ESRF
The European Synchrotron

# ESRF HIGHLIGHTS 2018

## Contents

Francesco Sette

# DEAR ESRF USER, DEAR READER

I am delighted to be able to share with you some of the accomplishments of 2018 – a year that has held particular significance for the ESRF.

On 10 December 2018, the User Service Mode (USM) of operation with the ESRF's original storage ring was halted. Since then, the dismantling process has begun and we bid farewell to this legendary storage ring – the first third-generation synchrotron source in the world – that has served the international scientific community with bright and reliable X-rays for the past 25 years. Yet we are also preparing for the restart of USM in September 2020. During the ongoing 20-month shutdown, a new and revolutionary X-ray source – the Extremely Brilliant Source (EBS) – will be installed and commissioned. It will be the world's first high-energy, fourth-generation synchrotron light source, and will provide ESRF users with an X-ray source of unprecedented brilliance and coherence. It is now time to start envisioning synchrotron research with qualitatively new opportunities, using both existing and future beamlines.

Importantly, the year 2018 also marked 30 years since the signature of the intergovernmental convention, which, in 1998, established the ESRF. Fittingly, we marked the occasion with a most productive year from a scientific point of view. Examples of the excellence and diversity of the science carried out at the ESRF in 2018 are reported here in this issue of the *ESRF Highlights*.

I would like to take the opportunity of this introduction, therefore, to retrace some of the ESRF's milestones with you, to present the status of the EBS programme, and to highlight some of the aspects of the outstanding ESRF user programme.

**30 years of science and innovation**

In 1988, 11 countries joined forces to create the first third-generation synchrotron light source, and a long-held European dream became a reality. This exceptional accelerator was the first of its kind to become operational worldwide. In February 1992, the first electrons were stored, and in September 1994, the ESRF user programme started. Compared to second-generation sources, this storage ring marked a revolution in synchrotron science by providing scientists with X-ray beams of unparalleled brilliance, thanks to the drastic reduction in the vertical size of the electron beam and to the use of undulator devices simultaneously on the majority of insertion device-based beamlines. With a factor of gain of $10^3$–$10^4$, this innovative X-ray source enabled new studies in the analytical characterisation of condensed and living matter – often down to single-atom resolution – and opened up new, non-destructive imaging possibilities for materials science and cultural heritage investigations. By guiding and inspiring the construction of all third-generation synchrotron radiation sources that exist today worldwide (approximately 30), it has contributed to many discoveries in fundamental and applied science at the ESRF and elsewhere, which – for some notable cases – have been recognised by Nobel prizes and other prestigious awards conferred to users of the ESRF and of other synchrotron laboratories. In Europe, synchrotrons and X-ray FELs together provide state-of-the-art facilities and instruments for a 24 000-strong user community (the largest scientific community in Europe), as well as providing services to industry for innovative R&D, and training and education for the next generation of synchrotron scientists and engineers.

Over 30 years, the ESRF has broken records for the brilliance and stability of its X-ray beams, for its scientific output of over 32 000 publications (around 2000 publications per year over the last ten years), and for the strength of its community of users. Today, the ESRF has 22 partner countries, from Europe and further afield, all sharing the same vision: to promote excellence in science across all frontiers. The ESRF has grown into a powerhouse of international scientific cooperation, an interdisciplinary hub where scientists from all fields, and from all countries, come together to exchange knowledge and to pioneer scientific ideas.

**EBS on track**

Opening up new possibilities for synchrotron science has been at the heart of the ESRF's mission from its inception 30 years ago and, indeed, is stated in its founding Convention. If 2018 has been an opportunity to look back at the ESRF's achievements, the EBS

shutdown is also the occasion to look towards our extremely brilliant future and to share with all our partners, users, and staff the excitement of the times ahead, in which the ESRF will continue pioneering synchrotron science for the benefit of global science and our society.

On 10 December 2018, USM with the ESRF's third-generation storage ring ended. The EBS project has officially entered a new stage, the fruit of our hard work of the last four years. The conception, engineering design, quality control and procurement of more than 10 000 components, and their timely assembly on-site, guided by strict project management and the expertise of ESRF staff, was carried out in parallel and full transparency with USM during the period 2015–2018. This made it possible to start the exchange between the old and the new storage rings in the ESRF tunnel according to the initial schedule. Teams have three months to dismantle the old storage ring and, from April 2019, they will have eight months to install the 32 new EBS storage ring arcs, which consist of 128 assembled-and-ready EBS girders. These girders support over 10 000 new components precision-aligned to within a few microns. According to the master schedule, the tunnel will be closed in November 2019, and the new EBS storage ring should be commissioned by March 2020, with user service resuming in September that year. The EBS programme will continue for a further few years, in parallel with USM (resumed in 2020). ESRF users will be able to exploit four brand-new flagship beamlines, as well as take advantage of the full refurbishment of many existing beamlines, an ambitious instrumentation programme with a focus on high-performance detectors, and cutting-edge experimental control and data analysis tools designed to exploit the enhanced performance of the new extremely brilliant X-ray source.

The new EBS beamlines will make it possible to probe complex materials at the atomic level in greater detail, with higher quality, and at a much faster rate. These new beamlines will help scientists to address major challenges facing our society, including the development of the next generation of drugs, biomaterials and sustainable materials, and to provide deep insights into the complex mechanisms governing living organisms. They will help elucidate our recent and ancient past, as manifested in historical artefacts and fossils. Moreover, they will provide unique opportunities for applied and innovation-driven research.

**User programme continues to reach record highs**

The 2018 ESRF user programme has been highly productive, beating ESRF records despite the 2018 beam period being two months shorter than usual due to the beginning of the EBS shutdown. Over 6500 user visits and more than 1700 experimental sessions were accommodated, following a record 2544 proposals submitted. The 2018 user programme greatly benefitted from high beam stability and intensity thanks to the top-up injection system that was developed for the new EBS storage ring.

Thanks to a strong collaboration between the ESRF, the EMBL, the ILL and the Institute of Structural Biology, the ESRF has also strengthened its services to the structural biology community, offering a full structural biology pipeline, from sample preparation, purification, cloning and crystallisation to X-ray, cryo-EM, neutron and NMR data-taking and analysis. As an example, after one year of operation using the same model as that of ESRF beamlines (access granted by peer-reviewed applications based on criteria of scientific excellence), the cryo-EM platform has achieved incredible success, with 66 user experiments (602 shifts – 200 days) and the first papers published in high-impact-factor journals (**see pages 46** and **52**).

In conclusion, 30 years after the beginning of the ESRF in 1988, the facility is ensuring its place at the forefront of X-ray research. EBS will be a powerful new instrument for the benefit of the international scientific community and for the next generation of young scientists interested in exploring nature's mysteries, from the complexity of condensed matter down to the single atom to the links between atomic structure and function. All this is possible thanks to the 22 nations working together towards a common dream, contributing with people, expertise and financial support for the benefit of a vast scientific community, and for the advancement of knowledge. I wish to express my profound gratitude to our partner countries for their constant support, to the ESRF users, to whom this edition of the *ESRF Highlights* is dedicated, for their outstanding scientific work, and to the ESRF staff for their commitment.

**FRANCESCO SETTE**
*Director General,*
*ESRF*

# 2018 AT THE ESRF

© Chantal Argoud

## Kilian Heeg, Young Scientist 2018

6 February – Kilian Peter Heeg was awarded the title of Young Scientist 2018 by the ESRF User Organisation in recognition of his pioneering work on light-matter interactions enabling resonant brilliance enhancement of X-ray pulses.

## Europhysics prize for RIXS

13 March – Giacomo Ghiringhelli and Lucio Braicovich were awarded the 2018 Europhysics Prize of the Condensed Matter Division of the European Physical Society (EPS), for their ground-breaking work on the development and scientific exploration of high-resolution resonant inelastic X-ray scattering (RIXS). The duo invented RIXS at the ESRF and were actively involved in the conception and construction of the world-leading RIXS spectrometer on ID32.

© Giacomo Ghiringelli

© The Austrian Academy of Sciences

## Austria strengthens collaboration with the ESRF

22 June – A new arrangement between Austria and the ESRF was signed at the historical headquarters of the Austrian Academy of Sciences in Vienna. Austria increased its association level to the ESRF from 1.3 to 1.75%, reflecting the increased use of the ESRF by its very successful and vibrant scientific community.

## ERC grants awarded to ESRF users

July - Hugh Simons, materials researcher at the Technical University of Denmark and user on ID06, was awarded a starting grant from the European Research Council. Simons is helping to develop the new technique of dark-field microscopy at the ESRF.

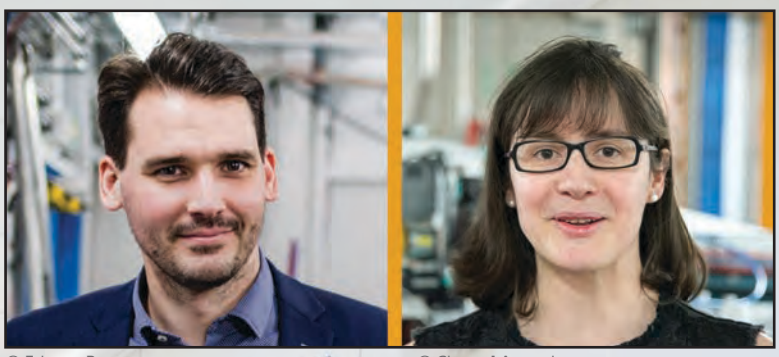

© Etienne Bouy

© Chantal Argoud

November - Marie-Ingrid Richard, of Aix-Marseille University and visiting scientist at ID01, was awarded a consolidator grant to develop coherent X-ray diffraction *in situ* and *operando* to explore nanostructures, focusing on catalysis and interfaces.

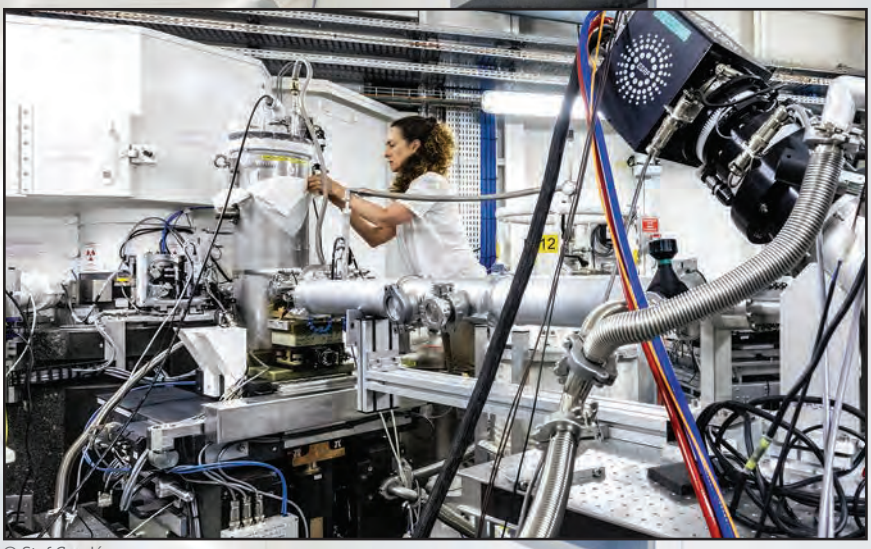

© Stef Candé

## Launch of ATTRACT fund for detection and imaging innovation

August – The ATTRACT project (https://attract-eu.com/attract-call) was launched. This pioneering initiative to couple world-class research laboratories and business-management experts aims to create a European innovation ecosystem that will accelerate the development of technologies and their progress to market. The call was a success, with 170 projects each receiving €100 000 in funding to bring their ideas to life.

## Training the next generation

September – Every year, the joint ESRF/ILL International Student Summer Programme brings together 20 international undergraduates to learn about X-ray and neutron science. From 2–28 September 2018, the students were assigned tutors and experimental projects in relation to their studies. The course included lectures combined with hands-on experiments on the beamlines.

© ILL/Serge Claisse

# 2018 AT THE ESRF

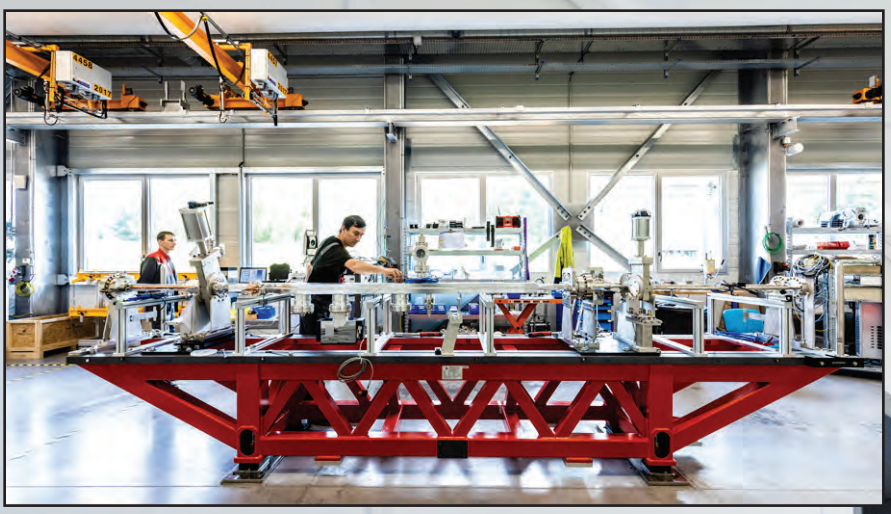

© Stef Candé

## ESRF–EBS confirmed as ESFRI roadmap

11 September – The European Strategy Forum on Research Infrastructures (ESFRI) presented the ESFRI Roadmap 2018 on Large Scale Research Infrastructures, confirming the ESRF–Extremely Brilliant Source (ESRF-EBS) as a major landmark project. ESRF–EBS is a €150M facility upgrade, over the period 2015–2022. With the construction of a brand-new storage ring, ESRF–EBS will be the world's first high-energy fourth-generation synchrotron light source.

## The ESRF Cryo-EM excels in its first year

31 October – Less than one year after the inauguration of the Titan Krios cryo-electron microscope (cryo-EM) at the ESRF, scientists published a first paper using data collected on the cryo-EM, known as beamline CM01. The results feature in a Nature publication describing the activation cycle of a serotonin receptor, which is targeted by medication against chemotherapy- and radiotherapy-induced nausea.

© Stef Candé

## ESRF celebrates 30 years of science

27 November - The ESRF celebrated its 30th anniversary in the presence of the representatives of its 22 partner countries. The event looked back at the ESRF's scientific accomplishments but also on the role that the ESRF has played in fostering peaceful cross-border collaboration in Europe and beyond. Congratulatory messages from Carlos Moedas, European Commissioner for Research, Science and Innovation, Ada Yonath and Sir Venki Ramakrishnan, winners of the Nobel prize for chemistry in 2009, and Frédérique Vidal, French Minister of Higher Education, Research & Innovation, demonstrate the impact of the ESRF on a global scale.


© Pierre Jayet

## South Africa extends commitment with ESRF

December - The South African scientific community has been very successful in recent years. This very positive outcome has resulted in the renewal of the association of South Africa to the ESRF under the same conditions as before, until the end of 2020.

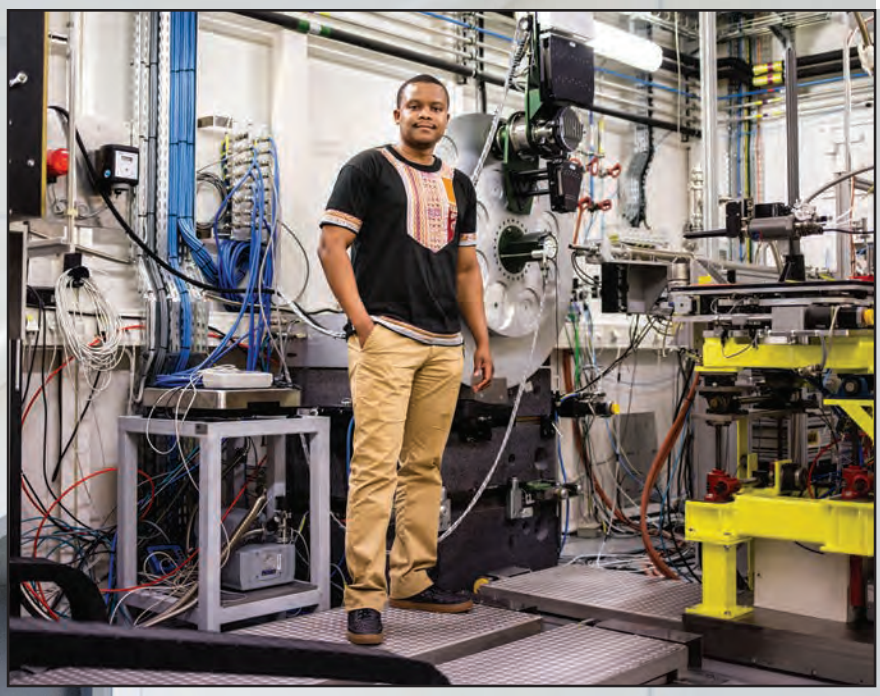

© Etienne Bouy


© Pierre Jayet

## Israel renews its association with the ESRF

27 November – Israel took the opportunity of the ESRF's 30th anniversary occasion to renew its scientific association with the ESRF for another five-year period, until 31 December 2023. The Israeli association will initially be at a level of 1.5% and will be increased to 1.75% from 2021 onwards.

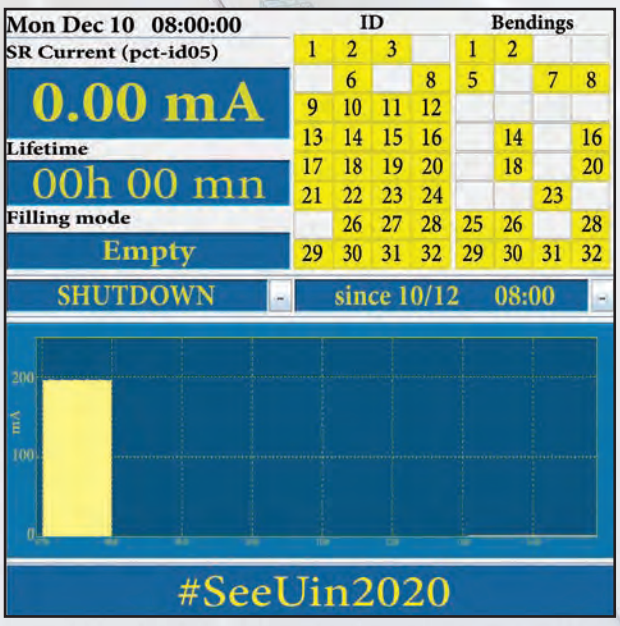


© Alexandra Mouillec

## EBS shutdown begins

10 December – Thirty years after the signature of the ESRF Convention, the ESRF's shining light was put in standby mode. The ESRF entered a 20-month shutdown period in order to dismantle its flagship storage ring to make way for the Extremely Brilliant Source (EBS) – the world's first high-energy fourth-generation storage ring. With X-ray brightness and coherent flux increased 100 times, additional new X-ray beamlines, and an ambitious instrumentation and data strategy, the new facility will be open for users in 2020.

# STATUS OF THE EBS

**In 2018, the last full year before the shutdown for the installation of the EBS storage ring, many key milestones were achieved, including the completion of the magnet construction and the girder assembly phase. Work has started on the new EBS flagship beamlines and further beamline upgrades are also under way.**

The past year marked the fourth year of the execution phase of the ESRF's Extremely Brilliant Source (EBS) project, which will see the implementation of a new lattice for the storage ring. This will reduce the operational horizontal emittance from 4 nm to about 100 pm, thus greatly increasing the brilliance and coherence of the X-rays and opening up new perspectives for experiments that are not conceivable today. Much of the work of the project in 2018 concentrated on the delivery of the components and equipment, as well as the completion of the assembly phase. A total of 120 out of 129 girders had been fully assembled by the end of the year, with the remaining girders assembled and ready to be installed in the storage ring by April 2019 (**Figure 1**). In addition to this, great efforts went into the organisation of the dismantling and installation phases, complex work that defines the logistical requirements, task sequences and resource needs for the next two years. Detailed preparations were made for the long shutdown that began in December 2018. Finally, a new timing system (**page 157**) was installed and used successfully in user service mode (USM). This is advantageous for improved flexibility and additional features that will be necessary for the new machine and beamlines.

**Fig. 1:** The production line of girders in assembly building ESRF 01. By the end of 2018, most of the EBS girders were assembled, ready for installation in the storage ring in spring 2019.

The seventh and eighth Machine Advisory Committee (MAC) meetings were held at the ESRF in May and November 2018. Committee members from leading institutes around the world came together to discuss the recent progress of the EBS project and to make recommendations for the six months ahead. In November, the MAC was impressed with the level of progress made over the year and congratulated the ESRF staff on the timely achievement of key milestones ready for the start of the long shutdown in December.

## MAIN MAGNET CONSTRUCTION COMPLETE

An important project milestone was reached in 2018 with the completion of the construction of the EBS magnets; the last DQ2 magnets were delivered at the beginning of October 2018. Tracing back to ideas and concepts in early 2013, right up to the magnets currently assembled on the girders, this has been a fascinating project. The project stands out in terms of innovation, in particular with regards to the combined function dipole-quadrupoles, permanent magnet dipoles and high-gradient quadrupoles (**Figure 2**), reflecting the capacity of the ESRF team to move forward in magnet technology.

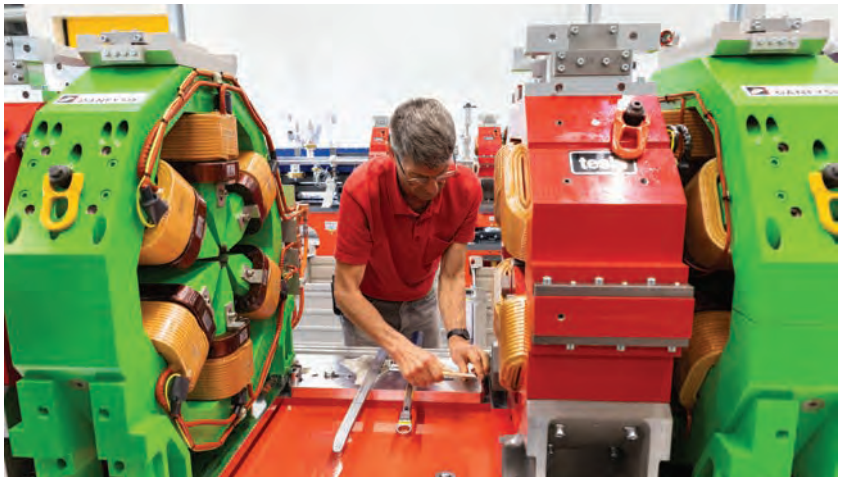

**Fig. 2:** Over 1000 new magnets have now been constructed, received and tested, including 132 permanent magnet dipoles and 983 innovative electromagnets, including sextupoles (left, green) and high-gradient quadrupoles (right, red).

## COMPLETION OF THE ASSEMBLY PHASE

On 25 October 2018, an event was held at the ESRF to celebrate approaching the end of the girder assembly phase and to thank the 12 Russian specialists who contributed to its success. The partnership with colleagues from the Budker Institute of Nuclear Physics (BINP) in Novosibirsk, Russia, allowed our two institutes to pool their knowledge and resources to work together on this phase. The team from BINP (**Figure 3**), headed by Sergei Gurov, brought with them valuable experience gained from working on the development, assembly and commissioning of several leading light sources worldwide.

Each EBS girder was assembled with up to 80 individual components, manufactured from companies all over Europe, making the process highly labour-intensive. The support of the BINP specialists was therefore vital in order to keep to the ambitious production schedule, allowing girders to be equipped with state-of-the-art magnets, vacuum chambers and the associated instrumentation at a maximum rate of four girders per week. Girder production was carried out in a dedicated building, ESRF 01, where three assembly lines were set up to install the equipment on the girders, as well as a 'clean room' area where the vacuum chambers were assembled. The girders were then transported via crane and lorry to their temporary external storage location.

This productive joint effort resulted in the completion, by the end of the year, of 114 of the 129 girders for the new storage ring, with the rest due to be completed in January 2019.

**Fig. 3:** A team of accelerator production experts from Budker Institute of Nuclear Physics (BINP) in Russia worked together with the ESRF team to assemble the girders for the new EBS storage ring.

## COMMISSIONING SIMULATION

In preparation for the EBS start-up in 2020, the Beam Dynamics group carried out an important commissioning simulation exercise during machine-dedicated time (MDT) shifts in October. The group simulated problems that could occur during commissioning and created a novel tool for signaling errors. The results were very positive and the MAC commended the work that had been done.

In the present ESRF storage ring, several settings have been defined to obtain accumulated stable beam. They include: 1) magnetic strengths for orbit, optics, coupling and lifetime correction and 2) beam position monitor (BPM) offsets. When a new storage ring is started up, all settings are unknown and need to be set, based on measurable observables. Lacking these settings, the presence of alignment errors results in the

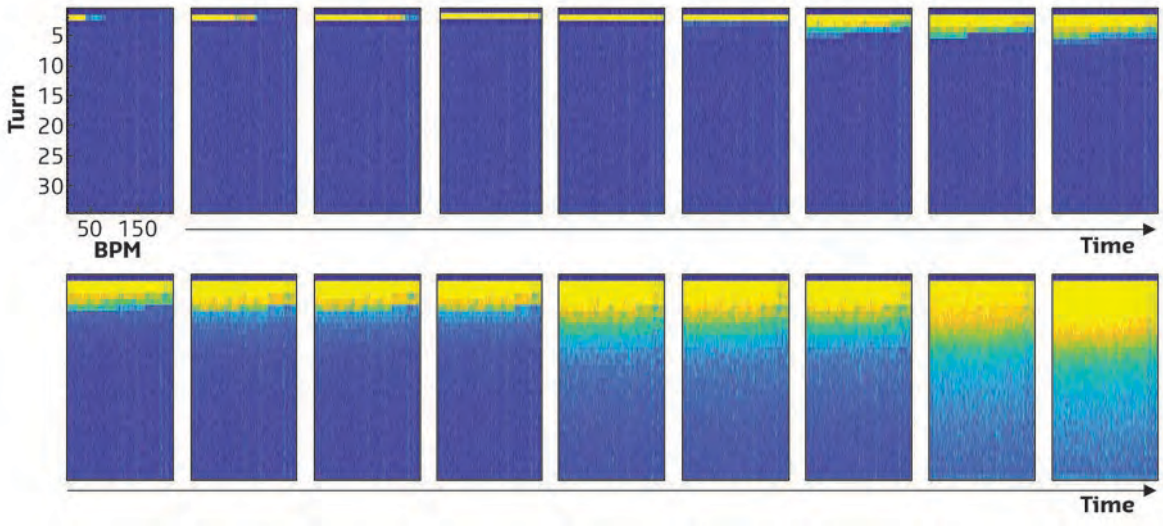


**Fig. 4:** Turn-by-turn BPM sum signal while progressing in the first-turn trajectory correction up to stored beam.

electron beam only travelling through one part of the storage ring circumference, limiting the signals available both in number and in intensity. Moreover, several issues can arise, such as failing power supplies or wrongly cabled correctors.

The objective of the commissioning-simulation MDTs was to start from present operating conditions in the storage ring and to remove features one by one in order to be left with a commissioning-like storage ring. At each of these steps, the group tried to recover stored beam using orbit steerers to correct the trajectory signal obtained in a single passage from turn-by-turn BPMs (**Figure 4**). The first test was to switch off the orbit steerers in order to focus on the trajectory correction, as everything else was still fixed at normal parameters. Once this procedure provided stored beam, it was applied, starting over with increasingly degraded conditions. The trajectory of the first turn could eventually be corrected in the simultaneous presence of: zero initial steerer strengths, random 500-µm rms BPM offsets, 20/224 random disabled BPMs, no optics and coupling correction, and theoretical main magnets strengths. When comparing the measured and expected trajectories, it was also possible to get an indication of the possible location of a switched-off quadrupole and to use the trajectory data to spot a wrongly cabled corrector.

Successful tests have also been carried out on the first-turn correction with intentionally mistuned injection parameters (energy and TL2 steering). This tool has been developed for the EBS storage ring on the EBS control system simulator, has been tested, and is ready to be used for the initial and most critical phases of the EBS commissioning.

## START OF THE DISMANTLING PHASE

On 10th December 2018, the beam was switched off, marking the start of the intensive dismantling phase of the EBS project. Preparatory work for the dismantling of the storage ring began the same day and lasted until the end of the year, and included the secure disconnection of electrical equipment, the draining of the fluids and cryogenic networks, the return to atmospheric pressure of vacuum equipment and the recovery of components to be re-used in the new machine. The removal of each piece of equipment from the storage ring began in January and is set to last three months, before installation of the new storage ring commences.

## PUBLIC BEAMLINE UPGRADE

In 2017, four beamline projects were selected for construction within the EBS project:

- EBSL1: Beamline for coherence applications
- EBSL2: Beamline for hard X-ray diffraction microscopy
- EBSL3: High-throughput, large-field phase-contrast tomography beamline
- EBSL8: Serial crystallography beamline

In 2018, work began on EBSL3 and EBSL8, with the technical design report (TDR) for EBSL3 finalised and accepted in November 2018. EBSL3 is a long beamline on a high-field 3-pole bending magnet source for imaging large objects over an extended range of length scales. Preparations for construction in 2019, during the long shutdown, continue. The draft of the TDR for EBSL8 is finished and will be reviewed in May 2019. EBSL8 is a long beamline for serial crystallography, located on port ID29 with end-station in the Chartreuse Hall. The construction of the infrastructure for the beamline is scheduled to start at the end of 2019.

**Fig. 5:** The cryo-EM, also known as beamline CM01, will remain open for experiments throughout the ESRF's shutdown for the installation of the EBS storage ring.

In parallel to the development of the EBS upgrade beamline portfolio, the regular beamline refurbishment programme is also progressing to schedule. The refurbishment of the X-ray microscopy beamline ID21 continues, with the installation of a new primary mirror system and a prototype cryo-cooled scanning double crystal monochromator (DCM). After validation, the new scanning DCM will be deployed on all public ESRF spectroscopy beamlines. For the refurbishment of the nuclear resonance beamline, a relocation of the beamline from port ID18 to port ID14 is foreseen. EBSL1, the project for the construction of a new coherence beamline, will then be realised on port ID18 as a long beamline.

Regarding the two new user platforms, HPLF-I and cryo-EM, the front end of the high-power laser has been delivered to beamline ID24 for commissioning. The first user experiments took place before the long shutdown with a maximum power of 15 J. The cryo-EM (designated as beamline CM01, see **Figure 5**) successfully started user operation in November 2017 and is now in routine operation with the first publications already published.

## CRG BEAMLINE UPGRADE

In 2018, infrastructure work was focused on the CRG beamlines, with BM20 and BM28 modified in preparation for the new source. The split of the double-branch beamlines BM26A/B and BM30A/B, and the construction of BM07 continues as planned. The Dutch-Belgian CRG DUBBLE has taken over the reactivated beamline BM14 to replace beamline BM26A after the long shutdown. One unavoidable consequence of the EBS is that the source points and beam trajectories for all bending magnet beamlines will change. Plans for the preparation of the bending magnet beamlines for EBS have been worked out and are now part of the master plan.

## INSTRUMENTATION AND DATA MANAGEMENT

The EBS project comprises an ambitious instrumentation and technology programme, which is required to gain the greatest benefit from the new source properties. In 2018, significant headway was made in data management and analysis. Version 0.8.0 of Silx (http://www.silx.org), a library of common software routines for analysing data from synchrotron sources, was released. Collaborative efforts to work on data analysis software with other ESFRI (European Strategy Forum on Research Infrastructures) laboratories have started, with PaNOSC (Photon and Neutron Open Science Cloud), a proposal to boost and harmonise data management and services across the ESFRI photon and neutron sources. The implementation of the ESRF Open Data Policy has started (http://www.esrf.fr/datapolicy), with metadata collected systematically on 12 beamlines, including the cryo-EM, and raw data archived for 10 years. Substantial efforts have been invested in the installation, configuration and use of cloud software, confirming its potential for a number of use cases. Tests have also been conducted successfully with a public cloud service provider, offering the possibility to our user community to continue the analysis of data acquired on the ESRF beamlines.

The detector development plan is running to schedule. Ten new high-performance pixel array detectors have been purchased, and a range of R&D collaborations are in progress for the development of new detectors, sensors, and related soft- and firmware.

Following the creation of a mechatronics task force and high-precision laboratory to strengthen expertise in this domain, further investments were made that enabled the development of an advanced control system for the crystal positioning in the double crystal monochromator prototype. Following fluid dynamics tests to reduce thermal stabilisation time, the DCM prototype was installed and commissioned on ID21 in November and December 2018.

In terms of optics and metrology, a fully automated press for the in-house production of compound refractive lenses was developed. A series of 50 micrometre-radius aluminium lenses is currently being produced, and studies for the production of 1D parabolic lenses have begun. Intensive tests of a prototype metrology system for the measurement of the surface figure of reflective optics are in progress.

**R. DIMPER, M. KRISCH, P. RAIMONDI, H. REICHERT and J. SUSINI**

# MATTER AT EXTREMES

As I write this introduction, the beamlines of the Matter at Extremes (MEx) group are running at full speed to take advantage of the present storage ring up until the very last photon is produced. In a few days, this wonderful machine, with its exquisite stability and reliability, will be dismantled to make way for the construction of the Extremely Brilliant Source (EBS). From an operational point of view, this year saw the implementation of the top-up filling mode in May, an important validation step prior to the transition to the new, lower-emittance storage ring. The MEx beamlines witnessed a very positive effect on operation, with higher average current coupled to reduced thermal drift-induced beam position instabilities.

The year 2018 has seen a clear increase in the synergetic use of the MEx beamlines. We are witnessing more and more user groups exploiting the specificity, the complementarity and the proximity of the MEx beamlines to answer a given science question using a combination of different X-ray techniques, such as X-ray diffraction (XRD), synchrotron Mössbauer spectroscopy (SMS) and X-ray absorption spectroscopy (XAS). Very recent work on new iron oxide phases led to publications with data from three different MEx beamlines. Ovsyannikov *et al*. (*Nat. Commun*. **9**, 4142, 2018) studied the effect of pressure on charge ordering in $Fe_4O_5$ using ID27, ID18 and the ex-ID09A beamline now on ID15B, while Sans *et al.* (*Nat. Commun*. **9**, 4554, 2018) probed the stability and nature of the volume collapse of $\varepsilon$-$Fe_2O_3$ on ID27, ID18 and BM23. Earlier this year, Andrault *et al.* (*Geochem. Perspect. Lett.* **6**, 5, 2018) suggested that mantle dynamics at the Archaean–to–Proterozoic transition could have induced a major evolution of the redox state at the Earth's surface, by measuring the $Fe^{3+}$ content in lower mantle bridgmanite using SMS on ID18 and XAS on ID24. Also, Morard *et al.* (*Geophys. Res. Lett*. **45**, 11074, 2018) contributed to solving a longstanding controversy on the melting curve of Fe, through a combined XRD (ID27) and XAS (ID24) study.

Unfortunately, many publications did not make it into this chapter. Data from **ID09A** led to a paper by Paliwoda *et al.* (*J. Mater. Chem. C* **6**, 7689, 2018) focusing on an emerging new class of layered stoichiometric materials with a large anisotropic dielectric constant highly sensitive to external stimuli. Dewaele *et al.* (*Nat. Commun*. **9**, 2913, 2018) reported the result of many years of work on ID27 illustrating the potential of toroidal diamond anvils for detailed measurements under extreme static pressures. More recently, Lomachenko *et al.* (*J. Am. Chem. Soc.* **140**, 17379, 2018) presented an extended X-ray absorption fine structure (EXAFS) study at BM23 on mixed-metal Ce-Zr metal–organic frameworks, explaining the dependence of thermal and chemical stability on Ce content. As in previous years, users on ID18 benefitted from fine spatial resolution (~10 µm) and from high (~0.5 meV) and ultra-high (~10 neV) energy resolution in studies of magnetic, electronic and vibrational properties of matter. This led to results highlighted both in this chapter and in many other impressive publications. Among these are, for example, the paper by Cini *et al.* (*Nat. Commun*. **9**, 480, 2018) on the magnetic properties of a monolayer of single molecule magnets, and that by Mikolasek *et al.* (*J. Am. Chem. Soc*. **140**, 8970, 2018), providing a complete set of elastic moduli of spin-crossover actuators.

In parallel to scientific activity, refurbishment programmes have kept beamline staff very busy throughout 2018. On **ID06-LVP**, the large-volume press has further extended its pressure domain, with a number of user experiments going beyond 30 GPa in 6/8 geometry, with and without ultrasonic measurements, using 7/3 assemblies. Deformation studies have been pushed to ~$10^{-6}$ strain rates, at high temperature and pressures exceeding 19 GPa. Finally, a variety of new carbides and anvil geometries have been tested and included into those available to users.

On **ID18**, for the first time, users could benefit from ultra-high energy resolution in studies of atomic dynamics, using a new instrument: the hard X-ray spectrograph. Extending the principles of spectrographic imaging from visible light to the hard X-ray regime, this device enables ~100 µeV energy resolution, while

efficiently capturing photons from a broad (~0.6 meV) spectral window.

On **BM23**, a five-crystal analyser spectrometer (funded by the French national research agency, ANR, in the frame of the EcoX project) was coupled to the micro-XAS facility, enabling studies of ultra-dilute systems by EXAFS with micron spatial resolution.

On **ID24**, phase I of the high power laser facility, HPLF-I, has reached several milestones, with the design of the new clean room hosting the 100 J laser in 2020, the design of the laser beam transport into the experimental hutch and the successful commissioning of its 15 J front end.

In parallel, the technical design report (TDR) for the future high-brilliance EXAFS beamline was completed and submitted. Finally, we have just received the go-ahead for the start of the TDR for the largest EBS project in the MEx group: the new high-flux nano-XRD beamline for science under extreme conditions on **ID27**, due in October 2019.

Apart from the preparation of TDRs and other ongoing beamline refurbishments, the year 2019 will also include the organisation of events to prepare our user community to better utilise the EBS. The MEx group is involved in two of them: a two-day workshop on *Nuclear Resonance Scattering at the Extremely Brilliant Source* (11–12 March 2019) and a one-week *Hands on! High-pressure school at the ESRF* event (17–22 June 2019), open to users interested in learning about the unique opportunities for high-pressure research at the ESRF with the EBS. Finally, the high-pressure laboratory will be operational throughout 2019 for loading of diamond anvil cells to be used at other facilities, or for in-house research experiments exploiting the Raman spectrometer or laser annealing.

During the down time, the MEx group will therefore remain very active.

**S. PASCARELLI**

# OXIDISED GARNETS FROM THE EARTH'S TRANSITION ZONE

**The surprising observation that iron is highly oxidised in majorite inclusions from deep diamonds provides evidence for oxidation-reduction reactions between iron and carbon inside the Earth.**

Diamonds are prized not only for their beauty and brilliance, but also for the rare glimpse that they provide into the deep interior of our planet. When they grow inside the Earth, they incorporate tiny pieces of their surroundings that are protected by the diamond host during its journey to the Earth's surface. Examining these small inclusions provides information about the conditions under which the diamonds and their inclusions grew.

Diamonds from the Jagersfontein kimberlite in South Africa contain inclusions of the mineral garnet (**Figure 6**). To determine their crystal structure, X-ray diffraction data were collected at DESY, in Germany, and single crystal X-ray refinements performed. The results showed that the inclusions are a special form of garnet called majorite that only occurs at high pressure.

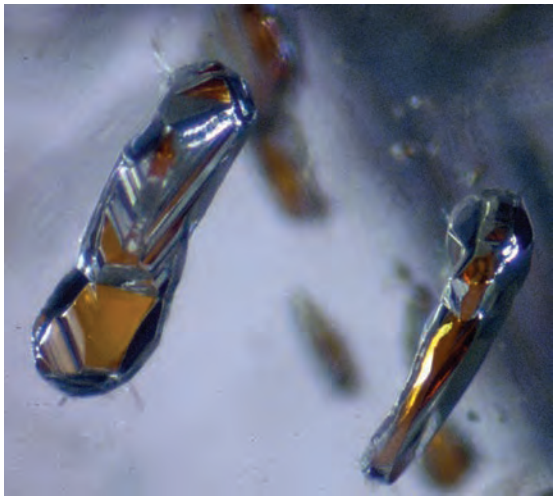

**Fig. 6:** Diamonds with garnet inclusions can form at depths down to 550 kilometres below the surface. The orange inclusions shown here are approximately 200 µm long. Photo: J. W. Harris, University of Glasgow.

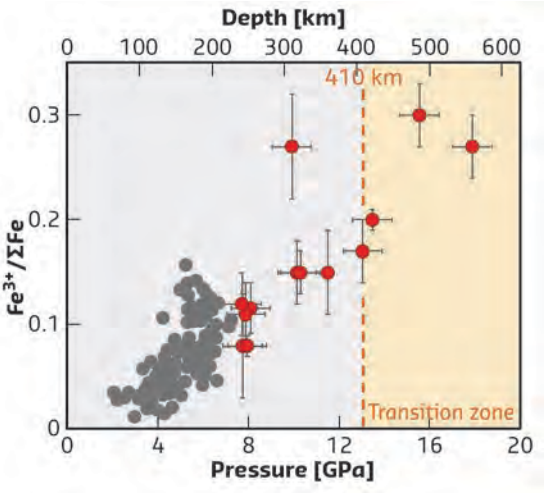


**Fig. 7:** The ferric iron content of majoritic garnets from Jagersfontein diamonds (this study, red circles) is much higher than of garnets from shallower depths (literature data, grey circles).

Despite being one of the dominant phases in the deep mantle, majoritic garnets are extremely rare, with only about 150-200 crystals reported in literature to date. Predominantly, this is because majoritic garnets break down on their ascent to the surface and can be found intact only in meteorites, or rarely, as inclusions in diamonds.

The novel synchrotron Mössbauer source at beamline **ID18** was used to determine the oxidation state of iron in the majorite inclusions. The oxidation state of Fe in Earth's mantle minerals controls such important parameters and processes as magma generation, the speciation and mobility of sulphur and oxygen in the Earth's interior, the deep carbon cycle, the formation of diamond, the recycling of oceanic crust back into the mantle, the chemical differentiation of the planet, and many others. The main three layers of the Earth – its crust, mantle and core – represent profound changes in the oxidation state of iron from ferric ($Fe^{3+}$) at the surface to mostly $Fe^{2+}$ in the silicate minerals in the upper mantle, transition zone and the lower mantle, and ultimately, to the $Fe^{0}$ in the core (**Figure 6**).

Measuring $Fe^{3+}$ concentrations in mantle minerals is the most common way of inferring the oxidation state of the mantle. The rationale behind this is relatively simple: the valence state of iron in a silicate phase depends on the activity of oxygen, thus, the relative abundances of $Fe^{3+}$ and $Fe^{2+}$ (and the $Fe^{3+}/Fe_{tot}$ ratio) of a mineral or melt should be indicative of the activity of oxygen in the environment in which it formed. From these investigations, it was found that the majoritic garnets contained iron in a highly oxidised form, in contrast to garnets from shallower depths, which are almost always more reduced (**Figure 7**).

The $Fe^{3+}/Fe_{tot}$ ratios in the studied garnets increased from 0.08 at approximately 240 km depth to 0.30 at approximately 500 km depth. It is also important to note that the majoritic garnets are at least twice as rich in $Fe^{3+}$ as any garnet from xenoliths of the upper mantle. These measurements of the ferric/ferrous ratios of majoritic garnets represent a significant advancement in the understanding of the deep mantle.

The analysis shows that the most likely scenario for iron oxidisation in these garnets is the simultaneous reduction of carbon, for example, from carbonate to diamond. This process may play an important role in the cycling of carbon through the deep Earth as well as providing a way to liberate oxygen from minerals where it would normally be locked up.

PRINCIPAL PUBLICATION AND AUTHORS

Oxidized iron in garnets from the mantle transition zone, E. S. Kiseeva (a), D. M. Vasiukov (b, c), B. J. Wood (a), C. McCammon (c), T. Stachel (d), M. Bykov (e), E. Bykova (c, e), A. Chumakov (f), V. Cerantola (f), J. W. Harris (g) and L. Dubrovinsky (c), *Nat. Geosci.* **11**, 144–147 (2018); doi: 10.1038/s41561-017-0055-7.
*(a) Department of Earth Sciences, University of Oxford (UK)*
*(b) Laboratory of Crystallography, University of Bayreuth (Germany)*
*(c) Bayerisches Geoinstitut, University of Bayreuth (Germany)*
*(d) Department of Earth and Atmospheric Sciences, University of Alberta (Canada)*
*(e) DESY Photon Science, Hamburg (Germany)*
*(f) ESRF*
*(g) School of Geographical and Earth Sciences, University of Glasgow (UK)*

# EXTENDED STABILITY OF CARBON DIOXIDE ABOVE 1 Mbar

**The extended form of carbon dioxide is stable even at 120 GPa and 2700 K, the thermodynamic conditions relevant to the Earth's lowermost mantle. This finding changes the view on the role and speciation of inorganic carbon in the terrestrial interior.**

Carbon dioxide, $CO_2$, is known as a common component of the atmosphere that has gained a negative image among the general public as a major greenhouse gas. On the other hand, exploration of the phase diagram of $CO_2$ is not only essential for understanding fundamental properties of this prototypic compound, but also relevant to the fate, distribution and chemistry of carbon in the Earth's deep reservoirs.

While the $CO_2$ molecule is one of the simplest, in its solid state it undergoes numerous structural changes as a function of pressure and temperature **[1]**. Below ~40 GPa, a series of molecular phases exist. Despite some initial controversies suggesting bent molecules and elongated C=O bonds, more recent experimental and theoretical studies have clarified that all of the molecular phases contain linear O=C=O building blocks interacting via weak van-der-Waals forces. At higher pressures, however, the structure and properties of $CO_2$ change dramatically. No wonder – it contains unsaturated bonds, and any unsaturation is known to be eventually violated at sufficiently high pressure. Such pressure-induced polymerisation is related to bond breaking and formation. This results in a huge energy barrier and at low temperature the transformation proceeds sluggishly, even at pressures higher than that of a nominal transition point. Indeed, compressing $CO_2$ at moderate temperatures (below 700 K) leads to amorphous carbonia **[2]**, an equivalent of silica glass consisting of a network with mixed threefold and fourfold carbon coordination and thus representing a kinetically trapped intermediate state. Under harsh temperature conditions such as laser heating, however, carbonia is transformed to an ordered crystalline covalent solid called $CO_2$-V **[3]**, isostructural to the partially collapsed β-cristobalite. $CO_2$-V seems, therefore, a thermodynamic ground state at extreme pressure.

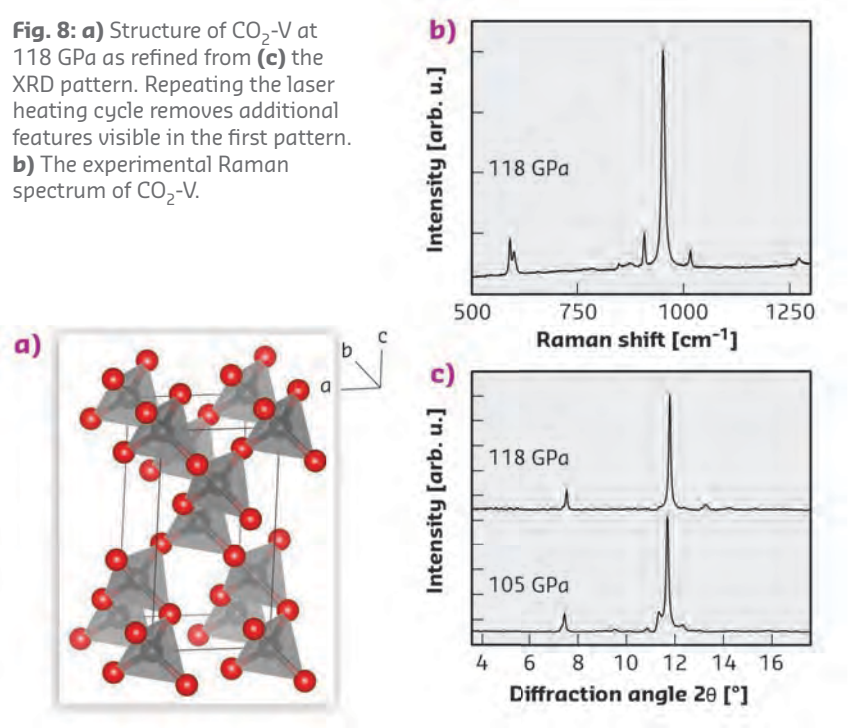


**Fig. 8: a)** Structure of $CO_2$-V at 118 GPa as refined from **(c)** the XRD pattern. Repeating the laser heating cycle removes additional features visible in the first pattern. **b)** The experimental Raman spectrum of $CO_2$-V.

While explaining the major part of the phase diagram of $CO_2$, these results raised further questions. First, none of the previous experiments were conducted at the high-pressure, high-temperature conditions mimicking those in the Earth's lowermost mantle. Second, some works performed in the pressure range up to 70 GPa indicated that $CO_2$ dissociates into its elements with a negative pressure–temperature slope, which could have implications for the oxygen fugacity in the deep mantle and the formation of so-called superdeep diamonds.

During experiments at **ID27**, a sample of $CO_2$ was compressed to ~120 GPa (1.2 million atmospheres) and laser-heated to a temperature of ~2700 K, which provoked the immediate formation of $CO_2$-V, as confirmed by Rietveld refinement, Raman spectra, as well as the equation of state, in perfect agreement with the extrapolated literature data (**Figure 8**). No dissociation was observed, but quite the opposite: the transient additional features in the X-ray diffraction (XRD) pattern disappeared after the second annealing, demonstrating that $CO_2$-V is the stable polymorph in this pressure–temperature range. The only additional phase revealed in the sample chamber were trace amounts of the high-pressure form of rhenium dioxide $ReO_2$, present close to the borders of the rhenium gasket, as a product of the chemical reaction between the Re gasket material and $CO_2$.

Discrepancies with literature data might be thus related to the earlier use of metal laser couplers, which might have reacted with $CO_2$, inducing its decomposition. This hypothesis is additionally supported by the current study, where the use of $MgCO_3$ as the laser absorber excluded the possibility of chemical reaction or catalysis in the central part of the chamber, while the observed reaction between the sample and gasket proceeded only in the lateral region. Besides, at very high pressure, extended phases are more favoured than molecular materials, which can actually hamper dissociation on compression.

These findings change the understanding of the role of $CO_2$ as the important volatile involved in the deep carbon cycle. While degassing of carbon-bearing magmas may release $CO_2$, it should not decompose in the Earth's deep mantle, adopting instead the extended crystalline structure or being able to form stable $CO_2$-containing phases. This presumption relies upon the reactivity of $CO_2$ with the surrounding minerals, which could further complicate the speciation and distribution of mantle carbon materials.


PRINCIPAL PUBLICATION AND AUTHORS

Crystalline polymeric carbon dioxide stable at megabar pressures, K. F. Dziubek (a), M. Ende (b), D. Scelta (a, c), R. Bini (a, c, d), M. Mezouar (e), G. Garbarino (e) and R. Miletich (b), *Nat. Commun.* **9**, 3148 (2018); doi: 10.1038/s41467-018-05593-8.

*(a) LENS, Sesto Fiorentino (Italy)*
*(b) Institute of Mineralogy and Crystallography, University of Vienna (Austria)*
*(c) CNR-ICCOM, Sesto Fiorentino (Italy)*
*(d) Dipartimento di Chimica "Ugo Schiff", University of Florence, Sesto Fiorentino (Italy)*
*(e) ESRF*

REFERENCES

[1] M. Santoro *et al.*, in *Carbon in Earth's interior*, American Geophysical Union, Wiley and Sons (2019).
[2] M. Santoro *et al.*, *Nature* **441**, 857–860 (2006).
[3] V. Iota *et al.*, *Science* **283**, 1510–1513 (1999).


# REVEALING THE STRUCTURE OF NITROGEN'S MOST COMPLEX POLYMORPH

**Nitrogen exhibits an exceptional polymorphism under extreme conditions. Here, one of the most elusive phases of this model system is resolved, revealing a crystalline structure with unexpected complexity.**

Nitrogen, the primary constituent of the air we breathe, exists as a simple diatomic molecule at ambient conditions. It may be surprising that nitrogen exhibits a diverse range of polymorphs in much the same way that water–ice is more famous for. The simplicity of the $N_2$ molecule makes it a model system for exploring pressure and temperature-induced changes in structure and bonding. Understanding these pressure-induced phenomena is significant to many scientific fields, varying from chemistry to astronomy, and the $N_2$ molecule provides an ideal testing ground for experiment–theory comparison. As such, the nitrogen phase-

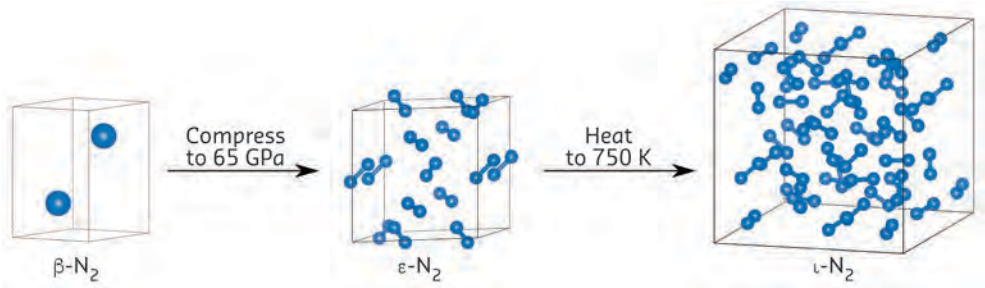


**Fig. 9:** Representation of the synthesis route to ι–$N_2$. The blue spheres in β-$N_2$ represent tumbling $N_2$ molecules. The blue spheres in ε–$N_2$ and ι–$N_2$ represent nitrogen atoms. ε–$N_2$ is represented in the rhombohedral axis setting.

diagram is a focus-point in current extreme conditions research and nitrogen's high-degree of polymorphism has not been observed in other simple molecular systems, such as hydrogen or oxygen.

One of the most elusive polymorphs of nitrogen is known as ι–$N_2$ (pronounced 'iota'–$N_2$). ι–$N_2$ is a molecular nitrogen polymorph that is only accessible via high-temperature, high-pressure conditions. Despite attracting considerable attention, the crystal structure of ι–$N_2$ has remained unknown since its original discovery over 15 years ago **[1]** and, until now, the ι–$N_2$ polymorph had never been recreated in the laboratory. In this work, a single crystal of ι–$N_2$ is synthesised in a resistively heated diamond anvil cell, which is a device for generating high-pressures comparable to those at the centre of the earth.

A representation of the synthesis route to ι–$N_2$ is shown in **Figure 9**. When compressed at ambient temperature, nitrogen solidifies into the β–$N_2$ polymorph at a pressure of 2.4 GPa. β–$N_2$ is characterised by tumbling $N_2$ molecules centred on a hexagonal close packed lattice. With further compression, nitrogen eventually reaches the ε–$N_2$ polymorph, which was heated to a temperature of 750 K at a pressure of 65 GPa for several minutes until it transformed into the elusive ι–$N_2$ crystal.

The ι–$N_2$ crystal was recovered to ambient temperature and brought to the high-pressure diffraction beamline **ID15B**. The single-crystal X-ray diffraction data revealed ι–$N_2$ to have an unusually complex molecular crystal structure characterised by 48 $N_2$ molecules arranged into an intriguing layered structure, making it, to the best of the authors' knowledge, the most complex molecular crystal ever observed in an elemental diatomic system. An example of a diffraction pattern from the ι–$N_2$ crystal is shown in **Figure 10**.

In collaboration with theoreticians at the University of Edinburgh, the energetic landscape and stability of the experimentally determined ι–$N_2$ structure was explored. *Ab initio* simulations found the ι–$N_2$ structure to display a surprising energetic favourability and random structure searches did not generate any structures more favourable than ι–$N_2$. Therefore, the uncovering of the ι–$N_2$ structure has implications for the traditional nitrogen phase diagram.

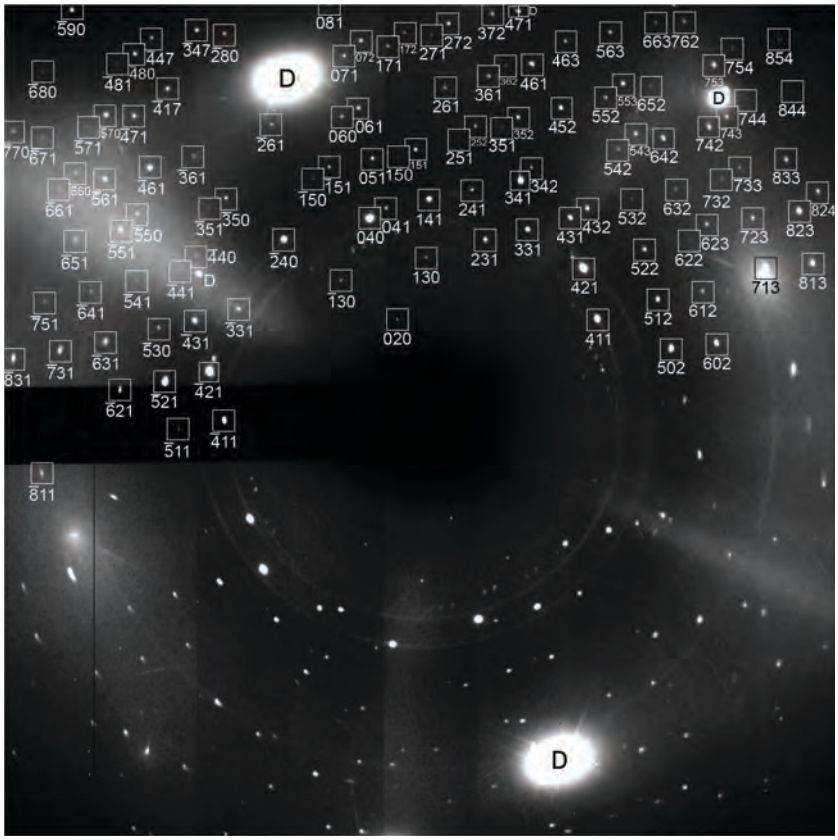


**Fig. 10:** Single crystal X-ray diffraction pattern of ι–$N_2$ at 56 GPa. The sample was rotated over a range of 60° in 0.5° increments. Squares mark nitrogen reflections with the given hkl indices. Diamond reflections are labelled with the letter D.

The ESRF and the University of Edinburgh have been at the forefront of discovering complex high-pressure structures over the last 10 years, finding a number of fascinating polymorphs that contain hundreds of atoms in light alkali and alkaline earth metals **[2–4]**. This recent study, performed in collaboration with researchers based in China, pushes in a new direction, revealing for the first time that simple molecular elements can also exhibit complex structures at

high pressures. These findings raise intriguing questions of whether unusual phases should be more widely expected, and could prompt further investigations into why such complex structures should appear at high pressures in elemental molecular solids.

PRINCIPAL PUBLICATION AND AUTHORS

Unusually complex phase of dense nitrogen at extreme conditions, R. Turnbull (a), M. Hanfland (b), J. Binns (c), M. Martinez-Canales (a), M. Frost (a, d), M. Marques (a), R. T. Howie (c) and E. Gregoryanz (a, c, e), *Nat. Commun.* **9**, 4717 (2018); doi: 10.1038/s41467-018-07074-4.

*(a) Centre for Science at Extreme Conditions and School of Physics and Astronomy, University of Edinburgh (UK)*
*(b) ESRF*
*(c) Center for High Pressure Science & Technology Advanced Research, Shanghai (China)*
*(d) SLAC National Accelerator Laboratory (USA)*
*(e) Key Laboratory of Materials Physics, Institute of Solid State Physics, Chinese Academy of Sciences (China)*

REFERENCES

[1] E. Gregoryanz *et al., Phys. Rev. B* **66,** 224108 (2002).
[2] C. L. Guillaume *et al., Nat. Phys.* **7**, 211 (2011).
[3] E. Gregoryanz *et al., Science* **320**, 1054–1057 (2008).
[4] I. Loa *et al., Nat. Mater.* **11**, 627–632 (2012).

# IS THERE A LIQUID–LIQUID TRANSITION IN DENSE FLUID NITROGEN?

**Nitrogen is an archetypal system to understand the effects of pressure on simple diatomic molecules. Using novel techniques for X-ray diffraction of fluids under extreme pressure and temperatures, the structure of fluid nitrogen was investigated along the melting line to 1.2 Mbar. The results challenge the theoretical prediction of a liquid–liquid transition.**

The triple bond of the nitrogen molecule is one of the strongest and most stable in nature, yet this bond is broken at sufficiently high pressure (P) and temperature (T) conditions. In the solid, this has been experimentally observed at pressures exceeding 110–150 GPa, where either an amorphous phase or the single-bonded cg-N are produced, respectively, at room and high T. In the fluid, shock-wave experiments suggested that molecular dissociation starts above 30 GPa and 6000 K, and that a fully dissociated metallic fluid is obtained at 120 GPa.

First-principle simulations were used to map the dense fluid and predicted two distinct domains: an atomic liquid beyond 30 GPa, 6000 K, in accordance with shock-wave results, and a polymeric fluid above 60 GPa and below 4000 K **[1]**. According to the same calculations, the transition line between the molecular and dissociated or polymeric liquid meets the melting line at 88 GPa, 2000 K, and is associated with a discontinuous jump of density below 4000 K that also induces an inversion of the melting curve **[2]**. Such first-order liquid–liquid transitions are very rare and this prediction stimulated a large

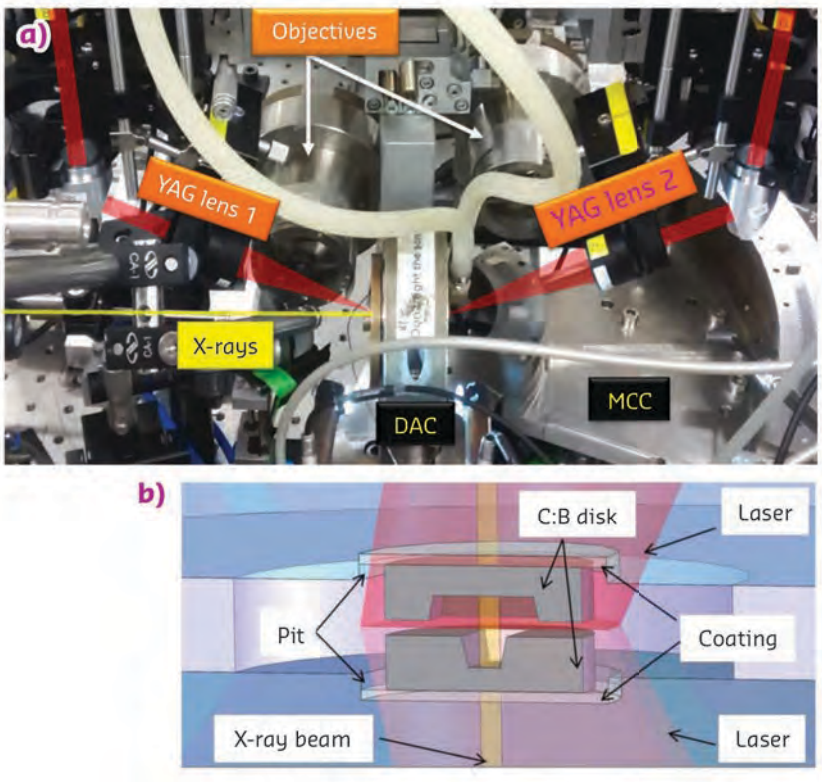


**Fig. 11: *a)*** Double-sided vertical laser heating system coupled to the Soller slits (MCC) for structure factor measurements on the ID27 beamline. **b)** Schematic cross-sectional view of the sample cavity located between the two diamond anvils of the DAC. The sample volume probed by the X-ray beam is at the intersection of the two slits engraved on the C:B disks. The two disks, of diameter 30 microns and thickness 10 microns, form a capsule heated from both sides by the laser beams.

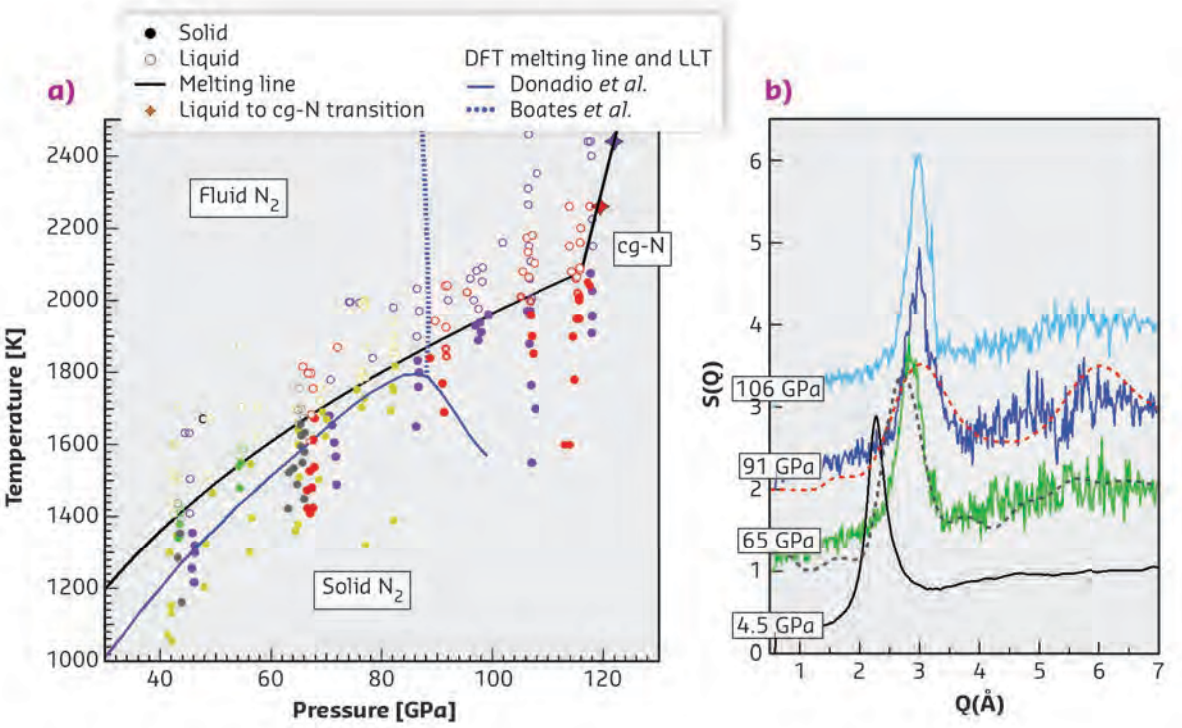


**Fig. 12: a)** Phase diagram of nitrogen. The symbols show the collected data points in the solid and liquid phases, the black line is the resulting melting curve, other lines are from first-principles calculations. **b)** Experimental (solid lines) and theoretical (dotted lines) structure factor of liquid nitrogen. The predicted changes in structure factor around 90 GPa related to the molecular to polymeric transition are not observed in experiments.

experimental effort to characterise this P–T range of the phase diagram. Furthermore, the strong similarities between the phase diagrams of fluid $N_2$ and fluid $H_2$ make the study of $N_2$ relevant to the much discussed molecular–metallic transition in $H_2$.

The existence of the polymeric or dissociated liquid would be unambiguously evidenced by structure factor measurements, but such measurements at megabar pressures and several thousands of degrees was considered a formidable technical challenge. To this aim, a new setup was developed and installed at **ID27** in the framework of the French ANR project, MOFLEX, which combines laser heating with a Soller slits system (**Figure 11a**). The latter, which is unique worldwide, enables the collection of high-quality diffraction images of fluids and amorphous materials composed of the lightest elements in the diamond anvil cell. To produce homogeneous heating of the sample, a laser absorber in the form of a micro-capsule, machined by a focused ion beam out of boron-doped diamond (C:B), was also developed (**Figure 11b**).

The evolution with the temperature of the nitrogen diffraction signal was measured along 24 isobars between 40 and 120 GPa, which made it possible to determine the melting temperatures through the appearance of diffuse scattering rings in the X-ray pattern coming from the liquid part of the sample. By contrast with simulations, the measured melting curve of nitrogen shows a monotonic increase of the melting temperature up to 116 GPa (**Figure 12a**). Above 116 GPa, the fluid crystallises directly into the extended cg-N phase, inducing a stiff increase of the melting line slope. Accurate structure factors of the liquid along the melting line (**Figure 12b**) were also measured, and show that fluid nitrogen remains molecular up to 116 GPa, with no evidence for the predicted liquid–liquid transition at 88 GPa.

The present work thus contradicts state-of-the-art density functional theory predictions and calls for more elaborate theoretical models to understand the phase diagram of nitrogen. It may, however, be conjectured that the transition occurs at higher P–T conditions, which constitute a challenge for future experiments.


PRINCIPAL PUBLICATION AND AUTHORS

Melting Curve and Liquid Structure of Nitrogen Probed by X-ray Diffraction to 120 GPa, G. Weck (a), F. Datchi (b), G. Garbarino (c), S. Ninet (b), J. A. Queyroux (a), T. Plisson (a), M. Mezouar (c) and P. Loubeyre (a), *Phys. Rev. Lett.* **119**, 235701-1 (2017); doi: 10.1103/PhysRevLett.119.235701.

*(a) CEA, Arpajon (France)*
*(b) Institut de Minéralogie, de Physique des Matériaux et de Cosmochimie (IMPMC), Sorbonne Université, Paris (France)*
*(c) ESRF*

REFERENCES

[1] B. Boates and S. A. Bonev, *Phys. Rev. Lett.* **102**, 015701 (2009).
[2] D. Donadio *et al.*, *Phys. Rev. B* **82**, 020102 (2010).

# SPIN-ORBIT COUPLING UNDER PRESSURE

**In the past decade, interest in iridium-based transition metal oxides (or iridates) has surged. This can be traced to the discovery that the strong atomic spin-orbit coupling inherent to the 5d Ir ion, which competes on the same magnitude as electronic correlations and crystal-fields, can result in a rich variety of unusual electronic and magnetic states [1, 2].**

Perhaps the most studied iridates have been the perovskites $Sr_2IrO_4$ and $Sr_3Ir_2O_7$. Both compounds adopt a 'spin-orbit induced' Mott insulating state. While this ground state has been shown to share many similarities with regular Mott insulators, it is unclear how far the analogy holds. Many phenomena are already known to differ in the strong spin-orbit coupling regime, such as unusual magnetic exchange interactions and topological non-trivial states. In this context, studying the insulator-metal transition (IMT) of a spin-orbit Mott insulator is of fundamental interest.

High-pressure can offer a clean way to induce IMTs in insulating materials. In general, it is expected that shortening atomic bonds increases the orbital overlap, which will result in wider electronic bands that eventually close the electronic band gap and yield a metallic state. $Sr_3Ir_2O_7$ is of particular interest in this regard. At ambient conditions, it possesses a small electronic band gap (~100 meV), which leads to the expectation that applying pressure should rapidly lead to metallisation.

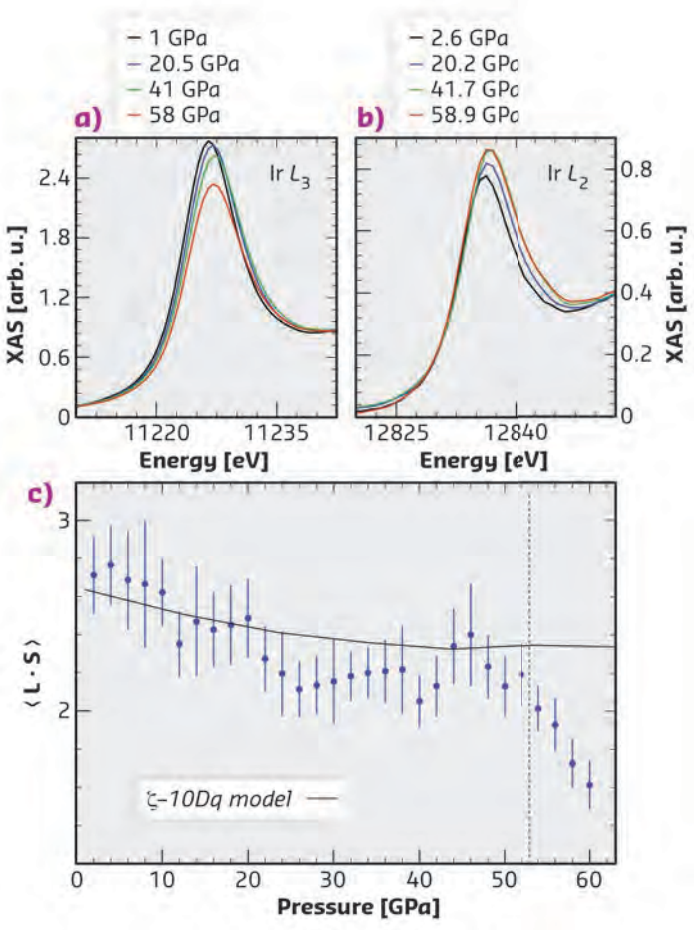


**Fig. 13:** X-ray absorption spectroscopy (XAS) data of $Sr_3Ir_2O_7$, showing the evolution of the Ir $L_3$ **(a)** and Ir $L_2$ **(b)** white lines with pressure. c) Expectation value of the spin-orbit coupling (blue dots), derived from the XAS data. The solid line shows the calculated value for a spin-orbit Mott insulator, which deviates from the data at around 54 GPa (dotted vertical line), where the structural transition and metallisation occur.

However, experiments have run contrary to these expectations. Initially, despite a number of attempts, metallisation of $Sr_3Ir_2O_7$ could not be achieved by applying pressure. Only recently, studies have extended the pressure range to beyond 50 GPa, revealing that a first order structural transition occurs at 54 GPa and, most probably at the same pressure, a transition to a metallic state occurs **[3, 4]**. This metallic state is highly unusual as conductance was only found within the basal plane, and an insulating nature persisted along the *c* axis of the crystals. This has led to the proposal that the high-pressure phase of $Sr_3Ir_2O_7$ is a confined metal state.

In order to examine further the electronic state of $Sr_3Ir_2O_7$ at high-pressure, an X-ray absorption spectroscopy (XAS) experiment was carried out on **ID24**. By studying the white line intensity at the Ir $L_2$ and $L_3$ edges, it is possible to extract the expectation value of the spin-orbit coupling (**Figure 13**). Crucially, this technique does not require any assumptions about the electronic state, and hence makes it possible to cleanly extract this parameter as a function of pressure. Furthermore, while similar studies in the literature used a monochromatic beam paired with long acquisition times, here energy dispersive XAS was chosen. This facilitated a rapid collection of XAS data, which allowed the pressure evolution of the spin-orbit coupling to be studied in unprecedented detail.

The data collected supports two conclusions. First, up to the structural transition at 54 GPa, the spin-orbit Mott insulating state provides an adequate description of the electronic ground state. The change in the expectation value of the spin-orbit coupling can be understood from the increased strength of the cubic crystal field at high pressure. This supports the notion that the spin-orbit Mott insulating state remains

relatively unperturbed up to these pressures. Secondly, above the structural transition, the expectation value of the spin-orbit coupling reduces further than can be explained by cubic crystal field effects.

This indicates that the transition to the high-pressure metallic phase alters the orbital character of the ground state wave function, suggesting a departure from the spin-orbit induced state known at ambient conditions. However, it is noted that even at the highest pressures, the spin-orbit coupling still plays a role in the electronic ground state. Thus, while this study provides insights into the nature of the high-pressure IMT in the spin-orbit Mott insulator $Sr_3Ir_2O_7$, further research is needed to fully characterise exactly what kind of metallic state emerges.


PRINCIPAL PUBLICATION AND AUTHORS

High-pressure insulator-to-metal transition in $Sr_3Ir_2O_7$ studied by X-ray absorption spectroscopy, C. Donnerer (a), M. Moretti Sala (b), S. Pascarelli (b), A. D. Rosa (b), S. N. Andreev (c), V. V. Mazurenko (c), T. Irifune (d), E. C. Hunter (e*), R. S. Perry (a) and D. F. McMorrow (a), *Phys. Rev. B* **97**, 035106 (2018); doi: 10.1103/PhysRevB.97.035106.

*(a) London Centre for Nanotechnology and Department of Physics and Astronomy, University College London, London (UK)*
*(b) ESRF*
*(c) Theoretical Physics and Applied Mathematics Department, Ural Federal University (Russia)*
*(d) Geodynamics Research Center, Ehime University (Japan)*
*(e) SUPA, School of Physics and Astronomy, and Centre for Science at Extreme Conditions, University of Edinburgh (UK)*
**Present address: Inorganic Chemistry Laboratory, University of Oxford (UK)*

REFERENCES

[1] B. J. Kim *et al., Phys. Rev. Lett.* **101**, 076402 (2008).
[2] W. Witczak-Krempa *et al., Annu. Rev. Condens. Matter Phys.* **5**, 57 (2014).
[3] C. Donnerer *et al., Phys. Rev. B* **93**, 174118 (2016).
[4] Y. Ding *et al., Phys. Rev. Lett.* **116**, 216402 (2016).


# SYNTHESIS OF $FeN_4$ UNDER PRESSURE: A HIGH-ENERGY-DENSITY POLYNITRIDE


**Iron tetranitride, $FeN_4$, was synthesised from elements above 1 Mbar in a laser-heated diamond anvil cell. The compound contains polymeric chains built of nitrogen atoms in its structure that makes it a high-energy-density material. This work shows a simple synthetic route to polynitrides of transition metals and demonstrates how methods of single-crystal X-ray diffraction can help in phase analysis of the high-pressure reaction products and understanding the organisation of their crystal structure.**


Nitrogen-rich compounds are among the best high-energy-density materials due to the remarkable difference in the average bond energy between the single N–N bond (160 kJ/mol), the double N=N bond (418 kJ/mol), and the triple N–N bond (945 kJ/mol). However, it is challenging to synthesise compounds with high nitrogen content. The large bond enthalpy of the triply bonded $N_2$ molecule makes nitrogen a generally unreactive element. In many reactions, the activation barrier for N≡N bond breaking requires temperatures higher than the decomposition temperatures of the target phases. Application of pressure is one of the ways to increase the chemical potential of nitrogen and to stabilise nitrogen-rich phases **[1]**.

The focus of this study was the synthesis of novel iron polynitrides. A tiny piece of iron foil was placed in a diamond anvil cell loaded with nitrogen, then the sample was first compressed to 1 Mbar and afterwards laser-heated to 2700 K. The reaction product was studied by means of single-crystal X-ray diffraction and Mössbauer spectroscopy at beamlines **ID27**, **ID11** and **ID18**. Although both starting reagents were in the form of powders, numerous single-crystalline grains were observed, belonging to an unknown phase that produced a high-quality diffraction pattern. Structural analysis showed that the major product of a chemical reaction between iron and nitrogen has the chemical formula $FeN_4$ and has a triclinic symmetry *P*-1. **Figure 14** shows the crystal structure of this novel compound. Each Fe atom is a member of two five-member Fe[$N_4$] metallacycles, which are parallel to the (1-10) lattice plane. Two more nitrogen atoms complete the coordination of the Fe atom to the distorted octahedron. The most intriguing feature of the crystal structure is displayed by nitrogen atoms forming infinite zigzag chains. $FeN_4$ is the first metal nitride with a reliably characterised crystal structure that features polymeric nitrogen chains.

The geometry of the nitrogen chains gives an insight into the bonding scheme of the compound.

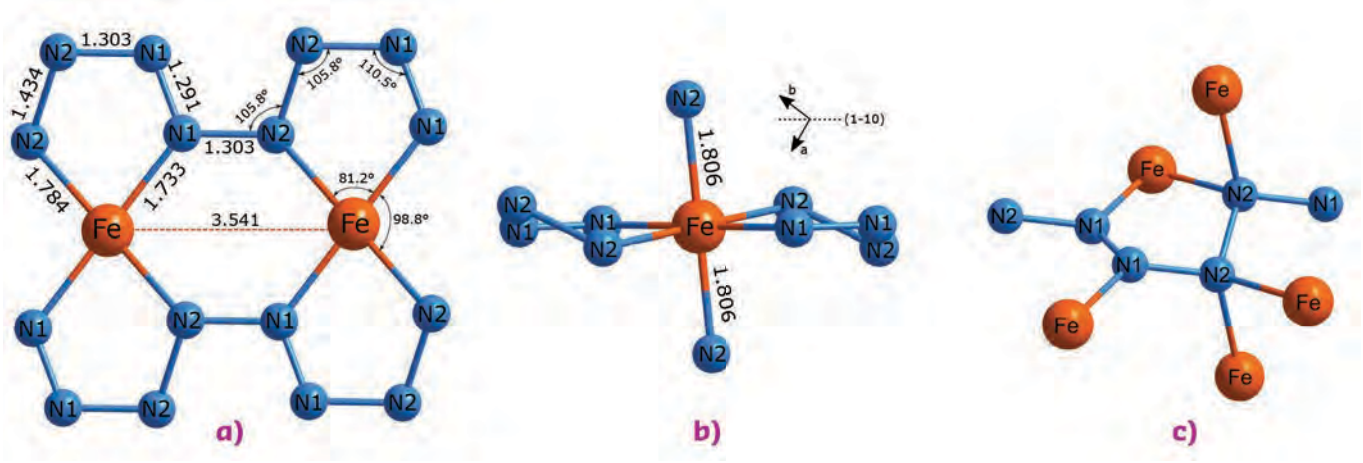


**Fig. 14:** Fragments of the crystal structure of $FeN_4$ at 135 GPa. ***a)*** A fragment of the crystal structure parallel to the (1-10) lattice plane featuring polymeric zigzag N–N chains. Out-of-plane atoms are not shown. **b)** The same fragment shown in a different projection with two additional nitrogen atoms belonging to neighbouring nitrogen chains. **c)** A fragment of the crystal structure showing the coordination geometry of the nitrogen atoms.

Half the nitrogen atoms ($N_1$) have only three neighbouring atoms in planar triangular geometry, whereas the other nitrogen atoms ($N_2$) have tetrahedral coordination. This directly suggests the $sp^2$ hybridisation of $N_1$ atoms and $sp^3$ hybridisation of $N_2$ atoms. Therefore, the nitrogen chains in $FeN_4$ can be considered as catena-poly[tetraz- 1-ene-1,4-diyl] anions $[-N\text{-}N\text{-}N{=}N\text{-}]_\infty$ (**Figure 15**). This agrees with the description of Fe atoms in the formal oxidation state +2, which is also suggested by the results of Mössbauer spectroscopy and electronic structure calculations.

The volumetric energy density of $FeN_4$ is estimated to be of 13–15.1 kJ/cm$^3$, which is much higher than that of common explosives: TNT (7.2–8.0 kJ/cm$^3$), 1,3,5-trinitroperhydro-1,3,5-triazine (RDX) (10.1 kJ/cm$^3$), and pentaerythritol tetranitrate (PETN) (10.6 kJ/cm$^3$). This study shows that laser heating of elemental metals in a nitrogen environment, at high pressure created by the diamond anvil cells, is a simple route to various polynitrides with peculiar crystal structures and promising chemical properties.

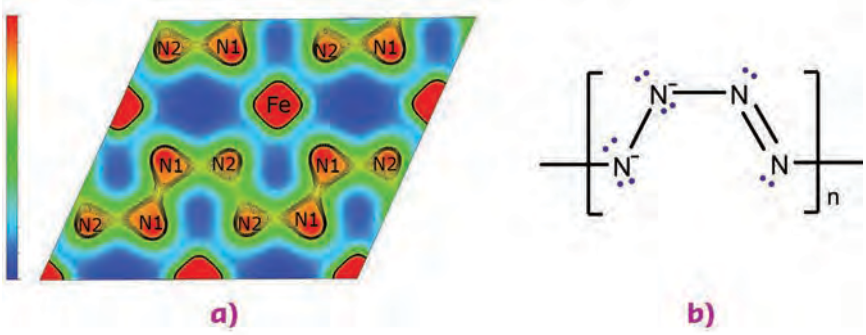


**Fig. 15:** ***a)*** The charge density map with zig-zag N–N chains in $FeN_4$ structure. **b)** A scheme of poly[tetraz- 1-ene-1,4-diyl] anion.

## PRINCIPAL PUBLICATION AND AUTHORS

Fe-N system at high pressure reveals a compound featuring polymeric nitrogen chains, M. Bykov (a), E. Bykova (b), G. Aprilis (c), K. Glazyrin (b), E. Koemets (a), I. Chuvashova (c), I. Kupenko (d), C. McCammon (a), M. Mezouar (e), V. Prakapenka (f), H.-P. Liermann (b), F. Tasnádi (g), A. V. Ponomareva (h), I. A. Abrikosov (g), N. Dubrovinskaia (c) and L. Dubrovinsky (a), *Nat. Commun.* **9**, 2756 (2018); doi: 10.1038/s41467-018-05143-2.
*(a) Bayerisches Geoinstitut, University of Bayreuth (Germany)*
*(b) Photon Science, DESY, Hamburg (Germany)*
*(c) Material Physics and Technology at Extreme Conditions, Laboratory of Crystallography, University of Bayreuth (Germany)*
*(d) Institut für Mineralogie, University of Münster (Germany)*
*(e) ESRF*
*(f) Center for Advanced Radiation Sources, University of Chicago (USA)*
*(g) Department of Physics, Chemistry and Biology (IFM), Linköping (Sweden)*
*(h) Materials Modeling and Development Laboratory, National University of Science and Technology 'MISIS', Moscow (Russia)*

## REFERENCES

[1] W. Sun *et al.*, *Chem. Mater.* ***29***, 6936–6946 (2017).

# Si-4H: SYNTHESIS OF AN UNEXPECTED POLYTYPE OF SILICON

**Pure hexagonal silicon was obtained via high-pressure, high-temperature synthesis in the large-volume press at ID06 combined with heating in vacuum. Structural characterisation shows it to be the nanostructured metastable 4H polytype (ABCB stacking), in contrast to the expected 2H structure (AB stacking). Optical measurements suggest it has a promising future as a photovoltaic material.**

Silicon (Si) is so far the protagonist of modern technology, being employed in a wide range of applications. At ambient conditions, Si has a cubic, diamond-like structure. This allotrope, known as Si-I, is an indirect bandgap semiconductor. Semiconductors are at the basis of modern electronics, as their conductivity can be switched on and off and their properties can be tuned by doping. In the case of photovoltaic application, Si efficiency is strongly limited by the indirect nature of its bandgap as absorption of solar light needs to be mediated by phonons *(i.e.* vibrations of the crystal lattice, that cause energy dissipation). Nevertheless, further developments and improvements are still possible for silicon, for example by adoption of new crystal structures and nanostructuring. A variety of Si allotropes with enhanced optoelectronic properties has been predicted. Among them, hexagonal allotropes of Si are of interest. Not only are they expected to enhance the absorption of visible light, but they could be transformed into direct bandgap semiconductors by applying stress **[1]**.

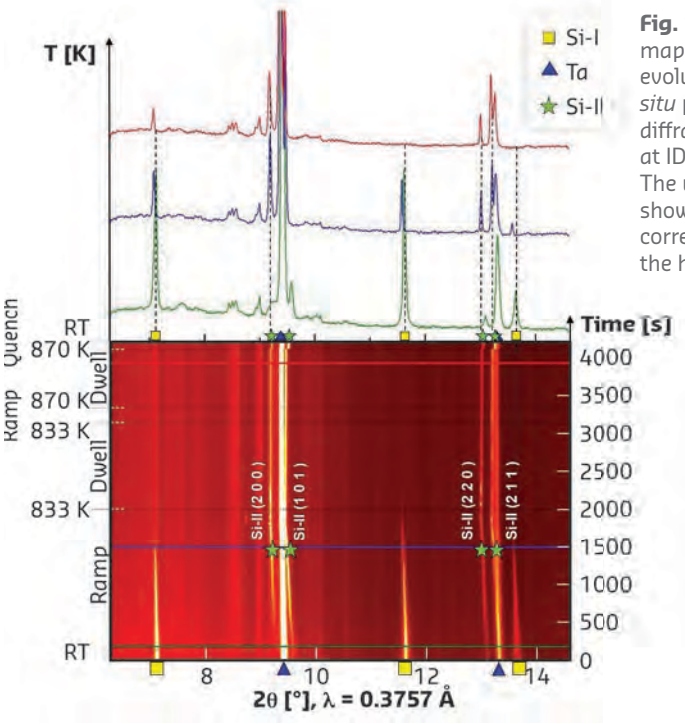


**Fig. 16**: Colour map showing the evolution of *in-situ* powder X-ray diffraction collected at ID06-LVP. The upper panel shows patterns corresponding to the horizontal lines.

High-pressure synthesis has become a method of choice for the development of new materials. New crystal structures become stable at extreme conditions and can often be recovered at ambient conditions. Furthermore, direct solid-to-solid transitions ensure the high purity of the synthesised materials and in some cases allow well-controlled nanostructuring, giving rise to bulk yet nanostructured samples, which are agglomerates of confined nanoparticles. In this way, the synthesis approach allows the simultaneous tuning of both the structure and the texture of the samples, which is a very desirable feature for material design.

Common silicon Si-I undergoes a transformation into the metallic Si-II phase (with β-tin structure) above 10 GPa, a pressure of interest because it is accessible for industrial production. During decompression, the Si-II phase does not transform back to the common Si-I, but to the metastable Si-III **[2]**. This allotrope can be recovered and used as a precursor for the synthesis of hexagonal Si-IV, which forms during slight heating at ambient pressure or under vacuum. Such hexagonal Si was reported more than 50 years ago and was believed to have a lonsdaleite-like structure (2H hexagonal polytype). However, so far, its existence had only been demonstrated for Si shells grown on GaP nanowires **[3]**.

Following the optimised conditions for the Si-III production **[2]**, *in-situ* high-pressure synthesis was performed at **ID06-LVP** (**Figure 16**), assuring the full transformation of Si-I → Si-II and recovering pure Si-III after decompression. The hexagonal Si phase was obtained by heating at ~473 K under vacuum. Resolution of the structure by complementary X-ray diffraction (XRD) and transmission electron microscopy (TEM) methods demonstrates that hexagonal Si obtained from high-pressure corresponds to the 4H polytype and thus has a different stacking sequence from the one expected for Si-IV (*i.e.* ABCB stacking instead of 2H characteristic sequence AB). A nanostructured morphology was also observed. The crystallites have a flake-like configuration, as they are strongly confined along the vertical direction (*i.e.* the *c* axis) by the presence of stacking faults. Such peculiar morphology is expected to strongly influence

the properties of this new material, possibly introducing strain and/or confinement effects able to improve the photovoltaic performances of Si-4H. The crystal structure resolution allowed comparison of Si-4H properties with *ab initio* simulations. Density functional theory was employed to compute nuclear magnetic resonance and Raman spectra based on the Si-4H structural model. Such calculations are in good agreement with experimental data, in which the signature of the numerous stacking faults is also identified.

In conclusion, high-pressure synthesis with *in-situ* control of the accomplishment of phase transformation has resulted in the formation of pure hexagonal Si with 4H structure in its bulk nanostructured form. The strong superposition between its emission spectra and visible light (**Figure 17**) sets this new material as one of the most promising candidates for future Si-based photovoltaics.

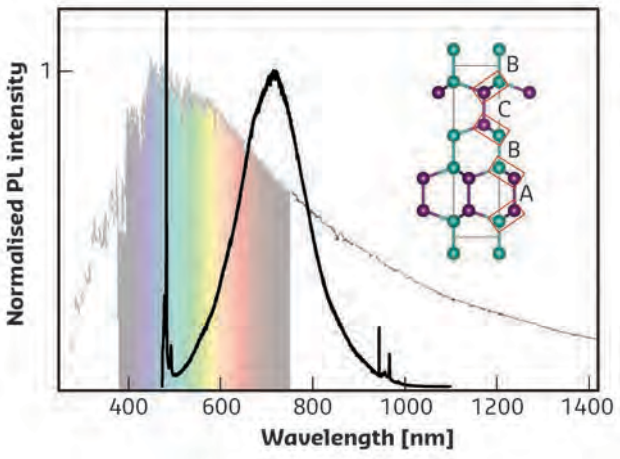


**Fig. 17:** Photoluminescence spectrum of nanostructured Si-4H collected at ambient conditions with a blue laser (λ = 460 nm). Solar spectrum irradiance is reported in the background.

PRINCIPAL PUBLICATION AND AUTHORS

Nature of Hexagonal Silicon Forming via High-Pressure Synthesis: Nanostructured Hexagonal 4H Polytype, S. Pandolfi (a), C. Renero-Lecuna (a, b), Y. Le Godec (a), B. Baptiste (a), N. Menguy (a), M. Lazzeri (a), C. Gervais (b), K. Spektor (c), W. A. Crichton (c) and O. O. Kurakevych (a), *Nano Lett.* **18**, 5989–5995 (2018); doi: 10.1021/acs.nanolett.8b02816.

*(a) Sorbonne Université, IMPMC Paris (France)*
*(b) Sorbonne Université, LCMCP Paris (France)*
*(c) ESRF*

REFERENCES

[1] C. Rödl *et al., Phys. Rev. B.* **92**, 045207 (2015).
[2] O. O. Kurakevych *et al., Inorg. Chem.* **55**, 8943–8950 (2016).
[3] H. I. Hauge *et al., Nano Lett.* **15**, 5855–5860 (2015).

# SEARCHING FOR THE ACTIVE PHASE IN Cu-Ni/$TiO_2$ MATERIALS: HYDROGEN PHOTOCATALYTIC PRODUCTION

**Microbeam X-ray absorption was combined with calculations of the light-matter interaction at the measurement cell to clarify the nature and chemistry of the active phase in a bimetallic co-catalyst. This study shows that a microsized X-ray probe is required to obtain a true structure–activity relationship to interpret photoactivity.**

Understanding how hydrogen is produced from renewable chemicals in a photocatalytic process is a topic of importance for the setting-up of new, green, industrial technologies. Non-noble metal $TiO_2$-based materials catalyse this reaction, but with limited activity. This limitation can be solved using bimetallic materials, and Cu-Ni appears to be one of the best candidates **[1, 2]**.

The performance of a Cu-Ni/$TiO_2$ system (and monometallic references) was analysed in the (continuous flow) gas-phase photocatalytic production of hydrogen from water/methanol mixtures. In titania materials, UV light decay from the surface occurs within a few microns **[3]** and calculation at the X-ray cell suggested the use of a 3 x 3 µm microbeam at **BM23** to scan the material perpendicularly to the external, illuminated surface (**Figure 18**). *Operando* XAS spectra at the Cu and Ni K-edges were thus obtained.

**Figure 19** presents the Cu K-edge XANES data. Among the positions scanned, the only one presenting differences when illuminated corresponds to the surface in both bi- and

monometallic samples. Below the surface, zones were observed where the contact with the gas atmosphere leads to a fully reduced phase. Copper was fully oxidised (initial state) for zones far from the surface where the reductant (methanol) had been totally consumed. Considering a rather modest modification at the Ni-edge (which does not show detectable changes by XAS and, as a monometallic reference, displayed low activity) and the study of the corresponding reduced and oxidised phases by EXAFS, it was concluded that a different chemical state is present in monometallic Cu and bimetallic Cu-Ni materials. At the surface, following illumination both materials show the co-existence of oxidised and reduced phases: a Cu-rich or pure Cu(0) reduced state(s) together with a CuO-like phase. Differences between the samples correspond to the extent of oxidation (larger in the bimetallic sample) and the way oxidised and reduced entities contact each other.

As displayed in **Figure 18** (surface position), the monometallic Cu sample shows a metal core–oxide shell structure, while the CuNi bimetallic material shows a finely dispersed reduced phase onto the (dominant) oxidised phase. This contradicts previous reports (not scanning the portion of the sample under the simultaneous action of light and reactant mixture) where (partially or fully) reduced entities were erroneously assigned as the active phase **[4]**. In the monometallic system, a metallic core facilitates the charge handling under light excitation, while the surface oxidised phase plays a key chemical role. Improved photoactivity by the CuNi sample is related to intimate contact between the Cu-rich zerovalent component and the dominant oxidised phase.

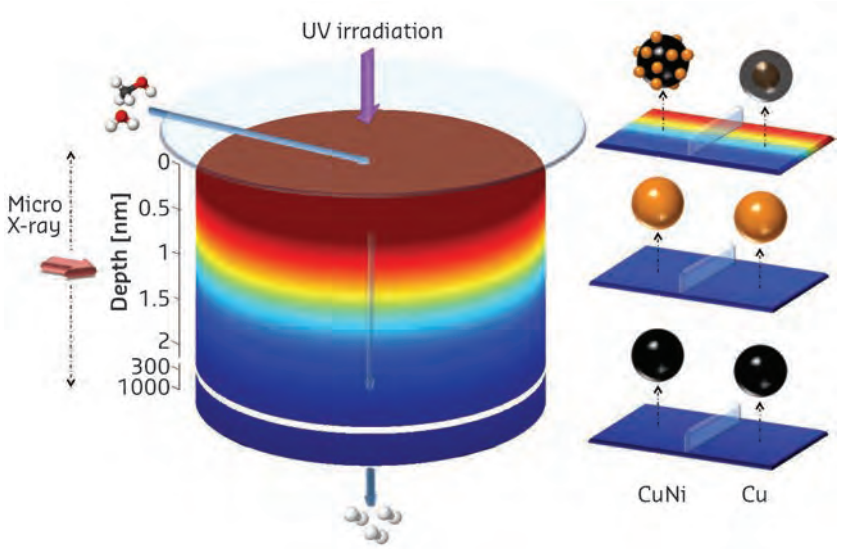


**Fig. 18:** Schematic view of the sample and experimental conditions. The sample is confined in a cell that allows simultaneous gas phase treatment and illumination from the top side. Arrows show the direction of the gas flow, illumination and incident X-ray microbeam. The X-ray microbeam probes non-noble metal chemical states and structure as a function of the depth from the surface. Panels on the right depict the most relevant metal-containing phases (Cu(0): brown, Cu(II): black) for different depths described by the light intensity received. Cu and CuNi samples are considered.

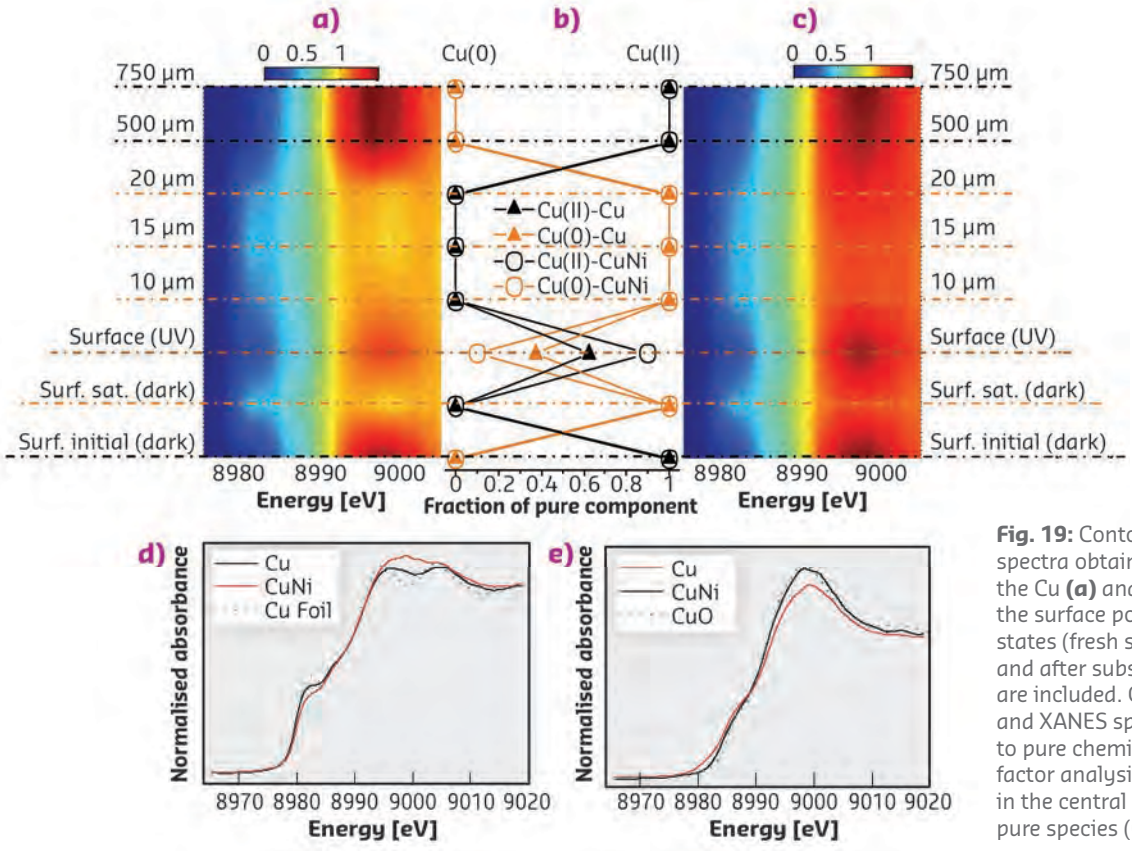


**Fig. 19:** Contour plot of Cu K-edge XANES spectra obtained under illumination for the Cu **(a)** and CuNi **(c)** samples. For the surface position, the two previous states (fresh sample at dark conditions and after subsequent gas saturation) are included. Concentration profiles **(b)** and XANES spectra **(d, e)** corresponding to pure chemical species obtained from factor analysis are included. Colours in the central panel are assigned to pure species (Cu(II): black, Cu(0): orange).

As a result, the key effect of Ni is to shape the contact between these two types of entities. Thus, the combination of micro-XANES and micro-EXAFS at relevant light/X-ray probe lengths unveils the true physicochemical basis of the photoactivity in hydrogen production materials.

PRINCIPAL PUBLICATION AND AUTHORS

Phase-Contact Engineering in Mono- and Bimetallic Cu-Ni Co-catalysts for Hydrogen Photocatalytic Materials, M. J. Muñoz-Batista (a), D. Motta Meira (b), G. Colón (c), A. Kubacka (a) and M. Fernández-García (a), *Angew. Chem. Int. Ed. Engl.* **57**(5), 1199–1203 (2018); doi: 10.1002/anie.201709552.

*(a) Instituto de Catálisis y Petroleoquímica, CSIC, Madrid (Spain)*
*(b) ESRF*
*(c) Instituto de Ciencia de Materiales de Sevilla, CSIC, Seville (Spain)*

REFERENCES

[1] Y. Xu & B. Zhang, *Catal. Sci. Technol.* **5**, 3084–3088 (2015).
[2] G. Colon, *Appl. Catal. A* **518**, 48–59 (2016).
[3] M. J. Muñoz-Batista *et al., J. Catal.* **330**, 154–166 (2015).
[4] (a) W.-T. Chen *et al., J. Catal.* **326**, 41–53 (2015); (b) J. B. Priebe *et al, ChemCatChem* **9**, 1025–1031 (2017).

# EXHAUST GAS CATALYSTS IN ACTION: *OPERANDO* TURBO-XAS FOLLOWS THE STATE OF Pt DURING REALISTIC DRIVING CYCLES

**Simplified tests of exhaust gas catalysts are known to fail to mimic real-life emissions from vehicles. Studying rapid structural changes in Pt-based aftertreatment catalysts under conditions resembling real operation, using turbo-XAS, could give insight into the origin of the differences between model laboratory tests and more realistic operation conditions.**

Legislation demands the reduction of $CO_2$ emission from on-road vehicles, entailing more efficient transformation of thermal energy to kinetic energy. However, this leads to lower exhaust gas temperature and pushes exhaust aftertreatment catalysts to their operational limits **[1, 2].** As a result, even small discrepancies in the predicted and real catalyst performance result in failure to meet emission legislation. Hence, kinetic models used to derive aftertreatment control algorithms must be validated for real-world driving rather than model test conditions. X-ray absorption spectroscopy (XAS) is an invaluable tool to identify the working state of catalytic active sites and presence of adsorbed species. This information is used to derive kinetic models and improve aftertreatment catalysts.

The main difference between typical laboratory test conditions and real-world driving lies in the very fast temperature variations that the catalyst experiences. Such temperature transients cannot be reproduced using conventional test benches

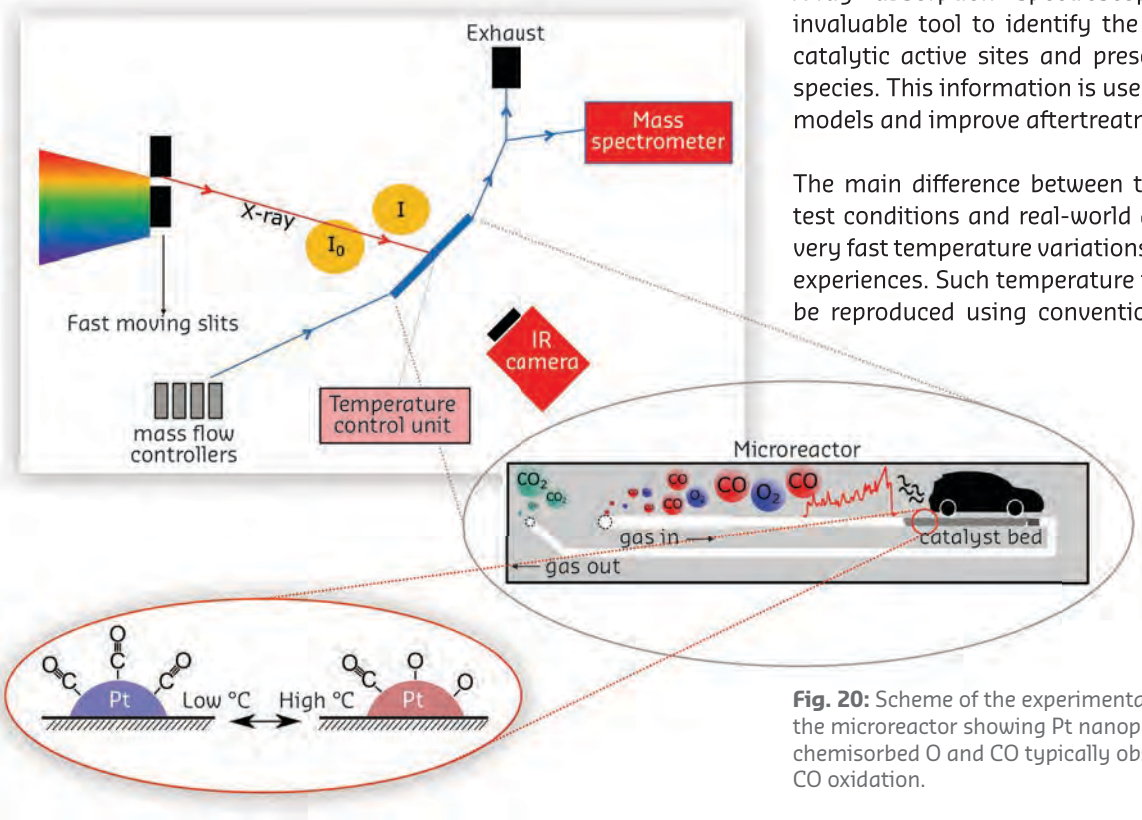


**Fig. 20:** Scheme of the experimental setup and the microreactor showing Pt nanoparticles with chemisorbed O and CO typically observed during CO oxidation.

and common *in-situ* cells due to high thermal mass of the used heater devices. Here, an *in-situ* microreactor **[3]** and an integrated heater with low thermal mass was used to accurately reproduce high temperature transients. Combined with fast fluorescence XAS measurements at beamline **ID24** (turbo-XAS) and complementary analysis of the outlet gas composition, the behaviour of Pt active sites in typical diesel oxidation catalysts (DOC) during CO oxidation were monitored under model test conditions and during realistic driving cycles.

**Figure 20** schematically shows the setup installed at **ID24**. The photon energy was selected from the polychromatic beam by fast-moving slits and total fluorescence yield was measured by two photodiodes. Pt $L_3$ XANES spectra were recorded at 1 Hz to follow the fast temperature transients, allowing quantification of the Pt oxidation state and the presence of adsorbed oxygen and CO molecules. Two catalysts were studied, representing basic $Pt/Al_2O_3$ and more advanced $Pt\text{-}CeO_2/Al_2O_3$ containing ceria as an oxygen storage component.

The New European Driving Cycle (NEDC) protocol employed (**Figure 21a**, blue curve) represents the inlet temperature of the $Pt/Al_2O_3$ catalyst in a typical aftertreatment system (temperature variation of 50 to 290 °C/min), shown together with the Pt oxidation state and $CO_2$ mass spectrometer (MS) signal for evaluating catalytic performance. Each ramp segment of the NEDC profile was matched to a corresponding peak in Pt oxidation state and $CO_2$ production, demonstrating sequential light-off and extinction of CO oxidation during the test cycle. When plotted against catalyst temperature (**Figure 21b**), both the Pt oxidation state and $CO_2$ production measured during the driving cycle showed significant deviation from the dependencies obtained during typical laboratory tests with slow temperature ramps. A significant decrease in light-off temperatures during transient NEDC testing compared to model laboratory tests is consistent with rapid desorption of CO compared to a conventional heat treatment and its slower re-adsorption during short cooling periods. Consistent and reproducible Pt oxidation state during several repeated NEDC cycles was observed for the $Pt\text{-}CeO_2/Al_2O_3$ catalyst, while $Pt/Al_2O_3$ demonstrated a large scatter of experimental points and continuous deactivation during repeated tests, confirming the vital role of ceria in stabilising Pt species against sintering and providing oxygen storage capacity.

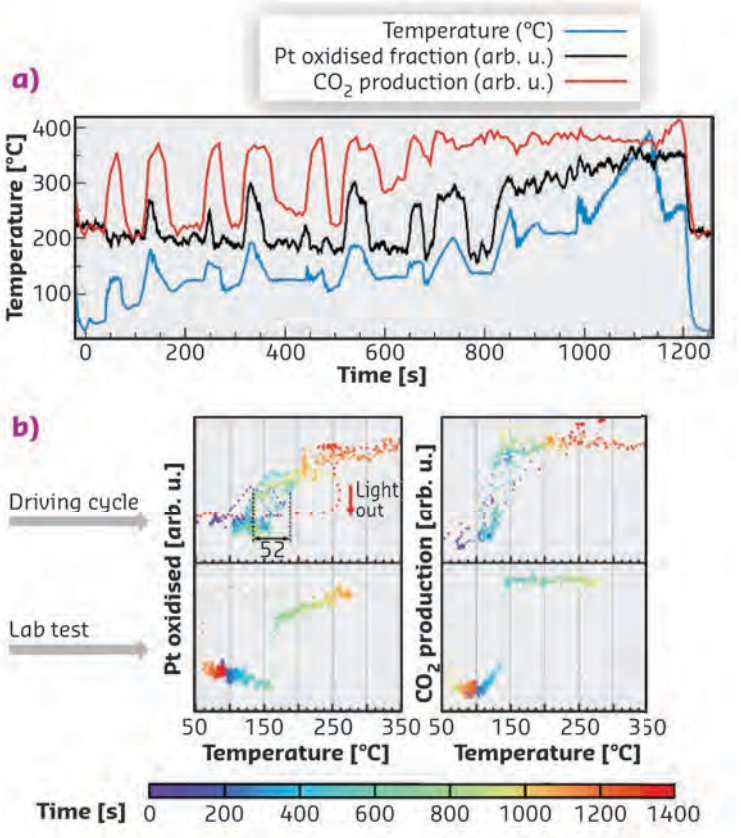


**Fig. 21: a)** System response over a $Pt/Al_2O_3$ catalyst (temperature, $CO_2$ production and fraction of oxidised Pt during NEDC testing). **b)** Correlation plots of temperature (°C), Pt oxidation state and $CO_2$ production (a.u.) during a single NEDC driving cycle and a typical laboratory test with slow temperature ramp for Pt /$Al_2O_3$; data points are color coded according to the time during the test (legend below the graph).

This study demonstrates a unique *operando* approach to studying DOCs under rapid transient temperature conditions corresponding to real driving cycles. Although such *operando* experiments are demanding during harsh transient regimes (up to 290 °C/min), turbo-XAS combined with an *in situ* cell with low heat capacity presents a useful method for observing structural changes during rapid temperature variation and explaining differences between real-life operation and model tests.

## PRINCIPAL PUBLICATION AND AUTHORS

Transient structural and catalytic behaviour of Pt-particles probed by operando spectroscopy during a realistic driving cycle, F. Benzi (a), T. L. Sheppard (a, b), D. E. Doronkin (a, b), D. M. Meira (c), A. M. Gänzler (a), S. Baier (a) and J.-D. Grunwaldt (a, b), *Catal. Sci. Technol.* **7**, 3999–4006 (2017); doi: 10.1039/c7cy00926g.
*(a) Institute for Chemical Technology and Polymer Chemistry (ITCP), Karlsruhe Institute of Technology (Germany)*
*(b) Institute of Catalysis Research and Technology (IKFT), Karlsruhe Institute of Technology (Germany)*
*(c) ESRF*

## REFERENCES

[1] E. S. Lox *et al.*, in *Handbook of Heterogeneous Catalysis*, G. Ertl, H. Knözinger, J. Weitkamp (Eds.), Wiley-VCH, 1569–1595 (2008).
[2] O. Deutschmann & J.-D. Grunwaldt, *Chem. Ing. Tech.* **85**, 595–617 (2013).
[3] S. Baier *et al., Rev. Sci. Instrum.* **86**, 1–24 (2015).

# DISCLOSING THE STRUCTURE OF CATALYTICALLY ACTIVE Mn-EXCHANGED MOF-5

**The exchange of redox-active ions in MOFs could lead to novel platforms combining the benefits of heterogeneous and homogeneous catalysts. XAS data has helped to shed light on the local structural and electronic properties of Mn(II) ions supported within the MOF-5 node, serving as selective catalysts for the epoxidation of cyclopentene.**

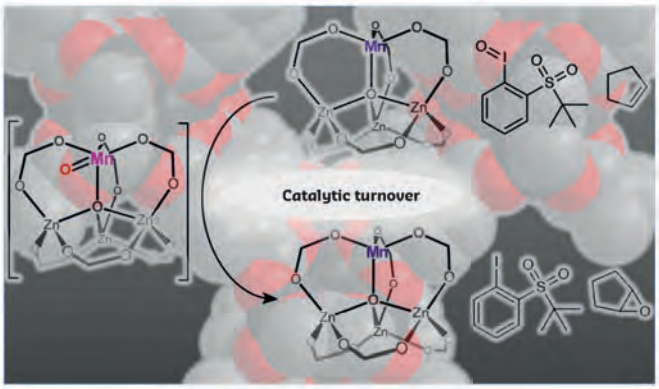


**Fig. 22:** Pictorial representation of the cyclopentene epoxidation reaction cycle over redox-active Mn ions exchanged in the MOF-5 node.

In catalysis, metal–organic frameworks (MOFs) could potentially combine the benefits of heterogeneous catalysts, such as ease of recovery and product separation, with those of homogeneous catalysts, most critically, steric and electronic tunability **[1–4]**. These fascinating systems are built by connecting metal-based nodes with organic linkers, yielding crystalline nanoporous materials with surface areas as high as some thousands of $m^2/g$. Post-synthetic modifications enabling the incorporation of additional redox-active metal ions into these materials currently represent the forefront of research in MOF-based catalysis.

In this context, this work demonstrates that Mn(II) ions supported within the unusually weak-field zinc-carboxylate nodes of $Zn_4O$-(terephthalate)$_3$ (MOF-5) engage in oxidative reactivity and serve as selective catalysts for the epoxidation of cyclopentene, through the likely intermediacy of a high-spin Mn(IV)–oxo complex (**Figure 22**).

Mn K-edge X-ray absorption spectroscopy (XAS) measurements performed at beamline **BM23** have been crucial to confirm the partial substitution of Zn(II) by Mn(II) in MOF-5. By comparing the experimental X-ray absorption near-edge structure (XANES) spectrum of Mn-MOF-5 with the ones of selected Mn-containing reference compounds, it was possible to verify the exchange of Mn(II) ions supported in the distorted all-oxygen ligand field of the MOF-5 node (**Figure 23a**). DFT-assisted extended X-ray absorption fine structure (EXAFS)

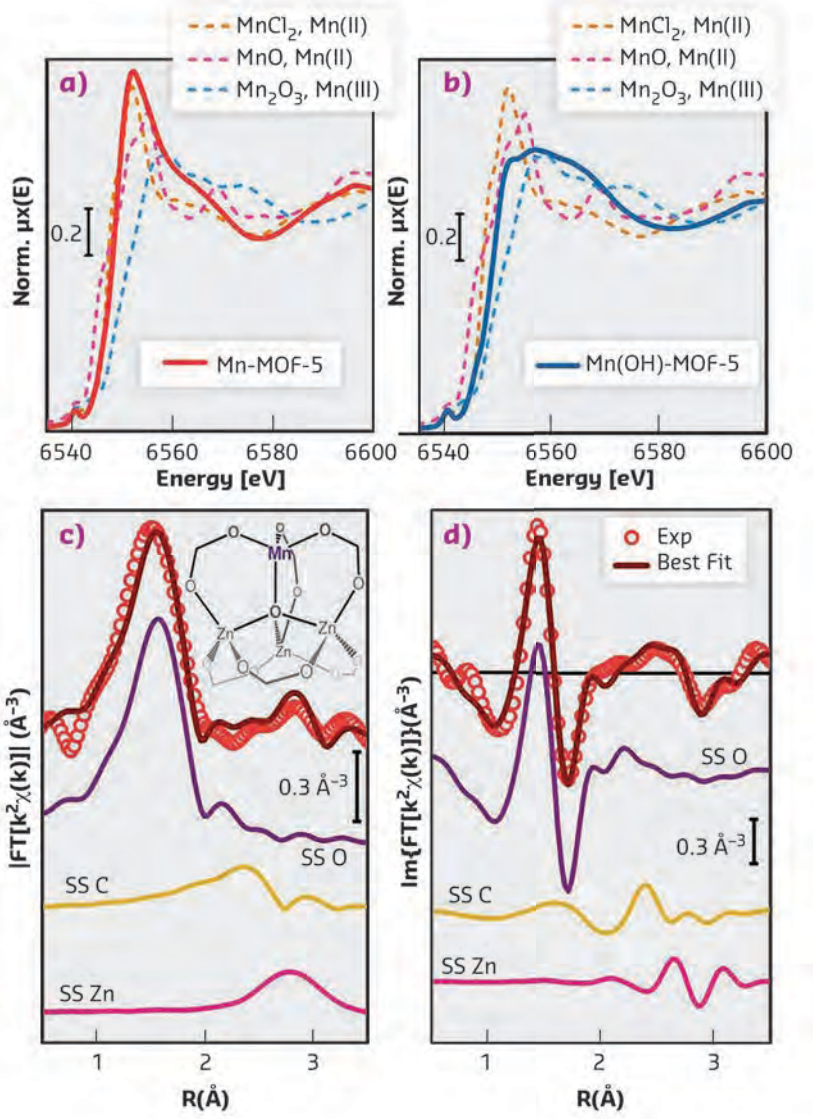


**Fig. 23:** Mn K-edge XANES spectra of **(a)** Mn(II)-MOF-5 and **(b)** Mn(III)(OH)-MOF-5 in comparison with selected Mn(II) and Mn(III) reference compounds. **c)** Magnitude and **(d)** imaginary part of the Fourier-transformed experimental and best-fit EXAFS spectrum of Mn(II)-MOF-5. The figure also reports the principal contributions to the EXAFS signal (vertically translated for clarity) as well as a scheme of the local Mn(II) coordination environment in the MOF-5 node.

analysis further supports the proposed local structure of the Mn(II) centres (**Figure 23c,d**), revealing mean Mn–O bond distance $R_{Mn-O}$ = 2.07 ± 0.01 Å and second-shell mean distances $R_{Mn\cdots C}$ = 3.00 ± 0.04 Å and $R_{Mn\cdots Zn}$ = 3.23 ± 0.03 Å.

The Mn(II) ion at the MOF-5 node engages in redox chemistry with a variety of oxidants. With $^{t}BuSO_2PhIO$, a soluble variant of the commonly used oxidant iodosyl benzene, it produces a putative Mn(IV)-oxo intermediate, which, upon further reaction with adventitious hydrogen, is trapped as a Mn(III)–OH species. XANES data ascertain the presence of Mn(III) in Mn(OH)-MOF-5 (**Figure 23b**). Although the edge position and the characteristic features in the XANES spectrum of Mn(OH)-MOF-5 are closer to that of Mn(III) in $Mn_2O_3$ than to those of Mn(II) in MnO and $MnCl_2$, it is clearly intermediate between Mn(II) and Mn(III) model compounds. This implies that Mn(OH)-MOF-5 contains a dominant fraction of Mn(III) together with a residual amount of Mn(II), in further agreement with EXAFS analysis as well as parallel electron paramagnetic resonance (EPR) studies.

Most intriguingly, the intermediacy of the high-spin Mn(IV)–oxo species is likely responsible for catalytic activity of the Mn(II)-MOF-5 'precatalyst', which, in the presence of $^{t}BuSO_2PhIO$, catalyses oxygen atom transfer reactivity to form epoxides from cyclic alkenes with >99% selectivity (catalytic cycle depicted in **Figure 22**). These results demonstrate that MOF nodes can serve as competent platforms for accessing terminal high-valent metal–oxo species, able to engage in catalytic oxygen atom transfer chemistry. The demonstrated reactivity and proposed intermediate highlight a unique opportunity with MOFs to study species of fundamental interest, in which local structural and electronic properties are successfully unravelled by XAS.

PRINCIPAL PUBLICATION AND AUTHORS

Selective Catalytic Olefin Epoxidation with Mn(II)-Exchanged MOF-5, A. W. Stubbs (a), L. Braglia (b, c), E. Borfecchia (b), R. J. Meyer (d), Y. Román-Leshkov (e), C. Lamberti (b, c) and M. Dincă (a), *ACS Catal.* **8**, 596–601 (2018); doi: 10.1021/acscatal.7b02946.

*(a) Department of Chemistry, Massachusetts Institute of Technology (USA)*
*(b) Department of Chemistry, NIS and CrisDi Interdepartmental Centers, INSTM Reference Center, University of Turin (Italy)*
*(c) International Research Institute "Smart Materials", Southern Federal University, Rostov-on-Don (Russia)*
*(d) Corporate Strategic Research, ExxonMobil Research and Engineering, Annandale (USA)*
*(e) Department of Chemical Engineering, Massachusetts Institute of Technology (USA)*

REFERENCES

[1] A. H. Chughtai *et al., Chem. Soc. Rev.* **44**, 6804–6849 (2015).
[2] D. Farrusseng *et al., Angew. Chem. Int. Ed.* **48**, 7502–7513 (2009).
[3] J. Gascon, *et al., ACS Catal.* **4**, 361–378 (2014).
[4] H. Furukawa *et al., Science* **341**, 1230444 (2013).

# MULTI-PHOTON SUPERRADIANCE FROM A NUCLEAR ENSEMBLE

**A prediction about the quantum-mechanical behaviour of resonant systems has been verified in experiments. After nuclei in a crystal were excited by a flash from an X-ray laser, the emission of X-rays was followed. A dramatic reduction in the time to emit the first photon was observed as the number of X-rays increased.**

One of the broad challenges of science is to understand the behaviour of groups of atoms based on the response of a single atom, which is usually much simpler. A facet of this is understanding the behaviour of a group of identical oscillators. An analogy is a collection of bells that all have the same tone: one can easily imagine the sound of a single bell struck once – a clear tone ringing out with a volume that decays away over time. Yet what happens if one gently taps all the bells in a large collection? Will the tone be the same as a single one? What about the volume? Does it matter if you tap them all at the same time?

The preceding questions can be answered using straightforward mathematics. However, the analogous questions become more complex in the quantum world of collections of atoms that emit light. In that world, light comes in photons and light intensity is measured in discrete packets of photons. Similar questions arise, but now one also has to ask how the response changes depending on the number of photons in the system.

A pioneering approach to these issues was developed by Robert Dicke **[1]**. He predicted a 'superradiant' state, where, when large numbers of photons or quanta are put into a system with

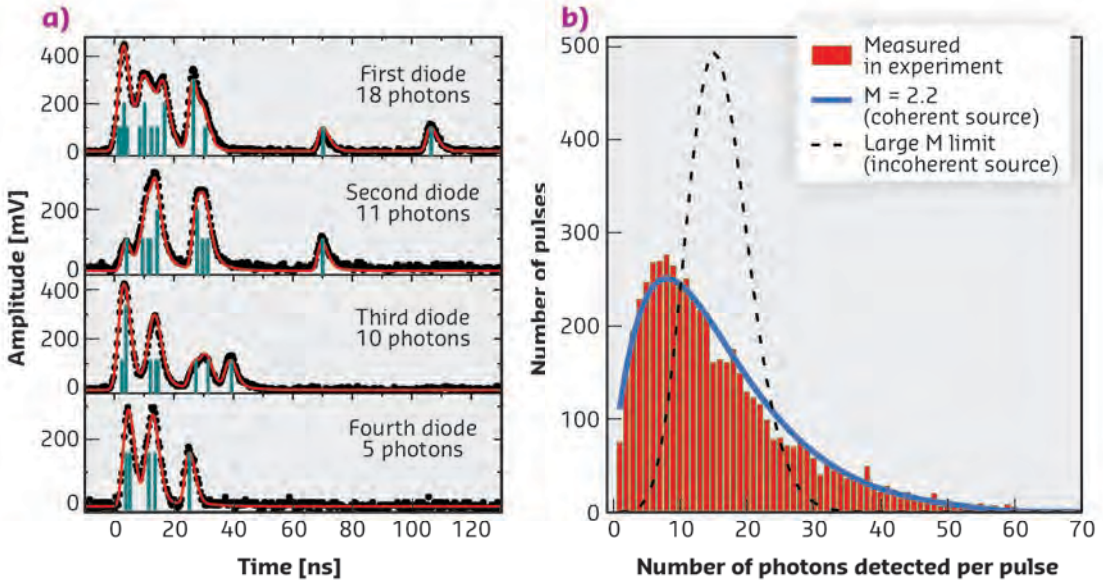


**Fig. 24:** Measuring the multi-photon emission after a single pulse of the XFEL. **a)** Scope traces from the avalanche photo diode (APD) detectors after one pulse of 44 photons and the fits used to analyse the distribution. **b)** The distribution of multi-photon events measured in the APD detectors, as compared with a model incorporating a coherent source with few modes ($M$ = 2.2) and an incoherent source (large $M$ limit).

many atoms, the decay of the excited system becomes much faster than for a single atom. In the context of the above analogy, his suggestion would mean that if one has a large number of bells that are excited together, they can ring loudly but the sound dies out much more quickly than the gentle fading of a single bell. The concept of superradiance has since been verified, and indeed, is a touchstone of quantum optics. However, Dicke also predicted that a very strong change in decay rate would occur even when the number of quanta in the system is much less than the number of atoms in the system. This was investigated in recent experiments at the SACLA free-electron laser and on beamline **ID18**.

The new work replaced the low-energy quanta envisioned by Dicke with high-energy X-rays, allowing the decay of the system to be followed, one quantum of X-ray light at a time. However, getting strong pulses of X-rays is much harder than for low energy light, and required the use

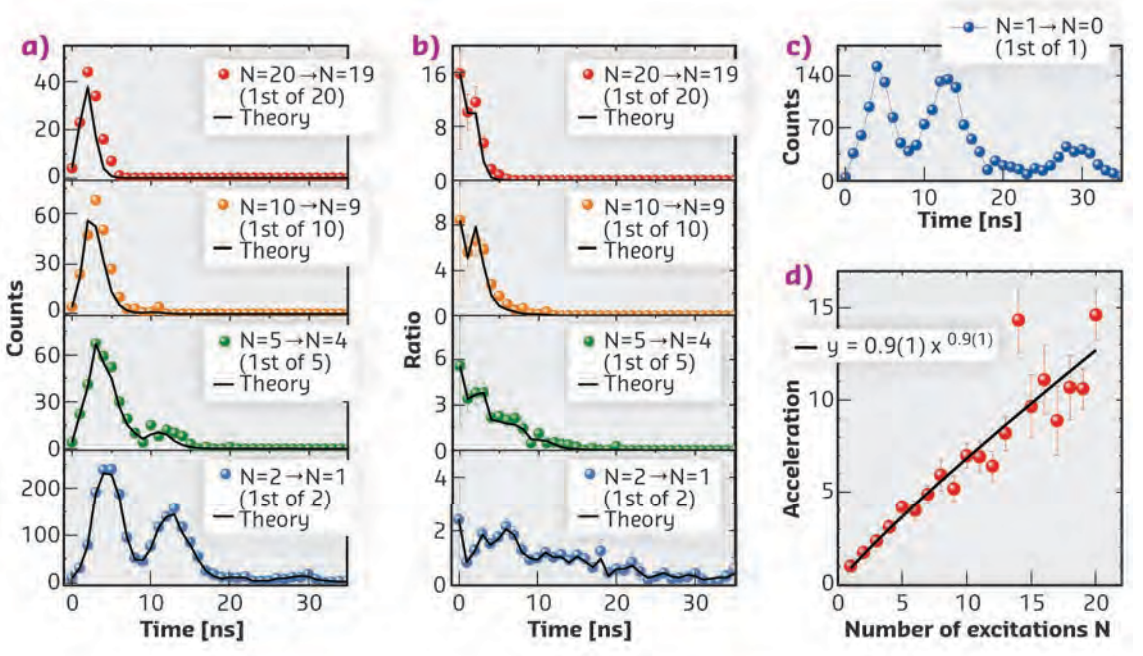


**Fig. 25:** Acceleration of the initial decay rate. The increase of the initial decay rate for the transitions from $N$ to $N$-1 excited states revealed **a)** by the accelerated decay of the first out of $N$ detected photon, $P_N^1(t)$, **b)** by the ratios $P_N^1(t)/P_1^1(t)$ of these data to the single-photon decay $P_1^1(t)$ (shown in **(c)**), and **d)** by the estimated acceleration rates $(P_N^1/P_1^1)|_{t->0}$. The solid lines in **(a, b)** are the calculations based on the statistical approach. The solid line in **(d)** is the power fit.

of an X-ray free-electron laser. Such sources have only become available recently, and of the few operating in the world, SACLA, at the RIKEN SPring-8 Center in Japan, was the first that could provide the required high energy. Using this source, it was possible to precisely follow the decay for up to 68 X-ray photons (**Figure 24**). The accelerated emission of the first photon (**Figure 25**) was observed to be in excellent agreement with Dicke's prediction **[1]**. The single-photon decay under the same experimental conditions was studied on ID18. From these experiments, an alternative picture of the decay properties was produced, based on a statistical approach, which will be valuable for the understanding of future work.

## PRINCIPAL PUBLICATION AND AUTHORS

Superradiance of an ensemble of nuclei excited by a free electron laser, A. I. Chumakov (a), A. Q. Baron (b), I. Sergueev (c), C. Strohm (c), O. Leupold (c), Yu. Shvyd'ko (d), G. V. Smirnov (e), R. Rüffer (a), Y. Inubushi (f), M. Yabashi (f), K. Tono (f), T. Kudo (b) and T. Ishikawa (b), *Nat. Phys.* **14**, 261–264 (2017); doi: 10.1038/s41567-017-0001-z.
*(a) ESRF*
*(b) RIKEN SPring-8 Center, Hyogo (Japan)*
*(c) DESY, Hamburg (Germany)*
*(d) Advanced Photon Source, Argonne National Laboratory, Illinois (USA)*
*(e) National Research Centre "Kurchatov Institute", Moscow (Russia)*
*(f) Japan Synchrotron Radiation Research Institute, Hyogo (Japan)*

## REFERENCES

[1] R. H. Dicke, Coherence in spontaneous radiation processes, *Phys. Rev.* **93**, 99–110 (1954).

# STRUCTURAL BIOLOGY

For reasons of which many readers will be aware, and which will undoubtedly be expanded upon in this edition of the *ESRF Highlights*, 2018 will be seen as a watershed year in synchrotron science. Indeed, the very small, ultra-brilliant X-ray beams that will be provided as a result of the ESRF–EBS upgrade will transform the science carried out not only in the field of structural biology but also in many other disciplines.

It is worth remembering, however, that the ESRF has already helped provide a revolution in structural biology, particularly in macromolecular crystallography (MX). In its initial operation phase, MX activities at the ESRF were mostly confined to the non-dedicated use of ID02 and ID09. Initial results, particularly from ID02, were startling. Structural biologists were able to visualise the three-dimensional structures of viruses, membrane proteins and large, biologically relevant complexes with hitherto unobtainable resolution thanks to small, powerful, low-divergence X-ray beams unavailable elsewhere in Europe. The commissioning of BM14 in 1996 coincided with the dawn of cryo-crystallography, helping to make previously complicated phasing experiments routine, and MX activities at the ESRF started to snowball.

The real explosion, however, came with the advent of the ID14 'quadriga' complex, which validated beyond any doubt the benefit of exploiting undulator-based beamlines in MX. This success led directly to the construction of **ID29** and then to **ID23**, a canted MX beamline complex which, building on pioneering and scientifically outstanding work carried out on ID13, included **ID23-2**, the world's first microfocus beamline entirely dedicated to MX.

After more than 10 years of operation, the ageing ID14 complex was superseded in 2014 by the construction of **ID30-A** & **B** as part of the ESRF's Phase I Upgrade Programme, further consolidating the facilities available to the ESRF structural biology user community. Operated in collaboration with EMBL Grenoble Outstation, and coupled with world-leading developments and methodology in automation hardware and software, diffraction data collected at the ESRF (including on the CRG MX facilities BM30A and, from 2002, BM14) have now contributed to more than 14 000 depositions in the Protein Data Bank.

The ESRF's commitment to structural biology has not stopped at MX. The re-deployment of ID14-3 as a dedicated BioSAXS beamline (since superseded by a new facility on **BM29**), the construction of the cryobench facility operated in collaboration with the Grenoble-based Institut de Biologie Structurale (IBS), and the very recent construction of the **CM01** cryo-electron microscopy facility have all significantly expanded the portfolio of complementary facilities available for the study of structural biology in Grenoble.

How will the ESRF–EBS upgrade benefit its structural biology user community? The short answer is almost certainly: increased resolution. Not only will the quality of diffraction data – from even the smallest of crystals – improve, time-resolved MX experiments will become much more tractable. To this latter end, the EBSL8 project will see the current ID29 replaced by a wide-bandpass beamline dedicated to time-resolved MX with most experiments based around synchrotron serial crystallography. This will be coupled to the relocation of an upgraded cryobench facility (to be renamed the *in crystallo* optical spectroscopy laboratory or icOS-Lab). The technical design report for the new beamline has recently been submitted and we expect first users in early 2022.

Work on the ESRF–EBS project aside, perhaps the major structural biology development that occurred at the ESRF in 2018 was the ramping up to full operation of the CM01 cryo-EM facility, operated in collaboration with our partners on the EPN campus (EMBL, IBS and ILL). Here, we present two highlights based on work carried out at CM01. The first of these, by Polovinkin and colleagues (**page 46**), presents structures of different conformational states of the serotonin 5-HT3 receptor, providing crucial insights into the activation cycle of this important molecule, which is targeted by drugs that alleviate some of the undesirable side effects of radiotherapy or chemotherapy. The second, by a consortium of French research groups, sheds light on the biogenesis and function of the bacterial Type VI secretion system (T6SS), a key virulence factor during bacterial infections (**page 52**). These two

articles will undoubtedly be the first of many CM01-based investigations to appear in the *ESRF Highlights*.

We noted in the introduction to the structural biology chapter of the 2017 *ESRF Highlights* that an increasing proportion of structural biology research is targeted at the design of new, improved therapeutic agents and at providing an increased understanding of the molecular basis of diseases and their treatments (**pages 35, 40, 46, 47, 49** and **52**). Several articles presented here reflect this trend. Also on the increase is the study of the potential use of biological macromolecules in biotechnology applications, including in the generation of hydrogen (**page 41**), optogenetics (**page 34**) and the creation of artificial enzymes (**page 38**). Nevertheless, much of structural biology remains focused on providing an improved understanding of biological processes, with examples included here helping to further elucidate mechanisms involved in the action of the GroEL/GroES chaperonin system (**page 37**), in cell signalling (**page 47**), gene expression (**page 51**) and even in DNA replication (**page 54**), which is fundamental to all living organisms.

We have also included in this selection an article reviewing methodological developments carried out in the ESRF Structural Biology group (**page 43**). As readers will see, such developments have recently focused on methods for serial/multi-crystal data collection. Such experiments have, and will continue to, become more prevalent in synchrotron-based MX, and during the construction of the EBS storage ring we will be devoting ourselves to further improving the experimental possibilities that will be available in 2020 when we welcome back users to our facilities.

Finally, January 2019 will see Stephanie Monaco leave the Structural Biology group in order to take up a position as deputy head of the ESRF User Office. Over more than a decade and a half, Stephanie's contribution to the success of the group's industrial user programme has been exceptional, as has her contribution in many other areas of high importance to our user community. We wish Stephanie every success in her new venture.

**G. LEONARD AND C. MUELLER-DIECKMANN**

# FIRST CRYSTAL STRUCTURE OF NATIVE CHANNELRHODOPSIN 2

**Channelrhodopsin 2 (ChR2) is the first and major tool of optogenetics but previous efforts to describe its high-resolution structure had failed. In this study, the molecular structures of ChR2 and its mutant, C128T, are solved. The structures suggest a consistent mechanism for channel functioning and open up new avenues for protein engineering for optogenetic applications.**

The first channelrhodopsin (ChR), from the green freshwater algae *Chlamydomonas reinhardtii*, was characterised in 2001. In 2003, the function of ChR2, a light-sensitive selective cation channel, was also elucidated. These proteins belong to the family of microbial rhodopsins, comprising seven-helical transmembrane proteins with a retinal cofactor covalently bound to a conserved lysine residue. Under light illumination the retinal isomerises, the protein undergoes a cycle of structural changes (photocycle) and the channel opens. It was predicted, and then shown, that when ChR2 is heterologously expressed in a plasma membrane the electrical potential across the membrane can be modulated by light, by opening and closing the ion channel. In the case of neural cells, this photocurrent mimics neuronal signal transduction and fires a single neuron. The new field of optogenetics emerged with this discovery. At present, ChR2 is an indispensable technique in neuroscience and it is expected that it may find applications in medicine. Indeed, clinical trials using channelrhodopsin 2-based gene therapy as a means of treating age-related muscular degeneration are currently being performed.

Several ChR2 mutations are known to modify its properties; such modifications include increasing the photocurrent it generates, altering its ion selectivity and changing its excitation wavelength. Such an array of mutations makes it possible to choose a tool for concrete optogenetic experiments in living cells. However, most of these mutations were generated using a directed evolution method or were based on structures of similar proteins, and they thus do not lead to desirable improvements of the optogenetic properties of ChR2. The existing structure of a C1C2 chimera (a fusion of the five first α-helixes of ChR1 and the two last α-helixes of ChR2) does not explain all the properties of the native channel, and thus cannot be used as a completely reliable basis for the rational design of enhanced optogenetic tools.

New approaches to membrane protein expression and crystallisation were developed in this work, making it possible to collect the high-quality crystallographic data required to determine the crystal structures of both wild type ChR2 and its C128T mutant at 2.4 and 2.7 Å resolution, respectively. Analysis of the structures, obtained at beamline **ID23-1**, showed that the core structure of channelrhodopsin consists of four cavities (extracellular cavity 1 (EC1), EC2, intracellular cavity 1 (IC1), and IC2, see **Figure 26**) separated by three flexible constrictions that act as gates (extracellular gate (ECG), central gate (CG), and intracellular gate (ICG)). The cores of ECG and ICG (R120 and

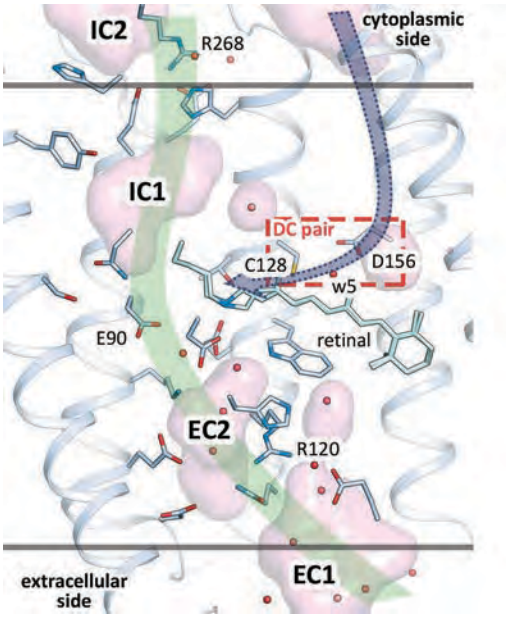


**Fig. 26:** Four cavities and three gates forming the ChR2 channel pore. The DC gate is highlighted with a red box. Pathways for the putative ion channel and the reprotonation of the Schiff base are shown in green and grey, respectively.

R268, respectively) are conserved in all ChRs. The retinal Schiff base (RSB) is connected by hydrogen bonds to amino acids E123 and D253 and is the key part of the CG, further connected with two other gates through an extended H-bond network mediated by numerous water molecules. Based on the crystal structures, a molecular mechanism of the channelrhodopsin function was proposed. When the protein is exposed to blue light, the retinal isomerises and the chain of water molecules breaks, causing a synchronised opening of the three gates and producing a pore extending the entire length of the protein. The DC gate (C128 and D156 pair) is separated from the gates in the channel pathway and is bridged by hydrogen bonds through the water molecule w5 (**Figure 26**). It stabilises α-helices 3 and 4 and provides connection from D156, a possible proton donor, to the RSB. The presence of hydrogen bonds provides structural insights into how the DC gate controls the ChR2 gating lifetime.

The results obtained represent a milestone in optogenetics. They enable a better understanding of how light-controlled channels work and open up the possibility of constructing new channels with specific properties for use in certain optogenetic scenarios.

PRINCIPAL PUBLICATION AND AUTHORS

Structural insights into ion conduction by channelrhodopsin 2, O. Volkov (a), K. Kovalev (a, b, c, d), V. Polovinkin (a, b, c, e), V. Borshchevskiy (c), C. Bamann (f), R. Astashkin (b, c), E. Marin (c), A. Popov (g), T.s Balandin (a), D. Willbold (a, b, h), G. Büldt (c), E. Bamberg (f), V. Gordeliy (a, b, c), *Science* **358**, eaan8862 (2017); doi: 10.1126/science.aan8862.

*(a) Institute of Complex Systems–6: Structural Biochemistry, Research Centre Jülich (Germany)*
*(b) Institut de Biologie Structurale Jean-Pierre Ebel, Université Grenoble Alpes–CEA–CNRS, Grenoble (France)*
*(c) Moscow Institute of Physics and Technology (Russia)*
*(d) Institute of Crystallography, University of Aachen (Germany)*
*(e) ELI Beamlines, Institute of Physics, Czech Academy of Sciences (Czech Republic)*
*(f) Max Planck Institute of Biophysics, Frankfurt am Main (Germany)*
*(g) ESRF*
*(h) Institut für Physikalische Biologie, Heinrich-Heine-Universität* Düsseldorf (Germany)

# STRUCTURE OF A NEWLY DISCOVERED CLASS OF UBIQUITIN E3 LIGASE

**Ubiquitination is a prevalent posttranslational modification involving the covalent attachment of the small protein ubiquitin to protein substrates. E3 ligase enzymes, of which there were understood to be three main classes, transfer ubiquitin to lysine residues within their specific substrates. A high-resolution structure of a novel class of ubiquitin-ligating enzyme reveals the unappreciated mechanistic diversity and substrate scope of these important enzymes.**

Protein ubiquitination regulates a vast array of cellular processes involved in both health and disease **[1]**. E3 ligases (E3s) operate at the end of a multienzyme cascade (E1-E2-E3) and typically conjugate the carboxy terminus of ubiquitin to lysine residues, forming an amide-linked isopeptide bond. Hundreds of E3s exist and were thought to be made up of only three main classes – HECT, RING and RBR **[2]**. Data collection at beamline **ID23-1** led to the high-resolution structure determination of a fourth class of E3 ligase. This RING-Cys-Relay (RCR) E3 found in the neuronal MYCBP2/Phr1 protein changes the way we should think about protein ubiquitination.

HECT and RBR E3s bind the upstream 'ubiquitin-charged' E2 enzymes and form a covalent intermediate with ubiquitin through linkage to a single catalytic cysteine residue. The RCR E3, however, has not one but two catalytic cysteine residues (**Figure 27**). The upstream cysteine accepts ubiquitin from the upstream E2 and the residue resides within a dynamic region termed the mediator loop. This loop region was found to be disordered within the obtained structural model and it is proposed, supported by biochemical experiments, that the inherent flexibility of this mediator loop, allows the RCR E3 to transfer the attached ubiquitin molecule to a downstream catalytic cysteine residue. The two cysteine residues are found in a novel zinc-binding protein fold dubbed the tandem cysteine domain. Such a ubiquitin relay mechanism has never been observed for E3s before, but is reminiscent of the protein splicing mechanism of inteins **[3]**.

Why the RCR E3 enzyme uses the relay mechanism is not clear but it may be due to its unexpected substrate specificity. Once the downstream cysteine receives the ubiquitin, it can transfer it to threonine residues, thereby forming a chemically distinct ester bond between substrate

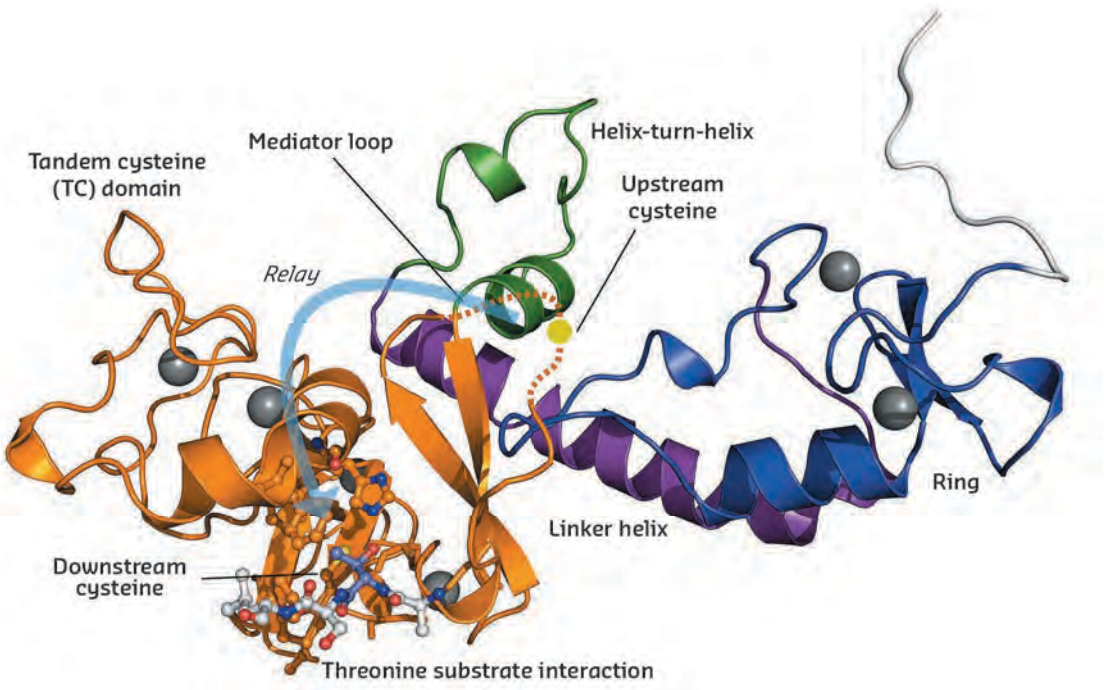


**Fig. 27:** Crystal structure of the RCR E3 ligase machinery from MYCBP2. RING domain (blue) serves as a docking site for the ubiquitin-charged E2 enzyme. The ubiquitin is transferred from E2 to the upstream catalytic cysteine residue. The residue is in a mobile region known as the mediator loop. Movement of the mediator loop allows relay of the ubiquitin to a downstream catalytic residue. Both of these residues reside within a novel zinc-binding domain known as the tandem cysteine domain (orange). A crystal packing interaction places a threonine-containing motif proximal to the downstream site.

and ubiquitin. Insights into the structural basis of this threonine selectivity were obtained from a fortuitous packing interaction in the crystal. An N-terminal threonine motif in the crystallisation construct was found to be docked into the active site of a neighbouring molecule centred around the downstream catalytic cysteine (**Figure 28**). A histidine residue appears to serve as a general base, pointing towards the threonine side chain hydroxy group. Furthermore, the methyl group of the threonine side chain docks into a hydrophobic pocket formed by a cluster of three phenylalanine residues. One explanation for the relay mechanism is that these active site requirements for threonine selectivity are incompatible with the direct transfer of ubiquitin from the E2 enzyme. Consistent with this, the downstream cysteine appears to be otherwise inaccessible but the mediator loop is optimally tuned to deliver the bulky ubiquitin cargo to it.

As MYCBP2 has a role in driving a neurodegenerative process known as Wallerian degeneration, the structural characterisation of the novel, and seemingly unique, E3 ligase machinery may offer therapeutic opportunities for the treatment of a range of neurological conditions.

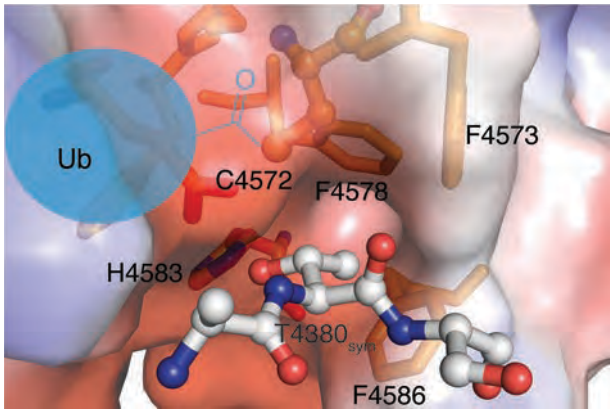


**Fig. 28:** A packing interaction appears to mimic a threonine-containing substrate peptide. H4583 acts as a general base, pointing towards the threonine side chain hydroxy group. Phenylalanines F4573, F4578 and F4586 form a hydrophobic pocket that can act as a selectivity determinant for the threonine side chain. C4572 is the downstream catalytic cysteine that becomes charged with ubiquitin via the relay mechanism. The threonine hydroxy group is positioned to attack the activated thioester bond in the charged E2–ubiquitin conjugate.

## PRINCIPAL PUBLICATION AND AUTHORS

Activity-based E3 ligase profiling uncovers an E3 ligase with esterification activity, K.-C. Pao (a), N. T. Wood (a), A. Knebel (a), K. Rafie (b), M. Stanley (b), P. D. Mabbitt (a), R. Sundaramoorthy (b), K. Hofmann (c), D. M. Van Aalten (b) and S. Virdee (a), *Nature* **556**, 381–385 (2018); doi: 10.1038/s41586-018-0026-1.
*(a) MRC Protein Phosphorylation and Ubiquitylation Unit, University of Dundee (UK)*
*(b) Division of Gene Regulation and Expression, School of Life Sciences, University of Dundee (UK)*
*(c) Institute for Genetics, University of Cologne (Germany)*

## REFERENCES

[1] A. Hershko and A. Ciechanover, *Annu. Rev. Biochem.* **67**, 425–479 (1998).
[2] N. Zheng and N. Shabek, *Annu. Rev. Biochem.* **86**, 129–157 (2017).
[3] K. V. Mills *et al., J. Biol. Chem.* **289**, 14498–14505 (2014).

# A NEW TWIST IN THE MECHANISM OF THE BACTERIAL GroEL/GroES CHAPERONIN SYSTEM

**The chaperonin GroEL (a cylindrical double-ring complex) and its cofactor, GroES, mediate protein folding. The two rings of GroEL have been found to transiently separate in an ATP-dependent reaction. Crystal structures of a GroEL mutant with covalently linked rings have been solved and support the conclusion that ring separation is part of the chaperonin cycle.**

Proteins are synthesised as linear chains of amino acids but must fold into unique three-dimensional structures for functional activity. To fold efficiently on a biologically relevant time scale, many proteins rely the assistance of molecular chaperones to avoid misfolding and aggregation in the crowded cellular environment.

The best-studied chaperonin system is the bacterial GroEL and its cofactor, GroES **[1]**. GroEL consists of two heptameric rings of ~60 kDa subunits that are stacked back-to-back. Each ring provides a cavity for the binding of protein substrate. GroES is a heptameric ring of ~10 kDa subunits that binds and dissociates from the ends of the GroEL cylinder in a reaction cycle allosterically controlled by the GroEL ATPase activity. A non-folded substrate protein binds at the inside rim of the cylinder to hydrophobic residues exposed by the apical GroEL domains. Binding of ATP, followed by GroES, displaces the substrate protein into an enclosed cage for folding to occur unimpaired by aggregation.

How GroEL ring opening and closing is orchestrated by ATP binding and hydrolysis, and the exact nature of the structural intermediates in the folding cycle are questions that are only partially understood. GroES can either bind to only one ring of GroEL (asymmetric cycle, GroEL:GroES complexes populated) or to both rings (symmetric cycle, GroEL:GroES$_2$ complexes populated) **[1]**. Consequently, the two rings have been proposed to function in substrate folding either sequentially or in parallel, respectively. The relative contribution of these proposed reaction mechanisms to overall chaperonin action is a matter of debate.

Analysis of the GroEL/GroES reaction revealed that the two GroEL rings transiently separate during the chaperonin folding cycle. Ring separation occurs upon ATP binding to the free ring (the trans-ring) of the asymmetric GroEL:ADP:GroES complex (**Figure 29**) and can result in ring exchange between GroEL complexes.

To test the functional relevance of this step in the chaperonin cycle, cysteine residues were engineered into the GroEL ring-ring interface, which formed covalent disulphide bonds, preventing ring separation. Crystal structures of this cysteine mutant were determined in two conformational states at beamline **ID30A-1** (MASSIF-1) by screening a large number of crystals to identify the best-diffracting volumes in large crystals by X-ray rastering, as implemented in an automated data collection workflow **[2]**. The resulting crystallographic models suggest that formation of the disulphide bonds does not distort the structure compared to wild-type GroEL (**Figure 30**), consistent with biochemical characterisation, which revealed normal ATP-regulated inter-ring allostery. However, in contrast to wild-type GroEL, the disulphide-bonded GroEL mutant populates only symmetric GroEL:GroES$_2$ complexes (**Figure 30**), as proposed in the symmetric reaction cycle.

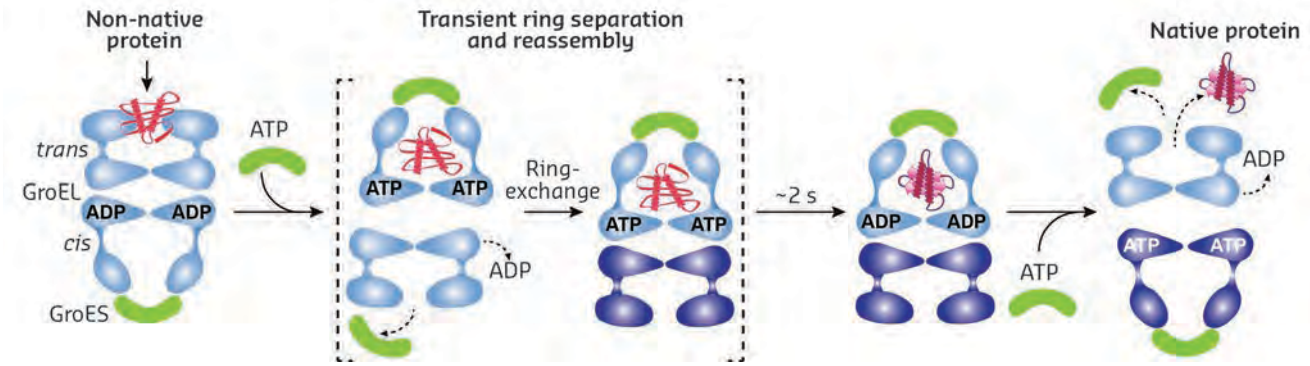


**Fig. 29:** A schematic of the reaction cycle of GroEL and GroES in protein folding. Substrate protein binds to the open ring of GroEL:ADP:GroES complex. ATP and GroES binding trigger conformational changes that result in the release of bound substrate into a nano-cage for folding to proceed in isolation. Concomitantly, the GroEL rings separate and can exchange. The encapsulated protein attempts to fold to the native state during the time needed for ATP hydrolysis (~2 s at 37°C). Finally, binding of ATP and GroES to the opposite ring opens the cage and the native protein is released.

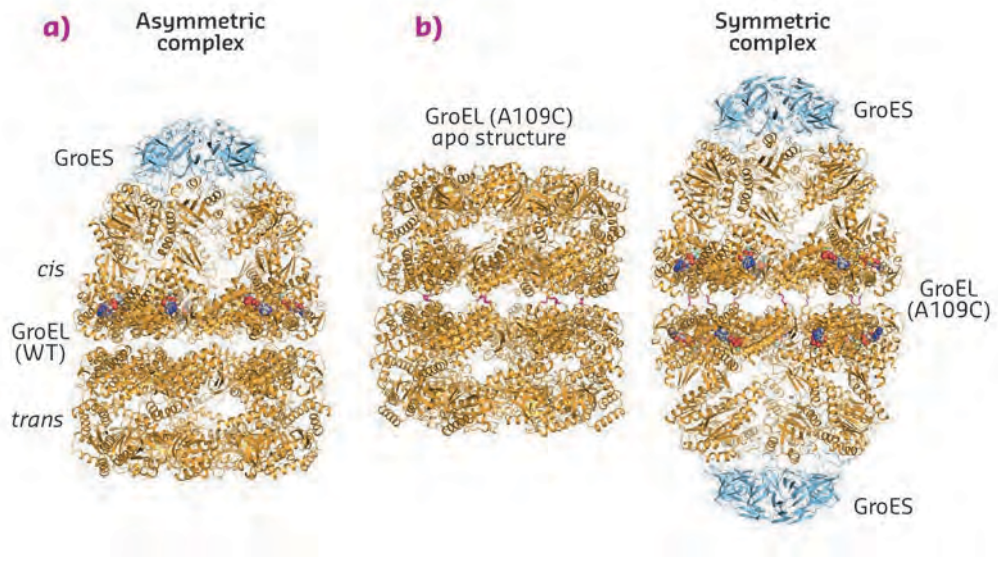


**Fig. 30:** ***a)*** Ribbon representation of the GroEL:ADP:GroES asymmetric complex (PDB 1PQC). **b)** Crystal structures of apo-GroEL mutant (A109C) (left panel; PDB 5OPW) and the symmetric complex (right panel; PDB 5OPX). The disulphide bonds between the rings are shown in magenta with the bound ADP molecules shown in a space-filling representation (multicoloured).

Furthermore, the mutant displayed a reduced efficiency in substrate protein release and binding. Consistent with the essential function of GroEL/GroES in *Escherichia coli*, the mutant could not substitute for wild-type GroEL *in vivo*, especially under conditions of heat stress, when pre-existing proteins unfold and increasingly interact with the chaperonin system. These results suggest that enforcing a symmetric reaction cycle reduces the functionality of the chaperonin.

This study of the bacterial GroEL/GroES system provides a mechanistic model for the chaperonin reaction. This could lead to several applications, given that homologs of GroEL occur in mitochondria (Hsp60) and in chloroplasts (Cpn60). Mutations in the human Hsp60 cause hereditary spastic paraplegia and chloroplast Cpn60 is required for the folding of Rubisco, the abundant photosynthetic enzyme that catalyses the fixation of atmospheric carbon dioxide.


PRINCIPAL PUBLICATION AND AUTHORS

GroEL Ring Separation and Exchange in the Chaperonin Reaction, X. Yan (a), Q. Shi (b), A. Bracher (a), G. Miličić (a), A. K. Singh (a), F. U. Hartl (a) and M. Hayer-Hartl (a), *Cell* **172**, 605–617 (2018); doi: 10.1016/j.cell.2017.12.010.

*(a) Max Planck Institute of Biochemistry, Martinsried (Germany)*
*(b) iHuman Institute, Shanghai (China)*

REFERENCES

[1] M. Hayer-Hartl *et al., Trends Biochem. Sci*. **41**, 62–76 (2016).
[2] M. W. Bowler *et al., J. Synchrotron Radiat*. **22**, 1540–1547 (2015).


# A MULTI-DRUG RESISTANCE REGULATOR TRANSFORMED INTO AN ARTIFICIAL HEME ENZYME


**An artificial heme enzyme was created through the self-assembly of hemin and the lactococcal multi-drug resistance regulator (LmrR). Although X-ray diffraction data suggest the enzyme is inactive, catalytic activity was observed. This work proposes that structural dynamics in the protein may be key to achieving catalytic activity and should be taken into account in the design of artificial enzymes.**


Enzymes are increasingly utilised in organic synthesis, due to their ability to catalyse reactions with high efficiency, specificity and stereoselectivity. The application of biocatalysts mostly relies on exploiting their natural biological activities, using these as starting points for protein engineering towards altered substrate specificity and stereoselectivity. Alternatively, enzymes can be created by a supramolecular approach, by anchoring a non-protein catalyst to a non-catalytic protein scaffold. This latter approach was successfully used here to create an artificial heme enzyme based on the lactococcal multi-drug resistance regulator protein LmrR.

LmrR is a DNA-binding multi-drug induced regulator of antibiotic resistance in *Lactococcus lactis*. It forms a homodimer with a large central hydrophobic pore at the dimeric interface, which serves as the drug-binding site **[1]**. Two tryptophan residues (Trp96 and Trp96') in the central pore are essential for the binding of

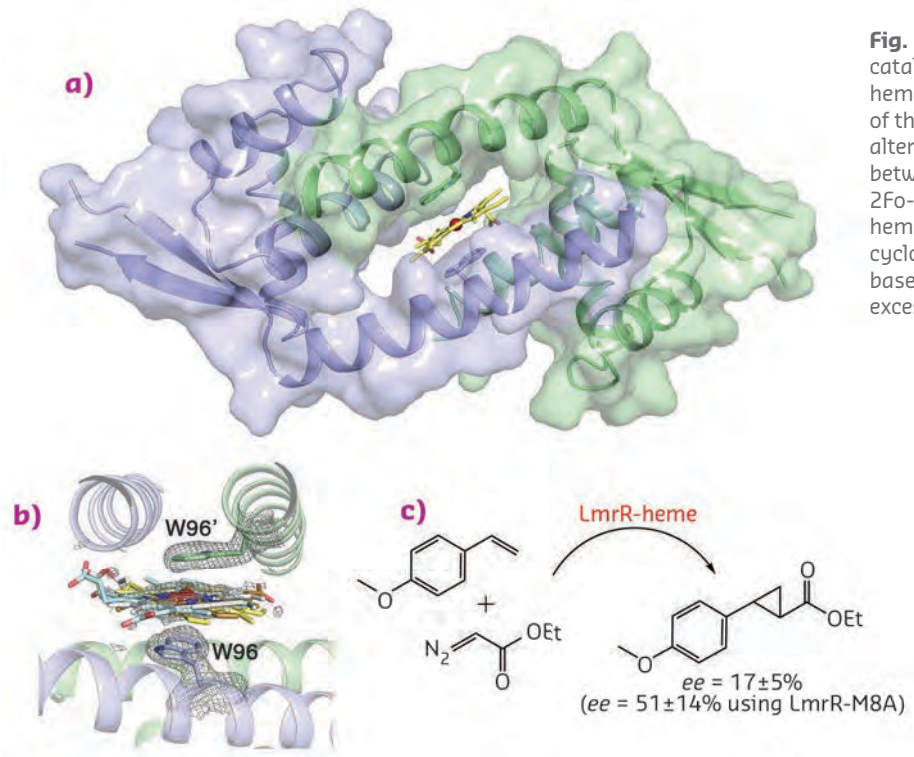


**Fig. 31:** Structure and activity of the LmrR-heme catalyst. ***a)*** Overall crystal structure of the LmrR–heme complex (PDB ID: 6FUU). **b)** Close-up view of the heme-binding site, showing the modelled alternate binding modes of the heme stacked in between the side chains of the W96/W96' pair. 2Fo-Fc omit electron density for W96, W96' and the heme is shown as a mesh. **c)** The enantioselective cyclopropanation reaction catalysed by the LmrR-based artificial heme enzyme. The enantiomeric excess (*ee*) is for the trans isomer of the product.

ligands, which are mostly planar heterocyclic compounds. Previous studies showed that the drug-binding pocket of LmrR is highly suitable for the creation of a novel active site through the anchoring of a catalytically active copper complex **[2]**. Using a similar approach, a heme group was added to the protein in order to create an artificial heme protein catalyst. Using X-ray diffraction data collected at beamline **ID30A-3** (MASSIF-3), the crystal structure of the LmrR–heme complex was determined at 1.75 Å resolution (**Figure 31a**). The structure confirms that the heme is stacked in between the side chains of W96/W96'. Due to a lack of specific stabilising interactions with its polar substituents, the heme adopts alternate binding modes, resulting in considerable disorder (**Figure 31b**). As a consequence, clear electron density is observed only for the porphyrin ring. In all binding modes, the heme iron is shielded on either side of the heme by the indole ring of W96 and W96' and lies at an average distance of around 4 Å from the carbon atoms, thus suggesting cation–π interactions.

The LmrR–heme protein displayed good activity and moderate enantioselectivity in the catalytic cyclopropanation of styrenes (**Figure 31c**), both of which were further improved by site-directed mutagenesis and optimisation of reaction conditions. The observed activity of the LmrR–heme protein seems difficult to reconcile with the crystal structure, showing a bound heme that appears inaccessible to substrates. Molecular dynamics studies, however, indicate that the protein–heme assembly is highly dynamic, and that the artificial enzyme can open up to allow formation of precatalytic structures. This work illustrates the versatility of LmrR as a scaffold for artificial metalloenzyme design and shows how such enzymes can be applied in the catalysis of new-to-nature reactions.

## PRINCIPAL PUBLICATION AND AUTHORS

An artificial heme enzyme for cyclopropanation reactions, L. Villarino (a), K. E. Splan (b), E. Reddem (a), L. Alonso-Cotchico (c), C. Gutiérrez de Souza (c), A. Lledós (c), J.-D. Maréchal (c), A. M. Thunnissen (d) and G. Roelfes (a), *Angew. Chem. Int. Ed.* **57**, 7785–7789 (2018); doi: 10.1002/anie.201802946.

*(a) Stratingh Institute for Chemistry, University of Groningen (The Netherlands)*
*(b) Department of Chemistry, Macalester College Saint Paul, Minnesota (USA)*
*(c) Departament de Química, Universitat Autònoma de Barcelona (Spain)*
*(d) Groningen Biomolecular Sciences and Biotechnology Institute, University of Groningen (The Netherlands)*

## REFERENCES

[1] P. K. Madoori *et al., EMBO J.* **28**, 156–166 (2009).
[2] J. Bos *et al., J. Am. Chem. Soc.* **137**, 9796–9799 (2015).

# EPITOPE SPECIFICITY DETERMINES ACTIVITY OF ANTI-CANCER ANTIBODIES

**Monoclonal antibodies directed against immune receptors are providing potent tools for treating cancer and autoimmune disease. The structures of antibodies binding to these receptors can deliver information that is critical to the understanding and development of next generation immune-therapeutics.**

Antibodies are not only creating blockbuster drugs to treat autoimmune disease **[1]**, they also offer a realistic hope of curing certain cancers **[2]** by activating the immune system. One promising antibody target is CD40, a tumour necrosis factor receptor (TNFR) superfamily member expressed on antigen-presenting cells involved in regulating adaptive immunity **[3]**.

Monoclonal antibodies (mAb) targeting CD40 show activities ranging from agonistic (activatory) to antagonistic (inhibitory) but the rules determining activity are unclear. Using a comprehensive panel of mAb and a range of *in-vitro* and *in-vivo* approaches, agonistic activity was shown to be largely dependent on mAb epitope. Receptor domain deletion studies revealed a correlation between binding position and activity, with mAb binding to domains proximal to the membrane producing antagonistic responses, and membrane-distal mAb inducing agonistic responses (**Figure 32**). A crystal structure determined at beamline **ID23-1** showed an agonistic antibody fragment bound to CD40 and revealed the precise binding epitope. Superposition with the trimeric ligand-receptor complex showed that this interaction would not compete with binding of CD154 **[3]**, the physiological ligand of CD40 (**Figure 32**).

Agonism has previously been shown to be promoted through interaction of the mAb constant regions with FcγRIIB on adjacent cells **[1, 2]**. The current study therefore provides further insight into the structural requirements for this process. For the numerous mAb tested, those engaging epitopes in CRD1, the most membrane-distal CD40 domain, were agonistic (ChiLob 7/4, SGN40, CP870,893 and Lob 7/2), whereas those that bound CRD2-4 were not (**Figure 32**). These observations support the hypothesis that agonistic activity reflects a requirement for the mAb Fc to engage FcγRII on adjacent cells, while steric constraints prevent optimal FcγRIIB engagement for mAb that bind epitopes closer to the membrane.

Structure determinations like the one undertaken help rationalise these differences in biological activity. A simple sequence comparison can be used to highlight differences in antibody recognition for antibodies that bind similar epitopes, in the same domain, as shown for the comparison of the crystal structure with the SGN40 antibody, for which the precise structure is unknown (**Figure 33**). The knowledge obtained will allow the fine-tuning of anti-CD40 mAbs for desired activity. On-going work, based on a crystal structure determined at **ID23-2**, takes antibody flexibility into account, using

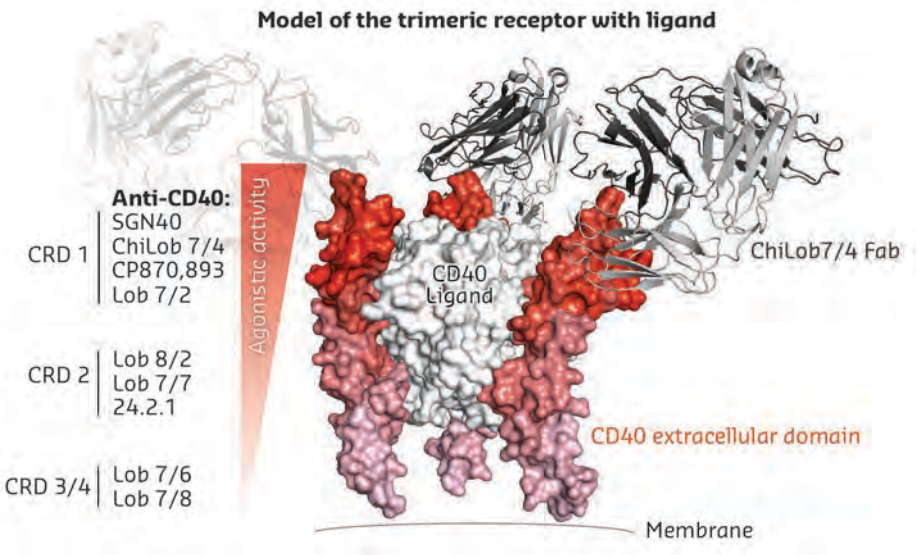


**Fig. 32:** Superposition of the structure of the complex between the extracellular portion of the CD40 receptor and the F(ab) fragment of the monoclonal antibody ChiLob 7/4 (PDB: 6FAX) with a CD40 receptor / ligand complex (PDB: 3QD6). The figure gives an impression of the potential spatial arrangement in the fully ligand-assembled trimeric receptor, with the cell surface indicated at the bottom. Epitope mapping for a number of antibodies grouped by binding to the individual CD40 cysteine rich domains (CRD, left) revealed that agonistic activity is associated with epitopes further away from the membrane. Antibodies produced for this study were Lob 7/2, Lob 7/6, Lob 7/7, Lob 7/8 and Lob 8/2; presently in clinical trials are ChiLob 7/4 **[5]**, SGN40, *dacetuzumab* **[6]** and CP870,893 **[7]**); the antibody 24.2.1 was generated from a patent-published sequence **[8]**.

a combination of small-angle scattering data collected at **BM29** and molecular dynamics simulations **[4]** to derive a dynamic picture of the interactions between antibody and cellular targets. This is relevant for other mAb targets, especially those targeting similar TNFRs capable of immune regulation.

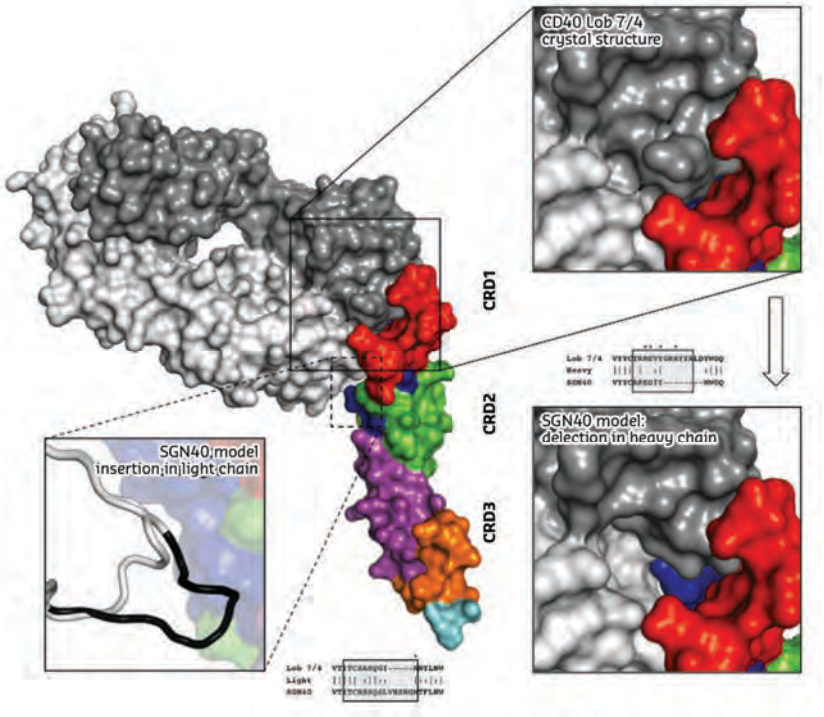


**Fig. 33:** The structure of the ChiLob 7/4 F(ab) fragment (grey) in complex with the extracellular portion of the CD40 receptor highlighting the cysteine rich domains (CRD) by colour (PDB 6FAX). A simple modelling exercise for the antibody SGN40 reveals epitope variation for mAb binding, predicting loss of one interaction with CRD1 (boxed) and gain of another interaction with CRD2 (dashed box); this would place the binding epitope for SGN40 further down the CD40 scaffold compared with ChiLob 7/4:CD40. These structure-based predictions rationalise the biological data obtained with epitope mapping studies.


PRINCIPAL PUBLICATION AND AUTHORS

Complex interplay between epitope specificity and isotype dictates the biological activity of anti-human CD40 antibodies, X. Yu (a), H. T. Chan (a), C. M. Orr (a), O. Dadas (a), S. G. Booth (a), L. N. Dahal (a), C. A. Penfold (a), L. O'Brien (a), C. I. Mockridge (a), R. R. French (a), P. Duriez (b), L. R. Douglas (b), A. R. Pearson (c), M. S. Cragg (a, d), I. Tews (d, e), M. J. Glennie (a) and A. L. White (a), *Cancer Cell* **33**, 664–675 (2018); doi: 10.1016/j.ccell.2018.02.009.

*(a) Antibody and Vaccine Group, Cancer Sciences Unit, University of Southampton Faculty of Medicine (UK)*
*(b) Protein Core Facility, University of Southampton Faculty of Medicine (UK)*
*(c) Hamburg Centre for Ultrafast Imaging & Institute for Nanostructure and Solid State Physics, University of Hamburg (Germany)*
*(d) Institute for Life Sciences, University of Southampton (UK)*
*(e) Biological Sciences, University of Southampton (UK)*

REFERENCES

[1] M. Croft *et al., Nat. Rev. Drug Discov.* **12**, 147–168 (2013).
[2] R. H. Vonderheide and M. J. Glennie, *Clin. Cancer Res.* **19**, 1035–1043 (2013).
[3] I. S. Grewal and R. A. Flavell, *Annu. Rev. Immunol.* **16**, 111–135 (1998).
[4] E. J. Sutton *et al.*, *Biophys. J.* **115**, 289–299 (2018).
[5] P. Johnson *et al.*, *Clin. Cancer Res.* **21**, 1321–1328 (2015).
[6] M. Hussein *et al.*, *Haematologica* **95**, 845–848 (2010).
[7] R. H. Vonderheide *et al.*, *J. Clin. Oncol.* **25**, 876-883 (2007).
[8] US patent 2009/0130715.


# STRUCTURAL INSIGHT INTO $O_2$-TOLERANCE OF A MEMBRANE-BOUND [NiFe]-HYDROGENASE USING HIGH-PRESSURE OXYGEN CRYSTAL DERIVATISATION

**Hydrogen is one of the seven currently available renewable energy resources. Its production is mainly linked to energy-generating power plants using fossil fuels. In recent years, the focus for clean hydrogen production has moved to biological sources, such as hydrogenases, through direct bio-photolysis and biofuel cells.**

Hydrogenases are the crucial players in biological hydrogen conversion. Whereas most are irreversibly inactivated by oxygen, a small subgroup of [NiFe]-hydrogenases remains active under aerobic conditions. This makes them attractive targets for studies on the mechanisms of $O_2$-tolerance. An important member of this subgroup is the membrane-bound, oxygen-tolerant [NiFe]-hydrogenase of the Knallgas (hydrogen oxidising) bacterium *Ralstonia eutropha* (*Re*MBH) **[1, 2].** Previous studies revealed major differences in the hydrophobic

tunnel network between $O_2$-sensitive and $O_2$-tolerant hydrogenases **[3]**, but, until now, the actual route of $O_2$ travel through these enzymes remained elusive, mainly due to the technical limitations of visualising weakly interacting gases like $O_2$ in the crystal structures of proteins. This study aimed to track the route of $O_2$ in *Re*MBH using X-ray crystallography in conjunction with a novel high-pressure oxygen device and an improved soak-and-freeze technique developed at the ESRF **[4, 5]**.

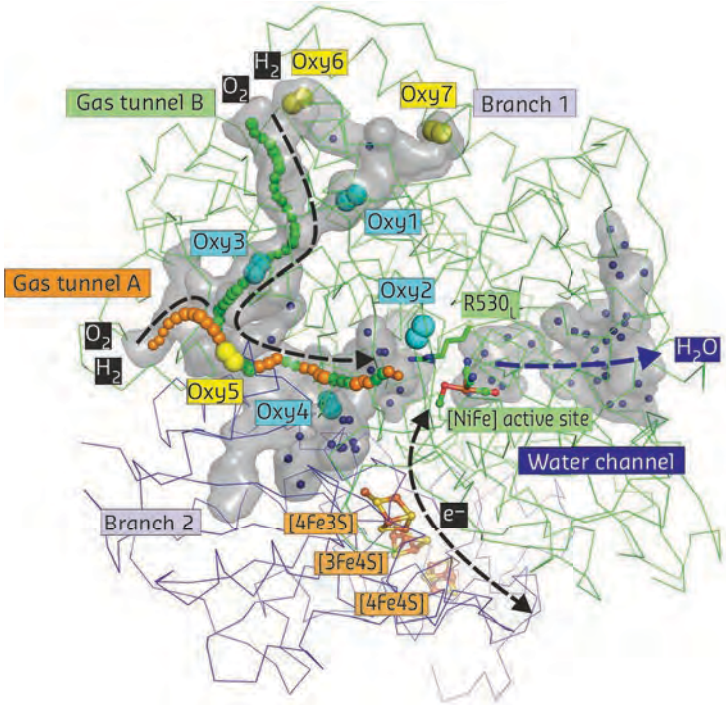


**Fig. 34:** Substrate/product flow in *Re*MBH (PDB entry 5MDL). OXY1-7 are shown in cyan and yellow spheres.

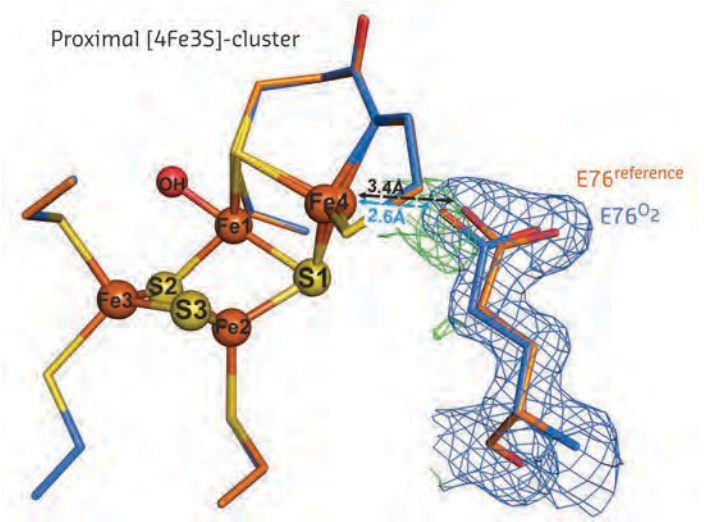


**Fig. 35:** Superposition of $O_2$-derivatised (blue) and non-derivatised (orange) *Re*MBH shows an $O_2$-dependent movement of Glu76 towards the FeS-cluster (shown in the 2*m*Fo-*D*Fc [blue mesh] and $Fo^{O2} - Fo^{Reference}$ [green mesh] electron density maps contoured at 1σ and 3σ, respectively.)

*Re*MBH is composed of three subunits: a large subunit with a deeply buried [NiFe]-active site where the reversible catalytic reaction $H_2 \Leftrightarrow 2e^- + 2H^+$ takes place; a small subunit containing an electron relay of three different [FeS]-clusters (**Figure 34**, $e^-$ black dashed arrow) that transfer the electrons derived from $H_2$ oxidation to the third subunit, a membrane-integral cytochrome, $b_{562}$.

The active site and the protein exterior are linked through a complex hydrophobic tunnel network (**Figure 34**, grey surface). Under $O_2$ attack, electrons are redirected from the electron relay to the [NiFe]-active site to reduce $O_2$ to water (**Figure 34**, $O_2$ and $e^-$ black dashed arrows). The water molecules are released through a nearby water channel (**Figure 34**, blue dashed arrow).

In the soak-and-freeze technique application, which differs fundamentally from other derivatisation methods, crystals are flash frozen in the corresponding liquefied gas while still under high pressure. This facilitates crystal derivatisation using difficult-to-handle, highly mobile gases like krypton or even molecular oxygen. To determine the migration pathway of $O_2$ to the active site, *Re*MBH crystals were harvested using specially designed sample supports for a higher throughput and direct use at the beamline. Twelve crystals were $O_2$-derivatised in a cryogenic oxygen pressure cell at 56 – 70 bar for between 15 – 70 minutes. Crystals were flash-frozen in liquefied oxygen and transferred to liquid nitrogen before data collection at beamline **ID29**.

This improved method of crystal derivatisation made it possible to show the $O_2$-pathway within the hydrophobic tunnel network of a hydrogenase. Through comparison of $Fo^{O2}$ – $Fo^{Reference}$ difference electron density maps calculated using an $O_2$-derivatised data set and a non-derivatised reference data set, seven molecular oxygen positions were detected within the *Re*MBH tunnel system, describing a continuous pathway between the protein exterior and the active site. The $O_2$ routes were later confirmed by computational methods (molecular dynamics simulations and protein tunnel calculations using the program *CAVER* **[6]**). Unexpectedly, the $O_2$-derivatisation also led to structural changes at the proximal FeS-cluster (**Figure 35**), which is located next to the active site. This unique [4Fe3S]-cluster is believed to be involved in recovery from $O_2$ attack by redirecting electrons to the active site for oxygen reduction. The structural changes suggest a connected mechanism between the active site, the [4Fe3S]-cluster, and its surrounding amino acids for regulation of enzyme activity under aerobic conditions.

PRINCIPAL PUBLICATION AND AUTHORS

Tracking the route of molecular oxygen in O2-tolerant membrane-bound [NiFe] hydrogenase, J. Kalms (a*), A. Schmidt (a), S. Frielingsdorf (b), T. Utesch (b), G. Gotthard (c), D. Von Stetten (c**), P. Van der Linden (c, d), A. Royant (c, e), M. A. Mroginski (b), P. Carpentier (c, f), O. Lenz (b) and P. Scheerer (a), *Proc. Natl. Acad. Sci. USA* **115**(10), e2229–e2237 (2018); doi: 10.1073/pnas.1712267115.
*(a) Charité-Universitätsmedizin Berlin, Institut of Medical Physics und Biophysics (CC2), Group Protein X-ray Crystallography and Signal Transduction, Berlin (Germany) (b) Institut für Chemie, Technische Universität Berlin (Germany) (c) ESRF (d) Partnership for Soft Condensed Matter (PSCM), Grenoble (France) (e) Université Grenoble Alpes, CNRS, CEA, IBS, Grenoble (France). (f) Université Grenoble Alpes, CNRS, CEA, Institut de Biosciences et Biotechnologies de Grenoble (BIG)-Laboratoire Chimie et Biologie des Métaux (LCBM), Grenoble (France) * Present address: Institute for Structural and Chemical Biology (LISCB), University of Leicester (UK) ** Present address: European Molecular Biology Laboratory (EMBL), Hamburg Outstation c/o DESY (Germany)*

REFERENCES

[1] J. Fritsch *et al., Nature* **479**, 249–252 (2011).
[2] S. Frielingsdorf *et al., Nat. Chem. Biol.* **10**, 378–385 (2014).
[3] J. Kalms *et al., Angew. Chem. Int. Ed. Engl.* **55**, 5586–5590 (2016).
[4] P. Van Der Linden *et al., J. Appl. Crystallogr.* **47**, 584–592 (2014).
[5] B. Lafumat *et al., J. Appl. Crystallogr.* **49**, 1478–1487 (2016).
[6] E. Chovancova *et al., PLOS Comput. Biol.* **8**, e1002708 (2012).

# DEVELOPING SERIAL SYNCHROTRON CRYSTALLOGRAPHY AT THE ESRF

**Aiming at the recent renewed interest in multi-crystal techniques, scientists at the ESRF and at the EMBL Hamburg have developed new workflows for serial synchrotron crystallography (SSX), incorporating improvements in mesh scan analysis techniques, the development of user-friendly dataset analysis and merging software, and methodology to increase the success of SSX-based experimental phasing.**

Even relatively weak X-ray sources can cause significant radiation damage in macromolecular crystals at room temperature, given enough time. In the very earliest days of macromolecular crystallography, partial data sets from multiple crystals were thus frequently required to assemble a complete dataset **[1]**. With the introduction of cryo-cooling, however, it became possible to routinely collect complete diffraction datasets from single crystals and such multiple crystal techniques were all but forgotten. Recently, spurred by major developments at X-ray free electron lasers and synchrotron sources, multi-crystal techniques have seen a renewed interest, and a wide variety of cryo- and ambient temperature sample delivery platforms that facilitate these have been developed.

In the Structural Biology group at the ESRF, particular effort has been made towards enabling so-called 'fixed target' approaches. In particular, the 'mesh-and-collect' workflow was developed **[2]**. This automatically makes a diffractive map of a user-specified region of a fixed target, followed by the automatic collection of partial datasets from each position identified in the map. However, these kind of experiments introduce new challenges, such as the identification of the boundaries of crystals and regions where multiple crystals overlap. They also make the classic problem of non-isomorphism significantly more complex. If these challenges can be overcome, multi-crystal techniques offer exciting possibilities for pushing the boundaries of *in crystallo* dynamics and experimental phasing. To this end, three studies have recently been published, describing work performed by ESRF scientists and their collaborators.

Proper centring of a crystal in the X-ray beam and accurate estimation of crystal sizes have a crucial impact on the final quality of data. Melnikov *et al.* have developed an analysis method (*MeshBest*) for X-ray mesh/grid scans for determining the dispositions and characteristics of protein crystals contained in a sample holder (**Figure 36**). First, mesh scan images recorded at grid points in the sample area are analysed for the presence of protein diffraction with the program *Dozor*. Next, mesh scan areas are grouped based on diffraction pattern similarity, and a 'crystal map' illustrating different crystal areas in the sample holder can be built (including regions that contain overlapping crystals). The resulting information provides better estimates of absorbed doses to be used in mesh-and-collect experiments and, in some

cases, incident beam sizes could be dynamically changed to match the crystal size.

Once partial datasets have been collected, users are confronted with the potential problem of non-isomorphism between crystals. Newly developed tools to address this problem include down-weighting poor or poorly merging datasets, grouping datasets via correlations on reflection intensities using cluster analysis **[3]**, and grouping datasets based on merging statistics via genetic algorithms **[4]**. While cluster analysis has seen widespread use, there has been a notable lack of user-friendly software to streamline its use. Santoni *et al.* have recently released the *ccCluster* program (**Figure 37**). *ccCluster* calculates the correlation coefficient of all the common reflections between all the possible pairs of datasets and uses it to define a distance. Next, a hierachical cluster analysis based on those distances allows the user to define groups with high correlation, each of which can be merged via the software interface. This allows different populations of partial datasets to be

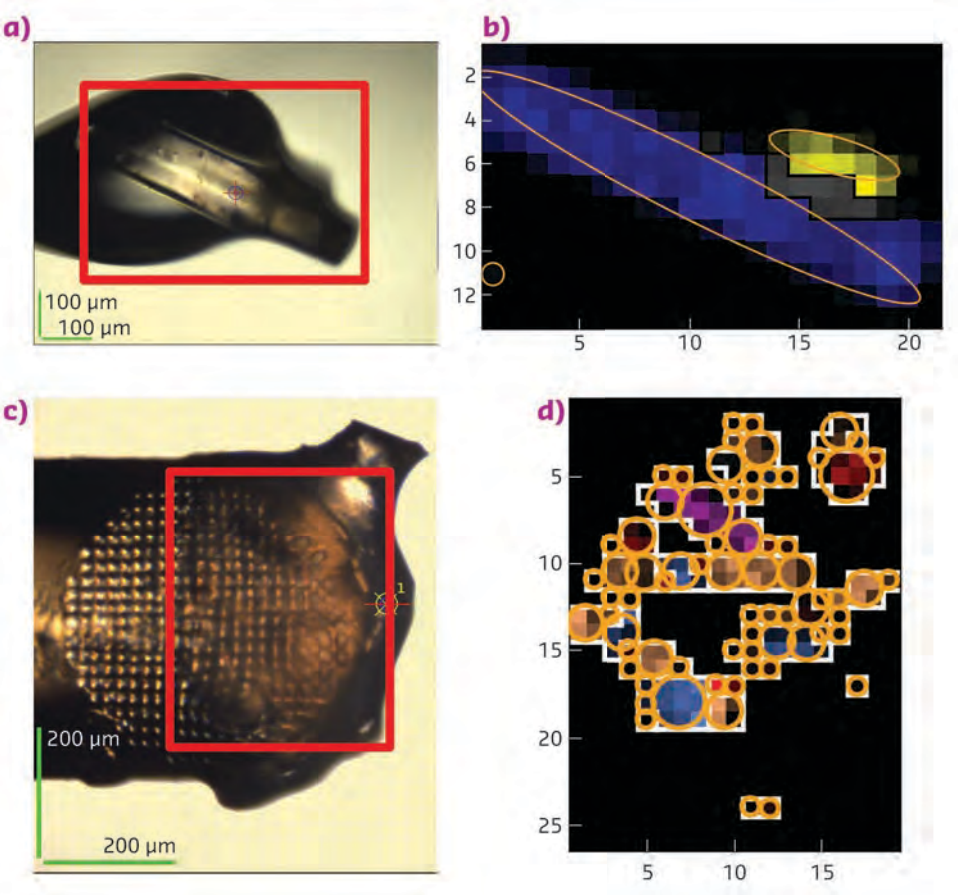


**Fig. 36:** Application of *Dozor-MeshBest* analysis. Here, two examples are presented. **a)** Analysis of a single crystal of thermolysin. Here, a mesh scan was performed in the area indicated by the red rectangle and subsequent analysis revealed the presence of a small satellite crystal (yellow in the crystal map shown in **(b)**). The crystal areas were then approximated with ellipses. **c)** Analysis of NarQ crystals distributed on a micromesh sample holder. A mesh scan was performed in the area indicated by the red rectangle and the analysis determined the dispositions of the crystals in the area, as shown on the crystal map in **(d)**. Multi-crystal 'mesh-and-collect' **[1]** data collection could then be carried out at the positions indicated by orange circles, potentially varying beam size at each position corresponding to the circle size.

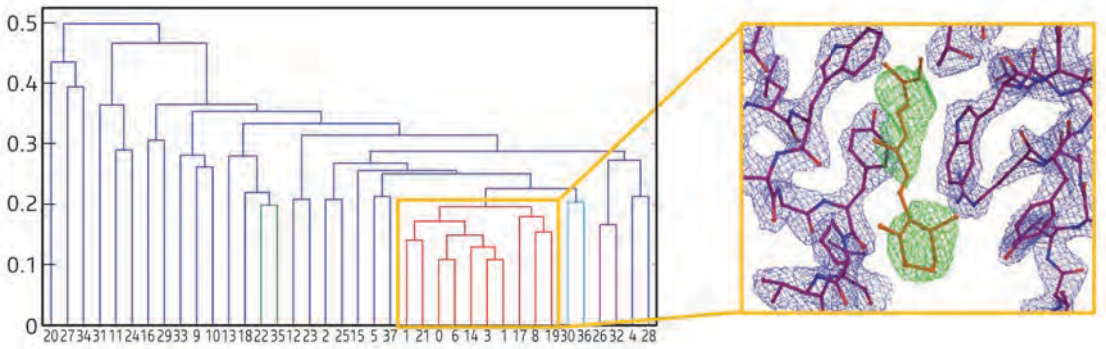


**Fig. 37:** An example of hierarchical cluster analysis applied to protein serial crystallography. The software *ccCluster* was used to compare 38 partial datasets. The dendrogram helps to find those that are most isomorphous. The partial data sets in the orange square are those used to solve the protein structure shown in the inset (electron density shown as a blue mesh). The quality of the resulting data set is high enough to allow the visualisation of a ligand in a $F_{calc} - F_{obs}$ difference map (green mesh).

easily and appropriately grouped, and can lead to large improvements in data quality compared to simply merging all available data.

Multi-crystal experiments can be especially problematic in experimental phasing. One method of experimental phasing that is particularly sensitive is radiation damage-induced phasing (RIP, **[5]**). In a RIP experiment, specific radiation damage to sensitive chemical groups in the crystal can be used to determine the structure of the entire molecule. However, the signal can easily be lost in noise due to non-isomorphism and/or non-specific radiation damage. These two problems made it unclear whether RIP could work for multi-crystal experiments. Foos *et al.* showed that not only can it work, but when paired with a genetic algorithm it can greatly increase the success rate of phasing (**Figure 38**). This is due to optimising the selection of partial datasets to merge, and to the greatly increased data quality at a given dose afforded by using many crystals.

Together, these developments will extend the usability and utility of multi-crystal data collection at the ESRF and elsewhere, and provide the foundation for further advances in this exciting new field.

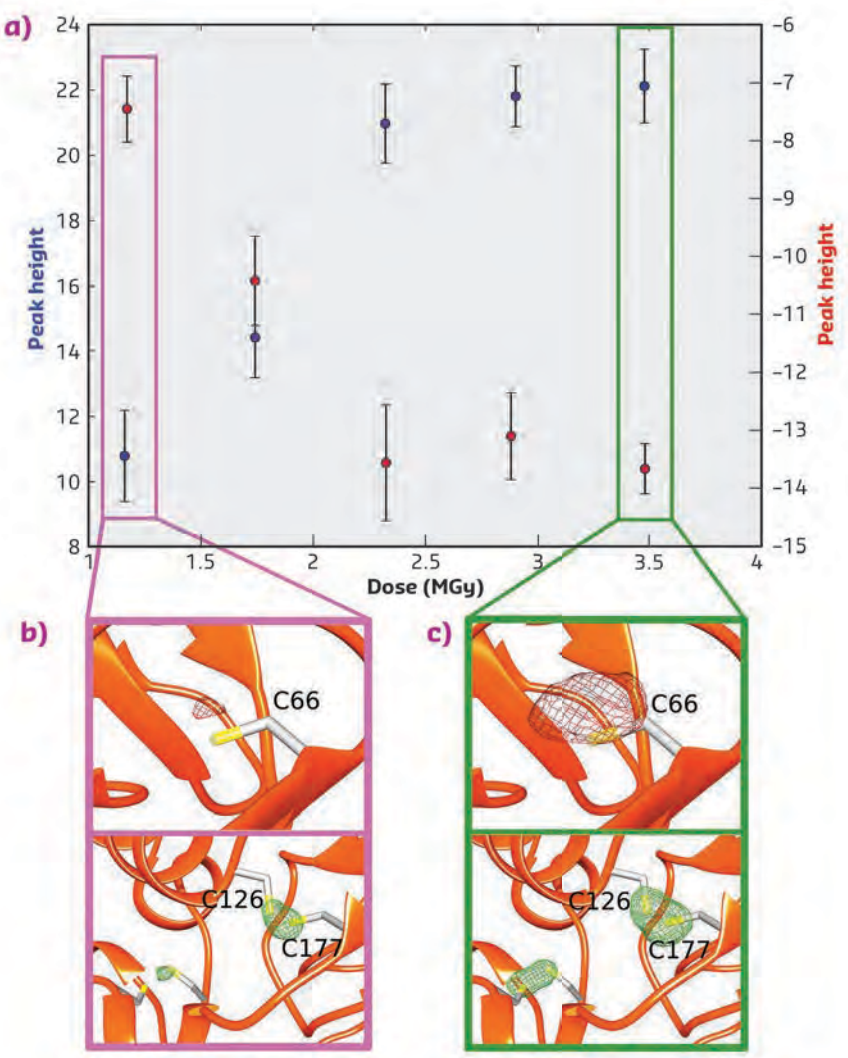


**Fig. 38: a)** RIP peak height as a function of absorbed dose in a SSX experiment using crystals of thaumatin. Maximum (blue point) and minimum (red point) peak heights (σ) in the model-phased $F_{before} - F_{after}$ difference electron-density maps. Average values in circles, with error bars. **b)** and **c)** Model-phased RIP difference electron-density maps calculated for the SSX RIP data at two doses. Difference density is shown as a green mesh contoured at 6σ. Negative difference electron density shown as red mesh contoured at 6.5σ.

## PRINCIPAL PUBLICATIONS AND AUTHORS

The complex analysis of X-ray mesh scans for macromolecular crystallography, I. Melnikov (a), O. Svensson (a), G. Bourenkov (b), G. Leonard (a) and A. Popov (a), *Acta Cryst.* ***D74,*** 355–365 (2018); doi: 10.1107/S2059798318002735.

Hierarchical clustering for multiple-crystal macromolecular crystallography experiments: the ccCluster program, G. Santoni (a), U. Zander (c), C. Mueller-Dieckmann (a), G. Leonard (a) and A. Popov (a), *J. Appl. Cryst.* **50**, 1844–1851 (2017); doi: 10.1107/S1600576717015229.

X-ray and UV radiation-damage-induced phasing using synchrotron serial crystallography, N. Foos (a), C. Seuring (d, e), R. Schubert (e, f, g), A. Burkhardt (h), O. Svensson (a), A. Meents (d), H. N. Chapman (d, e, i) and M. H. Nanao (a), *Acta Cryst.* ***D74***, 366–378 (2018); doi: 10.1107/S2059798318001535.

*(a) ESRF*
*(b) European Molecular Biology Laboratory, Hamburg Outstation (Germany)*
*(c) European Molecular Biology Laboratory, Grenoble Outstation (France)*
*(d) Center for Free-Electron Laser Science, Deutsches Elektronensynchrotron (Germany)*
*(e) The Hamburg Centre for Ultrafast Imaging (Germany)*
*(f) Integrated Biology Infrastructure Life-Science Facility at the European XFEL (XBI) (Germany)*
*(g) Institute for Biochemistry and Molecular Biology, University of Hamburg (Germany)*
*(h) Photon Science, Deutsches Elektronensynchrotron (Germany)*
*(i) Department of Physics, University of Hamburg (Germany)*

## REFERENCES

[1] J. Kendrew *et al.*, *Nature* **185**, 422–427 (1960).
[2] U. Zander *et al.*, *Acta Cryst.* ***D71***, 2328–2343 (2015).
[3] R. Giordano *et al.*, *Acta Cryst.* ***D68***, 649–658 (2012).
[4] U. Zander *et al.*, *Acta Cryst.* ***D72***, 1026–1035 (2016).
[5] R. Ravelli *et al.*, *Structure*, **11**, 217–224 (2003).

# SEVERAL SNAPSHOTS OF THE 5-HT3 SEROTONIN RECEPTORS IN ACTION

**Several three-dimensional structures of an important serotonin receptor involved in fast neurotransmission have been obtained. The structures reveal how the neurotransmitter serotonin and the anti-emetic drug tropisetron bind to the receptor. The structures also unveil how this receptor moves during its working cycle, and therefore help to clarify how it operates at the molecular level.**

Serotonin is a versatile neurotransmitter and neurohormone that plays diverse roles in, for example, mood regulation, development and gastrointestinal mobility. Among the large set of serotonin receptors, the 5-HT3 serotonin receptor is the best known through its pharmacology; 5-HT3 receptor inhibitors are widely used in drugs that alleviate nausea and vomiting for cancer patients undergoing radiotherapy or chemotherapy.

This study attempts to understand how the 5-HT3 receptors operate at the molecular level. Sitting in the membrane of an excitable cell (typically a neuron), the receptors provide cation-selective pores through the membrane that transiently open when serotonin is bound to the receptors. When these ions rush through the pores, the electrical potential of the cell is modified. The 5-HT3 receptors are thus ligand-activated ion channels and participate in fast neurotransmission, both in the central nervous system and in peripheral systems such as the enteric nervous system.

The 5-HT3 receptor was imaged using cryo-electron microscopy and four conformations were obtained at resolutions ranging from 3.2 Å to 4.5 Å. These conformations represent snapshots of the receptor along its functional cycle. They provide information on how its structure changes when the receptor is working. For instance, one inhibited conformation reveals what the binding site looks like when an antagonist (the anti-emetic drug tropisetron) is present. Another active conformation shows how the binding site is re-arranged when serotonin is bound, and also features an open pore permeant to cations. Of the four conformations imaged, the one with the best resolution (3.2 Å) was obtained using data from the Titan Krios cryo-electron microscope at beamline **CM01**. In this structure, the disposition of bound serotonin and its interactions can be seen in detail and without ambiguity. Serotonin fits tightly within its binding pocket in an orientation consistent with functional and binding studies, surrounded by a 'cage' of aromatic residues (**Figure 39**, inset).

While it was straightforward to assign the inhibited and active conformations to physiological states, two other intermediate structures – obtained in complex with serotonin but featuring a closed pore – were more complex to interpret. After integrating the structures with complementary functional experiments, including measuring the electric function of mutant receptors to probe motions in the pore, and carrying out *in silico* molecular dynamics simulations, it was proposed that the intermediate structures correspond to pre-active states. Put together, the data gave an insight into the molecular mechanism of operation of 5-HT3 receptors (**Figure 40**).

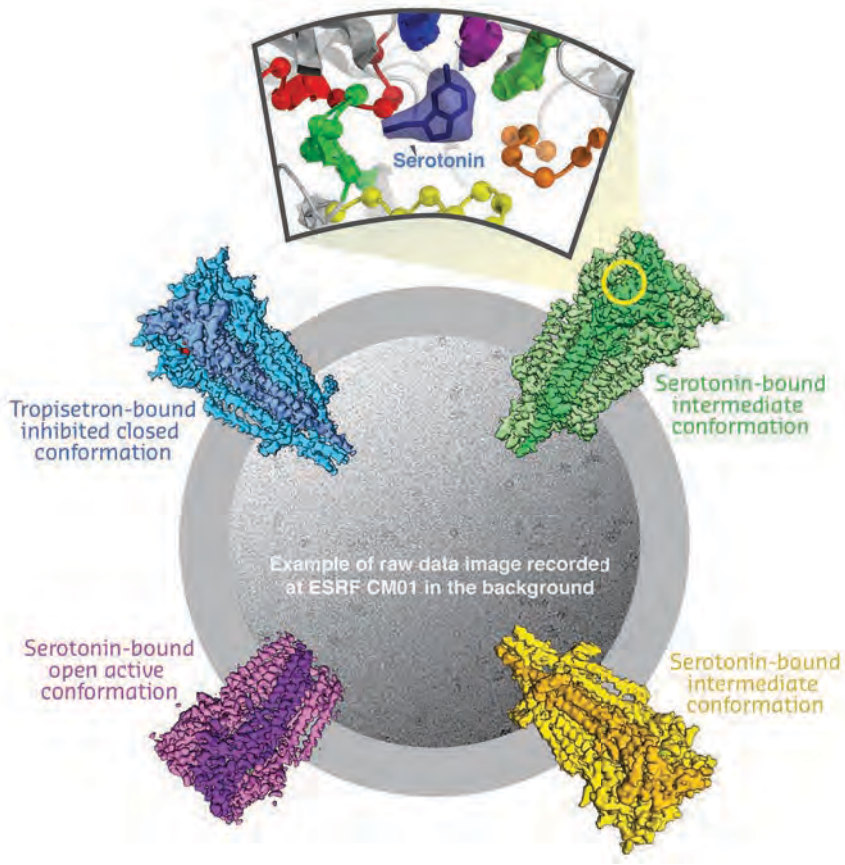


**Fig. 39:** The four conformations of the 5-HT3 serotonin receptor obtained by cryo-electron microscopy are shown. The green conformation was obtained at CM01 using several thousand images, such as the one presented in the background. An inset represents the binding site of serotonin with the experimental information shown as a blue surface.

The serotonin 5-HT3 receptor belongs to a family of proteins that also features receptors activated by acetylcholine (responsible for cigarette addiction) and by GABA (the target of drugs like Valium). In 2018 alone (in the experimental session during which the structures of the 5-HT3 receptors were elucidated), other researchers solved structures of its acetylcholine- or GABA-activated cousins **[1, 2]**, marking a notable acceleration in the pace of research in this field.

Together, these fundamental studies may help the rational design of new drugs targeting this important family of receptors.

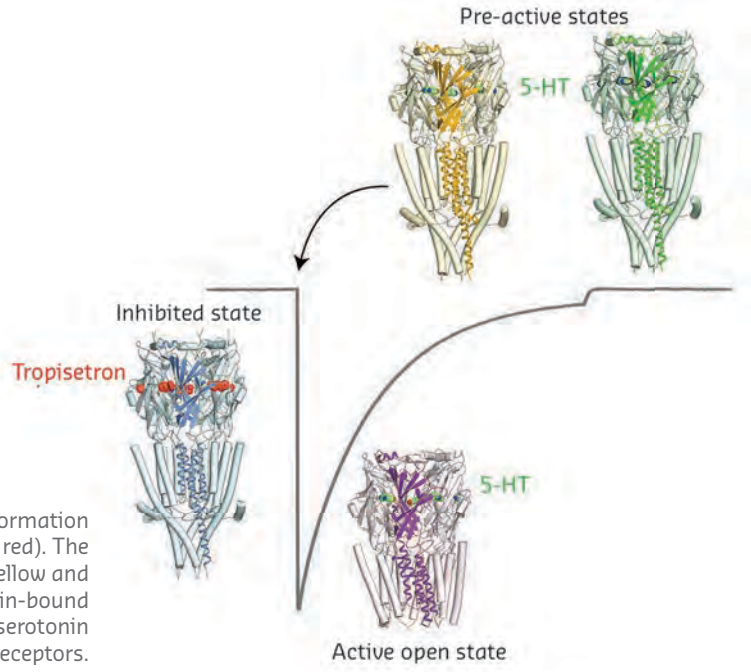


**Fig. 40:** Of the four conformations obtained, the blue conformation represents an inhibited state, stabilised by tropisetron (in red). The purple conformation represents an open, active state. The yellow and green conformations are likely to represent pre-active serotonin-bound states. The grey line illustrates the electrical response to serotonin recorded in a cell expressing 5-HT3 receptors.


PRINCIPAL PUBLICATION AND AUTHORS

Conformational transitions of the serotonin 5-HT3 receptor, L. Polovinkin (a), G. Hassaine (b), J. Perot (a), E. Neumann (a), A. A. Jensen (c), S. Lefebvre (d), P.-J. Corringer (d), J. Neyton (a), C. Chipot (e, f, g), F. Dehez (e, f), G. Schoehn (a) and H. Nury (a), *Nature* **563**, 275–279 (2018); doi: 10.1038/s41586-018-0672-3.

*(a) CNRS, Université Grenoble Alpes–CEA–IBS, Grenoble (France)*
*(b) Theranyx, Marseille (France)*
*(c) University of Copenhagen (Denmark)*
*(d) Channel Receptors Unit, CNRS UMR 3571, Institut Pasteur, Paris (France)*
*(e) Université de Lorraine, CNRS, LPCT, F-54000 Nancy (France)*
*(f) Laboratoire International Associé CNRS and University of Illinois at Urbana–Champaign, Vandoeuvre-les-Nancy (France)*
*(e) University of Illinois at Urbana–Champaign, Urbana (USA)*

REFERENCES

[1] R. M. Walsh *et al., Nature* **557**, 261–265 (2018).
[2] P. Miller *et al., bioRxiv* (2018); doi: 10.1101/338343.


# SUPPRESSION OF IMMUNE SIGNALLING BY THE INFLUENZA A VIRUS NS1 PROTEIN

**Crystal structures of the E3 ligase TRIM25 in its apo form and bound to influenza A virus NS1 reveal the mechanism by which NS1 suppresses TRIM25-catalysed RIG-I ubiquitination and thus the anti-viral host response.**

Infection by pathogens such as influenza virus is sensed by specific proteins of the innate immune system that constantly survey cells for invaders. The detection of viral components initiates a signalling cascade that results in the release of proteins that alert surrounding cells to mount an anti-viral defence. A combination of crystal structures and biochemical experiments have provided insight into the mechanism used by the influenza A virus non-structural protein 1 (NS1) to suppress the host immune response.

Infection of cells by pathogens is sensed by pattern recognition receptors (PRRs), which induce an appropriate host immune response. One such receptor is RIG-I, which senses viral RNA and activates a signalling pathway that results in the production of anti-viral interferons and pro-inflammatory cytokines **[1]**. A key step in this pathway is the ubiquitination of RIG-I by the E3 ubiquitin ligase TRIM25, which promotes RIG-I oligomerisation and downstream signalling **[2]**. This activity can be inhibited by the NS1 protein from influenza A virus to prevent RIG-I-mediated interferon expression **[3]**.

TRIM25 belongs to the TRIM family of RING-type E3 ligases. It consists of an N-terminal TRIM motif comprising the catalytic RING domain, B-box domains and a long coiled coil (CC) region

that mediates dimerisation of the protein in an anti-parallel manner. The C-terminal portion of TRIM25 contains a PRYSPRY domain that recognises the substrate RIG-I, to allow its modification with K63-linked polyubiquitin chains.

While the structure of the complete human TRIM25 homodimer remains elusive, a CC-PRYSPRY (residues 189-630) construct was crystallised. Using beamline **ID29**, diffraction spots were resolvable along a long *c*-axis of 827 Å, resulting in a 3.6 Å-resolution data set. The structure showed, for the first time, how and where the PRYSPRY domain is bound to the CC domain, although the linker between the domains is disordered (**Figure 41a**). Small-angle X-ray scattering (SAXS) carried out at **BM29** showed that the PRYSPRY domain–CC interaction is labile in solution but, nevertheless, disruption of the interaction by mutation results in the loss of TRIM25's ability to ubiquitinate RIG-I.

Crystal structures of complexes between the TRIM25 CC and influenza A NS1 were determined using data from Diamond Light Source. They show that NS1 effector domain (ED), but not its RNA binding domain (RBD), binds to the TRIM25 CC. Interestingly, the EDs of a given NS1 homodimer contact two different TRIM25 dimers, suggesting a mechanism whereby NS1-mediated higher order oligomerisation of the TRIM25-NS1 complex might be an important factor in the antiviral mode of action of NS1 (**Figure 41b**).

Superposition of the TRIM25 CC-PRYSPRY crystal structure with that of NS1-bound TRIM25 CC reveals that the PRYSPRY domain and NS1 both bind to the end of the coiled coil, though on opposite sides (**Figure 41c**). However, while the binding surfaces on the CC overlap only minimally, binding of NS1 necessitates the displacement of an extended loop of the coiled coil region, which is incompatible with simultaneous binding of the PRYSPRY. Taken together, the data suggest that NS1 does not interfere with RIG-I recognition by TRIM25 *per se*, but instead prevents the PRYSPRY domain from adopting a functionally competent conformation, in which the substrate RIG-I can get sufficiently close to RING domain-bound E2-ubiquitin conjugate to be modified with a K63-linked polyubiquitin chain (**Figure 42**).

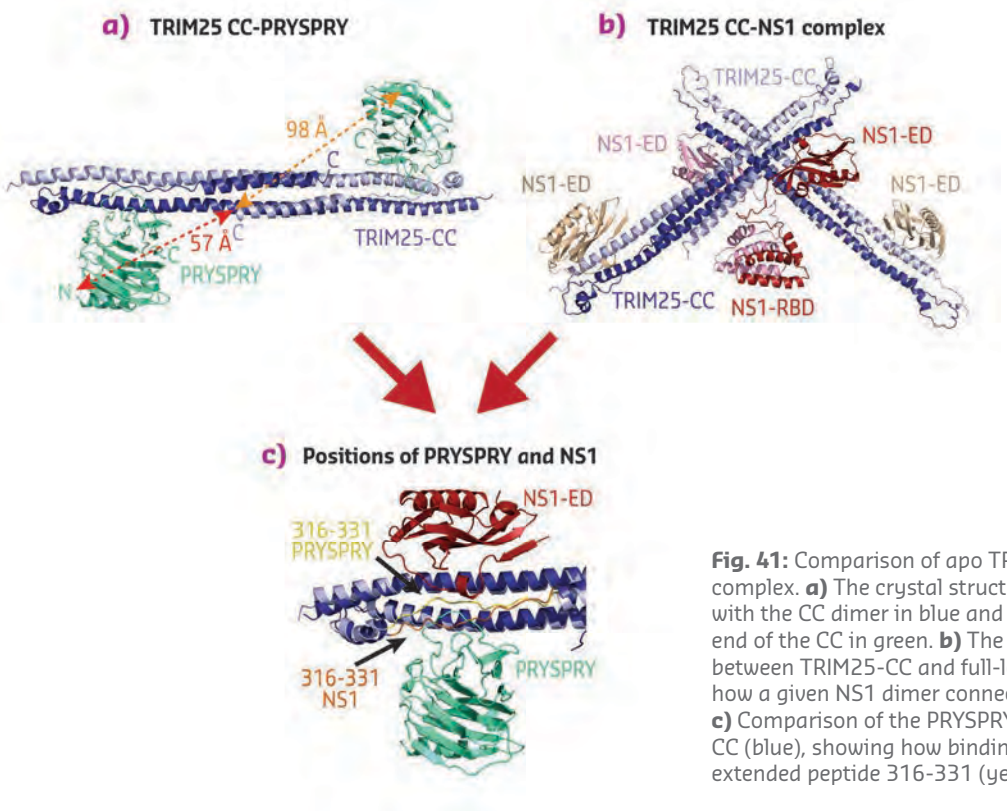


**Fig. 41:** Comparison of apo TRIM25 and a NS1-bound TRIM25 complex. **a)** The crystal structure of a TRIM25 CC-PRYSPRY fragment, with the CC dimer in blue and the PRYSPRY domains, located either end of the CC in green. **b)** The crystal structure of the complex between TRIM25-CC and full-length NS1 (asymmetric unit), showing how a given NS1 dimer connects 2 TRIM25-CC dimers. **c)** Comparison of the PRYSPRY (green) and NS1 (red) positions on the CC (blue), showing how binding of NS1 changes the position of CC extended peptide 316-331 (yellow and orange).

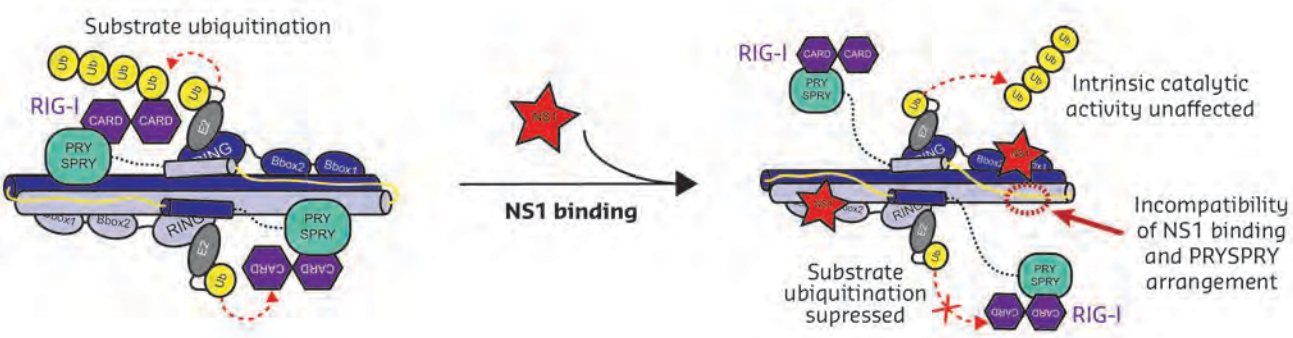


**Fig. 42:** Schematic diagram showing a model for how binding of NS1 may suppress substrate (RIG-I) ubiquitination by TRIM25.

PRINCIPAL PUBLICATION AND AUTHORS

Molecular mechanism of Influenza A NS1-mediated TRIM25 recognition and inhibition, M. G. Koliopoulos (a), M. Lethier (b), A. G. Van der Veen (c), K. Haubrich (d), J. Hennig (d), E. Kowalinski (b), R. V. Stevens (a), S. R. Martin (e), C. Reis e Sousa (e), S. Cusack (b) and K. Rittinger (a), *Nat. Commun.* **9**, 1820 (2018); doi: 10.1038/s41467-018-04214-8. CC BY 4.0. Figures adapted from original publication.

*(a) Molecular Structure of Cell Signalling Laboratory, The Francis Crick Institute, London (UK)*
*(b) European Molecular Biology Laboratory, Grenoble (France)*
*(c) Immunobiology Laboratory, The Francis Crick Institute, London (UK)*
*(d)* Structural and *Computational Biology Unit, European Molecular Biology Laboratory, Heidelberg (Germany)*
*(e) Structural Biology Science Technology Platform, The Francis Crick Institute, London (UK)*

REFERENCES

[1] S. Reikine *et al.*, *Front. Immunol.* **5**, 342 (2014).
[2] M. U. Gack *et al.*, *Nature* **479**, 916–920 (2007).
[3] M. U. Gack *et al.*, *Cell Host Microbe* **5**, 439–449 (2009).

# POTENTIAL THERAPEUTIC MOLECULES FOR THE SPECIFIC TREATMENT OF ACUTE MYELOID LEUKAEMIA

**Treatments for acute myeloid leukaemia (AML) that are based on the inhibition of casein kinase 1A1 (CKIα) target only a small group of patients exhibiting a specific form of the disease. Here, crystal structures of a new class of molecules with an improved anti-leukaemia profile reveal the molecular mechanisms of their activity.**

Acute myeloid leukaemia (AML) is an aggressive cancer of the bone marrow, causing production of abnormal white blood cells, red blood cells, and platelets. While recent investigations have shed light on its biological diversity and topography **[1]**, there has only recently been significant evolution in anti-AML therapies, which now include epigenetic modification of leukaemia cells **[2]**. Another potential anti-AML treatment is the activation of the tumour suppressor p53, which is reduced in AML due to an increased activation of the major p53 antagonist MDM2 **[3, 4]**. An obvious way of achieving this is via the development of MDM2 inhibitors **[5]**. However, an alternative approach is the inhibition of casein kinase 1A1 (CKIα).

In this work, a set of inhibitor molecules (A-series; **Figure 43a**) with very high levels of CKIα inhibition were produced. The crystal structures of the A86-CKIα (**Figure 43b**) and A86-CKIδ complexes were then determined at 2.3 Å and 1.6 Å resolution, respectively, using diffraction data collected at **ID30A-1**. A86 binds in the ATP binding pocket of CKIα where it interacts via hydrogen bonds to atoms of the amino acid residues Leu93 and Asp99, which form part of the CKIα hinge region. These two residues are conserved across the casein kinase 1 (CK1) family, and the crystal structure of the A86-CKIδ complexes confirms that these interactions form a common mechanism of CK1 inhibition by A86.

Some molecules in the A-series show high levels of potency only in leukemic cells, while

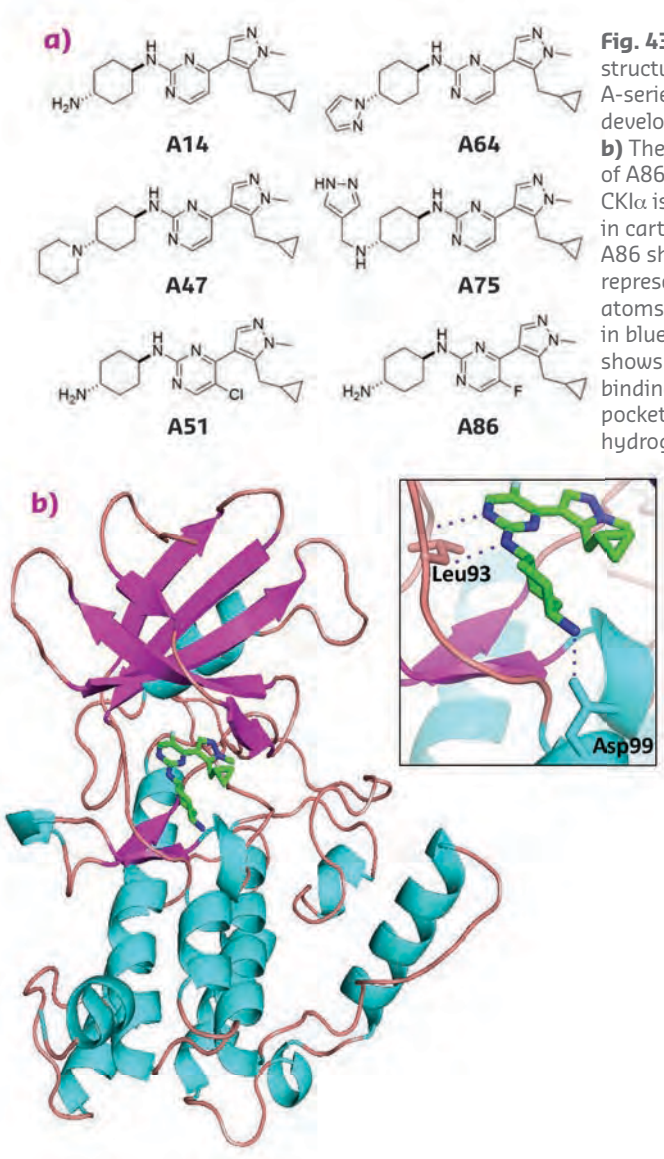


**Fig. 43: a)** Chemical structures of some of the A-series CKI inhibitors developed in this work. **b)** The crystal structure of A86-CKIα complex. CKIα is represented in cartoon style with A86 shown in stick representation (carbon atoms in green, nitrogen in blue). The inset shows a close-up of A86 binding in the CKIα ATP pocket, highlighting hydrogen bonds (blue dashed lines) and the hinge region Leu93 and Asp99, both of which are conserved in CK1 family members.  Figures adapted from original publication.

others are leukaemia-inactive. An assay of the binding of the major A-series molecules to important transcriptional kinases showed that the leukaemia-active compounds A51 and A86 strongly bind to, and show high inhibition of, CDK7 (TFIIH) and CDK9 (P-TEFb), two of the seven currently known transcriptional kinases. CDK7 enables transcriptional initiation, which is then paused until CDK9 facilitates transcription elongation. In contrast, the binding of leukaemia-inactive A64 to CDK7 and CDK9 is only moderate and poor, respectively. The crystal structure of P-TEFb (CDK9-cyclin T1) in complex with A86 (**Figure 44a**) was determined to 3.2 Å resolution, again using diffraction data collected on **ID30A-1.** A comparison of this crystal structure with that of CK1α-A86 (**Figure 44b**) shows that the inhibitor binds to the ATP pockets of the two kinases in a very similar manner, explaining the co-targeting of CKIα and CDK9 by A86.

In summary, a new category of kinase inhibitors has been discovered which, by co-targeting CKIα and the catalytic subunits of the transcriptional kinases CDK7 (TFIIH) and CDK9 (P-TEFb) in leukaemia cells, stabilise p53 production and eliminate the expression of the p53 master regulator and target gene MDM2. This combination of p53 activation and the transcriptional silencing of leukaemia-associated genes provides a huge step forward in the development of new anti-AML therapeutics.

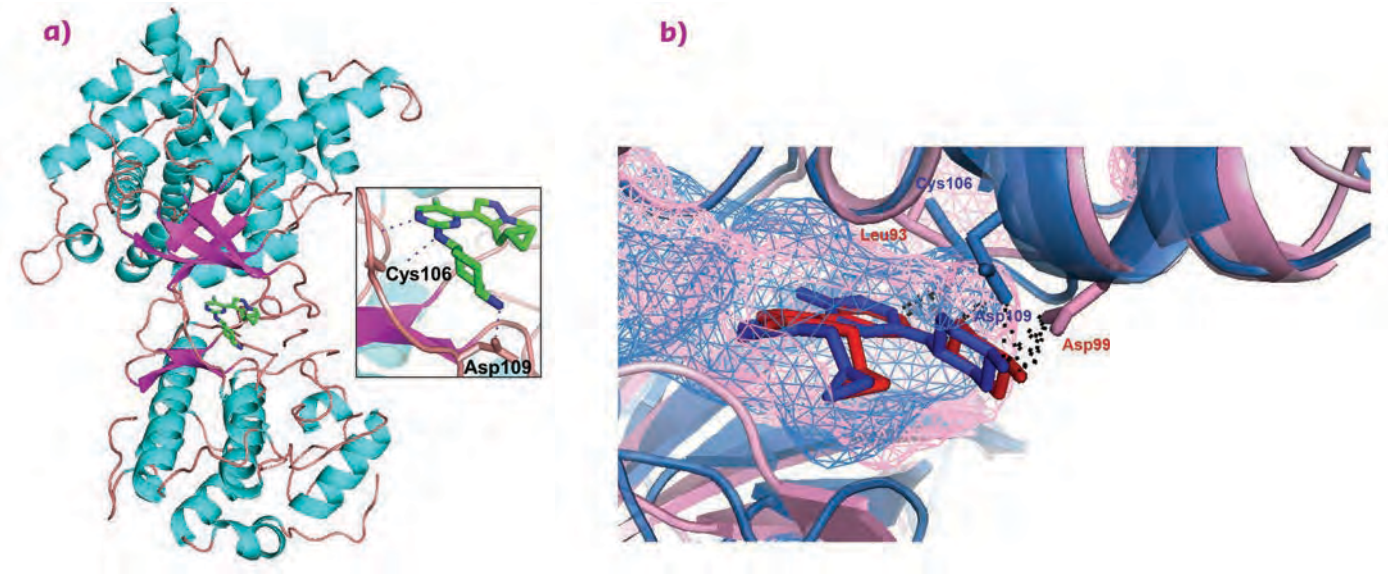


**Fig. 44: a)** The crystal structure of the complex formed between P-TEFb (CDK9-CycT1) and A86. Representation and colour scheme as shown in **Figure 43**. The inset shows a close-up of A86 binding in the P-TEFb ATP pocket (hydrogen bonds in blue dashed lines). **b)** A superposition of A86-CKIα (pink) and P-TEFb-A86 (blue) complexes focusing on ligand binding regions. Solvent accessible cavities are shown as pink and blue meshes, respectively.  Figures adapted from original publication.

## PRINCIPAL PUBLICATION AND AUTHORS

Small Molecules Co-targeting CKIα and the Transcriptional Kinases CDK7/9 Control AML in Preclinical Models, W. Minzel (a), A. Venkatachalam (a), A. Fink (a), E. Hung (a), G. Brachya (a), I. Burstain (a), M. Shaham (a), A. Rivlin (a), I. Omer (a), A. Zinger (a), S. Elias (a, b), E. Winter (c), P. Erdman (e), R. Sullivan (e), L. Fung (e), F. Mercurio (e), D. Li (f), J. Vacca (f), N. Kaushansky (g), L. Shlush (g), M. Oren (h), R. Levine (i), E. Pikarsky (a, d), I. Snir-Alkalay (a) and Y. Ben-Neriah (a), *Cell* **175**, 171–185 (2018); doi: 10.1016/j.cell.2018.07.045.

*(a) The Lautenberg Center for Immunology and Cancer Research, Institute of Medical Research Israel-Canada, Hebrew University-Hadassah Medical School (Israel)*
*(b) Department of Hematology, Hadassah Medical Center, Hebrew University-Hadassah Medical School (Israel)*
*(c) Bioinformatics Unit of the I-CORE Computation Center, Hebrew University-Hadassah Medical School (Israel)*
*(d) Department of Pathology, Hadassah Medical Center, Hebrew University-Hadassah Medical School (Israel)*
*(e) BioTheryX Inc., San Diego (USA)*
*(f) WuXi AppTec, Shanghai (China)*
*(g) Department of Immunology, Weizmann Institute of Science (Israel)*
*(h) Department of Molecular Cell Biology, Weizmann Institute of Science (Israel)*
*(i) Center for Hematologic Malignancies, Memorial Sloan Kettering Cancer Center, New York (USA)*

## REFERENCES

[1] E. Papaemmanuil *et al.*, *N. Engl. J. Med.* **374**, 2209–2221 (2016).
[2] J. Bradner *et al.*, *Cell* **168**, 629–643 (2017).
[3] K. Kojima *et al.*, *Exp. Hematol.* **44**, 791–798 (2016).
[4] B. Vogelstein *et al.*, *Nature* **408**, 307–310 (2000).
[5] A. Levine and M. Oren, *Nat. Rev. Cancer* **9**, 749–758 (2009).

# DECIPHERING THE MOLECULAR MECHANISM OF p300 ACTIVATION

**p300 is a chromatin-modifying enzyme, which regulates gene expression. X-ray diffraction data have helped to decipher the molecular mechanism that allows switching between inactive and active states of p300 and to understand the link between cellular signalling and the regulation of p300 activity, thus explaining why gene transcription is associated with chromatin acetylation.**

Eukaryotic cells have developed mechanisms to package DNA into chromatin. The nucleosome is the basic unit of chromatin, which consists of 147 base pairs of DNA wrapped around a histone octamer consisting of two copies of each histone: H2A, H2B, H3 and H4. During gene transcription, chromatin is remodeled and the nucleosome structure disrupted, allowing activation of specific genes. p300 is a chromatin-modifying enzyme with a histone acetyltransferase (HAT) activity. It introduces post-translational modifications (PTM) by covalently attaching acetyl groups to lysine residues on the nucleosome histone tails, producing a destabilisation of the nucleosome structure and thus activating gene expression. Such modifications on chromatin are sometimes considered to form an 'epigenetic layer' of the genome that ultimately controls genome function.

While it has been known for more than 50 years that chromatin acetylation is coupled to gene activation, the precise molecular mechanism has remained unclear. This work reports that transcription factor dimerisation activates the enzymatic function of p300. A critical regulatory element that controls p300 activity is a positively charged and lysine-rich auto-inhibitory loop (AIL) embedded in the HAT domain. This auto-inhibitory loop is highly acetylated when p300 is incubated with dimeric transcription factors (TF) but not when p300 is incubated alone or in the presence of inactive, monomeric TF (**Figure 45a**).

To understand the molecular mechanisms of p300 activation, diffraction data were collected at beamline **ID29** from the crystals of the core domain of the protein p300, which contains PTM reader domains (Bromo_PHD), a regulatory domain (RING) and the catalytic domain (HAT). The crystals diffracted to 3.1 Å resolution and the structure was determined by molecular replacement. This revealed two p300 molecules in an antiparallel arrangement, in which the AIL is loop-swapped with a neighbouring copy, in the crystallographic asymmetric unit (**Figure 45b**). In monomer II, the AIL extends away from the HAT domain and interacts with the substrate binding pocket of monomer I. Here, the RING domain of the monomer I is in an outward rotated conformation ~39° away from the HAT active site, resulting in an overall displacement by ~22 Å (**Figure 45c**). The outward conformation of the RING domain is stabilised by the interaction with the AIL of monomer II, thus resulting in a more open HAT active site, apparently to enable trans-acetylation of the AIL and activation of p300.

To understand this trans-auto-acetylation mechanism further, computational simulations were performed of the core domain of p300 in different states: inactive de-acetylated and active

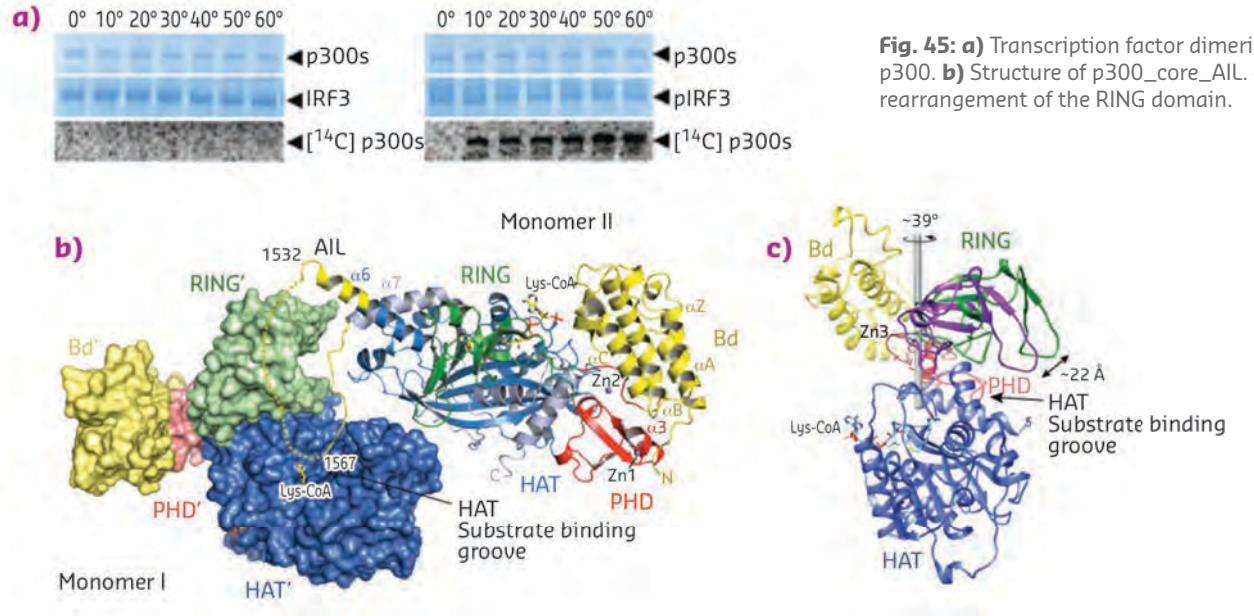


**Fig. 45: a)** Transcription factor dimerisation activates p300. **b)** Structure of p300_core_AIL. **c)** Structural rearrangement of the RING domain.

acetylated states of the AIL. These simulations revealed electrostatic interactions between the AIL and the RING domain and HAT substrate binding site in the inactive and de-acetylated form of p300. In contrast, in the acetylated and active state, no such interactions were seen. Accordingly, MALLS analysis showed that the de-acetylated form of p300 adopts a more compact conformation, due to the dynamic interaction of the AIL with the HAT substrate-binding site, while the acetylated form adopts a more open conformation.

Based on these findings, a model for p300 activation and signal integration to chromatin is proposed (**Figure 46**). The hypothesis is that in the basal state, p300 is in an inactive conformation, in which the AIL is de-acetylated and extends close to the enzyme's active site. This conformation of the AIL prevents the access of lysine-rich substrates. Cellular signalling initiates phosphorylation of TF, resulting in their dimerisation and activation. The activated-dimeric TF are then shuttled to the nucleus, where they are in their DNA-binding competent conformations, can engage two copies of p300 and increase the likelihood of AIL to be captured *in trans* by a second p300 molecule.

In summary, these findings help to understand how cellular signalling, TF activation and dimerisation controls p300 activation, thus explaining the long-standing observation that gene transcription is associated with chromatin acetylation. As p300 activation and concomitant chromatin acetylation is dependent on TF-mediated activation, chromatin acetylation arises in a DNA sequence-specific manner. Thus, histone-modifications do not form an independent 'epigenetic layer' of the genome but arise due to a DNA-targeted signalling reaction.

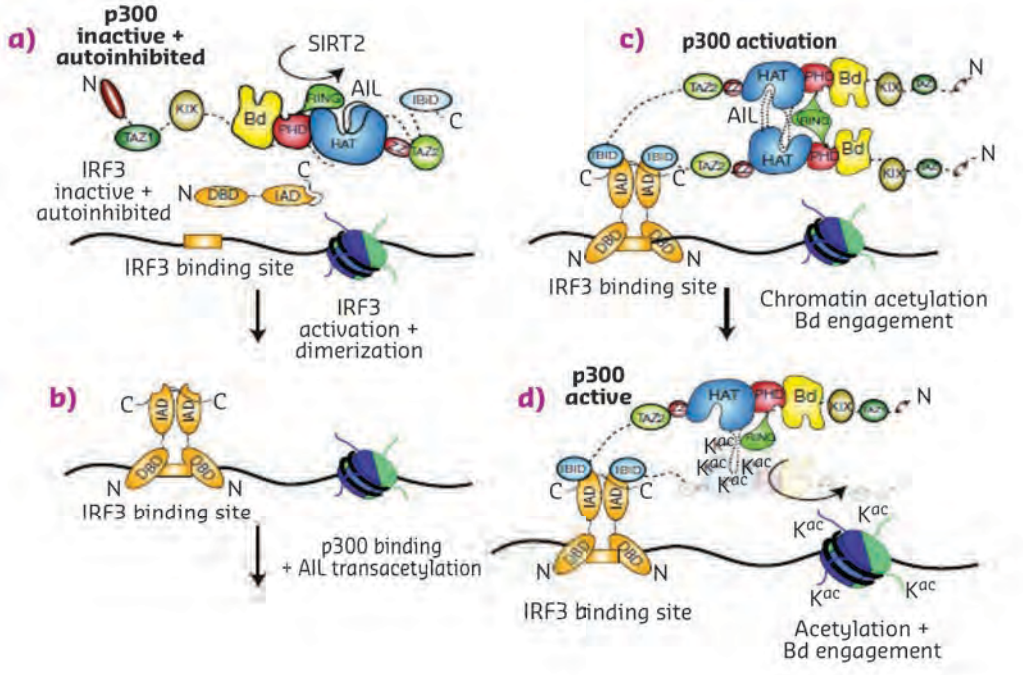


**Fig. 46:** Molecular model of p300 activation.

PRINCIPAL PUBLICATION AND AUTHORS

Transcription factor dimerization activates the p300 acetyltransferase, E. Ortega (a), S. Rengachari (a), Z. Ibrahim (a, b), N. Hoghoughi (c), J. Gaucher (a, e), A. Holehouse (d), S. Khochbin (c) and D. Panne (a, b), *Nature* **562**, 538–544 (2018); doi: 10.1038/s41586-018-0621-1.

*(a) EMBL, Grenoble (France)*
*(b) Leicester Institute of Structural and Chemical Biology, Leicester (UK)*
*(c) CNRS, Université Grenoble Alpes, Grenoble (France)*
*(d) Department of Biomedical Engineering and Center for Biological Systems Engineering, Washington University in St. Louis (USA)*
*(e) Université Grenoble Alpes, INSERM U1042, HP2 Laboratory, Grenoble (France)*

# BUILDING THE BLOCKS OF A BACTERIAL NANO-CROSSBOW

**The bacterial Type VI secretion system (T6SS) is a key player in microbial competition and is an important virulence factor during bacterial infections. Here, the cryo-electron microscopy structure of the wedge protein complex of the T6SS from enteroaggregative *Escherichia coli* (EAEC) is unveiled, offering detailed insights into its biogenesis and function.**

Bacterial Type VI secretion systems (T6SS) belong to the family of contractile injection systems (CIS) that also includes bacteriophages and high-molecular-weight tailocins **[1, 2]**.

CIS comprise a tail composed of an inner tube wrapped by a sheath, built under a baseplate. The T6SS tail tube/sheath is a 100 nm-long cytoplasmic structure. It is made up of TssB/C subunits that polymerise to form the contractile sheath that surrounds the attacking arrow, and is composed of an inner tube of stacked Hcp hexameric rings tipped by the trimeric VgrG puncturing spike. Various signals induce structural rearrangements of the sheath, leading to its contraction and the propulsion of the Hcp-VgrG arrow into the target cell. Assembly of the tail tube/sheath is initiated at the baseplate. During T6SS biogenesis, the baseplate docks to a trans-envelope complex composed of TssJ, TssL and TssM. By connecting the tail to the membrane complex and initiating tail tube/sheath polymerisation, the baseplate is a central piece of the T6SS machinery. In addition, as shown in **Figure 47**, by binding cargo effectors through VgrG, the T6SS baseplate also serves as an effector-sorting platform **[3]**. Besides the critical role of the T6SS baseplate complex, crucial information is still lacking on its biogenesis and architecture. Recently, the 8.5 Å-resolution structure of an assembled T6SS baseplate revealed its overall shape, but did not provide detailed information on the molecular organisation of its subunits.

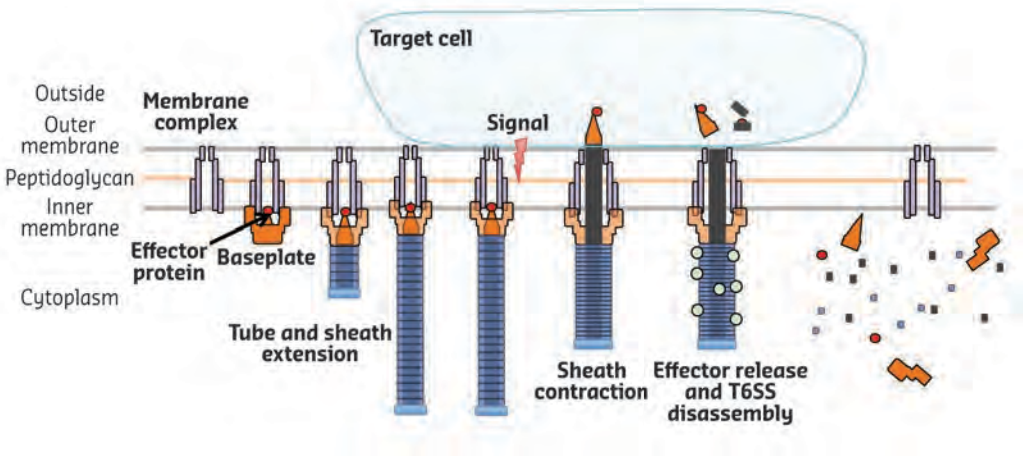


**Fig. 47:** Type VI secretion assembly and function. The membrane complex, composed of TssJ, TssL and TssM, is inserted in the bacterial cell envelope. The baseplate, a protein complex made of VgrG, TssK, TssF, TssG and TssE, binds to the membrane complex and mediates the Hcp tube and TssB/C sheath assembly in the bacterial cytoplasm. Upon contact with the target cell, the sheath contracts and expels the VgrG spike and Hcp tube through the membrane complex, delivering the effector proteins carried by the VgrG spike or within the Hcp tube. The ClpV ATPase then dissembles the sheath. The baseplate complex might disassemble while the membrane complex remains in the cell envelope for another round of assembly and secretion.

This study took a hybrid approach, combining cryo-electron microscopy, biochemical analysis, native mass spectrometry, evolutionary covariance, and molecular modelling to unveil the assembly pathway of the T6SS baseplate, and reports the detailed structure of the TssKFGE baseplate wedge complex from the model organism enteroaggregative *Escherichia coli* (EAEC) (**Figures 48a** and **48b**). The TssKFGE complex was purified and then visualised by cryo-electron microscopy at beamline **CM01**. A 4.6 Å-resolution reconstruction of the complex was obtained, which, combined with biochemical data, reveals that TssG is the keystone of the baseplate edifice (**Figure 48b**). This elongated protein is the backbone of the wedge complex contacting two copies of TssF on each side and two TssK trimers through two long loops. This structure also highlights unanticipated structural and functional conservation with orthologous bacteriophage proteins.

Finally, the atomic model of the T6SS wedge complex was fitted into the recent reconstruction of the fully assembled baseplate to provide unprecedented structural and

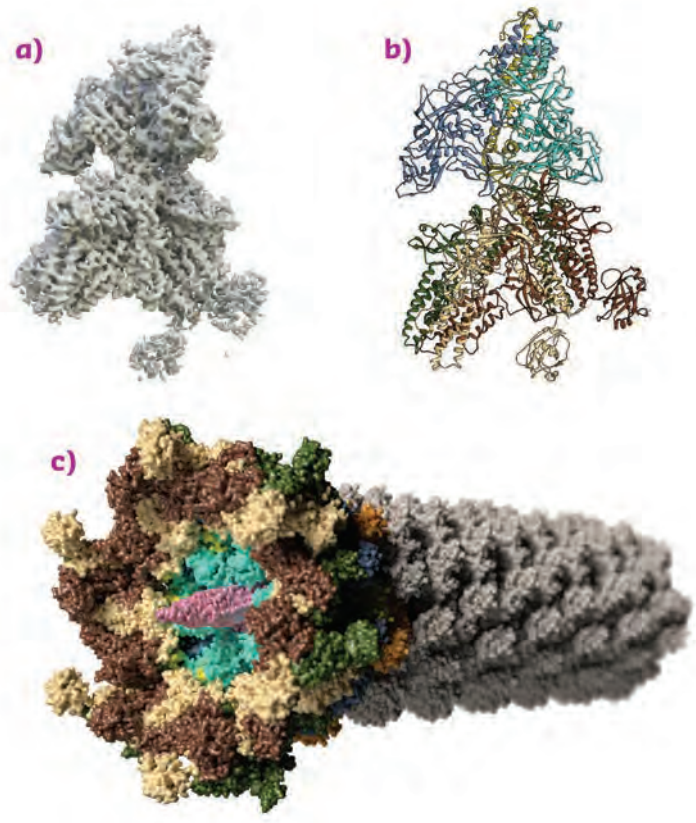


**Fig. 48: a)** A reconstruction of the TssKFGE complex visualised by cryo-EM at 4.6 Å resolution. **b)** An integrative approach using modelling, native mass spectrometry and biochemistry was used to analyse the density map and build an atomic model of the complex. In this ribbon representation, TssG is in yellow, TssF subunbits in dark and light blue. Two TssK trimers (each subunits in beige, dark green and brown) are bound to TssG. **c)** Molecular model of an assembled baseplate enclosing the VgrG spike, and bound to the Hcp tube and TssB/C sheath.

functional understanding of the T6SS baseplate (**Figure 48c**). Due to the conservation of T6SS wedge complexes among pathogenic bacteria, the atomic model of the TssKFGE complex will facilitate the design of anti-T6SS compounds targeting hot spots of the baseplate assembly, paving the way towards new therapeutic avenues to replace or help classical antibiotherapies.


PRINCIPAL PUBLICATION AND AUTHORS

Biogenesis and structure of a type VI secretion baseplate, Y. Cherrak (a), C. Rapisarda (b, c), R. Pellarin (d), G. Bouvier (d), B. Bardiaux (d), F. Allain (d), C. Malosse (e, f), M. Rey (e, f), J. Chamot-Rooke (e, f), E. Cascales (a), R. Fronzes (b, c) and E. Durand (a, g), *Nat. Microbiol.* **3**, 1404–1416 (2018); doi: 10.1038/s41564-018-0260-1.
*(a) Laboratoire d'Ingénierie des Systèmes Macromoléculaires, Institut de Microbiologie de la Méditerranée, UMR7255, Aix-Marseille Université – CNRS (France)*
*(b) Institut Européen de Chimie et Biologie, University of Bordeaux (France)*
*(c) CNRS UMR 5234 Microbiologie Fondamentale et Pathogénicité, Paris (France)*
*(d) Institut Pasteur, Structural Bioinformatics Unit, Department of Structural Biology and Chemistry, CNRS UMR 3528, C3BI USR 3756, Paris (France)*
*(e) USR 2000, CNRS, Institut Pasteur, Paris (France)*
*(f) Mass Spectrometry for Biology Unit, Institut Pasteur, Paris (France)*
*(g) Laboratoire d'Ingénierie des Systèmes Macromoléculaires, Institut de Microbiologie de la Méditerranée, UMR7255, INSERM, Marseille (France)*

REFERENCES

[1] N. M. Taylor *et al., Mol. Microbiol.* **108**, 6–15 (2018).
[2] M. Brackmann *et al., Trends Cell Biol.* **27**, 623–632 (2017).
[3] C. Rapisarda *et al., Annu. Rev. Microbiol.* **72**, 231–254 (2018).


# PYROPHOSPHATE HYDROLYSIS IS AN INTRINSIC AND CRITICAL STEP OF THE DNA SYNTHESIS REACTION


**The blueprint of life resides in DNA. DNA polymerases (dPols) ensure accurate duplication of DNA and of the genetic information it contains. dPols are also central to multiple applications in research and biotechnology. Multiple snapshots of the primary chemical reaction catalysed by dPols shed new light on this process that is fundamental to living organisms.**


In all living organisms, genome duplication is primarily mediated by enzymes known as DNA polymerases (dPols). DNA replication is semi-conservative, with the two strands of the double helix serving as templates for the synthesis of two new strands to give rise to two new double helical DNA molecules. To synthesise new DNA, dPols catalyse the template-dependent incorporation of deoxynucleoside triphosphates (dNTPs) into the primer strand, extending the new strand – known as the primer strand – in the 5' to 3' direction through the formation of a phosphodiester bond (pB bond) between the α-phosphate of the incoming dNTP and the 3'- hydroxyl group of the terminal primer nucleotide **[1]**. $Mg^{2+}$ ions play a critical role in this polymerisation reaction. The reaction also involves breakage of the bond between the α-phosphate and, the bridging oxygen (αO bond) between the α- and β-phosphates within the dNTP. This latter process results in the release of pyrophosphate (PPi).

The nucleotide incorporation reaction catalysed by dPols is believed to have a low free-energy change **[2]**. The PPi moiety is thought to be cleaved by an accompanying pyrophosphatase enzyme to ensure that the reaction is energetically favourable and moves in the forward direction **[3]**. However, dPols are also utilised in applications such as DNA sequencing and the polymerase chain reaction **[4]**. In these applications, DNA synthesis occurs in the absence of any pyrophosphatase enzyme and therefore it was unclear how the reaction proceeds in the forward direction.

Here, time-resolved crystallography was used to study DNA synthesis by DNA polymerase IV (*Escherichia coli*) and periodic snapshots of the reaction were obtained. The method involves incubating crystals of dPol:DNA:dNTP with $Mg^{2+}$ ion for different periods. Crystals were then cryo-cooled, diffraction data collected at beamline **ID29** and the resulting electron density maps used to observe the progress of the reaction. A total of 14 snapshots representing different stages of the reaction were obtained and analysed. The structural observations were further validated using biochemical assays performed on DNA polymerase IV and other DNA polymerases.

The results show that the DNA synthesis reaction may involve the following sequence of events (**Figure 49**): First, the dNTP and $Mg^{2+}$ ions bind the DNA polymerase active site. $Mg^{2+}$ binding

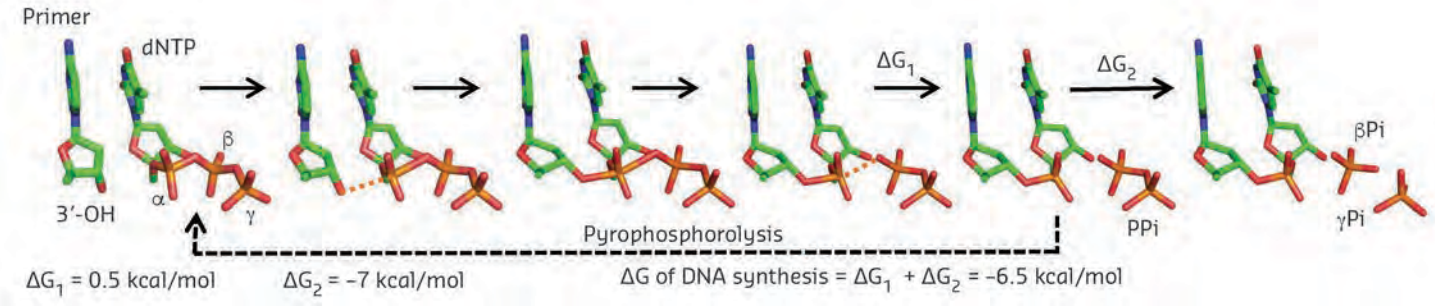


**Fig. 49:** The reaction scheme, as deduced from time-resolved crystallography, for DNA synthesis in the active site of a DNA polymerase. The phosphodiester bond is formed first, resulting in the appearance of a covalent pentacoordinate transition state, followed by release of PPi. After PPi is released, pyrophosphorolysis can reverse the reaction, but a hydrolysis, inherent to the reaction, of PPi to Pi prevents this reversal.

causes a change in the pucker of the primer 3'-deoxyribose from C2'-endo to C3'-endo resulting in a decrease in the distance between the primer 3'-OH and the α-phosphate of dNTP and an enhancement of the angle between 3'-OH, α-phosphate of dNTP and the bridging oxygen between the α- and β-phosphates. These changes facilitate nucleophilic attack by the deprotonated 3'-$O^-$ on the α-phosphate allowing the creation of a pB between the α-phosphate of dNTP and the 3'-OH of the primer nucleotide and resulting in the formation of a covalent pentacoordinate transition state. This is followed by dissolution of the αO bond and release of the pyrophosphate (PPi) moiety. PPi is then hydrolysed into two phosphate ions (Pi) followed by diffusion out of the active site of Pi and $Mg^{2+}$. The hydrolysis of PPi prevents pyrophosphorolysis that can reverse the synthesis reaction and thus ensures that replication proceeds smoothly **[5]**. The next step involves DNA translocation so that the newly incorporated nucleotide moves out of the nucleotide-binding site and a new cycle of DNA synthesis starts. The identity of the incoming nucleotide will be determined by the next unpaired nucleotide from the template DNA.

This study suggests that hydrolysis of the pyrophosphate moiety is an inherent and critical step in the DNA synthesis reaction catalysed by dPols (**Figure 49**). Consequently, the nucleotide incorporation reaction is energetically favourable in the absence of pyrophosphatase enzymes. Additionally, DNA synthesis was observed to be a two $Mg^{2+}$ ion stepwise associative substitution nucleophilic ($S_N2$) reaction, wherein the formation of pB and dissolution of αO occur sequentially and not concomitantly. Overall, the study provides new insight into the mechanism used by dPols to synthesise DNA during DNA replication.

## PRINCIPAL PUBLICATION AND AUTHORS

Pyrophosphate hydrolysis is an intrinsic and critical step of the DNA synthesis reaction, J. Kottur (a) and D. T. Nair (a), *Nucleic Acids Res.* **46**, 5875–5885 (2018); doi: 10.1093/nar/gky402.

*(a) Regional Centre for Biotechnology, Haryana, NCR Delhi (India)*

## REFERENCES

[1] T. A. Steitz, *J. Biol. Chem.* **274**, 17395–17398 (1999).
[2] L. Peller, *Biochemistry* **15**, 141–146 (1976).
[3] J. D Watson *et al.*, in *Molecular Biology of the Gene (7e)*, Pearson, USA (2013).
[4] J. Aschenbrenner and A. Marx, *Curr. Opin. Biotechnol.* **48**, 187–195 (2017).
[5] M. Pandey *et al., PLoS One* **3**, e1389 (2008).

# COMPLEX SYSTEMS AND BIOMEDICAL SCIENCES

The main challenge for the Complex Systems and Biomedical Sciences (CBS) beamlines in 2018 was to prepare for the smaller, more intense beams from the Extremely Brilliant Source (EBS). Several beamlines need new primary slits, attenuators and improved monochromator cooling to tackle the increased power density in the centre of the beam. Faster detectors are also essential and three EIGER 2 detectors were ordered for ID02, ID10 and ID17. With new detectors taking up to 1000 images per second, the computing infrastructure will also be upgraded. Another important project is to replace SPEC, the beamline control system that has been used since 1993, with the new Python-based program, BLISS. BLISS was successfully implemented on ID10 and used in several user experiments in the second half of 2018. Another mission for the beamlines is to generate industrial income, and ID09 and ID17 welcomed first industrial users in 2018.

**ID02**, the beamline for small angle scattering, had a very productive year. Ongoing work on cardiac muscle employing ultra-small-angle X-ray (USAXS) diffraction revealed new structural features along the activation pathway. In addition, ultra-small-angle X-ray photon correlation spectroscopy (XPCS) reached a new level of maturity, enabling dynamic studies of anisotropic magnetic colloids and active Janus particles, which are yielding promising results. The industrial use of the beamline also peaked this year, with an increase in revenue of 30%.

The surface science beamline **ID03** made important improvements in instrumentation such as the continuous scan mode, which increases data acquisition rates substantially. With the expected completion of EBS in September 2020, surface science will enter a new era, where improvements in coherence and flux will make it possible to follow the dynamics and local structure of surfaces in *operando* where transient surface phenomena determine the characteristic properties. Furthermore, due to the increased measurement speeds, it will be possible to track and unravel new surface processes that are beyond reach today.

The activities on **ID09**, the beamline for structural dynamics, were focused on finishing the upgrade project, UPBL9b, with the installation of a white-beam toroidal mirror in the first experimental hutch, EH1. With EBS, the new mirror should reach a focus of < Ø 25 µm, which is particularly important for time-resolved serial Laue crystallography (TRSLC). A collaboration with Alke Meents and the CFEL institute in Hamburg is aimed at speeding up the acquisition rates in TRSLC, by acquiring up to 1000 Laue patterns per second. The new techniques will make it possible to monitor biological processes, triggered by light, in proteins that were hitherto impossible to crystallise. The new Jülich Chopper for pump-probe experiments at 3 kHz was tested successfully in October 2018. Exposure times will be shortened by a factor three, which is important for X-ray spectroscopy on dilute samples. The new Von Hamos Spectrometer for X-ray emission spectroscopy (XES) was also successfully installed. The atom-specific information from XES is an important supplement to the large-scale information from scattering. ID09 was used in several industrial experiments. In one example, memory chips were exposed to intense 100 ps pulses while the chips were operating. The short and intense X-ray pulse mimics the effect of heavy iron bombardment in satellite electronics in space (**page 159**).

The 2018 activities on **ID10** were focused on ensuring that the beamline will benefit fully from the increased brilliance and coherence of EBS. The BLISS control software was tested in XPCS with fast detectors like the Maxipix and the EIGER. BLISS was also used to measure multi-speckle dynamics on the µs timescale. Coherent X-ray diffraction imaging (CXDI) also made a big step forward in nano-tomographic imaging of amorphous and crystalline samples, allowing the phase determination of materials. The last activity before the shutdown was devoted to XPCS studies of the dynamics of soft materials with the EIGER 500K detector and using high-energy X-rays at 21 keV. Soft matter and biological systems will benefit enormously from the increase in brilliance at higher energies with EBS.

The surface section on ID10 focused mainly on organic electronic materials and self-assembly of nanoparticles at fluid–liquid interfaces, which were studied using the new double-crystal beam deflector. ID10 is also a partner in the European project *Formation of 2D materials on liquid metal catalysts* (LMCat: 2020-FETOPEN). The first X-ray and Raman studies of chemical vapour deposition (CVD)-grown graphene on molten Cu *in situ* were performed successfully. A special reactor was built for CVD growth of 2D materials on molten metallic surfaces. It will be available to users at the end of 2020.

2018 was another successful year for the biomedical beamline **ID17**. The breakdown of publications reflects almost perfectly the distribution of beam time between imaging applications (69%), microbeam radiation therapy (22%), and radiation biology (9%). Several upgrades were implemented, most notably for the dual-energy Laue monochromator and the pink beam CT setup, which can now operate in low- (~11 µm) and high-resolution (0.7–3.1 µm) modes simultaneously. Finally, several grant proposals were submitted, hopefully providing a significant boost for the imaging and MRT programmes in the future.

In 2018, the five laboratories of the **BMF** (BioMedical Facility) served and provided expertise to users carrying out *in-vitro* and *in-vivo* experiments at a dozen different beamlines. Requests for support have almost doubled with respect to 2017 in terms of the number of experiments performed and the use of the laboratories.

The laboratories in the Partnership for Soft Condensed Matter (**PSCM**) were requested by more than 200 user experiments from 28 different beamlines, as well as by 75 ESRF in-house research experiments. The last call for new PSCM partnerships attracted 15 expressions of interest from European institutes in October 2018, among which, three or four will soon be selected as new PSCM partners.

**M. WULFF**

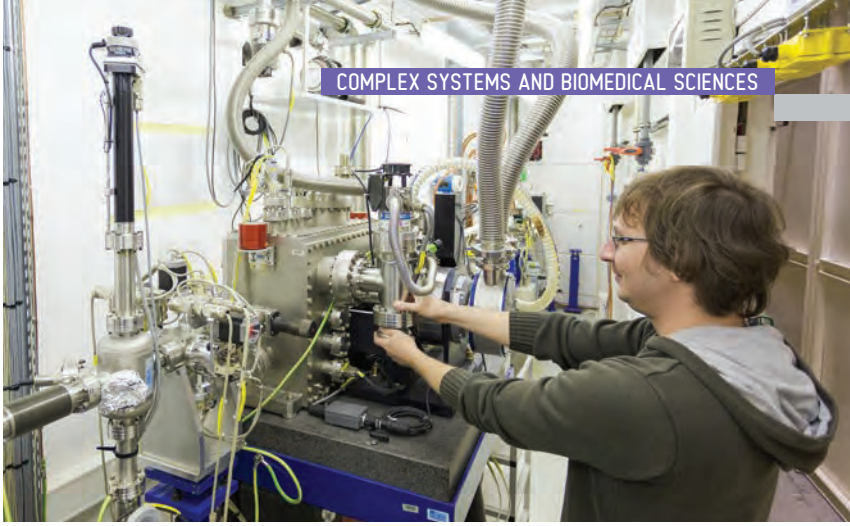

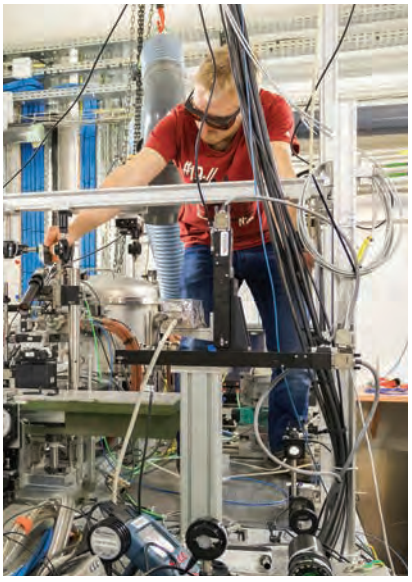

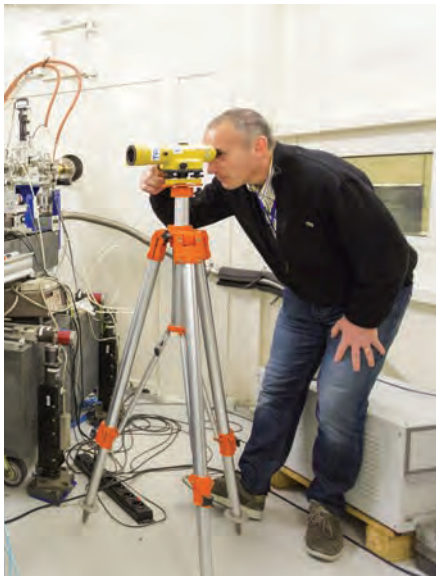

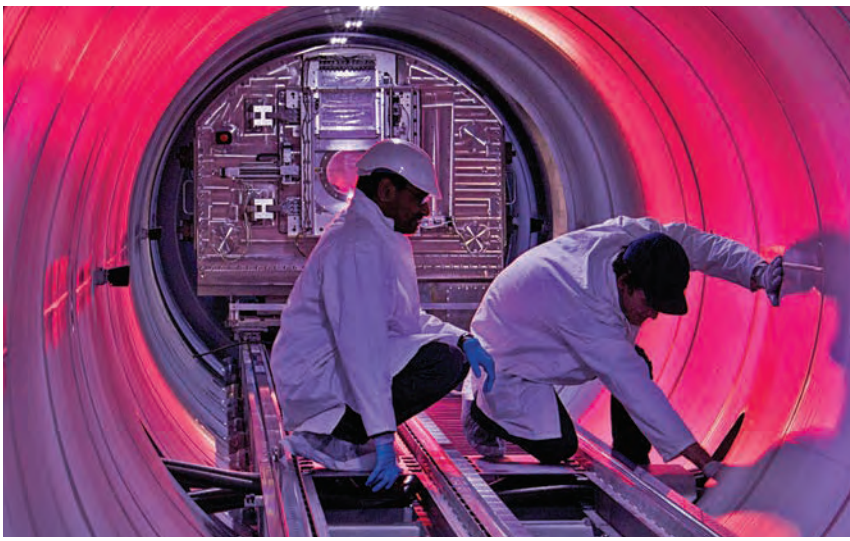

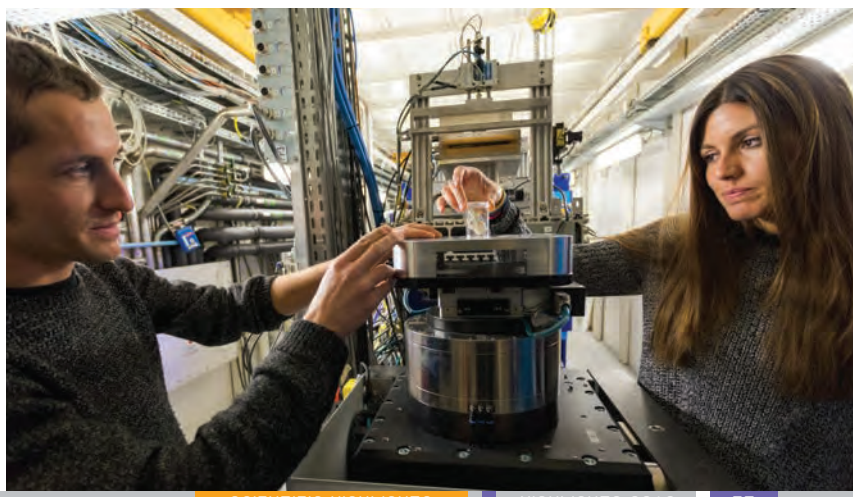

# INWARD GROWTH BY NUCLEATION

**Mixtures of soap and doughnut-shaped sugar molecules spontaneously form concentric tubes with diameters about a thousand times larger than the molecules themselves. The mechanism behind this process was identified, and it may be applicable to many similar systems.**

The superstructures that occur in self-assemblies of crystalline membranes often share a set of common morphologies: they form hollow shells, single- or multiwalled (nano)tubes, or lamellae. Nanotubes are found in self-assemblies of amphiphilic peptides and the allotropes of carbon. The same morphologies are found in living systems such as microtubules, bacterial protein shells and bacterial chlorosomes. The striking morphological similarities between these seemingly unrelated systems suggest the driving forces underlying their self-assembly mechanisms are common to many of these systems, depending more on the interplay between membrane rigidity and the high energy cost of maintaining the edges of membranes than on the nanoscopic details of the individual systems. Moreover, these types of systems often share a remarkable degree of monodispersity. As such, this suggests the existence of a well-defined formation mechanism, common to a broad range of crystalline membrane systems.

The self-assembly of sodium dodecyl sulphate (SDS) and β-cyclodextrin (β-CD) leads to superstructures representative of crystalline membrane materials. Earlier work **[1]** explored the rich phase behaviour of the SDS/β-CD system, showing the presence of multiwalled microtubes, polyhedral capsids and lamellar phases. A common feature of all these superstructures is a rigid crystalline bilayer membrane, with a well-ordered internal structure that is identical regardless of the higher-order organisation.

In this work, the self-assembly of the SDS/β-CD system into concentric hollow microtubes *in situ*, was followed using time-resolved small- and ultrasmall-angle X-ray scattering (SAXS, USAXS) at beamline **ID02**. The assembly process was initiated by a rapid temperature quench from about 75 °C to 25 °C in a few milliseconds. After a concentration-dependent waiting time, the appearance of structures at a broad range of length scales was observed, consistent with the formation of monodisperse single-walled SDS/β-CD tubes (see **Figure 50**). By modelling the observed scattering patterns by the form factor of a hollow cylinder, a decrease in mean inner cylinder radius concurrent with an increase in cylinder wall thickness was noted, indicating that microtubes grow inward from the originally formed single-walled microtubes.

The distribution of waiting times follows the non-linear scaling with SDS/β-CD concentration that is predicted by the classical nucleation theory for critical nuclei in two dimensions. Moreover, when the experimental time is rescaled according to classical nucleation theory, all trajectories of inward growth collapse onto a single curve, indicating that the full kinetics of inward growth is determined by a nucleation process. The mechanism of inward growth, shown in **Figure 51**, can therefore be explained by the successive nucleation of new, discrete cylinders inside previously existing ones, constrained in their size by the size of the original tube.

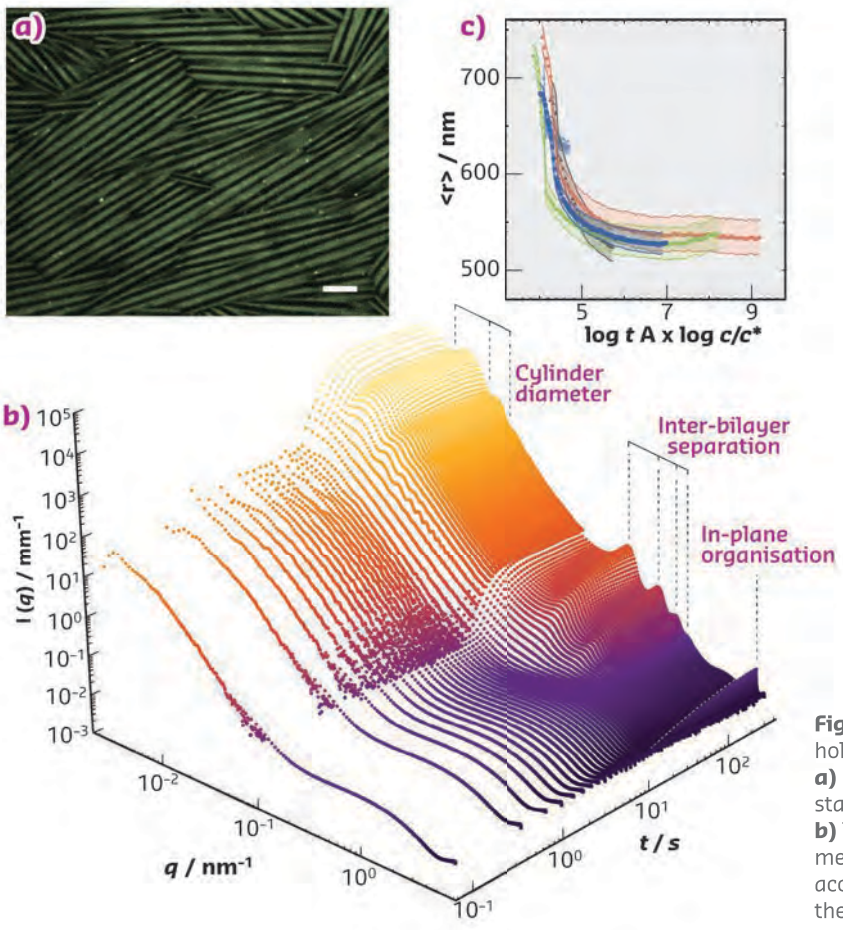


**Fig. 50:** Self-assembly of β-CD and SDS into concentric hollow microtubes, lamellar phases or polyhedral capsids. **a)** Confocal microscopy image of SDS/β-CD microtubes, stained with Nile red fluorescent dye. Scale bar is 5 μm. **b)** Time-resolved one-dimensional SAXS/USAXS profiles measured in a typical experiment. **c)** When rescaled according to classical nucleation theory, the trajectories of the mean cylinder radius collapse onto a single curve.

The mechanism proposed depends on properties that are insensitive to the specific chemistry of the system and, as such, is thought to have a far more general applicability.

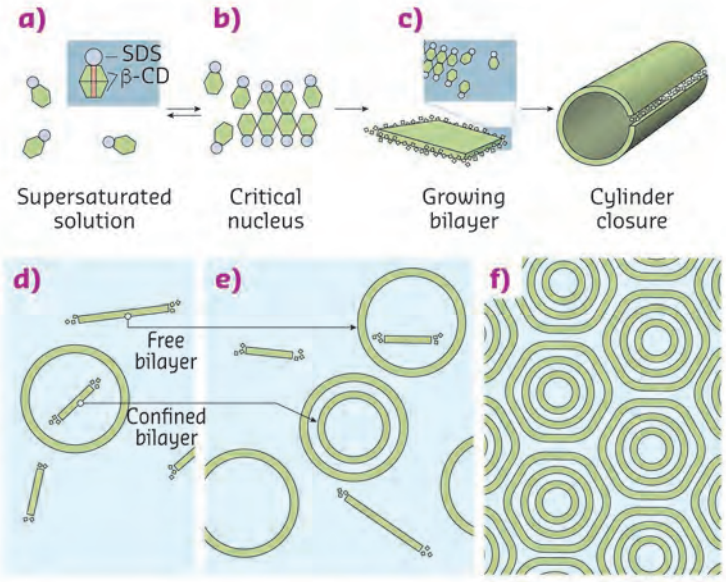


**Fig. 51:** Proposed mechanism of microtube formation. **a)** SDS/β-CD complexes in solution nucleate into **b)** ordered bilayers, governed by directional hydrogen bonding with their neighbours. **c)** When the bilayer reaches a certain size, it becomes advantageous to close the ring, gaining bond free energy at the cost of bending free energy. **d)** Since nucleation and growth are not separated, new bilayers keep nucleating, both inside and outside pre-existing tubes. **e)** Bilayers that nucleated outside pre-existing tubes form new tubes. Bilayers that nucleated inside pre-existing tubes are restricted in size and form concentric inner cylinders. **f)** Due to the large amount of material that is accommodated in the bilayers in a limited space, a dense packing of concentric cylinders is obtained.

PRINCIPAL PUBLICATION AND AUTHORS

Inward growth by nucleation: Multiscale self-assembly of ordered membranes, J. Landman (a, b, c), S. Ouhajji (a), S. Prévost (d), T. Narayanan (b), J. Groenewold (e, a), A. P. Philipse (a), W. K. Kegel (a) and A. V. Petukhov (a, c). *Sci. Adv.* **4**, eaat1817 (2018); doi: 10.1126/sciadv.aat1817.

*(a) Van 't Hoff Laboratory for Physical and Colloid Chemistry, Utrecht (Netherlands)*
*(b) ESRF*
*(c) Laboratory of Physical Chemistry, Eindhoven University of Technology (Netherlands)*
*(d) Institut Laue-Langevin, Grenoble (France)*
*(e) Guangdong Provincial Key Laboratory of Optical Information Materials and Technology and Institute of Electronic Paper Displays, South China Normal University, Guangzhou (China)*

REFERENCES

[1] S. Yang *et al., Nat. Commun.* **8**, 15856 (2017).

# HOW AN ICOSAHEDRAL VIRUS PACKAGES ITS RNA GENOME

**The spontaneous reconstitution of a plant icosahedral virus was probed by time-resolved small-angle X-ray scattering. The genome acts as an assembly template for the protein subunits making up the viral capsid.**

Cowpea chlorotic mottle virus (CCMV) is an icosahedral single-stranded RNA virus infecting a variety of beans. Four segments of RNA encoding the viral genome are shared between three distinct protein shells, called capsids, necessary for viral replication. The capsids, which protect the RNA genome, are made of 90 dimeric subunits (**Figure 52a**) arrayed onto a solid structure with 20 faces, an icosahedron. Each subunit possesses two flexible, highly positively charged domains that interact electrostatically with the genome. A delicate balance of interactions between subunits, combining a short-range, mostly hydrophobic attraction and a long-range, electrostatic repulsion, holds the capsid. The survival of the virus partly relies on its ability to self-assemble rapidly, in an error-free manner, inside the host cell. Although coarse-grained simulations have identified different pathways leading to the assembled virus from its components, very few experimental measurements were available up to now, due to the difficulty of following the fate of biological molecules over a wide range of timescales.

In this work, CCMV was reconstituted from purified protein subunits and genomic RNA, and its spontaneous assembly was probed by time-resolved small-angle X-ray scattering (SAXS) at beamline **ID02**. The forward scattering intensities allowed an estimation of the mean number of subunits bound on the genome as a function of time and, subsequently, the binding timescale, $\tau_{bind}$, while structural information was inferred from the form factors. An empty capsid self-assembles sequentially and requires a precise positioning of the subunits over the course of the assembly **[1, 2]**. For a full virus, the genome acts as an assembly template and captures a large number of subunits to form a disordered nucleoprotein complex (**Figure 52b**).

The latter slowly self-organises, typically during one hour at room temperature, while continuing

to capture the missing subunits, and eventually leads to a fully assembled virus. Equilibrium measurements at various subunit-to-genome mass ratios revealed that the binding energy of subunits on the genome is moderate (*i.e.*, ~$7k_BT_0$ where $k_B$ is the Boltzmann constant and $T_0$ the room temperature). *In vivo*, a weak binding energy may allow the subunits to select the viral genome specifically, which is a crucial feature in the crowded environment of the cytoplasm. Relaxation experiments carried out at different temperatures showed that the self-organisation of nucleoprotein complexes into viruses requires crossing a high energy barrier, $E_a$, estimated to be $20k_BT_0$ (**Figure 53a**). The assembled viruses (**Figure 53b**) are structurally indistinguishable from the native ones. In particular, they display a hollow core that arises from the fact that the genome is packed against the interior wall of the capsid due to the electrostatic interactions. In the last series of experiments, a synthetic polyelectrolyte, namely poly(styrene sulfonic acid) (PSS), was packaged into capsids (**Figure 53c**) in conditions where viruses cannot build up. The equilibrium state was reached in only two minutes. PSS has a hydrophobic backbone so its excluded volume is smaller than that of RNA. Its compaction therefore requires less energy and its templating effect is enhanced. PSS-filled capsids were fairly spherical and regular but exhibited defects that suggest the icosahedral symmetry is not respected.

The elucidated pathways of genome packaging might be advantageous to virus survival for two reasons: (i) The building blocks are first associated rapidly thanks to nonspecific but moderate electrostatic interactions, and (ii) the high energy barrier between nucleoprotein complexes and viruses provides enough time to select the viral genome and correct the errors of assembly. A detailed understanding of assembly pathways could promote the development of therapeutic strategies against viral replication.

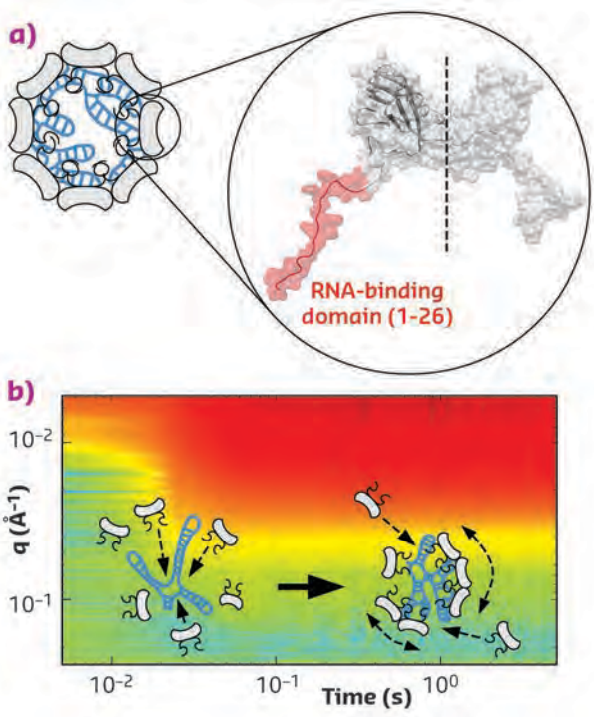


**Fig. 52: a)** Schematic representation of a virus with dimeric subunits (light grey) and the RNA genome (blue), and the molecular structure of a subunit with one of its two RNA-binding domains (red). **b)** Experimental scattering intensities of self-assembling viruses. The drawing depicts the fast binding of subunits onto the genome, then the slow self-organisation of nucleoprotein complexes.

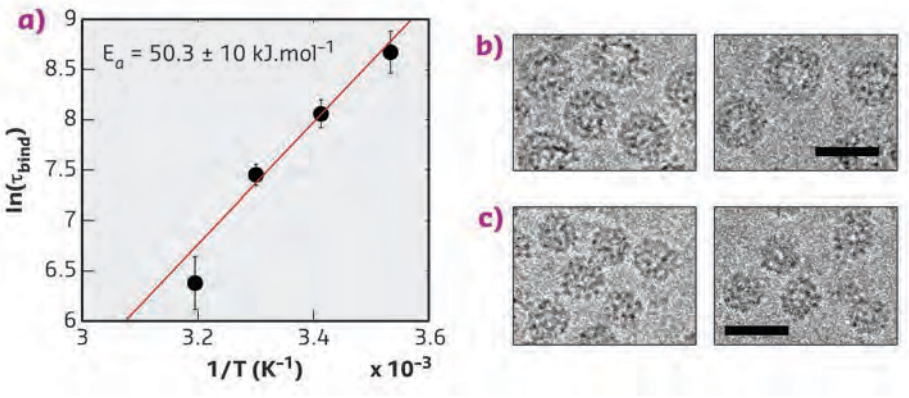


**Fig. 53: a)** Arrhenius plot of the binding timescale, $\tau_{bind}$, for the relaxation of nucleoprotein complexes into viruses. The red line is a linear fit that gives the activation energy $E_a$. Cryo-transmission electron microscopy images of **b)** assembled viruses and **c)** PSS-filled capsids. Scale bars are 30 nm.

## PRINCIPAL PUBLICATION AND AUTHORS

Nonequilibrium self-assembly dynamics of icosahedral viral capsids packaging genome or polyelectrolyte, M. Chevreuil (a, b), D. Law-Hine (a), J. Chen (a), S. Bressanelli (b), S. Combet (c), D. Constantin (a), J. Degrouard (a), J. Möller (d), M. Zeghal (a) and G. Tresset (a), *Nat. Commun.* **9**, 3071 (2018); doi: 10.1038/s41467-018-05426-8.
*(a) Laboratoire de Physique des Solides, Orsay (France)*
*(b) Institute for Integrative Biology of the Cell (I2BC), Gif-sur-Yvette (France)*
*(c) Laboratoire Léon Brillouin (LLB), Gif-sur-Yvette (France)*
*(d) ESRF*

## REFERENCES

[1] G. Tresset *et al.*, *J. Am. Chem. Soc.* **135**, 15373–15381 (2013).
[2] D. Law-Hine *et al.*, *Soft Matter* **12**, 6728–6736 (2016).

# OXIDES AND CATALYTIC CO OXIDATION

**Catalytic CO oxidation, one of the reactions in automotive catalytic converters, is a seemingly simple reaction between CO and $O_2$ molecules, yet, surprisingly, the phase responsible for the catalytic activity is still debated. A study of Rh and Pd model catalysts resolves the controversy and could provide important design principles for oxidation catalysts.**

It is well established that CO oxidation can be catalysed by metallic Pd and Rh surfaces. During adsorption, $O_2$ dissociates and the resulting atomic oxygen easily reacts with co-adsorbed CO to form $CO_2$, which desorbs to close the catalytic cycle. At realistic pressures, mixed adsorbate structures rarely form, but one of the reactants tends to dominate the surface. At low temperatures, the surface is covered by CO, which blocks $O_2$ dissociation. This surface is referred to as 'CO-poisoned' and is associated with low catalytic activity. Increasing the temperature leads to CO desorption and the formation of free surface where $O_2$ can dissociate and react. At high enough temperatures, the reaction continues until all CO is removed and the surface becomes covered by O. Adsorbed oxygen, however, cannot block the adsorption of CO and this surface possesses high catalytic activity.

The transition from the low to high active state is referred to as catalytic ignition. For the ignited catalyst, the CO oxidation reaction is no longer determined by the intrinsic activity of the catalyst but by the transport of reactants to the catalytic surface, a state often referred to as mass transfer-limited. In this situation, the gas composition close to the catalyst is depleted in CO, and the surface is exposed to an oxidising atmosphere of $O_2$ and $CO_2$. Several studies have shown that an oxide may form in conjunction with the ignition. This may be interpreted as the oxide being responsible for the activation, but it has been shown that the oxide forms first after the ignition, as a result of the changed gas composition **[1]**. This does not, however, show whether the reaction occurs or is faster on the oxide or the metal.

At the heart of the problem, the metallic surface, after ignition, is so active that only a fraction of the surface is needed to keep the catalyst in its active state. It is therefore difficult to determine whether the reaction happens on the oxide surface or on metallic surface patches in between oxide islands that almost completely cover the surface.

In order to distinguish between these situations, the deactivation (rather than the activation) of the catalyst was studied. By lowering the temperature, the reaction is slowed such that a larger part of the surface needs to be active in order to stay in the high-active state. If the reaction happens on the metallic surface, it leads to a continuous reduction in oxide coverage, while if the oxide is at least as active as the metal, the oxide will stay until the catalyst deactivates.

**Figure 54** shows the results from an experiment of CO oxidation over Pd(100) at beamline **ID03**, where the catalytic activity and surface structure were followed by mass spectrometry and surface X-ray diffraction (SXRD), respectively, while slowly lowering the temperature. The signal from a thin epitaxial oxide stayed nearly constant until the catalyst deactivated, showing that this oxide was at least as active as the metallic surface. Similarly, an ultrathin (one-layer thick) Pd oxide film was found to be highly active.

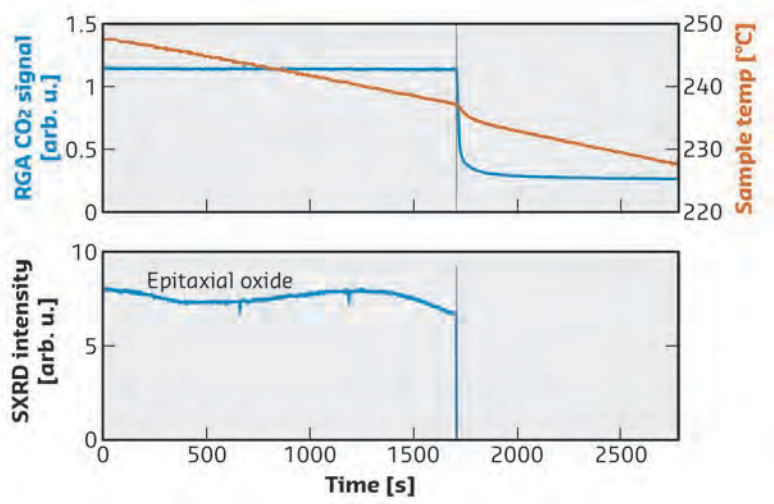


**Fig. 54:** Mass spectrometry, temperature and SXRD data during deactivation of catalytic CO oxidation over epitaxial PdO. The disappearance of the oxide in conjunction with the deactivation shows that the Pd oxide is at least as active as the metal.

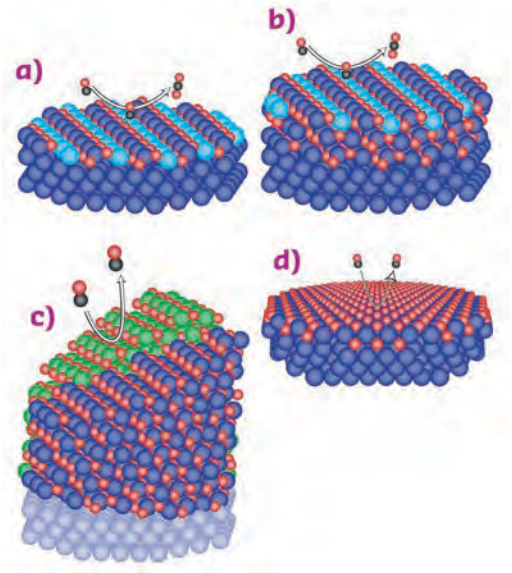


**Fig. 55:** Models of **a)** ultra-thin Pd surface oxide, **b)** thin epitaxial PdO, **c)** thick polycrystalline PdO and **d)** ultra-thin Rh surface oxide. **a)** and **b)** expose coordinatively undercoordinated Pd atoms (light blue), which act as active sites.

In contrast, if the Pd oxide growth is too thick, it shows low activity, and Rh oxides are less active than the metal, independent of thickness. As illustrated in **Figure 55**, the active oxides expose coordinatively unsaturated metal atoms that act as active sites, where CO can adsorb and react. The thick Pd oxide, on the other hand, exposes only fully saturated Pd atoms, while Rh oxides are completely oxygen-terminated. Hence, these oxides do not allow CO to adsorb and react.

Knowledge about the activity of different oxide phases can be used, for instance, to decrease the effect of oxygen poisoning on Pd-based catalysts. A bimetallic system where the PdO grows on top of a more noble metal might be able to stabilise the active PdO film.

PRINCIPAL PUBLICATION AND AUTHORS

The Role of Oxides in Catalytic CO Oxidation over Rhodium and Palladium, J. Gustafson (a), O. Balmes (b), C. Zhang (a), M. Shipilin (c), A. Schaefer (d), B. Hagman (a), L. R. Merte (b, d), N. M. Martin (d), P.-A. Carlsson (d), M. Jankowski (e), E. J. Crumlin (f) and E. Lundgren (a), *ACS Catal.* **8**, 4438–4445 (2018), doi: 10.1021/acscatal.8b00498.
*(a) Lund University (Sweden)*
*(b) MAX IV Laboratory, Lund (Sweden)*
*(c) Stockholm University (Sweden)*
*(d) Chalmers University of Technology, Göteborg (Sweden)*
*(e) ESRF*
*(f) Advanced Light Source, Berkeley (USA)*

REFERENCES

[1] S. Blomberg *et al.*, *J. Synchrotron Rad.* **25**, 1389–1394 (2018).

# PICOSECOND X-RAY SCATTERING REVEALS THE STRUCTURAL DYNAMICS OF IRON-COMPLEXES WITH ANOMALOUSLY LONG-LIVED CHARGE-SEPARATED STATES

**Fe complexes with N-heterocyclic carbene (NHC) ligands represent a new class of photo-sensitive materials with potential application in solar cells due to their exceptionally long-lived charge transfer (CT) states. Why is the lifetime of the charge-separated state much longer in these complexes? The study of a prototype NHC complex demonstrates that the NHCs improve their solar cell properties by destabilising and distorting the so-called metal-centred state in the photo cycle to the ground state.**

Transition metal complexes (TMCs) have been studied for decades due to their rich photophysical and photochemical properties. The tunability of the optical absorption bands makes TMCs useful in photodriven nanomachinery, photocatalysis, photosensitising and photoinduced water splitting. For a long time, the most efficient metals in these complexes were Ru and Ir. They have microsecond long charge-separated states – the so-called metal-to-ligand charge transfer (MLCT) states – that are used to convert photon energy to chemical or electric energy in solar cells. However, Ru and Ir are rare and toxic and therefore harmful for large-scale industrial solar applications. Recent efforts are therefore focused on photosensitisers that use cheap and environmentally benign first-row transition metals such as Fe.

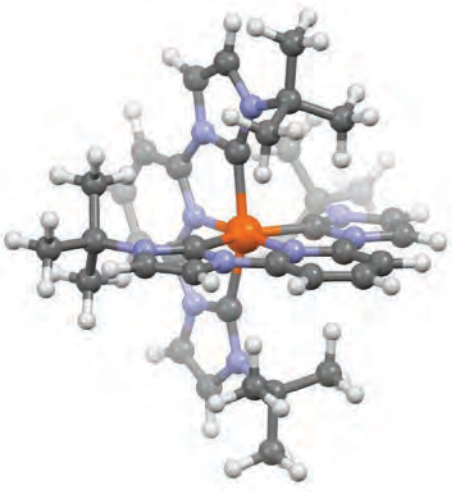

**Fig. 56:** Structure of the photo-sensing molecule $[Fe(btbip)_2]^{2+}$ studied in this work. (Atom labels: orange: Fe, blue: N, grey: C, white: H.)

Fe compounds, however, display substantially different excited state dynamics. In contrast to Ru and Ir complexes, the so-called metal-centred (MC) states are low in energy for Fe complexes, which leads to very short MLCT lifetimes on the 100 femtosecond timescale. Only recently, a 100-fold increase in the MLCT lifetime was obtained using N-heterocyclic carbene (NHC) ligands around the Fe. The energy of the unwanted MC states is raised, effectively prolonging the MLCT lifetime. The new approach is paving the way for using Fe complexes in photodriven applications, as well as opening up new studies of the photophysics and photochemistry of Fe-based TMCs.

While NHC ligands are known to be effective in increasing the MLCT lifetime in Fe compounds, their exact effect on the photoinduced dynamics is not well understood. Specifically, the structural dynamics of the MLCT decay via the MC states is not known. Understanding the role of the MC states in this process is important for the design of new complexes with improved properties.

To investigate the MLCT decay and the properties of the MC states, a novel NHC complex was studied – $[Fe(btbip)_2]^{2+}$, shown in **Figure 56** – in which the

MC state dominates the deactivation cascade. The lifetime of the MC state is found to be ~200 ps, significantly shorter than the nanosecond MC states in traditional Fe complexes. The short lifetime indicates a high degree of destabilisation from the NHC ligands, making this complex perfect for investigating the NHC effect on the MC states. To study the structural dynamics of the complex, time-resolved wide-angle X-ray scattering (WAXS) was used on beamline **ID09**, making it possible to characterise the excited state molecular structure with 100 ps temporal and sub-angstrom spatial resolution.

The results show that the MC state is a quintet with spin S=2, in contrast with some spectroscopic works suggesting a triplet character (**Figure 57**). The refinement of the molecular structure in the excited state shows that, compared to the ground state, the first Fe coordination shell expands anisotropically by 0.2 Å and 0.3 Å along the equatorial and axial direction. Compared to traditional complexes, where the expansion is isotropic with an amplitude of 0.2 Å, the structural changes in the present study is unusually large. This indicates that the NHC ligands not only destabilise the MC state energetically, but also structurally distort it. The new experiments agree with theoretical predictions and confirm the role of the NHC ligands in increasing the MLCT lifetimes.

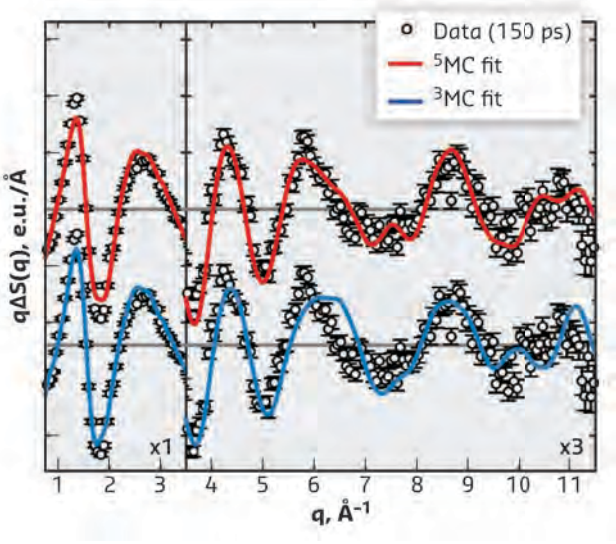


**Fig. 57:** Capturing the short-lived metal-centred state in the Fe–Carbene complex from time-resolved WAXS data taken on beamline **ID09** 150 ps after laser excitation. Comparison of the theoretical $^3$MC and $^5$MC signals indicates that the decay from MLCT state proceeds via the $^5$MC state.

PRINCIPAL PUBLICATION AND AUTHORS

Tracking the Picosecond Deactivation Dynamics of a Photoexcited Iron Carbene Complex by Time-Resolved X-ray Scattering, D. Leshchev (a), T. C. Harlang (b, c), L. A. Fredin (d), D. Khakhulin (e), Y. Liu (f), E. Biasin (c), M. G. Laursen (c), G. E. Newby (a), K. Haldrup (c), M. M. Nielsen (c), K. Wärnmark (f), V. Sundström (b), P. Persson (d), K. S. Kjær (b, c) and M. Wulff (a), *Chem. Sci.* **9**, 405–414 (2018); doi: 10.1039/c7sc02815f.
*(a) ESRF*
*(b) Department of Chemical Physics, Lund University (Sweden)*
*(c) Molecular Movies Group, Department of Physics, Technical University of Denmark (Denmark)*
*(d) Theoretical Chemistry Division, Lund University (Sweden)*
*(e) European XFEL, Schenefeld (Germany)*
*(f) Centre for Analysis and Synthesis, Department of Chemistry, Lund University (Sweden)*

# GOLD NANORODS AS ULTRAFAST PHOTO-THERMAL TRANSDUCERS

**The suitability of using gold nanorods as photo-thermal transducers was tested by recording the structural relaxations in nanorods excited by femtosecond laser pulses. The structural changes were probed by picosecond X-ray pulses. The photo-thermal and photo-acoustic responses are accompanied by irreversible changes in shape.**

Photonic applications of metallic nanoparticles include the exploration of photo-thermal phenomena when particle-laden materials are subjected to intense short laser pulses. Nanoscale heat release and cavitation phenomena in aqueous suspension of nanorods can be explored for so-called theranostics: thermal modification of tissue or nanobubbles as contrast agents. Gold nanorods have attracted a lot of attention in the last few years due to their ability to tailor shapes, and, therefore, their optical response, through a strong photonic resonance in the near-IR, the transparency window for biological tissue **[1]**.

However, the reversible and non-reversible dynamics are very diverse and include particle heating, bubble formation, particle reshaping or various destructive laser interactions. Time-resolved X-ray scattering was used to investigate a gold nanorod suspension in order to study these phenomena with picosecond time resolution **[2]**. While wide-angle X-ray scattering (WAXS) at beamline **ID09** gives information about the particle lattice (temperature, melting) and the water pressure (formation of nanobubbles), small-angle X-ray scattering (SAXS) probes the shape of the particles. Difference SAXS patterns probe the selective excitation of rods aligned with the laser polarisation. **Figure 58** shows the onset

of the asymmetry of the pattern as a function of delay. Nanorods of 93 nm length and 22 nm width contract towards a spherical shape, while still being in the solid state (80 J/m$^2$). Above the melting fluence, they undergo shape oscillations before ending as spheres (220 J/m$^2$).

Thus, the different relaxation channels can be selected as a function of external parameters such as the time delay and laser power. A compilation of the observed relaxations is shown in **Figure 59** as a relaxation (phase) diagram. While particle heating and cooling can be observed at the lowest fluences, bubbles around the hot particles start to form above 20 J/m$^2$. Rod contraction starts for the prealigned rods to finally involve all particles at elevated fluences.

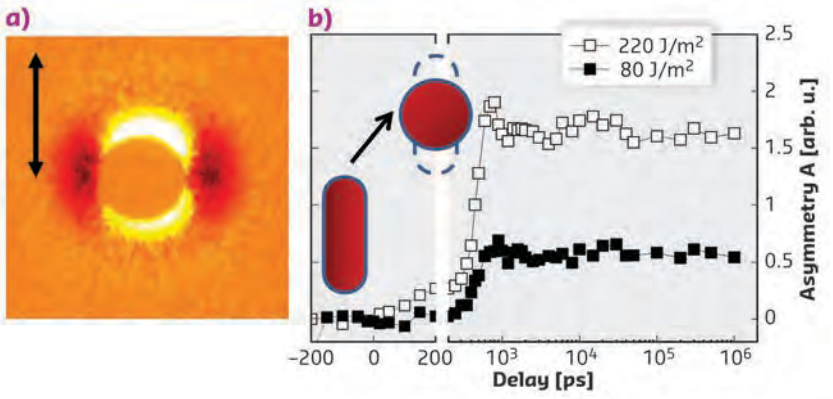


**Fig. 58: a)** Difference SAXS pattern taken 1 µs after laser excitation. The asymmetry is due to preferential relaxation of the nanorods that are aligned parallel to the laser polarisation (double arrow). **b)** The dynamics involves the relaxation to spheres, at the speed of sound, which is seen by the rise of the pattern's asymmetry after 600 ps. At 220 J/m$^2$, the excited rods become liquid and undergo oscillatory relaxation.

In photo-thermal applications, repeated heating or photoacoustic action over a long irradiation time is required. It turns out that reversible, strong reactions, such as bubble formation, are not easy to isolate from destructive reactions in terms of laser power. Thus, the window for sustained excitation is limited. On the other hand, irreversible morphology changes could be useful for nanoscale structuring, e.g., by exploiting laser-optical permanent writing in nanoparticle-loaded materials.

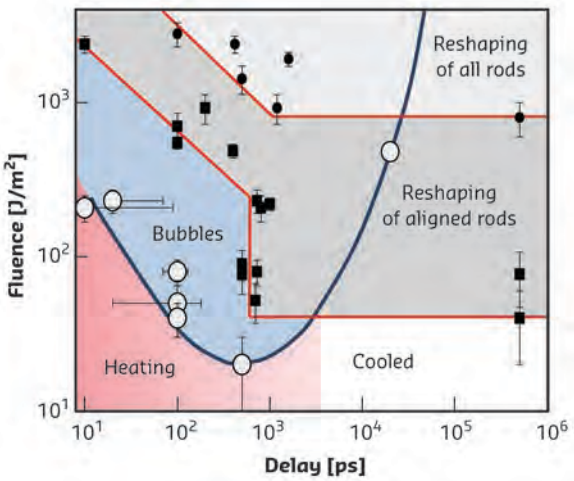


**Fig. 59:** Diagram of the different relaxations as a function of the laser/X-ray time delay and the laser fluence. The fully reversible cycle is restricted to fluences < 30–40 J/m$^2$.

PRINCIPAL PUBLICATION AND AUTHORS

Thermal dynamics of pulsed-laser excited gold nanorods in suspension, A. Plech (a), S. Ibrahimkutty (a), S. Reich (a) and G. Newby (b), *Nanoscale* **9**, 17284–17292 (2017); doi: 10.1039/c7nr06125k.
*(a) Institute for Photon Science and Synchrotron Radiation, Karlsruhe Institute of Technology (Germany)*
*(b) ESRF*

REFERENCES

[1] E. Boulais *et al.*, *J. Phys. Chem. C*, **117,** 9386 (2013).
[2] A. Siems *et al.*, *New J. Phys.* **13,** 043018 (2011).

# WATCHING CONDUCTIVE SUPERLATTICES GROW – INSIGHTS FROM X-RAY SCATTERING AT THE LIQUID/AIR INTERFACE

**The growth of conductive nanocrystal superlattices with the aid of molecular cross-linkers was monitored in real time using X-ray scattering from the liquid/air interface. This provides unique insight into the mechanism of the formation of such materials with applications as light emitters in television screens. Understanding the various stages of the synthesis is an important step to further improve the device performance.**

Spontaneous and directed assembly of semiconductor nanocrystals (NCs) into ordered superlattices is an intriguing field in nanoscience **[1]**. Mostly, the as-prepared NCs are poorly conductive due to their insulating ligand shell. The self-assembly of the NCs into well-ordered and conductive superlattices is anticipated to lead to cross-linked nanostructures with new physical properties. One effective strategy in this regard is ligand exchange with organic semiconductor (OSC) molecules at the liquid/air interface **[2]**.

In view of the rising significance of the fabrication of conductive NC superlattices, the understanding of their formation is very important. *In-situ* X-ray experiments during self-assembly and ligand

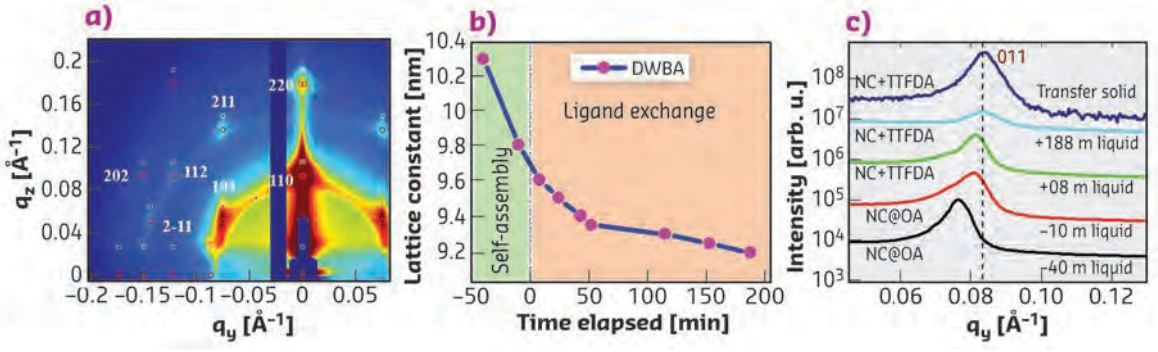


**Fig. 60:** ***a)*** GISAXS pattern of the NC superlattice on a liquid surface. Red circles (transmitted) and white boxes (reflected) are the simulated spots for a *bcc* superlattice.
**b)** Temporal evolution of the lattice parameters.
**c)** (011) peak positions of the superlattices at different conditions.

exchange at the liquid surface can potentially elucidate the complex structural evolution of the superlattice. This requires a special setup for tilting the X-ray beam, as the liquid surface cannot be inclined, in contrast to scattering experiments on solid substrates **[3]**. Such an *in-situ* experiment was recently performed on beamline **ID10** using real-time grazing-incidence small-angle X-ray scattering (GISAXS). The key to the success was the proper design of a cell for the liquid surface, controlled injection of the superlattice components and an optimised combination of solvents **[4]**.

The real-time self-assembly of oleic acid (OA)-stabilised, 6.8 ± 0.2 nm PbS NCs from a hexane:octane (1:1) solution at the acetonitrile/air interface was monitored. The ligand exchange with tetrabutylammonium tetrathiafulvalenedicarboxylate ($[TBA]_2$TTFDA) was followed and the structural evolution determined. **Figure 60a** shows a typical GISAXS pattern of the NC superlattice during self-assembly. Applying the distorted wave Born approximation (DWBA), the scattering peaks in each of the GISAXS patterns are simulated to extract the lattice parameters. The pattern can be fit to a body-centered cubic (*bcc*) structure with *Im-3m* space group (SG) symmetry oriented with the $[110]_{SL}$-axis perpendicular to the liquid surface and an initial lattice constant $a$ = (10.3 ± 0.05) nm. The scattering peaks in the GISAXS images during self-assembly and after ligand injection show a high resemblance, indicating that neither solvent evaporation nor ligand exchange noticeably alters the symmetry of the superlattice.

The contraction of the lattice parameters during the self-assembly (green region) and ligand exchange (orange region) is evident from **Figure 60b**. It contracts by 5% (from 10.3 to 9.7 nm) over a period of 45 min, followed by another contraction of 6% due to ligand exchange of the superlattice (from 9.7 to 9.2 nm) during a reaction time of 188 min. A comparison of the line profiles through the (011) in-plane peak of the respective GISAXS patterns in **Figure 60c** further demonstrates this continuous contraction on the liquid surface, the sequence of which is illustrated in **Figure 61**. Previous experiments at beamline ID10 of superlattices assembled at the liquid/air interface without utilising OSC molecules as cross-linkers have shown that this contraction is mostly reversed upon lifting the superlattice from the liquid onto a dried support **[5]**. In contrast, it was found that NCs cross-linked with the OSC retain their interparticle spacing of 1.1 nm after drying on a solid substrate. This is consistent with a 'locked-in' superlattice due to the rigid, bidentate cross-linker, TTFDA. This is further supported by the fact that the final interparticle distance equals the molecular length of TTFDA.

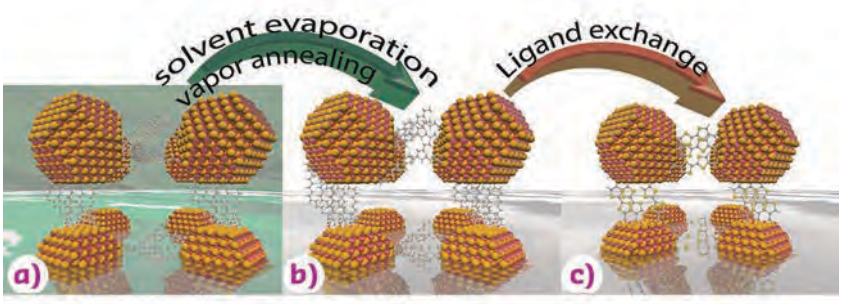


**Fig. 61:** Idealised schematics of the sequential contraction of the superlattice.
**a)** OA-capped NCs form a *bcc* superlattice
**b)** Solvent evaporation invokes a first contraction.
**c)** Ligand exchange induces further contraction.

## PRINCIPAL PUBLICATION AND AUTHORS

Monitoring Self-Assembly and Ligand Exchange of PbS Nanocrystal Superlattices at the Liquid/Air Interface in Real Time, S. Maiti (a), A. André (b), R. Banerjee (c), J. Hagenlocher (a), O. Konovalov (d), F. Schreiber (a, e) and M. Scheele (b, e), *J. Phys. Chem. Lett.* **9**, 739–744 (2018); doi: 10.1021/acs.jpclett.7b03278.
*(a) Institute of Applied Physics, University of Tübingen (Germany)*
*(b) Institute of Physical and Theoretical Chemistry, University of Tübingen (Germany)*
*(c) Department of Physics, Indian Institute of Technology, Gandhinagar (India)*
*(d) ESRF*
*(e) Center for Light–Matter Interaction, Sensors & Analytics LISA+, University of Tübingen (Germany)*

## REFERENCES

[1] C. B. Murray *et al.*, *Annu. Rev. Mater. Sci.* **30**, 545–610 (2000).
[2] M. Scheele *et al.*, *Phys. Chem. Chem. Phys.* **17**, 97–111 (2015).
[3] S. Maiti *et al.*, *J. Phys. Condens. Matter* **25**, 395401 (2013).
[4] S. Maiti *et al.*, *J. Phys. Chem. Lett.* **9**, 739–744 (2018).
[5] W. Van der Stam *et al.*, *Nano Lett.* **16**, 2608–2614 (2016).

# RESPONSE OF NORMAL TISSUE TO HIGH-DOSE MICROBEAM IRRADIATION

**The radiation tolerance of normal tissues constitutes the limit of the radiation dose applied to a tumour. This study shows that the technique of synchrotron microbeam irradiation (MBI) allows the deposition of very high doses in the microbeam paths but does not severely affect different types of normal surrounding tissues.**

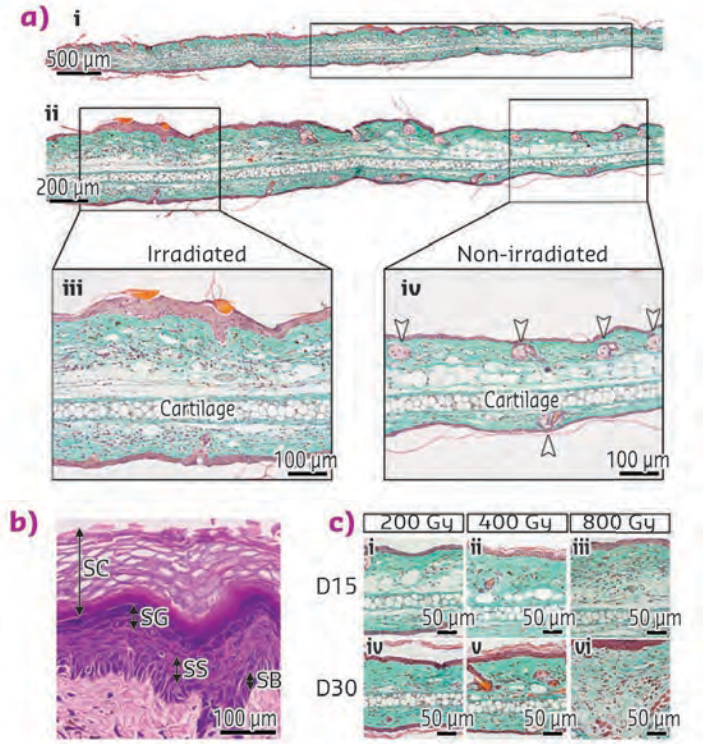


**Fig. 62:** Epidermal and dermal reaction. **a)** Transverse sections of entire ear (i) and zoom in the same ear (ii) containing irradiated (iii) and non-irradiated (iv) areas. Top: dorsal surface. Arrowheads indicate sebaceous glands. **b)** Illustration of hyperkeratotic zone in the epidermis after 800 Gy (day 30: D30) with enlarged stratum corneum (SC), stratum granulosum (SG) and stratum spinosum (SS). **c)** Histological assessment of tissue edema.

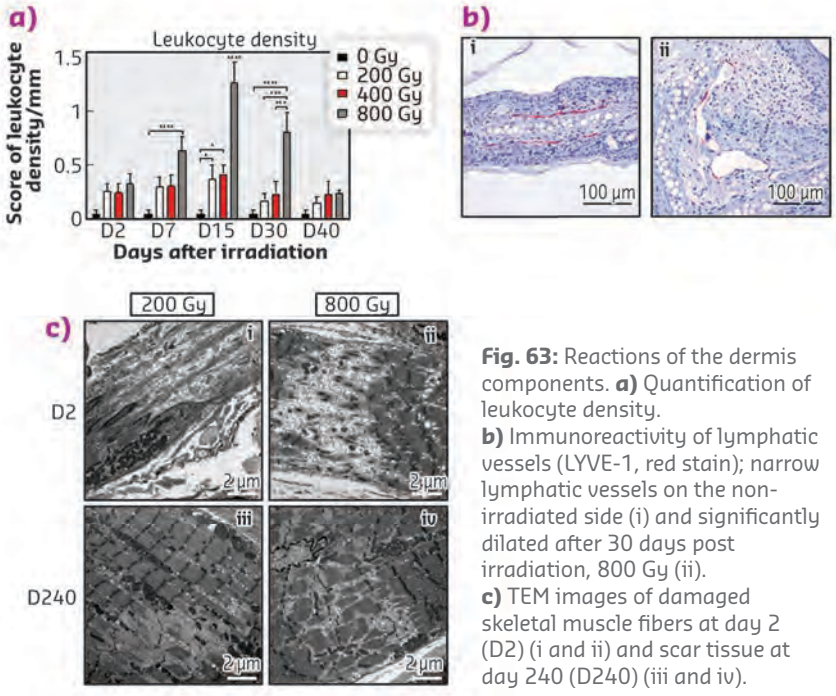


**Fig. 63:** Reactions of the dermis components. **a)** Quantification of leukocyte density. **b)** Immunoreactivity of lymphatic vessels (LYVE-1, red stain); narrow lymphatic vessels on the non-irradiated side (i) and significantly dilated after 30 days post irradiation, 800 Gy (ii). **c)** TEM images of damaged skeletal muscle fibers at day 2 (D2) (i and ii) and scar tissue at day 240 (D240) (iii and iv).

Radiotherapy has significant anti-tumour effects on cancer cells but also deleterious consequences in the healthy surrounding tissue. The tolerance of normal tissue constitutes the limit of the radiation dose applied to the tumour. An alternative method of radiotherapy, developed on **ID17**, called synchrotron microbeam radiation therapy (MRT), is based on the spatial micro-fractionation of the incident X-rays. This technique allows the delivery of high doses of radiation (hundreds of Gy) to tumours **[1]**, without inducing severe damage to normal tissues in the vicinity **[2]**.

This study analyses the effects of microbeam irradiation (MBI) on normal mouse ears, a model containing an epidermis, a dermis, striated muscle fibres, ear cartilage, blood and lymphatic vessels. Moreover, this part of the mouse has a lower hair density, resembling, at least in part, human skin. The ears were irradiated with 200 Gy, 400 Gy and 800 Gy and analysed 2 days, 7 days, 15 days, 30 days and 240 days after irradiation. The thickness of the epidermis, the dermis, and the entire ear were measured employing Goldner stained slices. The inflammatory responses to the different irradiation doses were studied on hematoxylin and eosin (H&E) stained slices. The immunofluorescent staining made it possible to quantify and evaluate the lymphatic vessels. Finally, the skeletal muscle cells were analysed by electron microscopy.

Only MRT at 800 Gy induced a significant increase in the thickness of the ear from day 15 until day 30 after irradiation, including both the epidermis and the dermis compartment (**Figure 62**). The dermis enlargement appears to be associated with a transitory edema, between 15 and 30 days after MBI (**Figure 62c**). In parallel, the leukocyte infiltration was increased at the same time points (**Figure 63a**). A dramatic enlargement of the lymphatic vessels estimated by lymph vessel surface (**Figure 63b**) was very prominent at day 15 and decreased at day 30, but was still evident at day 240 after irradiation. The cartilage does not undergo any morphological alterations over the entire period of investigation after all the applied doses. The striated skeletal muscle seems to be susceptible to MRT and showed destruction of muscle fibres in the microbeam path at all doses, starting from 2 days after irradiation

(**Figure 63c**, **i** and **ii**). The micro-scars within the muscle fibres were still visible 240 days after treatment (**Figure 63c**, **iii** and **iv**).

In conclusion, these results demonstrate a high normal tissue resistance to MRT. The very few side effects induced on all tissue components for doses up to 400 Gy allow the consideration of MRT irradiation with this dose as a promising future strategy for treating tumours without causing severe damage to the surrounding normal tissue.


PRINCIPAL PUBLICATION AND AUTHORS

Effects of synchrotron X-ray micro-beam irradiation on normal mouse ear pinnae, M. Potez (a), A. Bouchet (a), J. Wagner (a), M. Donzelli (b, c), E. Bräuer-Krisch (b), J. W. Hopewell (d), J. Laissue (a) and V. Djonov (a), *Int. J. Radiat. Oncol. Biol. Phys.* ***101***, 680–689 (2018); doi: 10.1016/j.ijrobp.2018.02.007.

*(a) Institute of Anatomy, University of Bern (Switzerland)*
*(b) ESRF*
*(c) Joint Department of Physics, The Institute of Cancer Research and the Royal Marsden Hospital, London (UK)*
*(d) Green Templeton College, University of Oxford (UK)*

REFERENCES

[1] M. A. Grotzer *et al.*, *Phys. Medica* **31**, 564–567 (2015).
[2] L. M. Smyth *et al.*, *Int. J. Radiat. Biol.* **3002**, 1–10 (2016).


# EMERGING CLINICAL APPLICATIONS OF SYNCHROTRON-GENERATED MICROBEAMS

**Research has shown that microbeam arrays delivering incident doses from 300–600 Gy generate the equivalent of a microsurgical incision over the cortex and hippocampus. These microbeam incisions generate no neurological deficit when delivered to eloquent cortex, offering new tools to treat seizures originating from brain regions not amenable to surgical resection.**

Synchrotron-generated microbeams have been extensively characterised as a new experimental treatment for brain tumours. The irradiation of normal brain and spinal cord with microbeam arrays is characterised by a distinct tissue-sparing effect. Incident doses between 300 and 600 Gy are well tolerated by the central nervous system, with no histological evidence of brain damage outside the beam paths **[1–3]**. Microbeam radiosurgery (MRS) is performed at beamline **ID17**, either by directing beams to the target in a convergent isocentric fashion (creating a 'hot spot' where the dose is enhanced by the overlapping of the beams) or interlacing 2-to-4 microbeam arrays over the target.

A recent development of microbeam research is the use of microbeam transections to modulate pathological activity over eloquent brain cortex through the selective cutting of horizontal axons connecting adjacent columns. Microbeam arrays are placed over selected cortical areas in order to hit tangentially and cut the horizontal axons connecting adjacent cortical columns, thus replicating the effects of microsurgical cortical transections, a procedure aiming to disconnect an epileptic focus located in eloquent cortex (**Figure 64**). Cutting the horizontal axons required for the spreading of epileptic activity is an effective way to control seizures without inducing neurologic dysfunction, which would be necessarily associated to a resective or ablative procedure on eloquent cortex. Synchrotron-generated microbeams have been used to create transections over the sensorimotor cortex **[4]**, the visual cortex **[5]** and the hippocampus **[6]**. Sensorimotor cortex microbeam transections generated fast abolition of status epilepticus induced by focal cortical injection of kainic acid while motor function was preserved **[7]**. This novel experimental application of microbeams provides a new and attractive tool to modulate cortical function by transecting the fibres connecting the cortical columns while keeping intact the neurological functions sub-served by the columns.

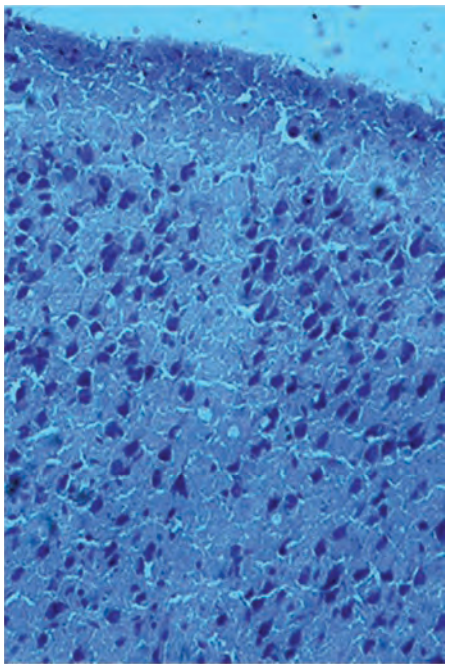

**Fig. 64:** Sensorimotor cortex transection six months after irradiation, Nissl staining; intact pyramidal neurons originating in the corticospinal tract are clearly visible adjacent to the transection, which is characterised by a cell void.

**Figure 65** shows a microbeam array through the hippocampus, a structure known to be very sensitive to conventional irradiation, which can disrupt neurogenesis, causing hippocampal atrophy and radio-induced dementia. An array of nine parallel beams, with a width

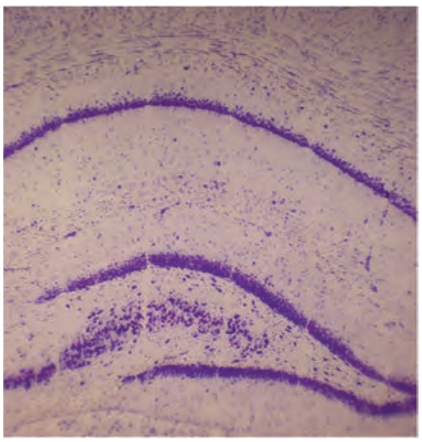

of 75 microns and spaced 400 microns apart, delivering an incident dose of 600 Gy, generated hippocampal transections without atrophy or distortion of the overall anatomy. Hippocampal neurogenesis, typically disrupted by whole brain radiation, was also preserved. The wide spatial interface between the unhindered tissue in the valleys and the tissue receiving peak doses within the microbeam paths facilitated widespread vascular recolonisation of the necrotic regions, thus preventing the dissolution of the tissue architecture induced by delayed vascular effects. It appears that the neoplastic vasculature is unable to replicate this fast repair of the segments hit by the peak dose, facilitating the development of radionecrosis over the irradiated tumour **[8]**.

Microbeam transections, either placed over neocortical seizure foci or through the hippocampus, could prove to be an excellent tool to add to the current radiosurgical techniques used to control seizures, and their use can be extended to modulate the cortical functions in a wide variety of functional brain disorders.

**Fig. 65:** Synchrotron-generated hippocampal transaction shown on Nissl staining obtained three months after delivery of an array of nine parallel microbeams to a healthy Wistar rat. Microbeam size was 75 μm and spacing across the beams was 400 μm. Incident dose was 600 Gy. Clear-cut transections through the hippocampus are visible, with no radionecrosis, edema, or evident behavioural or cognitive deficits observed.

### PRINCIPAL PUBLICATION AND AUTHORS

Synchrotron-generated microbeams induce hippocampal transections in rats, E. Fardone (a, i), B. Pouyatos (b) E. Bräuer-Krisch (a), S. Bartzsch (c, d) H. Mathieu (b), H. Requardt (a), D. Bucci (e), G. Barbone (f), P. Coan (f, g), G. Battaglia (e), G. Le Duc (a), A. Bravin (a) and P. Romanelli (h), *Sci. Rep.* **8**, 184 (2018); doi: 10.1038/s41598-017-18000-x.

*(a) ESRF*
*(b) Grenoble Institut des Neurosciences, Inserm U836, Université Joseph Fourier (France)*
*(c) Department of Radiation Oncology, Klinikum rechts der Isar, Technical University of Munich (Germany)*
*(d) The Institute of Cancer Research, London (UK)*
*(e) I.R.C.C.S. Neuromed, Pozzilli (Italy)*
*(f) Department of Physics, Ludwig Maximilians University, Garching (Germany)*
*(g) Department of Clinical Radiology, Ludwig Maximilians University, Munich (Germany)*
*(h) Brain Radiosurgery, Cyberknife Center, Centro Diagnostico Italiano (CDI), Milan (Italy)*
*(i) Present Address: Department of Biological Science and Program in Neuroscience, Florida State University (USA)*

### REFERENCES

[1] P. Romanelli and A. Bravin, *Neurol. Res*. **33**(8), 825–31 (2011).
[2] J. A. Laissue *et al., Int. J. Cancer* **78**, 654–660 (1998).
[3] F. A. Dilmanian *et al., Proc. Natl. Acad. Sci. USA* **103**, 9709–9714 (2006).
[4] E. Fardone *et al., Nature Sci. Rep.* **7**(1), 14290 (2017).
[5] P. Romanelli *et al., Phys. Med*. **31**(6), 642–6 (2015).
[6] E. Fardone *et al., Sci. Rep*. **8**(1), 184 (2018).
[7] P. Romanelli *et al., PLoS One* **8**(1), e53549 (2013).
[8] M. Miura *et al., Br. J. Radiol*. **79**, 71–75 (2006).

# HYDROGEL STABILISATION: CROSSLINKING WITHOUT DISADVANTAGES

**Hydrogels are porous soft materials of up to 99.9 % water. Crosslinking stabilises the structures but usually reduces the pore size, which is unfortunate for many biomedical applications. This work presents an alternative route to crosslinking fibrous gels, using small-angle X-ray scattering (SAXS) to demonstrate that the gel architecture is not compromised in the crosslinking step.**

Cells and their direct surroundings obtain their stiffness and mechanical integrity through the presence of fibrous networks, made from, for instance, actin, fibrin and collagen. In water, these networks form gels with extraordinary properties **[1, 2]**. The gels, typically formed at very low concentrations, can become 100 times stiffer upon deformation. Hundreds of synthetic or semi-synthetic polymers have been generated by scientists aiming to copy nature's advanced functional soft materials. Commonly, however, these synthetic gels form static, non-responsive, high-density networks, with pore structures too small to allow nutrient diffusion and cell migration **[3]**.

Recently, synthetic hydrogels were developed based on polyisocyanides (PIC) that uniquely

display the characteristics of biological gels, both in network architecture and in mechanical responsiveness **[4]**. It was found that parameters such as concentration **[5]**, temperature, polymer structure **[6, 7]** and ionic strength of the solution **[8]** could be used to tailor the linear and nonlinear mechanical properties of the gel, and that, as in nature, composites offer infinite possibilities to tune the mechanics **[9]**.

The polymers that make the PIC gels have unusual thermal behaviour. At low temperatures they dissolve in water, but at the gelation temperature, the polymer chains become hydrophobic. Consequently, the chains bundle and a gel is formed (**Figure 66a**). Further increasing the temperature stiffens the gels (**Figure 67a**). This thermal behaviour is fully reversible; cooling to below $T_{gel}$ yields the polymer solution again.

In this work, crosslinks were introduced into the gel to capture the gel (mechanical) properties at a specific temperature (**Figure 66b**). Common crosslinking approaches for synthetic gels, however, require a high density of the crosslinkers, which block the large pores in the PIC that are so important for its applications. An alternative route was developed that crosslinks selectively inside the bundles and conserves the architecture.

After mixing the components and heating to the desired crosslinking temperature (that sets the mechanics), the gel was allowed to set for 15 minutes and cooled to 5 °C. **Figure 67b** shows that the mechanical properties strongly depend on the crosslinking temperature, while **Figure 67c** illustrates that after reheating to 50 °C, all gels behave similarly again.

SAXS experiments on beamline **BM26** allowed the architecture of the gel to be monitored during

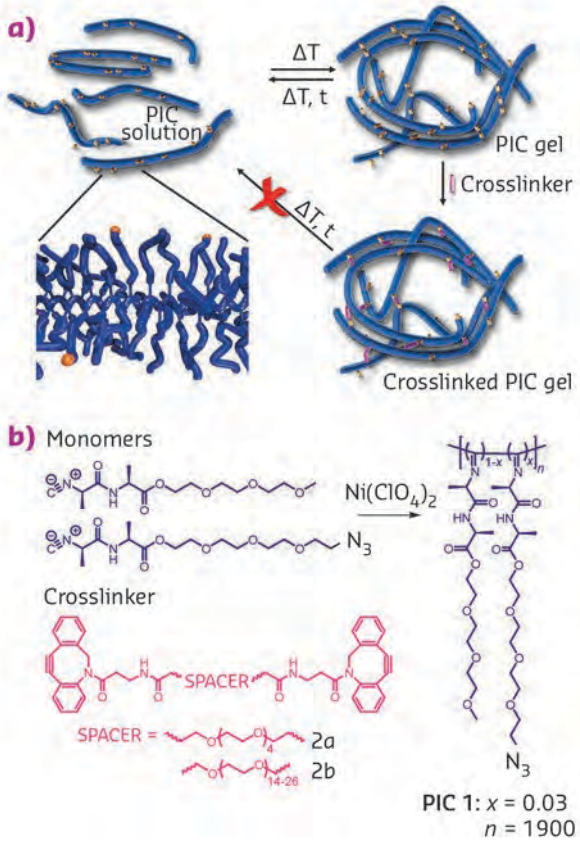


**Fig. 66: a)** Selective crosslinking inside the bundles stabilises the gel indefinitely, but does not impact the gel architecture. **b)** Molecular structures of the PIC polymer (with $N_3$ group for cross-linking) and of the crosslinkers used in this work.

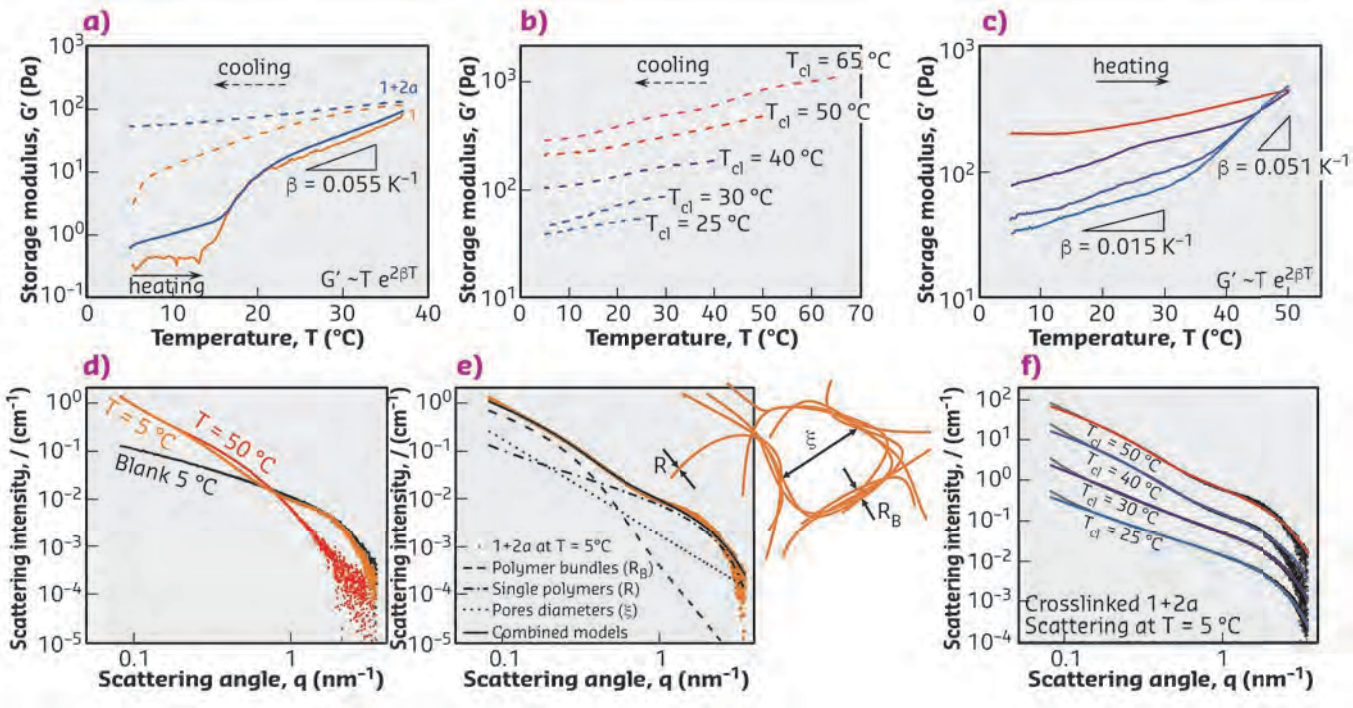


**Fig. 67: a)** A gel is formed above $T_{gel}$ > 16 °C. Gelation is irreversible with the crosslinker present (blue data). **b, c)** The stiffness of the gel at, for instance, 20 °C depends on the crosslinking temperature $T_{cl}$, but on reheating to 50 °C, all gels behave similarly. **d)** SAXS profiles before crosslinking at $T$ = 5 °C (polymer solution, black), at $T$ = 50 °C (gel, red) and a crosslinked gel at $T$ = 5 °C. **e)** The scattering profile of the latter is a composite of different length scales. **f)** The gel architecture is independent of the crosslinking temperature.

gel, formation, crosslinking and subsequent cooling (**Figure 67d–f**). The data were fit to a composite model that adds scattering contributions of molecularly dissolved polymers, bundled polymers in the network and the network structure itself:

$$I(q) = I_{polymers}(q) + I_{bundles}(q) + I_{network}(q)$$

where the first two terms follow Kholodenko's wormlike chain model **[10]** and the last term the Ornstein-Zernike model **[11]**. Key parameters are the polymer and bundle diameters ($R$, $R_B$) and the pore size ($\xi$). It was found that in the gel, the contribution of molecularly dissolved polymers is minimal. After cooling a crosslinked gel to 5 °C, however, SAXS indicates that a fraction of the polymer chains dissolve again. The fact that the average bundle diameter at 5 °C increased shows that only the thick bundles remain. As the mechanical properties change very little upon cooling, it is concluded that the thickest bundles primarily carry all mechanical stresses in the gel. The smaller ones play a marginal role.


## PRINCIPAL PUBLICATION AND AUTHORS

Crosslinking of fibrous hydrogels, D. C. Schoenmakers (a), A. E. Rowan (b) and P. H. J. Kouwer (a), *Nat. Commun.* **9**, 2172 (2018); doi: 10.1038/s41467-018-04508-x.

*(a) Institute for Molecules and Materials, Radboud University (Netherlands)*

*(b) AIBN, University of Queensland (Australia)*

## REFERENCES

[1] C. Storm *et al., Nature* **435**, 191–194 (2005).
[2] M. L. Gardel *et al., Science* **304**, 1301–1305 (2004).
[3] B. V. Slaughter *et al., Adv. Mater.* **21**, 3307–3329 (2009).
[4] P. H. Kouwer *et al., Nature* **493**, 651–655 (2013).
[5] M. Jaspers *et al., Nat. Commun.* **5**, 5808 (2014).
[6] P. H. Kouwer *et al., Chin. Chem. Lett.* **29**, 281–284 (2018).
[7] M. Jaspers *et al., Biomacromolecules* **17**, 2642–2649 (2016).
[8] M. Jaspers *et al., Adv. Funct. Mater.* **25**, 6503–6510 (2015).
[9] M. Jaspers *et al., Nat. Commun.* **8**, 15478 (2017).
[10] A. L. Kholodenko, *Macromolecules* **26**, 4179–4183 (1993).
[11] L. S. Ornstein and F. Zernike, *KNAW Proc.,* 793–806 (1914).



## ACKNOWLEDGEMENT

The work was financially supported by the NWO Gravitation grant 024.001.035 and the NWO grant BM26-02773.


# CONVERTING CARBON DIOXIDE INTO ETHYLENE USING COPPER FOAMS AND POLYMERS

**The results of *in-situ* and *ex-situ* X-ray diffraction experiments support a convenient catalyst modification strategy based on coating metallic electrocatalysts with polymers, which significantly improves the efficiency for hydrocarbon formation. This could be used to enhance $CO_2$ reduction to $C_2^+$ products used in industry, such as ethylene, ethane and acetate.**

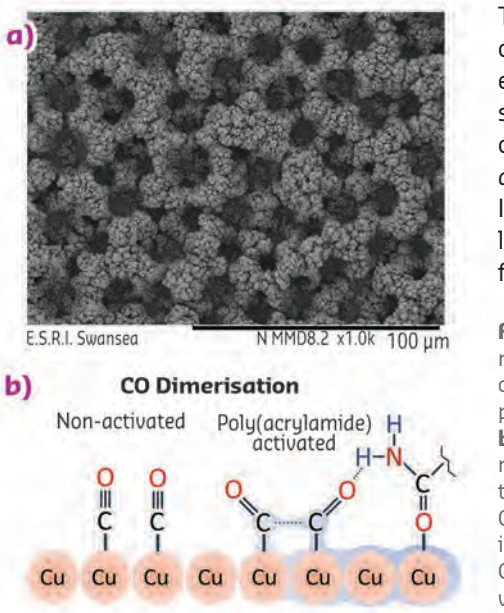


**Fig. 68: a)** A scanning electron microscopy image of the porous copper foam decorated with poly(acrylamide). **b)** A depiction of the computer-modelled stabilising effect of the poly(acrylamide) on the $CO_2$ reduction reaction intermediates. ©2018 American Chemical Society. Reprinted with permission.

There is growing awareness of the need to reduce $CO_2$ emissions from the power sector, but decarbonisation of industry, transport and domestic heating has stalled. In part, this is due to the lack of financial incentive for carbon capture and conversion into value-added products in industry. Considerable research focuses on capturing and storing harmful carbon dioxide emissions but an alternative to expensive long-term storage is to use the captured $CO_2$ as a resource to make useful materials.

The reduction of $CO_2$ can be facilitated using a range of metals as electrocatalysts. Copper is unique among metals as it reduces $CO_2$ to $C_2^+$ products such as ethylene, ethane and acetate. The current ethylene market could absorb about 1.5% of the world's $CO_2$ emissions (500 Mt/year), with a current market value of $500/t, providing industry with the incentive to install carbon capture, utilisation and storage technologies. There is, therefore, a need to develop scalable high-surface-area catalysts for higher throughput hydrocarbon formation.

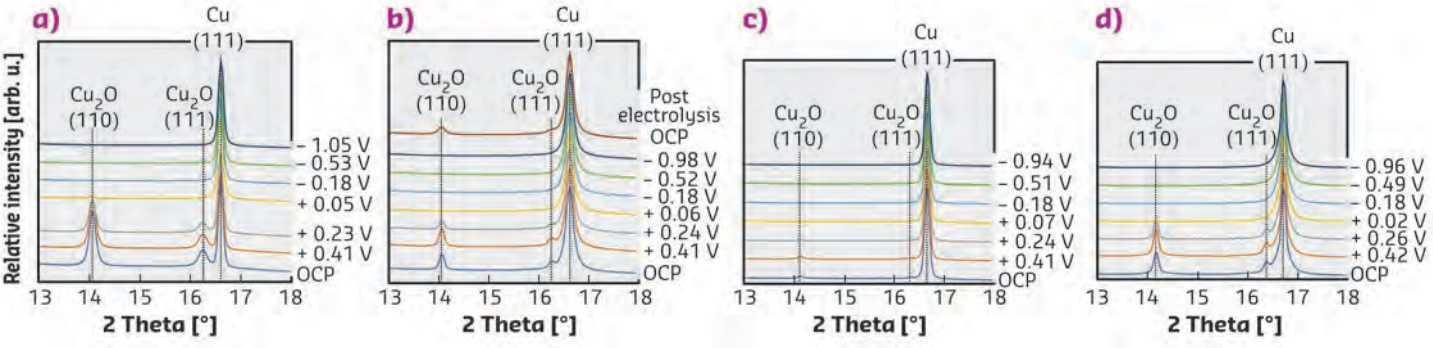


**Fig. 69:** Grazing angle X-ray diffractograms of copper foams with **a)** no additive, **b)** poly(acrylamide), **c)** poly(acrylic acid) and **d)** poly(allylamine). Copper foams were immersed in aqueous 0.1 M $NaHCO_3$ saturated with $CO_2$, all potentials reported vs RHE. ©2018 American Chemical Society. Reprinted with permission.

The efficiency of conversion is measured by the faradaic efficiency, which is the number of electrons converted to product divided by the number of electrons put in. The structure of copper affects its catalytic activity, with the crystal faces being important for the product distribution.

In this study, a porous copper foam electrocatalyst that converted $CO_2$ to ethylene with a faradaic efficiency of 13% was used. However, the addition of poly(acrylamide) doubled its faradaic efficiency to an average of 26% with peak values as high as 30%. The hypothesis is that the poly(acrylamide) modified the surface of the copper electrocatalyst to provide a stabilising effect for key intermediates during the conversion of $CO_2$ to ethylene (**Figure 68**). These effects were modelled using *ab initio* molecular dynamic simulations, but experimental evidence was required to corroborate these findings.

*Ex-situ* X-ray diffraction (XRD) experiments were performed in order to understand the preferred orientations of copper within the copper foams and to discover what effect the modification with polymers had. The results showed that all the foams had peaks corresponding to copper and cuprous oxide. However, the polymers appeared to suppress the formation of copper oxides. The copper crystalline phases were similar across all foams, which indicates that the polymer additives do not adsorb onto specific sites for preferential inhibition of crystalline phases.

*In-situ* XRD experiments were carried out on beamline **ID03**. This work was key to substantiating the hypothesis that the poly(acrylamide) provided a stabilising effect by ruling out already reported effects from crystalline phase distribution and copper oxide. Spectra were recorded during the conversion of $CO_2$ at various potentials (**Figure 69**). Initially, the reduction of surface oxidised copper ($Cu_2O$) to copper metal ($Cu^0$) was observed through the decay of the $Cu_2O$ (111) and (100) peaks with more negative applied potential. This decay was independent of surface modification. Subsequently, an increase in the $Cu_2O$ peak was observed over an hour at open circuit potential as the surface copper was oxidised upon exposure to the electrolyte solution. The product distribution of the electrocatalysis was unaffected by the quantity of surface cuprous oxide present and the enhancement in ethylene production efficiency could be attributed purely to the modifying effect of the poly(acrylamide) on the copper foam surface.

Modification of electrodeposited copper foam with poly(acrylamide) leads to a significant enhancement in faradaic efficiency for ethylene, whereas the methane yield is unaffected. Effects from crystalline phase distribution and copper oxide phases are ruled out as the source of enhancement through X-ray photoelectron spectroscopy (XPS) and *in-situ* XRD analysis. Poly(acrylamide) with copper acts as a multipoint binding catalytic system, where the interplay between activation and stabilisation of intermediates results in enhanced selectivity toward ethylene formation. Modification with poly(acrylic acid), which has a similar structure to poly(acrylamide), also shows some enhancement in activity but is unstable, whereas poly(allylamine) completely suppresses $CO_2$ reduction in favour of the hydrogen evolution reaction.

This study expands the work on copper foams whose large surface area and ease of synthesis offer favourable scalability compared to other reported materials. The results offer an additional, independently tuneable parameter for the optimisation and design of more efficient catalysts for $CO_2$ reduction.

PRINCIPAL PUBLICATION AND AUTHORS

Poly-Amide Modified Copper Foam Electrodes for Enhanced Electrochemical Reduction of Carbon Dioxide, S. Ahn (a), K. Klyukin (b), R. J. Wakeham (a), J. A. Rudd (a), A. R. Lewis (a), S. Alexander (a), F. Carla (c), V. Alexandrov (b) and E. Andreoli (a), *ACS Catal.* **8**(5), 4132–4142 (2018); doi: 10.1021/acscatal.7b04347

*(a) Energy Safety Research Institute, Swansea University (UK)*
*(b) Department of Chemical and Biomolecular Engineering, University of Nebraska (USA)*
*(c) ESRF*

# X-RAY NANOPROBE

This year's selection of scientific highlights is a fitting representation of the multidisciplinary nature of the applications and scientific fields covered by the ESRF's X-ray Nanoprobe (XNP) group. Three of our 10 presented articles deal with high-resolution brain imaging and the structural imaging of nerves (**pages 76**, **83** and **86**). The uniqueness of the resolution – far beyond that the optical microscopes – along with the three-dimensional information and the structural information obtainable through elastic scattering make X-ray nanoprobes of growing importance in biomedicine. This area is covered in particular by **ID16A**, thanks to its particular environment, which combines high-vacuum and cryogenics. Its worldwide uniqueness for biological samples makes ID16A not only a highly requested beamline, but also an instrument that brings synchrotron radiation to a new area of biomedicine.

As in previous years, the majority of the selection focuses on the structural and chemical imaging of materials at steadily increasing resolution and speed. These parameters are already, to some extent, brilliance-limited, and will experience a boost with the Extremely Brilliant Source (EBS). In order to handle this in a user-friendly manner, the new control software BLISS has been successfully deployed at **ID13**. It will replace the old SPEC control software to allow for the enhanced speed and higher complexity of EBS experiments from 2020. An efficient fast-scanning mode, available within this new control framework, has been already applied for significantly improved data-acquisition performance during one of the last user experiments with the previous source in December 2018. In order to mitigate the risk of radiation damage during scanning diffraction experiments on biological samples (induced by the expected increase of nanobeam flux density by more than an order of magnitude), an in-vacuum cryogenic sample-scanning stage, compatible with nanobeam small- and wide-angle scattering (SAXS/WAXS), has been developed within a collaborative Partnership for Soft Condensed Matter (PSCM) project (Pontoni *et al.,* PSCM and Salditt *et al.,* Göttingen University, Germany). A first prototype of this device passed a very successful test at ID13's nanobranch in summer 2018. For future fast, high-temperature, *in-situ*, nanodiffraction, material science applications, a micro-electrical-mechanical (MEMS) chip-based microsample heater has been integrated into the beamline's nanosetup (collaboration LTP MI-1216: Kubec *et al.,* Fraunhofer Inst., Germany and Keckes *et al.,* Erich Schmidt Inst., Austria) and sample temperatures of over 1 000 K were reached during *in-situ* experiments in November 2018.

The supply of *operando* conditions at **ID01** has seen an increase in requests, and the beamline staff have responded to it by designing and supplying easy-to-use, high-temperature environments compatible with gas-atmospheres and electrochemical environments. These are compatible with the nanobeams and also with the full-field diffraction microscope available to users at ID01. Bragg coherent diffraction imaging (CDI) is used with increasing robustness and the in-house experience in this field benefits the user community. This technique, essentially limited today by the available coherent flux, will certainly see deployment over a vast energy regime and, more specifically, at 7–11 keV and 19.5–21 keV, where ID01 can reliably supply nanofocused beams. For most techniques available on ID01, a robust metadata structure is now implemented, making it possible for users to easily visualise their datasets online during their experiments and also setting a sound basis for the subsequent exploration and publication of the results.

Diversity of techniques and scientific fields is also the trademark of beamline **ID16B**. Several types of sample environments can be combined with small beams, high flux and energy tenability. Over the past year, there has been an increased number of experiments combining two or more techniques simultaneously from those available on the beamline: X-ray absorption spectroscopy (XAS), X-ray fluorescence (XRF), X-ray diffraction (XRD), X-ray excited optical luminescence (XEOL), X-ray beam-induced current (XBIC) methods and nanotomography. The installation and commissioning of the fixed-figure Kirkpatrick-Baez (KB) mirrors optimised for XAS allowed an increase in the flux by a factor of 10 in the energy range between 6 to 14 keV, reducing

the measurement time and improving the data quality considerably. With an eye on preparing the beamline for the new conditions provided by the EBS, everything required to start using faster readout electronics for the XRF detectors is ready. The upgrade of the detectors is planned to take place during the EBS shutdown. This shutdown will also be used to improve the performance of the XAS and nanotomography techniques in terms of quality and acquisition time. Furthermore, the spectrometers used to measure the XEOL signal will be upgraded to allow continuous acquisition.

Most of the XNP beamlines have been built or fully refurbished over the past few years and, following suit, a significant amount of time in 2018 was dedicated to the refurbishment of **ID21**. The three optic hutches were almost fully emptied and re-equipped with new instruments. Notably, a new pair of double mirrors was installed and commissioned, offering better mechanical stability and better optical quality, with a more homogeneous beam and, ultimately, a higher horizontal resolution in the microscope. The energy range (2.1–9.1 keV) has been extended to 11.5 keV thanks to an additional Pt coating. In addition to this, a large set of equipment was also installed for the commissioning of the first prototype of the new double crystal monochromator, specially designed for spectroscopy. Over the year, software developments have been implemented, in particular to ease data processing and analysis, making it more systematic and traceable. Also, an electronic log book is now available, offering efficient recording of the experiments. In parallel, significant efforts have been dedicated to the preparation of the third part of the **ID21** technical design report, which focuses mainly on the specification and design of a new, state-of-the-art cryo-nanoscope for spectroscopy. The detailed design of this new microscope will be a major activity for ID21 during the EBS shutdown.

**T. SCHÜLLI**

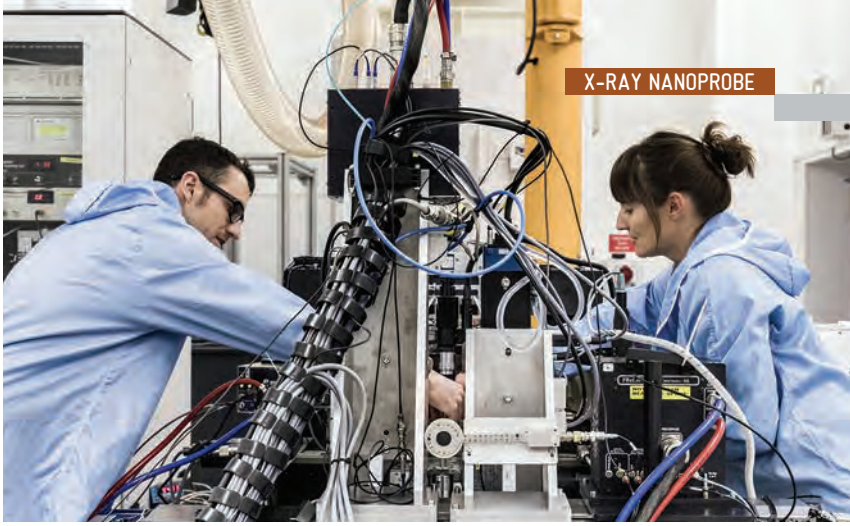


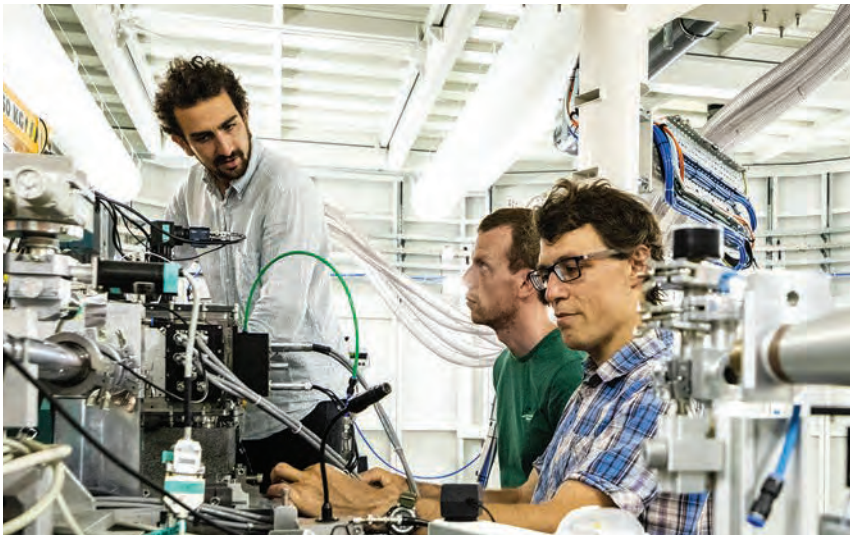

# PROBING THE ORIENTATION OF FERROELECTRIC NANODOMAIN WALLS WITH X-RAY NANODIFFRACTION

**The ability to characterise and manipulate domain structures in ferroelectric materials is crucial to their successful applications in future nanoelectronic devices. X-ray nanodiffraction imaging sheds new light on the local arrangements of nanodomain walls and their evolution with temperature.**

Almost 100 years after the first reports of ferroelectricity, and boasting an incredibly diverse portfolio of successful technological applications, ferroelectrics continue to amaze and surprise. Even for 'classic' perovskite ferroelectrics such as lead titanate ($PbTiO_3$), understanding of their behaviour, gained from decades of experience with bulk materials, is constantly being challenged by the new structures and properties being discovered in ferroelectrics with reduced dimensions. Epitaxial heterostructures such as thin films, multilayers and superlattices, which allow the electrical and mechanical boundary conditions to be controlled with great ease, have provided a particularly fruitful playground for discovering new, emergent behaviour. Some of the most intriguing properties are those that arise from the presence of domain structures and, especially, at domain boundaries. Just like any interface, domain walls break the local symmetry of the host material and therefore can have distinct, intrinsic properties of their own that often dominate the behaviour of nanoscale materials, where the density of such walls becomes very large. Enhanced electrical conductivity, emergent magnetism and unusual polarisation distributions are just a few examples of such properties found at ferroelectric domain walls.

Extremely large domain wall densities can be induced in a controlled fashion when ultrathin ferroelectric layers are confined between dielectric spacers, making ferroelectric-dielectric superlattices an ideal model system for studying nanoscale domain walls and their influence on the macroscopic functional properties. In $PbTiO_3$-$SrTiO_3$ superlattices, such domains form periodic stripes just a few nanometres across **[1, 2]**. The large domain wall density means that even tiny domain wall displacements result in large enhancements of the overall dielectric response of these artificially layered materials **[3]**, while the ferroelectric layers themselves can even exhibit negative capacitance behaviour **[4]**. It is therefore imperative to better understand the structure and dynamics of domain walls in these model systems as well as to develop scalable methods for controlling the domain structure. Unfortunately, the small length scales and complex morphology associated with these buried domain structures present many challenges for their characterisation using conventional techniques such as piezoresponse force microscopy and electron microscopy.

To probe the domain structure locally, X-ray nanodiffraction measurements were performed on $PbTiO_3$-$SrTiO_3$ superlattices deposited on

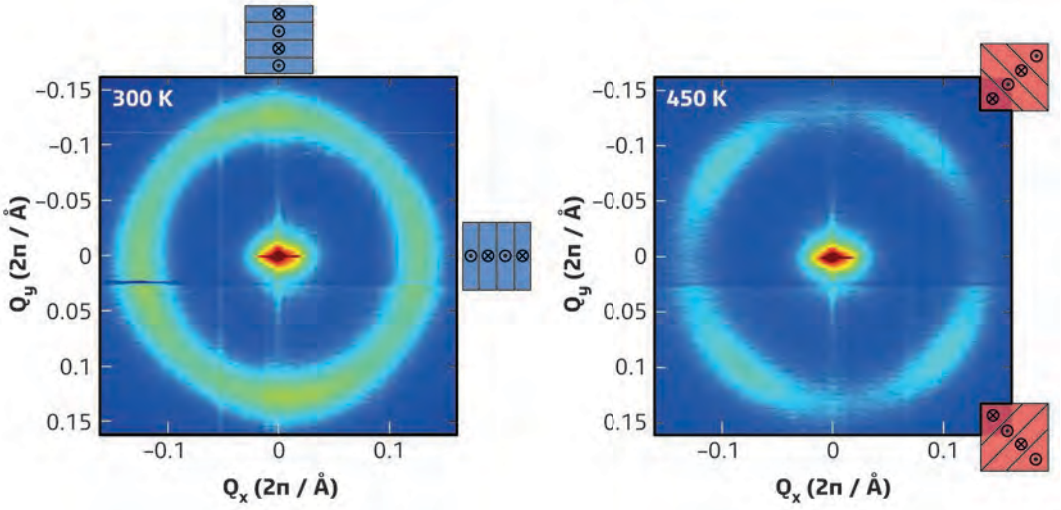


**Fig. 70:** In-plane reciprocal space maps around the (002) Bragg peak of a $PbTiO_3$-$SrTiO_3$ superlattice showing a preference for (100) domain walls at room temperature and (110) walls at 450 K.

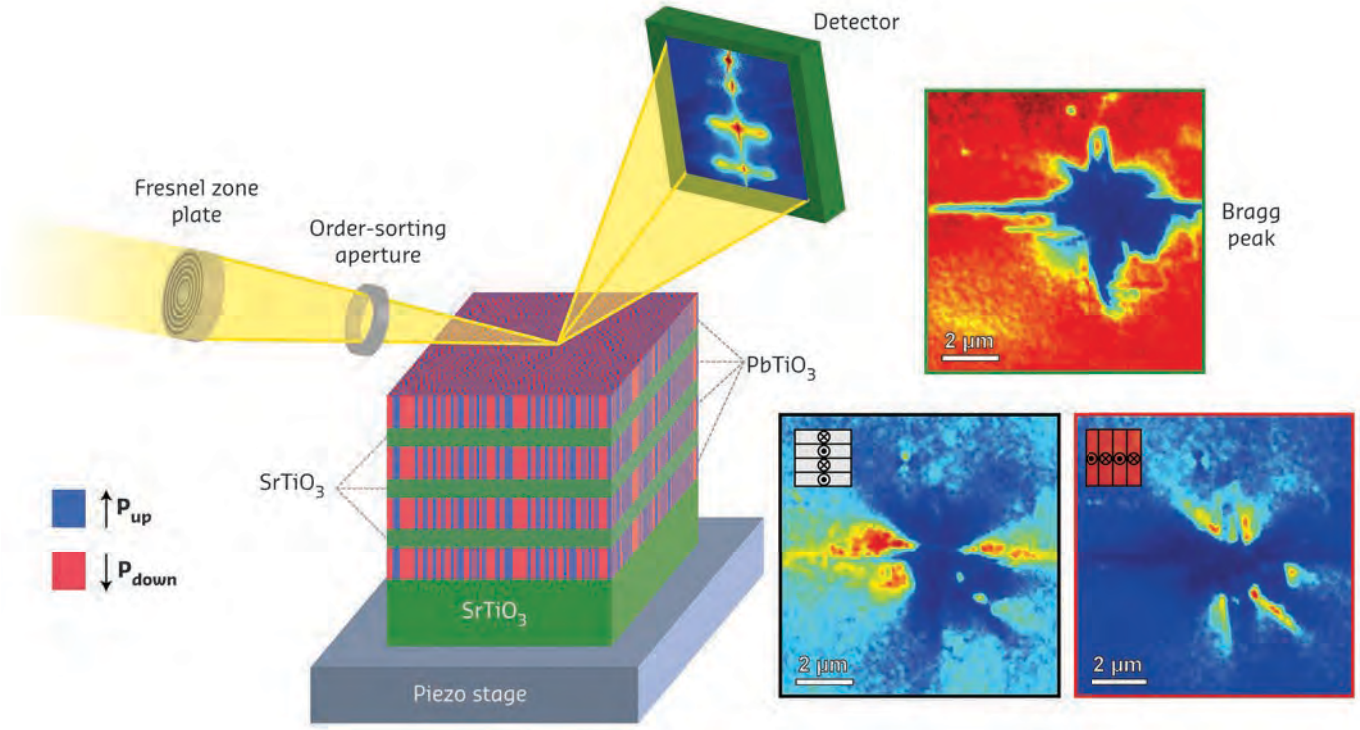


**Fig. 71:** Schematic of the setup used at beamline **ID01**. The diffracted intensity from a focused X-ray beam is used to map the local variations in ferroelectric domain wall orientation in a superlattice. Maps of domain satellite intensities corresponding to different domain wall orientations reveal domain wall alignment along defect features visible in the Bragg peak intensity map.

cubic $SrTiO_3$ substrates at the **ID01** beamline **[5]**. Macroscopic diffraction measurements as a function of temperature revealed a change of preferential orientation from (100) to (110) domain walls on heating (**Figure 70**), providing the experimental evidence of an earlier theoretical prediction of such behaviour. The focused beam and fast-scanning capability of the beamline was then used to map the intensity of the diffraction satellites from the periodic domain structure as a function of position, and hence image the regions with different orientation of the ferroelectric domain walls (**Figure 71**). Particularly interesting behaviour was observed in the vicinity of a structural defect, where domain walls were observed to align preferentially along features associated with the defect. 3D reciprocal space mapping as a function of position on the sample revealed that these features were accompanied by inhomogeneous distribution of strain and substantial strain gradients, implying that domain wall orientation could be controlled by manipulating strain. Indeed, physical discontinuities in the sample created by milling away parts of the superlattice using an ion beam were found to induce preferential alignment of domain walls along the edges of the ion-milled features, consistent with other recent work **[6]**.

These findings illustrate the potential of X-ray nanodiffraction as a valuable technique for characterising nanoscale domain structures, and demonstrate how domain wall orientations can be manipulated using temperature and sample patterning, offering an additional route to tuning the functional properties of ferroelectric heterostructures.

## PRINCIPAL PUBLICATION AND AUTHORS

Domain Wall Orientations in Ferroelectric Superlattices Probed with Synchrotron X-Ray Diffraction, M. Hadjimichael (a), E. Zatterin (a, b), S. Fernandez-Peña (c), S. J. Leake (b) and P. Zubko (a),

*Phys. Rev. Lett.* **120**, 037602 (2018); doi: 10.1103/PhysRevLett.120.037602.

*(a) London Centre for Nanotechnology and Department of Physics and Astronomy, University College London (United Kingdom)*

*(b) ESRF*

*(c) Department of Quantum Matter Physics, University of Geneva (Switzerland)*

## REFERENCES

[1] P. Zubko *et al., Nano. Lett.* **12**, 2846 (2012).
[2] P. Zubko *et al., Ferroelectrics* **433**, 127 (2012).
[3] P. Zubko *et al., Phys. Rev. Lett.* **104**, 187601 (2010).
[4] P. Zubko *et al., Nature* **534**, 524–528 (2016).
[5] S. Leake *et al., J. Mat. & Des.* **119**, 470–471 (2017).
[6] J. Park *et al., Nanoscale* **10**, 3262 (2018).

# CORRELATED DISORDER IN MYELIN ULTRASTRUCTURE FLUCTUATIONS

**Living matter is a quasi-stationary, out-of-equilibrium state; in this physical condition, investigating structural fluctuations at the nanoscale can aid in understanding its properties and functionalities. The ultrastructural fluctuations of myelin in its out-of-equilibrium functional state have been studied. Myelin fluctuations show a particular class of correlated disorder that deteriorates as the system degenerates towards thermodynamic equilibrium.**

Most processes occurring in nature take place far from thermodynamic equilibrium. This is the case of biological matter in the living state. Here, myelin has been used as a model system of out-of-equilibrium living matter **[1]**. The scheme of the myelin ultrastructure is made of the stacking of cytoplasmatic (*cyt*), lipidic (*lpg*), extracellular (*ext*) and another lipidic (*lpg*) layer (**Figure 72a**). In the equilibrium state, it is known that myelin has a quasi-crystalline ultrastructure, but there is no information on its structural fluctuations at the nanoscale in the non-equilibrium state. Scanning micro X-ray diffraction (SμXRD) at **ID13** was used to map structural fluctuations of myelin at the nanoscale in the sciatic nerve of *Xenopus laevis*.

Typical X-ray diffraction profiles, I(*s*), vs. transfer moment $s=2\sin(\theta)/\lambda$, measured at various 1 μm$^2$ spots in a freshly obtained nerve, are shown in **Figure 72b**. All X-ray diffraction profiles measured in each pixel of selected regions of interest (ROI), were employed in a Fourier analysis to extract the electron density distribution (EDD) of myelin, shown in **Figure 72c**. From the differences between two adjacent maxima in the EDD profiles, the widths of the inter-membrane spaces at the cytoplasmic ($d_{cyt}$) and extracellular ($d_{ext}$) appositions and the thickness of the lipid bilayer ($d_{lpg}$) were obtained. From these quantities, the period of the structural unit $d_\lambda=2d_{lpg}+d_{ext}+d_{cyt}$ was obtained.

In order to measure the structural fluctuations of myelin and their spatial correlation, an appropriate conformational parameter, ξ, was introduced, given by the ratio between hydrophilic and hydrophobic layers $\xi = (d_{ext}+d_{cyt})/2d_{lpg}$. This parameter univocally characterises the state of myelin. Typical maps of ξ measured on a central 80 x 80 μm$^2$ ROI of 'fresh' and 'unfresh' (measured after 18 hours, in order to investigate ageing effects) nerves are shown in **Figure 73a** and **Figure 73b**, respectively. The red spots represent areas where hydrophilic layers are larger, while in the blue spots they become smaller and the thickness of the hydrophobic layers increases.

The results show that the myelin fluctuations in the functional living state show a correlated disorder, characterised by a fat-tailed probability distribution of the hydrophobic-hydrophilic

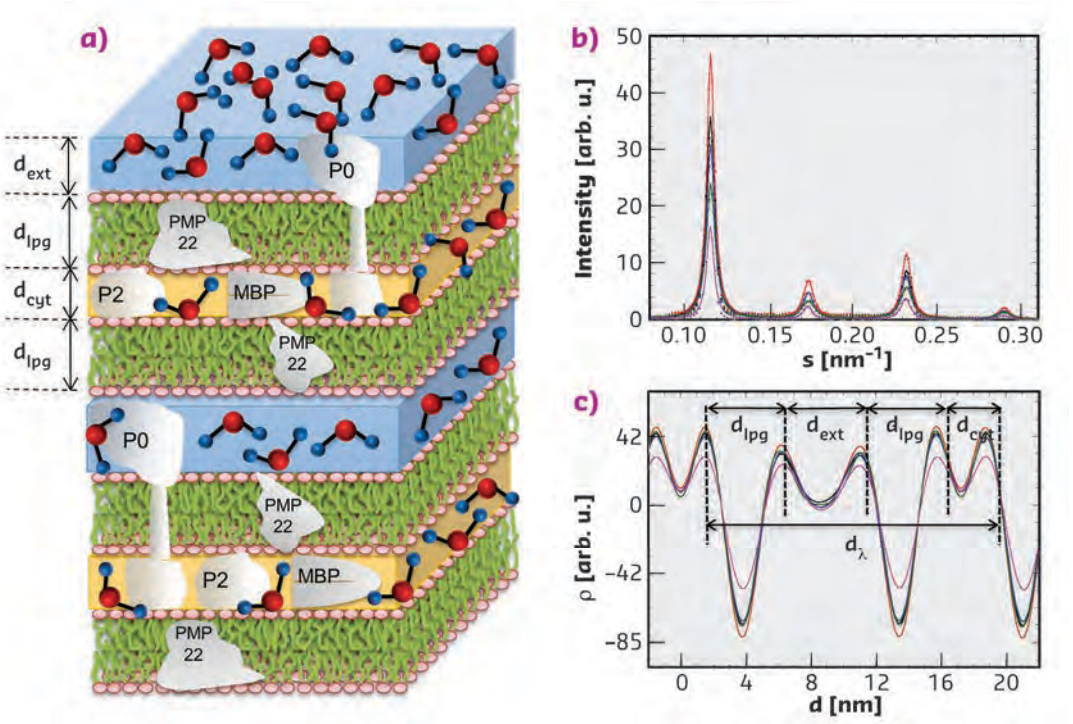


**Fig. 72: a)** Pictorial view of the myelin ultrastructure made of polar lipid groups with thickness $d_{lpg}$, intercalated by two hydrophilic layers: the Schwann cell cytoplasm and the extracellular apposition with thickness $d_{cyt}$ and $d_{ext}$, respectively. The specific myelin sheath proteins PMP22, P0, P2 and MBP are schematised. **b)** X-ray diffraction patterns measured in the fresh sample, at different sample spots. **c)** Electron density distribution computed from the diffraction patterns shown in **(b)**.

conformational parameter, ξ. This behaviour is typical of a non-equilibrium-state tuned close to a critical point **[2]**. The probability density function (PDF) of ξ has been modelled by a Lévy stable distribution (**Figure 73c**), which provides a general statistical description of complex signals deviating from equilibrium **[3, 4]**. This is supported by the experimental data for the aged phase, where the structural fluctuations are frozen, losing the correlated disorder; indeed, here, ξ distribution changes to a Gaussian line shape function, which is peculiar of a static state approaching equilibrium (**Figure 73c**).

The results open new perspectives for developing SμXRD with focused mesoscale X-ray beams in next generation synchrotron sources to characterise biological systems in out-of-equilibrium state **[5, 6]**. Besides its impact on fundamental statistical physics, this research could have implications for biomedicine, where moving the clinical investigation from structural morphology to structural dynamics is expected to open new possibilities for detecting early degenerated states, *e.g.*, those related to neurodegenerative diseases.

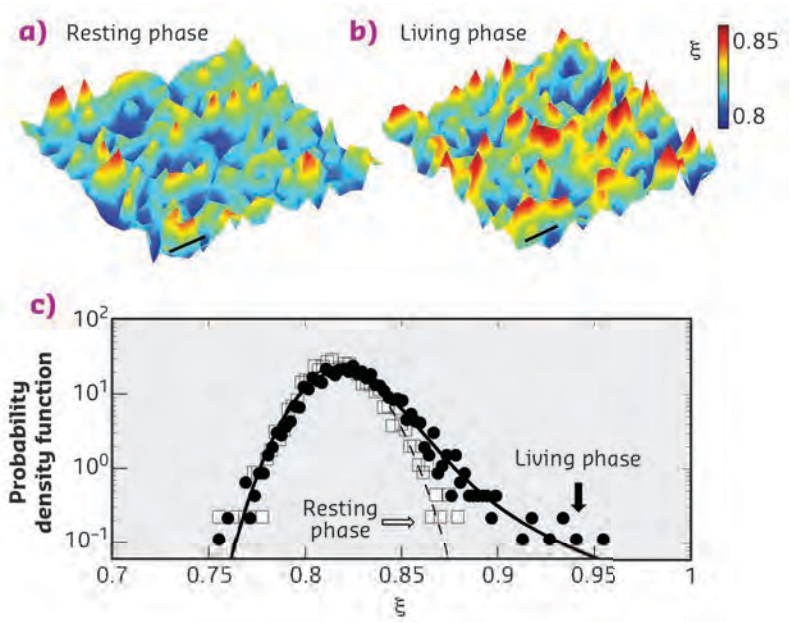


**Fig. 73:** Map of the conformational parameter, ξ, in a selected ROI of the **a)** unfresh and **b)** fresh nerve. The bar corresponds to 10 μm. **c)** Probability density function (PDF) of ξ in the unfresh (open squares) and in the fresh (full circles) sample in semi-log plot. The Levy PDF curve found in the fresh sample (continuous line) is reported. The fat tail in the distribution deviates, assuming a Gaussian profile (dashed line) in the unfresh sample.


PRINCIPAL PUBLICATION AND AUTHORS

Nanoscale correlated disorder in out-of-equilibrium myelin ultrastructure, G. Campi (a), M. Di Gioacchino (a, b, c), N. Poccia (d), A. Ricci (b), M. Burghammer (e), G. Ciasca (f) and A. Bianconi (a, b, g), *ACS Nano* **12**(1), 729–739 (2018); doi: 10.1021/acsnano.7b07897.

*(a) Institute of Crystallography, CNR (Italy)*
*(b) Rome International Center for Materials Science Superstripes (RICMASS) (Italy)*
*(c) Department of Science, Nanoscience section, Roma Tre University (Italy)*
*(d) Department of Physics, Harvard University, Massachusetts (USA)*
*(e) ESRF*
*(f) Physics Institute, Catholic University of Sacred Heart, Rome (Italy)*
*(g) National Research Nuclear University, Moscow Engineering Physics Institute (Russia)*

REFERENCES

[1] N. Poccia, *et al., Sci. Rep.* **4**, 5430 (2014).
[2] T. Mora and W. Bialek, *J. Stat. Phys.* **144**, 268–302 (2011).
[3] P. Barthelemy *et al., Nature* **453**, 495–498 (2008).
[4] N.E. Humphries *et al., Nature* **465**, 1066–1069 (2010).
[5] G. Campi *et al., Acta Biomater.* **23**, 309–316 (2015).
[6] G. Campi *et al., Nanoscale* **9**, 17274–17283 (2017).


# THREE-IN-ONE ON THE NANOSCALE

**Semiconductor devices rely largely on the controlled separation of charge carriers in internal electric fields – by strain and/or chemical potentials. It is now possible to simultaneously gain information on the chemical composition, the valence (*i.e.* oxidation state), and the location of the charge separation at very high spatial resolution. As this is possible during operation of the device, this method can be used to understand the working principle of heterogeneous devices.**

A light-emitting nanowire heterostucture diode was studied, in which segments of Si–GaAs–Ga–Si were stacked in sequence. In order to understand the operation of the device, and to draw up the corresponding electronic band diagram, it was necessary to identify the phase of the Ga segment in the device, the doping level of the silicon segments, as well as the active region of the functional device.

The measurements relied on raster-scanning the nanofocused X-ray beam at **ID16B** with a size of about 80 nm across the sample and measuring the characteristic X-ray fluorescence (XRF), as

shown in **Figure 74**. As a result, the elemental composition of the scanned area was accurately determined. By comparing the As–Ga ratio in the Si segments of the structure, it was possible to verify that the silicon segments are highly doped with As, thus being n-type.

The simultaneously recorded current, given by the excitation and separation of charge carriers by the incoming photons (such as in a solar cell), was then analysed as a function of the position of the X-ray beam. The highest intensity of the X-ray beam-induced current (XBIC) measurements was obtained in the GaAs segment towards the interface between the GaAs and Ga segment, clearly identifying this as the active region of the device.

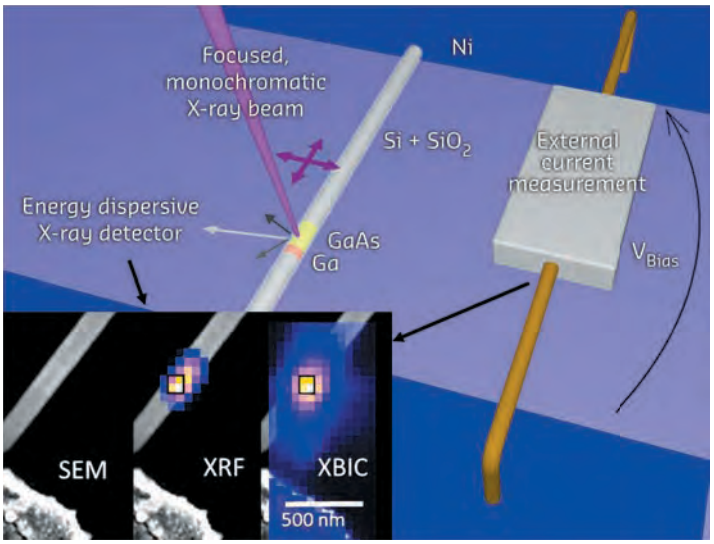


**Fig. 74:** Measurement on nanowire heterostructures. A monochromatic, focused, hard X-ray beam was raster-scanned across the sample. At each point, the characteristic X-ray fluorescence and the current through the sample was measured. The insets show a scanning electron microscope (SEM) image and the Ga K-line fluorescence data, and the XBIC current overlaid on the SEM image. The measurement was repeated for a set of incoming X-ray energies.

Finally, the energy of the incoming monochromatic X-rays was varied around the Ga K-absorption edge at 10.37 keV. With X-ray absorption near edge structure (XANES) spectroscopy, the oxidation state of Ga can be determined. In this experiment, the energy was systematically varied for a number of raster-scans across the sample. The selection of the data shown in **Figure 75** shows the XANES information at high spatial resolution. The shift of the absorption edge in the obtained spectra (**Figure 75b**) clearly revealed that a significant fraction of the Ga segment in the devices was in the metallic state. By overlaying all three information channels, it was possible to conclusively determine the electronic band diagram of the complex nanostructure, showing that the unusual LED heterostructure relies on a Schottky diode forming between the metallic Ga and the semiconducting GaAs.

This experiment illustrates how XANES and XBIC mapping can be combined to identify the properties of a complex semiconductor nanostructure, in *operando* mode. A further significant advantage of this synchrotron-based method is found in the high penetration length of hard X-rays. This greatly reduces the sample preparation effort usually required for electron microscopy methods. In future, this will enable direct measurements on finished solar cells and batteries while they are in use, without the need to change them structurally.

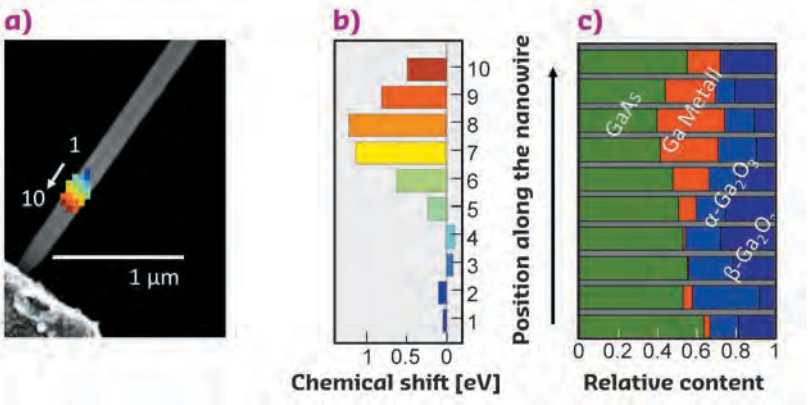


**Fig. 75:** Energy and spatial resolution: the onset of absorption of the incoming X-ray beam at the K-edge of gallium is shifted as a function of position along the nanowire **(a, b)**. When compared to the corresponding reference spectra, this shift indicates the presence of metallic gallium (**c**, red) at positions 5-10.

PRINCIPAL PUBLICATION AND AUTHORS

*In operando* X-ray imaging of nanoscale devices: Composition, valence, and internal electrical fields, A. Johannes (a), D. Salomon (a), G. Martinez-Criado (a, b), M. Glaser (c), A. Lugstein (c) and C. Ronning (d), *Sci. Adv.* **3**, 12, eaao4044 (2017); doi: 10.1126/sciadv.aao4044.

*(a) ESRF*
*(b) Instituto de Ciencia de Materiales de Madrid, CSIC, Madrid (Spain)*
*(c) Institute for Solid State Electronics, Technische Universität Wien (Austria)*
*(d) Institute of Solid State Physics, Friedrich-Schiller-University Jena (Germany)*

# REVEALING THE MANUFACTURING TECHNIQUES OF LOUIS DUCOS DU HAURON IN HIS EARLY COLOUR PHOTOGRAPHS

**Louis Ducos du Hauron (1837–1920) was one of the pioneers of colour photography. Since patenting a first three-colour printing process in 1869, he tirelessly sought to improve his processes. This work focuses on how he printed positives, through an extended bibliographic review and the microanalysis of fragments from three of his photographs. This sheds light on a largely ignored but major contributor to the history of photography.**

Ducos du Hauron dedicated his entire life to elaborating physical-chemical processes for colour photography. This work specifically focused on his 'three-colour print' technique: three black and white negatives of the same view were first produced with the camera using three coloured (orange, green, and purple) filters (**Figure 76a**). Then, three semi-transparent monochrome positive images; blue, red, and yellow, were printed from these three negative plates, respectively (**Figure 76b**). The three monochrome prints were then aligned and assembled to generate the final colour print (**Figure 76c**).

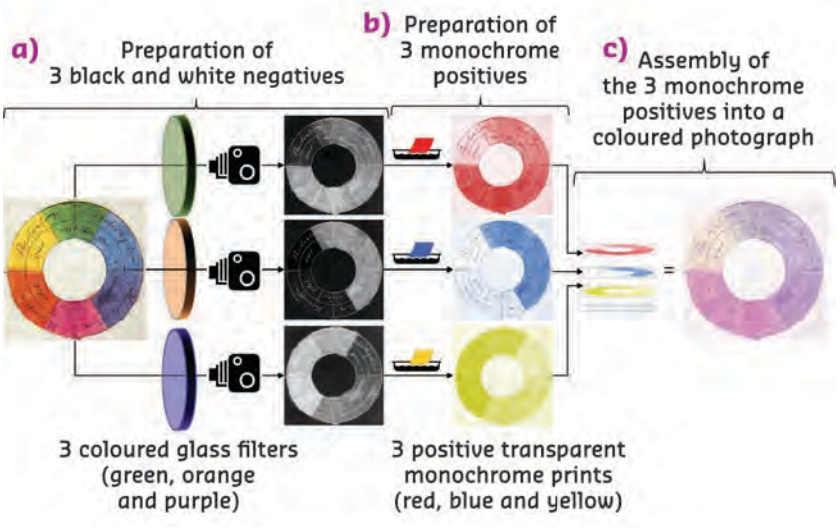


**Fig. 76:** General principle of three-colour carbon printing developed by Ducos du Hauron.

The present research was carried out with a dual approach. On one hand, an in-depth bibliographic review was made of the many protocols Ducos du Hauron published, revealing several complex multistep recipes with a clear rational in the methodological evolution of the processes and the ingredients used. Recipes are sketched in details in the supporting information of the publication **[1]**. However, this historical evolution is not linear as early recipes were continuously improved, concomitant with the elaboration of completely different methods, making the overall chronological review challenging.

On the other hand, micro-Fourier transform infrared (μFTIR) spectroscopy, micro X-ray fluorescence (μXRF) spectrometry and Cr K-edge micro X-ray absorption near edge structure (μXANES) spectroscopy analyses were performed at **ID21** on tiny fragments sampled in three colour photographs produced by Ducos du Hauron. The aim was to identify the organic and inorganic components constitutive of the three positive monochromes, and compare them with ingredients described in the various recipes.

First, microscopic observations revealed that each monochrome was indeed composed of two layers: a coloured and a transparent layer. The presence of gelatin and Cr(III) in all the coloured layers is in agreement with the use of the carbon-printing technique: a gelatin film, light-sensitised by the addition of dichromate salts, is exposed to light under the negative plates. In light-exposed areas, Cr(VI) is reduced to Cr(III) and gelatin is insolubilised while the unexposed gelatin could be later dissolved in hot water. Gelatin can be coloured by using stable and water-insoluble pigments. In the studied samples, Prussian blue pigment was identified by μFTIR and μXRF in the blue monochrome and carmine by μRaman in the red monochromes. The transparent layers were made of gelatin in two photographs and of collodion in one photograph.

The composition of the first two photographs agrees with the so-called gelatin 'cuirasse' method, as described in 1870 and 1878 by the Ducos du Hauron brothers: an uncoloured gelatin layer is applied to the developed coloured gelatin films to fill in the holes (which correspond to light areas of the photographs) and, after immersion in an alum bath, to harden the final monochrome. A higher Al concentration was indeed observed in these transparent gelatin layers. Other materials, such as natural vegetal resin, lead and ricinoleic acid, were identified, and were ascribed to the use of varnish, lead-based driers and castor oil, respectively. Ducos' texts

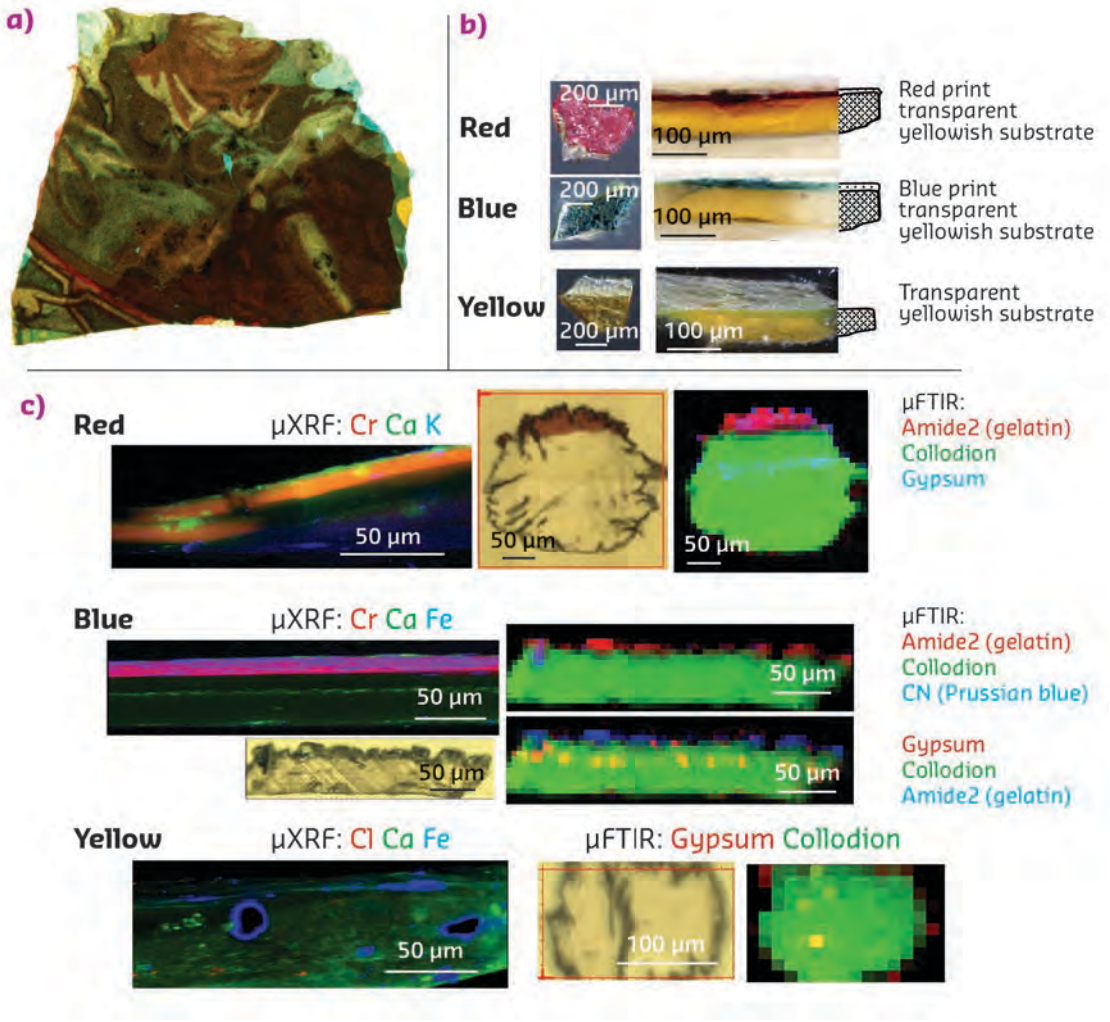


**Fig. 77: a)** Photograph of a piece of a colour print from the Niepce museum (© Niepce museum). **b)** Visible-light images and **c)** µFTIR and µXRF maps of the fragments from the red, blue, and yellow prints, showing the nature and distribution of the main components.

provide precise comments about the pros and cons of these various materials in photography. As an example, castor oil is probably responsible for the yellow aspect of the collodion layers in the photograph shown in **Figure 77**.

In summary, this study brought to light complex multi-step recipes based on optics, photochemistry (carbon-print), organic and inorganic chemistry. Thanks to the high resolution provided by the synchrotron microscopes, the various ingredients involved were identified and localised through their spectroscopic signature and confirm the relevance of synchrotron spectromicroscopy for the characterisation of historical photographs. The impressive correlation between texts and chemical analyses calls for a wider application to photography history.

## PRINCIPAL PUBLICATION AND AUTHORS

Rediscovering Ducos du Hauron's Color Photography through a Review of His Three-Color Printing Processes and Synchrotron Microanalysis of His Prints, M. Cotte (a, b), T. Fabris (b), J. Langlois (c), L. Bellot-Gurlet (d), F. Ploye (e), N. Coural (c), C. Boust (c, f), J.-P. Gandolfo (g), T. Galifot (h) and J. Susini (a), *Angew. Chem. Int. Ed. Engl.* **57**(25), 7364–7368 (2018); doi:10.1002/ange.201712617.

*(a) ESRF*
*(b) Laboratoire d'Archéologie Moléculaire et Structurale (LAMS), UMR 8220, UPMC/CNRS, Sorbonne Universités, Paris (France)*
*(c) Centre de Recherche et de Restauration des Musées de France (C2RMF), Palais du Louvre, Paris (France)*
*(d) MONARIS, UMR 8233 UPMC/CNRS, Sorbonne Universités, Paris (France)*
*(e) Photographs Conservator, Paris (France)*
*(f) UMR 8247 PCMTH, Chimie ParisTech (IRCP)*
*(g) Ecole nationale supérieure Louis-Lumière, La Plaine Saint-Denis (France)*
*(h) Musée d'Orsay, Paris (France)*

## REFERENCES

[1] https://onlinelibrary.wiley.com/action/downloadSupplement?doi=10.1002%2Fanie.201712617&file=anie201712617-sup-0001-misc_information.pdf

# ORIGIN OF THE BRIGHT PHOTOLUMINESCENCE OF SILVER CLUSTERS CONFINED IN LTA ZEOLITES

**XEOL-EXAFS is combined with TD-DFT-based computational modelling and time-resolved optical spectroscopy to unravel the structural and electronic properties of photoluminescent silver clusters in zeolite.**

Clusters of a few metal atoms have physical properties distinct from single atoms and larger nanoparticles. Like molecules, they have discrete energy levels allowing electronic transitions conferring remarkable photoluminescent properties **[1]**.

To protect them against aggregation, metal clusters can be stabilised in water-dispersible organic scaffolds such as peptides, proteins, DNA, and polymers or in solid-state matrices such as glasses and zeolites. Zeolites are aluminosilicates found naturally or produced synthetically on an industrial scale and they are used for a wide range of domestic and industrial applications. They consist of a rigid and well-defined crystalline framework made of molecular-scale channels and cavities that are perfectly suited to host small clusters.

Silver clusters that self-assemble in the cavities of faujasite (FAU) and Linde Type A (LTA) zeolites upon heat treatment or X-ray irradiation have homogeneous, photostable and efficient green-yellow emissions reaching unity **[2, 3]**. This makes them outstanding candidates for light-based applications such as wavelength converters for light-emitting diodes (LEDs) and luminescent tags. Despite their attractive photoluminescence properties, little is known about their structural and electronic properties.

In a new approach, X-ray excited optical luminescence (XEOL)-detected extended X-ray absorption fine structure spectroscopy (EXAFS) was used at beamline **BM08** (LISA CRG). XEOL at the Ag K-edge exclusively detects the XAFS signal (**Figures 78a** and **78b**) from the atoms constituting the emissive species.

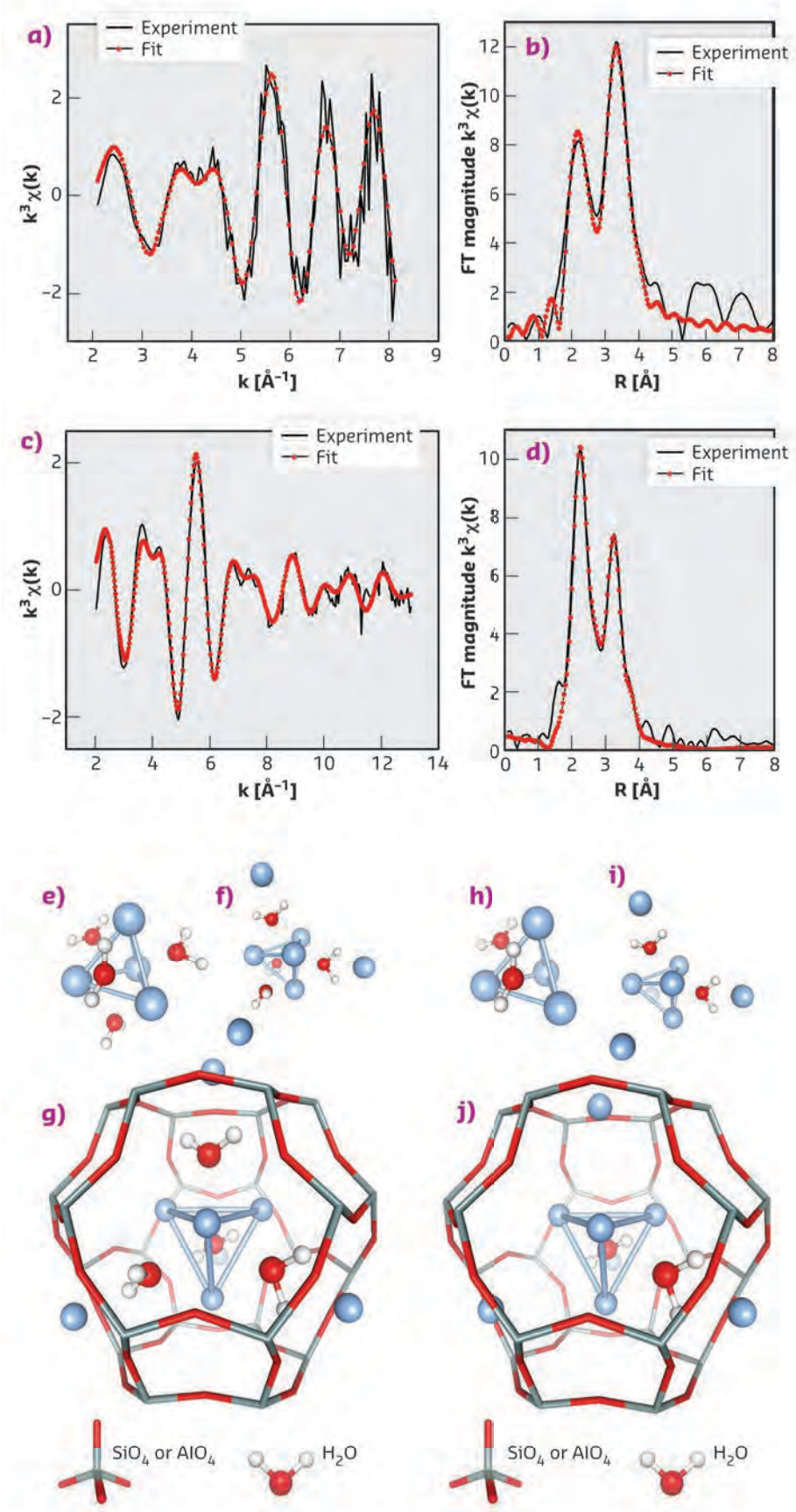


**Fig. 78:** Ag K-edge XEOL and transmission-detected EXAFS and Fourier transform (FT) of heat-treated $Ag_3K_9$-LTA and derived structures. **a)** XEOL-detected and **c)** transmission-detected $K_3$-weighted Ag K-edge EXAFS with **b)** the phase corrected XEOL-detected FT and **d)** transmission-detected FT best fits. Structures of **e)** $Ag_4(H_2O)_4$ and **h)** $Ag_4(H_2O)_2$, including $Ag_R$ cations (**f** and **i**) and embedded in the sodalite cage (~0.66 nm free diameter) (**g** and **j**), respectively.

This innovative technique allowed a selective determination of the structure of the emitting Ag species in LTA zeolite in the presence of charge-balancing $K^+$ ions ($Ag_3K_9$-LTA), providing new insight compared to earlier work **[3]**.

The three-dimensional structures of the silver clusters were then determined by combining the XEOL fitting results with those obtained from conventional transmission-detected EXAFS (**Figures 78c** and **78d**) collected at beamlines **BM08** (LISA CRG) and **BM26** (DUBBLE CRG). With this technique, the luminescence of silver LTA zeolites was unambiguously assigned to a mixture of two doubly-charged four-atom tetrahedral hydrated silver clusters, $Ag_4(H_2O)_x^{2+}$ (x = 2 and 4), positioned at the centre of sodalite cages of the LTA zeolite (**Figures 78e** to **78j**).

The structures obtained experimentally were confirmed computationally with geometry optimisations by using density functional theory (DFT) methods, while time-dependent DFT (TD-DFT) was applied to calculate the optical transitions. This theoretical modelling indicates that the remarkable optical properties resulting from this structure originate from a confined super-atom quantum two-electron system, in which hybridised silver and water oxygen orbitals are highly delocalised over the cluster.

Upon excitation, one electron of the s-type highest occupied molecular orbital (HOMO) $^1S_0$ is promoted to the p-type lowest unoccupied molecular orbitals (LUMO) $^1P$, perturbed by the water ligand field interaction, and relaxes through enhanced system inter-crossing into green luminescent long-lived microsecond triplet states, $^3P$, as presented in **Figure 79**. These calculated transitions were confirmed by time-resolved optical spectroscopy.

This study may be extended to other materials containing few-atom clusters made of silver and, perhaps, other metals. This new understanding may yield an entire class of materials with tailored properties based on luminescent silver clusters that should find technological applications in the near future.

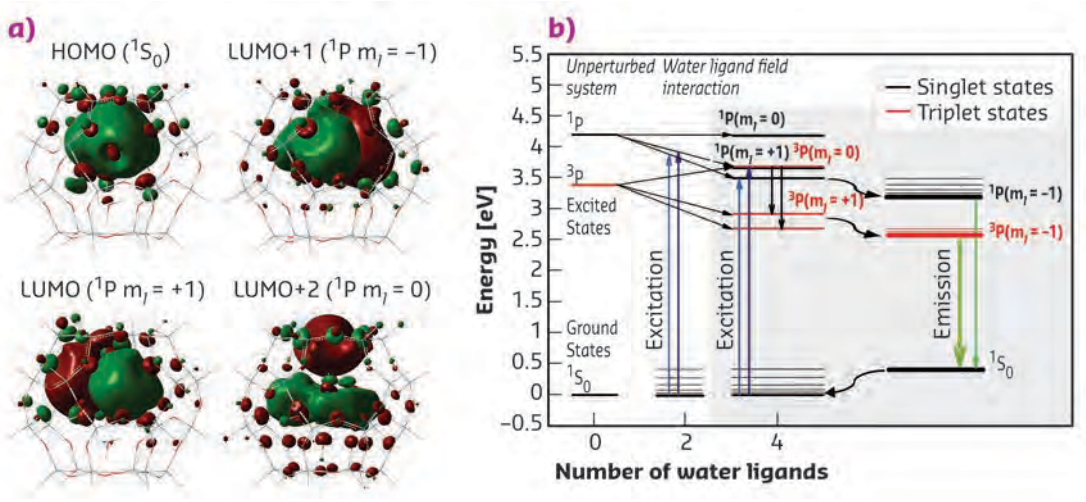


**Fig. 79:** Frontier orbitals of $Ag_4(H_2O)_4(Si_{24}H_{24}O_{36})^{2+}$ and energy level diagram of $Ag_4(H_2O)_2^{2+}$ and $Ag_4(H_2O)_4^{2+}$ clusters in $Ag_3K_9$-LTA. **a)** Frontier orbitals consist of one single symmetric s-type HOMO ($^1S_0$) and three singlet one-node p-type $^1P$ ($m_l$ = -1, +1 or 0) LUMOs ($p_x$, $p_y$, $p_z$) delocalised over all the silver and oxygen atoms of the cluster. **b)** Energy level diagram showing the ground state $^1S_0$ and the excited states $^3P$ and $^1P$ of water-free unperturbed $Ag_4^{2+}$ clusters and the ground state $^1S_0$ and the six singlet $^1P$ and triplet $^3P$ excited states of $Ag_4(H_2O)_2^{2+}$ and $Ag_4(H_2O)_4^{2+}$ perturbed by water ligand field interaction. Blue arrows represent the allowed transitions while the green arrows represent the luminescent transitions between the relaxed states.

## PRINCIPAL PUBLICATION AND AUTHORS

Origin of the bright photoluminescence of few-atom silver clusters confined in LTA zeolites, D. Grandjean (a), E. Coutiño-Gonzalez (b), N. T. Cuong (c, d), E. Fron (b), W. Baekelant (b), S. Aghakhani (a), P. Schlexer (e), F. D'Acapito (f), D. Banerjee (f), M. B. J. Roeffaers (g), M. T. Nguyen (d), J. Hofkens (b) and P. Lievens (a), *Science* **361**, 686–690 (2018); doi: 10.1126/*science*.aaq1308.
*(a) Laboratory of Solid State Physics and Magnetism, KU Leuven (Belgium)*
*(b) Molecular Visualization and Photonics, KU Leuven (Belgium)*
*(c) Faculty of Chemistry, Hanoi National University of Education (Vietnam)*
*(d) Department of Chemistry, KU Leuven (Belgium)*
*(e) Dipartimento di Scienza dei Materiali, Università di Milano-Bicocca (Italy)*
*(f) ESRF*
*(g) Centre for Surface Chemistry and Catalysis, KU Leuven (Belgium)*

## REFERENCES

[1] H. Hakkinen, *Adv. Phys. X* **1**, 467–491 (2016).
[2] G. De Cremer *et al., J. Am. Chem. Soc.* **131**, 3049–3056 (2009).
[3] O. Fenwick *et al., Nat. Mater.* **15**, 1017–1022 (2016).

# THREE-DIMENSIONAL NANO-IMAGING OF HUMAN BRAIN TISSUE

**X-ray nanoholotomography allows large-scale, label-free, direct imaging with isotropic voxel sizes down to 25 nm. It is especially attractive for the non-destructive hierarchical imaging of human tissues, as it avoids physical slicing and, therefore, complements well-established histology and electron microscopy approaches.**

Pathologists generally examine micrometre-thin tissue slices by means of optical microscopy. The analysis helps to exclude or to identify diseases. More recently, high-resolution hard X-ray microtomography (µCT) has been applied to complement histology by adding the third dimension **[1, 2]**. The lateral spatial resolution of the optical micrographs of the histological slices, however, has been at least a factor of two better than for µCT. Through the combination of X-ray optics and the phase contrast mode at the nano-imaging beamline **ID16A**, the spatial resolution has been greatly improved, reaching deep into the nanometre range (*i.e.*, well beyond the optical limit). The embedding of the human brain tissue into paraffin, as is clinical practice in neuropathology departments, results in an amazing contrast, allowing for the identification of a variety of nanometre-sized anatomical features. Many anatomical features become evident even if one sets dedicated staining protocols aside. Consequently, the imaging technique, which has been developed and implemented at ID16A, can be regarded as a milestone in the establishment of nanoanatomy as a fundamental chapter of nanomedicine.

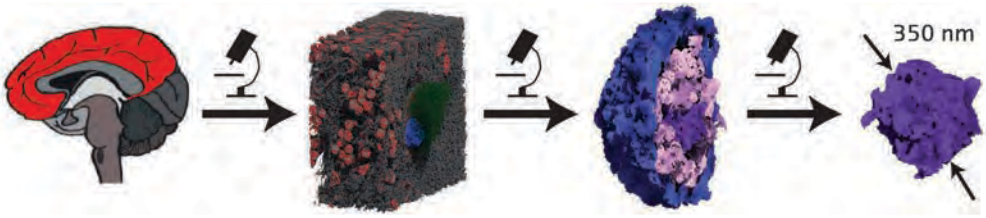


**Fig. 80:** Hierarchical brain imaging down to the true nanometre scale. Hard X-ray nanoholotomography bridges the resolution gap in three-dimensional imaging between microtomography and electron microscopy with tissue ablation.

The term 'holotomography', coined in 1999 **[3]**, relates to in-line Gabor holography introduced in 1948 **[4]** and stems from the combination of holographic and tomographic reconstructions. The term holography was introduced by D. Gabor to indicate that the method records the complete wave front (*i.e.*, amplitude and phase). Therefore, the holographic reconstruction, which is done numerically, recovers both the real and imaginary parts of the refractive index. For in-line holography, a partially coherent beam interferes with itself so that no separate reference beam is required. Thus, in-line holography is considered the poor man's holography, but is, in fact, the original and the oldest one.

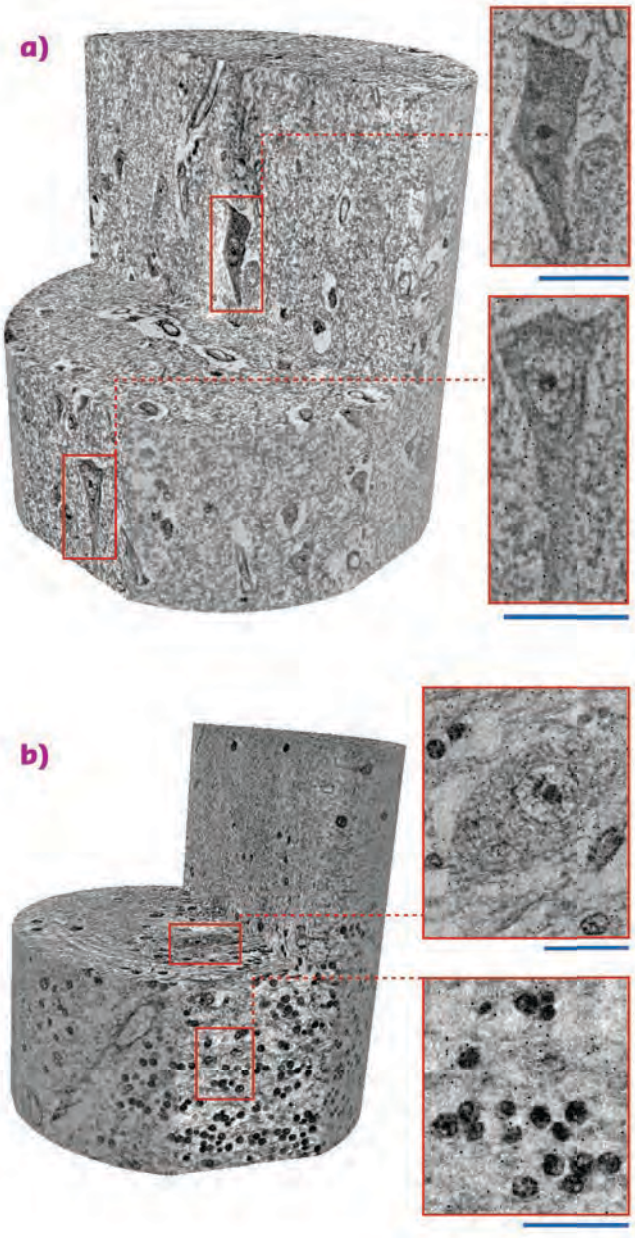


**Fig. 81:** Datasets with 100 nm voxels allow the three-dimensional imaging of **a)** human neocortex and **b)** human cerebellum tissues with sufficient resolution to identify individual biological cells post mortem

Hard X-ray nanoholotomography (XNH) is regarded as non-destructive because it does not require physically slicing the specimen and multiple measurements exhibit the same result, even after long X-ray exposure. The 180° acquisition and tomographic reconstruction creates a virtual three-dimensional model without destroying the original object; here the selected human brain tissues were treated according to the standard protocols in pathology for a wide variety of daily diagnoses.

XNH has numerous advantages with respect to the established techniques. First, the penetration depth of the hard X-rays is much larger than for visible light and electrons, which makes mechanical slicing of specimens usually investigated in research and clinical applications obsolete. Second, the employment of local phase tomography allows for hierarchical imaging (see **Figure 80**). This multiscale approach includes a fast overview scan of a volume close to one cubic millimetre in order to select a region of interest. This region can be subsequently investigated with voxel volumes three orders of magnitude smaller. Third, after XNH, the same tissue can be used for the well-established histological analysis.

**Figure 81** represents two local tomograms of human brain tissues, namely neocortex and cerebellum. The volume rendering of the brain tissue, after clinically relevant tissue preparation, but without cutting, highlights the electron microscopy-like data quality at 100 nm voxel length. The virtual cutting planes illustrate the presence of cellular and even subcellular features, which include cell somata, dendrites, nuclear envelopes, nucleoli, and structures within the nucleus. The scale bars correspond to a length of 20 µm. It is known that the desired spatial resolution restricts the volume accessible. Local tomography approaches allow for the combination of volumes measured separately within the same object, so that a significant portion of the human brain can be imaged. As the handling of data with tera- to petabyte size advances, visualisation of the entire brain with nanometre resolution could become available during the next decade.

PRINCIPAL PUBLICATION AND AUTHORS

Hard X-ray nanoholotomography: large-scale, label-free, 3D neuroimaging beyond optical limit, A. Khimchenko (a), C. Bikis (a), A. Pacureanu (b), S.E. Hieber (a), P. Thalmann (a), H. Deyhle (a), G. Schweighauser (c), J. Hench (c), S. Frank (c), M. Müller-Gerbl (d), G. Schulz (a), P. Cloetens (b) and B. Müller (a), *Adv. Sci.* **5**, 1700694 (2018); doi: 10.1002/advs.201700694.
*(a) Biomaterials Science Center (BMC), Basel (Switzerland)*
*(b) ESRF*
*(c) Institute of Pathology, Basel (Switzerland)*
*(d) Musculoskeletal Research Group, Basel (Switzerland)*

REFERENCES

[1] A. Khimchenko *et al.*, *NeuroImage* **139**, 26 (2016).
[2] S. E. Hieber *et al.*, *Sci. Rep.* **6**, 32156 (2016).
[3] P. Cloetens *et al.*, *Appl. Phys. Lett.* **75**, 2912 (1999).
[4] D. Gabor, *Nature* **161**, 777 (1948).

# CRYSTALLOGRAPHIC ORIENTATION OF FACETS AND PLANAR DEFECTS IN FUNCTIONAL NANOSTRUCTURES

**The physico-chemical properties of nanostructures depend on their surface facets. This work exploits a pole figure approach to determine the orientation of a nanostructure using a nanofocused X-ray beam. This enables facets to be rapidly indexed and planar defects to be identified. The methodology provides a unique insight into the connection between structure and properties of nanomaterials.**

Understanding how facets develop on a nanocrystal is essential to controlling the crystal's geometric shape, which, in turn, is critical to controlling the crystal's chemical and electronic properties. A thorough understanding of the formation of facets at the surface is required to optimise their properties. The study of nanocrystal shape evolution is a critical topic in the field of nanomaterials when it comes to rationally engineering nanocrystals with desirable surface structures, and hence properties.

Morphologies of nanocrystals can be characterised by high-resolution transmission electron microscopy. Significant progress has recently been achieved, pushing the resolution to atomic level in nanocrystals as large as 100 nm. However, for larger particles, this is more challenging. In all cases, microscopy requires

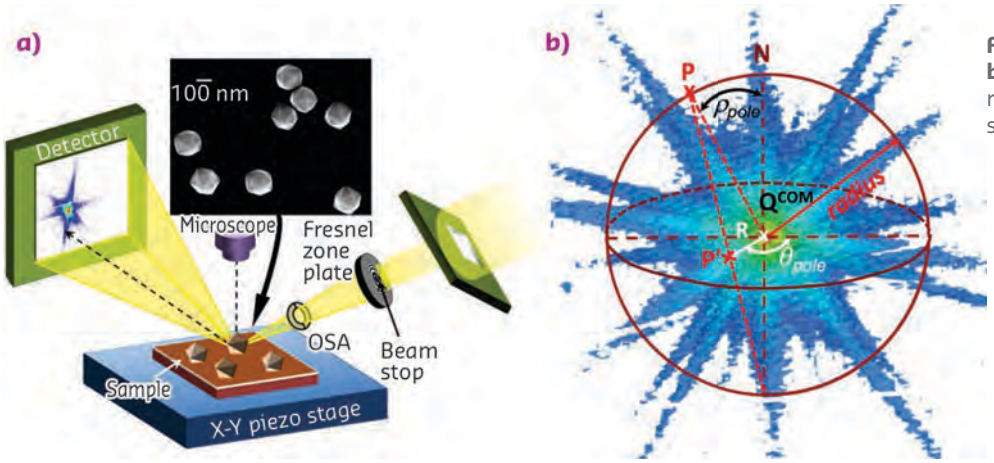


**Fig. 82: a)** Experimental set-up. **b)** 3D reciprocal space pattern around one reflection of a single nanoparticle before stereographic projection.

orienting the sample to have the beam parallel to the various facets to be indexed. Therefore, other approaches that enable a direct identification of all surface facets simultaneously should be explored.

Coherent X-ray diffraction imaging (CXDI) is a lens-less imaging technique whereby the intensity local to each Bragg peak encodes the internal displacement field and the shape of the illuminated object. Identifying a single Bragg reflection is often straightforward if the crystal growth axis is known. Here, a method to identify the facets present on a crystal is demonstrated, providing a fast, on-the-fly method to monitor facet modulation. Using the experimental setup demonstrated in **Figure 82a**, a 3D data set at a given (hkl) Bragg reflection is measured on a single nanostructure using a nanofocused X-ray beam (**Figure 82b**). From the stereographic projection of this 3D data set, the surface facets and planar defects can be characterised and indexed (**Figure 83**). Contrary to microscopy, the sample is aligned once: one single rocking-curve (few degrees) provides access to all the facets and the crystal orientation can be extracted.

In order to resolve the internal structure, it is necessary to measure multiple Bragg reflections. The technical challenge of rotating a crystal through many axes to measure additional Bragg peaks is significant and often requires additional sample characterisation. It is also demonstrated that the orientation matrix can be determined to sufficient accuracy to easily locate and measure multiple Bragg reflections from the same object.

This technique was applied at beamline **ID01**. The coherent beam was focused to 700 nm x 400 nm using a Fresnel Zone Plate or Kirkpatrick-Baez (KB) mirrors, in order to illuminate a single nanowire or nanoparticle. To illustrate the possibilities, two types of nanostructure were mapped: epitaxial core-shell InGaN/GaN multiple quantum-wells grown on GaN nanowires, and randomly oriented, single, high-index, faceted platinum (Pt) particles.

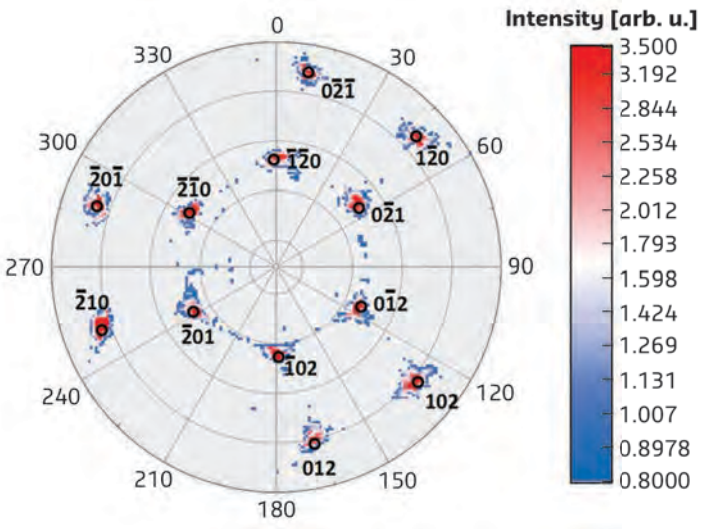


**Fig. 83:** Stereographic projections of the 3D reciprocal space map of a highly faceted Pt particle.

InGaN ternary alloys are of great importance due to their potential to provide tunable emission over most of the solar spectrum using one single crystalline material by simply adjusting the alloy composition. The nanostructure geometry can have a significant impact on both light extraction and collection efficiencies. InGaN ternary alloys incorporated in multiple quantum-well barriers also exhibit competitive emission and absorption properties. For this example, the crystallographic orientation of the side facets, as well as planar defects along a single core-shell InGaN/GaN multiple quantum-wells on a GaN nanowire, have been determined. Pole figures reveal new types of defects, as well as their location along the wire.

Regarding the second showcase, platinum is one of the most effective industrial catalysts in use today. Determining how facets evolve during catalysis is highly desirable in order to set up structure–activity, structure–selectivity and structure–stability relationships in heterogeneous catalytic systems. The method reveals uncommon faceting in the measured tetrahexahedral-model Pt particles, which were prepared by an electrochemical method.

This approach is a promising tool for structural characterisation of nanostructures and, due to the penetration power of hard X-rays, it could be especially useful for embedded structures where techniques like scanning electron microscopy or transmission electron microscopy are unable to probe. The non-invasive nature of CXDI, as well as the pole figure analysis, is particularly well adapted to study nanoscale materials during *in situ* and *operando* experiments such as catalysis, thermal treatment or corrosion, allowing facet and planar defect identification to be performed.

PRINCIPAL PUBLICATION AND AUTHORS

Crystallographic orientation of facets and planar defects in functional nanostructures elucidated by nano-focused coherent diffractive X-ray imaging,
M.-I. Richard (a, b), S. Fernández (a, b), J. Eymery (c, d), J. P. Hofmann (e), L. Gao (e), J. Carnis (a, b), S. Labat (a), V. Favre-Nicolin (b), E. J. Hensen (e), O. Thomas (a), T. U. Schülli (b) and S. J. Leake (b), *Nanoscale* **10**, 4833–4840 (2018); doi: 10.1039/c7nr07990g.
*(a) Aix Marseille Université, IM2NP-CNRS, Marseille (France)*
*(b) ESRF*
*(c) Université Grenoble Alpes (France)*
*(d) CEA, INAC-MEM, Grenoble (France)*
*(e) Laboratory of Inorganic Materials Chemistry, Department of Chemical Engineering and Chemistry, Eindhoven University of Technology (The Netherlands)*

# ORGAN–TO–CELL 3D DISSECTION OF ALZHEIMER'S DISEASE PATHOLOGY

**X-ray phase-contrast tomography was applied to dissect global pathology in an Alzheimer's disease mouse model. Comparison of the physiological versus pathological states of crucial disease targets at organ through to cellular levels enabled the visualisation of the angiopathy, as well as the internal structures of the plaques and their interaction with the microenvironment.**

The complex neuropathology of Alzheimer's disease (AD), a neurodegenerative disorder associated with progressive mental deterioration, involves synaptic and cognitive dysfunction, neuroinflammation, brain angiopathy, neuronal cell death, and gross brain atrophy **[1]**. Further understanding of its causes and progression requires the investigation of crucial neuropathological signatures at the fine level, which has not so far been possible with standard 2D and 3D techniques.

In this context, micro- and nanoscale X-ray phase-contrast tomography (XPCT), respectively with voxel sizes of 0.7 µm at Tomcat-SLS in Villigen, Switzerland and 50 nm at beamline **ID16A**, has been applied to dissect the neuropathology of the disease at whole-brain and cellular levels in the AD mouse model most relevant to human pathology. The brain of these APP/PS1 mice displays amyloid-β (Aβ)

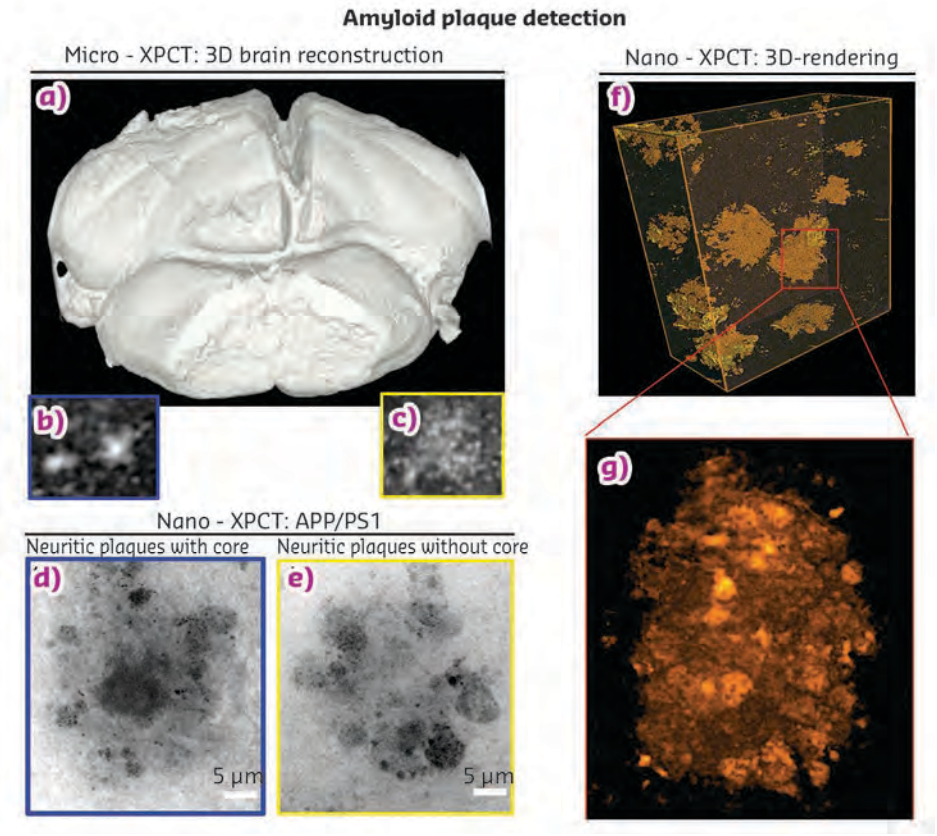


**Fig. 84: *a)*** 3D XPCT-rendering of the mouse brain. **b, c)** Micro-XPCT images of two different kinds of Aβ plaques in APP/PS1 mouse hippocampus. **d, e)** Nano-XPCT enables a deep investigation of cored and non-cored neuritic plaques (scale bar = 5 µm). **f)** 3D rendering of deposited Aβ plaques and **g)** of a single Aβ plaque.

plaques from the age of 6–8 months, accompanied by intense inflammation, atrophy, and vascular damage at later ages. Micro-XPCT-rendering of the hippocampus in AD mice confirmed the presence of plaques, while imaging inside the plaques through nano-XPCT demonstrated clear differences in plaque structure, enabling their classification as neuritic cored or non-cored (**Figures 84 a–g**).

Angiopathy is a now well-recognised aspect of AD neuropathology **[2]**, and abnormality of vessel walls and volume restriction are the main causes of brain hypo-perfusion in AD **[3]**. Micro-XPCT 3D-rendering showed vascular compromise in an AD mouse brain, with clear evidence of vessel loss and interruptions (**Figures 85a** and **85b**). At the cellular level, nano-XPCT enabled the exploration of the intra-capillary lumen and vessel walls, and revealed the presence of deposits (**Figure 85c**) that are likely attributable to deposited Aβ, thus providing vital information on the angiopathic mechanism at capillary level, which is difficult to obtain with standard techniques.

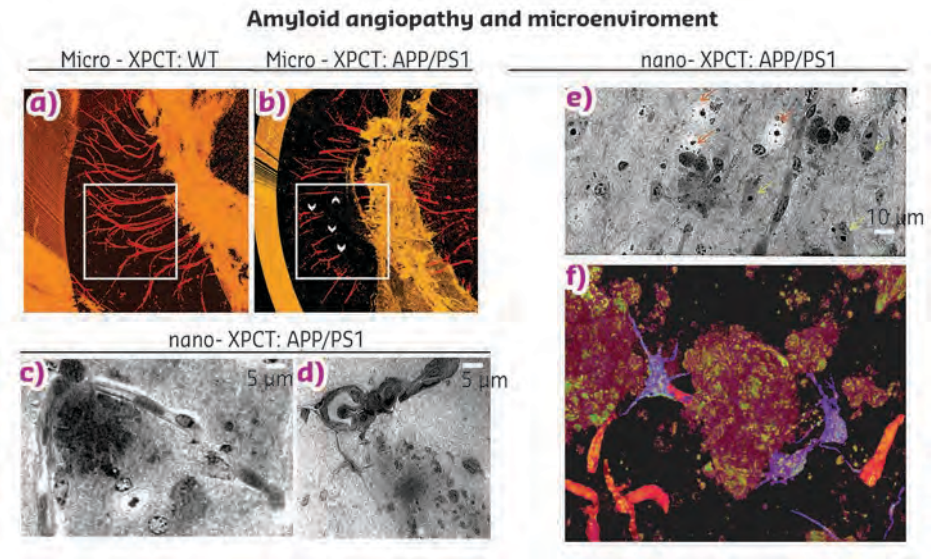


**Fig. 85: a, b)** Micro-XPCT 3D-renderings of **a)** normal vasculature in WT and **b)** cerebral vessel alterations in APP/PS1 mice. **c, d)** Nano-XPCT images of APP/PS1 mouse brain capillaries demonstrating the presence of Aβ deposits inside the lumen and plaques in close proximity to vessels, with **d)** showing an apparent interaction between a deposited plaque and a capillary through astrocyte end-feet (scale bar = 5 µm). **e)** Nano-XPCT image showing both healthy (yellow arrows) and suffering (orange arrows) neurons (scale bar = 10 µm). **f)** 3D-rendering of the microenvironment in APP/PS1 mouse brain. Violet: astrocytes; red: capillaries; brown: plaques; green: dystrophic neurites.

Through nano-XPCT, the status of the glial barrier was also explored. Under physiological conditions, this consists of astroglial end-feet surrounding the blood–brain barrier (BBB) and covering the majority of the parenchymal vasculature, and promotes efficient brain waste elimination, including Aβ. In the AD mouse brain, an astrocyte interconnecting a neuritic plaque with an apparently damaged capillary (**Figure 85d**) was observed. In the same zone, it was also possible to identify both suffering neurons next to plaques and more distant healthy neurons (**Figure 85e**). Nano-XPCT also provided detailed imaging of the microenvironment typifying an AD brain and its cellular complexity (**Figure 85f**), making it possible to detect the presence of astrocytic processes around plaques, as in the brain of AD patients **[4]**, and to detect connections between plaques and capillaries through astrocytic end-feet.

The possibility to faithfully image brain conditions in 3D and in such an exhaustive manner, without tissue manipulation, is a unique opportunity to virtually dissect the neuropathology down to nano-sized details, thereby gaining a more comprehensive understanding of it. Most importantly, through XPCT it will be possible to evaluate the efficacy of new therapeutic approaches in experimental models at the level of the multiple crucial neuropathological targets of AD and other neurodegenerative diseases.

## PRINCIPAL PUBLICATION AND AUTHORS

Exploring Alzheimer's disease mouse brain through X-ray phase contrast tomography: from the cell to the organ, L. Massimi (a), I. Bukreeva (a, b), G. Santamaria (c), M. Fratini (a, d), A. Corbelli (c), F. Brun (a), S. Fumagalli (c), L. Maugeri (a, d), A. Pacureanu (e), P. Cloetens (e), N. Pieroni (a), F. Fiordaliso (c), G. Forloni (c), A. Uccelli (f, g), N. Kerlero de Rosbo (f), C. Balducci (c) and A. Cedola (a, b), *Neuroimage* **184**, 490–495 (2018); doi: 10.1016/j.neuroimage.2018.09.044.
*(a) Istituto di Nanotecnologia, Consiglio Nazionale delle Ricerche, Rome (Italy)*
*(b) Dipartimento di Fisica, Università Sapienza, Rome (Italy)*
*(c) IRCCS Istituto di Ricerche Farmacologiche Mario Negri, Milan (Italy)*
*(d) IRCCS Fondazione Santa Lucia, Rome (Italy)*
*(e) ESRF*
*(f) DINOGMI, Università degli Studi di Genova (Italy)*
*(g) Ospedale Policlinico San Martino, Genoa (Italy)*

## REFERENCES

[1] D. M. Holtzman, *et al., Cold Spring Harb. Perspect. Med*. **2**, 11 (2012).
[2] A. R. Nelson *et al., Biochim. Biophys. Acta* **1862**, 887 (2016).
[3] N. Allen *et al., Neuropathol. Appl. Neurobiol.* **40**, 136 (2014).
[4] C. Duyckaerts *et al., Acta Neuropathol*. **118**, 5 (2009).

# A PINCH OF SALT FOR SOLAR CELLS

**The incorporation of Rb into Cu(In,Ga)$Se_2$ solar cells significantly improves their performance. Clear indications of the origin of the beneficial effect of Rb are obtained by correlating the distribution of Rb with microstructural elements of the Cu(In,Ga)$Se_2$ absorber.**

Thin film solar cells based on the compound semiconductor Cu(In,Ga)$Se_2$ have reached conversion efficiencies of over 22 % and even outperform multicrystalline silicon solar cells. The recent push in efficiencies was mainly achieved by applying an alkali fluoride post-deposition treatment using heavy alkali elements like K, Rb or Cs. It is still under discussion how the heavy alkali elements lead to the improved solar cell performance compared to Na supplied by the glass substrate. Therefore, the aim of this work was to reveal the origin of the beneficial effect of a pure RbF post-deposition treatment.

A Cu(In,Ga)$Se_2$ absorber grown on a Mo-coated ferritic stainless steel foil was investigated. After the growth of the absorber, a RbF post-deposition treatment was applied and a thin CdS buffer layer was deposited subsequently. Electrical characterisation of complete solar cells showed an increase of the conversion efficiency by 2.4 % absolute due to the RbF treatment.

In order to investigate the incorporation of Rb and to determine its spatial distribution, a 190-nm-thin cross-sectional lamella of the layer stack was prepared using a focused ion beam. This lamella was analysed via high-resolution X-ray fluorescence (nano-XRF) with a spot size of approximately 50 x 50 $nm^2$ at beamline **ID16B**. Additionally, different electron microscopy techniques were performed at the same lamella, correlating the Rb distribution with the microstructure and the optoelectronic properties of the absorber.

**Figure 86a** shows a scanning transmission electron microscopy image of the cross-sectional lamella taken in partial high-angle annular dark-field geometry. The Cu(In,Ga)$Se_2$ absorber exhibits a polycrystalline structure with grains ranging over the entire depth of the approximately 2-µm-thick absorber layer. The nature of the grain boundaries was investigated by means of electron backscatter diffraction. **Figure 86b** shows the resulting inverse pole figure map, in which the orientation of each grain is given by a certain colour. Comparing the orientation of neighbouring grains yields the type of grain boundary formed by these adjacent grains. Highly symmetrical and benign Σ3 twin boundaries are highlighted. All other grain boundaries are random grain boundaries, which are known to be detrimental to the solar cell performance.

The spatial distribution of Rb inside this polycrystalline Cu(In,Ga)$Se_2$ absorber was determined by moving the lamella stepwise through the X-ray nanobeam and recording the created X-ray fluorescence at each spot, as shown schematically in **Figure 86c**.

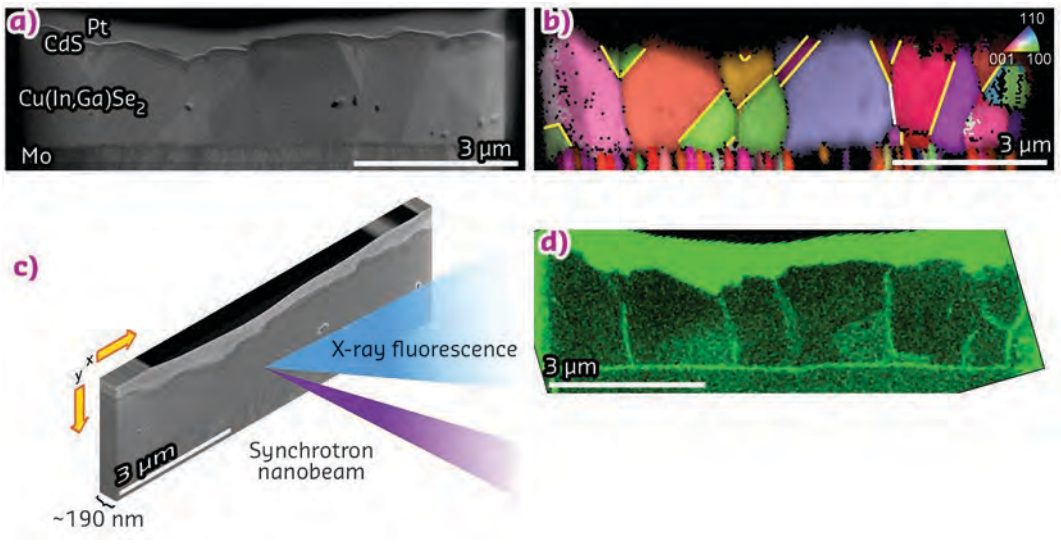


**Fig. 86:** Cu(In,Ga)$Se_2$ microstructure and Rb distribution measured with nano-XRF. **a)** Electron microscopy image of the Cu(In,Ga)$Se_2$ absorber revealing different micrometre-sized grains. **b)** Colour-coded map of the grain orientation. Σ3 twin boundaries are marked by yellow lines. **c)** Schematic of the nano-XRF measurement at ID16B. **d)** Rb intensity map. The strong signal on top of the absorber originates from the protective Pt layer, whose signal overlaps with that of Rb. Inside the Cu(In,Ga)$Se_2$, Rb clearly accumulates at random grain boundaries but not at Σ3 twin boundaries and at the Mo back contact.

The resulting map of the Rb intensity is presented in **Figure 86d**. Rubidium clearly segregates only at random boundaries and not at Σ3 twin boundaries. It is assumed that Rb passivates these detrimental random grain boundaries, thereby improving the electronic properties of the material and thus the device performance. This is supported by cathodoluminescence measurements performed at the same lamella. Additionally, Rb is detected close to the Mo back contact. This may cause a reduction of the contact resistance between absorber and back contact, as supported by the electrical characterisation, and may also contribute to the observed improvement of the solar cell efficiency.

By applying a combination of synchrotron-based nano-XRF and different electron microscopy techniques, it was possible to provide clear indications of the origin of the beneficial effect of Rb in $Cu(In,Ga)Se_2$ thin film solar cells. Subsequent studies of a $Cu(In,Ga)Se_2$ solar cell grown on a glass substrate and then subjected to a RbF post-deposition treatment further demonstrates that the conclusions drawn here for a pure RbF treatment are similarly valid for high-efficiency devices already containing Na and K from the glass **[1]**.


PRINCIPAL PUBLICATION AND AUTHORS

Rubidium segregation at random grain boundaries in $Cu(In,Ga)Se_2$ absorbers, P. Schöppe (a), S. Schönherr (a), R. Wuerz (b), W. Wisniewski (c), G. Martinez-Criado (d, e), M. Ritzer (a), K. Ritter (a), C. Ronning (a) and C. S. Schnohr (a), *Nano Energy* **42**, 307–313 (2017); doi: 10.1016/j.nanoen.2017.10.063.

*(a) Institut für Festkörperphysik, Friedrich-Schiller-Universität Jena (Germany)*
*(b) Zentrum für Sonnenenergie- und Wasserstoff-Forschung Baden-Württemberg (Germany)*
*(c) Otto-Schott-Institut für Materialforschung, Friedrich-Schiller-Universität Jena (Germany)*
*(d) Instituto de Ciencia de Materiales de Madrid (Spain)*
*(e) ESRF*

REFERENCES

[1] P. Schöppe *et al., ACS Appl. Mater. Interfaces* **10**(47), 40592–40598 (2018).


# SULFUR IN GLASS INCLUSIONS IN MANTLE MINERALS AS AN INDICATOR FOR REDOX PROCESSES IN SUBDUCTION ZONES

**Magmatism on Earth mainly occurs at mid-ocean ridges and subduction zones, where it is generated by mantle melting at different redox conditions. This study examines the role of sulfur in redox reactions within subduction zones by determining the sulfur valence state in glass inclusions in mantle minerals.**

Most magmatism on Earth starts in the Earth's mantle, either by decompression melting, as in the case of mid-ocean ridges, or by fluid addition from the descending subducted plate (slab), as in the case of subduction zones (**Figure 87**). Although the magma source is similar in both cases, subduction zone-related rocks are generally more oxidised than those at mid-ocean ridges. The reason for this oxidation is controversially debated and has been attributed to the slab fluid, magmatic differentiation or degassing. As the oxidation state controls the mobility of multivalent elements, it is crucial to elucidate the oxidation mechanism in order to understand important geological processes, such as volcanic degassing and the formation of ore deposits.

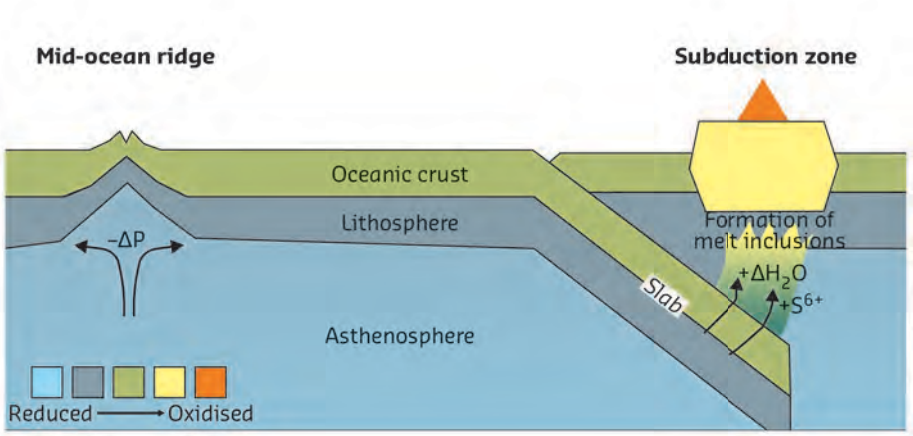


**Fig. 87:** Schematic illustration showing mantle melt generation at mid-ocean ridges and subduction zones by decompression melting (-ΔP) and fluid addition (+$\Delta H_2O$). Colours refer to oxidation state (unscaled, from reduced to oxidised). Oxidation in subduction zones is caused by slab derived sulfate (+$S^{6+}$).

The oxidation state of rocks and melts is usually determined from the iron (Fe) valence state in minerals and melts, and expressed as $Fe^{3+}/\Sigma Fe$ ($Fe^{3+}/[Fe^{3+}+Fe^{2+}]$), or alternatively from the sulfur (S) valence state in melts expressed as $S^{6+}/\Sigma S$ ($S^{6+}/[S^{6+}+S^{2-}]$). This study investigates the S distribution and valence states of glass (formerly melt) inclusions in spinel (**Figure 88**) from mantle rocks using micro X-ray fluorescence (XRF) and X-ray absorption near-edge structure (XANES) at **ID21**, in combination with other analytical techniques to understand the role of sulfur in redox processes in subduction zones. The XRF maps and XANES spectra were collected in fluorescence mode using a Si (111) double-crystal monochromator and a micro-focused beam of 0.4 x 0.8 $\mu m^2$. In order to minimise beam damage in the glasses, which may generate $S^{4+}$ by photon reduction **[1]**, a 6-µm-thick Al foil was used as an attenuator to reduce the incident photon flux on the sample. The XRF maps were collected before the XANES measurements to locate the melt inclusions within the spinel mineral grains (**Figure 88**).

The investigated glass inclusions (10–50 µm across; **Figure 88**) were trapped as melts in spinel (Al-Cr-Fe-Mg-oxide) minerals at mantle conditions and brought to the Earth's surface in lavas from two subduction zone volcanoes:

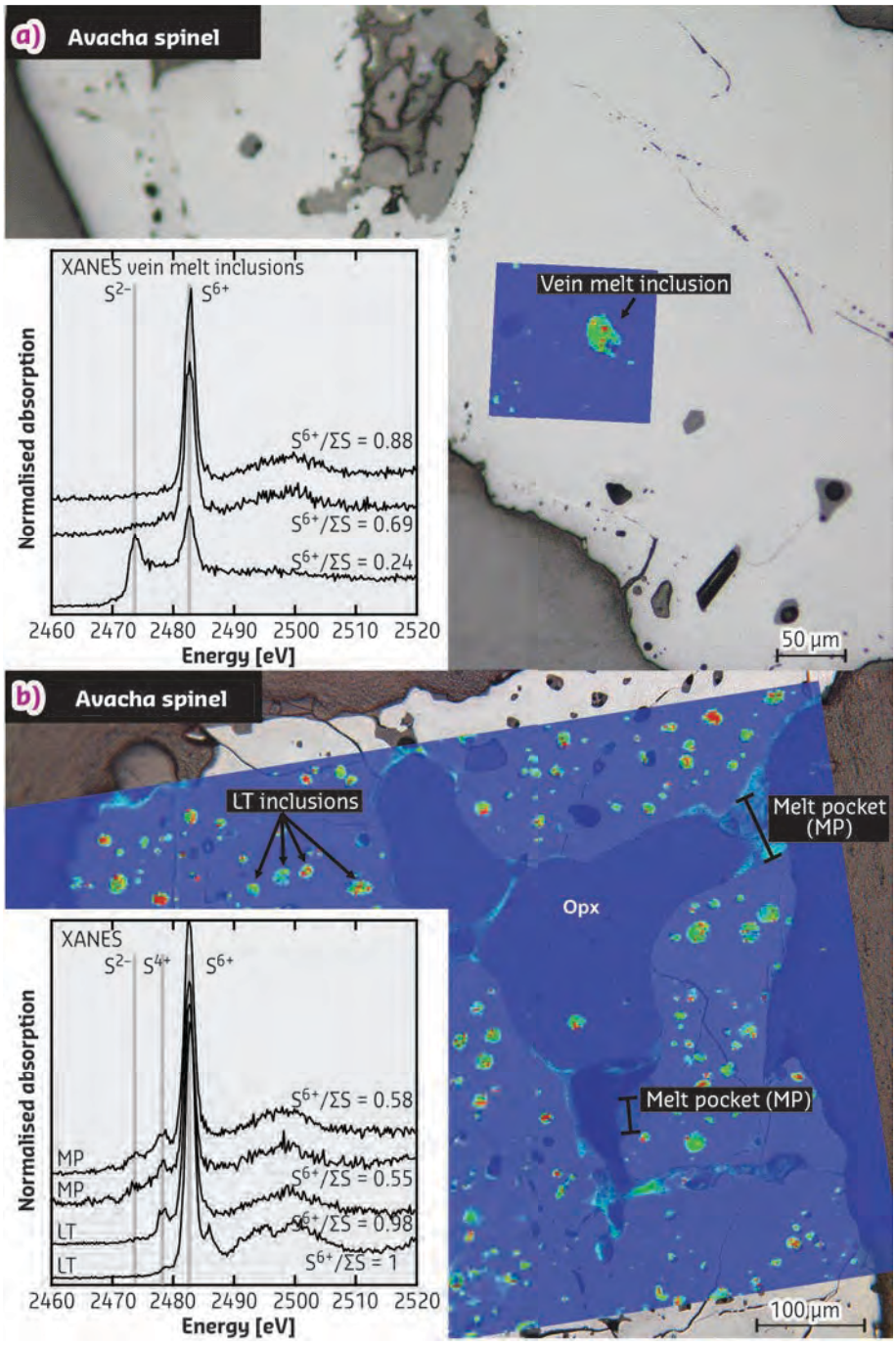


**Fig. 88:** Sulfur distribution and speciation in spinel-hosted glass inclusions. Reflected light images of two Avacha spinel grains, **a)** and **b)**, with representative XANES spectra of glass inclusions and calculated $S^{6+}/\Sigma S$. Coloured inlays show the abundance of S in the spinel and glass inclusions determined by µXRF mapping (heat map; red = high S concentration; blue = low S concentration).

Avacha in the Kamchatka (Russia) and Ritter in the West Bismarck (Papua New Guinea) volcanic arcs, respectively. Within the melt inclusions, sulfur is distributed heterogeneously (**Figure 88**). All melt inclusions contain $S^{6+}$ (sulfate), which is either incorporated in the glass structure or in crystalline anhydrite ($CaSO_4$). Some inclusions additionally contain $S^{2-}$ (sulfide) within the glass or as crystalline Fe-S compounds. The presence of $S^{4+}$ is related to minor beam damage of the glasses during the measurements. The sulfate content of the melt inclusions ($S^{6+}/\Sigma S$) can be calculated from the XANES spectra **[1]** and varies from 0.24 to 1 depending on the contribution of crystalline $S^{2-}$-bearing compounds to the spectrum considered.

The redox conditions of the mantle during formation of the melt inclusions can be calculated from their $S^{6+}/\Sigma S$ ratio **[1]**. The calculations reveal more oxidising conditions of the mantle in subduction zones compared to what is expected for the mantle underlying mid-ocean ridges. A combination of these data with the S isotope composition of the melt inclusions (determined by secondary ion mass spectrometry, SIMS) and the Fe valence state of spinel measured by electron probe microanalysis (EPMA) indicates that oxidised S must have been added to the mantle by a slab-derived agent over the redox mechanism: $SO_4^{2-}{}_{(slab)} + 8FeO_{(mantle)} \Rightarrow S^{2-} + 4Fe_2O_{3(mantle)}$. The results imply that these oxidising agents can link the slab fluid with the magma sources in the mantle and affect the redox budget of subduction zones.

## PRINCIPAL PUBLICATION AND AUTHORS

Oxidising agents in sub-arc mantle melts link slab devolatilisation and arc magmas, A. Bénard (a, b, c), K. Klimm (d), A. B. Woodland (d), R. J. Arculus (a), M. Wilke (e), R. E. Botcharnikov (f, g), N. Shimizu (h), O. Nebel (b), C. Rivard (i) and D. A. Ionov (j), *Nat. Commun.* **9**, 3500 (2018); doi: 10.1038/s41467-018-05804-2.

*(a) Australian National University, Canberra (Australia)*
*(b) Monash University, Melbourne (Australia)*
*(c) University of Lausanne (Switzerland)*
*(d) Goethe Universität Frankfurt (Germany)*
*(e) Universität Potsdam (Germany)*
*(f) Leibniz Universität Hannover (Germany)*
*(g) Gutenberg Universität Mainz (Germany)*
*(h) Woods Hole Oceanographic Institution (USA)*
*(i) ESRF*
*(j) Université de Montpellier & UMR-CNRS (France)*

## REFERENCES

[1] M. Wilke *et al. Rev. Mineral. Geochem.* **73**, 41–78 (2011).

# ELECTRONIC STRUCTURE, MAGNETISM AND DYNAMICS

The EMD group comprises the beamlines ID12, ID20, ID26, ID28 and ID32, as well as the sample environment unit, which serves all ESRF and CRG beamlines. All EMD beamlines carry out spectroscopy experiments and the introduction of top-up operation in most filling modes was highly appreciated by the beamlines because the improved thermal stability translates into more stable energy calibration. The theoretical spectroscopy tool *Crispy* (**page 162**) that the ESRF has developed in collaboration with the University of Heidelberg was presented at several schools and workshops and is seeing increasing popularity, with more than 500 downloads. The software supports calculation of X-ray absorption spectroscopy (XAS), X-ray emission spectroscopy (XES), resonant inelastic X-ray scattering (RIXS) and X-ray photoelectron spectroscopy (XPS), including polarisation control with X-ray magnetic circular dichroism (XMCD) and linear dichroism (LD). *Crispy* is also turning out to be an ideal tool for teaching X-ray spectroscopy in ligand field multiplet theory.

The sample environment unit, which manages an equipment pool and develops new instrumentation, has seen an increase in demand for the adaptation of small furnaces for specific experiments. The developments address common problems for *in-situ* experimental setups, such as temperature stability and specific geometry constraints. As a result, the offer and diversity of the equipment in the pool have increased this year with designs made in-house and acquisitions of commercial solutions. The expertise of the sample environment unit in robotics is in high demand, for example, on beamline ID19 for tomography applications and also for the dismantling of the current machine to make space for the Extremely Brilliant Source (EBS).

The major technical achievement on beamline **ID12** is the first detection of XMCD spectra in the hard X-ray range at temperatures as low as 300 mK. A dilution cryostat was inserted in a bore of a 7 T split-coil superconducting magnet, which allowed the recording of XMCD spectra at the L-edges of 5d transition metals in paramagnetic molecules that are designed as building blocks for a new generation of molecular magnets. This end-station is now fully operational and is complementary to the high-field XMCD setup, allowing measurements under magnetic fields of up to 17 T. With this achievement, beamline ID12 offers unique possibilities for fundamental research in magnetism. This is illustrated by investigations of giant magnetocaloric effect by Guillou *et al.* (**page 94**) and with studies on a new class of 2D molecular materials interesting for spintronic applications by Pedersen *et al.* (**page 104**).

Research activities at **ID20** encompass hard condensed matter physics, chemistry, material- and geoscience. This year, the ID20 team worked hard to develop new sample environments, such as a new and extremely flexible diamond anvil cell for experiments at extreme pressure conditions. As these *Highlights* go to press, the team on ID20 is assembling and testing a new spectrometer that will allow the measurement of the polarisation of the scattered beam in RIXS experiments at the Ir $L_3$ edge. As remarkable scientific contributions of this past year, we highlight a study on the evolution of the magnetic excitations in $NaOsO_3$ through its metal-to-insulator transition (Vale *et al.*, **page 95**), as well as an experiment that demonstrated the parametric down-conversion of X-rays into the optical regime (Schori *et al.*, **page 105**).

The tender X-ray range between 1.5 and 5 keV can now be explored using a new X-ray emission spectrometer on **ID26**. It allows the measurement of the L-lines of 4d transition metals, the M-lines of actinides and the K-lines down to Al. The instrument employs 11 cylindrical Johansson crystals that are fabricated in the ESRF crystal analyser laboratory (CAL). A large-area gas-proportional counter suitable for low energies has also been developed by the ESRF. A cryostat has been commissioned and a cell for *in-situ* experiments was tested in the vacuum chamber of the spectrometer. It is the most efficient instrument for high-energy-resolution fluorescence detected (HERFD) XAS in this energy range. The spectrometer was financed by the EcoX Equipex project overseen by the French national research agency, ANR. First users carried out experiments in May 2018. This instrument opens up a new realm for spectroscopic studies at the ESRF. The ID26 highlights in this volume show research on magnesium–sulfur batteries

(Robba *et al.,* **page 97**) and a blue phosphor (Amidani *et al.,* **page 107**).

The **ID28** side station, dedicated to the study of diffuse scattering and complementing the high-energy-resolution instrument, has been running in user operation since March 2017. Five papers have already been published as a result of this tandem operation, including one by Girard *et al.* (**page 108**). The beamline is subject to a growing demand by the user community for joint experiments. A uniaxial strain device that has been developed and tested over the past few years has been used to induce a 3D charge order in an yttrium-based cuprate that was characterised on ID28. The results of this study were published in *Science* by Kim *et al.* (*Science* **362**, 1040, 2018). A dedicated cryostat for the background-suppressed measurements of diffraction under uniaxial strain conditions has been commissioned and is available for user operation.

During the past year, the main emphasis for **ID32** has been to scientifically exploit the instruments. Many high-quality papers have been published, of which examples are given in these *Highlights*. Beyond work on the cuprates by Hepting *et al.* (**page 111**) and Peng *et al.* (**page 99**), and on the nickelates by Lu *et al.* (**page 101**), there have also been new studies on cerium compounds, titanates and cobaltates, to name a few, on the RIXS branch. On the XMCD branch, experiments using the full surface science preparation facility, together with the fast sweeping 9 T high-field magnet, promise some very interesting papers in the coming year. An upgrade of the beamline optics is underway to further improve the energy resolution of the RIXS instrument.

The staff of the EMD group will spend the EBS shutdown helping with the dismantling and assembly of the machine, visiting universities and other facilities and writing publications. We will have time to work on projects at the beamlines that we were not able to do during the busy operation time with beam, and users will find many new features at the beamlines when they return in 2020.

**P. GLATZEL**

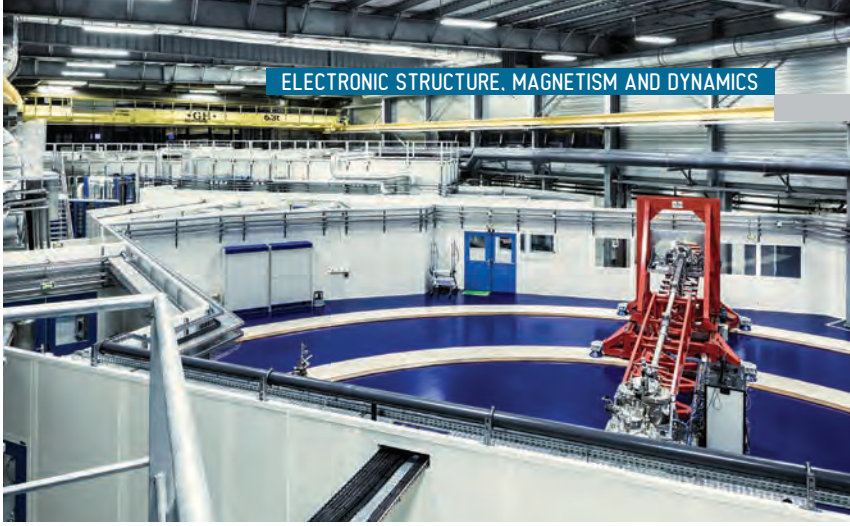

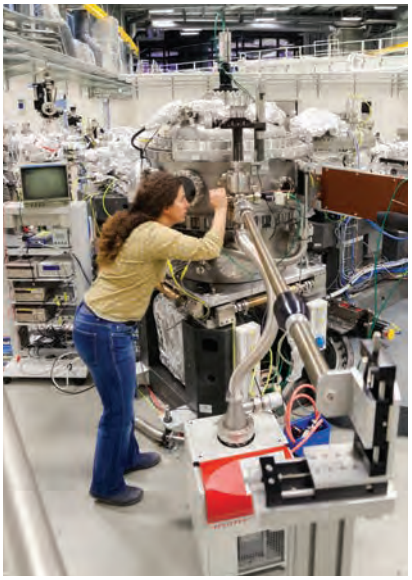

# ANHYSTERETIC FIRST-ORDER MAGNETIC TRANSITION WITH GIANT MAGNETOCALORIC EFFECT IN $Eu_2In$

**A particularly sharp, strongly first-order ferromagnetic-to-paramagnetic transition has been discovered in the rare-earth intermetallic $Eu_2In$. This transition is remarkable due to the combination of large latent heat, small volume discontinuities and negligible hysteresis. Some insight into its mechanism is gained by using X-ray absorption spectroscopy and magnetic circular dichroism.**

Magnetic transitions commonly lead to the emergence of important properties and are at the heart of many materials' functionalities of materials. They are technologically important, in particular due to their associated effects, such as magnetostriction, magnetovolume, magnetic shape memory, magnetoresistance or magnetocaloric effect. In a majority of materials, these effects are due to continuous second-order transitions, spreading over a large temperature range. First-order magnetic transitions (FOMTs) have the potential to concentrate the coupled phenomena around sharp discontinuities; they are however rare. For some applications, isosymmetric FOMTs are among the most desirable, as energy losses associated with hysteresis may often be controlled. Unfortunately, only a few such materials are known and they are almost exclusively based on transition metals. This paucity is primarily related to the uniqueness of the underlying mechanism, rooted in the itinerant electronic behaviour common in transition metals. Yet, an intriguing isosymmetric FOMT has been discovered in the rare-earth compound $Eu_2In$.

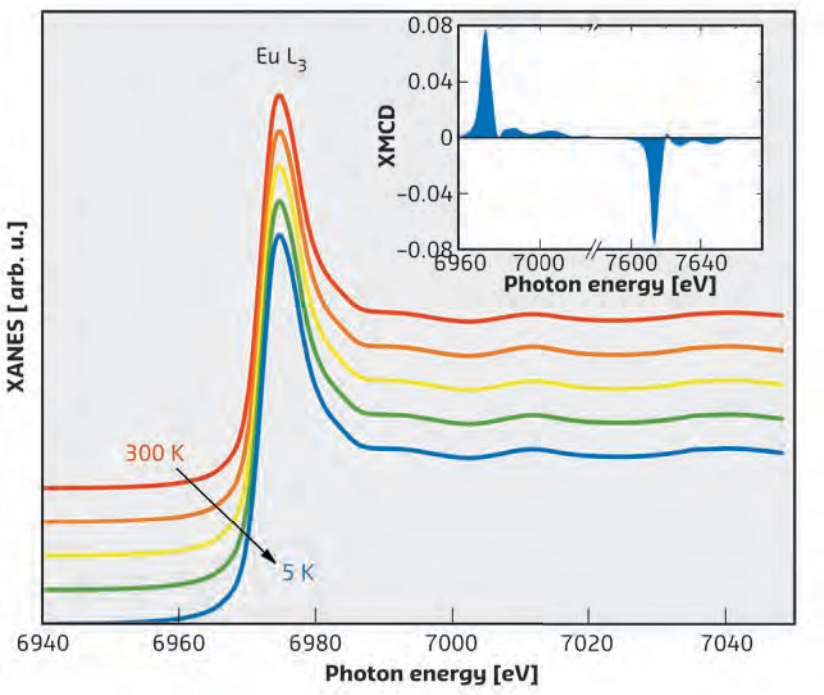


**Fig. 89:** XANES spectra in $Eu_2In$. Inset: XMCD at Eu $L_{2,3}$ edges (5 K and 3 T).

$Eu_2In$ samples were the object of thorough chemical, physical, and theoretical characterisations. Using density functional theory, an active participation of the Eu-5d/In-4p states in triggering the transition and a rather unique electronic structure presenting a charge transfer from In to Eu are predicted, which results in an unusual magnetic exchange mechanism and finite Eu-5d/In-4p magnetic moments. The 6s, 6p and 5d states of Eu are nearly completely hybridised with the more populated 5p states of In, in such a way that the Eu-s,p,d states fall within the envelope of In-p states. The Eu-4f states are centered just 2 eV below the Fermi level, and also hybridise with the p states of In. Nearly identical Eu-5d and In-5p exchange splitting across the Fermi level are observed, as well as similar magnetic moments of 0.22 and 0.24 $\mu_B$/atom, on Eu-5d and In-5p states, respectively.

It was crucial for the understanding of the FOMT in $Eu_2In$ and the validation of the theoretical predictions to get an experimental insight into the electronic structure of Eu. The question of the valence was vital, as closely related EuTX ternaries are famous for exhibiting first-order valence fluctuations. Europium $L_{2,3}$ edges (2p→5d) X-ray absorption near edge structure (XANES) spectroscopy and magnetic circular dichroism (XMCD) spectra, carried out at **ID12**, are shown in **Figure 89**. XANES spectra at low temperature present single white line shapes at the Eu $L_3$ edge, peaking at ~6974 eV. Determining the valence by the conventional spectral decomposition into Lorentzian peaks and arctangent, an average valence of +2.03 for Eu is obtained. XANES spectra measured as a function of temperature confirm the absence of valence fluctuations and a drastic change in the local crystalline environment of the europium atoms across the FOMT. The sizable XMCD signals observed at both Eu $L_2$ and $L_3$ edges are comparable with more ionic europium materials, wherein divalent $Eu^{2+}$ configurations are well-established and bring support to bulk magnetisation measurements and first-principle calculations that the Eu atoms carry at least 7 $\mu_B$/Eu.

**Figure 90** shows the low temperature–field dependence of magnetic circular dichroism and heat capacity, demonstrating that $Eu_2In$ is a ferromagnet with a large saturation magnetisation (14.4 $\mu_B$/f.u. from bulk magnetisation) and presents an exceptionally high heat-capacity peak at the Curie temperature at 55 K. The ferromagnetic transition in $Eu_2In$ and the mechanism at its origin breaks new ground in many aspects. Contrary to the common wisdom that strongly first-order magnetic transitions are necessarily associated with substantial crystallographic changes and hysteresis, $Eu_2In$ forms a counterintuitive example with a very large latent heat and an exceptionally high magnetocaloric effect, but with minuscule lattice discontinuities as well as negligible thermal and magnetic hystereses.

In summary, $Eu_2In$ demonstrates that an instability leading to a FOMT can be realised in rare-earth intermetallics in the absence of any structural or valence fluctuations. More generally, this work, as well as other systematic studies of giant magnetocaloric materials at **ID12 [1, 2]**, highlights the interest of XANES and XMCD spectroscopies to unveil the underlying microscopic mechanisms of first-order magnetic transitions.

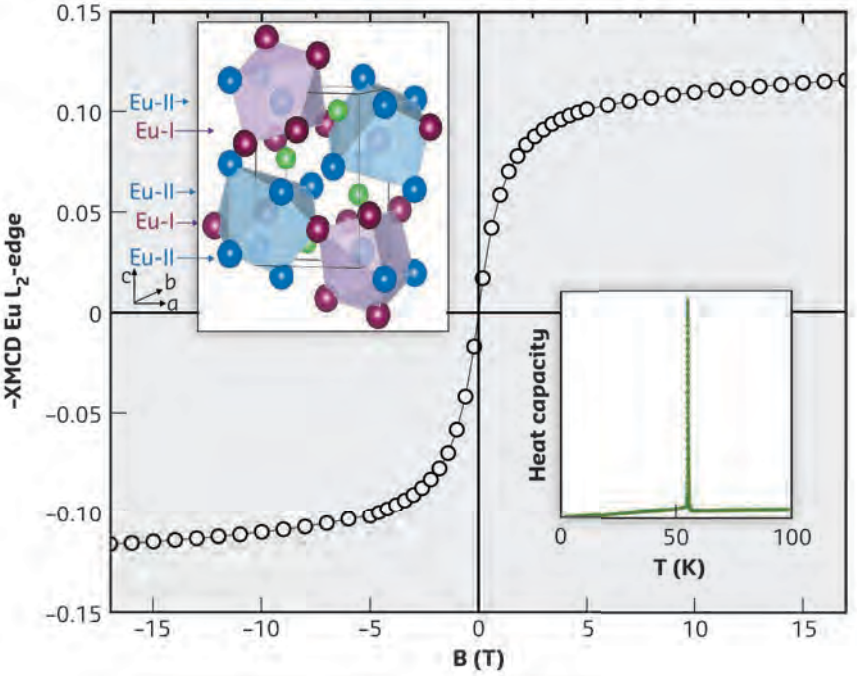


**Fig. 90:** Magnetic field dependence of the XMCD (at 5 K and 7613 eV). Insets: $Eu_2In$ crystal structure and heat capacity.

PRINCIPAL PUBLICATION AND AUTHORS

Non-hysteretic first-order phase transition with large latent heat and giant low-field magnetocaloric effect, F. Guillou (a), A.K. Pathak (a), D. Paudyal (a), Y. Mudryk (a), F. Wilhelm (b), A. Rogalev (b) and V. K. Pecharsky (a, c), *Nat. Commun.* **9**, 2925 (2018); doi: 10.1038/s41467-018-05268-4.
*(a) The Ames Laboratory, U.S. Department of Energy (USA)*
*(b) ESRF*
*(c) Department of Materials Science and Engineering, Iowa State University (USA)*

REFERENCES

[1] F. Guillou *et al.*, *Phys. Rev. B* **92**, 224427 (2015).
[2] F. Guillou *et al.*, *Appl. Phys. Lett.* **108**, 122405 (2016).

# EVOLUTION OF THE MAGNETIC EXCITATIONS IN $NaOsO_3$ THROUGH ITS METAL-INSULATOR TRANSITION

**$NaOsO_3$ is a material in which the electronic and magnetic degrees of freedom are intimately linked. This study shows a continuous evolution of the magnetic excitations with increasing temperature. This provides a unique description of the RIXS response between the localised and itinerant limits, which is not well understood theoretically.**

The metal-insulator transition (MIT) is of enduring interest in condensed matter physics as it embodies the essence of many-body phenomena. The ubiquitous Mott-Hubbard MIT is characterised by coupling between the electronic and magnetic degrees of freedom with the lattice. This typically leads to structural distortion at the (first-order) MIT, along with the formation of long-ranged magnetic order in the insulating phase.

A number of 5d transition metal oxides (TMOs) exhibit MITs that do not conform to this paradigm. One notable example is the perovskite $NaOsO_3$ ($5d^3$), which undergoes a continuous MIT at 410 K. This occurs concomitant with the onset of antiferromagnetic order, leading to suggestions that $NaOsO_3$ may be a rare example of a Slater insulator in three dimensions. In a weak-coupling Slater picture, the onset of antiferromagnetism is in itself the driving force for the MIT. Yet, a

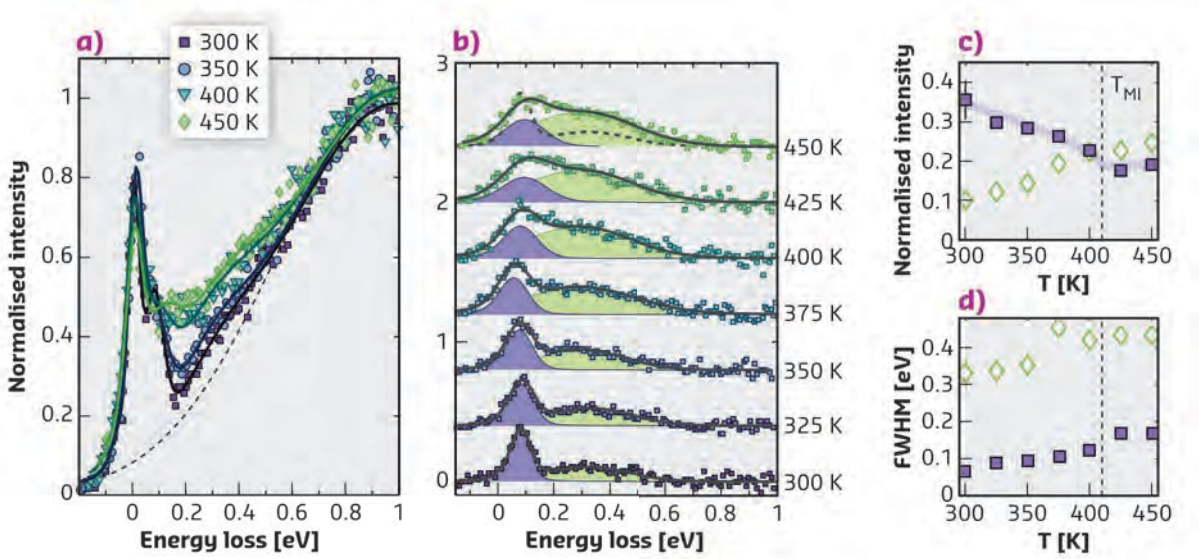


**Fig. 91:** Analysis of RIXS spectra collected at (5, 2.75, 4). **a)** Representative low-energy RIXS spectra, each of which is normalised to the *d–d* excitations at 1 eV energy loss (dashed line). **b)** Spectra with elastic line and *d–d* contributions subtracted off. Added are the best fit to the data (black solid line), and relative components of the magnon peak (purple) and high-energy continuum (green). Dashed line superimposed on 450 K plot is the best fit to 300 K data for comparison. **c, d)** Fitted peak intensity **(c)** and intrinsic FWHM **(d)** of the magnon peak (filled squares) and high-energy continuum (open diamonds) as a function of temperature.

defining feature of 5d TMOs is the presence of significant spin-orbit coupling (SOC), seemingly at odds with the weak-coupling Slater picture.

The dynamics of $NaOsO_3$ were studied through the MIT using resonant inelastic X-ray scattering (RIXS) at the Os $L_3$ edge (10.871 keV). This technique is uniquely sensitive to electronic and magnetic excitations as a function of energy and momentum transfer. The data were collected at **ID20**, the only instrument currently capable of performing Os $L_3$ RIXS measurements with an energy resolution better than 50 meV.

**Figure 91** shows representative RIXS spectra collected as a function of temperature. A clear evolution of the excitations occurs through the MIT. Well-defined gapped spin-wave excitations can be observed at 300 K (deep in the antiferromagnetic insulating phase). These are consistent with a previous study **[1]**, and demonstrate that $NaOsO_3$ is close to the localised limit. With increasing temperature, the spin waves weaken and become progressively more damped. This occurs concurrently with an increase of spectral weight at higher energies. The most likely cause for the damping is found to be scattering from particle-hole excitations (Landau damping), which is the dominant mechanism for metallic and itinerant systems.

**Figure 92** shows RIXS spectra collected at 450 K (deep in the paramagnetic metallic phase) as a function of momentum transfer. It was found that the data in this regime could be well described by diffusive (overdamped) spin fluctuations within a weakly antiferromagnetic Fermi liquid (WAFL) model.

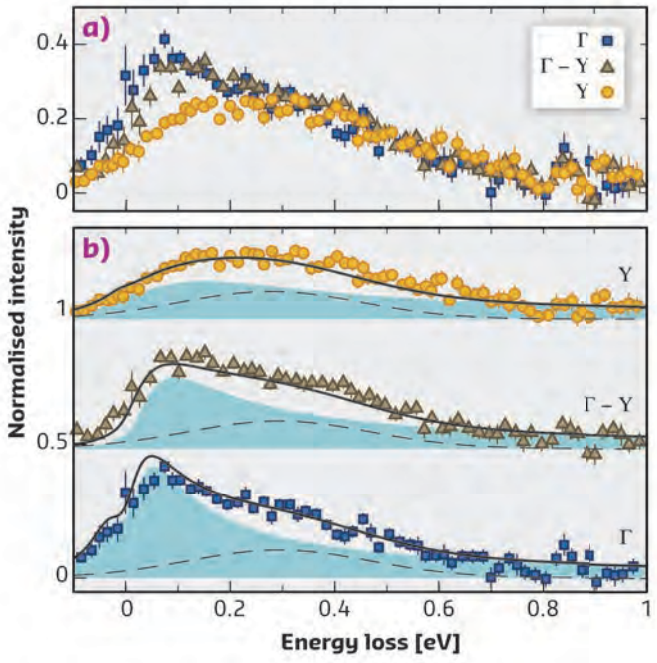


**Fig. 92:** Paramagnetic spin fluctuations in $NaOsO_3$ at 450 K. **a)** Experimental data collected at various crystal momenta. For clarity, the elastic line and high-energy intra-$t_{2g}$ excitations have been subtracted. **b)** Comparison of WAFL model (solid line) with experimental data. Filled area indicates contribution from paramagnetic spin fluctuations. Dashed line is a momentum-independent high-energy contribution, which likely results from inter-band particle-hole excitations.

The magnetic excitations in $NaOsO_3$ appear to evolve continuously through its MIT. This is indicative of the significant coupling between the electronic and magnetic degrees of freedom in this system, and has two important ramifications. Firstly, the fact that the WAFL model provides a good description of the data at 450 K implies that weak correlations persist in the metallic, paramagnetic phase. This, in turn, suggests that $NaOsO_3$ is proximate to, but not within, the ideal Slater picture. Moreover, $NaOsO_3$ provides an ideal test case for the study of magnetic excitations between the localised and itinerant limits. One can note similarities between the observed behaviour with that seen in the overdoped cuprates. The distinction in $NaOsO_3$, however, is that this occurs purely as a function of temperature, and without the complication of carrier doping inducing disorder, for example.


PRINCIPAL PUBLICATION AND AUTHORS

Evolution of the Magnetic Excitations in $NaOsO_3$ through its Metal-Insulator Transition, J.G. Vale (a, b), S. Calder (c), C. Donnerer (a), D. Pincini (a, d), Y.G. Shi (e, f), Y. Tsujimoto (f), K. Yamaura (f, g), M. Moretti Sala (h), J. van den Brink (i), A.D. Christianson (c, j) and D.F. McMorrow (a), *Phys. Rev. Lett.* **120**, 227203 (2018); doi: 10.1103/PhysRevLett.120.227203, and *Phys. Rev. B* **97**, 184429 (2018); doi: 10.1103/PhysRevB.97.184429 (joint submission).

*(a) London Centre for Nanotechnology and Department of Physics and Astronomy, University College London (UK)*
*(b) Laboratory for Quantum Magnetism, École Polytechnique Federale de Lausanne (EPFL), (Switzerland)*
*(c) Neutron Scattering Division, Oak Ridge National Laboratory, Tennessee (USA)*
*(d) Diamond Light Source (UK)*
*(e) Beijing National Laboratory for Condensed Matter Physics and Institute of Physics, Chinese Academy of Sciences (China)*
*(f) Research Center for Functional Materials, National Institute for Materials Science, Ibaraki (Japan)*
*(g) Graduate School of Chemical Sciences and Engineering, Hokkaido University (Japan)*
*(h) ESRF*
*(i) Institute for Theoretical Solid State Physics, IFW Dresden (Germany)*
*(j) Department of Physics and Astronomy, University of Tennessee (USA)*

REFERENCES

[1] S. Calder *et al., Phys. Rev. B* **95**, 020413 (2017).


# MAGNESIUM–SULFUR BATTERY MECHANISM STUDIED BY RIXS/XAS SPECTROSCOPY AT THE SULFUR K EDGE

**The magnesium–sulfur battery is an attractive alternative for future energy storage solutions. A combination of *operando* RIXS and XAS spectroscopy at the sulfur K edge has been used to follow the electrochemical sulfur conversion in the cathode during discharge and to determine the working mechanism of Mg–S batteries.**

Magnesium is one of the promising materials for negative electrodes for post-lithium batteries. In combination with a sulfur cathode, a system with high theoretical energy density, and that employs abundant and low-cost active materials, is obtained. A first concept for the Mg–S battery was presented in 2011 **[1]**. Since then, there has been a growing interest in this system. However, issues such as high polarisation, capacity fade and self-discharge are still to be successfully solved. Some solutions have been proposed over time; nevertheless, the lack of fundamental knowledge about the working mechanism has hindered significant advances. So far, the characterisation of Mg–S cathodes and their connected processes has focused on surface-based X-ray photoelectron spectroscopy (XPS) analysis **[2, 3]**, while the bulk electrochemical reactions in Mg–S battery cathodes have not been investigated.

X-ray absorption (XANES) and resonant inelastic X-ray scattering (RIXS) at the sulfur K edge can provide insight into the bulk electrochemical mechanism of Mg–S batteries. In order to study bulk reactions in the cathode, a tender X-ray emission spectrometer **[4]** was employed at **ID26** to perform RIXS measurements on the Mg–S battery cathode in *operando* mode. Complementary to RIXS, XANES measurements were performed simultaneously using the diode installed in the vacuum chamber of the spectrometer (**Figure 93a**). As previously demonstrated **[5]**, these techniques can be used to detect polysulfides with increased sensitivity and resolution. The resonant excitation condition sharpens and enhances the polysulfide signal, different sulfur species produced electrochemically within the cathode are resolved in the spectra and can be followed precisely through the battery discharge (**Figure 93b**).

The discharge curve of the Mg–S system exhibits two well-defined plateaus (**Figure 94**). The evolution of the polysulfide and MgS signals was followed precisely through the discharge and linked to the electrochemical behaviour of the system (**Figure 94**). Relative amounts of separate components (sulfur, Mg polysulfides and MgS) measured with XANES were determined by linear combination fitting, yielding values consistent with the ones obtained from the RIXS measurements and providing a clean, reliable picture of sulfur electrochemistry (**Figure 94**).

The reduction of sulfur in the cathode starts with the formation of polysulfides during the high-voltage plateau and is in the agreement with *operando* XRD measurements, where the disappearance of sulfur diffraction peaks was observed. During the low-voltage plateau, reduction of sulfur ceases and polysulfides are further reduced to MgS. The low-voltage plateau therefore corresponds to the equilibrium between polysulfides and precipitated MgS. Around 80% of sulfur is converted into MgS during the first discharge. Noticeable differences between XANES spectra, corresponding to MgS produced electrochemically and the synthesised standard, were observed. To investigate possible reasons, additional measurements employing $^{25}$Mg solid-state NMR spectroscopy were performed. Analysis showed poor crystallinity of electrochemically obtained MgS and tetrahedral coordination of Mg ions, resembling wurtzite-type structures, in contrast to the octahedral rock-salt structure of the synthesised sample. This suggests the

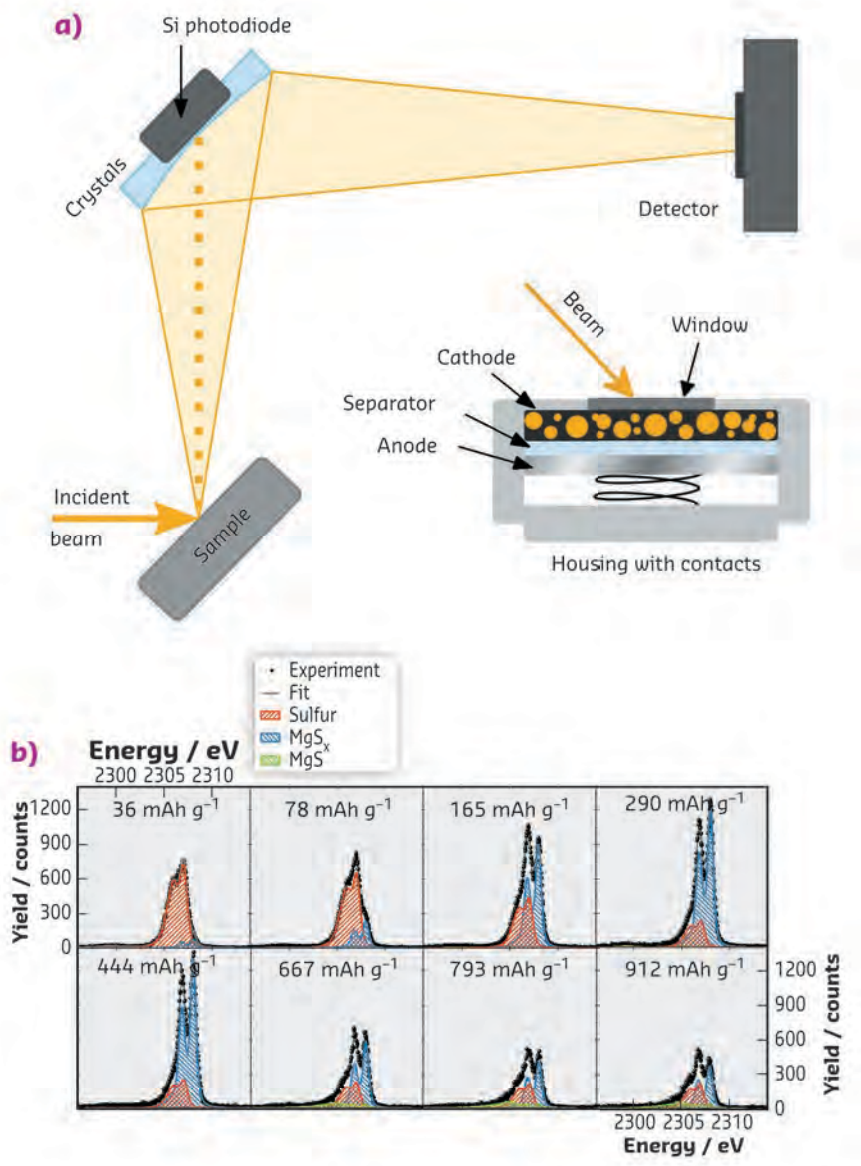


**Fig. 93: *a)*** Schematic representation of the experimental setup and cell configuration for *operando* measurements. **b)** Sequence of normalised *operando* sulfur RIXS spectra at the excitation energy of the polysulfide pre-edge resonance, showing the formation of polysulfides during the discharge.

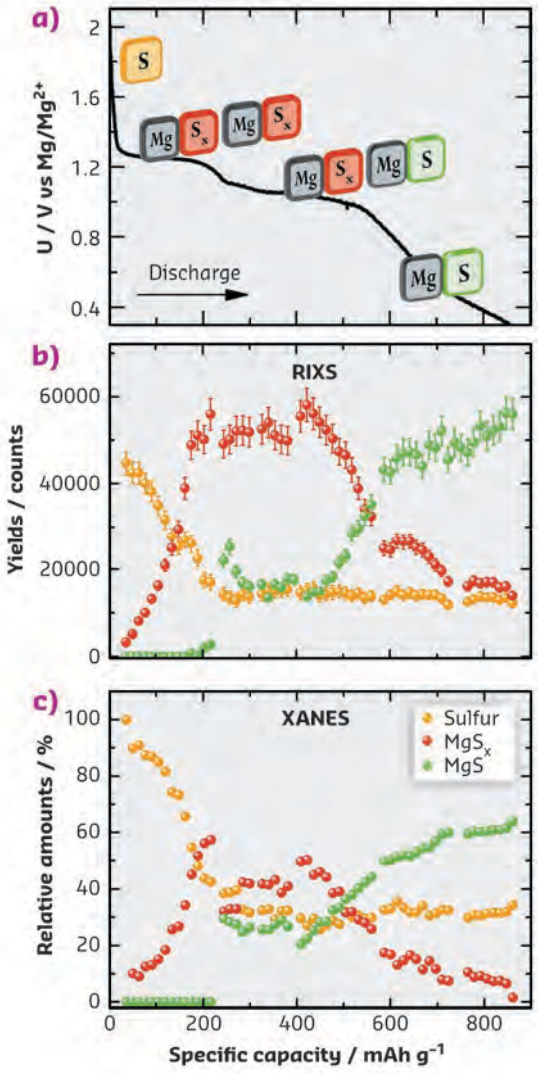


**Fig. 94:** Discharge voltage profile of a Mg–S battery with depicted compounds predominant in each segment of the discharge **(*a*)**, normalised absolute yields of RIXS measurements **(b)** and relative amounts of separate sulfur compounds, determined with XANES **(c)**, representing the evolution and disappearance of sulfur, MgS and polysulfides during discharge.

possibility of high volumetric changes during cycling, which could be one of the reasons for the fast-capacity fading.

In conclusion, *operando* RIXS and XAS measurements at the sulfur K edge, combined with laboratory X-ray diffraction (XRD) and solid-state nuclear magnetic resonance (NMR) spectroscopy, were used to quantitatively follow sulfur reduction in the cathode to determine the bulk electrochemical mechanism of Mg–S batteries. With this insight, important steps to improve the system and its characteristics can be identified.


## PRINCIPAL PUBLICATION AND AUTHORS

Mechanistic Study of Magnesium–Sulfur Batteries, A. Robba (a, b), A. Vizintin (a), J. Bitenc (a), G. Mali (a), I. Arčon (c, d), M. Kavčič (c), M. Žitnik (c), K. Bučar (c), G. Aquilanti (e), C. Martineau-Corcos (f, g), A. Randon-Vitanova (h) and R. Dominko (a), *Chem. Mater.* **29**, 9555-9564 (2017); doi: 10.1021/acs.chemmater.7b03956.


*(a) National Institute of Chemistry, Ljubljana (Slovenia)*
*(b) Faculty of Chemistry and Chemical Technology, University of Ljubljana (Slovenia)*
*(c) Institut Jožef Stefan, Ljubljana (Slovenia)*
*(d) University of Nova Gorica (Slovenia)*
*(e) Elettra-Sincrotrone Trieste S.C.p.A. (Italy)*
*(f) Institut Lavoisier, Versailles (France)*
*(g) CEMHTI-CNRS, Orléans (France)*
*(h) HONDA R&D Europe GmbH, Offenbach (Germany)*


## REFERENCES


[1] H. S. Kim *et al.*, *Nat. Commun.* **2,** 427 (2011).
[2] Z. Zhao-Karger *et al.*, *Adv. Energy Mater.* **5,** 1401155 (2014).
[3] X. Yu *et al.*, *ACS Energy Lett.* **1,** 431–437 (2016).
[4] M. Kavčič *et al.*, *Rev. Sci. Instrum.* **83**, 033113 (2012).
[5] M. Kavčič *et al.*, *J. Phys. Chem. C* **120**, 24568–24576 (2016).


# UNEXPECTED CHARGE DENSITY WAVES IN A FAMILY OF CUPRATE SUPERCONDUCTORS


**High $T_c$ superconductors are well known for their overwhelming complexity; they are a source of innumerable surprises. Using resonant inelastic X-ray scattering (RIXS), a robust charge order in highly doped cuprates has been discovered, disrupting once again the common views and theories about cuprates.**


In layered cuprates, superconductivity sets in with exceptional stability when the $CuO_2$ planes are doped by the 'right' amount of holes, which disrupt the long-range two-dimensional antiferromagnetic order of the parent compounds but preserve the short-range spin correlation. Charge carriers are thus under the effect of mutual interactions that can give rise to competing phenomena, eventually manifesting themselves as unusual transport properties, including superconductivity. This scenario includes the formation of charge order (CO), *i.e.* spontaneous modulations of the local charge density with a spatial wavelength commensurate or incommensurate to the lattice structure.

Long after having been predicted theoretically **[1]**, CO has been observed indirectly by neutron scattering and nuclear magnetic resonance (NMR) spectroscopy **[2, 3]**, and then directly by X-ray scattering **[4, 5]** in several families of cuprates, so that it is now considered ubiquitous in cuprates below the optimal level of doping $p_{opt}$ = 0.16 holes/Cu. In some cases, but not always, CO competes with superconductivity, so that it weakens below the $T_c$ and gets stronger

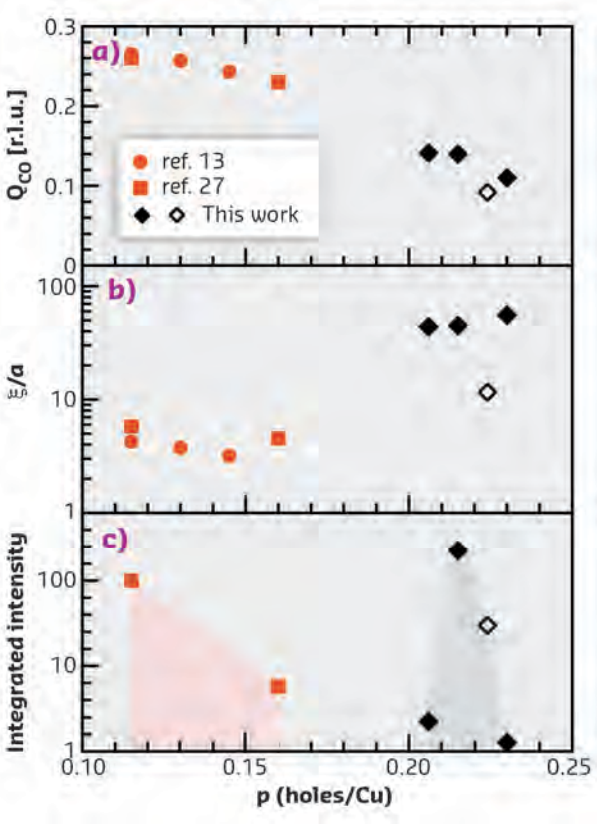


**Fig. 95:** The doping dependence of the charge order properties in single layer Bi2201. The incommensurate wave vector $Q_{CO}$, the correlation length ξ and the intensity of the scattering peak depend on the doping $p$ differently in the underdoped ($p \leq 0.16$) and in the overdoped ($p > 0.19$) regions of the phase diagram.

when superconductivity is supressed by magnetic fields. This picture confines the CO phenomenon to within a sub-region of the phase diagram, relating it to the well-known 'pseudo-gap' in the electronic structure. It is named 'underdoped' because the hole density is less than that needed for the maximum $T_c$.

Using RIXS at the Cu $L_3$ absorption edge at **ID32**, a new unexpected form of CO has been discovered in overdoped Pb-$Bi_2Sr_2CuO_{6+\delta}$ (Bi2201), a compound with a single $CuO_2$ layer per unit cell. The correlation length obtained from the sharpness of the scattering peak is of the order of 50 unit cells, much larger than in the underdoped samples measured previously (see **Figure 95**). The wave vector of the CO ($Q_{CO} \sim 0.14$ reciprocal lattice units) is different from that of the underdoped Bi2201; however, it is in-line with the extrapolation of the trend known at low doping, suggesting that the two regimes are connected by a common microscopic origin. Another surprising property of this CO is that it is independent of temperature: neither the onset of superconductivity at low $T$ nor the thermal disorder up to almost 300 K significantly modify the intensity and the width of the scattering peak.

The consequences of this discovery are depicted in the phase diagram in **Figure 96**. A new regime of CO, outside the pseudo-gap underdoped region, is labelled CO2. This means that theories requiring a connection between the pseudogap and charge order cannot explain CO2. Its origin from Fermi surface nesting or folding has also been ruled out by performing angle-resolved photoemission spectroscopy measurements. A unifying theory is thus proposed, descending from the initial prediction made 25 years ago **[1, 6]**. In this view CO is the result of an attractive interaction among charges that is insufficient to reach criticality, and thus long-range order at low $T$, which is nevertheless emerging at high doping of Bi2201 due to the presence of a particularly large van Hove singularity close to the Fermi level.

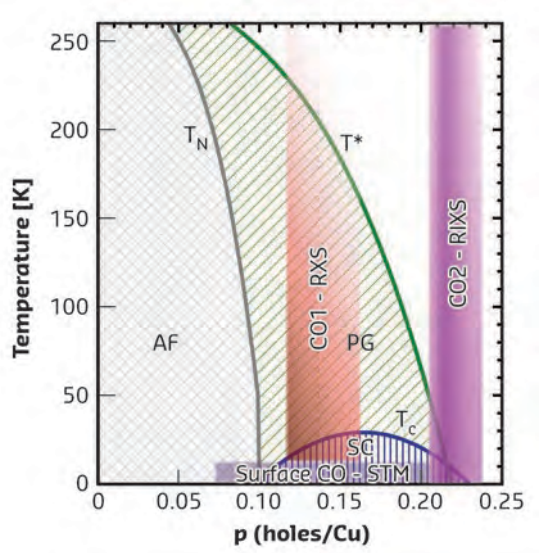


**Fig. 96:** The phase diagram of Bi2201 highlighting the various CO regions. The antiferromagnetic (AF) parent compound (p = 0) becomes superconducting (SC) in a domed region peaking around p = 0.16. A pseudo-gap (PG) is observed in the electronic structure of the superconductors above $T_c$ and below $T^*$. Charge order had been observed by STM at low $T$ over a wide range of doping, but only in a narrower interval with resonant X-ray scattering (CO1), always inside the PG region. The new RIXS data have unveiled charge order (CO2), almost insensitive to temperature, in the overdoped regime.

## PRINCIPAL PUBLICATION AND AUTHORS

Re-entrant charge order in overdoped $(Bi,Pb)_{2.12}Sr_{1.88}CuO_{6+\delta}$ outside the pseudogap regime, Y. Y. Peng (a), R. Fumagalli (a), Y. Ding (b), M. Minola (c), S. Caprara (d, e), D. Betto (f), M. Bluscke (c), G. M. De Luca (g, h), K. Kummer (f), E. Lefrançois (c), M. Salluzzo (f), H. Suzuki (c), M. Le Tacon (i), X. J. Zhou (b), N. B. Brookes (f), B. Keimer (c), L. Braicovich (a), M. Grilli (d, e) and G. Ghiringhelli (a, j), *Nat. Mater.* **17**, 697–702 (2018); doi : 10.1038/s41563-018-0108-3.
*(a) Politecnico di Milano (Italy)*
*(b) Institute of Physics, CAS Beijing (China)*
*(c) Max Planck Institute for Solid State Research, Stuttgart (Germany)*
*(d) Università di Roma La Sapienza (Italy)*
*(e) CNR-ISC, Rome (Italy)*
*(f) ESRF*
*(g) Università di Napoli Federico II (Italy)*
*(h) CNR-SPIN, Naples (Italy)*
*(i) Karlsruhe Institute of Technology* (Germany)
*(j) CNR-SPIN, Milan (Italy)*

## REFERENCES

[1] C. Castellani, *et al., Phys. Rev. Lett.* **75**, 4650 (1995).
[2] J. M. Tranquada *et al., Nature* **375**, 561 (1995).
[3] T. Wu *et al., Nature* **477**, 191–194 (2011).
[4] G. Ghiringhelli *et al., Science* **337**, 821 (2012).
[5] J. Chang *et al., Nat. Phys.* **8**, 871 (2012).
[6] S. Caprara *et al., Phys. Rev. B* **95**, 224511 (2017).

# RIXS UNVEILS EXOTIC MAGNETISM IN RARE-EARTH NICKELATES

**Rare-earth nickelates exhibit an unusual spin- and bond-ordered electronic ground state. Using high-resolution resonant inelastic X-ray scattering (RIXS), the magnetic excitations in $NdNiO_3$ were observed for the first time. Combined with a theoretical model, the results provide direct insight into the magnetic dynamics and exchange interactions of the rare-earth nickelates.**

Metal oxides exhibit a wide range of electronic and magnetic properties, largely due to the strong interactions and correlations between the individual electrons. In particular, the plethora of novel physics and functionalities that have emerged in thin oxide films and at oxide interfaces have made them a key ingredient for developing new concepts for modern electronic devices **[1, 2]**. Many of these designs are based on artificial heterostructures whose functionalities depend on the synergic interaction between different active elements across interfaces. To selectively probe the electronic and magnetic properties of the different functional components is therefore not only important for the fundamental understanding of the correlated-electron physics in these complex materials, but also crucial for the rational design and realisation of future oxide-based devices.

Perovskite rare-earth nickelates ($RNiO_3$) are a class of oxides that go through a metal-insulator transition when the temperature is lowered. In the insulating state, the $RNiO_3$ exhibit a rock-salt-type bond order with two inequivalent Ni sublattices hosting two different magnetic moments ($S_A > S_B$, **Figure 98a**). The moments order in a four-sublattice 90-degree spiral structure along the pseudocubic body diagonal, which has no analogue in insulating oxides, and its underlying mechanism has hitherto remained elusive. One of the main obstacles to understanding the peculiar magnetism of $RNiO_3$ lies in the difficulties associated with probing the different local spin states of the two inequivalent Ni sites and their corresponding exchange interactions.

In this study, the energy-selectivity of RIXS was exploited to investigate the electronic and magnetic properties of the different Ni sites in a $NdNiO_3$ film using the unprecedented high resolution of the ERIXS spectrometer at beamline **ID32**. The main experimental results are shown in **Figure 97**. The charge fluctuation in the metallic phase of $NdNiO_3$ gives rise to the two X-ray absorption spectroscopy (XAS) peaks A and B **[3]**, as shown in **Figure 97b**, which are associated with starkly different RIXS spectra in **Figure 97a**. The charge fluctuation is then suppressed in the insulating state, as different electronic configurations condense onto the two different Ni sites, thereby setting distinct excitation energies for the two sites. This is also confirmed by a realistic model calculation of the RIXS spectra. One can thus turn the energy-selectivity of RIXS into site-selectivity to probe the magnetic excitations ('magnons') originated from the two different Ni moments separately.

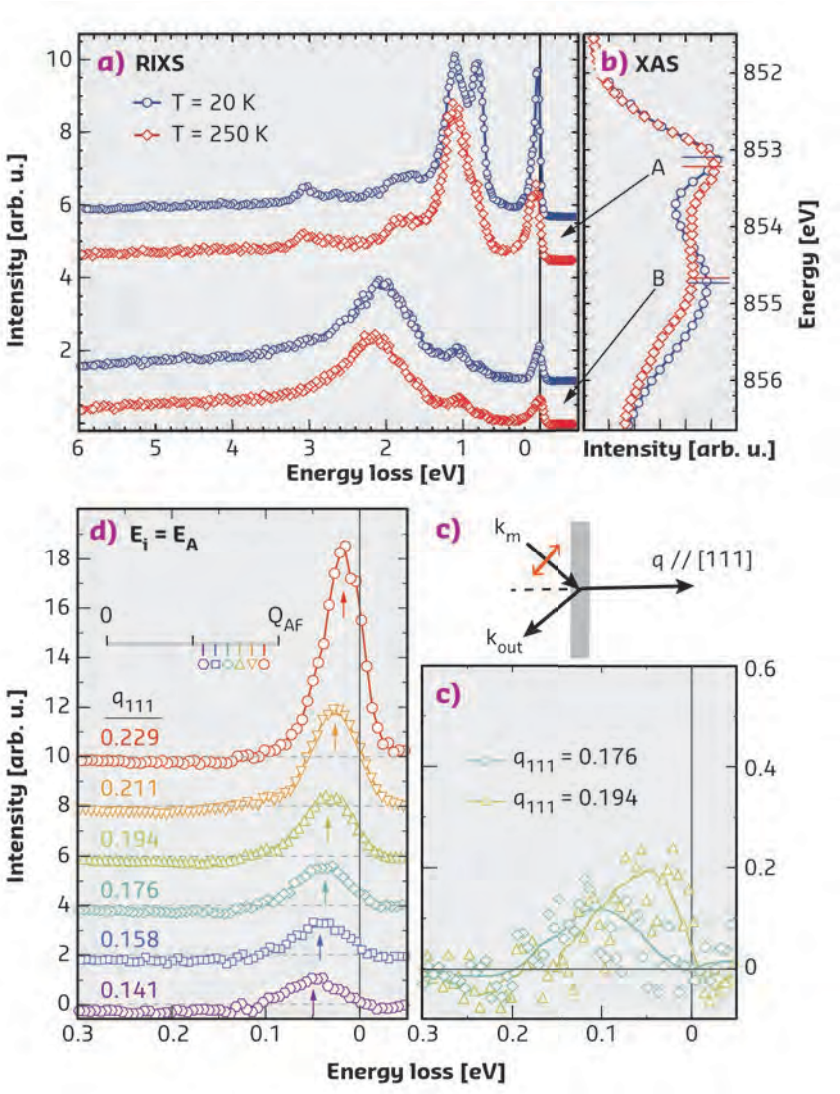


**Fig. 97: a)** RIXS spectra and **b)** XAS for the $NdNiO_3$ film at temperatures below and above the metal-insulator-transition temperature $T_{MIT}$. The incident photon energy in **(a)** is tuned to the resonant peaks A and B marked by bars in panel **(b)**. The scattering geometry is sketched in panel **(c)**. **d, e)** Magnon scattering intensity at different momentum transfer **q**//[111] (denoted by $q_{111}$) obtained with incident photon energy tuned to A and B, respectively.

The magnetic RIXS spectrum was mapped over a large momentum space for incident photon energy $E_A$ and $E_B$ (**Figures 97d** and **97e**). The magnons show a clear dispersion with $E_i = E_A$, whereas the spectra recorded with $E_i = E_B$ show vanishing spectral weight with almost non-discernible dispersion. Using a spin model that assumes strong competition between ferromagnetic double exchange and antiferromagnetic superexchange interactions between neighbouring Ni sites, the magnetic ground state and the magnon dispersion were successfully reproduced and explained for the first time (**Figure 98**), allowing for the extraction of exchange parameters with high accuracy. This study provides an example for the application of RIXS in oxide thin films and heterostructures that contain several functional materials and/or inequivalent structural sites.

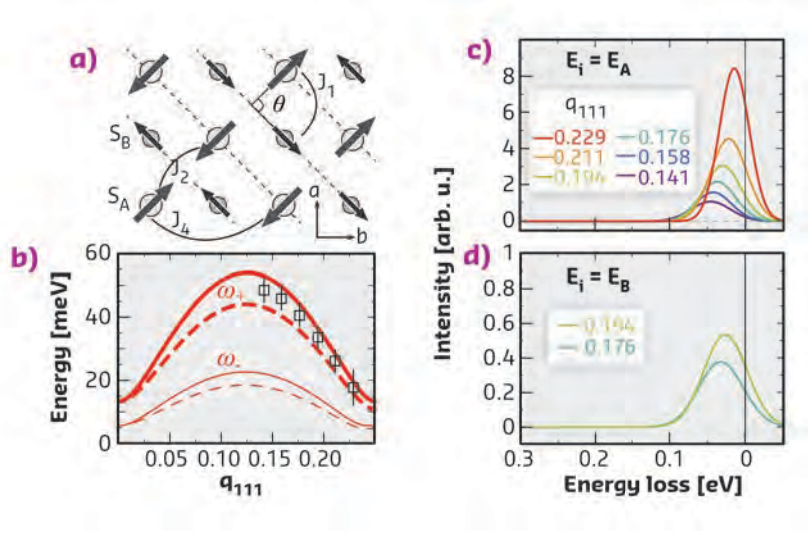


**Fig. 98: a)** Schematic of the magnetic structure of $R$NiO$_3$. It can be viewed as stacking of alternating ferromagnetic $S_A$ and $S_B$ planes along [111], as indicated by the dashed lines. **b)** Calculated spin-wave dispersion along [111] for two kinds of domains (solid lines for *hkl* and $\bar{h}\bar{k}l$, and dashed for $h\bar{k}\bar{l}$ and $\bar{h}k\bar{l}$). Each includes two branches (thick and thin) due to the disproportionated spins. Open symbols are experimental data from **Figure 97d**. **c, d)** Calculated RIXS spectra of magnon excitations for the experimental geometry at $E_i = E_A$ and $E_B$.

PRINCIPAL PUBLICATION AND AUTHORS

Site-Selective Probe of Magnetic Excitations in Rare-Earth Nickelates Using Resonant Inelastic X-ray Scattering, Y. Lu (a), D. Betto (b), K. Fürsich (a), H. Suzuki (a), H.-H. Kim (a), G. Cristiani (a), G. Logvenov (a), N.B. Brookes (b), E. Benckiser (a), M.W. Haverkort (c), G. Khaliullin (a), M. Le Tacon (d), M. Minola (a) and B. Keimer (a), *Phys. Rev. X* **8**, 031014 (2018); doi: 10.1103/PhysRevX.8.031014.
*(a) Max-Planck-Institut für Festkörperforschung, Stuttgart (Germany)*
*(b) ESRF*
*(c) Institut für Theoretische Physik, Universität Heidelberg (Germany)*
*(d) Institut für Festkörperphysik, Karlsruher Institut für Technologie (Germany)*

REFERENCES

[1] H. Y. Hwang *et al., Nat. Mater.* **11**, 102 (2012).
[2] M. Bibes *et al., Adv. Phys.* **60**, 5 (2011).
[3] R. J. Green *et al., Phys. Rev. B* **94**, 195127 (2016).

# EFFECT OF THE ACTIVE-SITE STRUCTURE ON THE ACTIVITY OF COPPER MORDENITE IN THE CONVERSION OF METHANE INTO METHANOL

**Materials with monomeric and oligomeric copper sites that are active in the direct conversion of methane into methanol possess different reactivity towards methane and water. Here, it is shown for the first time that oligomeric copper species exhibit high activity under both aerobic and anaerobic activation conditions, whereas monomeric copper sites produce methanol only in aerobic processes.**

The direct conversion of methane into methanol is an important process industrially, as it provides a sustainable route from an abundant and clean component of natural gas to one of the main precursors for the synthesis of chemicals. A promising aerobic stepwise process over copper-exchanged zeolites has been suggested; however, a detailed understanding of the mechanism of such a zeolite-catalysed conversion is still missing **[1, 2]**.

It has recently been shown that selective anaerobic oxidation of methane is possible **[3]**; where water is used both to provide oxygen to regenerate the zeolite active sites and to stabilise reaction intermediates to drive the otherwise endothermic $Cu^I$ oxidation reaction. Instead of using oxygen, only the presence of water is required, while the reactivation of the zeolite material is done in an inert atmosphere. Such a water-facilitated redox process requires

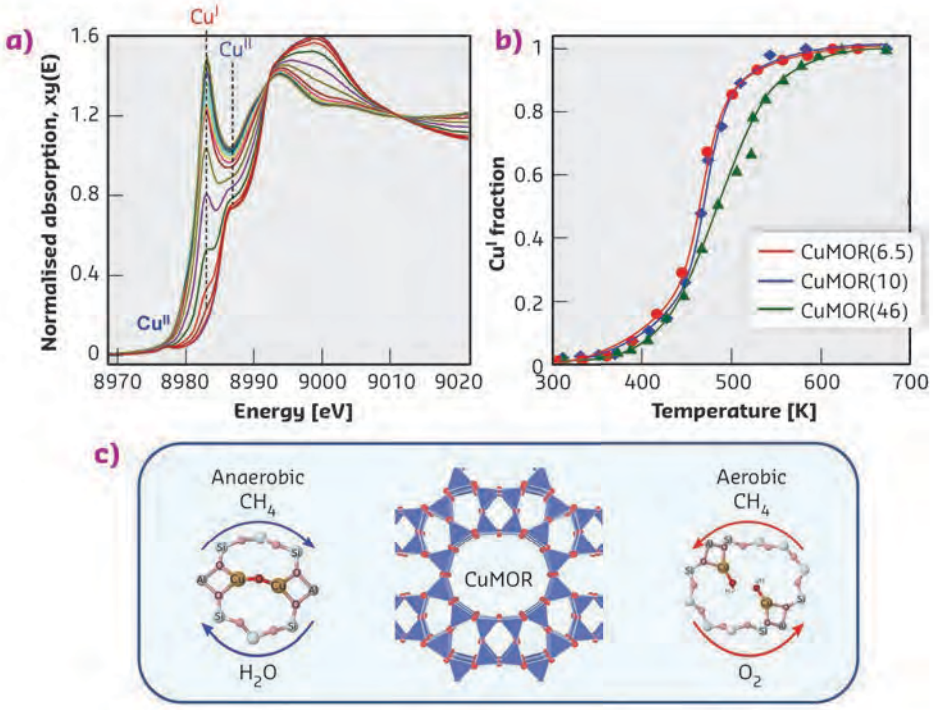


**Fig. 99: a)** Cu K-edge XANES spectra acquired during TPR of CuMOR(Si/Al = 6.5) with methane. **b)** Results of linear combination fitting of XANES results in the course of TPR-$CH_4$. **c)** Scheme representing the aerobic and anaerobic looping protocols for methane conversion into methanol.

at least two copper atoms to stoichiometrically oxidise methane into methanol, thus suggesting the presence of active sites containing several copper atoms. However, the intrinsic activity of copper species of different sizes is still a subject of debate.

This work demonstrates the influence of the Si/Al ratio of the zeolite mordenite on the possible configurations of the active copper oxide sites, and therefore on the activity of the material in the process of aerobic and anaerobic conversion of methane into methanol. Infrared spectroscopy of probe molecules (nitrogen monoxide and hydrogen) indicated the dominant formation of copper monomeric species for the samples with a high Si/Al ratio, in contrast to the samples with Si/Al ratio higher than 10, where a mixture of copper sites with different nuclearity was detected. Laboratory tests showed the gradual increase of the selectivity and methanol yield per mole of copper with an increase of the Si/Al ratio, which might be associated with different redox properties. To assess them, a temperature-programmed reaction (TPR) of copper mordenite samples with methane was monitored by means of *in situ* X-ray absorption spectroscopy (XAS) at beamline **BM31**. Cu K-edge X-ray absorption near edge structure (XANES) spectra showed the gradual conversion of $Cu^{II}$ species into $Cu^{I}$ within the temperature range of 300-700 K (**Figure 99a**). Linear combination fitting (LCF) analysis of the spectra acquired for different samples (**Figure 99b**) demonstrated that the reduction of all samples starts at ~400 K and then progressively accelerates with the rise of temperature. CuMOR(6.5) and CuMOR(10) demonstrated similar redox properties, with almost full reduction of $Cu^{II}$ into $Cu^{I}$ at 650 K. In contrast, the reduction of the CuMOR(46) material showed a more gradual reduction until the temperature of 750 K. This indicates lower reactivity of copper monomeric species of CuMOR(46) towards methane.

Combining XAS and infrared spectroscopy with reactor tests, it is possible to show that monomeric and oligomeric copper species display different activities towards methane in both aerobic and anaerobic pathways, as well as towards water under anaerobic conditions. This difference is probably related to the stabilising effect of the water molecules interacting with active copper sites. Together, the data can serve as a basis for the further improvement of existing systems and the design of novel materials for the direct conversion of methane into methanol.

## PRINCIPAL PUBLICATION AND AUTHORS

The Effect of the Active-Site Structure on the Activity of Copper Mordenite in the Aerobic and Anaerobic Conversion of Methane into Methanol, V. L. Sushkevich (a), D. Palagin (a) and J. A. van Bokhoven (a, b), *Angew. Chem. Int. Ed.*, **57**, 8906–8910 (2018), doi: 10.1002/anie.201802922.
*(a) Paul Scherrer Institut, Villigen (Switzerland)*
*(b) Institute for Chemical and Bioengineering, ETH Zurich (Switzerland)*

## REFERENCES

[1] M. H. Groothaert *et al., J. Am. Chem. Soc.* **127**, 1394–1395 (2005).
[2] P. Tomkins *et al., Acc. Chem. Res.* **50**, 418–425 (2017).
[3] V. L. Sushkevich *et al., Science* **356**, 523–527 (2017).

# A REDOX 'NON-INNOCENT' APPROACH TO 2D CONDUCTIVE MAGNETS

**Materials that combine high-temperature magnetic order and high electrical conductivity are interesting candidates for applications in spintronics. An appealing approach for the synthesis of such multifunctional materials is the combination of reducing metal ions and redox 'non-innocent' organic ligands. Such synergy can give rise to strong magnetic interactions as well as high electronic delocalisation.**

Magnetic and electrically conductive metal–organic frameworks (MOFs) are an exciting class of materials due to their potential applications in next-generation electronic devices. MOFs are usually composed of metal ions and redox-inactive or 'innocent' organic linkers, a combination that does not favour electronic communication between different structural components. A strategy to overcome this difficulty is based on the use of redox-active ('non-innocent') ligands, which possess frontier-orbital energies close to those of the metal ions, allowing a strong electronic delocalisation.

In the present work, this concept was applied for the synthesis of the layered coordination solid, $CrCl_2(pyrazine)_2$ (**Figure 100**). $Cr^{2+}$ is virtually impossible to stabilise in a coordination environment composed of aromatic amines, and thus $Cr^{3+}$ complexes with ligand-based radicals are formed. This metal–ligand redox process is also found in the case of $CrCl_2(pyrazine)_2$, in which the reducing power of $Cr^{2+}$ ions leads to an electron transfer between the metal centre and the organic ligand, giving rise to $Cr^{3+}$ and a singly reduced pyrazine scaffold.

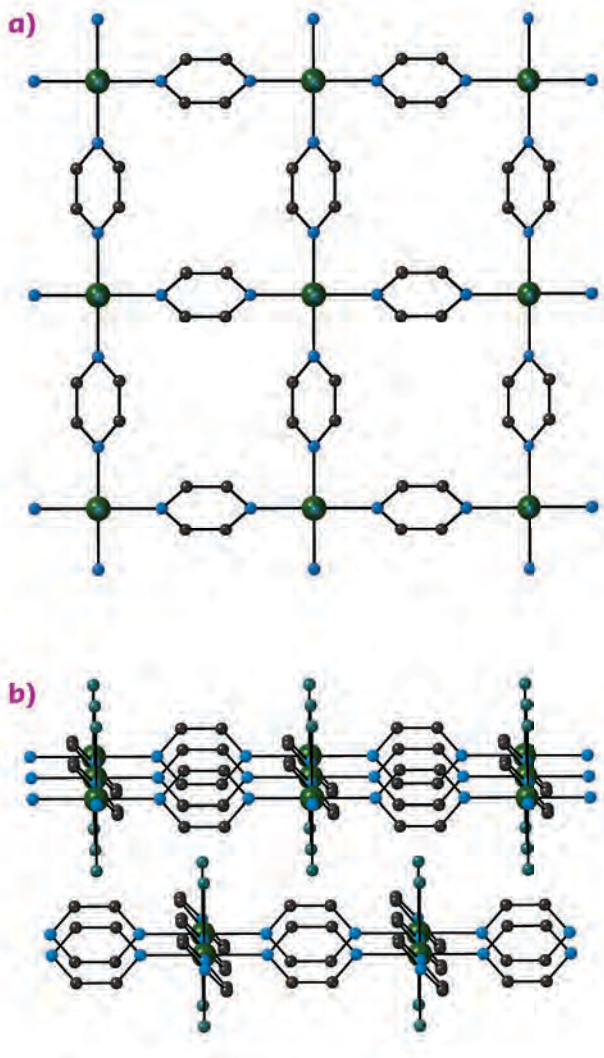


**Fig. 100:** Structure of $CrCl_2(pyrazine)_2$, showing **a)** a single layer along the crystallographic *c* direction and **b)** the stacking of the layers along the same direction. Colour code: Cr, dark green; Cl, light green; C, dark grey; N, blue; H are omitted for clarity.

In the absence of typical bond lengths expected for a $Cr^{2+}$ coordination sphere, the X-ray crystal structure of $CrCl_2(pyrazine)_2$ supports the presence of a Cr ion in its +3 oxidation state. The definitive confirmation came from X-ray absorption spectroscopy (XAS) measurements carried out at beamline **ID12** at the Cr and Cl K-edges. XAS spectra were collected for $CrCl_2(pyrazine)_2$ and two reference compounds named [Cr(II)] and [Cr(III)] featuring the same $\{CrN_4Cl_2\}$ first coordination sphere but having established oxidation states of +2 and +3, respectively. The XAS spectra of $CrCl_2(pyrazine)_2$ and [Cr(III)] were found to overlap, and the almost identical pre-edge features unequivocally assign the +3 oxidation state (**Figure 101**). These results also confirm the redox activity of the coordinated pyrazine, which plays a key role in magnetic and electrical properties of this layered material. Extremely strong magnetic interactions between $Cr^{3+}$ and the organic radical spins gives rise to a ferrimagnetic order below 55 K, while the extensive overlap between the pyrazine $\pi$- orbitals and the Cr 3*d* orbitals leads to large electron delocalisation throughout the material, inducing high electrical conductivity at room temperature. X-ray magnetic circular dichroism (XMCD), also performed at **ID12**, made it possible to experimentally determine the local Cr moment in this 2D material. The XMCD spectra of both $CrCl_2(pyrazine)_2$ and the [Cr(III)] reference compound have essentially the same shapes, confirming the identical local electronic structure of the Cr ions in these systems (**Figure 101**).

The intensity of the [Cr(III)] XMCD spectrum can be scaled by a factor of 0.75 to overlap with that of $CrCl_2(pyrazine)_2$. Taking into account the bulk magnetisation measurements of [Cr(III)], the local Cr magnetic moment was calculated in

the layered compound. As confirmed by density functional theory (DFT) calculations, the resulting magnetisation value is significantly reduced from the theoretical one. It is hypothesised that this effect arises from the strong degree of electronic delocalisation in $CrCl_2(pyrazine)_2$, which is absent in the [Cr(III)] model complex.

In conclusion, this work illustrates a new way of designing magnetic and highly conductive 2D MOFs using reducing transition metal ions and redox-active organic ligands.

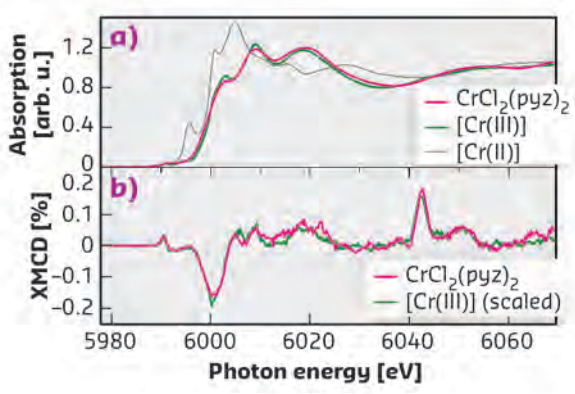


**Fig. 101: *a)*** XAS and XMCD spectra for $CrCl_2(pyrazine)_2$ (pyz: pyrazine) and the [Cr(III)] and [Cr(II)] reference compounds. ***b)*** Corresponding XMCD spectra of $CrCl_2(pyrazine)_2$ and the [Cr(III)] reference (intensity downscaled by 25%) recorded at 3 K and 17 T.

PRINCIPAL PUBLICATION AND AUTHORS

Formation of the layered conductive magnet $CrCl_2(pyrazine)_2$ through redox-active coordination chemistry,
K. S. Pedersen (a, b, c), P. Perlepe (a, b, d, e), M. L. Aubrey (f), D. N. Woodruff (g), S. E. Reyes-Lillo (h, i, j, k), A. Reinholdt (k), L. Voigt (c), Z. Li (l), K. Borup (m), M. Rouzières (a, b), D. Samohvalov (a, b), F. Wilhelm (n), A. Rogalev (n), J. B. Neaton (h, l, o), J. R. Long (f, p, q) and R. Clérac (a, b), *Nat. Chem.* **10**, 1056–1061 (2018); doi: 10.1038/s41557-018-0107-7.
*(a) CNRS, CRPP, UMR 5031, Pessac (France)*
*(b) Univ. Bordeaux, CRPP, UMR 5031, Pessac (France)*
*(c) Department of Chemistry, Technical University of Denmark (Denmark)*
*(d) CNRS, ICMCB, UMR 5026, Pessac (France)*
*(e) Univ. Bordeaux, ICMCB, UMR 5026, Pessac (France)*
*(f) Department of Chemistry, University of California Berkeley (USA)*
*(g) Department of Chemistry, University of Oxford (UK)*
*(h) Molecular Foundry, Lawrence Berkeley National Laboratory (USA)*
*(i) Department of Physics, University of California Berkeley (USA)*
*(j) Departamento de Ciencias Físicas, Universidad Andres Bello, Santiago (Chile)*
*(k) Department of Chemistry, University of Copenhagen (Denmark)*
*(l) Department of Physics and Astronomy – Centre for Storage Ring Facilities (ISA), Aarhus University (Denmark)*
*(m) Center for Materials Crystallography, Department of Chemistry and iNano, Aarhus, (Denmark)*
*(n) ESRF*
*(o) Kavli Energy Nanosciences Institute at Berkeley (USA)*
*(p) Department of Chemical and Biomolecular Engineering, University of California Berkeley (USA)*
*(q) Materials Sciences Division, Lawrence Berkeley National Laboratory (USA)*

# ATOMIC-SCALE RESOLUTION SPECTROSCOPY OF VALENCE CHARGES WITH SYNCHROTRON RADIATION

**This work demonstrates a novel technique that provides spectroscopic and structural information on valence electrons in a single measurement by using synchrotron radiation. In contrast to other techniques, this approach enables the measurements of atomic scale interactions of valence electrons, hence provides new access to microscopic-scale effects.**

The understanding of the interactions of valence electrons is essential for the understanding of physical, chemical and biological phenomena. Although optical radiation is extensively used to study the properties of valence electrons, optical radiation spectroscopy methods do not provide atomic-scale information, due to their long wavelengths. While X-ray Bragg diffraction experiments can reveal structural information at the atomic scale, they cannot provide spectroscopic information on valence electrons. Thus, understanding the microscopic nature of valence electron interactions remains a great challenge.

Nonlinear interactions of X-rays and long wavelengths provide insight into the microscopic structure of chemical bonds, the valence electron density of crystals, and light–matter interactions at atomic-scale resolution **[1].** The high resolution stems from the short wavelengths of X-rays, whereas the long wavelength field is used to select the interactions with the valence electrons. The effect could be considered as X-ray diffraction from optically modulated charge densities. In analogy to Bragg diffraction, atomic-scale resolution can be achieved by measuring the intensities for diffractions from different atomic

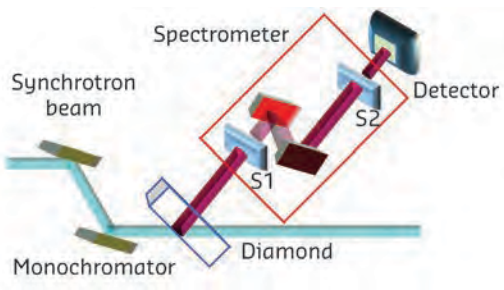


**Fig. 102:** Schematic of the experimental setup. A monochromatic beam was scattered from the sample in the horizontal plane. The diffraction was from the diamond(220) atomic planes. The scattering plane of the analyser was normal to the scattering plane of the sample. S1 and S2 are the slits before the analyser and before the detector, respectively. The analyser was a Si(440) and the detector was an avalanche photodiode.

planes, but, in contrast to Bragg diffraction, in the nonlinear process the intensity is proportional to the Fourier coefficient of the valence electrons and not to the coefficient of the core electrons.

To date, only Glover *et al.* have observed nonlinear wave mixing between X-rays and optical radiation by using the first hard X-ray free-electron laser **[2]**. It is challenging to perform further progress with this effect because it requires high optical intensities, which are above the radiation damage threshold of most materials.

This work demonstrates the nonlinear effect of parametric down-conversion (PDC) of X-rays into the optical regime. In PDC the input photons interact with vacuum fluctuations to generate correlated X-ray (signal) and optical (idler) photon pairs. Since the photons are always generated in pairs, and since the process conserves energy and momentum, the generation rate, the photon energy, and the angle of propagation of the generated X-ray photons are perfectly correlated with the long wavelength photons. Consequently, it is sufficient to measure the X-ray signal to probe the properties of the sample at energies corresponding to long wavelength photons**.** Several demonstrations of PDC into extreme ultraviolet are reported **[3, 4]**, but the extension of this method into the optical regime is more challenging due to the proximity of the photon energy to the input photon energy.

Experiments were conducted at beamline **ID20** and at Diamond Light Source (UK), using a collimated monochromatic beam at 9 and 11 keV to illuminate a diamond crystal for the generation of the PDC, collecting the emitted X-ray photons with a system described in **Figure 102**.

**Figure 103a** shows the spectrum of the effect. The peak on the left corresponds to the elastic scattering, and the broad peak is the PDC signal. The peak is observed at 7.1 eV, where the efficiency of the PDC is the largest. This energy is near the bandgap of the diamond crystal, where the density of states of the valence electrons is the highest. This observation demonstrates the ability to measure valence electron spectral dependencies.

The rocking curve of the PDC X-ray signal was measured at an idler energy of 2.2 eV, as shown in **Figure 103b**. The small peak on the left is the residual elastic, and the peak centred at 15 mdeg from the origin is the PDC signal. The Fourier coefficient of the susceptibility obtained from the measurement is comparable to the theoretical prediction and to the result of the X-ray and optical mixing experiment **[2]**.

This is the first observation of the PDC of X-rays into optical radiation, an effect that could be used as a new tool to probe microscopic valence charge densities and optical properties of materials on the atomic scale. This novel tool can be used to test and improve the understanding of condensed-matter physics.

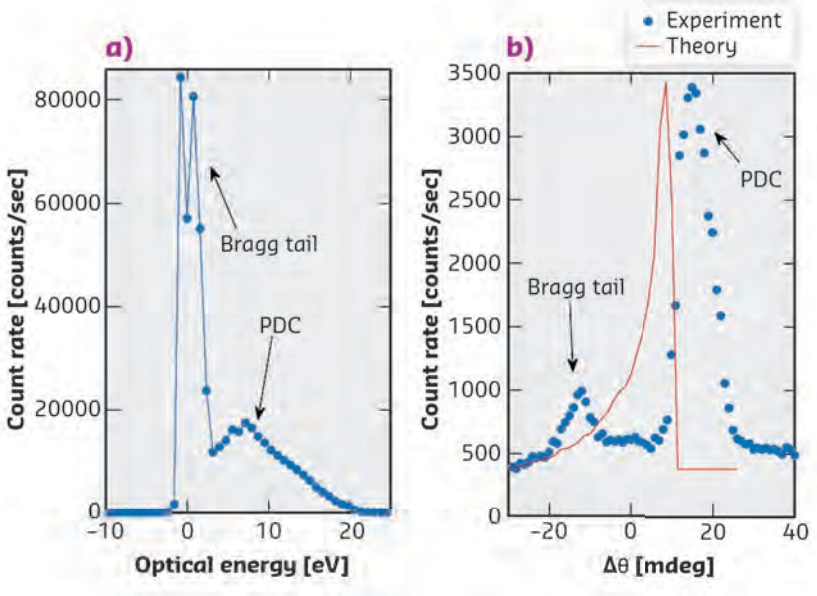


**Fig. 103: a)** X-ray signal count rate as a function of the analyser detuning from the photon energy of the input beam. The left sharp peak corresponds to the elastic scattering and the broad peak is the PDC signal. **b)** X-ray signal count rate as a function of the pump deviation angle from the phase matching angle. The idler central wavelength was 550 nm (~2.2 eV). The blue dots are the experimental results and the solid red line is calculated from theory.

## PRINCIPAL PUBLICATION AND AUTHORS

Parametric Down-Conversion of X-Rays into the Optical Regime, A. Schori (a), C. Bömer (b), D. Borodin (a), S. P. Collins (c), B. Detlefs (d), M. Moretti Sala (d), S. Yudovich (a) and S. Shwartz (a), *Phys Rev. Lett.* **119**, 253902 (2017).
*(a) Physics Department and Institute of Nanotechnology, Bar-Ilan University (Israel)*
*(b) European XFEL (Germany)*
*(c) Diamond Light Source (UK)*
*(d) ESRF*

## REFERENCES

[1] I. Freund and B. F. Levine, *Phys. Rev. Lett.* **25**, 1241 (1970).
[2] T. E. Glover *et al., Nature* (London) **488**, 603 (2012).
[3] K. Tamasaku *et al. Nat. Phys.* **7**, 705 (2011).
[4] D. Borodin *et al. Appl. Phys. Lett.* **110**, 131101 (2017).

# UNDERSTANDING THE DEGRADATION OF A BLUE PHOSPHOR AT THE ATOMIC LEVEL

**The atomic modifications responsible for the degradation of one of the brightest blue phosphors used in technological applications have been studied. Using element-selective X-ray spectroscopy combined with a UV-vis probe it was found that irradiation induces oxidation of $Eu^{2+}$ and the formation of killer centres that hamper remaining $Eu^{2+}$ to emit.**

White light emitting diodes (LEDs), plasma screens and fluorescent lamps are only some of the many daily-life objects exploiting inorganic phosphors to emit visible light. In this class of materials, light is emitted by luminescence centres – typically transition metal or rare-earth atoms incorporated in a transparent host crystal at concentrations of a few atomic percent. The electronic interactions in the partially filled d- and f-shell, and the influence of the nearest neighbouring atoms (via the ligand field), create a manifold of electronic states (multiplets) where the energy difference between the ground state and the first excited states is a few eV. When the luminescent centres are excited, directly or via energy transfer from the host crystal, visible light can be emitted in the de-excitation cascade.

The stability of the light emitted under working conditions is crucial in the technological use of phosphors **[1]**. Prolonged irradiation – LEDs are supposed to last for 50 000 hours – may induce modifications at the atomic level that degrade the luminescence efficiency. This is the case for one of the most employed blue phosphors, $BaMgAl_{10}O_{17}$ doped with $Eu^{2+}$ (BAM:Eu), which sees its bright blue luminescence redshift and degrade after prolonged exposure to ultraviolet excitation light. The alteration acting at the atomic level that is responsible for BAM:Eu degradation has been investigated before and explanations pointing to the degradation of the host crystal and of the energy transfer mechanism, as well as of the dopant itself, have been proposed **[2, 3]**. Nonetheless, a satisfactory explanation of the degradation process is still missing. Ideally, one would simultaneously probe the electronic structure of the luminescent centres and the luminescence efficiency while inducing progressive degradation. This investigation was recently performed on **ID26**, exploiting the X-rays as a probe of the local electronic structure, as excitation source for the luminescence and as an accelerated source of damage.

High-energy resolution fluorescence detected (HERFD) X-ray absorption near-edge structure (XANES) was measured at the Ba $L_3$ edge during X-ray irradiation and using a UV-vis spectrometer to simultaneously acquire emission spectra (**Figure 104**). The Ba XANES remained unchanged after an irradiation time that reduced the blue luminescence to less than 1% of the initial value, indicating that the structure of the host lattice was not degraded. Focusing on the Eu dopants, a series of fast HERFD XANES acquired at the Eu $L_3$

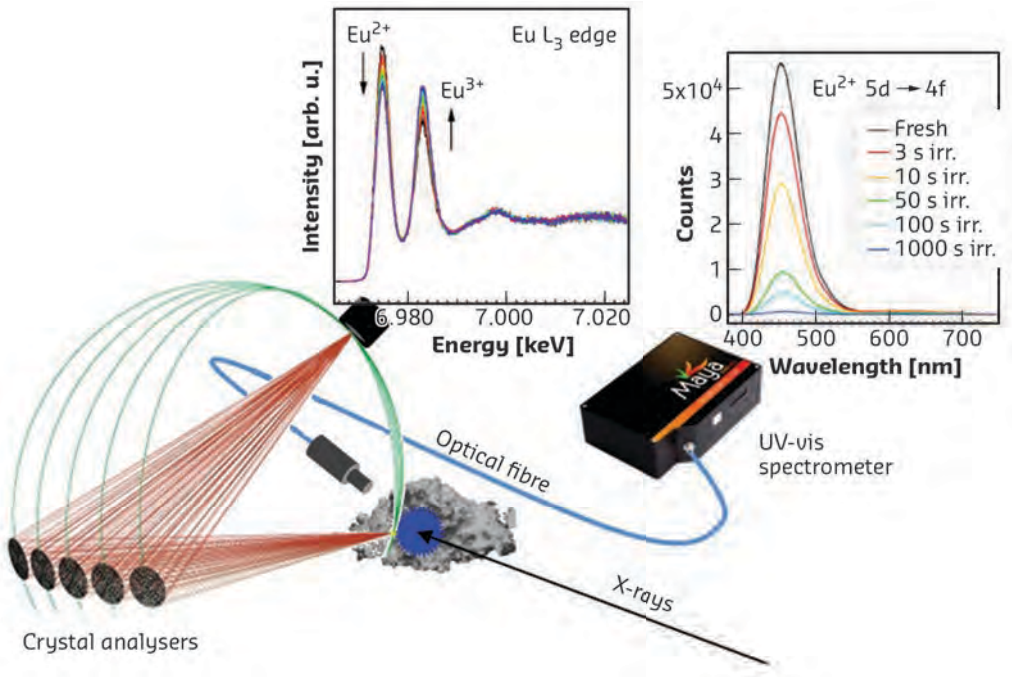


**Fig. 104:** Scheme of the experimental setup to collect the luminescence emitted by the sample during X-ray irradiation and the HERFD XANES at the same time. $Eu^{2+}$ oxidation is observed in Eu $L_3$ edge HERFD XANES and degradation of blue luminescence is simultaneously measured with a UV-vis spectrometer.

edge revealed that irradiation rapidly oxidises $Eu^{2+}$ to $Eu^{3+}$ (**Figure 104**), suggesting that this could be the cause for luminescence degradation.

To correlate oxidation and degradation, the maximum of $Eu^{2+}$ absorption and the luminescence during exposure to X-rays were sampled simultaneously. The comparison of the decay times of the luminescence intensity and of the oxidation of $Eu^{2+}$ revealed that the luminescence decreases at a considerably faster rate. In addition, a fraction of $Eu^{2+}$ dopants are resistant to oxidation. Thus, potentially emitting $Eu^{2+}$ centres are still present in the sample while luminescence is virtually zero. Oxidation is not solely responsible for the degradation and other processes are involved.

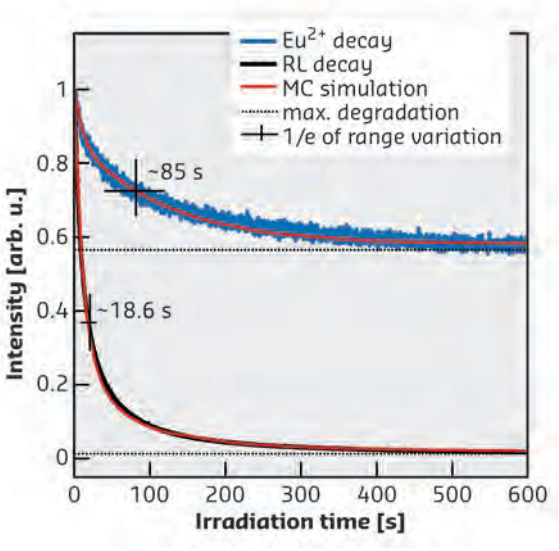


**Fig. 105:** The decay of $Eu^{2+}$ XANES peak (blue) and of the integrated luminescence (black) during irradiation are compared to the results of the Monte Carlo simulation (red lines).

To clarify this point, a Monte Carlo simulation was performed that, in a first step, modelled the $Eu^{2+}$ oxidation by random X-ray events hitting a sublattice of Ba and Eu atoms. Secondly, a quenching sphere centred on the newly formed $Eu^{3+}$ was introduced to simulate the formation of a killer centre close to the $Eu^{3+}$ that induces luminescence quenching of $Eu^{2+}$ ions inside the sphere. The decay profiles of $Eu^{2+}$ valence change and of blue luminescence were well reproduced by the simulation with a quenching radius of 24 Å (**Figure 105**). This value is compatible with the Eu–Eu distance at which luminescence emission decreases because energy is exchanged between impurities rather than being emitted.

In conclusion, simultaneously measuring the electronic structure and the luminescence emission during progressive degradation has revealed that the degradation of this europium-doped phosphor is due to the partial oxidation of $Eu^{2+}$ and to the simultaneous formation of killer centres that quench the remaining $Eu^{2+}$ luminescence centres.

PRINCIPAL PUBLICATION AND AUTHORS

Oxidation and Luminescence Quenching of Europium in $BaMgAl_{10}O_{17}$ Blue Phosphors, L. Amidani (a), K. Korthout (b), J. J. Joos (b), M. van der Linden (a, c), H. F. Sijbom (b), A. Meijerink (d), D. Poelman (b), P. F. Smet (b) and P. Glatzel (a),

*Chem. Mater.* **29**, 10122–10129 (2017); doi: 10.1021/acs.chemmater.7b03918.

*(a) ESRF*
*(b) Lumilab, Department of Solid State Sciences, Ghent University (Belgium)*
*(c) Inorganic Chemistry and Catalysis, Debye Institute for Nanomaterials Science, Utrecht University (The Netherlands)*
*(d) Condensed Matter and Interfaces, Debye Institute for Nanomaterials Science, Utrecht University (The Netherlands)*

REFERENCES

[1] P. F. Smet and J. J. Joos, *Nat. Mater.* **16**, 500 (2017).
[2] B. Howe and A. L. Diaz, *J. Lumin.* **109**, 51 (2004).
[3] B. Dawson *et al., Chem. Mater.* **16**, 5311 (2004).

# FERROELECTRIC AND ANTIFERROELECTRIC INSTABILITIES COMPETING IN $Bi_2SiO_5$

**$Bi_2SiO_5$ has recently emerged as a promising ambient-temperature, lead-free ferroelectric. Here, the competition between ferroelectric and antiferroelectric instabilities is analysed by investigating the characteristic temperature-dependent phonon energies at the centre and edge of the Brillouin zone, respectively.**

In the ferroelectric (FE) $Bi_2SiO_5$ (BSO), the ferroelectricity arises from the tilt of the quasi-one-dimensional (1D) chains formed by $SiO_4$ tetrahedral units (**Figure 106**, inset) **[1]**, providing an alternative to perovskite-type FEs, such as in $PbTiO_3$ or $BiFeO_3$, where the ferroelectricity arises from the cation off-centring. These findings recently opened the way towards the engineering of new tetrahedra-based FEs.

The soft phonon mode in BSO, which drives the FE transition at $T_C$, corresponds to a torsion of the $SiO_4$ units along the 1D tetrahedral chains. The freezing of this phonon was evidenced at the

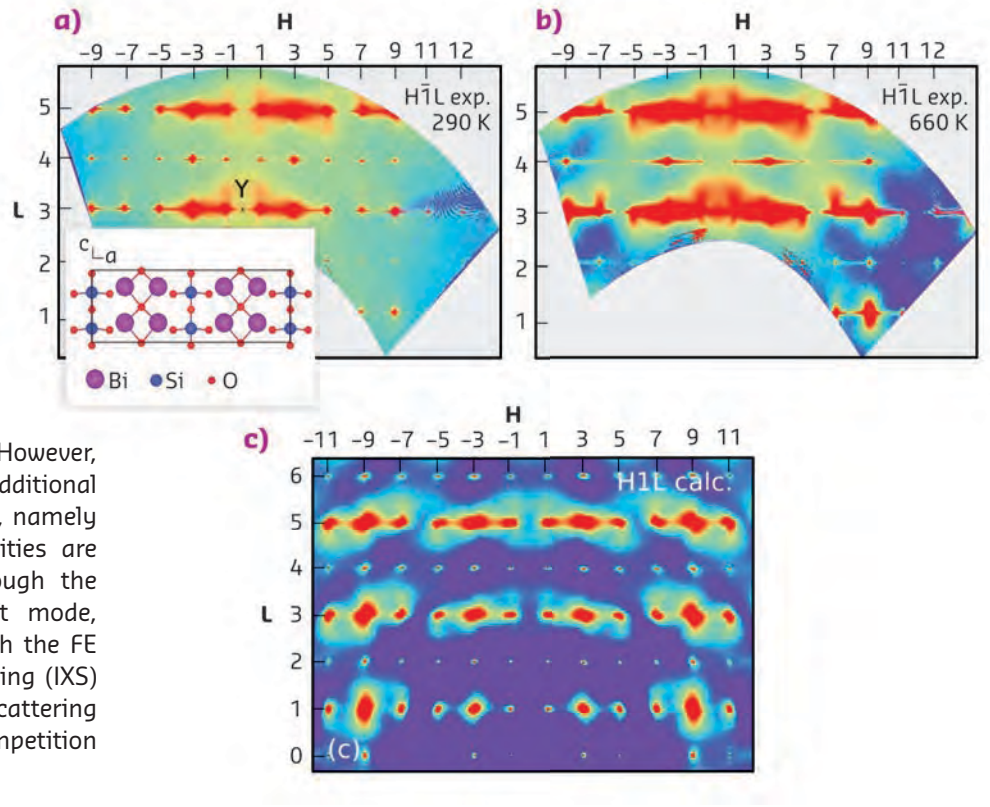


**Fig. 106:** Reconstructed TDS maps for the FE phase in the $H\bar{1}L$ plane measured **a)** at RT conditions, **b)** close to $T_C$ at $T$ = 660 K, and **c)** calculated from DFT. Inset: the crystal structure of BSO in the ferroelectric phase.

Γ point using Raman spectroscopy **[1]**. However, *ab initio* calculations predicted additional instabilities at the Brillouin zone edges, namely at the *Y* and *S* points. Such instabilities are usually related to AFE ordering, through the condensation of an AFE optical soft mode, suggesting, for BSO, a competition with the FE instability. Here, inelastic X-ray scattering (IXS) was combined with thermal diffuse scattering (TDS) experiments to analyse this competition between FE and AFE states.

TDS studies are particularly efficient when coupled with spectroscopic investigations and state-of-the-art *ab initio* calculations **[2]**. Specifically, a fast mapping of reciprocal space prior to an IXS experiment allows the identification of regions of interest, which can then be explored in more detail by energy-resolved spectroscopic measurements. To this end, a new diffractometer optimised for diffuse scattering studies has recently been designed, constructed and commissioned at beamline **ID28**, as a side-station to the existing high-resolution IXS spectrometer.

Experimental reconstructed reciprocal space maps measured with the side-station in the $H\bar{1}L$ plane at room temperature (RT) ($T<<T_C$) and $T$ = 660 K (close to $T_C$) are shown in **Figures 106a** and **106b**, respectively. They show elongated rod-like objects oriented along the [100]. The comparison with theoretical maps based on density functional theory (DFT) phonon dispersion calculations (**Figure 106c**), makes it possible to disentangle the contributions from static disorder and lattice dynamics. Here the diffuse signal is unambiguously related to a low-energy phonon branch along the Γ – *Y* direction, where the DFT calculations predict an AFE instability **[1]**. The strong temperature dependence of the diffuse rods upon approaching $T_C$ from below suggests the softening of an unstable phonon. In particular, the TDS intensity at the *Y* point, which is minimal at RT, becomes maximal close to the transition, indicating a strong dynamical anomaly at the Brillouin zone edge.

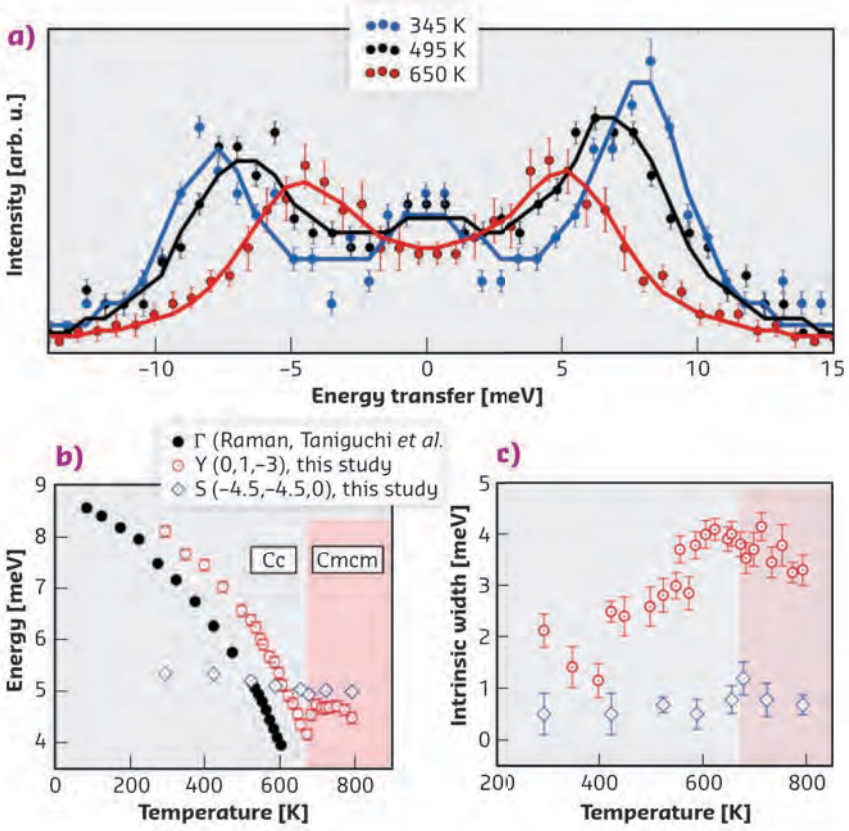


**Fig. 107:** RIXS spectra measured at the *Y* point for three different temperatures: 345 K (blue, $T<<T_C$), 495 K (black, $T<T_C$), and 650 K (red, $T\sim T_C$). **b)** Temperature evolution of the phonon energies at the *Y* point (red), *S* point (blue), and Γ point (black). **c)** Evolution with temperature of the intrinsic width of the phonon excitations at the *Y* and *S* points. Colour code same as in **(b)**.

In order to unveil the lattice dynamics underlying these TDS intensity distributions, a temperature-dependent IXS experiment was performed, providing the energy resolution in addition to the momentum resolution. A selected set of IXS spectra acquired at the *Y* point is shown in **Figure 107a** for the temperatures $T$ = 345 K ($T<<T_C$), $T$ = 495 K ($T<T_C$) and $T$ = 650 K (close to $T_C$). A pronounced softening of the *Y* point optical phonon is observed (**Figure 107b**), and compared to that of the FE optical soft mode **[1]**. The softening at the *Y* point is substantial but remains incomplete, and is accompanied by a considerable broadening due to the phonon overdamping (**Figure 107c**). In contrast, the *S* point mode showed only minor variations.

While the FE transition is driven by the complete softening of the FE mode at the Γ point, these results provide direct evidence for a strong competition between FE and AFE ordering at $T_C$. This work thus opens the way towards the exploration of the boundary between FE and AFE phases of BSO, and other similar systems, by means of an appropriate external perturbation, such as pressure or electric field.

This case study illustrates the possibilities offered at beamline ID28 by the combination of a diffuse scattering diffractometer with the high-resolution IXS spectrometer, which constitutes a unique experimental station worldwide, offering unprecedented capabilities in the studies of lattice dynamics in condensed matter.


PRINCIPAL PUBLICATION AND AUTHORS

Competing structural instabilities in $Bi_2SiO_5$, A. Girard (a), H. Taniguchi (b), S. M. Souliou (c), M. Stekiel (a), W. Morgenroth (a), A. Minelli (c), A. Kuwabara (d), A. Bosak (c) and B. Winkler (a), *Phys. Rev. B* **98**, 134102 (2018); doi: 10.1103/PhysRevB.98.134102.

*(a) Institut für Geowissenschaften, Goethe Universität Frankfurt (Germany)*
*(b) Department of Physics, Nagoya University (Japan)*
*(c) ESRF*
*(d) Nanostructures Research Laboratory, Japan Fine Ceramics Center (Japan)*

REFERENCES

[1] H. Taniguchi *et al.*, *Angew. Chem. Int. Ed.* **52**, 8088 (2013).
[2] A. Bosak *et al.*, *J. Phys. D: Appl. Phys.* **48,** 504003 (2015).


# LONG-ANTICIPATED ACOUSTIC PLASMONS REVEALED IN HIGH-TEMPERATURE SUPERCONDUCTORS

**Three-dimensional charge collective modes were observed in electron-doped copper oxides by resonant inelastic X-ray scattering (RIXS). The modes are reminiscent of acoustic plasmons predicted for layered copper oxides and are thought to play a substantial role in mediating high-temperature superconductivity.**

In the quest for novel functional materials with superconducting transition temperatures $T_c$ close to room temperature, it can be key to understand the mechanisms leading to a relatively high $T_c$ in other materials, such as the layered copper oxides. Despite more than 30 years of intense research, however, these mechanisms have not yet been fully clarified. One of the outstanding puzzles from the field of copper oxides is whether high-temperature superconductivity emerges as a consequence of the saving of kinetic energy or other potential energy **[1]**, and its relation to the distinct layered structure of stacked $CuO_2$ planes.

Addressing this issue, this study aimed at finding evidence for acoustic plasmons, which are branches of specific charge collective modes with a three-dimensional character due to interplanar Coulomb interaction. Their presence was argued to be energetically related to the energy savings associated with the superconducting

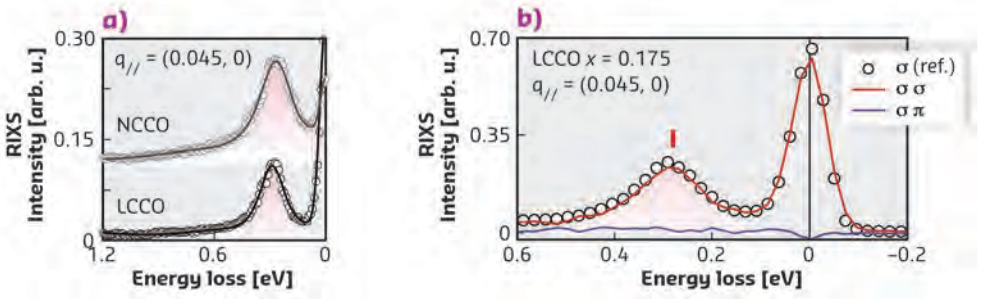


**Fig. 108: a)** RIXS spectra of NCCO ($x$ = 0.15) and LCCO ($x$ = 0.175) for incident photon energies tuned to the Cu $L_3$-edge at $T \approx 20$ K. **b)** Polarisation-resolved RIXS. Charge excitations are detected in the parallel polarisation channel (σσ, red line) and magnetic excitations in the crossed-polarisation channel (σπ, blue line).

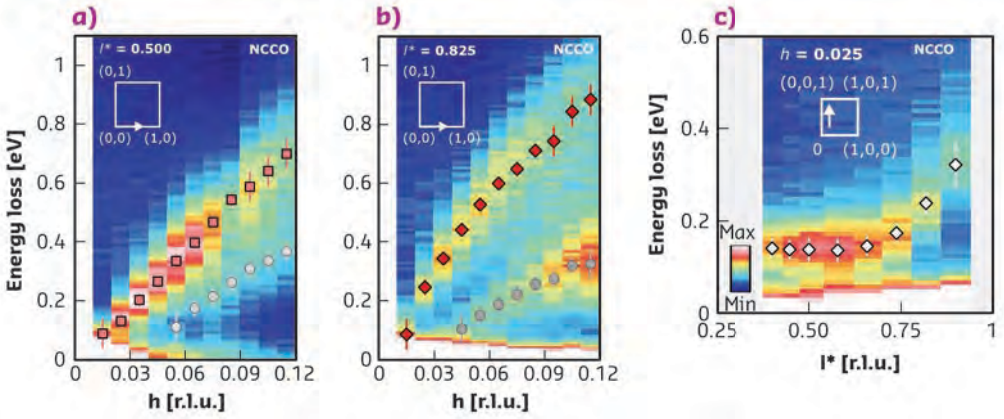


**Fig. 109: a)** and **b)** RIXS intensity maps of NCCO ($x$ = 0.15) as a function of in-plane momentum transfer along the $h$-direction at fixed out-of-plane momenta $l$* = 0.5 and $l$* = 0.825. Red and grey symbols indicate least-squares-fit peak positions of the plasmon and the paramagnon, respectively. **c)** RIXS map for momentum transfer along the out-of-plane direction at $h$ = 0.025. White symbols indicate fitted peak positions of the plasmon.

transition **[1]**. Furthermore, the investigation of acoustic plasmons could be highly relevant, as it was proposed that they contribute about 20% of the value of the high $T_c$ of copper oxides **[2]**.

The present work focused on the enigmatic 'zone-centre' mode of the electron-doped copper oxides $Nd_{2-x}Ce_xCuO_4$ (NCCO) **[3]** and $La_{2-x}Ce_xCuO_4$ (LCCO) (**Figure 108a**). Previous speculation about its origin has included intra-band transitions, collective modes of a quantum phase **[3]** and plasmons. In this work, it was possible to attribute the zone-centre mode unambiguously to the acoustic plasmon due to new information, that is, the pure charge origin of the mode (**Figure 108b**), distinct three-dimensional dispersion (**Figure 109**) and the dependence on the Ce doping concentration $x$, together with determinant quantum Monte Carlo (DQMC) calculations. On the technical side, the polarisation analyser of beamline **ID32**, revealing the mode's pure charge origin, and the continuous scanning capabilities of the RIXS spectrometer, were critical for the success of the experiment.

As an implication of the observation of three-dimensional plasmon modes, future models describing the charge dynamics of copper oxides, at the very least, should include a layered two-dimensional character. The energy of the plasmon extrapolates to zero at the projected zone centre, which indicates a negligible single electron hopping between adjacent $CuO_2$ planes, leaving the Coulomb interaction as the sole source of interplanar coupling. Such restriction of the charge to the two-dimensional planes may enhance the effects of quantum confinement at the heart of topological theories for superconductivity. Finally, using RIXS to probe plasmons opens new routes to study artificial quantum materials, such as plasmonic nanostructures, with a range of applications from sensors to photonic and electronic devices for communications.

## PRINCIPAL PUBLICATION AND AUTHORS

Three-dimensional collective charge excitations in electron-doped copper oxide superconductors, M. Hepting (a, i), L. Chaix (a, ii), E. W. Huang (a, b), R. Fumagalli (c), Y. Y. Peng (c, iii), B. Moritz (a), K. Kummer (d), N. B. Brookes (d), W. C. Lee (e), M. Hashimoto (f), T. Sarkar (g), J. F. He (a, iv), C. R. Rotundu (a), Y. S. Lee (a), R. L. Greene (g), L. Braicovich (c, d), G. Ghiringhelli (c, h), Z. X. Shen (a), T. P. Devereaux (a) and W. S. Lee (a), *Nature* **563**, 374–378 (2018); doi: 10.1038/s41586-018-0648-3.

*(a) Stanford Institute for Materials and Energy Sciences, SLAC National Accelerator Laboratory and Stanford University (USA)*
*(b) Department of Physics, Stanford University (USA)*
*(c) Dipartimento di Fisica, Politecnico di Milano (Italy)*
*(d) ESRF*
*(e) Department of Physics, Binghamton University (USA)*
*(f) Stanford Synchrotron Radiation Lightsource, SLAC (USA)*
*(g) Center for Nanophysics and Advanced Materials, University of Maryland (USA)*
*(h) CNR-SPIN, Politecnico di Milano (Italy)*
*Present addresses*
*(i) Max-Planck-Institute for Solid State Research (Germany)*
*(ii) Université Grenoble Alpes, Institut Néel (France)*
*(iii) Department of Physics, University of Illinois (USA)*
*(iv) Department of Physics, University of Science and Technology (China)*

This work is supported by the U.S. Department of Energy (DOE), Office of Science, Basic Energy Sciences, Materials Sciences and Engineering Division, under contract DE-AC02 76SF00515.

## REFERENCES

[1] A. J. Leggett, *J. Phys. Chem. Solids* **59**, 1729 (1998).
[2] V. Z. Kresin and H. Morawitz, *Phys. Rev. B* **37**, 7854 (1988).
[3] W. S. Lee *et al.*, *Nat. Phys.* **10**, 883 (2014).

# *OPERANDO* XAS OBSERVATION OF Mo TRANSFORMING TO ITS ACTIVE PHASE FOR CONVERTING METHANE TO AROMATICS

**The direct conversion of methane to aromatics is desirable because methane is cheaply available. The most studied catalyst for this reaction is a molybdenum-based catalyst where Mo atoms are dispersed in the pores of a silico-aluminate. However, the nature of the active phase is still under debate. Here, *operando* XAS at the Mo K-edge defined the active sites under relevant conditions and aided the discovery of alternative ways to produce the active site.**

Methane can be converted to benzene and naphthalene at temperatures above 600 °C. Molybdenum (Mo) supported on a zeolite is the most active catalyst to date, but it is not well understood how it is able to activate methane and why the performance of Mo is superior to other metals. The reaction is thermodynamically limited with benzene yields of 7.8–21.5 at.% between 650 and 800 °C. In addition, much improvement is still needed as the catalyst suffers from fast deactivation due to deposition of carbonaceous species.

A better understanding of the reaction pathway and structural information about the active Mo phase aides the improvement of the catalytic system. However, a fast blackening of the catalyst due to the deposition of carbonaceous deposits, means that many spectroscopic techniques, like infra-red (IR) or ultraviolet-visible (UV Vis) spectroscopy cannot be used to characterise the active site of this catalyst. A major reason why XAS spectroscopy has become a critically useful probe of the catalysts' structure is that it is element-specific, applicable to a broad range of elemental concentrations (from tens of ppm to wt.%), and can be used at reactive atmospheres and high temperature.

*Operando* characterisation of molybdenum species up to 800 °C still poses challenges for the design of an *operando* cell. The present study was performed in a plug-flow reactor developed by the Néel institute in collaboration with the King Abudullah University of Science and Technology (KAUST) **[1, 2]**. The setup makes it possible to flow, or pulse, methane to a catalyst bed heated to reaction temperature, while analysing the products on a mass-spectrometer (MS) and simultaneously measuring XAS,

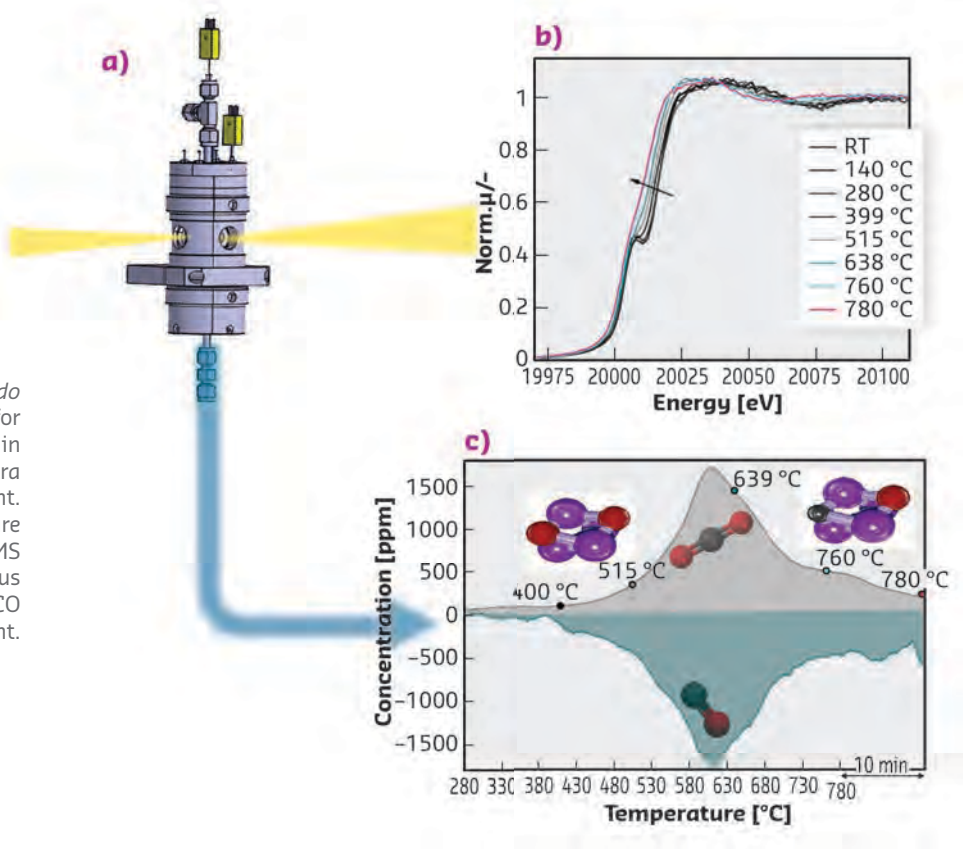


**Fig. 110: a)** Technical drawing of the *operando* reactor cell. The window openings allow for collection both in transmission as well as in fluorescence mode. **b)** *Operando* XANES spectra collected at BM16 during the CO treatment. **c)** The moments where XANES spectra are taken are indicated in the graph of the MS signal for consumption of CO and simultaneous production of $CO_2$ measured during the CO treatment.

either in transmission or fluorescence detection mode (**Figure 110**). Mo is usually found in its oxidic phase on the as-synthesised catalyst and transforms progressively to an (oxy-) carbide upon contact with methane at 700 °C. Benzene production is only observed after the transformation of Mo to its active phase is complete. During this activation, carbonaceous deposits, in the form of large immobile aromatic compounds, deposit simultaneously.

A CO treatment is proposed to produce the active phase of Mo prior to the reaction with methane. The advantage of this approach is that it can create the active site without the formation of carbonaceous deposits, which are responsible for the deactivation of the catalyst. For the as-synthesised catalyst, X-ray absorption near-edge structure (XANES) spectra recorded at **BM16** show a strong pre-edge feature at 20 008 eV attributable to a 1*s*–4*d* quadrupole/dipole transition, characteristic for distorted Mo oxide. During CO treatment, clear changes in the pre-edge peak were detected, accompanied by a total shift of the rising absorption edge by about 4.2 eV (**Figure 110**). At the same time CO consumption and $CO_2$ evolution are observed on the MS indicating the oxygen removal, while some carbon is left behind as carbidic carbon. The changes in the pre-edge feature and the rising edge during CO treatment are similar to what is observed when pulsing methane to the catalyst before benzene is formed. When methane reacts with the CO-treated sample, benzene forms with no delay, confirming that an active catalyst equivalent to the one forming under methane is produced with the CO-treatment. $^{13}C$ nuclear magnetic resonance (NMR) measurements on the samples activated in CO confirm the absence of any carbonaceous deposits other than carbidic carbon. Additional mass spectrometry studies with isotopically labeled CO and $CH_4$ have demonstrated how dynamic the carbon within the active Mo (oxy-) carbide is, since it can be transferred into the final products of the reaction.


PRINCIPAL PUBLICATION AND AUTHORS

On the dynamic nature of Mo sites for methane dehydroaromatization, I. Vollmer (a), B. van der Linden (a), S. Ould-Chikh (b), A. Aguilar-Tapia (c), I. Yarulina (a, b), E. Abou-Hamad (b), Y. G. Sneider (d), A. I. Olivos Suarez (a), J.-L. Hazemann (c), F. Kapteijn (a) and J. Gascon (a, b), *Chem. Sci.* **9**, 4801–4807 (2018); doi: 10.1039/c8sc01263f.
*(a) Delft University of Technology, Delft (The Netherlands)*
*(b) King Abdullah University of Science and Technology, Thuwal (Saudi Arabia)*
*(c) Institut Néel, Grenoble (France)*
*(d) Sapienza Università, Rome (Italy)*

REFERENCES

[1] B. AlSabban *et al., Appl. Catal. B* **213**, 177–189 (2017).
[2] A. Aguilar-Tapia *et al., Rev. Sci. Instrum.* **89**, 035109 (2018).


# METAL–HYDROGEN SYSTEMS WITH AN EXCEPTIONALLY LARGE AND TUNEABLE THERMODYNAMIC DESTABILISATION

**This work presents a new approach to tailoring the interaction of certain metals with hydrogen. Using interface strain, the ability of yttrium and gadolinium to reversibly absorb hydrogen can be significantly altered, leading to tuneable equilibrium hydrogen pressure at room temperature. This leads to novel optical hydrogen sensors with a large sensing range.**

Reversible hydrogen absorption in metals is exploited for many applications, such as hydrogen storage, hydrogen sensing, rechargeable batteries and catalysis **[1-4]**. The ability of metals to reversibly absorb hydrogen at a given temperature and pressure is governed by the thermodynamics of the metal–hydrogen interaction. For reversible hydrogen storage, metals that can absorb more than 5 wt.% hydrogen with an equilibrium hydrogen pressure of 1–10 bar at temperatures between 25 and 150 °C are required. Unfortunately, a majority of existing metal hydrides do not meet these requirements. Strategies such as alloying, nanosizing, nanoconfinement, and interfacial effects have been tested to alter the thermodynamics of metal–hydrogen systems **[5-7]**. However, none of these approaches has so far led to a controllable and large enough tuning of metal-hydrogen interaction.

This work reports that the equilibrium (de)hydrogenation pressure of some metals can be precisely tuned by the addition of insoluble

(non-alloying) dopant. Adding small amounts of zirconium to yttrium thin films leads to a large increase of the equilibrium hydrogen pressure.

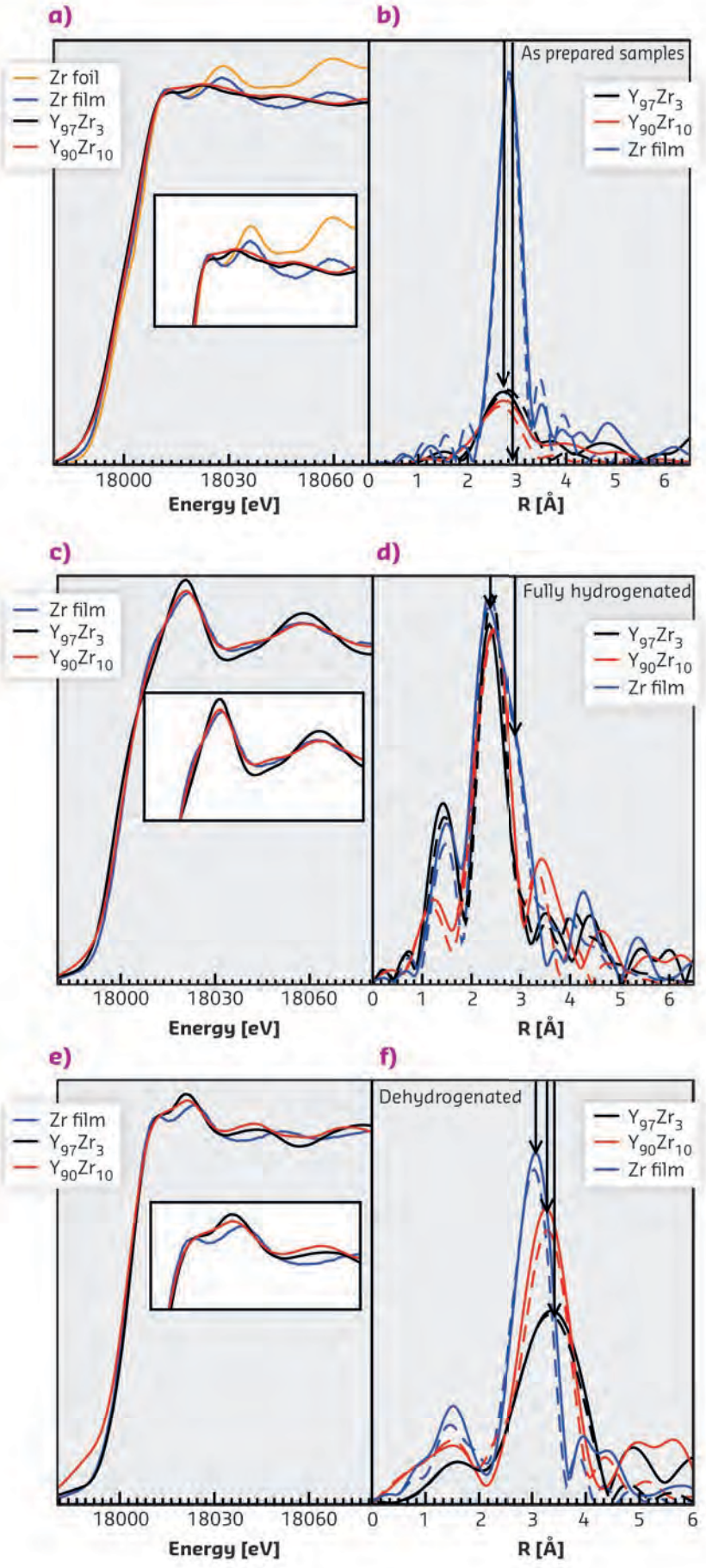


A thin layer of Pd (10-30 nm) was added to $Y_xZr_{1-x}$ thin films to catalyse hydrogen sorption in Y. A 5 nm Ti layer was deposited between the Y and Pd layers to prevent alloying of the Y and Pd (as depicted in **Figure 112**). By varying the amount of Zr in the $Y_x$ $Zr_{1-x}$ thin films from 0-13 atomic %, a continuous and well-defined increase in the equilibrium hydrogenation pressure was observed for the formation of yttrium trihydride ($YH_3$), from $10^{-1}$ to $10^4$ mbar at room temperature.

To investigate the origin of these remarkable thermodynamic effects, X-ray absorption near-edge structure (XANES) and extended X-ray absorption fine structure (EXAFS) measurements were carried out at beamline **BM26**, at the yttrium and zirconium K-edges (17 038 and 17 998 eV, respectively). The data suggest that the effect is due to lattice strain arising from the compression of the yttrium lattice by $ZrH_x$ nanoclusters (**Figure 111**). The lattice compression hinders the volume expansion needed to accommodate hydrogen in Y, leading to destabilisation of the yttrium hydride ($YH_x$) phase with respect to the metal. The lattice compression increases with an increase in the Zr content, implying that more pressure is needed to expand the Y lattice. As a result, the equilibrium hydrogen pressure of $YH_2 \leftrightarrow YH_3$ can be precisely and continuously tuned from $10^{-1}$ to $10^4$ mbar at room temperature by varying the Zr concentration from 0 to 13 at.%. The effect is maintained over several hydrogenation/dehydrogenation cycles and is accompanied by a strong optical change due to the $YH_2 \rightarrow YH_3$ metal insulator transition. At this transition, metallic face centred cubic (*fcc*) $YH_2$ transforms into the hexagonal $YH_3$ phase with a bandgap of around 2.7 eV. The ability to precisely tune the equilibrium hydrogen pressures of $YH_2 \leftrightarrow YH_3$ now allows the realisation of an optical hydrogen sensor that indicates the ambient hydrogen pressure over five orders of magnitude by an eye-visible colour change (**Figure 112**).

In summary, this work demonstrates a metal–hydrogen system with an exceptionally large and tuneable thermodynamic destabilisation induced by lattice strain. This shows that the addition of certain dopants can lead to unprecedented effects on the hydrogen sorption properties of metals, which opens new avenues for rationally tailoring the properties of metal–hydrogen systems to desired applications.

**Fig. 111:** Local structure analysis with XAS. XANES spectra of **a)** the as-deposited, **c)** fully hydrogenated, and **e)** dehydrogenated thin films. Phase uncorrected FT of the EXAFS spectra of the **b)** as-deposited, **d)** fully hydrogenated, and **f)** dehydrogenated Zr and Y–Zr thin films. The dashed lines are the fits of the EXAFS data, and the arrows are guides.

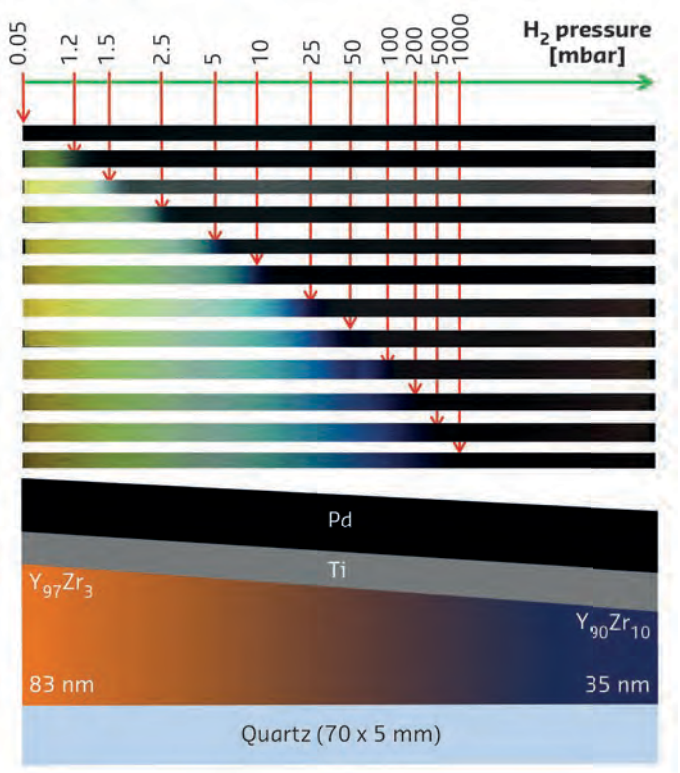


**Fig. 112:** The top image shows the visible colour changes associated with the formation of $YH_3$ in the thin film upon exposure to hydrogen, while the bottom shows the configuration of the sensor (70 × 5 mm $Y_{97}Zr_3$–$Y_{90}Zr_{10}$ gradient thin film). The pictures represent consecutive stages in time of the thin film hydrogenation at different $H_2$ pressures. The positions of the colour front (indicated by the arrows) clearly depend on the hydrogen pressure and Zr concentration.

## PRINCIPAL PUBLICATION AND AUTHORS

Metal–hydrogen systems with an exceptionally large and tunable thermodynamic destabilization, P. Ngene (a), A. Longo (b, c), L. Mooij (d), W. Bras (c) and B. Dam (d), *Nat. Commun.* **8**, 1846 (2017);
doi: 10.1038/s41467-017-02043-9.
*(a) Inorganic Chemistry and Catalysis, Debye Institute for Nanomaterials Science, Utrecht University (The Netherlands)*
*(b) Istituto per lo Studio dei Materiali Nanostrutturati ISMN-CNR, Palermo (Italy)*
*(c) ESRF*
*(d) Materials for Energy Conversion and Storage (MECS), Department of Chemical Engineering, Delft University of Technology (The Netherlands)*

## REFERENCES

[1] R. Mohtadi and S.-i. Orimo, *Nat. Rev. Mater*. **2**, 16091 (2016).
[2] R. Mohtadi *et al., J. Phys. Condens. Matter* **28**, 353001 (2016).
[3] M. B. Ley *et al., Mater. Today* **17**, 122–128 (2014).
[4] K. Møller *et al., Energies* **10**, 1645 (2017).
[5] A. Schneemann *et al., Chem. Rev.* (2018).
[6] J. Yang *et al., Chem. Soc. Rev* **39**, 656–675 (2010).
[7] P. E. de Jongh and P. Adelhelm, *ChemSusChem* **3**, 1332–1348 (2010).

# STRUCTURE OF MATERIALS

This year was notably dedicated to user service, and as many user experiments as possible were accommodated before the shutdown for the Extremely Brilliant Source (EBS) upgrade. Most of the Structure of Materials (SOM) beamlines were reviewed during 2018 with very positive feedback from the review panels.

On **ID06**, we spent most of 2018 developing a better understanding of the new experimental capabilities of the hard X-ray microscope. As a result, a series of technical papers has been published. The findings were put to good use during commissioning experiments with close collaborators, exploring data acquisition strategies in diverse fields ranging from classical metallurgy to functional materials and biominerals. With this, the foundations for user operation of the dark-field microscope and the design of EBSL2 are firmly in place. The team is looking forward to opening the dark-field X-ray microscope to external users.

Beamline **ID11** hosts many experimental techniques, from microstructure imaging to the solution and refinement of atomic crystal structures. High-energy X-ray beams and fast 2D detectors have been a common theme this year. *In-situ* pair distribution function (PDF) analysis by Albéric *et al.* (**page 118**) could show that ion impurities control the crystallisation of amorphous calcium carbonate. Work on Ti-alloys by Bönisch *et al.* (**page 135**) highlights the role of synchrotron radiation in uncovering giant thermal expansion and a series of phase transitions in Ti-alloys during an *in-situ* study. Thanks to ID11 technical staff, the white beam attenuator system was upgraded in order to improve the beam coherence properties ready for EBS.

Operational since November 2016, **ID15A** is optimised for the rapid acquisition of multidimensional data on working chemical reactors, novel batteries and other systems of interest to the chemical and energy sectors. New experimental methods have been developed (five-dimensional imaging by X-ray diffraction, XRD) or extended for the first time into the very high-energy domain (stroboscopic XRD and SAXS-WAXS tensor tomography). As a result of the accompanying improvements in data acquisition, reduction and post-treatment, methods that were previously the domain of only limited and expert user communities and required substantial time investment are now routinely available for non-expert users. ID15A has also been optimised to carry out total scattering studies. The availability of advanced software and improved experimental capabilities, in addition to the extended measurement range in reciprocal space, make ID15A particularly effective for such studies.

The EBS beamline project EBSL3 at **BM18** is progressing well. BM18 is a high-throughput, large-field, phase-contrast tomography beamline with exceptional properties in terms of coherence, beam size, energy range, and foreseen automation levels, for applications from industry and palaeontology to biology and cultural heritage. The optics hutch infrastructure is now completed and the first radiation test was done just before the shutdown. The construction of the tunnel and the building that will host a 42-m-long white beam experimental hutch will start in 2019. The X-ray optics and beam tuning system will be installed during the shutdown. The first beam in the experimental hutch is expected in autumn 2020, followed by installation of the large sample stage and detector robots, and development of the automated control system. The first user experiments are anticipated in 2021.

Microtomography beamline **ID19** welcomes a special new team member this year: a sample changer robot compatible with the high-resolution as well as medium-resolution tomographic setups of the beamline. Self-learning procedures as well as pre-alignment using visible light imaging are under development. For time-resolved studies including shock, the development of a gas gun in the frame of LTP MI-1252 is almost finished: first shots have been carried out by non-experts and the installation of the final system is expected during the long shutdown. In addition to the selected articles, one should note the paper by Olbinado *et al.* **[1]** about the first time-resolved X-ray imaging of laser-induced compression waves as well as the paper by Liotti *et al.* **[2]** about time-resolved radiography in metallic alloys analysed with the help of machine learning algorithms.

At the high-resolution powder-diffraction beamline, **ID22**, improvements include a new spinner/oscillator to support the gas-adsorption capillary cell. The gas rig was much in demand throughout the year with several experiments following structural changes accompanying sorption and desorption of gasses into porous materials, especially metal–organic frameworks or zeolites. The production of a series of 3D-printed capillary holders should significantly reduce the time required to prepare samples for the high-speed sample spinner and sample-changing robot. The new holders have a built-in grip, removing the need to stick the capillaries into their holders. With thoughts for the performance of the beamline after the EBS upgrade, tests were also conducted with a high-energy pixel detector, kindly lent by Dectris. When used in conjunction with the analyser crystals, replacing the current nine scintillation counters, there are significant improvements in data quality, both in terms of resolution and counting statistics. We anticipate introducing this new configuration for user operation in 2020.

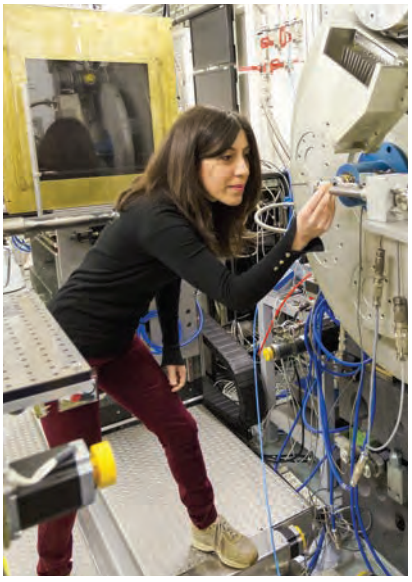

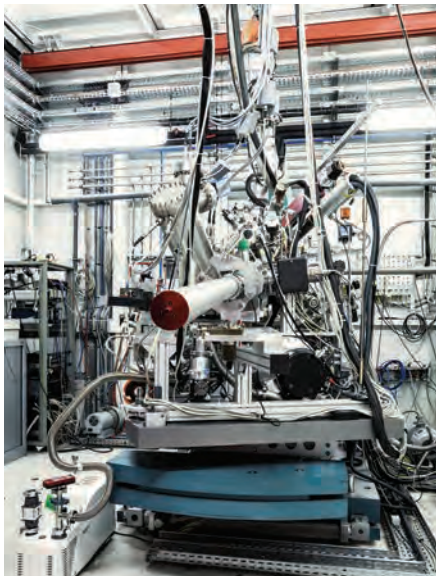

The high-energy beamline for buried interface structures and materials processing, **ID31**, has finished its third year of operation. The capabilities for electrochemical experiments have been greatly improved and a set of different cells and associated supporting equipment has been developed, including a new type of GID cell for *in-situ* characterisation of complex catalytic electrochemical systems in aqueous environments. Thanks to improved measurement geometry and the tightly focused high-energy X-ray beam with low divergences, the signal–to–noise ratio has improved 2000-fold, enabling electrochemical measurements on nanoparticles with millisecond time resolution. Furthermore, side by side experiments are now possible for better use of the beamline. In several experiments, users have operated the fuel cell test station in addition to their own sample setup, greatly enhancing the scientific output of a single experimental run.

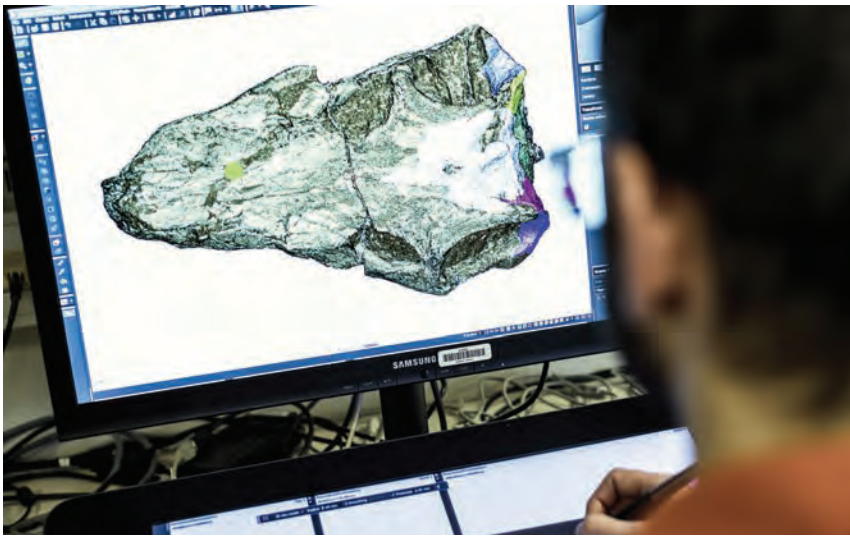


**V. HONKIMÄKI**

[1] Olbinado *et al.*, Ultra high-speed X-ray imaging of laser-driven shock compression using synchrotron light, *J. Phys. D: Appl. Phys.* **51**, 055601 (2018).
[2] Liotti *et al.*, Crystal nucleation in metallic alloys using X-ray radiography and machine learning, *Sci. Adv.* **4**, eaar4004 (2018).

# *IN-SITU* PDF ANALYSIS OF AMORPHOUS CALCIUM CARBONATE CRYSTALLISATION AND THE EFFECT OF WATER AND ION IMPURITIES ON ITS STRUCTURE AND STABILITY

**The stabilisation mechanisms of synthetic amorphous calcium carbonate (ACC) by water and inorganic ions were studied using *in-situ* calorimetric and scattering techniques. Inorganic additives affect the short-range structural rearrangement during dehydration of ACC. They control the molecular interactions of water within the mineral, thereby determining its kinetic stability but, surprisingly, have no effect on its thermodynamic stability.**

Amorphous calcium carbonate (ACC) is employed by many organisms across various phyla as a precursor phase in the crystallisation of biogenic calcium carbonate minerals. It is commonly deposited as a hydrated phase, in the presence of inorganic ions and organic molecules, and successively transforms to a crystalline polymorph, leading to biominerals with superior properties and fascinating shapes **[1, 2]**. This common biological strategy has inspired the development of new synthetic routes for controlling the morphology, the phase and the physical properties of various materials **[3]**. The key to the transformation of ACC lies in its (meta)stability. Under ambient conditions ACC is unstable but by adjusting the level of inorganic and organic additives and/or of water, its longevity can be tuned **[1]**. However, the way these compositional changes affect ACC stability and transformation mechanisms was unknown until recently, mostly because the energetic landscape of the crystallisation is experimentally difficult to probe, and, owing to the intrinsic elusive (lack of long-range) structure of amorphous materials **[4–6]**. In this contribution, novel *in-situ* techniques were developed to

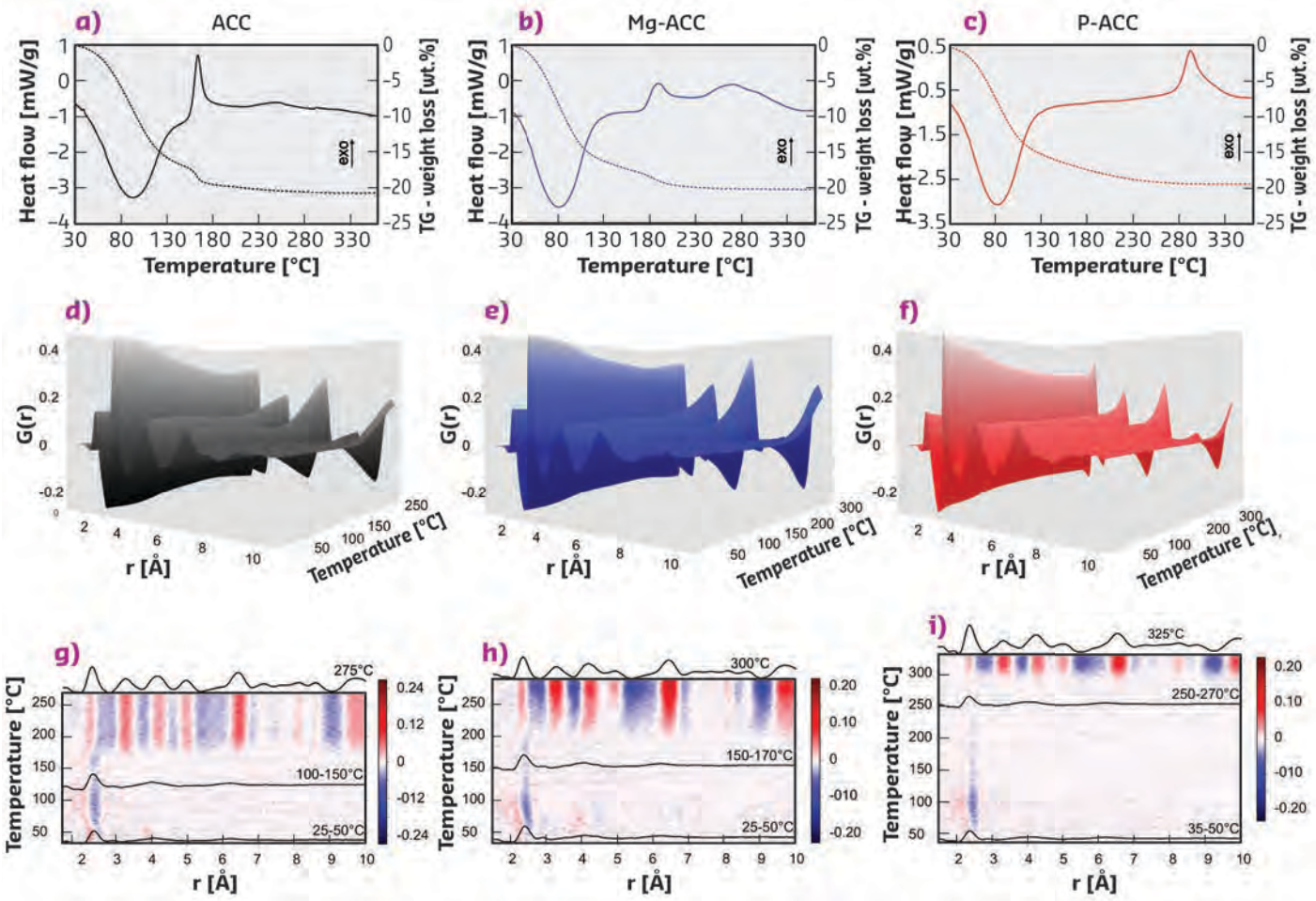


**Fig. 113: *a–c)*** Thermogravimetric and differential scanning calorimetry analyses, ***d–f)*** pair distribution function (PDF) from *in-situ* heating XRD measurements and ***g–i)*** differential dPDF/dT maps of respectively ACC, Mg-ACC, and P-ACC. Averaged PDFs at selected temperatures are superimposed on the maps (black curves).

study the effect of water, $Mg^{2+}$ and $PO_4^{3-}$ ions (commonly found in biology) on the dynamics of the structure of ACC during crystallisation and on the energetics of the phase transformation.

*In-situ* total X-ray scattering measured at **ID11** and acquired during the induced crystallisation of ACC, either by heating (**Figure 113**) or by humidity, allows the observation of small structural modifications by pair distribution function (PDF) analysis. The initial short- and medium-range orders of all studied ACC samples are similar; however, the use of *in-situ* methodologies shows that the magnitude and the extension of the local structure evolution during dehydration largely depends on the nature of additives (**Figure 113**). This suggests that interactions of ions with water are likely to play a role in ACC stability.

To determine whether the effect of the additives on ACC stability is thermodynamic (*i.e.*, due to changes in energy states of ACC) or kinetic (*i.e.*, due to mobility of the species), isothermal calorimetric coupled with microgravimetric analyses were performed. The rate of the transformation is critically dependent on the water content as well as on the presence and concentration of inorganic additives in ACC (**Figures 114a, b**). The higher the amount of structural water, the higher the ion mobility, resulting in fast crystallisation and low kinetic stability. Conversely, strong interactions between water and the ions, and incompatibilities of the additives within the final crystal polymorph, increase the kinetic stability of ACC. Surprisingly, the overall ACC thermodynamic stability (sum of binding energy and entropic terms) is independent of the hydration level (**Figure 114c**).

By controlling the water and ion concentrations, the longevity of the material can be tuned, as these factors govern the kinetics of ACC crystallisation. This seminal result entails a rethinking of the crystal growth mechanisms in organisms that involve calcium carbonate amorphous precursors, a widespread strategy in biomineralisation **[1]**.

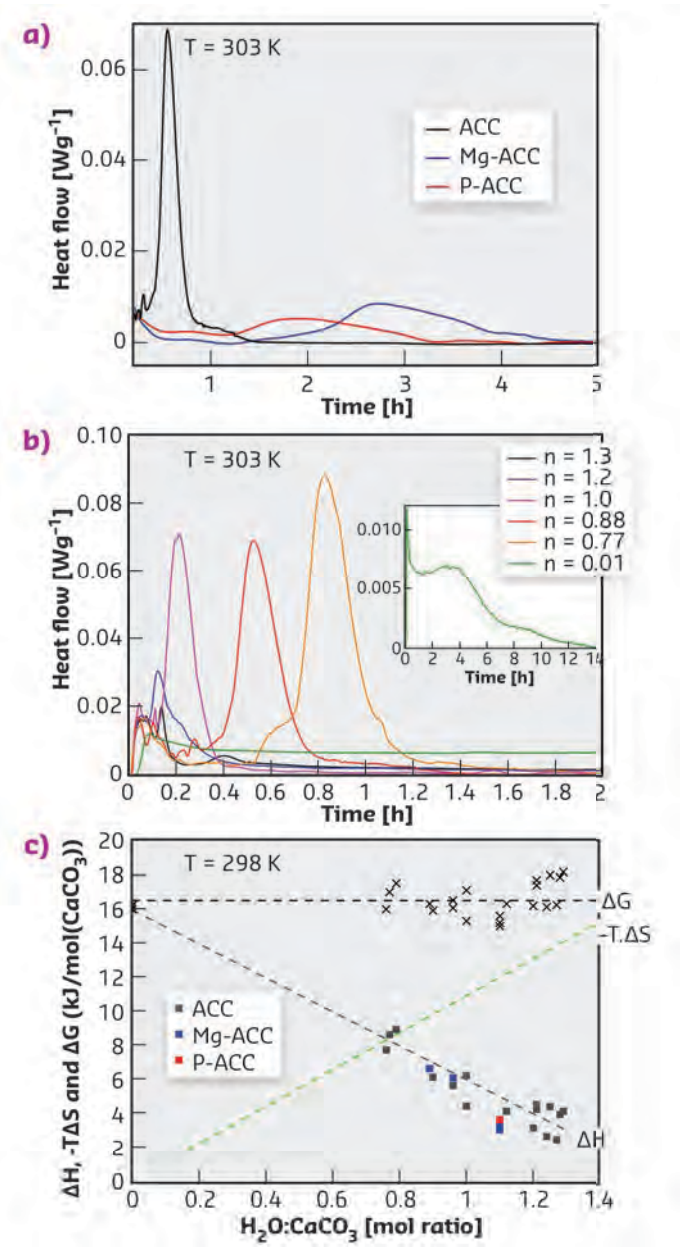


**Fig. 114:** Isothermal calorimetry measurements showing heat flow evolution during crystallisation induced by humidity (at 30 °C, *i.e.*, 303.15 K) of **a)** ACC, Mg-ACC and P-ACC with similar water content and **b)** differently hydrated ACC·$n$$H_2O$ samples without additives. **c)** The enthalpy of ACC relative to calcite ($\Delta H$) for ACC, Mg-ACC and P-ACC, $-T\cdot\Delta S$, $\Delta S$: molar entropy difference to calcite ($-T\cdot d\Delta S/dnH_2O$ = 10.9 kJ mol$^{-1}$ for $T$ = 298K **[7]**) and the molar free energy ($\Delta G = \Delta H - T\cdot\Delta S$) of ACC with different hydration levels with respect to calcite, with $T$ = 25 °C, *i.e.*, 298 K.

## PRINCIPAL PUBLICATION AND AUTHORS

The Crystallization of Amorphous Calcium Carbonate is Kinetically Governed by Ion Impurities and Water, M. Albéric (a), L. Bertinetti (a), Z. Zou (a), P. Fratzl (a), W. Habraken (a) and Y. Politi (a), *Adv. Sci.* **5**, 1701000 (2018); doi: 10.1002/advs.201701000.
*(a) Max-Planck Institute of Colloids and Interfaces, Potsdam-Golm (Germany)*

## REFERENCES

[1] L. Addadi *et al., Adv. Mater.* **15**, 959–970 (2003).
[2] Y. Politi *et al., Proc. Natl. Acad. Sci.* **105**, 17362–17366 (2008).
[3] Y. Politi and J. C. Weaver, *Science* **347**, 712–713 (2015).
[4] A. V. Radha *et al., Proc. Natl. Acad. Sci.* **107**, 16438–16443 (2010).
[5] Y. Levi-Kalisman *et al., Adv. Funct. Mater.* **12**, 43–48 (2002).
[6] F. M. Michel *et al., Chem. Mater.* **20**, 4720–4758 (2008).
[7] P. Raiteri and J. D. Gale, J. *Am. Chem. Soc.* **132**, 17623–17634 (2010).

# CREATING ULTRASTABLE METALLIC GLASSES ON COLD SUBSTRATES

**Ultrastable metallic glasses (UMGs) produced by physical vapour deposition possess extraordinary kinetic stability and mechanical properties. There is a well-accepted rule that ultrastability requires the use of high substrate temperatures close to the glass transition temperature, $T_g$. This rule has been challenged by demonstrating the possibility of producing ultrastable UMGs at room temperature (*i.e.* substrate temperature of only $0.43T_g$).**

Stability is a key parameter that controls the properties of glasses and their technological applications. The recent successful creation of organic **[1]**, polymeric **[2]** and even metallic **[3]** ultrastable glasses from physical vapour deposition has revolutionised the field of glasses and demonstrated a new route to obtain glassy materials with outstanding kinetic stability and mechanical properties.

Following a trial and error approach, an empirical recipe for producing ultrastable glasses has been proposed, based on deposition on substrates kept at temperatures close to the glass transition temperature, $T_g$. The physical idea behind this is that the hot substrate enhances the surface mobility, creating the kinetic and thermodynamic basis for the formation of stable glasses. In the case of metallic glasses (MGs), however, this requirement is incompatible with many technological applications. This work challenges this empirical rule by showing the formation of Zr-based UMGs at room temperature (*i.e.*, with a substrate temperature of only $0.43T_g$). The substantial enhancement in glass stability is achieved by lowering the deposition rate to ~1 nm min$^{-1}$. The slow rate of deposition gives the atoms enough time to rearrange on the surface and explore more stable configurations before being influenced by the presence of upcoming atoms.

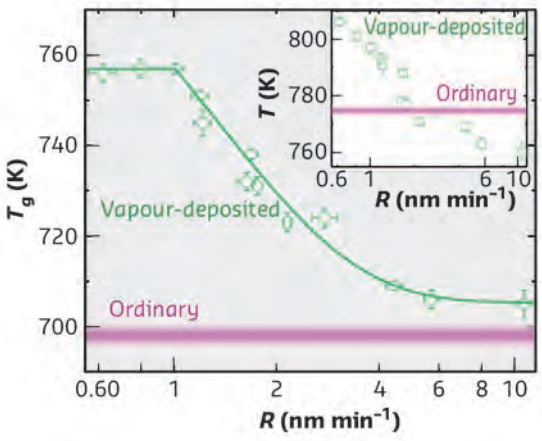


**Fig. 115:** Effect of deposition rate $R$ on the glass transition temperature $T_g$ and crystallisation temperature $T_x$ (the inset) for $Zr_{46}Cu_{46}Al_8$ MGs. The solid line at high $R$ is an exponential fit to the data; at low $R$ the $T_g$ keeps invariant. The error bars indicate the standard deviation of three to five measurements. The $T_g$ and $T_x$ with their variation ranges for the ordinary glass are presented by the shaded magenta areas for comparison.

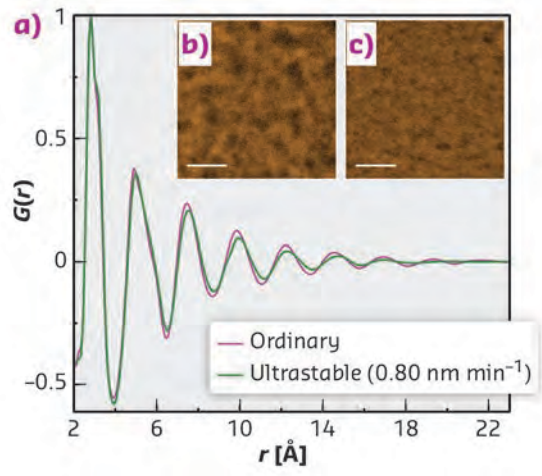


**Fig. 116:** Structure characterisation for the ordinary and the 0.80 nm min$^{-1}$ deposited ultrastable MGs. **a)** Pair distribution function $G(r)$. **b-c)** HADDF-STEM images of **(b)** the ordinary and **(c)** the ultrastable MGs. The scale bars are 5 nm.

A prototypical alloy of composition $Zr_{46}Cu_{46}Al_8$ was used to produce two types of samples; 20-µm-thick standard quenched MGs by the melt-spinning technique, and various µm-thick MGs produced by room temperature physical vapour deposition with different deposition rates, $R$. The two types of samples were studied by differential scanning calorimetry (DSC), *ex-situ* X-ray scattering, transmission electron microscopy and high-energy pair distribution function (PDF) analysis.

**Figure 115** summarises the results of the DSC measurements by showing the semi-log plot of $T_g$ vs. deposition rate $R$ for the vapour-deposited glasses, together with the $T_g$ of the ordinary glass produced by melt-spinning technique (shaded magenta area). Upon decreasing the deposition rate, $T_g$ increases exponentially, thus improving the ultrastability of the material, and reaches a maximum value of 757 K as $R \approx 1$ nm min$^{-1}$, which is 59 K higher than that of the ordinary glass. Interestingly, the onset temperature of crystallisation, $T_x$, also increases by lowering the deposition rate (inset in **Figure 115**) and suggests the higher stability against crystallisation of the ultrastable glasses.

With respect to ordinary glass, the ultrastable glass shows a distinct structure. **Figure 116a** presents the PDFs, $G(r)$, of the ordinary and the 0.80 nm min$^{-1}$ deposited ultrastable MGs measured by high-energy X-ray diffraction (XRD) at beamline **ID15A**. The $G(r)$ of the ordinary glass presents well-defined oscillations up to the eighth neighbouring shell, while the ultrastable glass

exhibits an ordered structure only up to the sixth shell. This means that the ordinary glass is more ordered at longer distances, and is characterised by more packed shells, as suggested by the shifts of the $G(r)$ peaks toward shorter distances. Additional structural characterisations with high-angle annular dark-field scanning transmission electron microscopy (HADDF-STEM) confirms the more homogeneous structure of the UMG (**Figure 116c**).

The production of UMGs with an increased $T_g$ up to ~60 K, a more homogeneous structure and a stronger resistance to crystallisation suggests that the relaxation dynamics at the surface of the glass could be much faster than expected, despite the low-temperature substrate. These results call for a reconsideration of the prerequisites for ultrastability of glasses.


PRINCIPAL PUBLICATION AND AUTHORS

Ultrastable metallic glasses formed on cold substrates, P. Luo (a, b), C. R. Cao (a, b), F. Zhu (c), Y. M. Lv (a, b), Y. H. Liu (a, b), P. Wen (a), H. Y. Bai (a, b), G. Vaughan (d), M. Di Michiel (d), B. Ruta (d, e) and W. H. Wang (a, b), *Nat. Commun.* **9**, 1389 (2018); doi: 10.1038/s41467-018-03656-4.

*(a) Institute of Physics, Chinese Academy of Sciences, Beijing (China)*
*(b) University of Chinese Academy of Sciences, Beijing (China)*
*(c) State Key Laboratory of Metal Matrix Composites, School of Materials Science and Engineering, Shanghai Jiao Tong University (China)*
*(d) ESRF*
*(e) Institut Lumière Matière, UMR5306 CNRS, Université Claude Bernard Lyon 1, Villeurbanne (France)*

REFERENCES

[1] S. F. Swallen *et al.*, *Science* **315**, 353–356 (2007).
[2] Y. Guo *et al.*, *Nat. Mater.* **11**, 337–343 (2012).
[3] H. B. Yu *et al.*, *Adv. Mater.* **25**, 5904–5908 (2013).


# MIXING INSTABILITIES DURING SHEARING IN METALS

**The dynamics of deformation during shearing in metallic multilayers have been captured using 3D X-ray synchrotron tomography. The observations include the formation of folds and vortices and delamination of layers. Numerical simulations show that metals behave as very viscous fluids. The process is similar to rock folding in geology.**

We tend to think of common metals as rigid solids. This perspective is challenged here as new evidence shows that metals behave as very viscous fluids when subjected to shear deformation, even at room temperature.

Interestingly, geologists have already shown that many large-scale geodynamical deformations taking place within the Earth over millions of years follow fluidic behaviour, for example, in phenomena such as rock folding and mountain building. Here, it is demonstrated that such behaviour is not restricted to large dimensions and durations. In fact, even during short-period deformations and at the micrometre scale, metals behave similarly.

These findings were made possible by a novel experimental strategy that enabled the morphological evolution within deforming solids to be captured in three dimensions for the first time. For this purpose, multilayers of copper-silver and copper-aluminium, representing a multiphase alloy, were created by alternately stacking individual 25-µm-thick foils of each material. Next, the multilayers were shear deformed using the high-pressure torsion (HPT) method, whereby the sample is squeezed between two anvils while one anvil is rotating, resulting in the formation of a disk-like sample. During high-pressure torsion, each radial cross-section (*i.e.*, plane with radius as its normal) is sheared to a slightly different extent due to the existence of a strain gradient along the radius of the disk. This causes a gradual evolution of morphology in the multilayer from its original phase-separated state to a relatively mixed-phase state in the resulting sample disk. The interfacial and morphological evolution undergone by the stack can then be discovered by looking at successive cross-sections at different radii, corresponding to different levels of strain, using 3D X-ray synchrotron tomography at beamline **ID19**. This technique revealed a host of morphological events including delamination of the layers, formation of folds and rotating vortices in the multilayers (**Figure 117**), which were not considered in previous atomic-scale mixing studies (*e.g.*, **[1]**).

These new observations resembled many similarities to morphologies found in rocks. Hence, a computer model originally designed for mountain building processes was adapted to simulate the experimental conditions.

The model identified the viscosity contrast (VC) and the stress exponent of the phases ($n$), as well as the strain rate ($\dot{\gamma}$), as the key factors driving the microstructural evolution. **Figure 118** shows the results of a simulation for a particular combination of (VC, $n$). In short, the results

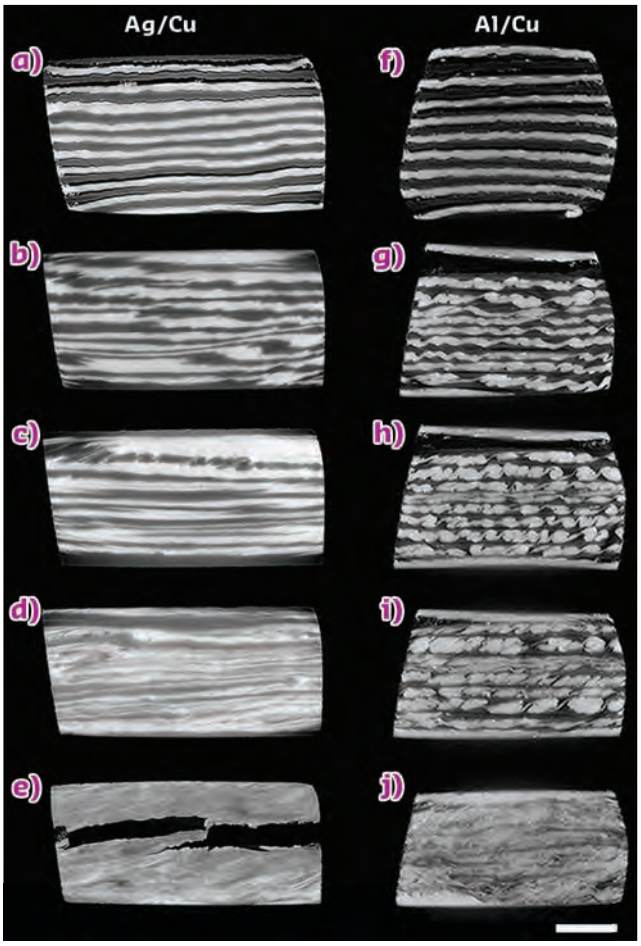


**Fig. 117:** Morphological evolution of multilayers upon shearing acquired by 3D X-ray synchrotron tomography. **a-e)** Selected snapshots of an Ag/Cu-multilayer that has been shear-deformed to a maximum strain of 393. The brighter phases are Ag. Here, the Cu layers predominantly delaminate before mixing takes place at the micrometre scale. **f-j)** Selected snapshots of an Al/Cu-multilayer, shear-deformed to a maximum strain of 236. The brighter phases are Cu. Here, the Cu layers initially fold in a quasi-regular manner and subsequently evolve into periodic vortices, before mixing takes place at the micrometre scale. In both sequences, the overall strain increases when going from the top to the bottom of each panel. The scale bar is 200 µm. The dark area within **(e)** is a crack that appeared after HPT deformation and during the cutting of the disk for tomography examination.

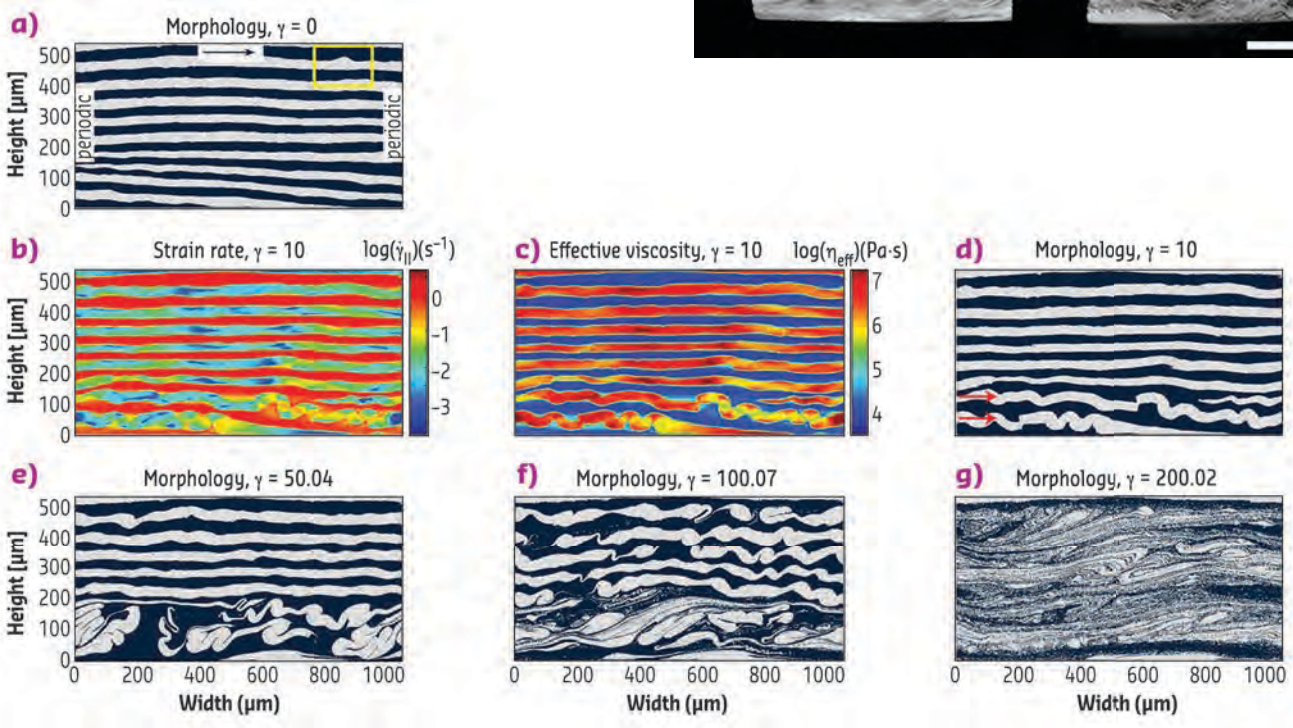


**Fig. 118:** Finite element simulation of shear deformation in a multilayer system. **a)** The computational cell showing the initial arrangement of the layers and the direction of shear at the top. Black (lower characteristic viscosity) and white (higher characteristic viscosity) layers denote the two different phases in each experiment, and the model domain is comparable in size to that of the samples used in 3D X-ray synchrotron tomography experiments. **b-g)** Simulation results for (VC = 10, $n$ = 3). **b-d)** Local strain rate ($\dot{\gamma}_{II}$), effective viscosity ($\eta_{eff}$), and morphology maps at shear strain $\gamma$ = 10, respectively. The arrows in **d)** point to two folding layers. **e-g)** Evolution of morphology with the increase of shear strain ($\gamma$) as indicated.

indicate that the same instability that causes kilometre-thick rock layers to fold on geological timescales is acting here at micrometre level.

The findings reveal the origin for a wealth of morphologies in deforming solids. While the experiments were performed on multilayers under shear, the model is not limited to samples of this type and could be applied to any material system regardless of its morphology. This makes the model a versatile tool to study a broad range of materials and material processing techniques.

PRINCIPAL PUBLICATION AND AUTHORS

Mixing instabilities during shearing of metals, M. Pouryazdan (a), B.J. Kaus (b), A. Rack (c), A. Ershov (d, e) and H. Hahn (a, f), *Nat. Commun.* **8**, 1611 (2017); doi: 10.1038/s41467-017-01879-5.
*(a) Institute of Nanotechnology, Karlsruhe Institute of Technology (Germany)*
*(b) Institute of Geosciences and Center for Computational Sciences, University of Mainz (Germany)*
*(c) ESRF*
*(d) Institute for Photon Science and Synchrotron Radiation, Karlsruhe Institute of Technology (Germany)*
*(e) Laboratory for Applications of Synchrotron Radiation, Karlsruhe Institute of Technology (Germany)*
*(f) Joint Research Laboratory Nanomaterials at Technische Universität Darmstadt (Germany)*

REFERENCES

[1] M. Pouryazdan *et al., Phys. Rev. B* **86**, 144302 (2012).

# A NEW STRUCTURAL DESCRIPTOR REVEALS THE OPERATION MODE OF NANOCATALYSTS

**The question of the role played by structural disorder in electrocatalysis has been intensively debated for years. A novel and original descriptor, surface distortion, provides the first experimental proof that both 'structurally ordered' and 'structurally disordered' catalysts can reach high activity for the oxygen reduction reaction, but through different approaches.**

The electrochemical activation of oxygen is the cornerstone of electrochemical conversion and storage devices, such as fuel cells, metal-air batteries, and electrolysers. Platinum (Pt) is known to be the only metal that efficiently and sustainably catalyses the oxygen reduction reaction (ORR) in acidic electrolyte, the reaction that limits the performance of low temperature proton-exchange membrane fuel cells (PEMFCs). Studies on Pt and PtNi single crystals have established that the ORR is best electrocatalysed on alloys and at (111) facets, leading to ORR enhancement on PtNi/C nanooctahedra relative to Pt/C nanoparticles **[1]**. However, due to the highly oxidising conditions of the PEMFC cathode (high electrochemical potential, presence of oxygen, acidic pH), the stability of this catalyst is poor in operating conditions, thus compromising its utilisation in real devices.

It has been found that structurally disordered PtNi nanocatalysts, such as hollow PtNi/C nanoparticles, porous PtNi/C nanoparticles, PtNi aerogels or PtNi nanowires, feature superior ORR activity relative to pure Pt/C. It has also been shown that ORR kinetics increase with the concentration of structural defects. Structural disorder is quantified with the values of microstrain, using the Rietveld refinement of wide-angle X-ray scattering (WAXS) patterns **[2, 3]**.

To reconcile these seemingly opposed approaches (targeting structural order vs. introducing structural disorder to better catalyse the ORR), a library of PtNi nanoalloys with distinct atomic composition, size, shape and degree of structural disorder was synthetised (**Figure 119a-h**), with their microstrain values determined at **ID31** (**Figure 119i**). Interestingly, microstrain was detected in all electrocatalysts (including the structurally ordered ones), except for pure monocrystalline Pt nanoparticles. However, thanks to *ab initio* calculations, the contributions of bulk and surface structural disorder were disentangled and a new parameter, the surface distortion (SD), was established.

In light of the SD descriptor, it appears that both structurally ordered (SD = 0) and structurally disordered materials (SD > 0) can reach high ORR activity (**Figure 120a**). However, as **Figure 120b** shows, such desirable ORR activity is achieved using different means. The structurally ordered catalysts feature homogeneously strained lattice parameters with desirable binding energy to the ORR intermediates. Any variation in structure is detrimental to their electrocatalytic activity.

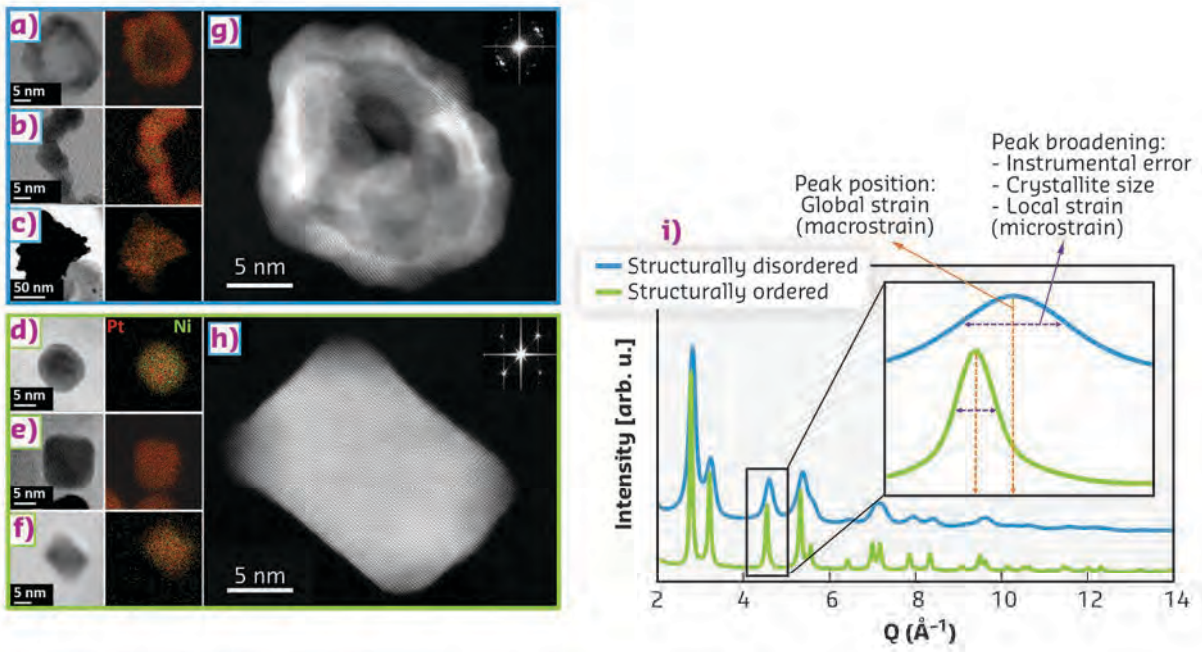


**Fig. 119:** Scanning transmission electron microscopy (STEM) images and X-ray energy dispersive spectroscopy (STEM/X-EDS) elemental maps of **a)** hollow PtNi/C, **b)** aerogel PtNi, **c)** sponge PtNi/C, **d)** sphere PtNi/C, **e)** cube PtNi/C and **f)** octahedron PtNi/C nanocatalysts. High-angle annular dark-field high resolution scanning electron microscopy (HAADF-HRSTEM) image with insertion of its associated fast Fourier transform pattern of **g)** hollow PtNi/C and **h)** cube Pt/C. The HAADF-HRSTEM images highlight the monocrystalline nature of the structurally ordered catalyst family (sphere PtNi/C, cube PtNi/C and octahedron PtNi/C), whereas the structurally disordered family (hollow PtNi/C, aerogel PtNi and sponge PtNi/C) features highly polycrystalline nanoparticles. **i)** Typical experimental WAXS powder diffraction patterns measured on structurally disordered and structurally ordered catalysts (here, hollow PtNi/C and cube Pt/C, respectively).

In contrast, the structurally disordered catalysts owe their high activity to their high degree of surface defectiveness. A multiplicity of catalytic site configurations co-exist on the surface of these catalysts, and those with closest-to-optimal binding to the ORR intermediates dominate the global ORR rate. Put simply, structurally ordered catalysts operate as a 'high-precision gun' and structurally disordered catalysts as a 'scattergun'.

Moreover, as shown in **Figure 120a**, the SD descriptor is capable of capturing the structural changes of bimetallic nanocatalysts during chemical or electrochemical ageing. The results show that the surface of structurally ordered catalysts buckles under the operating conditions of a PEMFC cathode, *i.e.*, leads to the appearance of an atomically rough surface, surprisingly close to that of the structurally disordered catalysts. In other words, these two families of catalysts are finally not so dissimilar in PEMFC cathode operating conditions.

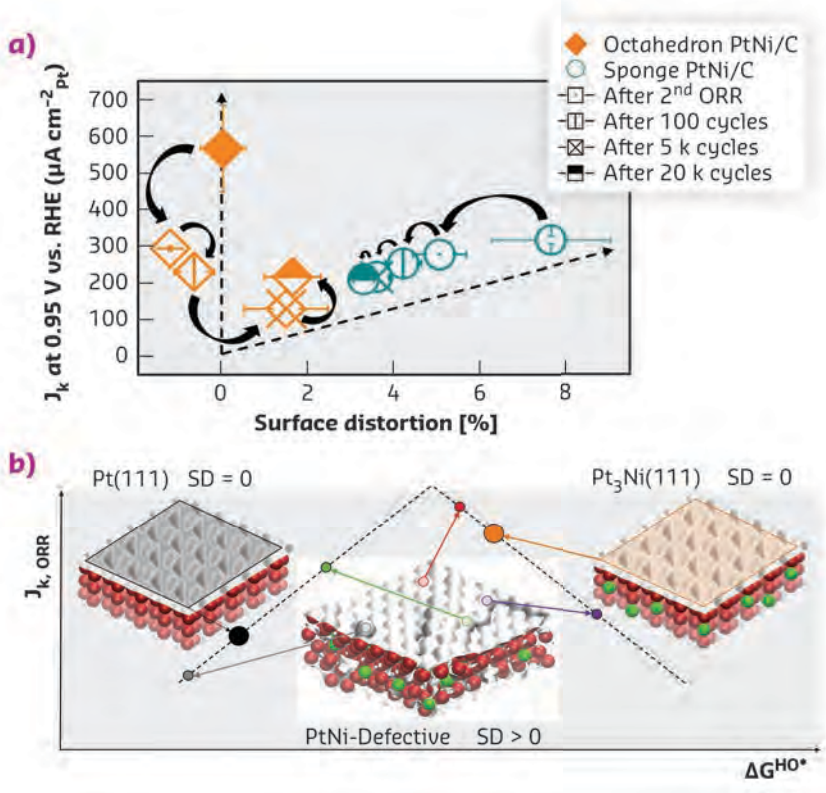


**Fig. 120: a)** Impact of electrochemical ageing (potential cycling in 0.1 M $HClO_4$ between 0.6 and 1.0 V vs. RHE at $T$ = 80 °C) on octahedron and sponge PtNi/C on ORR activity in light of the SD descriptor. **b)** DFT-derived schematic describing different approaches towards enhanced ORR kinetics: the 'scattergun' approach (SD > 0) vs. the 'high-precision gun' approach (SD = 0) for structurally disordered and structurally ordered catalysts, respectively.

PRINCIPAL PUBLICATION AND AUTHORS

Surface distortion as a unifying concept and descriptor in oxygen reduction reaction electrocatalysis, R. Chattot (a, b), O. Le Bacq (c), V. Beermann (d), S. Kühl (d), J. Herranz (e), S. Henning (e), L. Kühn (f), T. Asset (a), L. Guétaz (g), G. Renou (c), J. Drnec (b), P. Bordet (i), A. Pasturel (c), A. Eychmüller (f), T.J. Schmidt (e, j), P. Strasser (d), L. Dubau (a) and F. Maillard (a), *Nat. Mater.* **17**, 827–833 (2018); doi: 10.1038/s41563-018-0133-2.

*(a) LEPMI, Université Grenoble Alpes, Grenoble (France)*
*(b) ESRF*
*(c) Université Grenoble Alpes, CNRS, Grenoble INP, SIMAP (France)*
*(d) Electrochemical Energy, Catalysis and Material Science Laboratory, Department of Chemistry, Technische Universität Berlin (Germany)*
*(e) Electrochemistry Laboratory, Paul Scherrer Institut, Villigen (Switzerland)*
*(f) Physical Chemistry, Technische Universität Dresden (Germany*
*(g) Université Grenoble Alpes, CEA, Liten, Grenoble (France)*
*(i) CNRS, Institut Néel, Grenoble (France)*
*(j) Laboratory of Physical Chemistry, ETH Zurich (Switzerland)*

REFERENCES

[1] H. Mistry *et al.*, *Nat. Rev. Mater.* **1**, 1–14 (2016).
[2] L. Dubau *et al.*, *ACS Catal.* **6**, 4673–4684 (2016).
[3] R. Chattot *et al.*, *ACS Catal.* **7**, 398–408 (2017).

# WING BONES OF *ARCHAEOPTERYX* SHOW ADAPTATIONS TO ACTIVE FLIGHT

**The iconic, feathered dinosaur *Archaeopteryx* from the Late Jurassic of southeastern Germany combines skeletal features of land-living dinosaurs with the elaborate plumage of flying birds. New analysis demonstrates that its wing bones resemble those of modern birds in more ways than previously thought, which indicates the capacity of active flight.**

The well-preserved fossils of *Archaeopteryx* have been crucial in revealing the dinosaurian origin of modern birds. Nevertheless, the puzzling anatomy of its skeletons has remained difficult to interpret. Although *Archaeopteryx* shares features with the land-living dinosaurs that it is closely related to, impressions of feathers alongside its bones also show that *Archaeopteryx* must have sported an elaborate plumage resembling the feather arrangement of flying birds. Modern birds have an advanced flight apparatus that involves powerful muscles attached to a large, keeled breastbone, shoulder joints capable of moving the wing in a wide variety of directions, and a strongly reduced hand that controls wing shape during flight. *Archaeopteryx* lacks a fossilised breastbone altogether and its shoulder joints would not have enabled the full upstroke we see in modern birds. Because of these limitations, it is often concluded that *Archaeopteryx* was incapable of free flight, which begs the question of how it used its wings. To answer this question, the arm bones of *Archaeopteryx* were investigated in detail.

Several fossils of *Archaeopteryx* were studied using phase-contrast imaging at beamlines **BM05** and **ID19**. In addition, anterior limb bones of a selection of archosaurs – the animal group that encompasses crocodiles, pterosaurs, and dinosaurs including birds – were scanned at **BM05**, **ID17**, and **ID19** to provide the context

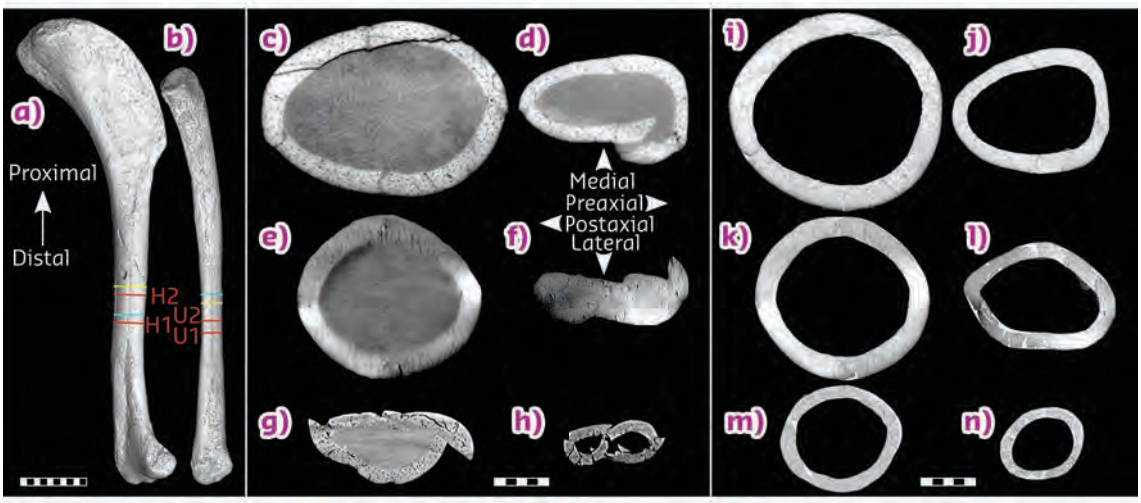


**Fig. 121:** Virtual cross sections of *Archaeopteryx* humeri and ulnae obtained with propagation-based synchrotron microtomography. **a)** Right humerus and **b)** left ulna of *Archaeopteryx* with sample locations indicated, scale bar 10 mm. Virtual cross sections of **c)** right humerus (H2) and **d)** right ulna of ninth specimen (U2), **e)** right humerus and **f)** right ulna of seventh specimen (blue samples), and **g)** left humerus and **h)** left ulna of fifth specimen (yellow samples). Reconstructed cross sections **(i)** of **(c)**, **(j)** of **(d)**, **(k)** of **(e)**, **(l)** of **(f)**, **(m)** of **(g)**, and **(n)** of **(h)**. Scale bars for **(c–n)** are 1 mm.

for explaining the conditions encountered in *Archaeopteryx*. Where earlier study concluded that the bones of *Archaeopteryx* were nearly avascular, suggesting reptilian-grade metabolic performance and growth **[1]**, full cross sections of the arm bones (**Figure 121**) revealed a vascular density approaching or within the range of modern birds, consistent with a more active lifestyle than would be assumed from bone nearly devoid of vascular canals. Archosaurs that are known to be or have been capable flyers (*i.e.* most birds and the extinct pterosaurs) all share wing bones with a relatively thin cortex. The hollowness of the bones of *Archaeopteryx* in cross section immediately confirms their affinity with flight. Limb bones evolve to cope with the forces that they are subjected to at minimal mass. Calculations adopted from mechanical engineering were used in order to quantify the resistance against torsional forces that are known to importantly influence the bone architecture of flying birds **[2]**. The study demonstrates that this resistance is particularly strong in birds that spend most of their time in the air, including those that employ a soaring flight strategy to save energy. *Archaeopteryx* can be placed among birds that prefer to spend most of their time on the ground but engage in brief, active aerial excursions when evading a predator or when crossing physical barriers. This behaviour can be seen in modern galliforms: the group including chickens, pheasants, quails, and turkeys (**Figure 122**).

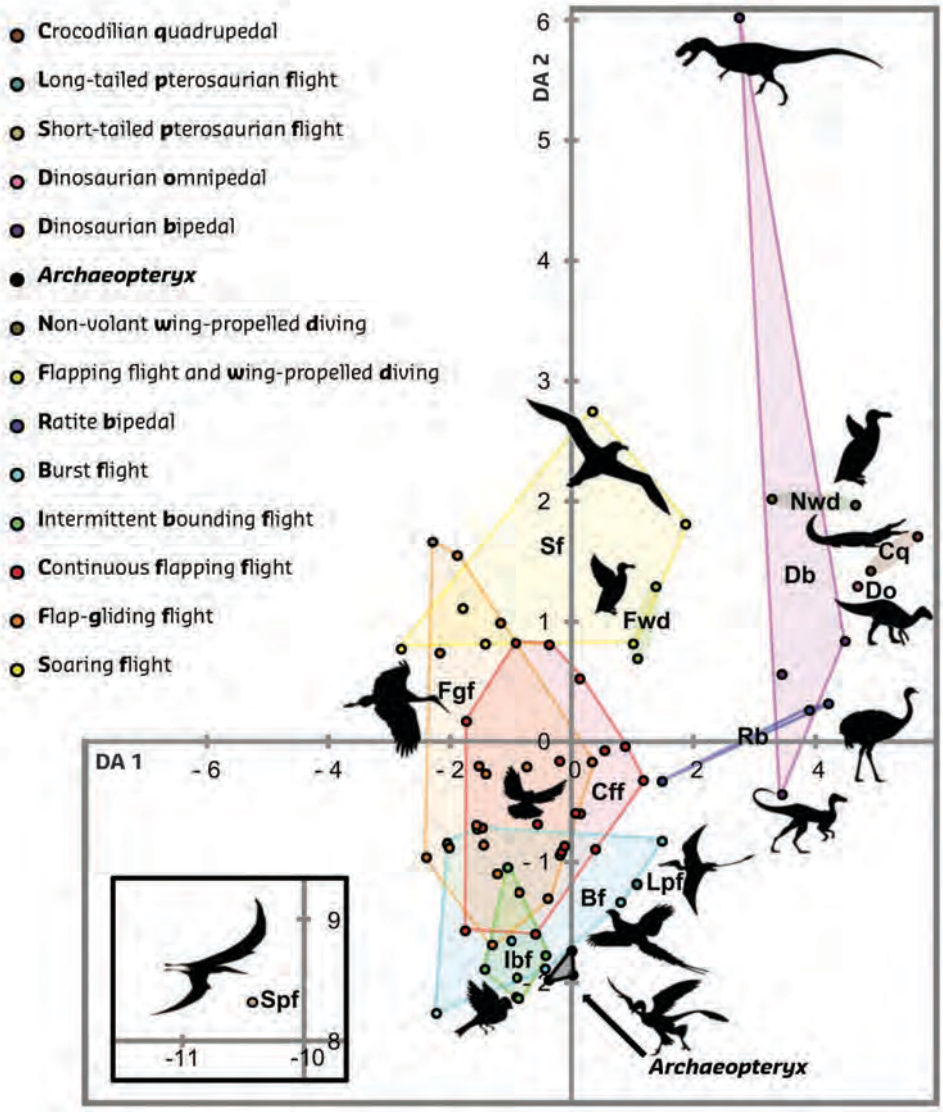


**Fig. 122:** Discriminant analysis (DA) plot of archosaurian species based on humeral and ulnar relative cortical thickness and mass-corrected torsional resistance. Dots indicate separate species, *Archaeopteryx* specimens plotted individually. Groups and associated silhouettes correspond with archosaurian locomotor strategies; non-pterosaurian flight modes represent avian flight modes.

These results indicate that *Archaeopteryx* must have used its wings for some form of incidental, active flight. By studying the joint tolerances in the flight apparatus and evaluating the surrounding bones for possible muscle attachment sites, it is proposed that sufficient flight forces might have been generated by a horizontally oriented flight stroke that superficially resembles the butterfly swimming stroke. Nevertheless, more research into the shoulder girdle and muscles will be required to demonstrate exactly how this dinosaur achieved the functional precursor of bird flight.

## PRINCIPAL PUBLICATION AND AUTHORS

Wing bone geometry reveals active flight in *Archaeopteryx*, D. F. A. E. Voeten (a, b), J. Cubo (c), E. de Margerie (d), M. Röper (e, f), V. Beyrand (a, b), S. Bureš (b), P. Tafforeau (a) and S. Sanchez (a, g), *Nat. Commun.* **9**, 923 (2018); doi: 10.1038/s41467-018-03296-8.
*(a) ESRF*
*(b) Department of Zoology and Laboratory of Ornithology, Palacký University Olomouc (Czech Republic)*
*(c) ISTeP – UMR 7193 UPMC-CNRS, Sorbonne Universités, Paris (France)*
*(d) Laboratoire d'éthologie animale et humaine-CNRS, Université de Rennes 1, (France)*
*(e) Bürgermeister-Müller-Museum, Solnhofen (Germany)*
*(f) Bayerische Staatssammlung für Paläontologie und Geologie, Munich (Germany)*
*(g) Evolutionary Biology Centre, Uppsala University (Sweden)*

## REFERENCES

[1] G. M. Erickson *et al., PLoS One* **4**, e7390 (2009).
[2] E. de Margerie *et al., Anat. Rec. A Discov. Mol. Cell. Evol. Biol.*, **282**, 49–66 (2005).

# UNRAVELLING ATOMIC-SCALE DEGRADATION PROCESSES OF OPERATING FUEL CELL ELECTROCATALYSTS

**A novel class of oxide-supported Pt electrocatalysts was studied using *in-situ* wide- and small-angle X-ray scattering under simulated fuel cell conditions. Understanding the structural and morphological properties of Pt nanoparticles and oxide support on the nanoscale allowed the identification of the most prominent degradation pathways, and thus aids in developing mitigation strategies.**

Electrification of the transportation sector requires the development of robust, electrochemical energy conversion devices, most prominently batteries and fuel cells. Low-temperature fuel cells replacing conventional internal combustion engines in medium- and long-range vehicles invariably use carbon-supported, Pt-nanoparticle electrocatalysts. While these materials are known for their excellent catalytic activity, they often fail in their harsh environment under working conditions of over several thousand operating hours. It is therefore highly important to understand the origin of degradation and the requirements for the long-term stability of such electrocatalysts in order to design durable fuel cells. More specifically, this work addresses the structural and morphological evolution and degradation of Pt nanoparticles supported on indium tin oxide (ITO) under simulated fuel cell operating conditions using different *in-situ* X-ray methods. Accelerated stress tests (AST) were applied to evaluate the electrochemical stability of the catalysts in fuel cell-relevant potential regimes. The Pt/ITO electrocatalyst showed contradictory behaviour of declining catalytic mass activity and stable electrochemical active surface area after 5000 AST cycles. This pointed towards the application of *in-situ* methods to unravel possible degradation phenomena on a fundamental level.

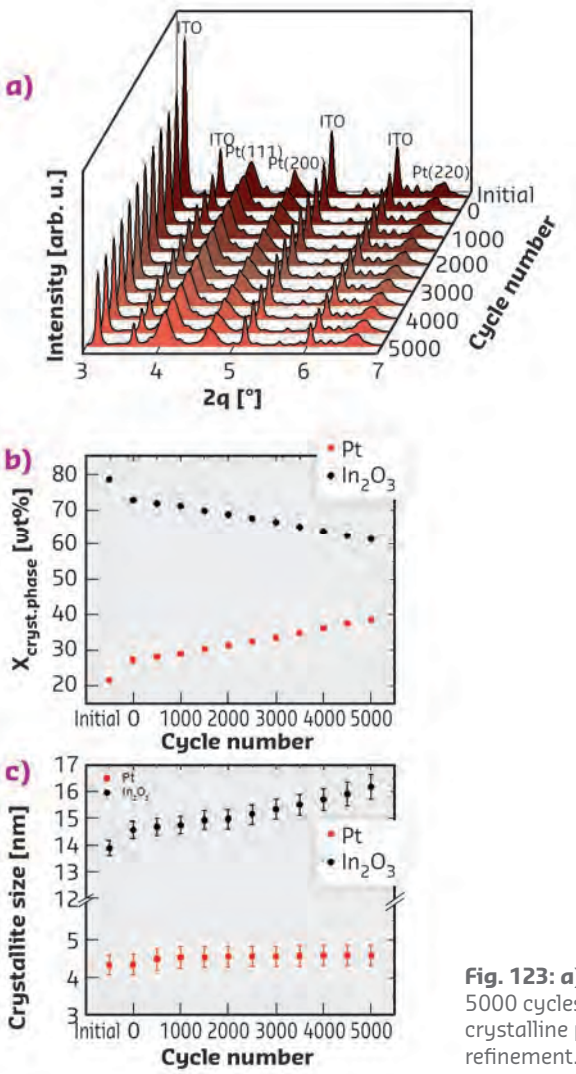


The combination of almost simultaneous wide- and small-angle X-ray scattering (WAXS and SAXS) at beamline **ID31** allowed the structural and morphological changes of the catalyst and support to be tracked in an *in-situ* electrochemical transmission setup. **Figure 123** shows the results of *in-situ* WAXS for Pt/ITO over 5000 cycles of the AST. The Pt diffraction peaks remained stable, while the intensity of ITO reflexes decreased (**Figure 123a**). This observation was further verified by Rietveld refinement as the crystalline weight fraction of ITO decreased from *ca.* 80% to 60% and the ITO crystallite size grew from *ca.* 14 nm to 16 nm (**Figure 123b, c**). In contrast, the Pt crystallite size remained constant at around 4.5 nm.

Furthermore, Pt-specific scattering curves were obtained from anomalous SAXS (ASAXS) measurements around the Pt K-edge (**Figure 124**). A clear feature above 0.1 Å, resulting from scattering of the nanoparticles, confirms a narrow Pt particle size distribution (PSD). Moreover, with fitting of these individual scattering curves, the PSD can be obtained for selected stages of the stability protocol

**Fig. 123: a)** *In-situ* wide-angle X-ray scattering patterns of a Pt/ITO electrocatalyst over 5000 cycles of the accelerated stress test (AST). **b)** The evolution of weight fractions of the crystalline phases and **c)** the crystallite sizes for Pt and ITO as determined from Rietveld refinement. 

(**Figure 124b**). A bimodal PSD was identified with a high fraction (99%) of around 4.5 nm Pt particles and a very small fraction (1%) of larger particles with a size of 9 nm, presumably agglomerates of two single smaller Pt particles. However, no changes in Pt particle sizes were observed during the AST, supporting the findings from the Rietveld analyses and, most importantly, demonstrating the very high stability of the catalytic Pt nanoparticles.

To conclude, *in-situ* WAXS and ASAXS analysis helped to understand the catalytic long-term performance of a novel class of fuel cell catalyst. It was confirmed that the morphology and structure of the ITO support crystallites were strongly affected by the AST conditions, as particle growth and amorphisation were found. This cathodic support corrosion was proposed to be co-affecting the performance stability of the Pt nanoparticles on an atomic level, leading to catalytic active site poisoning by sub-nanometer adlayers consisting of support metal ions.

This study offers insight into degradation mechanisms in oxide-supported Pt fuel-cell catalysts and contributes to the understanding of support-determining properties under fuel cell operating conditions. Overall, it highlights the importance of detailed knowledge of the catalyst–support couple for the development of durable fuel cells.

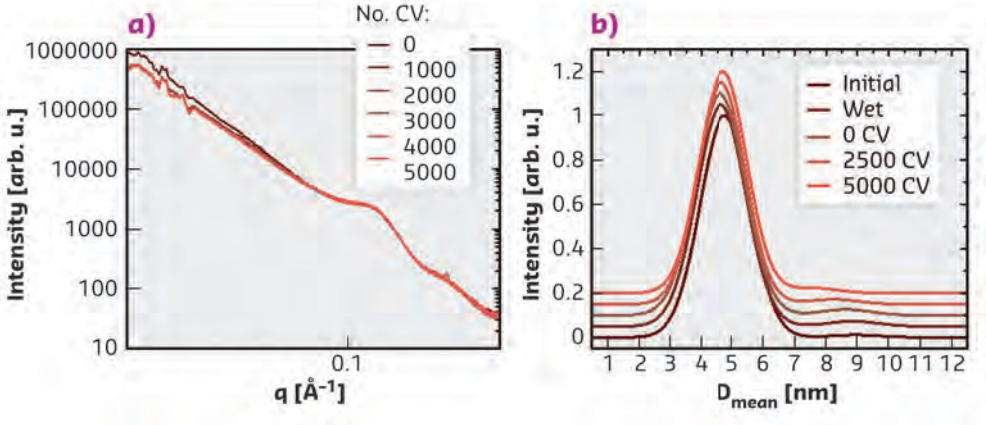


**Fig. 124: a)** *In-situ* anomalous small-angle X-ray scattering (ASAXS) curves of a Pt/ITO electrocatalyst over 5000 cycles of the accelerated stress test (AST). **b)** The *in-situ* particle size distributions (PSD) as obtained from fitting of the ASAXS curves. 

PRINCIPAL PUBLICATION AND AUTHORS

Unravelling Degradation Pathways of Oxide-Supported Pt Fuel Cell Nanocatalysts under *In Situ* Operating Conditions, H. Schmies (a), A. Bergmann (a), J. Drnec (b), G. Wang (c), D. Teschner (d), S. Kühl (a), D. J. Sandbeck (e), S. Cherevko (e), M. Gocyla (f), M. Shviro (f), M. Heggen (f), V. Ramani (c), R. E. Dunin-Borkowski (f), K. J. Mayrhofer (e) and P. Strasser (a),

*Adv. Energy Mater.* **8**, 1701663 (2017); doi: 10.1002/aenm.201701663.
*(a) Department of Chemistry, Technical University of Berlin (Germany)*
*(b) ESRF*
*(c) School of Engineering & Applied Science, Washington University in St. Louis (USA)*
*(d) Department of Inorganic Chemistry, Fritz-Haber-Institut der Max-Planck-Gesellschaft (Germany)*
*(e) Helmholtz-Institute Erlangen-Nürnberg for Renewable Energy, Forschungszentrum Jülich (Germany)*
*(f) Ernst-Ruska Centre for Microscopy and Spectroscopy with Electrons and Peter Grünberg Institute, Forschungszentrum Jülich (Germany)*

# STABILISATION AT ROOM TEMPERATURE OF THE TOPOLOGICAL WEYL SEMIMETAL PHASE IN EPITAXIAL $MoTe_2$ ATOMICALLY THIN FILMS

**Epitaxy of $MoTe_2$ on InAs(111) favours the formation of the orthorhombic ($T_d$) non-centrosymmetric phase, which is a topological type-II Weyl semimetal. Its stability at room temeperature is a result of tensile strain from the substrate, which stabilises an elongated interlayer antibonding state characteristic of $T_d$-$MoTe_2$.**

Topological Weyl semimetals **[1]**, often called the 'new 3D graphene', are a new state of matter that show linear dispersions (Dirac cones) in all three dimensions in reciprocal space, resembling massless light-like particles. Weyl fermions, predicted by quantum field theory as elementary particles, have never been observed in free space, so their low-energy 'incarnation' in semimetals offers a unique opportunity to merge high-energy elementary particle physics with condensed matter. It has been shown in the literature that bulk or free-standing films of the 2D material $MoTe_2$ adopt orthorhombic stacking at temperatures lower than 250 K, *i.e.*

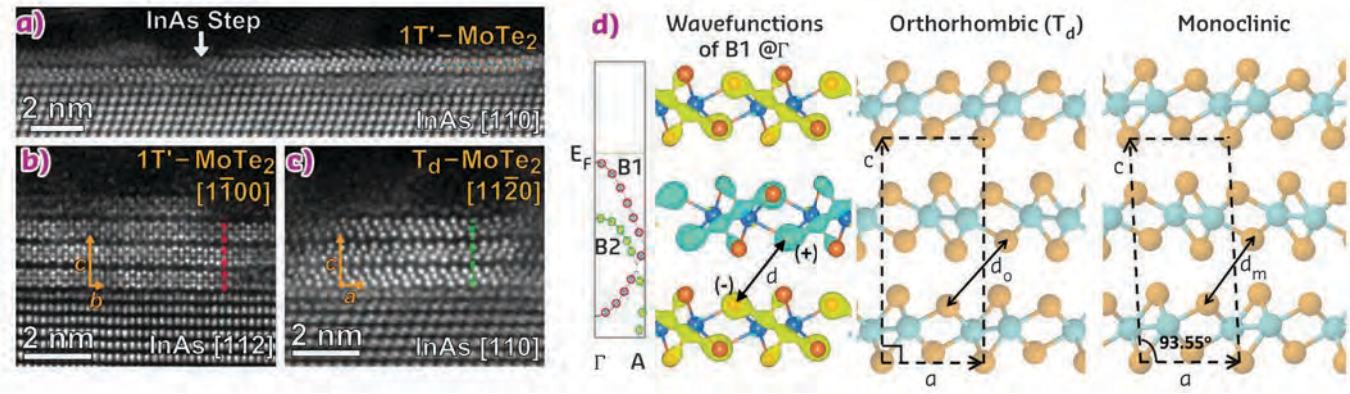


**Fig. 125:** HR-STEM of epitaxial $MoTe_2$ at room temperature. ***a)*** 1 ML of distorted 1T (1T′) $MoTe_2$ on InAs (111) substrate. **b, c)** Orthorhombic ($T_d$) stacking of the 1T′ $MoTe_2$. **d)** From left to right: portion of the band structure along ΓA, wave functions of band B1 at Γ showing the interlayer antibonding state between Te, orthorhombic ($T_d$) stacking and monoclinic stacking. © Wiley-VCH Verlag GmbH & Co. KGaA. Reproduced with permission.

non-centrosymmetric, and so $MoTe_2$ is classified as a type-II topological Weyl semimetal. At room temperature, $MoTe_2$ is stable in the monoclinic phase, and is centrosymmetric with trivial topology (no Weyl nodes exist).

This work demonstrates that atomically thin $MoTe_2$ films produced by molecular beam epitaxy are stabilised in the Weyl semimetal $T_d$ phase at room temperature as a result of the influence of the InAs(111)/Si(111) substrate. The $T_d$-$MoTe_2$ phase is directly probed by HRSTEM measurements (**Figures 125a-c**), where orthorhombic stacking is clearly observed. In-plane reciprocal space mapping, performed at beamline **BM32**, shows a complex diffraction pattern (**Figure 126a**) characterised by closely spaced triple diffraction spots, as a result of the overlapping of 60° and 120° rotated domains. These diffraction spots allow for an accurate estimation of the in-plane lattice constants *a* and *b* of the 2x1 reconstructed surface unit cell (**Figure 126 b-d**) characteristic of the $T_d$-$MoTe_2$ phase, while out-of-plane diffraction (*l*-scans) yields the out-of-plane lattice constant, *c*. It is concluded that, due to the influence of the substrate, the lattice parameters of the epitaxial films are enlarged with respect to experimental values obtained from bulk or free-standing films, which has important implications given that the electronic band structure is sensitive to the lattice parameters. Indeed, first principles calculations by density functional theory (DFT) predict that epitaxial films with enlarged lattice parameters have 8 Weyl points with energies only 1.1 and 12.9 meV below the Fermi energy, which makes them accessible to angular-resolved photoelectron spectroscopy (ARPES) and to transport measurements. It is worth noting, however, that the presence of rotation domains adversely affects the resolution of *in-situ* ARPES, so resolving the closely spaced Weyl points is difficult. Moreover, the enlarged lattice parameters affect the band structure along ΓA direction of the Brillouin zone so that the B1 band (**Figure 125d**) is fully occupied lying below the Fermi energy. The occupation of this band, which is made of interlayer antibonding states (**Figure 125d**), favours the orthorhombic $T_d$ phase with elongated Te-Te distances across the van der Waals gap, thus making the $T_d$ phase more stable than the monoclinic one at room temperature **[2]**.

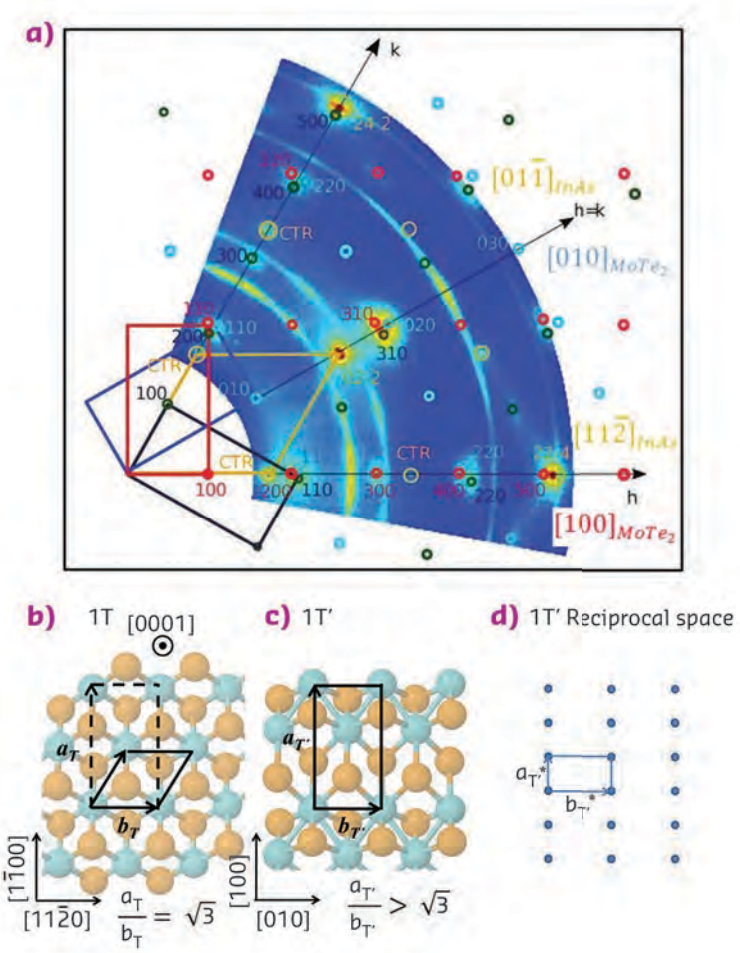


**Fig. 126:** Reciprocal space of epitaxial distorted (1T′) $MoTe_2$. ***a)*** In-plane reciprocal space mapping by GIXD at BM32. The rectangles show the surface unit cell of the reciprocal space corresponding to domains rotated by 60° between each other. **b)** The hexagonal surface unit cell of undistorted 1T $MoTe_2$ in real space. **c)** The 2x1 unit cell of the 1T′ $MoTe_2$. **d)** Reciprocal space of 1T′ $MoTe_2$ showing a surface unit cell. © Wiley-VCH Verlag GmbH & Co. KGaA. Reproduced with permission.

Since prototypical Weyl semimetals (*e.g.* TaAs) are 3D crystal structures mainly found in bulk form, discovering and engineering topological semimetals from the family of 2D transition metal dichalcogenide materials that are stable at room temperature (*e.g.* $T_d$-$MoTe_2$) could open the way for exploitation of their unique topological properties by fabricating thin epitaxial films and devices on suitable crystalline substrates.


PRINCIPAL PUBLICATION AND AUTHORS

Direct Observation at Room Temperature of the Orthorhombic Weyl Semimetal Phase in Thin Epitaxial $MoTe_2$, P. Tsipas (a), S. Fragkos (a), D. Tsoutsou (a), C. Alvarez (b, c), R. Sant (d), G. Renaud (b, c), H. Okuno (b, c) and A. Dimoulas (a), *Adv. Funct. Mater.* **28**, 1802084 (2018); doi: 10.1002/adfm.201802084.

*(a) NCSR DEMOKRITOS, Athens (Greece)*
*(b) Université Grenoble Alpes (France)*
*(c) CEA/INAC-MEM, Grenoble (France)*
*(d) Institut Néel CNRS, Grenoble (France)*



REFERENCES

[1] N. P. Armitage *et al., Rev. Mod. Phys.* **90**, 015001 (2018).
[2] H.-j. Kim *et al., Phys. Rev. B* **95**, 180101 (R) (2017).


# REVERSIBLE PHOTO-CONTROL OF FERROELECTRIC DOMAINS REVEALED AT MACROSCOPIC SCALE

**Ferroelectric materials exhibit a spontaneous polarisation in a certain range of temperatures that can be switched by applying an electric field. This work shows it is possible to achieve a reversible optical change of ferroelectric domain configuration, which may lead to a new generation of ferroelectric devices.**

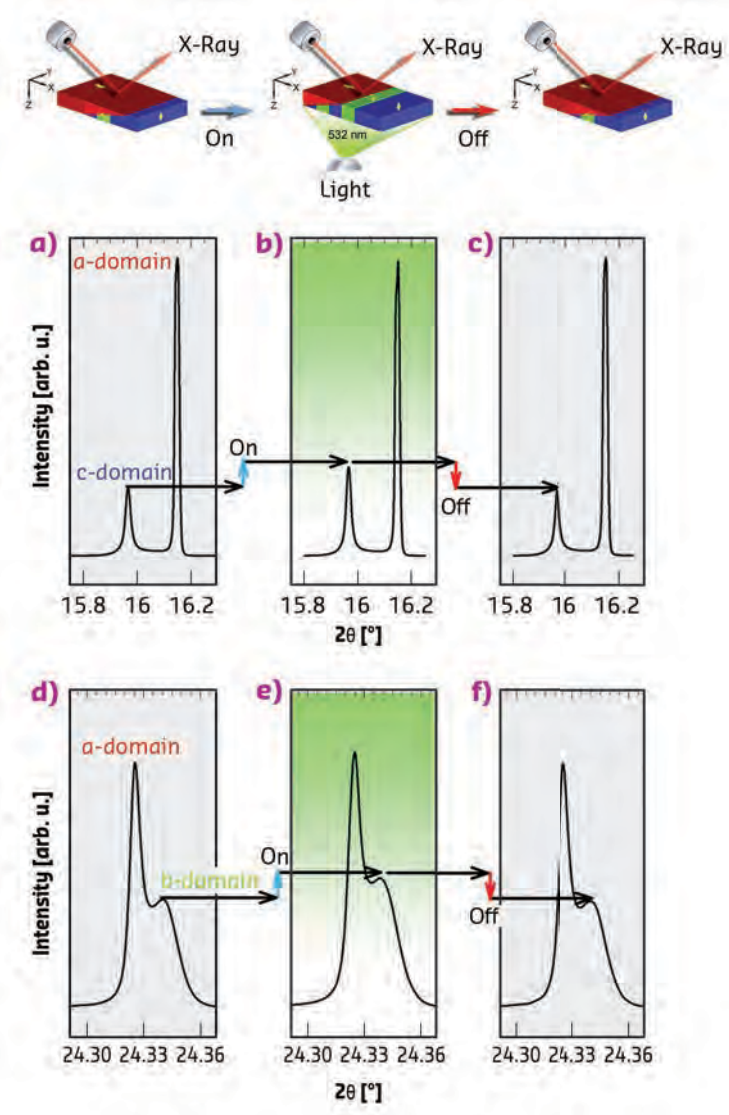


The optical control of ferroic properties is of great interest for the scientific community, since it involves the establishment of new paradigms for technology **[1-4]**. Optical control could solve two of the main drawbacks of the development and miniaturisation of next-generation ferroelectric devices: the feasibility of electrical contacts at smaller scales and the undesired heating of the devices. The possibility of controlling macroscopic polarisation with light while avoiding device heating and contacting would revolutionise the sector.

**Fig. 127: a-c)** Sequence of synchrotron radiation (λ = 0.5636 Å) high-resolution XRD patterns of (002)/(200) reflections corresponding to the off-on-off light succession. The *c*-domains contribution enhances when the light is on as a consequence of the light-induced domain wall motion. The reversible nature of the phenomenon is demonstrated, since the optically induced change in the domain structure disappears after the light is switched off.
**d-f)** Sequence of XRD patterns of (300)/(030) reflections showing the *b*-domains contribution emerges after the light is switched on.
The phenomenon reversibility is also revealed for *b*-domains contribution. Additionally, the schemes sequence shown at the top of **(a-c)** represents a simplified experimental setup as well as the light-induced change in the domains structure as a result of the illumination process. © 2018 Nature Publishing Group. Modified and reprinted with permission.

So far, few experimental studies have been devoted to the photo-control of ferroelectric properties, including the discovery of the ability to move ferroelectric domain walls by applying a coherent light source **[5]**. Since this stimulant effect was microscopically described, a fundamental question has arisen: What is the extent of the coupling between the light and ferroelectric polarisation? Few studies exist of light-matter coupling in ferroelectric materials, a phenomenon that may explain the evolution dynamics of complex domain structure and its correlations with the macroscopic response.

This work demonstrates that the macroscopic polarisation in a $BaTiO_3$ (BTO) single crystal can be reversibly switched by illumination with visible light. To identify *in situ* relative changes in the domain structures by applying a coherent light source, high-resolution X-ray diffraction (XRD) was used at beamline **BM25**. For experimentation in illumination conditions, a laser diode was coupled to the theta-two-theta diffractometer. The power and wavelength of the light source were 40 mW and 532 nm, respectively. Finally, the reversibility of the phenomenon was investigated by measuring XRD patterns for a set of on/off light cycles (**Figure 127**).

The changes in the polarisation, the reproducibility and reversibility of the process is investigated by means of *in-situ* sequential XRD patterns of a set of off-on-off illumination cycles (**Figures 127a-f**). The illumination generates a reversible domain switching, yielding a *c*- and *b*-domain volume increase at the expense of the volume of *a*-domains (**Figures 127a-c** and **127d–f**, respectively).

To prove that the structural change induced by light can generate a change in the macroscopic polarisation of the crystal, this study explores the macroscopic dielectric permittivity, ε´, under the same light source. **Figure 128** shows a light-induced change in the macroscopic dielectric permittivity of the BTO crystal. A notable variation in the real permittivity value occurs when the ferroelectric crystal is illuminated, showing that the local movement of domain walls is noted at the macroscopic scale as a change in dielectric properties.

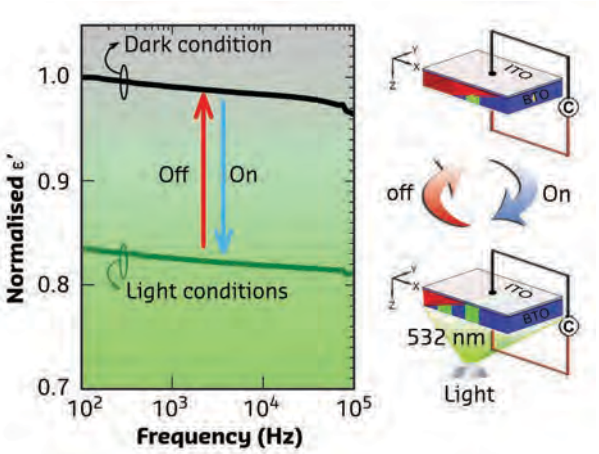


**Fig. 128:** Normalised real permittivity, ε´, of the BTO crystal before and upon optical excitation, as a function of the frequency. A notable variation in the real permittivity (~17% at 1 kHz) is shown in the panel as a result of a light-induced change in the macroscopic polarisation of the material. The dielectric constant values are normalised by taking into account the value in the dark condition at 1 kHz. On the right of the panel, a schemes sequence showing a simplified experimental setup to determine the real permittivity is displayed. © 2018 Nature Publishing Group. Modified and reprinted with permission.

Finally, this study demonstrates that the macroscopic polarisation of BTO single crystals can be reversibility controlled using only light. These results will serve as an inspirational source for further studies based on light-induced processes in ferroelectric materials, opening a new gate to the next generation of photo-stimulated ferroelectric devices.

## PRINCIPAL PUBLICATION AND AUTHORS

Reversible optical control of macroscopic polarization in ferroelectrics, F. Rubio-Marcos (a), D. A. Ochoa (b), A. Del Campo (a), M. A. García (a, c), G. R. Castro (d, e), J. F. Fernández (a) and J. E. García (b), *Nat. Photonics*, **12**(1), 29–32 (2018); doi: 10.1038/s41566-017-0068-1.

*(a) Department of Electroceramics, Instituto de Cerámica y Vidrio – CSIC, Madrid (Spain)*
*(b) Department of Physics, Universitat Politècnica de Catalunya – BarcelonaTech (Spain)*
*(c) Instituto de Magnetismo Aplicado 'Salvador Velayos', Universidad Complutense de Madrid (Spain)*
*(d) ESRF*
*(e) Instituto de Ciencia de Materiales de Madrid – CSIC (Spain)*

## REFERENCES

[1] C. Y. Ying *et al., Laser Photon. Rev.* **6**, 526–548 (2012).
[2] R. Guo *et al., Nat. Commun.* **4**, 1990 (2013).
[3] L. J. McGilly *et al., Nat. Nanotechnol.* **10**, 145–150 (2015).
[4] M.-M. Yang and M. Alexe, *Adv. Mater.* **30**, 1704908 (2018).
[5] F. Rubio-Marcos *et al., Nat. Comm.* **6**, 6594 (2015).

# POTASSIUM PASSIVATION BOOSTS LUMINESCENCE AND PHOTOVOLTAIC EFFICIENCY OF HALIDE PEROVSKITES

**This work demonstrates that potassium passivation via simple solution processing boosts the performance of perovskite-based solar cells by 'healing' defects and immobilising ion movement, which – to date – are the key barriers to the widespread adoption of potentially cheap perovskite solar cells.**

Halide perovskite materials have emerged as a serious rival to commercial thin film and silicon photovoltaic technologies, with excellent semiconductor properties. The efficiency at which they convert sunlight to electricity has surged in a few short years and, together with their inexpensive precursors and facile fabrication routes at low temperature, makes them a very promising candidate for next-generation solar cells and other semiconductor devices, such as light emitting diodes and photodetectors.

Despite the remarkable progress, there have been barriers that limit their ability to reach their full potential in both efficiency and long-term stability, which are key parameters for large-scale industrial production. The presence of tiny defects in the crystalline structure of perovskites leads to trapping of energised charges (electron or hole) before their energy can be harnessed. A second challenge is that the ions in the perovskite compounds can migrate under solar cell operation (when it is illuminated), which can generate new phases in the material and therefore change the optical bandgap and the colour of light the perovskite absorbs.

In this work, the chemical composition of perovskite thin films was tuned by adding potassium iodide to perovskite precursor inks, the components of which then self-assemble into thin films (**Figure 129a**). The developed technique is compatible with roll-to-roll processing in a similar way to newsprint, making it inexpensive and scalable. A combination of grazing-incidence wide-angle X-ray diffraction (GIWAXS) performed at beamline **BM28** and cross-sectional chemical mapping shows that the potassium halides form a 'decorative' layer on top of the perovskite. This has the effect of 'healing' the defects so that the energised charges can move more freely, while also immobilising the ion movement, which makes the material more stable with the desired bandgap. In particular, potassium stabilises the perovskite bandgaps needed for tandem solar cells – when a perovskite layer is added on top of a silicon solar cell or another perovskite layer – leading to more efficient harvesting of light from a wider region of the solar spectrum. The potassium also makes the materials more luminescent, a signature that the added potassium is helping to remove the detrimental impacts of defects in perovskites (**Figure 129b**). The GIWAX measurements on the potassium passivated perovskite films show a crystalline phase at a lower angle that grows with increasing potassium, representing a key finding on the formation of the passivating potassium rich phase in the perovskite thin films (**Figure 130**).

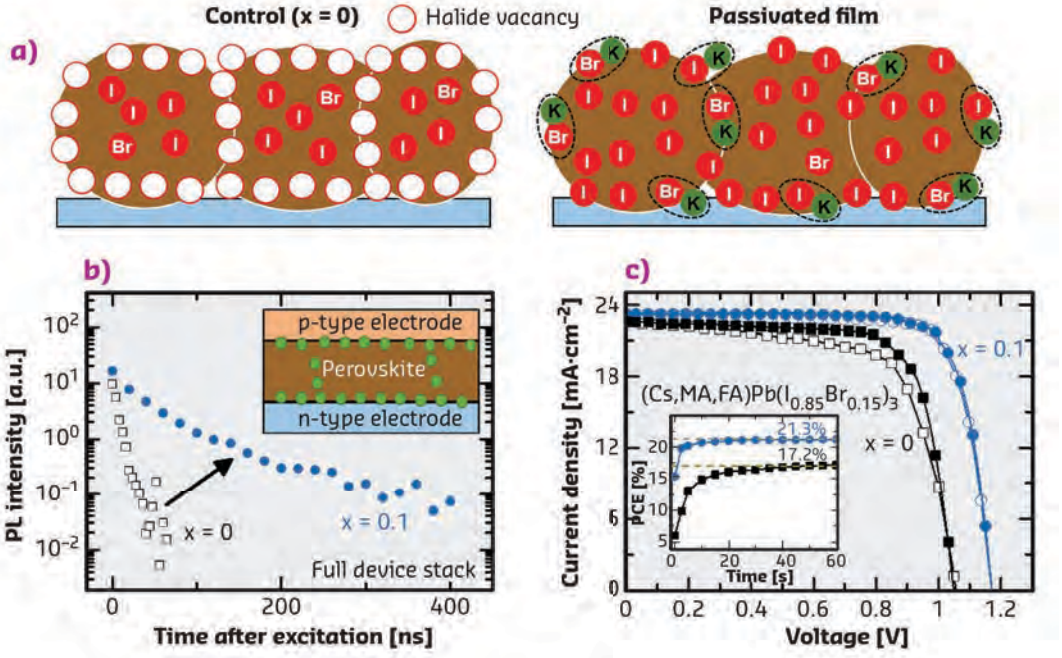


**Fig. 129: a)** Schematic of a cross section of a film showing halide-vacancy management in cases of excess halide, in which the surplus halide is immobilised through complexing with potassium into benign compounds at the grain boundaries and surfaces. **b)** Time-resolved photoluminescence decays of encapsulated (Cs,FA,MA) $Pb(I_{0.85}Br_{0.15})_3$ films (x = 0 and x = 0.1), when the perovskite is interfaced with both electrodes in a full device stack. **c)** Forward (open symbols) and reverse (closed symbols) *J–V* curves of the best-performing perovskite solar cells without (x = 0) and with (x = 0.1) potassium passivation, (AM1.5, 100 mW $cm^{-2}$). Inset, stabilised power output under the same conditions.

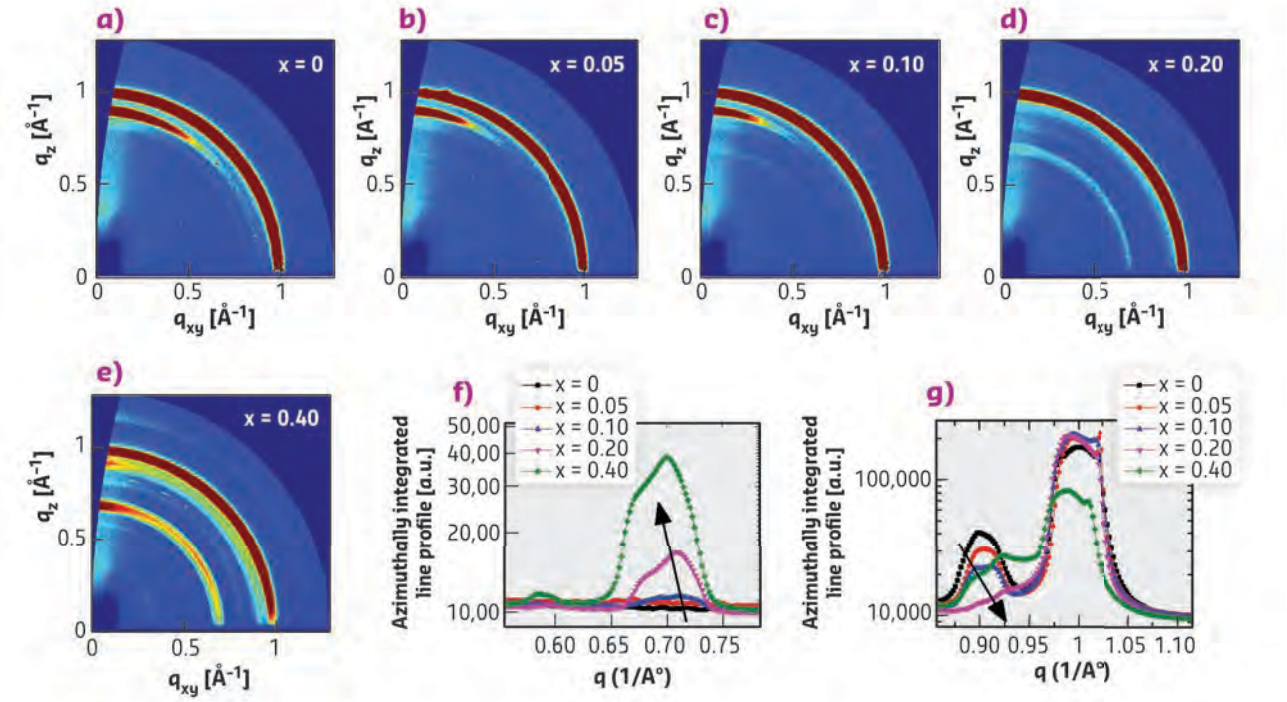


**Fig. 130:** GIWAXS measurements of passivated alloyed perovskite films. ***a-e)*** The diffraction patterns of thin perovskite films collected at low angle using GIWAXS for ***a)*** x = 0.00, ***b)*** x = 0.05, ***c)*** x = 0.10, ***d)*** x = 0.20 and ***e)*** x = 0.40. ***f, g)*** The high-resolution line profiles azimuthally integrated over the entire GIWAX profile for different fractions of potassium at ***f)*** 0.5 ≤ q ≤ 0.8 and ***g)*** 0.8 ≤ q ≤ 1.1.

The perovskite and potassium devices showed promising stability in tests, and were 21.5% efficient at converting light into electricity, which is similar to the best perovskite-based solar cells and not far below the practical efficiency limit of silicon-based solar cells, which is 29% (**Figure 129c**). Tandem cells made of two perovskite layers with ideal bandgaps have a theoretical efficiency limit of 45% and a practical limit of 35% – both of which are higher than the current practical efficiency limits for silicon.

PRINCIPAL PUBLICATION AND AUTHORS

Maximizing and stabilizing luminescence from halide perovskites with potassium passivation, M. Abdi-Jalebi (a), Z. Andaji-Garmaroudi (a), S. Cacovich (b), C. Stavrakas (a), B. Philippe (c), J.M. Richter (a), M. Alsari (a), E.P. Booker (a), E.M. Hutter (d), A.J. Pearson (a), S. Lilliu (e, f), T. J. Savenije (d), H. Rensmo (c), G. Divitini (b), C. Ducati (b), R. H. Friend (a) and S. D. Stranks (a), *Nature* **555**, 497–501 (2018); doi: 10.1038/nature25989.
*(a) Cavendish Laboratory, Department of Physics, University of Cambridge (UK)*
*(b) Department of Materials Science and Metallurgy, University of Cambridge (UK)*
*(c) Department of Physics and Astronomy, Uppsala University (Sweden)*
*(d) Department of Chemical Engineering, Delft University of Technology (Netherlands)*
*(e) Department of Physics and Astronomy, University of Sheffield (UK)*
*(f) The UAE Centre for Crystallography (United Arab Emirates)*

# LONG-RANGE SYMMETRY-BREAKING IN EMBEDDED FERROELECTRICS

**The characteristic functionality of ferroelectric materials is due to the symmetry of their crystalline structure. However, a new X-ray diffraction microscopy technique shows that, for many bulk ferroelectrics, this crystalline symmetry is broken. This has implications for understanding and engineering ferroelectric materials for a range of applications.**

The unique dielectric and electromechanical properties of ferroelectric materials enable a myriad of technologies from ultrasound imaging to high-speed digital memory. But, like many materials, these properties are at the mercy of the defects within them. Most ferroelectrics contain complex, hierarchical networks of grain boundaries, twin walls, dislocations and atomic vacancies, whose strain fields break the spatial symmetry of the materials' structure **[1]**. As ferroelectricity and polarisation are strongly coupled to the lattice symmetry, even

subtle distortions can have dramatic effects on properties. Defects present an opportunity for optimising ferroelectrics, but engineering them first requires the ability to characterise them at the scale of individual defects under the complex boundary conditions of real materials and devices.

This work used dark-field X-ray microscopy at beamline **ID06** to map the strain and symmetry around grain boundaries and twin (domain) walls buried within a millimetre-sized polycrystal of barium titanate ($BaTiO_3$) – a prototypical ferroelectric and ferroelastic perovskite. Earlier work on $BaTiO_3$ polycrystals **[2]** showed that, despite volume-averaged diffraction measurements confirming the expected tetragonal lattice symmetry, diffraction measurements from individual grains suggested the actual symmetry was much lower. Here, it was possible to identify which types of strain were responsible for the symmetry lowering and, crucially, the defects from which they originated.

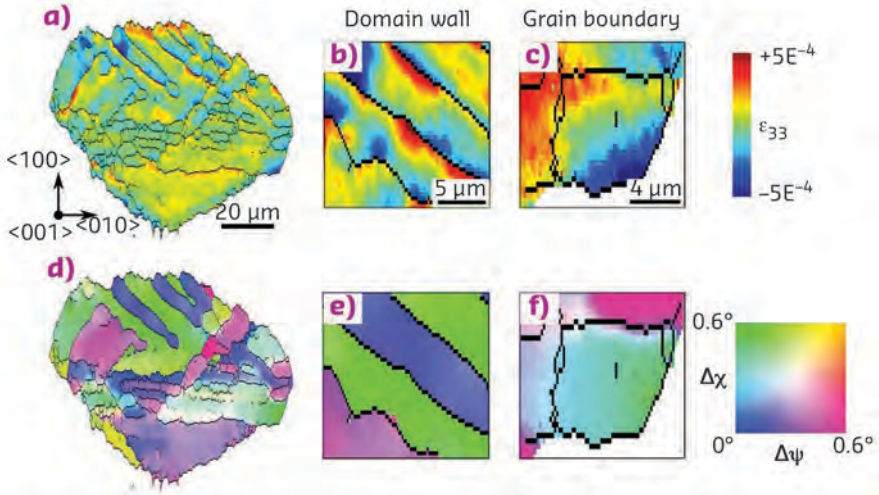


**Fig. 131:** Maps of lattice strain **(a-c)** and orientation **(d-f)** from the buried grain of $BaTiO_3$. The grain **(a, d)** contains a heterogeneous network of distortions originating from domain walls **(b, e)** and the grain boundary **(c, f)**. X-ray energy was 17 keV, using an X-ray magnification of 17, corresponding to a spatial resolution of 80 nm.

**Figure 131** shows that the distribution of axial strain and misorientation within the single, buried grain is consistent with bundles of domains separated by domain walls along {110} planes. While the axial strain is clearly correlated with the changes in domain orientation at the domain wall, the strain decay occurs over distances of 5 µm or more; an order of magnitude larger than reported from electron- or atomic force-based microscopy measurements **[3]**.

It is known that complex strain states may cause slower-than-usual decay from the twin walls **[4]**, however the large size of the grain (nearly 90 µm across) means that much of the material should be beyond the range of influence of the grain boundary. The long-ranging strain fields combined with appreciable misorientation gradients at the same locations imply that the local symmetry across the vast majority of the grain is much lower than the expected tetragonal symmetry.

But how does this widespread symmetry breaking influence the electric-field induced evolution of the domain structure? It is expected that reducing the domain wall density should also reduce the extent of the symmetry breaking; however, the results (**Figure 132**) showed the opposite: that the strain fields and symmetry breaking became much more severe after electrical poling. Notably, the deviation of the domain wall angles from their ideal {110} planes implies that the poling process favoured non-ideal domain orientations despite the increase in strain energy that presumably accompanies them.

A clear picture now emerges: long-range strains created by embedded grain boundaries and domain walls drastically lower the symmetry of entire grains and affect their response to applied electric fields. Macroscopic behaviour is therefore not strictly defined by the nominal symmetry but fundamentally affected by local heterogeneities deep within the bulk. Multiscale modelling approaches, based on data obtained *in situ* in dynamic conditions, are needed to account for the heterogeneous variation of the symmetry. Such multiscale data could be used to directly fit physical parameters for materials models **[5]**, which would create an opportunity to accurately simulate – and ultimately harness – the complex multiscale symmetry breaking from deeply embedded defects.

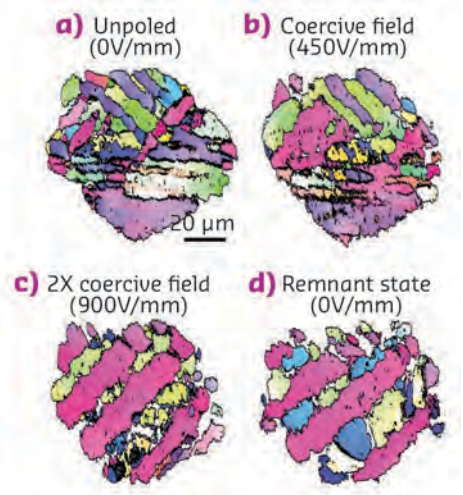


**Fig. 132:** Lattice orientation maps of the grain before **(a)**, during **(b, c)** and after **(d)** the *in-situ* application of electric fields to the bulk sample. For reference, the critical electric field for domain reorientation (coercive field) in $BaTiO_3$ is approximately 450 V/mm.

PRINCIPAL PUBLICATION AND AUTHORS

Long-range symmetry breaking in embedded ferroelectrics, H. Simons (a), A. Bjørnetun Haugen (b), A. C. Jakobsen (a), S. Schmidt (a), F. Stöhr (c), M. Majkut (d), C. Detlefs (d), J. E. Daniels (e), D. Damjanovic (f) and H. F. Poulsen (a), *Nat. Mater.* **17**, 814–819 (2018); doi: 10.1038/s41563-018-0116-3.
*(a) Department of Physics, Technical University of Denmark (Denmark)*
*(b) Department of Energy Conversion and Storage, Technical University of Denmark (Denmark)*
*(c) DTU Danchip, Technical University of Denmark (Denmark)*
*(d) ESRF*
*(e) School of Materials Science & Engineering, UNSW Sydney (Australia)*
*(f) Group for Ferroelectrics and Functional Oxides, Swiss Federal Institute of Technology in Lausanne – EPFL (Switzerland)*

REFERENCES

[1] M. E. Lines and A. M. Glass, *Principles and Applications of Ferroelectrics and Related Materials*, Oxford University Press, Oxford, 2001.
[2] J. E. Daniels *et al.*, *Sci. Rep.* **6**, 22820 (2016).
[3] A. K. Tagantsev, L. E. Cross and J. Fousek, *Domains in Ferroic Crystals and Thin Films*, Springer, New York, 2010.
[4] R. J. Harrison and E. K. Salje, *Appl. Phys. Lett.* **99**, 151915 (2011).
[5] J. Zhang *et al.*, *Acta Mater.* **129**, 229–238 (2017).

# REVEALING HOW MARTENSITE IN Ti-ALLOYS EXPANDS AND DECOMPOSES

**Ti-alloys are central to advancements in aerospace and biomedical engineering today. At the heart of the Ti-alloy design is the interplay between crystallographic phases, enabling engineers to adjust their properties towards application requirements. Recent experiments at ID11 revealed their uncommon thermal expansion behaviour and demonstrated novel precipitation pathways for α-phase.**

Ti-alloys are candidate materials for load-bearing and functional components in biomedical and aerospace applications as they offer a large design space through various competing athermal and diffusive phase transformations. However, to advance these technologies beyond the current state-of-the-art, alloys with tailored mechanical and functional properties are needed. This can be achieved by designing novel microstructures via bespoke thermomechanical processing paths. Their successful development, in turn, requires accurate knowledge of how these alloys respond to variations of temperature **[1, 2]**. However, deriving the alloys' response to temperature changes by *ex-situ* methods is stymied by their complex metallurgy. *In-situ* diffraction methods utilising synchrotron radiation are therefore the first choice to capture structural changes taking place in rather narrow temperature and time intervals directly at the critical temperature.

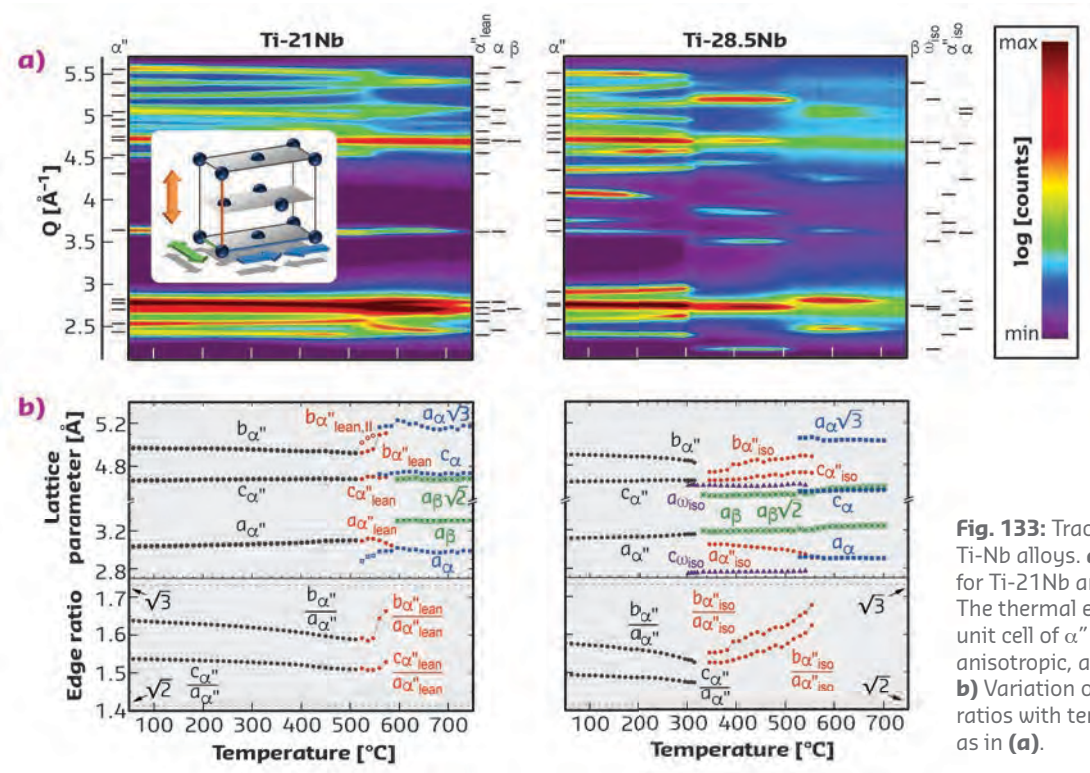


**Fig. 133:** Tracking structural changes in Ti-Nb alloys. **a)** Evolution of diffractograms for Ti-21Nb and Ti-28.5Nb during heating. The thermal expansion of the orthorhombic unit cell of α" martensite is highly anisotropic, as illustrated in the inset. **b)** Variation of lattice parameters and edge ratios with temperature for the same alloys as in **(a)**.

The aim of the present study was to track phase reactions and transformations *in situ* at elevated temperatures for selected Ti-Nb alloys. The diffraction data collected at **ID11** made it possible to clearly demarcate critical temperatures, such as start and end temperatures of concurrent reactions, where calorimetry otherwise provides only rough values. Furthermore, temperature-induced changes of the crystallographic unit cells were easily revealed.

During heating, several new phases appeared, including α, β, and $\omega_{iso}$. In addition, the formation of Nb-depleted α", denoted $\alpha"_{lean}$, and $\alpha"_{iso}$, was revealed. **Figure 133a** shows the diffractograms for two compositions studied: Ti-21Nb and Ti-28.5Nb. From these diffractograms, the lattice parameters were extracted (**Figure 133b**).

This analysis revealed that thermal expansion rates of orthorhombic α" martensite in Ti-Nb are among the largest (both positive and negative) reported for solid crystalline metallic systems, be they isotropic or anisotropic. The reflections of α" and, correspondingly, its lattice parameters, shifted with temperature due to thermal expansion, the shift being stronger the more Nb was present. Importantly, thermal expansion of α" martensite is highly anisotropic: *a* and *c* spacings expand for all compositions while the *b* spacing contracts for most compositions. Aside from reaching unprecedented giant values, the thermal expansion rates of the present alloys can be adjusted across a wide range by simply modifying their composition. This represents a significant advantage over many ceramics, in which thermal expansion is often difficult to control.

When further heated, the disappearance of α" martensite during heating involves different transformation sequences depending on composition. For instance, the high-temperature diffraction data made it possible to follow the process of α" decomposition into α and β phases observed for Ti-21Nb *in situ*. In this process, $\alpha"_{lean}$ progressively rejects Nb, thereby approaching equilibrium α. This is reflected by the behaviour of the unit cell aspect ratios (**Figure 133b**). When heated, α" martensite becomes more cubic-like, whereas, when decomposing, this assimilation is reverted and α" eventually turns into hexagonal close packed α-phase.

In the Nb-richer Ti-28.5Nb alloy variant, a very different sequence was revealed. Martensite did not decompose on heating but reverted to austenite β. Experiments demonstrated that if heating continued, α formation proceeds via a transitional phase, $\alpha"_{iso}$, which is similar to α" martensite. In this process, the crystal structure of $\alpha"_{iso}$ progressively became more similar to α. Notably, while the orthorhombic crystal structure of α" had so far been largely associated with diffusion-free formation during rapid cooling, these observations brought to light that α-precipitation is often mediated by the diffusion-based formation of α"-like phases. These results may help engineer advanced Ti-alloys with improved mechanical properties and/or thermal expansion control.

## PRINCIPAL PUBLICATION AND AUTHORS

Giant thermal expansion and α-precipitation pathways in Ti-alloys, M. Bönisch (a, b, g), A. Panigrahi (c, d), M. Stoica (a, h), M. Calin (a), E. Ahrens (a), M. Zehetbauer (c), W. Skrotzki (b) and J. Eckert (e, f), *Nat. Commun.* **8**, 1429 (2017); doi: 10.1038/s41467-017-01578-1.
*(a) Institute for Complex Materials, IFW Dresden (Germany)*
*(b) Institute of Structural Physics, Technische Universität Dresden (Germany)*
*(c) Physics of Nanostructured Materials, University of Vienna (Austria)*
*(d) Institute of Minerals and Materials Technology, Bhubaneswar (India)*
*(e) Erich Schmid Institute of Materials Science, ÖAW, Leoben (Austria)*
*(f) Department of Materials Physics, Montanuniversität Leoben (Austria)*
*(g) Department of Mechanical Science and Engineering, University of Illinois at Urbana-Champaign (USA)*
*(h) Department of Materials, ETH Zürich, (Switzerland)*

## REFERENCES

[1] M. Bönisch *et al., Sci. Technol. Adv. Mater.* **14**, 055004 (2013).
[2] M. Bönisch *et al., J. Alloys Compds.* **697**, 300–309 (2017).

# REVEALING THE MECHANISMS OF DECOUPLED MICROSCOPIC PIEZOELECTRIC RESPONSE IN BISMUTH FERRITE USING HIGH-ENERGY X-RAY DIFFRACTION

**Electric-field-induced ferroelectric response as a function of frequency in bismuth ferrite has been investigated using time-resolved high-energy X-ray diffraction (XRD). An unusual frequency-dependent decoupling of microscopic ferroelectric responses was observed. An analytical model was produced to explain the results in terms of anisotropy of conductive mechanisms in given grain families.**

Ferroic domain walls are naturally occurring nanoscale interfaces that can possess distinct properties from their parent materials. Due to their length scale, they have generated great interest for applications such as domain wall nanoelectronics. The ferroelectric material $BiFeO_3$ has been shown to possess enhanced electrical conductivity at domain wall regions **[1]**. This ferroelectric material also displays Maxwell–Wagner-like frequency dispersion in its macroscopic piezoelectric response **[2]**. This dispersion, which is different from a prototypical linear frequency-dependent behaviour in classical ferroelectric materials, has been suggested to originate from the conductive domain walls **[2]**.

In this study, *in-situ* experiments were conducted on poled $BiFeO_3$ ceramics. The 78.5 keV (0.15794 Å) X-ray beam from the **ID15A** beamline was focused to a size of 200 µm x 200 µm (**Figure 134a**). The diffraction images were collected in the forward direction (transmission geometry). During the diffraction measurements, sub-coercive sinusoidal electric fields were applied in the poling direction at frequencies from 0.01 Hz to 1000 Hz.

This applied field was hardware synchronised with the framing of the Pilatus 2M CdTe detector images, such that diffraction information was obtained at specific time points within the electric field cycle. The lattice strain, domain texture and corresponding phase angle of the response to the field were extracted from the diffracting images. A simultaneous observation of *in-situ* macroscopic strain was achieved by using an optical displacement sensor coupled to the top surfaces of the sample (**Figure 134a**).

The lattice strain, change in non-180° domain texture, and macroscopic strain of ferroelectric $BiFeO_3$ during field application, along with their corresponding phase angle with respect to the electric field, was evaluated as a function of the frequency.

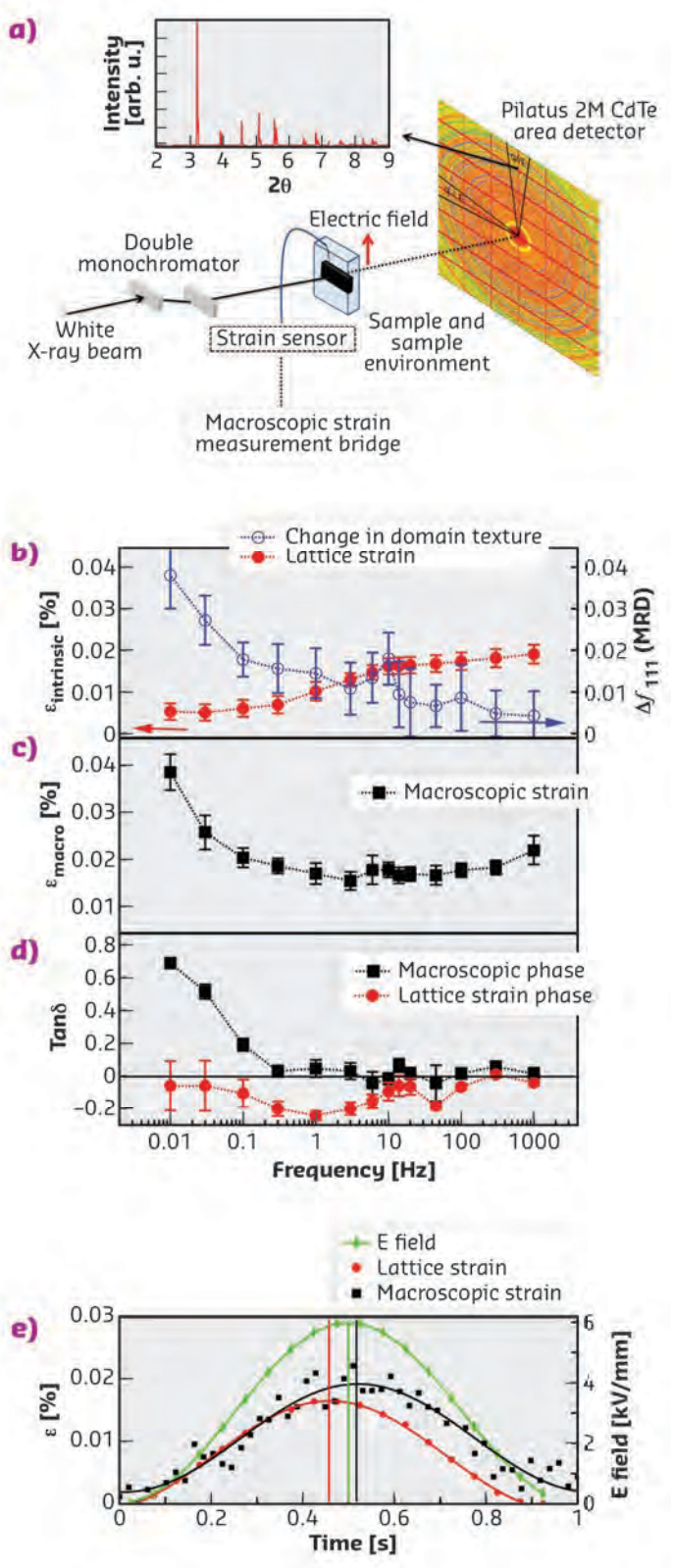


**Fig. 134: a)** Schematic of the experimental setup. **b)** Total lattice strain and change in non-180° $111_{pc}$ domain texture. **c)** Macroscopic strain. **d)** Tangent of the piezoelectric phase angle of macroscopic strain and lattice strain. **e)** Time dependence of driving electric field, macroscopic strain and lattice strain response at 6 kV/mm, 1 Hz unipolar electric field.

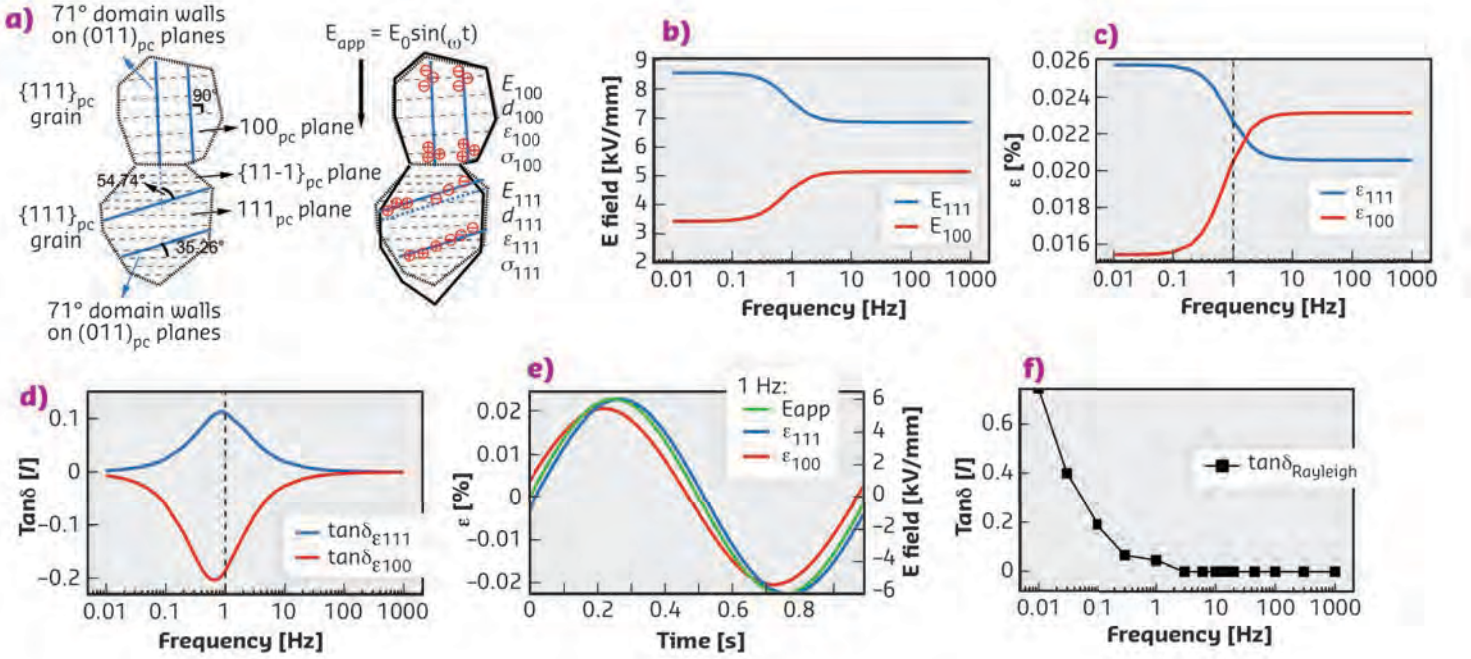


**Fig. 135:** ***a)*** Representative $\{100\}_{pc}$ and $\{111\}_{pc}$ grains in $BiFeO_3$ and charges distribution along 71° domain walls with external field. **b)** Redistributed effective fields in $\{100\}_{pc}$ and $\{111\}_{pc}$ grain families. **c)** Calculated frequency-dependent decoupling of strains. **d)** Phase angles of the strains. **e)** Time-dependent electric field and strains in two grains demonstrated for 1 Hz driving frequency. **f)** Rayleigh phase angle due to the significant non-linearity at frequencies below ~1 Hz.

Lattice strain and change in non-180° domain texture are surprisingly decoupled as a function of frequency, showing different trends in their fractional contributions to the macroscopic strain (**Figure 134b**). The macroscopic strain decreases sharply with increasing frequency from 0.01 Hz to ~3 Hz, showing the representative feature of Maxwell–Wagner dispersion (**Figure 134c**). The corresponding phase angle of macroscopic strain and lattice strain (**Figure 134d**) are positive and (unexpected) negative, indicating normal phase lagging and abnormal phase leading of the macroscopic strain and microscopic lattice strain with respect to the electric field, respectively (**Figure 134e**).

The Maxwell–Wagner dispersion and negative phase angle from *in-situ* XRD data suggests that local regions within the polycrystalline matrix have dispersive mechanisms with different time constants. The anisotropy in conductivity in homogeneous phase-pure $BiFeO_3$ is proposed to be due to the presence of conducting domain walls, oriented differently with respect to the applied field vector in different grain families (**Figure 135a**). Charge redistributes at the conductive domain walls on application of electric field with different time constant in different grains (**Figure 135a**), resulting in time-dependent effective field redistribution in these grains (**Figure 135b**). The redistribution of electric fields in these grains is analogous to effective fields in circuits where leaky capacitors (*i.e.* a capacitor and a resistor in parallel) with different capacitance and resistivity are connected in series. Such redistributed fields effectively cause complex frequency-dependent lattice strain, change in domain texture induced strain and their corresponding phase angles, as calculated using piezoelectric constitutive equations (**Figure 135c**, **d** and **e**). These calculations, incorporating Rayleigh nonlinearity at low frequency (**Figure 135f**), reproduce the *in-situ* experimental results well (*i.e.* decoupling of lattice strain and change in domain texture with frequency, phase leading of the lattice strain, and the nonlinearity at lower frequency).

The experimental data demonstrate how high-energy *in-situ* XRD can reveal undetermined structural perspectives of ferroelectric materials. Such behaviours would be invisible with a lower diffraction/time resolution or *ex-situ* methods.

## PRINCIPAL PUBLICATION AND AUTHORS

Revealing the mechanisms of decoupled microscopic piezoelectric response in bismuth ferrite using high-energy X-ray diffraction, L. Liu (a), T. Rojac (b), D. Damjanovic (c), M. Di Michiel (d) and J. Daniels (a), *Nat. Commun.* **9**, 4928 (2018); doi: 10.1038/s41467-018-07363-y.

*(a) School of Materials Science and Engineering, UNSW Sydney (Australia)*
*(b) Electronic Ceramics Department, Jozef Stefan Institute, Ljubljana (Slovenia)*
*(c) Group for Ferroelectrics and Functional Oxides, Swiss Federal Institute of Technology in Lausanne–EPFL, Lausanne (Switzerland)*
*(d) ESRF*

## REFERENCES

[1] J. Seidel *et al. Nat. Mater.* **8**, 229 (2009).
[2] T. Rojac *et al., Adv. Funct. Mater.* **25**, 2099–2108 (2015).

# MOLLUSCS USE THERMODYNAMICS TO CREATE COMPLEX MORPHOLOGIES WITH EXCEPTIONAL PROPERTIES

**A new model has been developed to describe how some molluscs create their complex shell ultrastructures. The model is an analogy to the directional solidification process well-known in classical material science. The results provide new tools for novel bioinspired and biomimetic bottom-up material design.**

Biomineralisation – the formation of 3D mineral–organic functional architectures by living organisms – serves as a source of inspiration for materials scientists and engineers seeking to recreate highly functional materials with structural, mechanical, optical, magnetic or sensing capabilities.

Molluscan shells, with their diversity of mineral morphologies and 3D mineral–organic architectures, and their exceptional mechanical efficiency, are a model system to understand the fundamental principles of mineral formation by living organisms. Molluscs appeared more than 500 million years ago, and they have developed hard and stiff mineralised outer shells for structural support and protection against predation **[1].** Their shells consist of parallel layers of mineral–organic hierarchical composite ultrastructures made of calcium carbonates. For example, the calcitic prismatic ultrastructure consists of elongated mineral columns glued together by an organic phase and an aragonitic nacreous ultrastructure, made of platelets surrounded by a relatively thin organic membrane **[2]**. While progress has been made in understanding the key mechanisms responsible for biotic calcium carbonate formation **[3-7],** morphogenesis of the spatially intricate shell ultrastructures was still poorly understood.

The morphology of the mollusc *Unio pictorum* was studied on **ID19**, using synchrotron-based absorption- and phase-contrast enhanced microtomography in order to visualise the 3D spatial arrangement of the dendritic–prismatic ultrastructure of the shell (**Figure 136**). The imaging data from **ID19** were complemented with X-ray diffraction measurements from **ID06** to provide additional information on crystal orientation in different parts of the shell. The data demonstrate continuous directional formation of the entire shell construct accompanied by an increasing degree of ordering, that occurs on two hierarchical levels. On the ultrastructural level, the transition proceeds from a dendritic, via more regular prismatic, into the highly ordered nacreous structure. On the level of the nanostructure, a progressive increase in nanoparticle alignment and texturing is achieved.

In both cases, the development of the entire shell shows a notable resemblance to directional solidification proceeding under a continuously decreasing driving force – the level of precursor supersaturation. To test this hypothesis, phase-field simulations were performed to mimic structural evolution during the formation of the shell. As shown in **Figure 137**, a clear and remarkable resemblance to the shell of *U. pictorum* was obtained, on both ultrastructural and nanostructural levels.

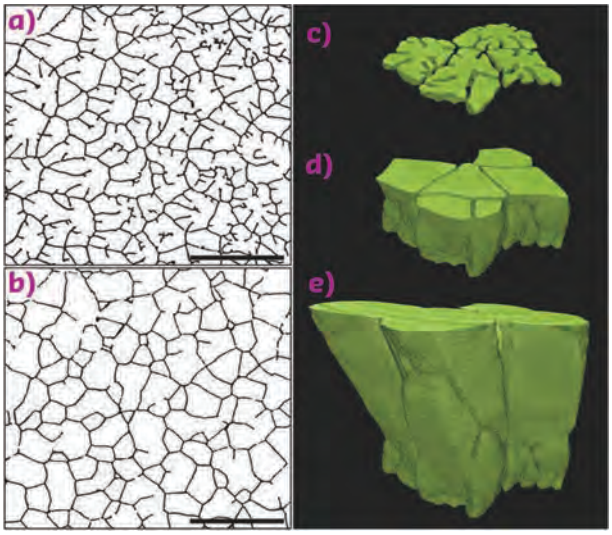


**Fig. 136:** Morphological analysis of the dendritic–prismatic ultrastructure in the shell of *U. pictorum*. **a, b)** 2D slices reconstructed from synchrotron-based microtomography data, (parallel to the surface of the shell), showing the dendritic and the prismatic morphology, closer to the periostracum and nacre, respectively. White areas correspond to the mineral component and black areas to the organic phase. Scale bars are 100 µm. **c-e)** 3D visualisation of tomographic segments showing different stages of structural evolution of the dendritic–prismatic ultrastructure: initial stage showing the dendritic morphology, intermediate stage showing transition to the prismatic morphology and the complete ultrastructure, respectively. Copyright Wiley-VCH Verlag GmbH & Co. KGaA. Reproduced with permission.

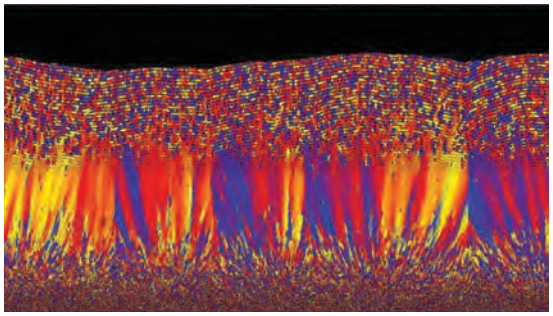

**Fig. 137:** Shell morphology as predicted by 2D phase-field simulation under decreasing supersaturation of the mineral phase. Orientation map: fluid shown in black, different colours represent different crystallographic orientations. Copyright Wiley-VCH Verlag GmbH & Co. KGaA. Reproduced with permission.

These results show that the formation of the different shell structures follows a self-assembly process guided by the physical and chemical environment that is set by the organism. It is demonstrated that the structural evolution of the entire shell of some molluscs – at the ultrastructural and the nanostructural levels – is a result of a continuous growth process with gradually changing boundary conditions, similar to the process of directional solidification, well known from classical materials science. This provides an understanding of the physical constraints governing the morphogenesis of shell ultrastructures, and thereby explains the limited variety of architectures observed in different molluscan clades.

The research greatly contributes to the general knowledge in this field, proposing a model that can be applied to describe the evolution of different shell architectures in many other species. This novel, comprehensive approach to understanding and mimicking mineral formation by living organisms also provides materials scientists with new clues about how to reproduce nature in the future.


PRINCIPAL PUBLICATION AND AUTHORS

Biomineralization as a Paradigm of Directional Solidification: A Physical Model for Molluscan Shell Ultrastructural Morphogenesis, V. Schoeppler (a), L. Gránásy (b), E. Reich (a), N. Poulsen (a), R. de Kloe (c), P. Cook (d), A. Rack (d), T. Pusztai (b) and I. Zlotnikov (a), *Adv. Mater.* 1803855 (2018); doi: 10.1002/adma.201803855.

*(a) B CUBE - Center for Molecular Bioengineering, Technische Universität Dresden (Germany)*
*(b) Institute for Solid State Physics and Optics, Wigner Research Centre for Physics, Budapest, (Hungary)*
*(c) EDAX, Tilburg (The Netherlands)*
*(d) ESRF*

REFERENCES

[1] H.A. Lowenstam and S. Weiner, *On Biomineralization*. Oxford: Oxford University Press (1989).
[2] J. D. Currey and J. D. Taylor, *J. Zool.* **173**, 395 (1974).
[3] G. Falini *et al., Science* **271**, 67 (1996).
[4] S. Weiner *et al., Trends Biochem. Sci.* **16**, 252 (1991).
[5] M. Suzuki *et al., Science* **325**, 1388 (2009).
[6] M. Suzuki et al., *Can. J. Zool*. **91**, 349 (2013).
[7] R. A. Metzler *et al., J. Am. Chem. Soc.* **132**, 6329 (2010).


# CAPTURE OF NITROGEN DIOXIDE WITHIN A METAL–ORGANIC FRAMEWORK


**This work demonstrates the first example of reversible adsorption of a notorious air pollutant, $NO_2$, in a robust metal–organic framework, MFM-300(Al), with high capacity and selectivity. The unusual helical monomer–dimer chains of $NO_2$ observed in MFM-300(Al) afford a fundamental understanding of host–guest interactions underpinning this selectivity, which will inspire the design of new functional materials for the mitigation of air pollution.**


Pollution from nitrogen oxides has been a long-standing concern and enormous efforts have been made to develop abatement technologies. Physisorption of gases by porous materials using supramolecular host–guest interactions is a promising approach that can give high reversibility and low energy penalty for system regeneration. Zeolites, metal oxides, mesoporous silica and activated carbons have been investigated for $NO_2$ adsorption, but these materials suffer from low adsorption capacities and material degradation upon contact with $NO_2$. This study reports the first isothermal adsorption of $NO_2$ with full reversibility in an ultra-stable porous metal–organic framework (MOF), MFM-300(Al).

Recognised for its high capacity in the capture and separation of gas mixtures from previous studies **[1, 2]**, MFM-300 (Al) shows a total $NO_2$ uptake of 14.1 mmol/g with the density of adsorbed $NO_2$ being 1.73 g/cm$^{-3}$ at 298 K and 1 bar. This is higher than that of liquid $NO_2$ and $N_2O_4$ at 1.45 g/cm$^{-3}$ and 1.44 g/cm$^{-3}$, respectively, at 294 K (**Figure 138a**). Significantly, the $NO_2$ uptake in MFM-300(Al) is reversible, and the host material can be regenerated with no loss of crystallinity or porosity for at least five cycles. Dynamic breakthrough experiments have also validated the high capacity of MFM-300(Al) for the removal of low concentrations of $NO_2$ from gas mixtures both under dry and humid conditions (**Figure 138b**).

To understand the underlying mechanism of this adsorption process at the molecular level, synchrotron powder X-ray diffraction (PXRD) data were collected at beamline **ID22** on samples

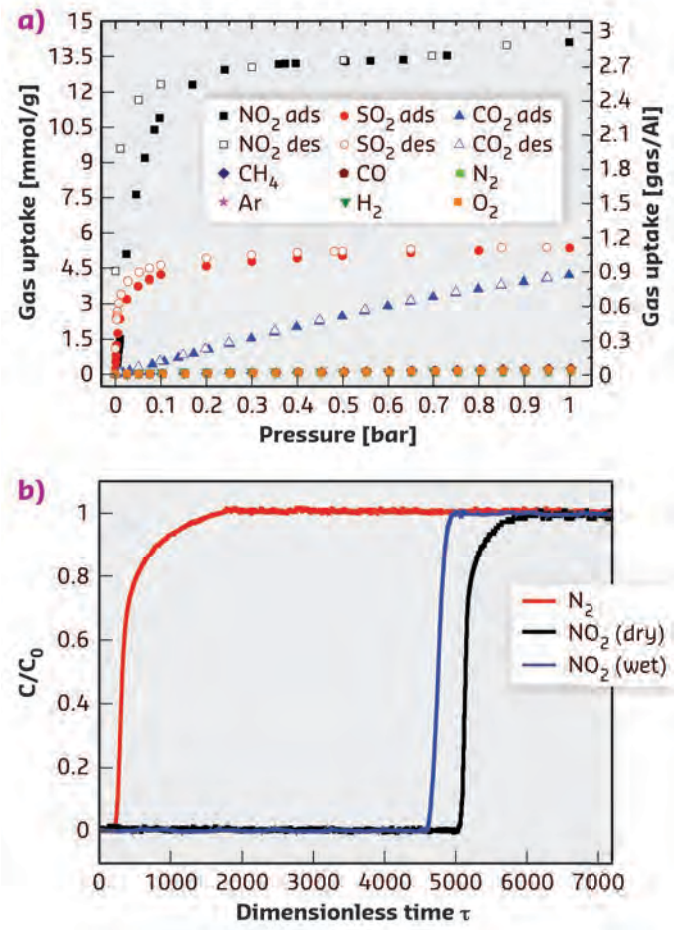


**Fig. 138:** ***a)*** Adsorption isotherms of $NO_2$, $SO_2$, $CO_2$, $CH_4$, $N_2$, CO, $H_2$, $O_2$ and Ar in MFM-300(Al) at 298 K. ***b)*** Dimensionless breakthrough curve of 0.5% $NO_2$ (5000 ppm) diluted in He/$N_2$ under dry and wet conditions at 298 K and 1 bar.

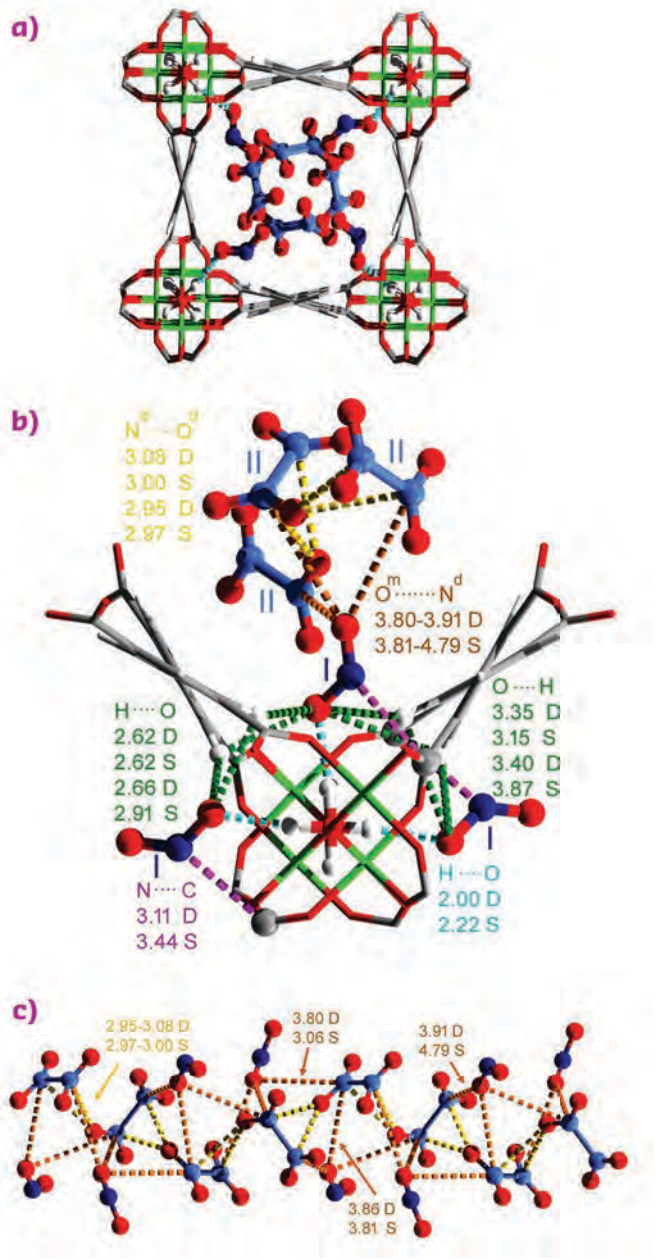


**Fig. 139:** ***a)*** Structural model for MFM-300(Al)·$(NO_2)_2$·$(N_2O_4)_2$ determined by high-resolution synchrotron PXRD and DFT calculations (Al: green; carbon: grey; oxygen: red; hydrogen: white; nitrogen: blue). ***b)*** Host–guest binding details showing the binding sites I and II. ***c)*** Structural view of the one-dimensional helical chain $(NO_2{\cdot}N_2O_4)_\infty$ within the channel of MFM-300(Al).

of $NO_2$@MFM-300(Al) at 298 K. The final structural model for MFM-300(Al)·$(NO_2)_2$·$(N_2O_4)_2$ was validated by Rietveld refinement and density functional theory (DFT) calculations (**Figure 139a**), and reveals two independent binding sites within the pore of MFM-300(Al). The $NO_2$ molecules at site I exhibit an end-on interaction to the HO-Al group through hydrogen bonds supplemented by additional four-fold supramolecular contacts of the O(δ-) centre of $NO_2$ to the aromatic hydrogen atoms H(δ+), and a strong dipole interaction between the N(δ-) centre of $NO_2$ molecule and the C(δ+) centre of the carboxylate group. $N_2O_4$ molecules at site II are located at the centre of the pore and interact primarily with the $NO_2$ molecules at site I via a three-fold intermolecular dipole interaction ($N^d\cdots O^m$). In addition, $N_2O_4$ molecules at site II form intermolecular dipole interactions with adjacent $N_2O_4$ molecules ($N^d\cdots O^d$). These are comparable to those observed in solid $N_2O_4$, as studied by neutron diffraction at 20 K **[3]**, confirming the restricted solid-state arrangement of the adsorbed $N_2O_4$ in MFM-300(Al). The presence of $NO_2$ and $N_2O_4$ molecules at sites I and II, respectively, affords a distinct 1D helical $(NO_2{\cdot}N_2O_4)_\infty$ chain running along the channel of MFM-300(Al) (**Figure 139c**), which represents the first example of the co-existence of $NO_2$ and $N_2O_4$ molecules within a crystalline matrix.

Various spectroscopic and computational methods, including Fourier transform infrared (FTIR), electron paramagnetic resonance (EPR) and inelastic neutron spectroscopy (INS) coupled with DFT and molecular dynamics (MD)

calculations, have also been applied to visualise directly these binding domains, and to interrogate the dynamics of host–guest interactions, and the reactivity and chemical behaviour of adsorbed $NO_2$ within MFM-300(Al).

These findings underpin the fundamental understanding of the chemical properties of guest molecules within porous hosts, and may also pave the way for the development of future capture and conversion technologies.


PRINCIPAL PUBLICATION AND AUTHORS

Reversible adsorption of nitrogen dioxide within a robust porous metal–organic framework, X. Han (a), H. G. Godfrey (a), L. Briggs (a), A. J. Davies (b), Y. Cheng (c), L. L. Daemen (c), A. M. Sheveleva (a, d), F. Tuna (a), E. J. L. McInnes (a), J. Sun (e), C. Drathen (f), M. W. George (b, g), A. J. Ramirez-Cuesta (c), K. M. Thomas (h), S. Yang (a) and M. Schröder (a), *Nat. Mater.* **17**, 691–696 (2018); doi: 10.1038/s41563-018-0104-7.
*(a) University of Manchester (UK)*
*(b) University of Nottingham (UK)*
*(c) Neutron Sciences Directorate, Oak Ridge National Laboratory (USA)*
*(d) International Tomography Centre SB RAS and Novosibirsk State University (Russia)*
*(e) Peking University, Beijing, (China)*
*(f) ESRF*
*(g) University of Nottingham, Ningbo (China)*
*(h) University of Newcastle upon Tyne (UK)*

REFERENCES

[1] S. Yang *et al.*, *Nat. Chem.* **4**, 887–894 (2012).
[2] S. Yang *et al.*, *Nat. Chem.* **7**, 121–129 (2015).
[3] Å. Kvick *et al.*, *J. Chem. Phys.* **76**, 3754–3761 (1982).


# UNDERSTANDING THE STRUCTURE OF LAYERED CUPRATE THIN FILMS

**Perovskite-related layered cuprates are considered the basis of conventional high-$T_c$ superconductors, but much remains to be understood about the interplay between their structure and properties. Epitaxial thin films of layered complex cuprates where the weakly coupled copper planes are oriented in the substrate surface plane are especially interesting, due to the simplified deconvolution of directionally dependent properties.**

One of the strategies is to study the mother system of this material type: perovskite $MCuO_{3-x}$. $LaCuO_{3-x}$ is considered one of the most promising systems in this respect. It exhibits a large versatility in oxygen off-stoichiometry and could help shed light on the role played by the mixture of $Cu^{3+}$ and $Cu^{2+}$ that is found in most high-$T_c$ superconductors. Copper valence in $LaCuO_{3-x}$ can be varied from only $Cu^{2+}$ in insulating orthorhombic $LaCuO_{2.5}$ (*i.e.*, $La_2Cu_2O_5$) all the way to only $Cu^{3+}$ in metallic tetragonal $LaCuO_3$. A metallic monoclinic phase exists for the interval $0.1 < x < 0.5$. (**Figure 140**). Studying the structure and properties of the intermediary valence compounds could help explain some of the strong correlation in these material types.

Unfortunately, layered cuprates are not the most straightforward type of material to deposit as thin films, especially by chemical methods. Copper oxides are notorious for catalytic decomposition of metal–organic precursors, which are used in techniques like chemical vapour deposition (CVD). This results in loss of compositional control during the growth phase.

In this study, the self-limiting nature of the atomic layer deposition (ALD) technique was utilised in order to overcome these challenges. Careful control of the copper precursor flux, precursor sublimation temperature and deposition temperature was shown to enable unmatched control of stoichiometry and uniformity in these thin films. Epitaxial thin films of $LaCuO_{3-x}$ (001) were deposited on single crystal substrates of $LaAlO_3$ $(100)_{pc}$, using commercially available cation precursors ($La(thd)_3$ and $Cu(acac)_2$). Ozone was used as the oxygen source to get a strongly oxidising environment.

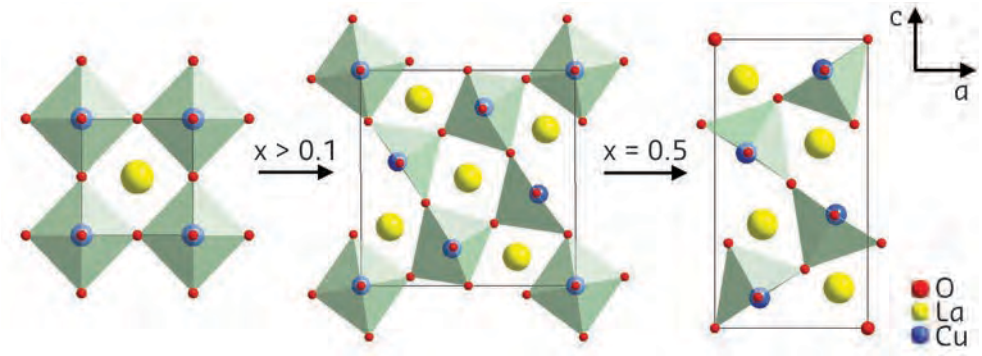


**Fig. 140:** The three different structures of $LaCuO_{3-x}$ found at different under-stoichometries of oxygen.

The thin films are amorphous as deposited by ALD, and a post-deposition annealing step is necessary to obtain crystalline films. The $LaAlO_3$ $(100)_{pc}$ substrates facilitate oriented crystallisation, with the (001)-planes of $LaCuO_{3-x}$ oriented parallel to the film surface. Different annealing parameters were used to enable control of the oxygen stoichiometry. Annealing in air at 650 °C for 15 minutes resulted in phase-pure, oriented, crystalline films. Annealing in oxygen at 900 °C for 10 hours increased the crystallinity, but from specular diffraction it was not possible to distinguish if the two treatments resulted in different crystal structures. Diffraction from the three variants of $LaCuO_{3-x}$ is very similar, and all specular reflections in from (00*l*)-planes are close to equal. Observing significant differences is only possible by moving far out in the reciprocal space. It was noted that a (640) reflection close to the substrate $(310)_{pc}$ would exist for the monoclinic phase, with no reflections from the orthorhombic phase nearby.

Studying this requires a diffraction setup that covers a relatively large *q*-range, and an area detector with sufficient resolution to deconvolute the $LaCuO_{3-x}$ (640) and $LaAlO_3$ $(310)_{pc}$ reflections. The versatile setup at beamline **BM01** offers the possibility to carry out these kinds of experiments. A flexible goniometer together with the Pilatus 2M detector gives the perfect conditions to study these small variations.

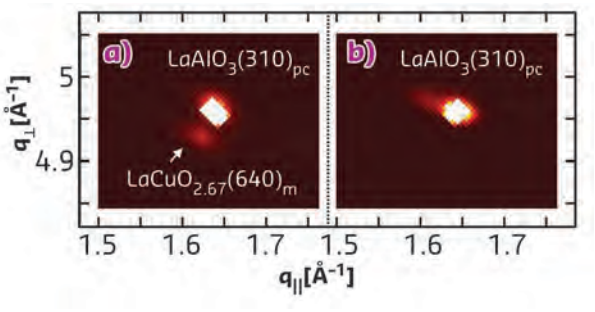


**Fig. 141:** Reciprocal space maps around the substrate $LaAlO_3$ $(310)_{pc}$ for **a)** the oxygen-annealed and **b)** air-annealed $LaCuO_{3-x}$ films. The substrate peak is pixelated due to overexposure.

The substrate (310) reflections were identified, and high-resolution reciprocal space mapping was carried out around this reflection for both air-annealed and oxygen-annealed samples (**Figure 141**). It is immediately clear that the (640)-reflection from the monoclinic structure only exists for the oxygen-annealed sample. Using X-ray photoelectron spectroscopy, the oxygen content was crudely estimated to $x = 2.67$ for the oxygen-annealed sample. Furthermore, 4-point probe resistivity measurements showed that the air-annealed samples are insulating, whereas oxygen-annealed samples exhibit metallic conductivity.

These observations support the following conclusions: that control of the chemistry and structure of thin films of $LaCuO_{3-x}$ can be obtained by the careful selection of deposition parameters and post-annealing conditions, and that the ability to probe the properties of these different structure-types may prove important to understanding the underlying mechanisms behind the properties of layered cuprate systems.


PRINCIPAL PUBLICATION AND AUTHORS

Phase Control in Thin Films of Layered Cuprates, H. H. Sønsteby (a), J. E. Bratvold (a), K. Weibye (a), H. Fjellvåg (a) and O. Nilsen (a), *Chem. Mater.* **8,** 1095 (2018), doi: 10.1021/acs.chemmater.7b05005.

*(a) University of Oslo, Department of Chemistry (Norway)*

REFERENCES

Sønsteby *et al.*, *Adv. Mater. Interfac.* **4**, 1600903 (2017).
Sønsteby *et al.*, *Chem. Comm.* **54**, 8253 (2018).


# CLEAN SEMICONDUCTOR BEHAVIOUR OF PEROVSKITE SOLAR CELLS PROBED BY SIMULTANEOUS CURRENT-VOLTAGE AND GIWAXS MEASUREMENTS

**By employing simultaneous *in-situ* GIWAXS and *operando* current-voltage measurements on metal-halide perovskite interdigitated-back-contact (IBC) solar cells, the remarkably clean semiconductor behaviour of perovskites films is shown to emerge in the earliest phase of conversion from the as-coated precursor film.**

Perovskite photovoltaics (PV) is one of the fastest-growing optoelectronic technologies, with device efficiencies currently exceeding 23% and with potential for low-cost production **[1]**. To further improve device performance, researchers are exploring a variety of optimisation strategies, such as thermal engineering. For most solution-processed perovskite materials, annealing

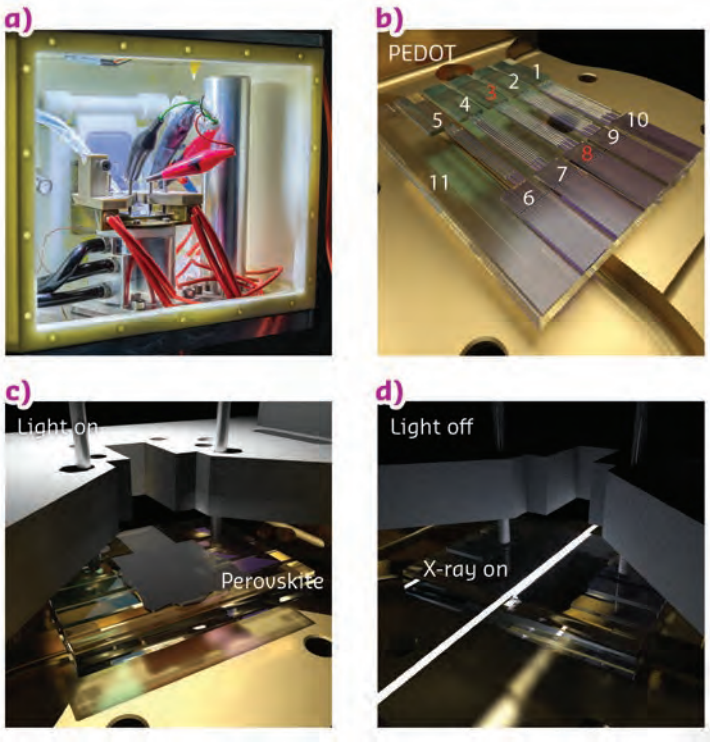


**Fig. 142:** Illustration of the measurement setup. **a)** Annealing chamber. **b)** Illustration of ITO interdigitated substrate electrodeposited with PEDOT (electrodes 1-5) and $TiO_2$ (electrodes 6-10). Electrode 11 is bare ITO. **c)** Illustration of the experimental setup for current-voltage sweeps performed *in situ* without X-rays. **d)** Illustration of the setup for diffraction pattern measurement (light off) with a 10 keV X-ray at grazing incidence.

temperature and duration are critical factors for optimised conversion of the as-coated precursor material into a functional polycrystalline perovskite film **[2]**. Optimisation is performed by recording current-voltage (JV) sweeps of a complete device placed on a hotplate under simulated solar illumination during annealing. However, this method is not feasible for perovskite solar cells because the perovskite material must be annealed before further layers completing the device can be deposited. Other solutions, including pre-annealing and completing the device stack, then measuring *ex situ* several solar cells for different annealing periods, are extremely time-consuming.

This work employs a new investigation method (**Figure 142**) that significantly reduces the workload required in the thermal engineering of perovskite solar cells and, at the same time, establishes a direct correlation between their opto-electrical and structural properties during annealing *in situ*. This is achieved by exploiting the concept of interdigitated back-contact (IBC) solar cells. Here the electron ($TiO_2$) and hole (PEDOT) selective electrodes are co-positioned on the back of the cell in an interdigitated fashion (**Figure 142b**) **[3]**. The main advantage of IBC solar cells is that the perovskite layer represents the final step of the device fabrication. Because the perovskite film is unobstructed by any top layer, *in-situ* annealing does not compromise the film formation. The perovskite film is

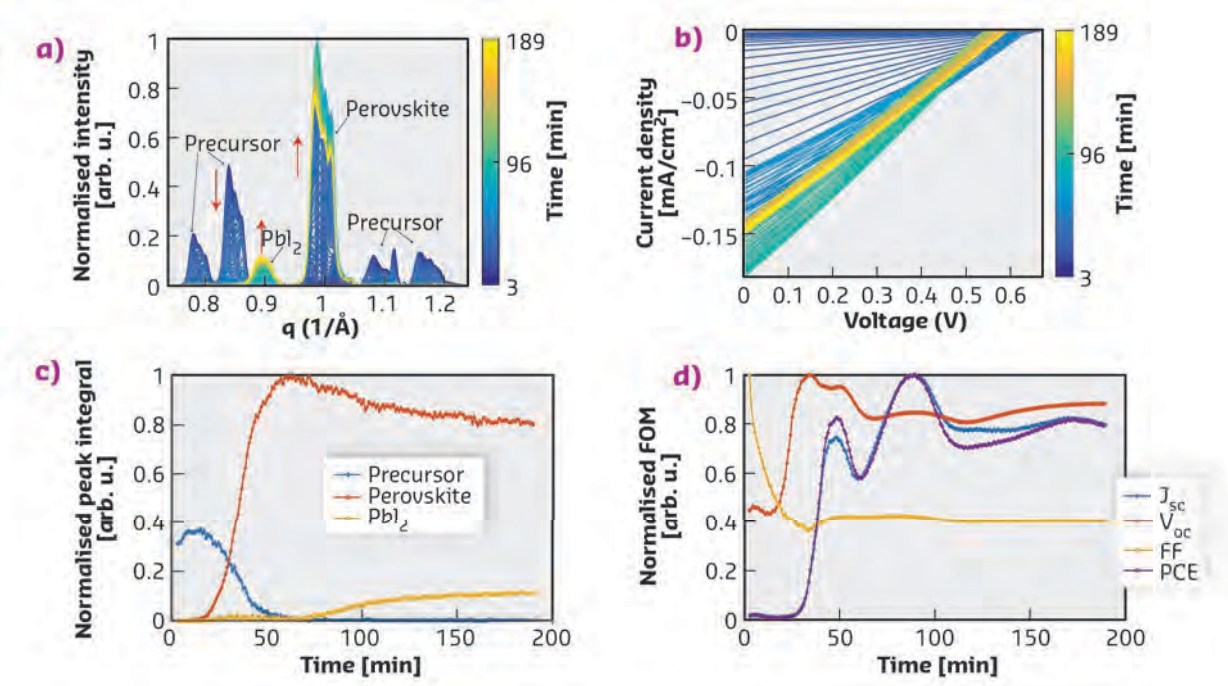


**Fig. 143:** Structural and opto-electrical parameters extracted from simultaneous GIWAXS diffraction patterns (under dark conditions) and current-voltage (under light conditions) measurement of perovskite ($CH_3NH_3PbI_3$) IBC solar cell during *in-situ* anneal at 88.2°C. **a)** Azimuthally integrated line profiles versus annealing time. **b)** IBC solar cell current-voltage sweeps measured under light. **c)** Integrated peak intensities of the second precursor peak, perovskite, and $PbI_2$ versus annealing time. **d)** Normalised FOM versus annealing time.

directly accessible by an X-ray beam, making IBC devices a great solution for simultaneous opto-electrical and grazing incidence wide-angle X-ray scattering (GIWAXS) measurements performed *in situ* during annealing. Using the setup at beamline **BM28**, this high-throughput thermal engineering route can be used on a variety of perovskite materials, along with the possibility of establishing a direct correlation between the figures-of-merit (FOM) of a solar cell and its structural properties.

**Figure 143** shows a summary of the photovoltaic and structural measurements on $CH_3NH_3PbI_3$ ($MAPI_3$) perovskite IBC solar cells. The remarkably clean semiconductor behaviour of perovskites is demonstrated by the high photovoltages measured at the first stages of perovskite conversion from precursors, at the percolation threshold for bulk conductance. Open circuit voltages ($V_{oc}$) reach maximum value before the precursor has fully converted into perovskite, when the fraction of precursor and perovskite crystals are comparable (**Figure 143c-d**). Short circuit currents ($J_{sc}$) and power conversion efficiencies (PCE) follow a trend similar to that of the perovskite peak intensity extracted from the GIWAXS measurements.

The behaviour of the FOM versus annealing time of IBC devices compares well with analogous profiles of conventional planar heterojunction solar cells, and these results can be generalised for other perovskite precursor routes (*e.g.*, $MAPbI_3$ prepared from MAI: $PbAc_2$, as well as the triple mixed cation $Cs_{0.5}(MA_{0.17}FA_{0.83})_{0.95}Pb(I_{0.83}Br_{0.17})_3$ (FA = formamidinium), and the mixed cation $(FAI)_{1.0}(MABr)_{0.2}(PbI_2)_{1.1}(PbBr_2)_{0.20}$). This measurement strategy is not limited to perovskite materials and is of interest for any solution-processable photovoltaic technology requiring thermal annealing.

PRINCIPAL PUBLICATION AND AUTHORS

*In situ* Simultaneous Photovoltaic and Structural Evolution of Perovskite Solar Cells During Film Formation,
M. Alsari (a), O. Bikondoa (b), J. Bishop (c), M. Abdi-Jalebi (a), L. Y. Ozer (d), M. Hampton (e), P. Thompson (f), M. Hoerantner (g), S. Mahesh (g), C. Greenland (c), J. E. Macdonald (e), G. Palmisano (d), H. J. Snaith (g), D. G. Lidzey (c), S. D. Stranks (a), R. H. Friend (a) and S. Lilliu (c, h),
*Energy Environ. Sci.* **11**, 383–393 (2018); doi: 10.1039/c7ee03013d. Article and figures adapted from this publication. CC by 4.0. Reproduced by permission of The Royal Society of Chemistry.
*(a) Cavendish Laboratory, University of Cambridge (UK)*
*(b) Department of Physics, University of Warwick (UK)*
*(c) Department of Physics and Astronomy, University of Sheffield (UK)*
*(d) Department of Chemical Engineering, Khalifa University of Science and Technology, Masdar Institute, Abu Dhabi (UAE)*
*(e) School of Physics and Astronomy, Cardiff University (UK)*
*(f) University of Liverpool (UK)*
*(g) Clarendon Laboratory, Department of Physics, University of Oxford (UK)*
*(h) The UAE Centre for Crystallography (UAE)*

REFERENCES

[1] H. J. Snaith and S. Lilliu, *Scientific Video Protocols* **1**, 1 (2018).
[2] S. Lilliu *et al., Cryst. Eng. Comm*. **18**, 5448–5455 (2016).
[3] L. M. Pazos-Outón *et al., Science* **351**, 1430–1433 (2016).

# CLUSTER BONDING IN THE SUPERCONDUCTING INTERMETALLIC COMPOUND $Be_{21}Pt_5$

**The complex crystal structure of the intermetallic compound $Be_{21}Pt_5$ features polyhedral cluster units as basic building blocks. Chemical bonding analysis in position space reveals their connection to the electronic structure and the multi-centre bonding in this fascinating group of compounds.**

Complex intermetallic compounds form periodic crystal structures containing hundreds to thousands of atoms per unit cell. The structure determination and the understanding of the chemical bonding in these intermetallic compounds remain challenging. Traditionally, the Hume-Rothery electron concentration rules are often used to explain the stabilisation of these complex structures, which suffer from a low number of valence electrons per atom **[1]**. However, the geometrical description of the crystal structure by means of so-called clusters, which is widely used in literature, has little connection to this reciprocal space approach.

Compounds of beryllium are a scarcely explored research field due to the difficult characterisation and handling. In this work, the new compound $Be_{21}Pt_5$ is synthesised and its crystal structure determined employing synchrotron and neutron

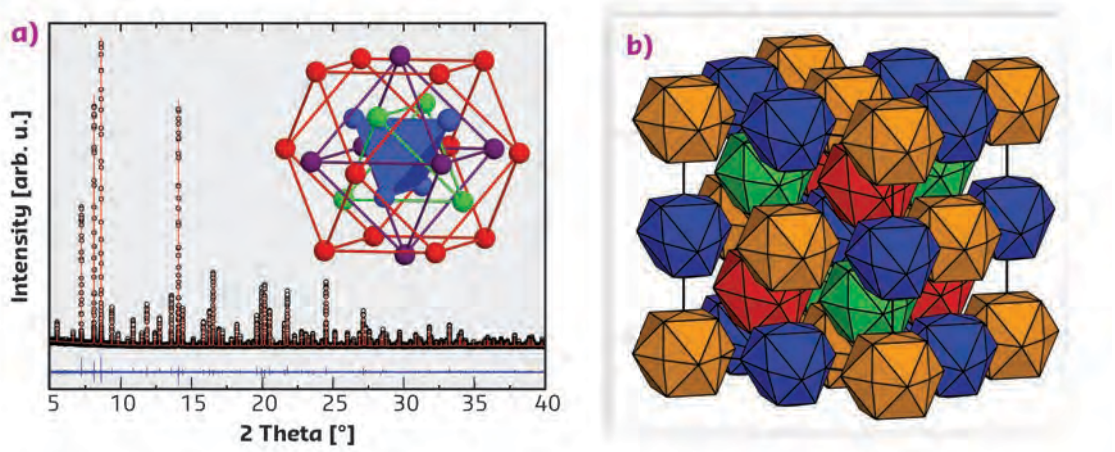


**Fig. 144: a)** Synchrotron powder diffraction pattern of $Be_{21}Pt_5$ recorded at BM20 with calculated profile (red) and difference plot (blue). Inset: Arrangement of atoms on consecutive polyhedra shells within the 26-atom cluster. **b)** Crystal structure of $Be_{21}Pt_5$. Arrangement of the four cluster types in the unit cell, represented by their outer cuboctahedron shell.

powder diffraction. Analysis of the chemical bonding using a position space approach revealed an insight into the relation between the observed cluster units and their role in chemical bonding.

The compound $Be_{21}Pt_5$ was prepared by arc-melting of the elemental metals and crystallises in a cubic structure with lattice parameter $a$ = 15.9042 Å. The high-resolution synchrotron powder diffraction data, recorded at beamline **BM20**, enabled structure solution in the space group $F\bar{4}3m$ (**Figure 144a**). Neutron diffraction data were used to complete the structure and refine the positions of the light beryllium atoms next to platinum.

The 416 atoms in the unit cell can be attributed to four types of cluster units, each containing 26 atoms. Atoms in the clusters are arranged on the vertices of four nested polyhedra shells, namely an inner tetrahedron, surrounded by the dual outer tetrahedron, inscribed in an octahedron and a cuboctahedron as the most outer shell (inset to **Figure 144a**). Two of the cluster types (orange and blue in **Figure 144b**) form a NaCl-like lattice and the two other cluster types (red and green) are at the centres of the formed cubes. The four cluster types differ in the ordering of Be and Pt atoms on the polyhedra shells, which is governed by the avoidance of direct contact between Pt atoms, leading to the large translational period. This is in line with the expected charge transfer from Be to Pt as confirmed by evaluation of the calculated electron density.

Analysis of the electron localisability indicator (ELI-D) in position space, whose maxima are interpreted as signatures of chemical bonding, gave insight into the interactions in $Be_{21}Pt_5$ **[2]**. ELI-D maxima at the centre of the cluster units, drawn in orange in **Figure 145**, indicate multi-centre intra-cluster bonding with contributions from up to 14 atoms of the respective cluster. These structural motifs are linked by regions of polar three-centre inter-cluster bonding, drawn as green domains in **Figure 145**. The extensive multi-centre bonding is a consequence of the low number of valence electrons available for bonding. Unexpectedly, $Be_{21}Pt_5$ is superconducting (with $T_c$ = 2 K), which is rarely observed for compounds with such complex crystal structures.

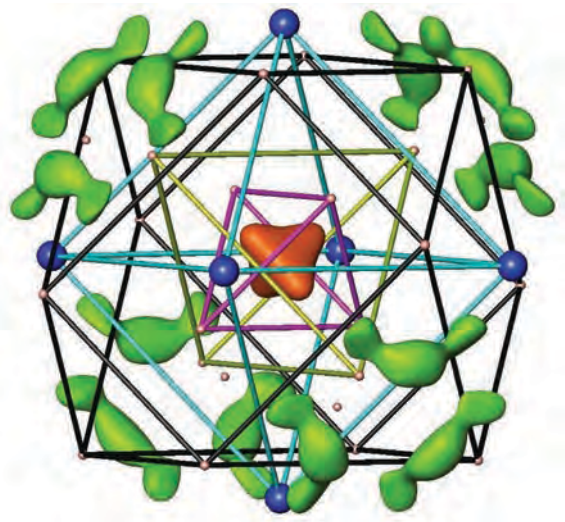

**Fig. 145:** Distribution of the electron localisability indicator (ELI-D) around a cluster unit. Domains in orange contain only contributions from atoms within the cluster (intra-cluster bonding), while domains in green contain contributions from atoms of neighbouring clusters (inter-cluster bonding). Platinum atoms in blue and beryllium atoms in orange.

The observed cluster bonding is a newly described interaction that opens a new avenue to understanding the chemical bonding in complex intermetallic compounds and ascribes chemical meaning to the traditional structure description based on cluster units.

## PRINCIPAL PUBLICATION AND AUTHORS

Cluster Formation in the Superconducting Complex Intermetallic Compound $Be_{21}Pt_5$, A. Amon (a), A. Ormeci (a), M. Bobnar (a), L. G. Akselrud (a, b), M. Avdeev (c), R. Gumeniuk (d), U. Burkhardt (a), Y. Prots (a), C. Hennig (e), A. Leithe-Jasper (a) and Y. Grin (a), *Acc. Chem. Res.* **51**, 214–222 (2018), doi: 10.1021/acs.accounts.7b00561.
*(a) Max-Planck-Institut für Chemische Physik fester Stoffe, Dresden (Germany)*
*(b) Ivan-Franko National University, Lviv (Ukraine)*
*(c) Australian Nuclear Science and Technology Organisation, Sydney (Australia)*
*(d) Technische Universität Bergakademie Freiberg, Freiberg (Germany)*
*(e) Helmholtz-Zentrum Dresden-Rossendorf, Dresden (Germany)*

## REFERENCES

[1] A. T. Paxton *et al., Proc. Royal Soc. Lond.* **453**, 1493 (1962).
[2] M. Kohout, *Faraday Discuss.* **135**, 43 (2007).

# INDUSTRIAL RESEARCH

2018 has been an extremely successful year for the ESRF in terms of commercial activities: commercial income has increased dramatically to over 3 million euros. This is thanks to higher demand for beam time as well as sales in instrumentation. Clients carried out more experiments than usual in the run-up to the pause in operation last December, perhaps to compensate for the 18 months of shutdown to install the Extremely Brilliant Source. Commercial access in 2018 was requested across a diverse set of sectors and over a wide range of beamlines.

Interestingly, while the most requested beamlines for imaging and protein crystallography confirmed and exceeded their industrial support, several beamlines traditionally less solicited by industry were also involved in commercial access. This shows that industrial demand can go beyond mainstream techniques, and that industrial needs can benefit from the most advanced capabilities offered by ESRF beamlines, even those usually considered as the domain of academic users. To give a few examples, a large automotive firm purchased X-ray Raman analysis on **ID20** to obtain a unique insight into the chemistry of batteries in *operando* conditions. Furthermore, the time-resolution capabilities of **ID09** have proved critical to providing important understanding on the radiation hardness of electronic components for the space environment. Finally, thanks to the performances and increased capacity allowed by a high-throughput instrument developed in collaboration with the IRT Nanoelec (www.irtnanoelec.fr), **BM05** has been very active in 2018 in serving the market of semiconductor substrates and monocrystals using topography.

This success goes hand in hand with outreach towards industry, including involvement in a range of European and national projects, such as NFFA (www.nffa.eu) and CALIPSOplus (www.calipsoplus.eu), developing more visibility for the ESRF and light sources in general. This close collaboration was also in evidence during the event Synergi2018 (https://synergi2018.b2match.io), held with the lead organisers of SINE2020 (www.sine2020.eu), and CALIPSOplus. Synergi2018 was held in Amsterdam, focusing on materials science and showing off what light and neutron sources can do for industry. We look forward to working together with our partners on Synergi2019, in Lyon, on chemistry!

Our CARAC workshop, highlighting Grenoble's portfolio of characterisation facilities, is now an annual event and is invaluable in putting facilities on the map for local and regional companies. This year, we were also delighted to be part of the 'Research Infrastructure Village' at the annual CARNOT event (https://rdv-carnot.com) for R&D and business, held in Lyon. Around 15 research infrastructures took part in the event, overseen by the French Ministry for Higher Education and Research. Again, we are looking forward to future editions of this village with even more visibility.

As well as European projects, the ESRF is also increasingly working in partnership with companies that specialise in helping clients to use advanced research infrastructures, such as Novitom. In this context, 2018 has been the first year that we have worked with the company Xploraytion, run by a former ESRF scientist with a strong background in bio-imaging. This collaboration has led to new contacts and the organisation of a workshop on how synchrotron X-rays can help the biomedical industry.

Another new collaboration is our partnership with Finden, a company providing analytical and scientific consultancy services, based in the United Kingdom. The Business Development Office (BDO) travelled to the headquarters of the chemical company BASF with the management team of Finden and key ESRF scientists to highlight the research possibilities in coatings and catalysts that the ESRF offers. Finden is an expert in spectroscopy and works with companies all over the world.

**Alliances with other research organisations**

As mentioned earlier, thanks to European projects, the ESRF has established tight links with other research infrastructure families, which has allowed us to reach bigger audiences. An example of these alliances is the European Analytical Research Infrastructures Village (www.eariv.eu), a joint initiative led by a set of transnational Horizon 2020 projects and regional initiatives that promotes opportunities for industry to interact with European large-scale analytical research infrastructures. EARIV is a network of eight projects, with 30 analytical research infrastructures spread across Europe, working together to develop a stronger regional integration with industry.

At the moment, EARIV is used as a marketing and visibility tool, drawing together resources from different stakeholders. It remains to be seen in which directions EARIV may go in the future as the European projects are completed. It could evolve into a tool for industry to quickly and easily connect with relevant experts and exploit the most appropriate, state-of-the-art research infrastructure tools.

Collaboration with the European Spallation Source, MAX IV and the Institut Laue-Langevin led to a workshop at the headquarters of Sandvik AB, a high-technology Swedish company specialised in tools and tooling systems for metal cutting, mining and rock excavation equipment, as well as stainless steel and special alloys. The workshop focused on how synchrotron X-rays and neutrons could help Sandvik's R&D needs in metallurgy and included case studies of research presented by scientists of the facilities. This enabled thorough discussions between Sandvik scientists and researchers from the facilities about specific challenges that Sandvik faces in its research and development programme.

**During the shutdown**

The shutdown for the installation of EBS is already upon us, but commercial work goes on with knowledge and technology transfer, and the manufacture and sale of advanced instrumentation. We also assist our beamtime clients to find other synchrotron sources able to support their R&D while we are closed. Although the beamlines are not available during the long closure, the CM01 cryo-electron microscope is still operational and available for commercial clients, as are all of the ancillary ESRF laboratories. These have been used, for example, to help support Synthelis, a local biotech, in a gene-to-structure pipeline in partnership with both ESRF and the EMBL Grenoble Outstation (see **page 153**).

The BDO team will be as busy as ever during the temporary closure, with a strong programme of outreach planned. We will keep in touch and provide news as the progress of the EBS moves forward, and we look forward to welcoming our clients, old and new, to the all-new ESRF in 2020.

**E. MITCHELL AND M. CAPELLAS ESPUNY**

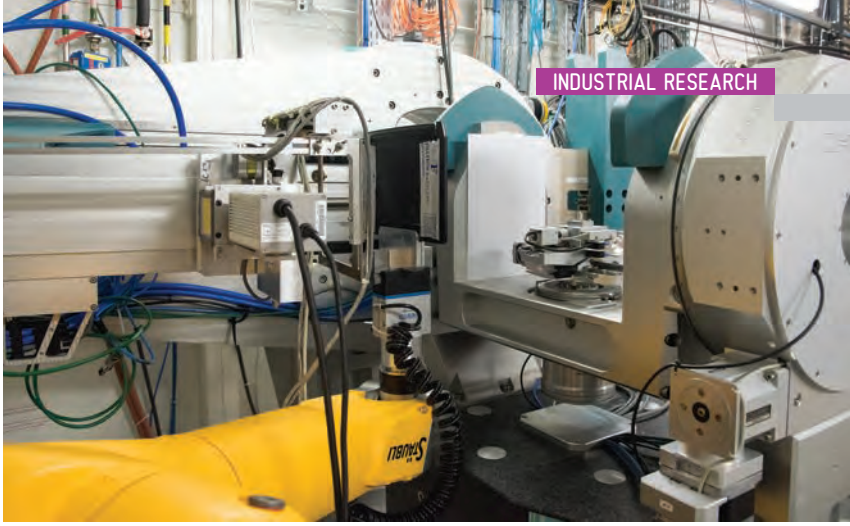


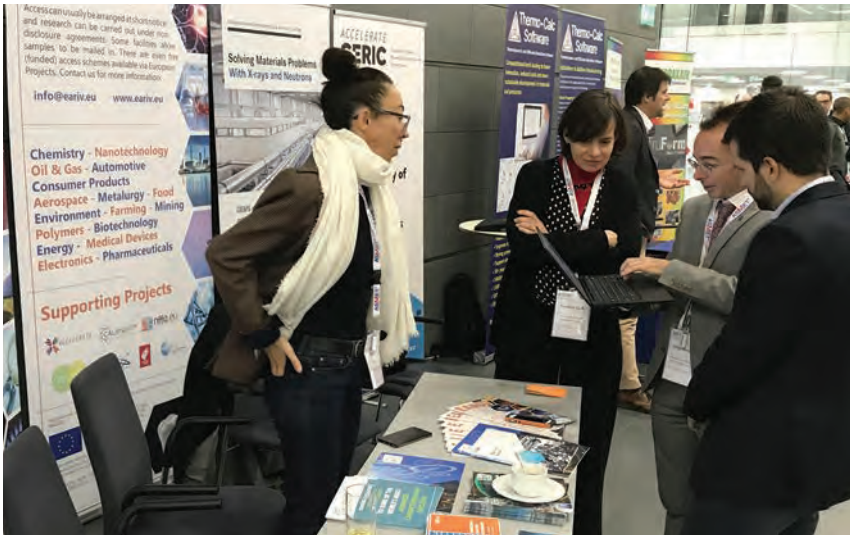



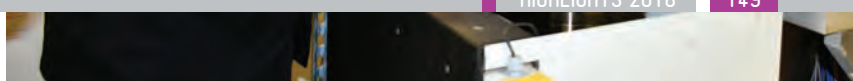

# INDUSTRIAL RESEARCH ON THE BEAMLINES

**Due to its proprietary nature, much of the commercial research carried out by industry at the ESRF cannot be disclosed. However, sometimes companies authorise the ESRF to discuss their work and they may even publish results or access the ESRF via the public programme. Below are a few examples from 2018.**

## IMPROVED THROUGHPUT OF TOPOGRAPHY AT BM05 USING ROBOTICS

As part of the IRT Nanoelec project, **BM05** integrated a new diffractometer in 2015 (**Figure 146**), resulting in topography measurements with higher precision and more varied experimental configurations. A six-axis robot was also installed, allowing automatic sample changing that can be synchronised with multi-image data acquisition sequences under software control, as well as automating the process of loading the X-ray-sensitive films required for high spatial resolution, large sensitive area imaging during white-beam topography experiments.


**Fig. 146:** The IRT diffractometer and robotic sample changer have sped up topography experiments at BM05, increasing its attractiveness for industrial clients.

The procedures involved in manually acquiring a single topography image take ~10 minutes – this is reduced to less than four minutes with the robot. As well as saving time, the need for manpower is greatly reduced. The diffractometer is well adapted for the characterisation of large samples, *e.g.* solar cells or quartz crystals (which may reach 5 kg). Six motorised axes enable the whole surface of a 200 x 200 $mm^2$ solar cell to be oriented in the X-ray beam and mapped.

Another example of topography measurements already carried out is the identification of local defects in 4 x 4 $mm^2$ synthetic diamond plates. To minimise the time and risks involved in changing these delicate samples, a support plate has been manufactured to hold an array of individual diamond samples by vacuum retention. The support plate is made of glassy carbon, a material that is both amorphous and near-transparent to the X-ray beam. Diamonds are loaded into the plate in a laboratory and then mounted on the diffractometer. Using the robot to change the X-ray films and position the support plate enables scientists to measure 20 diamonds sequentially.

The team at BM05 has used these systems for the measurement of silicon photovoltaic cells, diamonds, quartz, cadmium telluride and other crystals. The increase in efficiency and reduction in manpower required makes BM05 an attractive and cost-effective tool at the ESRF, both for scientific and commercial research.

# AIRBUS TESTS RADIATION RESISTANCE ON INTEGRATED CIRCUITS FOR SATELLITES

When satellites are sent to space, they sustain considerable stress from cosmic radiation and solar particles. The electronic components used inside satellites can malfunction if they are not robust enough against these ionising particles. Until now, engineers from Airbus had tested these components in cyclotron facilities, under heavy ions. Most of the cyclotrons provide high linear energy transfer of heavy ions, which are not capable of penetrating through significant thicknesses of materials. The advantage of synchrotron sources, then, is that X-rays can penetrate into different layers.

Following successful studies over the past 10 years, where scientists used X-ray beams to simulate the effects induced by heavy ions on planar devices, the team at Airbus decided to test out this methodology at the ESRF. At beamline **ID09**, they submitted 3D stacked memory devices to single pulses of X-rays and monitored how the device behaved (**Figure 147**).

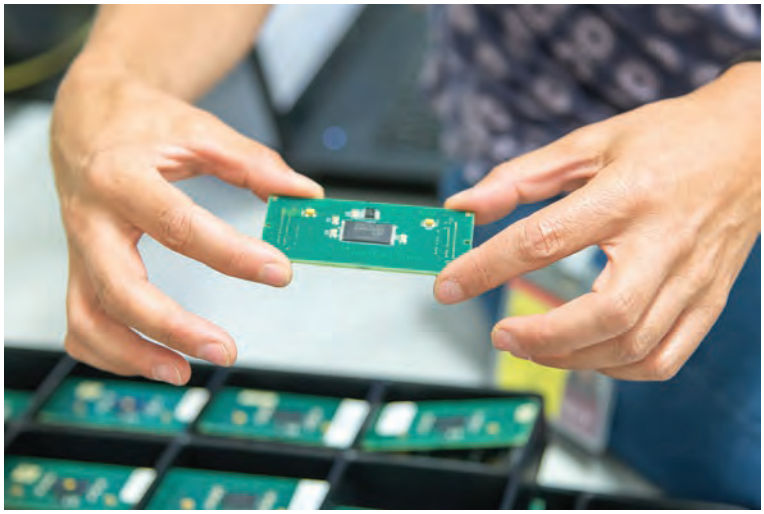

**Fig. 147:** The 3D stacked memory devices from satellites tested on ID09 for resistance to radiation.

This project is partly funded by DEMETER, an ECSEL Joint Undertaking, and a EU-driven, public-private partnership, funding innovation in electronic components and systems.

# CHARACTERISING 3D INTEGRATION SYSTEMS IN MICROELECTRONICS

In the microelectronics industry, one way to make devices smaller is to stack wafers vertically rather than horizontally – a method called 3D integration. This geometry requires new connections in order to transmit information between the different parts of the device: one such connection is copper pillars. During the assembly process, nano-to micrometre-sized defects and voids can appear in the pillars, changing their electrical and mechanical behaviour. Being able to characterise these often-inaccessible parts of the device is the key to the success of 3D integration.

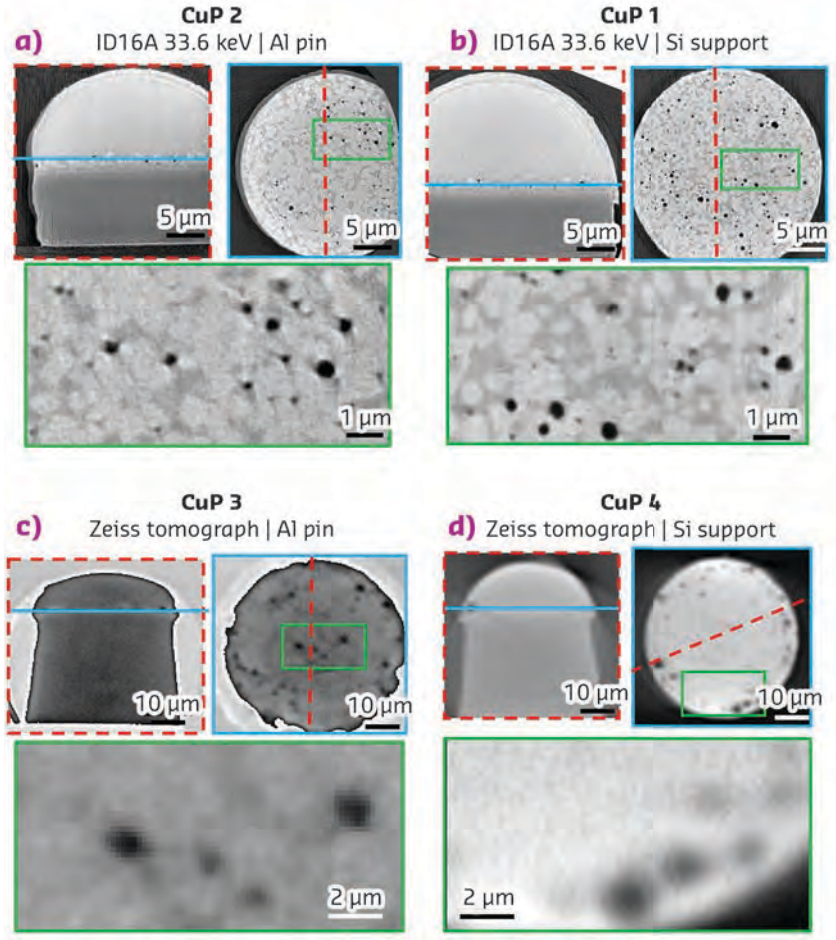


**Fig. 148:** The influence of the sample geometry on the reconstructed volumes. Figures **a)** and **b)** show results obtained from tomographies on ID16A, with copper pillars respectively isolated on an aluminium pin (CuP 2) and placed on a silicon support (CuP 1). Figures **c)** and **d)** show results from the lab tomograph, with similar sample geometries (resp. CuP 3 and CuP 4). Each figure contains an XZ view of the pillar (frame indicated by dashed red line), an XY view of the interface containing voids and intermetallic alloys (frame indicated by solid blue line), and a zoom-in view of the latter (frame indicated by solid green line).

A team of researchers from the CEA, ST Microelectronics and the ESRF investigated different techniques to characterise in 3D the copper pillars used in 3D integration. Computed tomography carried out on beamline **ID16A** offered vital information about the voids present in the pillars and about the intermetallic shapes (**Figure 148**). The contrast in synchrotron tomography makes it easy to segment the voids inside the final volume.

The next step for the team is to investigate how laminography combined with ptychography can further optimise 3D characterisation. This work was possible thanks to the support of the IRT Nanoelec and the ESRF.

PRINCIPAL PUBLICATION AND AUTHORS

3D high-resolution imaging for microelectronics: A multi-technique survey on copper pillars, A. Fraczkiewicz *et al.*, *Ultramicroscopy* **193**, 71–83 (2018); doi: 10.1016/j.ultramic.2018.04.012.

# MAKING SOLID OXIDE CELLS MORE DURABLE

Solid oxide cells (SOC) are promising energy conversion devices that can be used to produce electricity (fuel cell mode) or to produce hydrogen that can be stored for later energy demand (electrolysis mode). This technology offers high conversion efficiency due to the high operating temperature. However, degradation rates (cell voltage loss at a constant current density over time) are still too high to consider large-scale deployment of this technology.

Processes such as electrode poisoning, material instabilities, interdiffusion and reactivity, all caused by high operating temperatures, are thought to be behind this degradation. Also, the component of the $H_2$ electrode, Ni-YSZ cermet, is known to change its structure during operation, which could play a significant role in SOC deterioration.

In the framework of two projects funded by the European Union, SOLIDpower, a leading company in the field of high-temperature fuel cell technology, worked with scientists from the CEA and the ESRF to investigate the microstructural degradations after operation in electrodes. Following long-term durability tests at the CEA in fuel cell and electrolysis modes at high temperature (750 and 850 °C), samples from aged electrodes were taken to beamline **ID16A,** where X-ray nanotomography was used to study the microstructural evolution of the Ni-YSZ composite **(Figure 149)**.

The 3D analysis of the data revealed a nickel agglomeration after operation. The reorganisation of the nickel phase induces a decrease of the electrochemically active sites, which directly affects the SOC performances. The growth of the nickel particle was also found

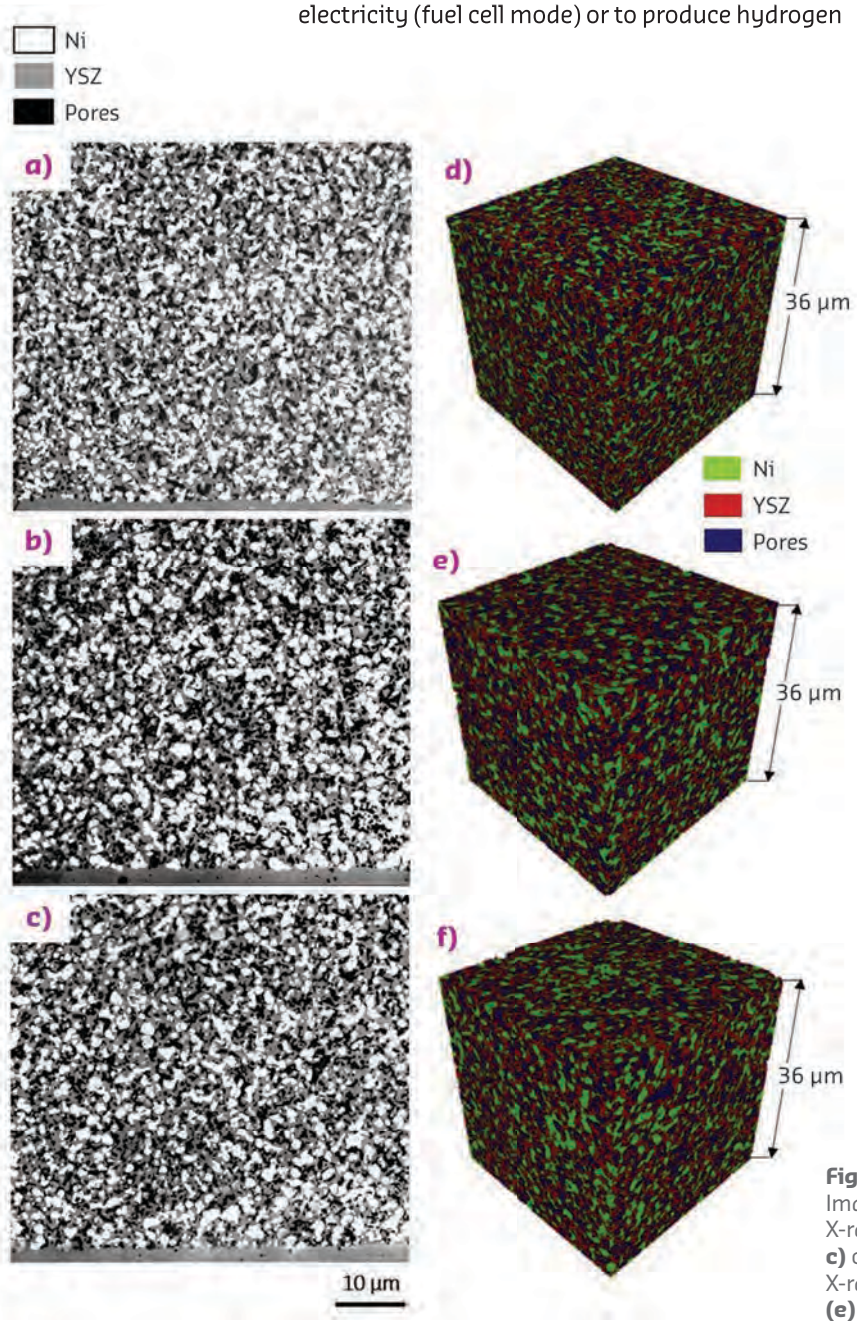


**Fig. 149:** Post-mortem characterisation of the $H_2$ electrode. Images of the electrode/electrolyte interface, obtained by X-ray nanotomography, for **a)** the pristine cell, **b)** cell 4 and **c)** cell 5. The corresponding volume renderings obtained by X-ray nanotomography are presented for **(d)** the pristine cell, **(e)** cell 4 and **(f)** cell 5.

to be thermally activated. Simulations of nickel coarsening using a sintering model show that microstructural changes in the $H_2$ electrode explain ~30% of the total degradation in fuel cell mode and ~25% in electrolysis mode at 850 °C after 1000–2000 hours of operation.

PRINCIPAL PUBLICATION AND AUTHORS

Impact of Nickel agglomeration on Solid Oxide Cell operated in fuel cell and electrolysis modes, M. Hubert *et al., J. Power Sources* **397**, 240–251 (2018); doi: 10.1016/j.jpowsour.2018.06.097.

## A UNIQUE GENE-TO-STRUCTURE SERVICE WITH SYNTHELIS

Synthelis is a Grenoble-based biotech with expertise in producing proteins that would otherwise be difficult or impossible to prepare. The company has teamed up with two EIROforum organisations, the EMBL Grenoble and the ESRF, to build an innovative gene-to-structure pipeline, exploiting the EMBL's crystallisation platform and the ESRF's diffraction analysis pipelines and protein purification expertise and equipment.

Synthelis acts as project manager, coordinating between its client and the laboratories at the institutes. In return, the ESRF and EMBL bring in expertise and access to equipment and technology for protein crystallography and diffraction analysis. The first client project drawing upon Grenoble's rich tapestry of structural biology expertise and platforms is now underway.

## PAC-G AND SERMA TECHNOLOGIES PROVIDE INDUSTRY WITH ADVANCED CHARACTERISATION

In 2018, the members of Platform for Advanced Characterisation – Grenoble (PAC-G), with the support of the IRT NanoElec, signed a first agreement with SERMA Technologies, a service and consulting company in the micro- and nano-electronics market (**Figure 150**).

The goal of this agreement is to provide innovative solutions, based on SERMA Technologies' knowledge of customer needs in the electronics market and on the PAC-G members' expertise in advanced characterisation. The partnership provides a key link from the market to advanced techniques to look inside materials, in order to open the way for new microelectronics devices.


**Fig. 150:** Jean Susini, director of research at the ESRF, following the signature of a partnership between PAC-G and SERMA Technologies to make advanced characterisation techniques available to industry.

# ENABLING TECHNOLOGIES

During the keystone year of 2018, the technical divisions have deployed all efforts to finalise the preparation of the Extremely Brilliant Source (EBS) storage ring installation. At the same time, work on major beamline and instrumentation projects was ramped up and several projects entered the implementation phase. A concise overview of EBS activities can be found in the Status of the EBS chapter of the Highlights (**page 8**).

The contributions in the present chapter give a flavour of the wide range of activity in technology developments, from a novel design of EBS vacuum chambers over a formalism to describe partially coherent X-rays in a quantitative fashion, to software developments in the crucial area of data analysis. The first two articles relate to the EBS storage ring. The first describes a novel vacuum chamber design, using bi-metallic explosion bonding between the steel and aluminium parts (**page 156**). The second one presents the new timing system for the EBS source, which was developed in-house and is based on the 'White Rabbit' technology from CERN (**page 157**). The third article nicely illustrates how complementary expertise from two research infrastructures can push technological limits further: thanks to a collaboration between the Paul Scherrer Institute (PSI) in Switzerland and the ESRF, the 500k and 2M PSI-EIGER detectors can now operate at frame rates of up to 22 kHz, a record for this type of detector (**page 158**). The fourth contribution underlines the importance of going beyond geometrical optics approaches to simulate partially coherent X-ray sources in order to predict the performance of optical elements and to provide crucial input to coherent imaging and scattering experiments (**page 160**). The last two highlights reflect the significant effort the ESRF has put into implementing a powerful and sustainable data analysis programme. A software toolkit, called silx, has been created to simplify the development and maintenance of scientific applications (**page 161**). For example, Crispy (**page 162**), a programme to calculate inner-shell spectroscopy spectra and ground state properties, uses the silx library for visualisation and for reading and writing data.

In addition to the results presented in the Highlights articles, 2018 has witnessed many other important accomplishments and activities in various technological areas:

In the frame of the detector development plan, beamline tests were conducted with the JUNGFRAU detector, in collaboration with colleagues from PSI, to evaluate the detector capabilities for storage ring applications, and several collaboration agreements with other European laboratories were signed. The liquid phase epitaxy laboratory improved grinding and polishing capabilities of orthosilicate scintillators, and freestanding 60 µm-thick crystals can now be made.

Regarding X-ray optics developments, 2D aluminium compound refractive lenses (CRL) are now being produced with the new lens press, and work on 1D linear lenses began in summer. The first Si (111) von Hamos crystal analysers with short curvature radius (R = 250 mm) and a series of Si (110) Johansson cylindrical analysers for the new **ID26** TEX spectrometer were manufactured.

The instrumentation beamline, **BM05**, continued to be a strategic tool for instrumentation developments such as the characterisation of detectors, scintillators, and X-ray optical components. In the frame of the H2020 EUCALL project (https://www.eucall.eu/), the BM05 team developed a portable speckle-based wavefront characterisation station and the associated software for the data analysis and wavefront reconstruction. The setup was utilised to perform acceptance tests of purchased CRLs and quality assessment of CRL prototypes.

Further developments of OASYS (http://ftp.esrf.eu/pub/scisoft/Oasys/readme.html), an open-source graphical environment for optics simulation software used in synchrotron facilities, comprised the integration of a software package for calculating coherence, COMSYL, and the upgrade of tools for power calculations.

Mechatronic concepts were incorporated in the prototype double crystal monochromator for spectroscopy and the nano-positioning and active stabilisation stage (NASS) end station for **ID31**. The complete refurbishment of the precision engineering laboratory will be completed in spring 2019.

Tests on cloud software for in-house and external IT provisioning continued in the frame of the CERN-led H2020 HNSciCloud project, a pre-commercial procurement (PCP) initiative engaging the IT industry and major European research infrastructures.

Significant progress has been made on the data policy with the implementation of long-term archiving for 10 years and DOI minting (first DOI: https://doi.esrf.fr/10.15151/ESRF-ES-90378880) for all publicly funded experiments. Twelve beamlines (including the cryo-electron microscope) have implemented the data policy (see http://www.esrf.eu/datapolicy for a list of beamlines), and work for a further six beamlines is in progress. Development of an electronic logbook and a new data portal has started and tests were carried out on some beamlines before the shutdown. Regarding the General Data Protection Regulation (GDPR), a risk assessment and a privacy impact assessment were completed, and software modifications are currently being implemented.

The cryo-electron microscope has been successfully integrated into the ESRF computing infrastructure. Images of 9 GB can now be written to central storage within 12 seconds, while the acquisition typically takes one minute.

The ESRF coordinates two H2020 projects – BEATS and PaNOSC. BEATS centres on the construction of a tomography beamline at SESAME and the long-term sustainability of this unique research infrastructure in Jordan. PaNOSC, standing for Photon and Neutron Open Science Cloud, will focus on FAIR data management principles and connects the participating ESFRI projects to the European Open Science Cloud (EOSC).

Finally, the ESRF continues to federate and coordinate joint developments with other research facilities, such as the IcePAP, TANGO, LImA, ISPyB, and mxCuBE collaborations, to mention only a few. The TANGO collaboration now comprises 11 partners, thus providing sufficient critical mass to initiate software developments of common interest to all partners.

**M. KRISCH AND R. DIMPER**

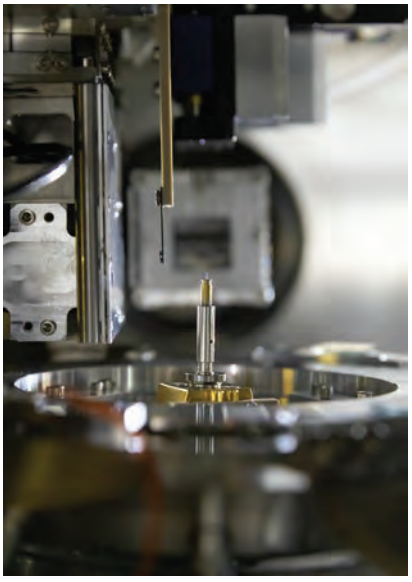

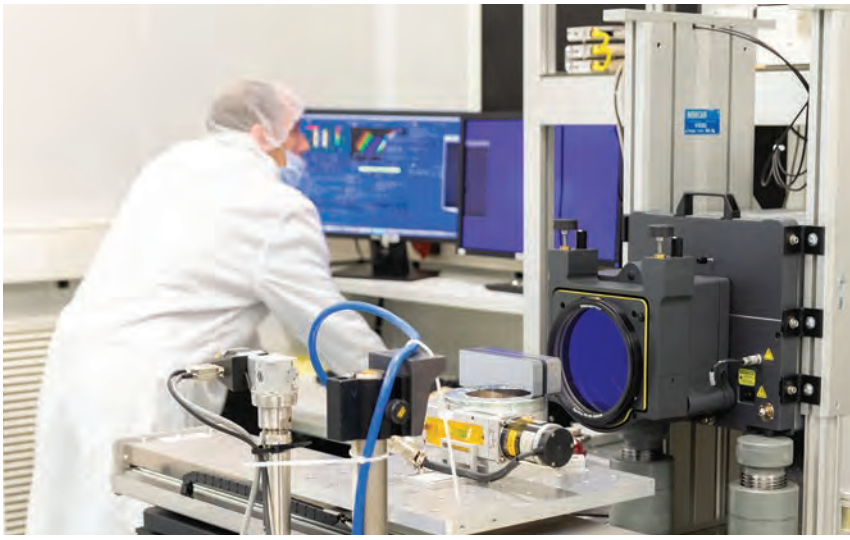

# NEW EBS BIMETALLIC VACUUM CHAMBERS

**Timely delivery of key components for the EBS storage ring is crucial to maintain the tight project schedule. To avoid a bottleneck in the supply of vacuum chambers for the new machine assembly, an additional series of chambers has been designed. This new design also includes bi-metallic explosion bonding zones (steel 316LN/aluminium Al2219).**

The EBS project requires the redesign of various key components of the storage ring, including vacuum chambers. The EBS lattice standard cell consists of 14 different vacuum chambers. One of the main differences between chambers is the design material: some are made of folded stainless steel (SS), some of aluminium (Al) bulk material. The initial design for chambers 6, 7 and 8 (series CH6/7/8) specified folded stainless steel sheets of highly complex geometry with a chamber length of up to 2.6 m. This design proved challenging for production, leading to problems regarding delivery times and dimensional and geometric tolerances. To relieve the tight production schedule and minimise bottlenecks in the supply chain, an additional aluminium chamber design was created: the bi-metallic CH6/7/8 **[1]**.

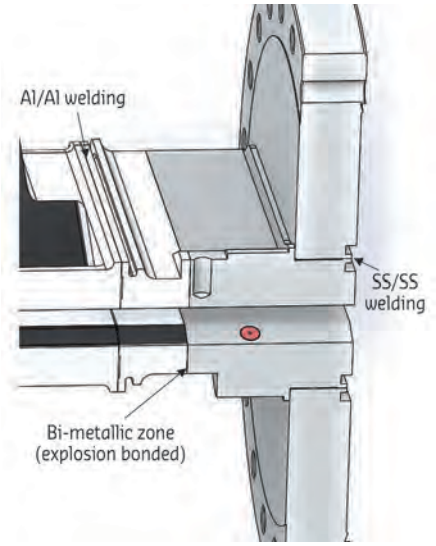


**Fig. 151:** Bi-metallic flange zone of CH8 exit.

The design phase for the new chamber series consisted of the classical iterative mechanical design steps: defining the general dimensions to guarantee the proper functioning and mechanical performances. After each design step, the design is verified by structural mechanical calculations with respect to the resistance against atmospheric pressure and thermal bake-out. Positive experience with the existing high-profile dipole chambers (fully constructed in aluminium) helped significantly during this phase.

This process resulted in the new chamber series design: the chamber bodies consist of two halves, machined out of single blocks of aluminium of up to 2.6-m-long (CH6/CH8). As these chambers contain bellows and beam position monitors (BPMs) made out of stainless steel, a transition between the chamber bodies and the stainless steel flange zones is necessary. This transition is realised by explosion-bonding of the body material, aluminium Al2219, to the flange material, 316LN stainless steel (**Figure 151**). By machining the bodies out of a single block, it is possible to obtain extremely tight tolerances, such as critical flange orientation of ±0.06°, typical body tolerances of ±0.05 mm and a requested flatness of the chambers of ±0.1 mm. The feasibility of these values had already been validated by the manufacturing and testing of the EBS dipole chambers. The chosen manufacturer, CECOM, in Italy, proved to have good experience with explosion bonding, satisfying performance constraints with regards to vacuum leak tightness and mechanical tolerances.

Calculations of under-vacuum deformations of the chamber structure initially revealed high deformations in the beam path section of magnitudes higher than the defined beam stay clear zone of ~1 mm. This issue was solved by adding particular bumps on both chamber halves in the chamber interior far from the beam zone that serve as mechanical struts. As a result, the deformations were lowered to the order of 0.1 mm. Bake-out simulations aiming to maintain a homogeneous temperature over the whole chamber surface of 150 °C ± 20 °C served to define the best routing for heating wires. The free convection of the surrounding air during the chamber bake-out was modelled by assuming a pessimistic convection coefficient of 17 $\frac{W}{m^2K}$ on the outer chamber surfaces.

The first chambers of this series, CH8, were delivered to the ESRF in September 2018. The

**Fig. 152:** Installation test of pre-series CH8 on girder in ESRF-01.

usual site acceptance tests were performed: dimensional checks of all highly important zones, such as absorber flanges and BPM blocks, by the alignment group, revealed very good overall dimensional results. A bake-out with chamber-integrated heating wires under closed-loop control, installed by the vacuum group, also ran well, pumping the chamber down to the required UHV level. The installation test on an equipped Girder 3 in the EBS assembly building, ESRF-01, was successful (**Figure 152**), and the chamber was used soon after to produce a complete girder. Two more chambers of the CH8 aluminium series were delivered in October 2018 and used in the EBS assembly, alleviating the production schedule accordingly.

AUTHORS

P. Brumund, F. Cianciosi and L. Goirand. *ESRF*

REFERENCES

[1] F. Cianciosi *et al., Proc. MEDSI 2018*. Paris, France (2018).

# AN ADVANCED TIMING SYSTEM FOR THE EBS SOURCE

**The ESRF timing system dating from the early 1990s has been upgraded to a state-of-the-art implementation developed in-house and based on the 'White Rabbit' technology from CERN [1]. The new system offers much more flexibility for signal generation and RF distribution, together with high-precision time-stamping capabilities.**

The heart of an accelerator is its timing system. It consists of the equipment that generates and delivers a diversity of clocks, pulses and precise timing information across the facility, such as the signals necessary to bring the electron bunches from the linear accelerator to the storage ring. The ESRF's original timing system was based on a centralised sequencer. From this central device, signals were distributed, duplicated, delayed and formatted in many ways through additional programmable devices, before being delivered to every place necessary for the operation of the machine and the synchronisation of certain time-critical beamline experiments.

The system, dating from the early age of the ESRF, was obsolete and needed refurbishment. Four years ago, the decision was made to replace it with a system better suited to the challenges of EBS, providing time-stamping as a necessary feature as well as a higher level of flexibility. This would not only benefit the accelerator complex but also the beamlines, where more and more experiments will require synchronisation with the new X-ray source. Replacing such a complex system with the facility still in operation could not be done in a single move. The chosen strategy was to devise a solution that allowed a progressive installation, preserving the user delivery schedule and offering the possibility of switching back to the old system.

After an initial prospection phase, the project team retained the White Rabbit technology from CERN for the new system. White Rabbit is an extension of the standard precise time protocol (IEEE 1588), achieving synchronisation of multiple nodes over a 125 MHz synchronous Ethernet network with subnanosecond accuracy. On top of the base technology, it was necessary to implement additional functionality to distribute the radiofrequency (RF) signal, uncorrelated to the White Rabbit clock, across the same network. The solution came from the so-called 'RF over Ethernet' feature, based on the distributed direct digital synthesis (DDDS) technology that allows the local reproduction of a given frequency at every node in parallel. The signal from the master RF clock (352 MHz) is directly connected to a dedicated White Rabbit master node that digitally synthesises the signal and continuously calculates phase and frequency corrections that are regularly broadcast across the whole network. At each node, a phase locked loop regenerates the evolutive RF signal locally. The degradation in the signal induced by this complex process is limited to a phase noise of about 7 picoseconds rms in a 10 Hz–1 MHz bandwidth, whatever the length of the connections between nodes, starting from a master source that exhibits 1 picosecond rms noise.

The implementation of the scheme presented above was possible thanks to the in-house development of the WHIST module **[2]** illustrated in **Figure 153**, which embeds: a) a SPEC board (CERN design) implementing the White Rabbit protocol; providing the embedded processing and resources required for the sequencer implementation, and b) an I/O board supporting RF over Ethernet hardware and various input and output signal connectors in standard ESRF electrical formats. The whole system consists of a set of WHIST modules distributed across the


**Fig. 153:** The WHIST module.

facility, placed close to the signal destinations and interconnected by an optical fibre network. The system is interfaced to the ESRF general communication network and it is configurable and controlled via dedicated TANGO device servers.

The new system was installed next to the original hardware. With limited modifications in cabling, switching between both was possible in about half an hour. This allowed for the progressive and extensive testing of the new timing system during machine-dedicated time (MDT) shifts, while preserving the old one for user mode operation. Since then, the timing network has grown to 14 interconnected WHIST units and, during this phase, it was possible to validate the whole system and test the accelerator in all the available filling pattern modes. In October 2018, it was decided to fully operate the accelerators with the new timing system during user mode, leading to the first implementation of the White Rabbit technology at storage-ring based X-ray sources. The system is now in place and, during the long 2019 shutdown, will be completed with additional modules to replace remaining old cabling and hardware. The timing system will thus be ready for the new EBS storage ring.

AUTHORS

N. Janvier, G. Goujon, A. Broquet, N. Tappret and G. Gautier. *ESRF*

REFERENCES

[1] J. Serrano *et al., Proc. IBIC 2013*, Oxford, UK (2013).
[2] G. Goujon *et al., Proc. ICALEPCS 2017*, Barcelona, Spain (2017).

# INTEGRATION OF HIGH-PERFORMANCE PSI-EIGER DETECTORS AT THE ESRF

**The PSI-EIGER 2D X-ray detectors provide photon-counting detection technology at exceptionally high frame rates. The integration of 500k- and 2M-pixel detectors on ESRF beamlines has required in-house engineering to exploit their full performance. Today, they are employed at frame rates of up to 22 kHz, a record for this type of detector.**

The EIGER detector is a fast photon-counting hybrid pixel detector developed at the Paul Scherrer Institute (PSI) in Switzerland for diffraction and scattering experiments. It is based on a 75-µm, square-pixel readout chip of the same name **[1, 2]**, bonded to a pixelated semiconductor sensor. A detector module consists of an 8 x 4 $cm^2$ single sensor connected to eight readout chips, and several modules can be tiled together to cover larger areas. Each pixel integrates a photon counter that can be configured with a variable number of bits. Extending the counter depth increases the dynamic range, but also increases the chip readout time and reduces the achievable frame rate, which can reach 22 kHz in the case of 4-bit operation. Although there are commercial detectors based on the same readout chip **[3]**, those devices do not fully exploit its capabilities. With this in mind, the ESRF established a collaboration with PSI aimed at integrating their higher performance modules on the ESRF beamlines and exploiting their full potential.

Currently, two variants of the PSI-EIGER detectors are in use at the ESRF: a half megapixel EIGER-500k (**Figure 154**), which is a single module device used at **ID02** and **ID10**, and a two-megapixel EIGER-2M, which consists of four modules and is in operation at **ID01** (**Figure 155**). The mechanics of the EIGER-2M are based on an in-house design ensuring in-vacuum operation to permit the installation of the detector inside the small-angle X-ray scattering (SAXS) tube of ID01. A specific cooling system was developed and a special setup built to test and improve the vacuum compatibility of the detector down to $2\times10^{-5}$ mbar.

The detector control and readout is highly parallelised, requiring 16 Ethernet connections in the case of the 2M version. The detector data

are transmitted through eight 10 GbE links with an aggregated maximum data bandwidth of up to 80 Gb/s. To deal with such a high data bandwidth, a readout infrastructure was designed based on state-of-the-art fibre optic technology and high-performance Ethernet switches to connect the detector to the backend computers. Regarding software integration, the development of the online data-streaming pipeline was particularly critical and challenging, given the very high data throughput produced by the detectors. Low-latency CPU scheduling and programming techniques were necessary to successfully manage such high frame-rates and data volumes, while ensuring data integrity and control software reliability. Based on the control and data acquisition software library from PSI, a LIMA plugin has been developed to read the data from the detector and to perform image composition 'on-the-fly', including correction of the images for inter-module gaps and, when necessary, expanding the image data from 4 to 8 bits for proper data alignment in the computer memory.

Before delivery to the beamlines, the detectors underwent a series of tests and calibration procedures in the 6–30 keV energy range, an assessment of their readout and noise performance, and a number of measurements in different experimental conditions and storage ring filling modes were taken to account and correct for photon pile-up effects.

After this work, the EIGER-500k detector operated at its maximum capacity, as summarised in **Table 1**. Operation at 22 kHz, which is a record for such type of detectors, has shown to be extremely useful in experiments such as X-ray photon correlation spectroscopy (XPCS), for which this device has enabled an increase in contrast by a factor of three and in time resolution by a factor of 25 compared to previous detectors **[4]**. Despite these results, work is not fully finished as limitations in the processing power of the beamline computers still prevent the use of the EIGER-2M detector at full capacity. The next stage of the project will focus on overcoming the current limitations with further software optimisations as well as by improving the performance of the computers and the data storage systems.

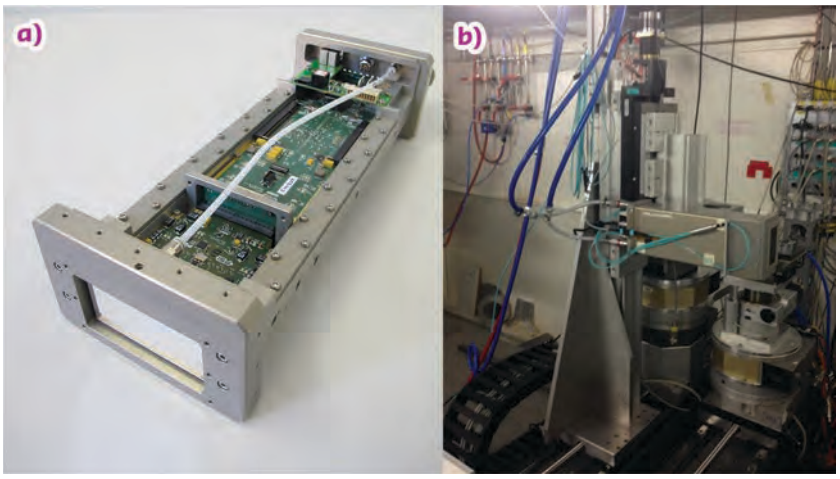


**Fig. 154: a)** EIGER-500k and **b)** test setup at **BM05**.

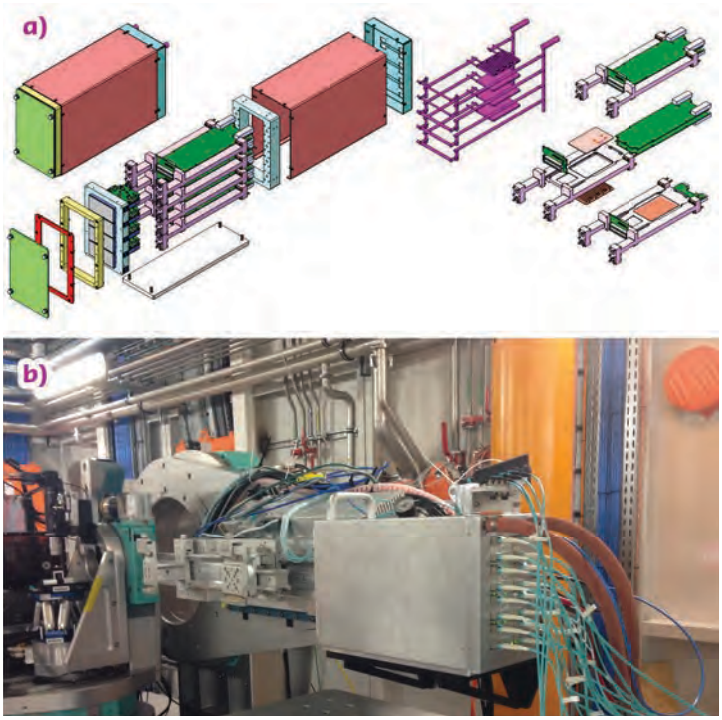


**Fig. 155: a)** EIGER-2M mechanical design and **b)** installation on ID01.

| Counter depth (bits) | Achieved frame rate (kHz) | Maximum number of images stored |
|---|---|---|
| 4 | 22 | 30 000 |
| 8 | 11 | 15 000 |
| 16 | 6 | 7500 |
| 32 | 0.3 | 3750 |

**Table 1:** Achieved performance in burst mode for the EIGER-500k.

AUTHORS

P. A. Douissard, M. Kocsis, A. Homs-Puron, R. Homs-Regojo, F. Calvelo and P. Fajardo. *ESRF*
B. Schmitt, G. Tinti, E. Froejd, M. Brueckner and D. Thattil. *PSI (Switzerland)*

REFERENCES

[1] R. Dinapoli *et al., Nucl. Instrum. Methods Phys. Res.* A **605**, 1 (2011).
[2] G. Tinti *et al., J. Instrum*. **10**, 3, (2015).
[3] https://www.dectris.com/products/eiger/overview
[4] T. Zinn *et al., J. Synchrotron Radiat*. **25**, 6 (2018).

# COHERENT MODES FOR SYNCHROTRON LIGHT

**EBS will increase the coherent fraction of the ESRF's synchrotron light. This coherence needs to be preserved all the way to the sample. Therefore, better optics and a better understanding of the coherence and its propagation in a beamline are needed. COherent Modes for SYnchrotron Light (COMSYL) is a new software package developed at the ESRF that uses advanced numerical methods to calculate the coherence.**

There are several ways to describe the coherence characteristics of a beam. Complicated functions like the mutual coherence function and the cross-spectral density (CSD) describe the correlation of the electric field in two spatial points. The concept of 'coherent fraction' represents the coherence of the beam using a number that is zero for an incoherent beam and one for a fully coherent beam. EBS will improve the coherent fraction by roughly two orders of magnitude with respect to the current ESRF storage ring.

The coherent fraction of a light beam can be estimated by simple approximation (the ratio of the diffraction-limited source over the phase-space volume of the source), but accurate values are derived from the theory of partial coherent optics. It is important to evaluate how the different optical elements of the beamline will preserve or degrade the coherent functions along the beamline.

The CSD completely describes the coherence of a beam. At a given plane distant $z$ from the source point, for a photon frequency $\omega$, the CSD is a 4-dimensional function that measures the correlation of the electric field between two points $(x_1,y_1)$ and $(x_2,y_2)$ in a plane. The computer resources to calculate, store and propagate the CSD are at the limit of present capabilities. For example, sampling the plane by $10^3$ pixels in each direction, the CSD will contain $(10^3)^4 = 10^{12}$ complex numbers (16 bytes), thus of the order of a few terabytes. The propagation of the CSD will require the calculation of the same number of 4D integrals. A solution to this problem is to expand the CSD in coherent modes.

This allows the representation of the 4D function as a sum of 2D functions: $CSD(x_1,y_1, x_2,y_2) = \Sigma\ \lambda_i\ \phi_i^*(x_1,y_1)\ \phi_i(x_2,y_2)$. If the sum is converging fast, only a limited number of modes contribute to the final CSD. This is expected for beams with relatively high coherence, such as those that will be produced by EBS. The coherent modes $\phi_i$ and the eigenvalues $\lambda_i$ are obtained by solving numerically the associated Fredholm equation $A_w[\phi_i] = \lambda_i\ \phi_i$, where $A_w$ is an integral operator with the CSD as a kernel. The coherent modes $\phi_i$ (typically images of megapixels) are obtained using iterative methods for diagonalising the associated matrix.

**Figure 156** shows the comparison of the cumulated occupation of the coherent modes spectrum for a U18 undulator tuned at 8 keV, computed for both the current ESRF and future EBS storage rings. For EBS, a few hundred modes are enough to recover most of the intensity. However, for the ESRF, the increase is much slower, thus the number of modes required for the same amount of total intensity is more than a thousand. The occupation of the first coherent mode is, by definition, the coherent fraction: 7% for EBS and about 0.2% for ESRF, *i.e.* a factor of 35 improvement!

A coherent fraction of 7% at the source level means that for an optimal coherent experiment one should remove 93% of the photons: the 'incoherent' ones. This is the role of the beamline. The beamline elements may modify the different modes in a different manner. The first coherent mode is always centred on-axis and the subsequent ones expand in space. Thus, a slit placed at a point where the beam is focused will remove intensity from the high modes, increasing

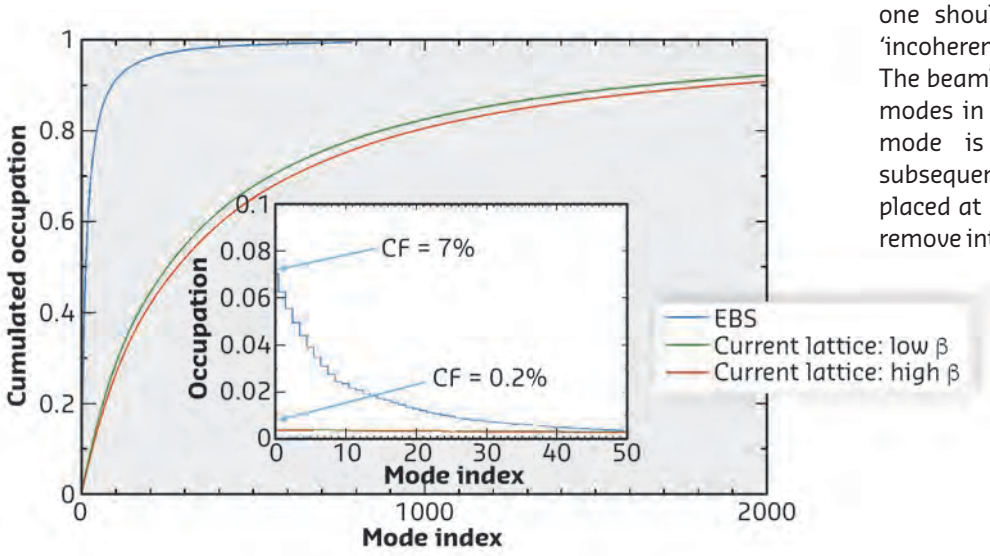


**Fig. 156:** Cumulated occupation of the coherent modes for the 2-m-long ESRF U18 undulator at its first harmonic (8 keV) for the new ESRF-EBS lattice and for the current ESRF lattice (high and low beta sections). The inset shows details of the occupation of the first modes and coherent fraction.

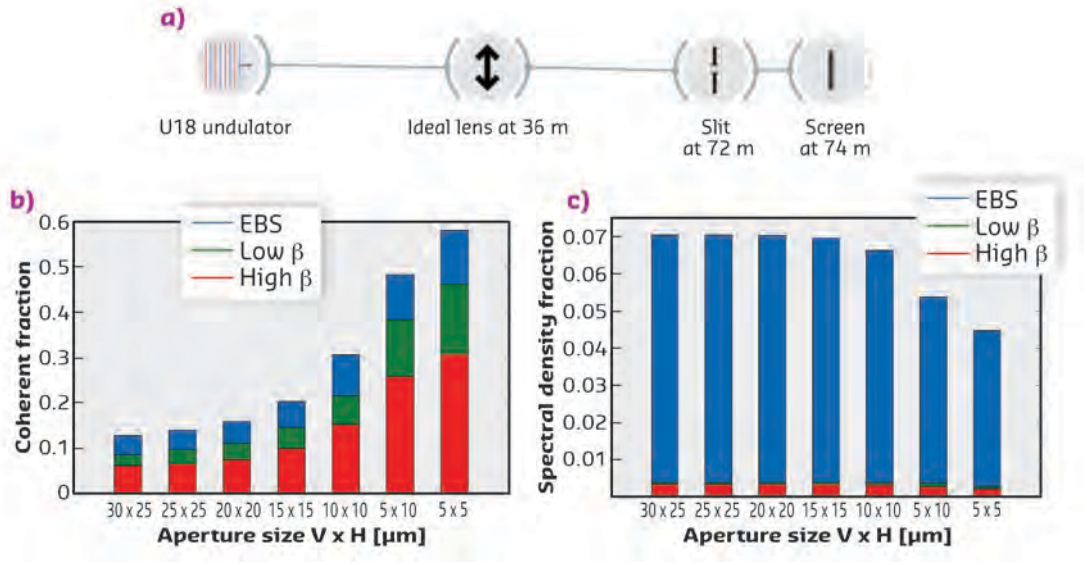


**Fig. 157: a)** Schematic view of a 1:1 imaging beamline. **b)** Coherent fraction of the beam after passing through a slit with different apertures. **c)** The fraction of transmitted intensity for the different slit apertures.

the occupation of the first one. **Figure 157** shows a simplified beamline with a focusing element that makes a one-to-one image of the source in the slit plane. The beam, cropped by the slit, is then propagated to a detector plane. The results shown quantify precisely the effect of the slit, which increases coherence with an unavoidable reduction of intensity. For EBS, the 5 x 5 µm slit raises the coherent fraction from 7% (at the source) to 58% after the slit, but the transmitted intensity is 4%. For a slit 25 x 25 µm, the coherent fraction is 14% and the intensity transmission 7%.

These calculations were performed at the ESRF NICE cluster. The calculation time depends on the size of the electron beam and the estimated number of modes. It can go from several hours to several days in several nodes, allocating up to few hundred gigabytes.

PRINCIPAL PUBLICATION AND AUTHORS

Coherent modes of X-ray beams emitted by undulators in new storage rings, M. Glass (a) and M. Sanchez del Rio (a), *EPL* **119**, 34004 (2017); doi: 10.1209/0295-5075/119/34004.
*(a) ESRF*

# SIL(E)X: THE COMMON ANCESTOR OF NEW SOFTWARE DEVELOPMENTS

**As part of its ambitious data analysis and management policy, the ESRF has developed a new software development toolkit in order to simplify the development and maintenance of scientific applications. Besides new applications, existing ESRF applications can also base their graphical user interfaces on this library in order to reduce and share maintenance efforts.**

In 2015, the ESRF realised that with the expected increase in data volumes and complexity that would be generated by EBS, and without any action, the already identified data-analysis bottleneck could only get narrower. Data management was therefore designated as a key priority and it was decided to start a long-term program to provide the appropriate infrastructure to tackle these challenges. Among other deliverables, the strategy foresees a common software development toolkit: a library of common software routines for analysing data from synchrotron sources and on which to base scientific software developments.

The Sclentific Library for eXperimentalists (silx) **[1, 2]** aims at providing the solid foundations on which scientific applications can be built. It derives its name and logo from the archaic name of flint, silex, a stone used as basis to build tools in prehistoric times, and as a nod to its toolkit function. In order to achieve its goal, modern software development practices have been followed. Started in 2016, silx is now at its ninth official release and is setting ESRF standards about how sustainable software should be developed: open source, public repository, code review, continuous integration, continuous documentation and user training.

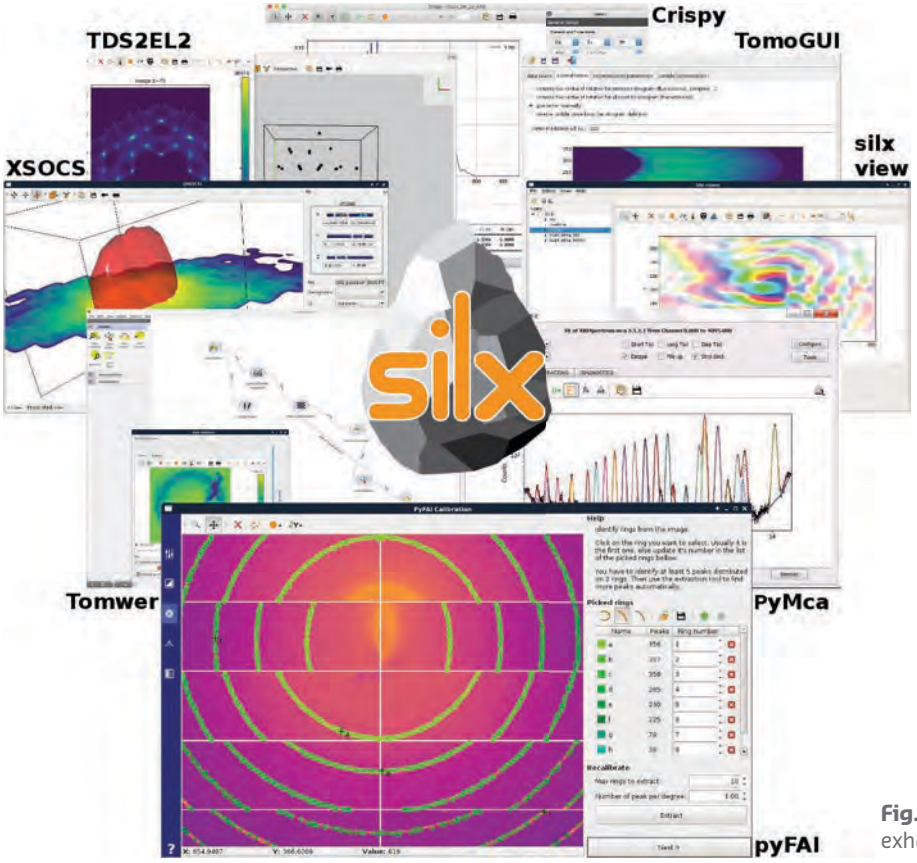


New code can only be added to the library if the functionality is described, it is accompanied by tests that can be run automatically and it has been reviewed by someone other than the developer(s). Today, the library contains about 110 000 lines of code and more than 1600 tests.

Silx has been developed by a team of software engineers and scientific software developers. Among other features, silx provides a common interface to access the data programmatically and graphically, widgets, data-visualisation tools (from 1D to 4D), efficient mathematic algorithms and a viewer. The list of applications using silx is growing: Crispy, Flint, Oasys, pyFAI, PyMca, PyNX, TDS2EL2, TomoGUI, Tomwer, XSOCS and XRStools, to name but a few (**Figure 158**). In the future, the library is expected to evolve according to the needs of the growing list of users and applications using it.

**Fig. 158:** Silx logo and screenshots of a non-exhaustive list of applications using it.

PRINCIPAL PUBLICATION AND AUTHORS

Data Analysis Unit, *ESRF*

REFERENCES

[1] http://www.silx.org
[2] http://github.com/silx-kit

# CRISPY: AN INTUITIVE INTERFACE FOR THEORETICAL SPECTROSCOPY

**A modern graphical user interface has been developed to perform theoretical calculations for inner-shell spectroscopies and ground state properties within the ligand field multiplet framework. Thanks to its usability, it has been widely adopted over the past year.**

Core-level spectroscopy is an element-selective probe of oxidation state, geometrical structure, and chemical bonding around the absorbing atom. The most common techniques, photoelectron and absorption spectroscopy, are used by many researchers for standard sample characterisation. The ESRF has, in recent years, made significant progress in the development of photon-in/photon-out spectroscopy (resonant inelastic X-ray scattering, X-ray emission spectroscopy), where the scattered X-rays are also analysed.

Experimental spectroscopy data are often evaluated by comparison to reference compounds. Theoretical spectroscopy provides deeper insight by maximising the amount of information that can be extracted from the experiments. The theoretical approaches can be broadly divided into two categories, depending on the strength of intra-atomic electron–electron interactions that, when dominant, can give rise to a large number of transitions. In this case, codes based on atomic multiplet theory have given good results. Conversely, density functional-based methods have been successfully applied

to model the experimental results when intra-atomic interactions are less important.

Multiplet-based approaches have historically relied on parametrised models using empirical values, a limitation imposed, in part, by the reduced computational resources at the time they were developed. They evolved from purely atomic models to models that include crystal field contributions (crystal field multiplets), or the interactions of the absorbing site and the surrounding atoms (ligand field or charge transfer multiplets). While recent developments allow for multiplet calculations to be performed using *ab initio* models, the use of semi-empirical or parametrised models can provide – in most cases – similar insight at a significantly reduced computational cost.

The computer programs for semi-empirical multiplet calculations were first developed in the early 1980s by Robert Cowan to calculate the electronic structure of atoms. They were subsequently extended by Theo Thole and others to also include the crystal field effects and hybridisation. Despite their success in calculating the core-level spectra of transition metals, lanthanides, and actinides, the complex user experience has limited their adoption by non-specialists. It was only later that the accessibility was significantly improved by packaging these ageing, but very useful, codes in graphical user interfaces (GUI). Another limitation was the difficulty in implementing new features and algorithms in the existing codebase. To address this second issue, entirely new software had to be developed. Using different theoretical foundations, Quanty **[1]** was developed by Maurits Haverkort to allow increased flexibility in the type of problem that a user can treat. Quanty is easier to use compared to the earlier codes and comes with extensive documentation. However, because it is a library of tools, the user has to write computer code to perform spectroscopy calculations, and therefore a rather steep learning curve remains that may require a significant time investment from users.

It is in this context that Crispy **[2]** was developed. The goal of the project was to provide an intuitive GUI to calculate the experiments performed on spectroscopy beamlines using semi-empirical multiplet models implemented in Quanty. Crispy was developed using the Python programming language and relies on a number of additional open-source scientific libraries that are part of the Python ecosystem. In particular, it uses the silx library developed at the ESRF for visualisation and for reading and writing data. Crispy runs an all major operating systems, has easy-to-use package installers for Windows and macOS, and, conforming with the ESRF's software policy, it is a free and open-source software.

The main window of the application is shown in **Figure 159**. With the current version, it is possible to calculate absorption (including circular and linear dichroism), photoemission, emission, and resonant inelastic scattering at different edges for transition metal ions, lanthanides, and actinides. Tutorials and extensive documentation on how to install and use the application can be found on the official website.

In addition to the online documentation, a series of hands-on tutorials have been organised to present Crispy to the user community. These took place during onsite events (ESRF User Meeting and HERCULES European School) and during external workshops and schools. Following these tutorials, the adoption of the application significantly accelerated, as shown by the increasing number of downloads – more than 500 during last year alone. While Crispy was specifically developed with the experimental spectroscopist in mind, it is refreshing to see that its ease of use has made it the perfect tool to introduce university students to the theoretical aspects of X-ray spectroscopy.

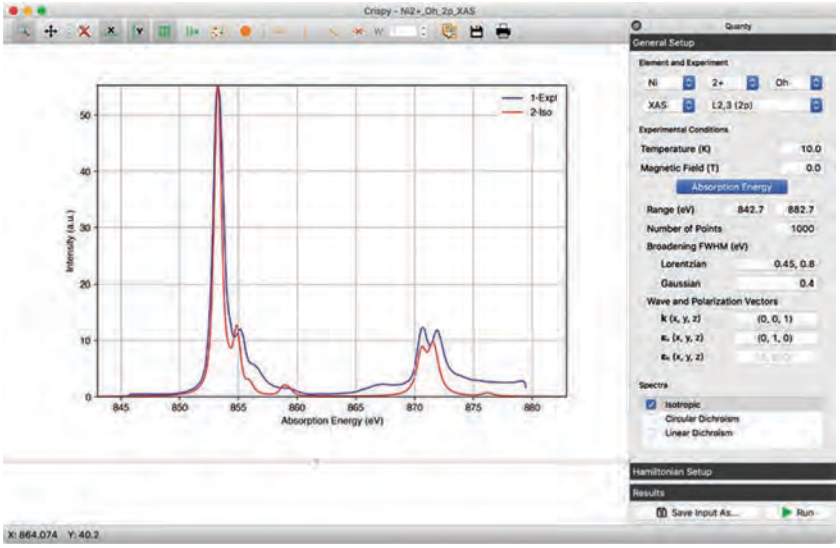


**Fig. 159:** The main window of the Crispy interface, showing the experimental and calculated X-ray absorption spectrum of NiO.

AUTHORS

M. Retegan and P. Glatzel. *ESRF*

REFERENCES

[1] http://www.quanty.org
[2] http://www.esrf.eu/computing/scientific/crispy

# ACCELERATOR AND SOURCE

The Accelerator and Source Division (ASD) is in charge of the production of synchrotron light from the ESRF's 6 GeV storage ring. Apart from operations, much of the division's activities in 2018 were focused on the Extremely Brilliant Source (EBS) project. Major progress was made in assembly, with the arrival of many more components onsite and the assembly of 12 to 16 new girders every month, as detailed in the *Status of the EBS* section of this report (**see page 8**). Despite the challenges faced by the increased workload of the project, the division has also continued to ensure excellent machine availability and reliability throughout 2018, including running maintenance campaigns, replacing ageing equipment and installing new diagnostics devices and a new timing system.

As a result of these efforts, the operation statistics for 2018 are very positive. A total of 5442 hours of beam was delivered out of 5527 scheduled hours, representing a very satisfactory availability of 98.47%. The Mean Time Between Failures (MTBF) was recorded at 104 hours. More information on the main parameters of the storage ring can be found on **page 168**.

The implementation of a new timing system took place during the machine-dedicated time (MDT) shifts in October 2018. The switchover went well and the system is working flawlessly. The operational applications for the operators and the Linac control have been updated to the new timing system. The addition of a feature that allows the distribution of a centralised RF-source frequency over the new White Rabbit network made it an ideal choice for replacing the existing timing distribution system. The aim is to provide improved flexibility and sub-nanosecond precision time-stamping through a dedicated optical fibre network.

An important project milestone was the construction and delivery of the EBS magnets, which was completed by the end of the year, with the reception of the last-awaited DQ2 magnets at the beginning of October 2018.

Regarding the assembly phase, great progress was made thanks to a successful partnership with colleagues from the Budker Institute of Nuclear Physics (BINP) in Novosibirsk, Russia. This allowed the two institutes to pool their knowledge and resources to work together to keep to the ambitious girder production schedule.

This year, major milestones have been met, and 2018's achievements would not have been possible without the dedication of ASD staff and the continuous support of the other ESRF divisions. I'd like to take this opportunity to thank all ESRF staff for their efforts in ensuring the successful completion of USM operation and the progress of the EBS project.

**P. RAIMONDI**

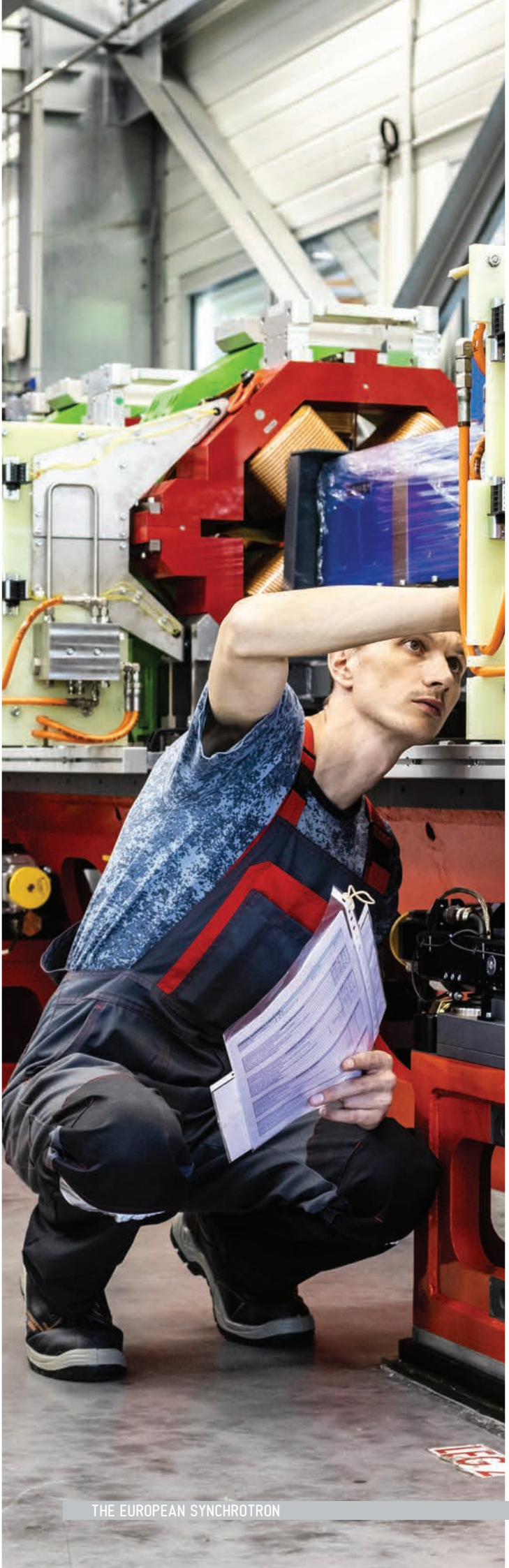

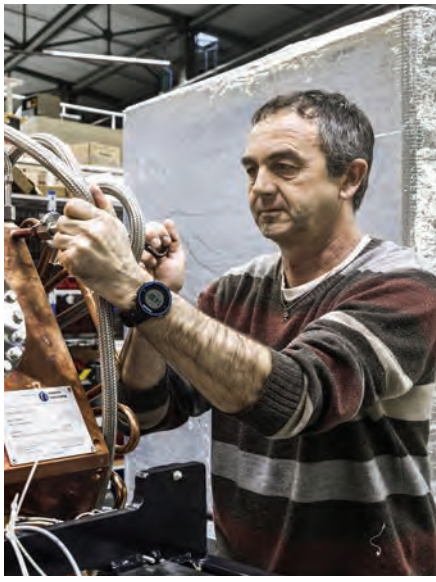

# SUMMARY OF ACCELERATOR OPERATION

Concerning the operation of the accelerators, 2018 represented not only the last year of X-ray delivery for the users with the present storage ring, but also a very intense period that brought many challenges in view of preparations for the Extremely Brilliant Source (EBS) project: maintaining high machine availability and beam quality, installing new equipment including a brand new timing system, and developing existing tools in perspective of EBS commissioning, such as diagnostics tools and beam dynamics simulation algorithms.

This last year of operation before EBS was indeed a success, with 5442 hours of beam delivered out of the 5527 that were scheduled. This represents an availability of 98.47%, compared with 98.28% in 2017. The number of failures was significantly lower in comparison to 2017, leading to a very good mean time between failures (MTBF) of 104 hours, compared to 65 hours in 2017. A summary of storage ring operation in 2018 is presented in **Table 2**.

One of the most notable operational achievements of 2018 is that, with the exception of the hybrid beam-filling mode, all of the other filling patterns have been delivered in top-up mode. This represents more than 11 000 refills over the year, highlighting once again the high level of reliability of the injector system, as well as the stability of the newly installed booster power supply system and the effectiveness of the beam cleaning process in the booster. Indeed, the booster beam-cleaning process, which is carried out in all relevant modes, avoids beam disturbances in the storage ring and therefore makes the refill process completely transparent to the users.

Another great achievement for operation occurred during the second run, when an all-time ESRF record was broken for continuous delivery – beam in 16-bunch top-up mode was successfully delivered for 13 days (*i.e.*, 312 hours) without the slightest hiccup (**Figure 160**).

As well as long periods without failures, some interruptions to the beam were experienced. The longest interruption occurred in August 2018, when a water hose was crushed between a vacuum vessel and the moving jaw of a permanent magnet. This resulted in the vacuum chamber becoming deformed into the path of the beam. Thanks to huge efforts by all the maintenance teams and experts who worked day and night, the intervention time (which included the replacement of a vacuum vessel, vacuum conditioning, alignment, removal and the re-installation of three insertion devices) lasted only 29 hours.

In addition to this, during the last three weeks of the year, the beam was delivered at a reduced intensity of 180 mA due to a leak in a radio frequency cavity that could not have been repaired during a short intervention.

| RUN NUMBER | 2018-01 | 2018-02 | 2018-03 | 2018-04 | 2018-05 | TOTAL 2018 |
|---|---|---|---|---|---|---|
| Start | 19/01/2018 | 23/03/2018 | 25/05/2018 | 17/08/2018 | 12/10/2018 | |
| End | 14/03/2018 | 16/05/2018 | 30/07/2018 | 08/10/2018 | 10/12/2018 | |
| Total number of shifts | 162 | 162 | 198 | 156 | 177 | **855** |
| Scheduled beam time (h) | 1003 | 1080 | 1294 | 1006 | 1144 | **5527** |
| Beam available w/o refill time (h) | 983.60 | 1073.30 | 1277.10 | 969.63 | 1126.88 | **5430.51** |
| Refill time (h) | 5.20 | 3.10 | 1.50 | 2.03 | 0 | **11.83** |
| Beam available including refill time (h) | 988.80 | 1076.40 | 1278.60 | 971.66 | 1126.88 | **5442.34** |
| **Availability** | **98.58%** | **99.67%** | **98.81%** | **96.59%** | **98.50%** | **98.47%** |
| Dead time for refills | 0.5% | 0.3% | 0.1% | 0.2% | 0% | **0.21%** |
| Dead time for failures | 1.4% | 0.3% | 1.2% | 3.4% | 1.5% | **1.53%** |
| Average intensity (mA) | 151 | 140 | 198 | 101 | 192 | **159.4** |
| Number of failures | 13 | 5 | 12 | 8 | 15 | **53** |
| **Mean time between failures (h)** | 77.2 | 216 | 107.8 | 125.8 | 76.3 | **104.3** |
| Mean duration of a failure (h) | 1.1 | 0.7 | 1.3 | 4.3 | 1.1 | **1.60** |

**Table 2:** Overview of storage ring operation in 2018.

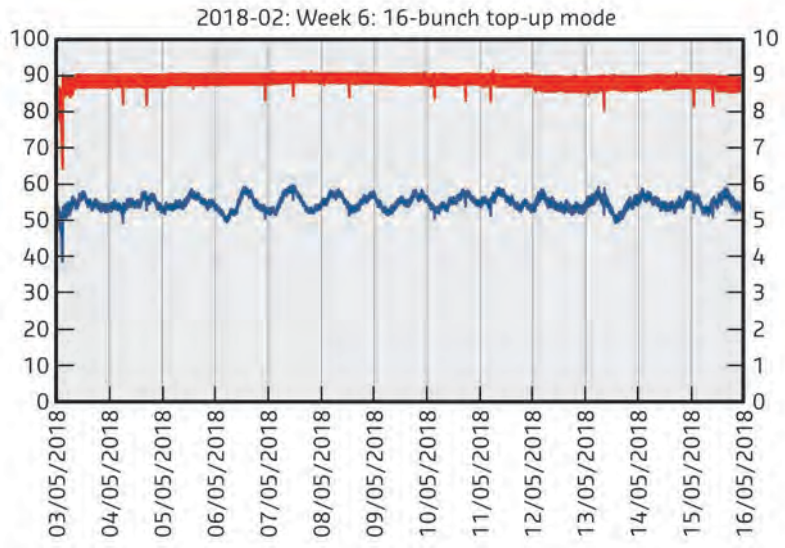


**Fig. 160:** Graph showing 13 days of delivery in 16-bunch top-up mode without a single failure.

# FILLING MODES AND TOP-UP

As shown in **Figure 161**, the distribution of the modes did not change significantly compared to 2017, with a large preference for the 7/8+1 filling pattern. The major change, as mentioned above, was the progressive introduction of the top-up mode for all of the filling patterns, including the cleaning in the booster, when relevant (**Figures 162** and **163**).

The beneficial side effect of these top-ups was the increase in the average intensity. In uniform filling mode, the average intensity with two refills per day was 176 mA. With top-up, this has reached an intensity of 197 mA with one refill every hour. Similarly, in 7/8+1 filling mode, the average intensity has increased from 175 mA to 201 mA, with one refill every 20 minutes. The most spectacular increase concerns the 4*8 mA filling mode, for which the average intensity with top-up has increased from 3.5 mA to 6.8 mA, *i.e.*, an increase of almost a factor two.

During delivery in top-up mode, the vertical emittance was permanently regulated in order to remain below 10 pm rad, as shown in **Figure 164**.

Finally, during the last few weeks of the year, an algorithm was developed to standardise the filling patterns. It consists of measuring the current in every electron bunch in order to refill, by priority, the least-filled bunches with the required intensity. When applied for a few hours, this algorithm leads to a very homogeneous filling pattern, which could be very important for experiments using particular bunches of the 16-bunch or the 4*10 mA filling patterns.

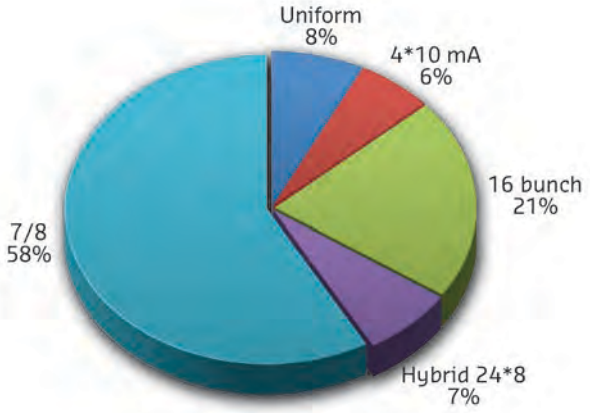


**Fig. 161:** Distribution of the filling modes in 2018.


**Fig. 162:** Uniform filling in top-up mode started in April 2018.


**Fig. 163:** 7/8 + 1 filling in top-up mode started in June 2018.

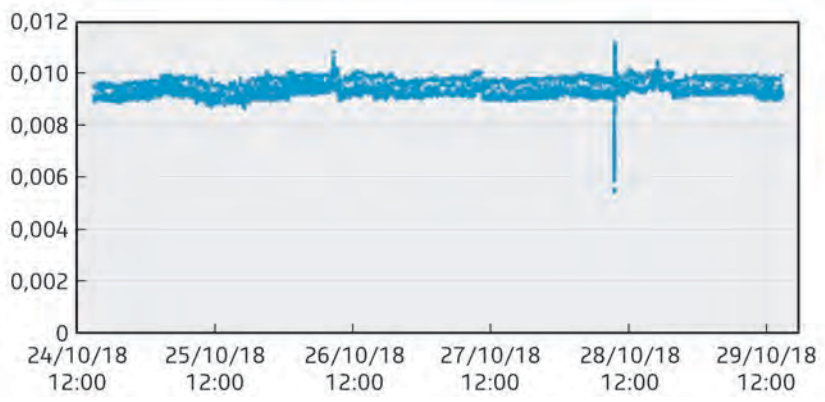


**Fig. 164:** Vertical emittance is regulated below 10 pm rad during top-up deliveries.

# APPENDIX 1: BEAM PARAMETERS OF THE STORAGE RING

**Table 3** presents a summary of the characteristics of the storage ring electron beam in optimal conditions.

| | | |
|---|---|---|
| Energy | [GeV] | 6.04 |
| Maximum current | [mA] | 200 |
| Horizontal emittance | [nm] | 4 |
| Vertical emittance | [pm] | 4 |
| Revolution frequency | [kHz] | 355 |
| Number of bunches | | 1 to 992 |
| Time between bunches | [ns] | 2.82 to 2816 |

**Table 3:** Principal characteristics of the electron beam.

**Table 4** gives the main optic functions, electron beam sizes and divergences at various source points. For insertion device source points, the beta functions, dispersion, sizes and divergences are calculated in the middle of the straight section. For bending magnets, two representative source points have been selected for each type of magnet (even or odd cell number), corresponding to magnetic fields of 0.4 T and 0.85 T. These points differ by the observation angles, of respectively 3 and 9 mrad from the entrance of the magnet.

Electron beam profiles are Gaussian and the size and divergence are presented in terms of rms values. The associated full width at half maximum sizes and divergences are 2.35 times higher. Horizontal electron beam sizes and divergences are given for the multibunch filling modes and apply to almost all filling patterns, except when the current per bunch is larger than 4.5 mA, for which a slightly larger size and divergence are attained because of the increased energy spread of the electron beam.

Vertical electron beam sizes and divergences are given for a vertical emittance of 4 pm, which is now the optimal condition for 2 x 1/3 and 7/8+1 filling modes. The vertical sizes and divergences are about 1.4 times larger in uniform filling mode (due to ion effects, which are partially corrected by the use of a vertical bunch-by-bunch feedback).

The lifetime, bunch length and energy spread mainly depend on the filling pattern. These are given in **Table 5** for a few representative patterns. Note that in 16-bunch and 4-bunch filling patterns, the energy spread and bunch length decay with the current (the value indicated in the table corresponds to the maximum current). The bunch lengths are given for the usual radiofrequency accelerating voltage of 9 MV (8 MV for 16-bunch and 4-bunch).

| | | Even ID (ID2, ID6...) | Odd ID (ID1, ID3...) | Even BM (ID2, ID6...) 3 mrad | Even BM (ID2, ID6...) 9 mrad | Odd BM (ID1, ID3...) 3 mrad | Odd BM (ID1, ID3...) 9 mrad |
|---|---|---|---|---|---|---|---|
| Magnetic field | [T] | Variable | Variable | 0.4 | 0.85 | 0.4 | 0.85 |
| Horiz. Beta function | [m] | 37.6 | 0.35 | 1.33 | 1.06 | 2.12 | 1.61 |
| Horiz. Dispersion | [m] | 0.134 | 0.031 | 0.062 | 0.051 | 0.089 | 0.075 |
| Horiz. rms e- beam size | [µm] | 413 | 50 | 99 | 85 | 132 | 113 |
| Horiz. rms e- divergence | [µrad] | 10 | 107 | 116 | 114 | 104 | 99 |
| Vert. Beta function | [m] | 2.95 | 2.97 | 41.7 | 42 | 32.1 | 32.2 |
| Vert. rms e- beam size | [µm] | 3.4 | 3.4 | 12.9 | 13 | 11.3 | 11.4 |
| Vert. rms e- divergence | [µrad] | 1.17 | 1.16 | 0.50 | 0.50 | 0.36 | 0.36 |

**Table 4:** Beta functions, dispersion, rms beam size and divergence at the various source points.

| Filling pattern | | Uniform | 7/8 + 1 | Hybrid | 16-bunch | 4-bunch |
|---|---|---|---|---|---|---|
| Number of bunches | | 992 | 870+1 | 24x8+1 | 16 | 4 |
| Maximum current | [mA] | 200 | 200 | 200 | 90 | 40 |
| Lifetime | [h] | 50 | 45 | 30 | 6 | 6 |
| Rms energy spread | [%] | 0.11 | 0.11 | 0.11 | 0.12 | 0.16 |
| Rms bunch length | [ps] | 20 | 20 | 25 | 48 | 55 |

**Table 5:** Current, lifetime, bunch length and energy spread for a selection of filling modes.

# FACTS AND FIGURES

## MEMBERS AND ASSOCIATE COUNTRIES

(AS OF JANUARY 2019)

### MEMBER COUNTRIES:

| | |
|---|---|
| 27.5% | France |
| 24% | Germany |
| 13.2% | Italy |
| 10.5% | United Kingdom |
| 6% | Russia |
| 5.8% | Benesync (Belgium, The Netherlands) |
| 5% | Nordsync (Denmark, Finland, Norway, Sweden) |
| 4% | Spain |
| 4% | Switzerland |

### ASSOCIATE COUNTRIES:

| | |
|---|---|
| 1.75% | Israel |
| 1.75% | Austria |
| 1.05% | Centralsync (Czech Republic, Hungary, Slovakia) |
| 1% | Poland |
| 1% | Portugal |
| 0.66% | India |
| 0.3% | South Africa |

## THE BEAMLINES

Details of the public ESRF beamlines as well as those operated by Collaborating Research Groups (CRG) are given in **Tables 6** and **7**. **Figure 165** shows the location of the beamlines in the experimental halls.

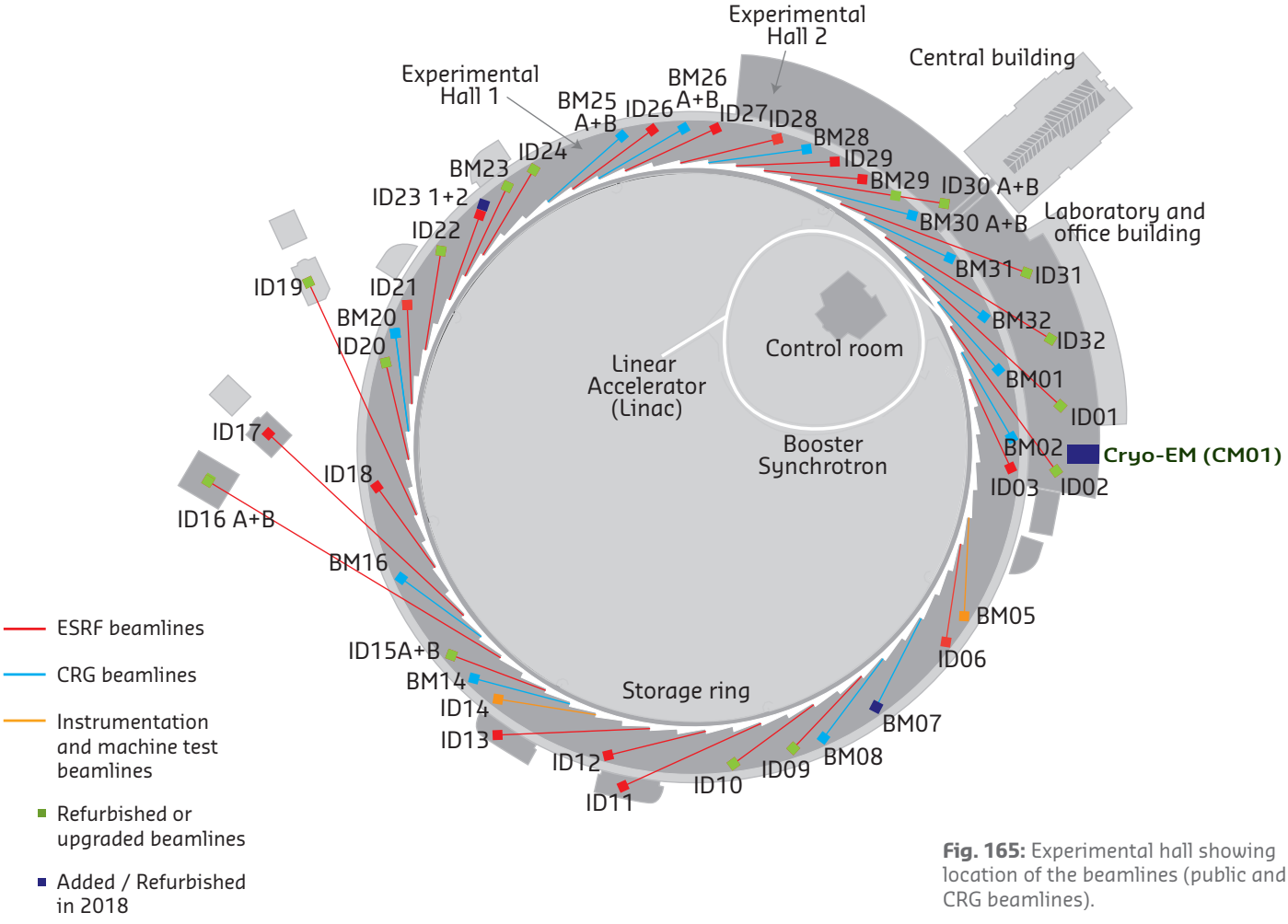


**Fig. 165:** Experimental hall showing location of the beamlines (public and CRG beamlines).

| SOURCE POSITION | NUMBER OF INDEPENDENT END-STATIONS | BEAMLINE NAME | STATUS | |
|---|---|---|---|---|
| ID01 | 1 | Microdiffraction imaging | Operational | since 12/14 |
| ID02 | 1 | Time-resolved ultra-small-angle X-ray scattering | Operational | since 07/14 |
| ID03 | 1 | Surface diffraction | Operational | since 09/94 |
| ID06 | 0.4 | Large volume press | Operational | since 10/13 |
| ID09 | 1 | Time-resolved structural dynamics | Operational | since 09/94 |
| ID10 | 1 | Soft interfaces and coherent scattering | Operational | since 06/12 |
| ID11 | 1 | Materials science | Operational | since 09/94 |
| ID12 | 1 | Polarisation-dependent X-ray spectroscopy | Operational | since 01/95 |
| ID13 | 1 | Microfocus | Operational | since 09/94 |
| ID15A | 0.85 | Materials chemistry and engineering | Operational | since 11/16 |
| ID15B | 0.75 | High-pressure diffraction | Operational | since 11/16 |
| ID16A | 1 | Nano-imaging | Operational | since 05/14 |
| ID16B | 1 | Nano-analysis | Operational | since 04/14 |
| ID17 | 1 | Medical | Operational | since 05/97 |
| ID18 | 1 | Nuclear scattering | Operational | since 01/96 |
| ID19 | 1 | Microtomography | Operational | since 06/96 |
| ID20 | 1 | Inelastic X-ray scattering | Operational | since 06/13 |
| ID21 | 1 | X-ray microscopy / IR spectroscopy | Operational | since 12/97 |
| ID22 | 1 | High resolution powder diffraction | Operational | since 05/14 |
| ID23 | 2 | Macromolecular crystallography MAD | Operational | since 06/04 |
| | | Macromolecular crystallography microfocus | Operational | since 09/05 |
| ID24 | 1 | Dispersive EXAFS | Operational | since 02/96 |
| ID26 | 1 | X-ray absorption and emission | Operational | since 11/97 |
| ID27 | 1 | High pressure | Operational | since 02/05 |
| ID28 | 1 | X-ray scattering II | Operational | since 12/98 |
| ID29 | 1 | Multiwavelength anomalous diffraction | Operational | since 01/00 |
| ID30A | 2 | Macromolecular crystallography | Operational | since 07/14 |
| ID30B | 1 | Macromolecular crystallography | Operational | since 04/15 |
| ID31 | 1 | Interfaces and materials processing | Operational | since 11/15 |
| ID32 | 1 | Soft X-ray spectroscopy | Operational | since 11/14 |
| BM23 | 1 | X-ray absorption spectroscopy | Operational | since 03/11 |
| BM29 | 1 | Bio SAXS | Operational | since 06/12 |
| CM01 | 1 | Cryo-EM | Operational | since 11/17 |

**Table 6:** List of the ESRF public beamlines.

| SOURCE POSITION | NUMBER OF INDEPENDENT END-STATIONS | BEAMLINE NAME | FIELD OF RESEARCH | STATUS |
|---|---|---|---|---|
| BM01 | 1 | Swiss-Norwegian BL | X-ray diffraction | Operational since 01/95 |
| BM02 | 1 | D2AM (French) | Materials science | Operational since 09/94 |
| BM08 | 1 | LISA (Italian) | X-ray absorption spectroscopy | Operational since 09/94 |
| BM16 | 1 | FAME-UHD (French) | X-ray absorption spectroscopy | Operational since 02/17 |
| BM20 | 1 | ROBL (German) | Radiochemistry | Operational since 09/98 |
| BM25 | 2 | SPLINE (Spanish) | X-ray absorption and diffraction | Operational since 04/05 |
| BM26 | 2 | DUBBLE (Dutch/Belgian) | Small-angle scattering | Operational since 12/98 |
| | | | EXAFS | Operational since 06/01 |
| BM28 | 1 | XMaS (British) | Diffraction, scattering and spectroscopy | Operational since 04/98 |
| BM30 | 2 | FIP (French) | Protein crystallography | Operational since 02/99 |
| | | FAME (French) | X-ray absorption spectroscopy | Operational since 08/02 |
| BM31 | 1 | SNBL II (Swiss-Norwegian) | X-ray absorption and diffraction | Operational since 09/16 |
| BM32 | 1 | IF (French) | X-ray diffraction and Laue microdiffraction | Operational since 09/94 |
| Operational in 2018: | | | | |
| BM14 | 1 | DUBBLE (Dutch/Belgian) | EXAFS | Operational since 05/18 |

**Table 7:** List of the Collaborating Research Group beamlines.

# USER OPERATION

User operation with public beam time at the ESRF in 2018 saw intense activity, as users, proposal review committees and beamline staff alike maximised the use of the ESRF beam before the 10 December shutdown for the installation of the new Extremely Brilliant Source (EBS).

All beamlines were fully operational with the exceptions of the X-ray microscopy beamline ID21 (partially closed for major refurbishment), the ROBL (BM20) and XMaS (BM28) CRG beamlines (unavailable in the second half of the year for works required to be EBS-ready for 2020), and beamline BM14, which was commissioned at the end of 2018 as a new DUBBLE CRG beamline. The year saw the highest ever demand for beam time in terms of number of proposals submitted and number of shifts requested, and around 36% of proposals were awarded beam time in this exceptionally shorter operation year. **Figure 166** shows the number of applications for beam time received since 2011, and clearly demonstrates the unprecedented interest in the ESRF from the user community in the post-Phase I / pre-EBS era, as well as the record provision of beam time and reception of users by the ESRF to satisfy the needs of the community.

Proposals for experiments are selected, and beam time allocations are made, by 12 peer review committees, called Beam Time Allocation Panels (**page 175**). These panels, composed of specialists mostly from the ESRF member and associate countries, review proposals for a subset of beamlines. The scientific areas of ESRF research activities reviewed by the panels are shown in **Table 8**.

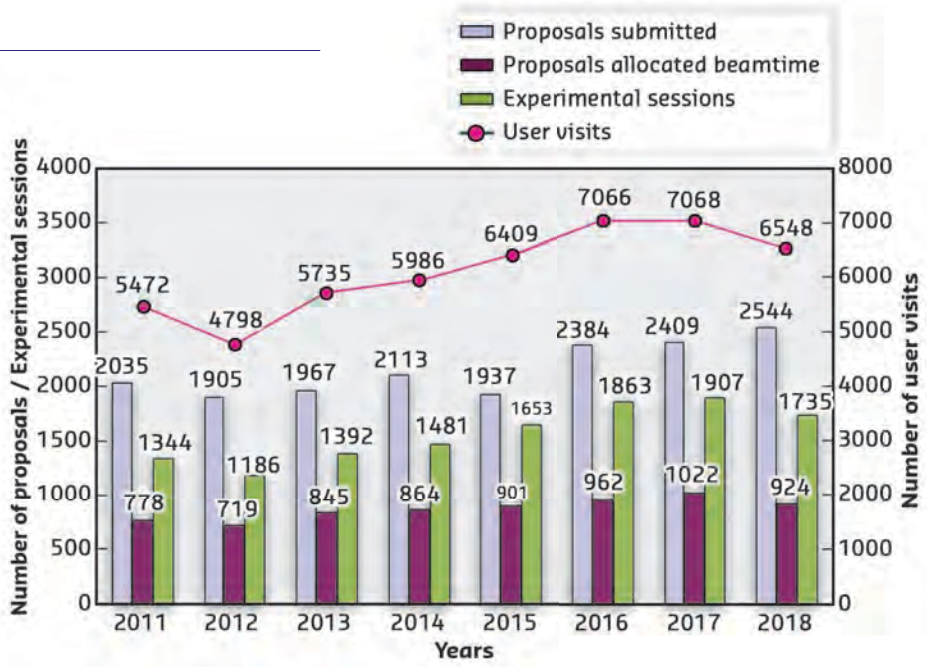


**Fig. 166:** Numbers of applications for beam time, experimental sessions and user visits, 2011 to 2018. 2018 figures for experimental sessions and user visits are up to 10 December 2018 (cryo-EM time delivered in early 2019 is not included).

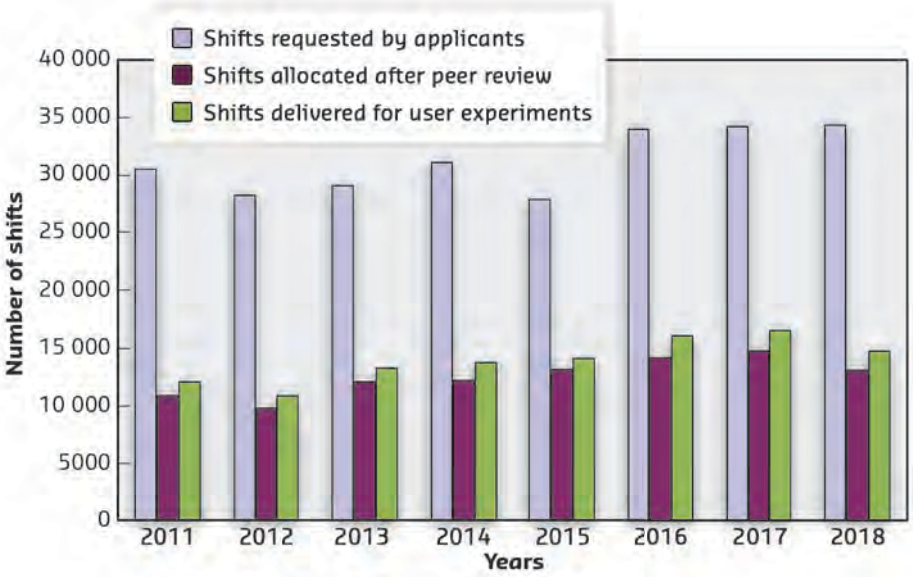


**Fig. 167:** Amount of beam time requested, allocated and delivered, 2011 to 2018. Beam time delivered for 2018 is up to the shutdown on 10 December and does not include the cryo-EM time delivered in early 2019.

**Table 8:** Shifts of beamtime requested and allocated for public user experiments, year 2018.

| Scientific field | Total shifts requested | Total shifts allocated |
|---|---|---|
| Chemistry | 5020 | 1525 |
| Earth Sciences | 2608 | 1029 |
| Environment | 981 | 280 |
| Hard Condensed Matter Science | 8450 | 2970 |
| Cultural Heritage | 240 | 75 |
| Life Sciences | 1782 | 741 |
| Applied Materials Science | 7065 | 1770 |
| Medicine | 1076 | 408 |
| Engineering | 425 | 66 |
| Methods & Instrumentation | 455 | 273 |
| Structural Biology | 3147 | 3056 |
| Soft Condensed Matter | 3082 | 924 |
| **Totals** | **34 331** | **13 117** |

The review committees met only once during this exceptional year, around six weeks after the deadline for submission of proposals (1 March 2018). There was no proposal submission deadline in September for beamtime in 2019 due to the EBS shutdown. The panels reviewed 2544 applications for beam time in 2018, an all-time record, and selected 924 (36.3%) in total. Requests for beam time, which is scheduled in shifts of eight hours, totalled 34 331 shifts and, of these, 13 117 shifts (38.2%) were allocated. The distribution of shifts requested and allocated by scientific area for 2018 is shown in **Table 8**, while the number of shifts requested, allocated and delivered per year since 2011 is shown in **Figure 167**.

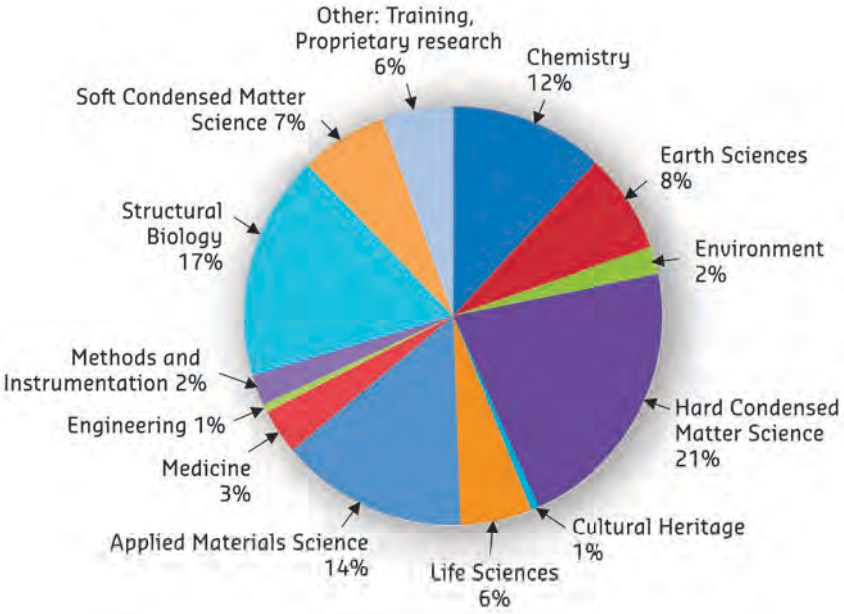


**Fig. 168:** Shifts delivered for experiments, 1 March to 10 December 2018, by scientific area, total 14 787.

The breakdown of shifts delivered for public experiments by scientific area up to 10 December 2018 is shown in **Figure 168**. These figures do not include time delivered on the cryo-EM in early 2019; final figures for operation year 2018, which ends on 1st March 2019, will include these additional shifts (72 further shifts currently allocated). The average duration of an experimental session in 2018 was eight shifts (just over three shifts for macromolecular crystallography (MX) experiments and just over 12 shifts for non-MX experiments).

The annual number of experimental sessions and user visits since 2011 is shown in **Figure 166** (again the 2018 figures do not include the remaining cryo-EM time delivered in January and February 2019). Since 2018, the figure for user visits includes sample dewars sent by users, and paid for by the ESRF, for structural biology experiments. Groups using structural biology beam time can now choose to request reimbursement of either travel and subsistence for a user or transport costs for a dewar of samples. In 2018, 317 sample dewars were paid for by the ESRF in the place of user reimbursement.

During 2018, the ESRF passed the remarkable milestone of 32 000 publications resulting from data taken either wholly or partially at the ESRF, or including ESRF staff as authors, since the facility first opened its doors in 1994. Yearly publication output from the ESRF has been systematically at a level of over 1800 for many years now, as shown in **Figure 169**. At time of press, 1604 publications had already been registered for 2018, giving a total of 32 256 publications accepted in peer-reviewed journals. This figure will continue to evolve, with the final number for this year expected to surpass 1800. Of these, around 300 every year are published in high impact factor journals (IF > 7).

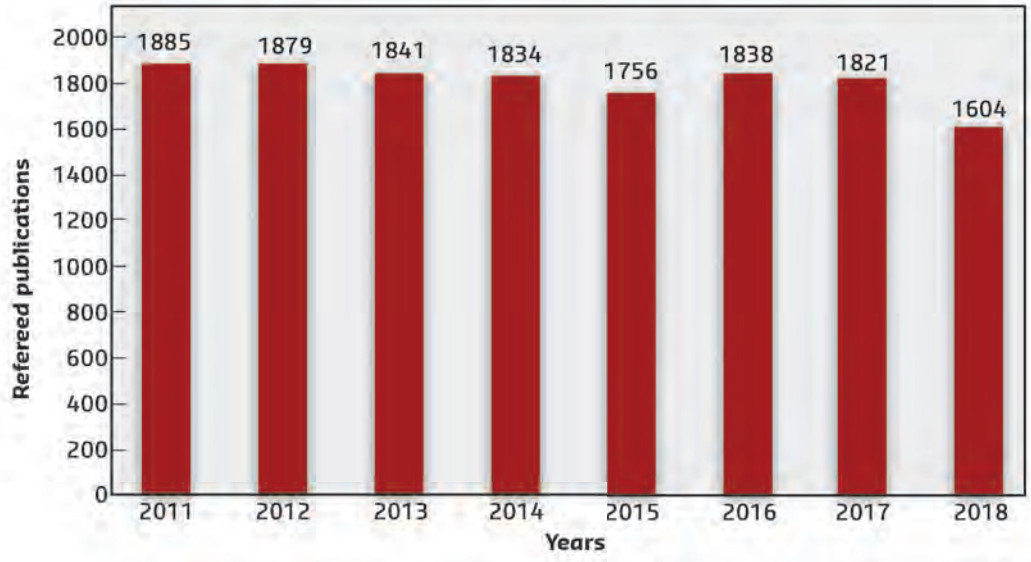


**Fig. 169:** Numbers of publications appearing in refereed journals reporting on data collected either partially or totally at the ESRF, 2011 to 2018. The number of publications for 2018 is not final at time of press.

# ADMINISTRATION AND FINANCE

The budget for 2018 includes additional contributions from Members and Scientific Associates of 11 242 kEUR dedicated to the ESRF-EBS Project. The ESRF-EBS expenditure budget amounts to a total of 41 857 kEUR including 6 053 kEUR of ESRF operating budget.

## Expenditure and income 2017

| Expenditure | | kEuro | Income | kEuro |
|---|---|---|---|---|
| Accelerator and Source | | | 2017 Members' contributions | 92 903,9 |
| Personnel | | 7 287,5 | Funds carried forward from 2016 | 4 852,0 |
| Recurrent | | 2 340,4 | Other income | |
| *Operating costs* | *2 103,6* | | Scientific Associates | 6 741,0 |
| *Other recurrent costs* | *236,8* | | Sale of beamtime | 2 146,9 |
| Capital | | 28 748,1 | Scientific collaboration and Special projects | 7 382,4 |
| *Accelerator and Source developments* | *28 748,1* | | Electricity overcosts brought to account | 514,0 |
| Beamlines, experiments and in-house research | | | Balance ESRF-EBS | 11 086,2 |
| Personnel | | 19 876,1 | Funds carried forward to 2018 | 907,0 |
| Recurrent | | 5 479,5 | | |
| *Operating costs* | *1 421,1* | | | |
| *Other Recurrent costs* | *4 058,4* | | | |
| Capital | | 10 317,6 | | |
| *Beamline developments* | *10 317,6* | | | |
| *Beamline refurbishment* | | | | |
| Technical and administrative supports | | | | |
| Personnel | | 31 976,9 | | |
| Recurrent | | 15 668,3 | | |
| Capital | | 3 932,1 | | |
| Unexpended committed funds | | | | |
| Funds carried forward to 2018 | | 907,0 | | |
| **Total** | | **126 533,4** | **Total** | **126 533,4** |

## Revised expenditure and income budget for 2018

| Expenditure | | kEuro | Income | kEuro |
|---|---|---|---|---|
| Accelerator and Source | | | 2018 Members' contributions | 94 820 |
| Personnel | | 7 148 | Funds carried forward from 2017 | 907 |
| Recurrent | | 3 843 | Other income | |
| *Operating costs* | *3 703* | | Scientific Associates | 7 653 |
| *Other recurrent costs* | *140* | | Income from industrial co.activity | 2 230 |
| Capital | | 34 070 | Scientific collaboration and Special projects | 7 272 |
| *Accelerator and Source developments* | *34 070* | | Balance ESRF-EBS | 21 818 |
| Beamlines, experiments and in-house research | | | | |
| Personnel | | 20 560 | | |
| Recurrent | | 5 819 | | |
| *Operating costs* | *1 680* | | | |
| *Other Recurrent costs* | *4 139* | | | |
| Capital | | 9 191 | | |
| *Beamline developments* | *9 191* | | | |
| Technical and administrative supports | | | | |
| Personnel | | 32 657 | | |
| Recurrent | | 14 641 | | |
| Capital | | 6 771 | | |
| **Total** | | **134 700** | **Total** | **134 700** |

## Expenditure 2017 by nature of expenditure

| | kEuro |
|---|---|
| **PERSONNEL** | |
| ESRF staff | 56 671,7 |
| External temporary staff | 16,5 |
| Other personnel costs | 2 452,3 |
| **RECURRENT** | |
| Consumables | 9 178,0 |
| Services | 11 611,2 |
| Other recurrent costs | 2 698,8 |
| **CAPITAL** | |
| Buildings, infrastructure | 914,9 |
| Lab. and Workshops | 1 506,3 |
| Accelator and Source incl. IDs and FEs | 28 748,1 |
| Beamlines, Experiments | 10 317,6 |
| Computing Infrastructure | 1 449,1 |
| Other Capital costs | 61,8 |
| Unexpended committed funds | |
| Funds carried forward to 2018 | 907,0 |
| **Total** | **126 533,4** |

## Revised budget for 2018 by nature of expenditure

| | kEuro |
|---|---|
| **PERSONNEL** | |
| ESRF staff | 57 748 |
| External temporary staff | 42 |
| Other personnel costs | 2 575 |
| **RECURRENT** | |
| Consumables | 9 098 |
| Services | 12 605 |
| Other recurrent costs | 2 600 |
| **CAPITAL** | |
| Buildings, infrastructure | 1 529 |
| Lab. and Workshops | 3 157 |
| Accelator and Source incl. IDs and FEs | 34 070 |
| Beamlines, Experiments | 9 191 |
| Computing Infrastructure | 1 985 |
| Other Capital costs | 100 |
| **Total** | **134 700** |

## 2018 manpower *(staff members present on 31/12/2018)*

| | Scientists, Engineers, Senior Administrators | Technicians and Administrative Staff | PhD Students | Total |
|---|---|---|---|---|
| **Staff on regular positions** | | | | |
| Accelerator and Source* | 36 | 40 | | 76 |
| Beamlines, instruments and experiments* | 225 | 95 | 19 | 339 |
| General technical services | 36 | 53 | | 89 |
| Directorate, administration and central services | 39 | 57 | | 96 |
| *Sub-total* | *336* | *245* | *19* | *600* |
| **Other positions** | | | | |
| Short term contracts | 25 | 19 | | 44 |
| Staff under “contrats de professionnalisation” | | 29 | | 29 |
| **Total** | **361** | **293** | **19** | **673** |
| *Scientific collaborators and consultants* | *9* | | | *9* |

** Including scientific staff on time limited contracts.*

# ORGANISATION CHART OF THE ESRF

(AS OF JANUARY 2019)

**Administrative and Finance Committee**
Chairperson: J. Pickett

**Council**
Chairperson:
M. Á. García Aranda
up to 3 delegates per Contracting Party

**Science Advisory Committee**
Chairperson: E. Weckert

**Machine Advisory Committee**
Chairperson: H.-H. Braun

**Director General**
F. Sette

**DG's Services:**
- Head of DG's Office/Secretary of Council: I. Echeverria
- Communication Group
- Internal Auditor
- Safety Group

## ACCELERATOR AND SOURCE
Director: P. Raimondi

- Beam dynamics and applications
- Power supplies
- Insertion devices
- Front-ends
- Radio frequency and linac
- Diagnostics
- Operation
- Secretariat

## ADMINISTRATION
Director: L-J. Sánchez Ortiz

- Personnel
- Finance
- Purchasing

- Joint ILL/ESRF
- Medical service

## EXPERIMENTS

Director: J. Susini

**Beamline groups:**
- Complex systems and biomedical sciences
- Structural biology
- X-ray nanoprobe

Director: H. Reichert

**Beamline groups:**
- Electronic structure, magnetism and dynamics
- Matter at extremes
- Structure of materials

**Scientific infrastructure**
- Theory group
- User office
- CRG liaison office
- Business Development Office
- Joint ILL/ESRF Library
- Secretariat

**Beam Time Allocation Panels**
- **C01** (ID01, ID03, BM25B, BM32) Chairperson: C. Lucas
- **C02** (ID11, ID15A, ID22, ID31) Chairperson: A. Abakumov
- **C03** (ID12, ID32) Chairperson: A. Severing
- **C04** (BM08, BM16, BM20, BM23, BM25A, BM26A, BM30B, BM31) Chairperson: J. Van Bokhoven
- **C05** (ID06-LVP, ID15B, ID27, BM01) Chairperson: P. Salmon
- **C06** (ID17, ID19) Chairperson: R. Cernik
- **C07** (ID16A, ID16B, ID21) Chairperson: F. Giannici
- **C08** (ID02, ID13, BM26B) Chairperson: A. Petukhov
- **C09** (ID09, ID10, BM02, BM28) Chairperson: A. Madsen
- **C10** (Structural Biology Beamlines) Chairperson: M. Degano
- **C11** (ID20, ID24, ID26) Chairperson: J. Rose
- **C12** (ID18, ID28) Chairperson: V. Giordano

## INSTRUMENTATION SERVICES AND DEVELOPMENT DIVISION
Head: M. Krisch

- Advanced analysis and modeling
- Detector and electronics
- Software
- X-ray optics
- Mechanical engineering

## TECHNICAL INFRASTRUCTURE DIVISION
Head: R. Dimper

- Management information systems and web
- Systems and communication
- Buildings and infrastructure
- EX2/CPER project team
- Survey and alignment
- Vacuum


**Cover**
Cover design by A. Moullec

**Photo credits:**
C. Argoud, E. Bouy, P. Jayet, @StefCandé and D. McBride.

## We gratefully acknowledge the help of:

C. Argoud, A. Bosak, J.F. Bouteille, B. Boulanger, N. Brookes, M. Capellas Espuny, J. Chavanne, D. Chenevier, K. Colvin, K. Clugnet, E. Dancer, M. Di Michiel, R. Dimper, I. Echeverría, A. Fitch, P. Gaget, S. Gerlier, P. Glatzel, L. Hardy, M. Hahn, V. Honkimäki, J. Jacob, E. Jean-Baptiste, M. Krisch, G. Le Bec, G. Leonard, E. Mitchell, A. Moullec, C. Mueller-Dieckmann, J. McCarthy, S. Pascarelli, P. Raimondi, H. Reichert, M. Retegan, J.L. Revol, S. Rio, B. Roche. A. Rogalev, E. Ryan, C. Sahle, K. Scheidt, T. Schülli, F. Sette, J. Susini, N. Theyencheri, Y. Watier, S. White, M. Wulff and all the users and staff who have contributed to this edition of the *Highlights*.

Editor
A. Joly
Layout
Pixel Project
Printing
Imprimerie du Pont de Claix



Communication Group
ESRF
CS 40 220
F38043 Grenoble Cedex 9 • France
Tel. +33 (0)4 76 88 20 56
Fax. +33 (0)4 76 88 25 42
http://www.esrf.eu